**Transactions of the ASME, Journal of Heat Transfer** (ISSN 0022-1481) is published monthly by The American Society of Mechanical Engineers, Three Park Avenue, New York, NY 10016. Periodicals postage paid at New York, NY and additional mailing offices. POSTMASTER: Send address changes to Transactions of the ASME, Journal of Heat Transfer, c/o THE AMERICAN SOCIETY OF MECHANICAL ENGINEERS, 22 Law Drive, Box 2300, Fairfield, NJ 07007-2300. **CHANGES OF ADDRESS** must be received at Society headquarters seven weeks before they are to be effective. Please send old label and new address. **STATEMENT from By-Laws.** The Society shall not be responsible for statements or opinions advanced in papers or ... printed in its publications (B7.1, Para. 3).


# Journal of Heat Transfer

**Published Monthly by ASME**

**VOLUME 131 • NUMBER 1 • JANUARY 2009 ( pp. 011301- 014504 )**

## RESEARCH PAPERS



(Contents continued on inside back cover)

This journal is printed on acid-free paper, which exceeds the ANSI Z39.48-1992 specification for permanence of paper and library materials. ♾™
♻ 85% recycled content, including 10% post-consumer fibers.

Journal of Heat Transfer Volume 131, Number 1 JANUARY 2009



The ASME Journal of Heat Transfer is abstracted and indexed in the following:

*Applied Science and Technology Index, Chemical Abstracts, Chemical Engineering and Biotechnology Abstracts (Electronic equivalent of Process and Chemical Engineering), Civil Engineering Abstracts, Compendex (The electronic equivalent of Engineering Index), Corrosion Abstracts, Current Contents, E & P Health, Safety, and Environment, Ei EncompassLit, Engineered Materials Abstracts, Engineering Index, Enviroline (The electronic equivalent of Environment Abstracts), Environment Abstracts, Environmental Engineering Abstracts, Environmental Science and Pollution Management, Fluidex, Fuel and Energy Abstracts, Index to Scientific Reviews, INSPEC, International Building Services Abstracts, Mechanical & Transportation Engineering Abstracts, Mechanical Engineering Abstracts, METADEX (The electronic equivalent of Metals Abstracts and Alloys Index), Petroleum Abstracts, Process and Chemical Engineering, Referativnyi Zhurnal, Science Citation Index, SciSearch (The electronic equivalent of Science Citation Index), Theoretical Chemical Engineering*

# Transient Method for Convective Heat Transfer Measurement With Lateral Conduction—Part I: Application to a Deposit-Roughened Gas Turbine Surface

**J. Bons**
Professor
Ohio State University,
2300 West Case Road,
Columbus, OH 43235

*The effect of lateral conduction on convective heat transfer measurements using a transient infrared technique over a rough surface is evaluated. The rough surface is a scaled model of gas turbine surface deposits. Comparisons are made between a full 3D finite volume analysis and a simpler 1D transient conduction model. The surface temperature history was measured with a high resolution infrared camera during an impulsively started hot gas flow over the rough test plate at a flow Reynolds number of 750,000. The boundary layer was turbulent with the peak roughness elements protruding just above the boundary layer momentum thickness. The 1D model underestimates the peak to valley variations in surface heat flux by up to a factor of 5 compared with the 3D model with lateral conduction. For the area-averaged surface heat flux, the 1D model predicts higher values than a 3D model for the same surface temperature history. This is due to the larger surface area of the roughness peaks and valleys in the 3D model, which produces a larger initial input of energy at the beginning of the transient. For engineering purposes, where the net heat load into the solid is desired, this lower 3D model result must be multiplied by the wetted-to-planform surface area ratio of the roughness panel. For the roughness model in this study, applying this correction results in a 25% increase in the area-averaged roughness-induced Stanton number augmentation for the 3D rough surface model compared with a flat 1D surface model at the same Reynolds number. Other shortcomings of the transient method for rough surface convective heat transfer measurement are identified.* [DOI: 10.1115/1.2976784]

*Keywords: transient heat transfer measurement, gas turbine roughness*

## Introduction/Background

The accurate measurement of convective heat transfer between a moving fluid and an adjacent solid is a subject of enduring engineering interest. Measurements are most commonly made in the steady-state mode, with either the surface temperature or surface heat flux prescribed while the other is measured to compute the local convective heat transfer coefficient $[h_c = q_s/(T_\infty - T_s)]$ at a given fluid temperature ($T_\infty$). Unfortunately, accurate steady-state measurements require careful accounting of conduction and radiative losses and often necessitate meticulously designed arrays of thin-foil surface heaters and associated "guard heaters" to approximate the prescribed wall boundary condition [1]. One option for avoiding some of these complicating factors is by employing the mass transfer analog through steady-state techniques such as naphthalene sublimation [2] and pressure sensitive paints [3], though these techniques require their own level of sophistication. Another option for accurate $h_c$ measurement is commonly referred to as the "transient" heat transfer method. Transient measurement techniques are a low-cost, efficient alternative that can produce accurate heat transfer measurements with a much shorter test time. These techniques are especially well suited for transient test facilities (e.g., shock tubes or blow-down type wind tunnels).

Transient techniques have been employed for over half a century in fields as far ranging as hypersonics [4] and solar collectors [5]. In particular, they have seen broad application in the gas turbine industry for cooled turbine blade design [6], analysis [7,8], and postproduction testing [9]. The critical measurement in the transient convective heat transfer method is the time history of surface temperature relative to some impulsively started flow event. The surface temperature can be measured either optically or through standard contact methods (e.g., surface thermocouple arrays) [10]. The two most common optical methods include liquid crystals and infrared imaging. Temperature-sensitive liquid crystals can be painted onto any smooth surface and calibrated in situ. The encapsulated crystals display visible bands of color when they are exposed to temperature changes by reflecting a single wavelength of light. The surface color time history can be imaged with a common charge coupled device (CCD) camera at higher resolution and much lower cost than an infrared camera. There are, however, several drawbacks to the liquid crystal technique [11]. Because the crystals are embedded into the surface coating, they are not located precisely at the surface nor are the thermal properties of the paint necessarily the same as those of the substrate. In addition, the temperature sensitivity of the crystals is not always in a convenient range (typically very near room temperature). Also, the color bands only provide information as to the local time delay for the surface to change from the isothermal (flow off) condition to the specific temperature associated with the particular color band. Infrared measurement, on the other hand, provides a continuous surface temperature history. This necessitates a different analytical processing technique. Finally, and perhaps most important for this study, liquid crystals are difficult to

Contributed by the Heat Transfer Division of ASME for publication in the JOURNAL OF HEAT TRANSFER. Manuscript received October 10, 2007; final manuscript received May 19, 2008; published online October 15, 2008. Review conducted by Gautam Biswas.

  

apply uniformly over rough surfaces. A nonuniform crystal distribution can create significant problems in interpreting heat transfer results. Even standard steady-state measurement techniques are challenged by rough surfaces due to the difficulty of ensuring a uniform surface heat flux or wall temperature condition [12,13]. As such, the subject of this study is the application of infrared thermography to the transient measurement of convective heat transfer over a rough surface.

## Analytical Development

The essential foundation of the transient heat transfer technique is the unsteady conduction equation. With the assumption of constant thermal properties and no heat generation, this equation can be written in Cartesian coordinates as

$$\frac{\partial^2 T}{\partial x^2} + \frac{\partial^2 T}{\partial y^2} + \frac{\partial^2 T}{\partial z^2} = \frac{1}{\alpha}\frac{\partial T}{\partial t} \tag{1}$$

or in one dimension only,

$$\frac{\partial^2 T}{\partial x^2} = \frac{1}{\alpha}\frac{\partial T}{\partial t} \tag{2}$$

The transient technique employs classical solutions to this equation for the specific case of a semi-infinite solid with uniform initial temperature. These initial and boundary conditions are explicitly stated as

$$T(x,0) = T_{\text{init}} \quad \text{and} \quad \lim_{x \to \infty} T(x,t) = T_{\text{init}} \tag{3}$$

Numerous heat transfer texts contain the solution of these equations for two of the most common cases [14,15]: (i) step change in surface temperature, $T(x=0, t>0)=T_s$, and (ii) step change in fluid temperature, $T_{\text{fluid}}(t>0)=T_\infty$, where $T_{\text{fluid}}(t\leq 0)=T_{\text{init}}$.

Since the governing equation (Eq. (2)) is linear, an arbitrary $T_s(t)$ or $T_\infty(t)$ distribution can be approximated as the summation of a series of steps. Then, using Duhamel's superposition theorem, the general solution of Eq. (2) is obtained. Using this approach, Cook and Felderman [16] and later Schultz and Jones [17] derived the following expression for the surface heat flux based on the general solution:

$$q_s(t) = \frac{\kappa}{\sqrt{\pi\alpha}} \sum_{i=1}^{n} \frac{T_s(\tau_i) - T_s(\tau_{i-1})}{\frac{1}{2}\left[\sqrt{t-\tau_i} - \sqrt{t-\tau_{i-1}}\right]} \tag{4}$$

Once the $q_s(t)$ distribution is calculated using Eq. (4), the transient IR method relies on an energy balance evaluated at the surface ($q_{s,\text{conv}}=q_{s,\text{rad}}+q_{s,\text{cond}}$) to calculate the convected heat flux to the surface ($q_{s,\text{conv}}$). The heat transfer coefficient is then computed as $h_c=q_{s,\text{conv}}/(T_\infty-T_s)$, where $q_{s,\text{conv}}$, $T_\infty$, and $T_s$ are all functions of time in the most general case.

## Finite Volume Method for Lateral Conduction

The subject of this paper is the transient IR technique accounting for lateral conduction on nonuniform (rough) surfaces. Since the method outlined above is only valid for 1D conduction, a finite volume discretization of the solid was employed. The 1D results are then used as a benchmark for comparison to assess the importance of lateral conduction for a generic rough surface topology. Since the 1D analysis is simpler to execute, there is a significant cost savings in terms of computational time. Thus, it is not uncommon for researchers to employ the 1D analysis even in cases with complex surface geometries (including roughness) [18–21]. More recently, some researchers have employed finite element analyses in conjunction with steady-state [22,23] and transient [9,24] heat transfer techniques to improve measurement accuracy in regions of steep surface temperature gradients. For example, Ling et al. [24] measured film cooling effectiveness ($\eta_{\text{fc}}$) using the transient liquid crystal technique. They compared results obtained from both 1D and 3D conduction models and found that in the region just downstream of the film cooling hole, the 1D model underpredicted $\eta_{\text{fc}}$ by up to 25%.

Brauckmann and von Wolfersdorf [22] employed a steady-state IR technique to a shaped film cooling configuration and showed that a 3D conduction model could be successfully employed to correct for the heat pick-up of the coolant fluid as it passes from the coolant plenum to the exit orifice. Nirmalan et al. [9] developed a procedure for nondestructively testing internal cooling passages of production turbine blades using a modified transient IR technique. They used a 1D solution as the initial condition for internal heat transfer coefficients in an iterative 3D ANSYS model of the turbine wall. Thus the final analysis does account for temperature variations through the wall thickness and lateral conduction. The authors reported an overall increase of 40% in predicted $h_c$ inside the coolant passage for the 3D model compared with the initial 1D prediction.

Based on these results, it is anticipated that accounting for lateral conduction on rough surfaces will have a significant influence on transient IR measurements of heat transfer coefficient. To conduct a formal assessment, a structured rectilinear grid was adapted to a rough surface topology originally generated by Bons et al. [25] shown in Fig. 1. The surface is a 20 times scale model of surface deposits generated on a thermal barrier coated (TBC) gas turbine sample in an accelerated deposition facility. Bons et al. showed that the surface character of this laboratory generated deposition roughness was similar in character to deposition that is commonly found on in-service power turbine hardware [26].

As shown in Fig. 1, the lateral directions are $y$ (83 mm) and $z$ (67 mm) while the $x$-direction is into the solid. The largest roughness peak is approximately 3.5 mm above the lowest valley for this topology. Cell temperatures are assigned to cell centers, allowing conservation of energy to be written for the $(i,j,k)$ cell as follows:

$$V\rho c_p \frac{\partial T_{i,j,k}}{\partial t} = q_{x_{i,j,k}} A_{x_{i,j,k}} + q_{y_{i,j,k}} A_{y_{i,j,k}} + q_{z_{i,j,k}} A_{z_{i,j,k}} - q_{x_{i+1,j,k}} A_{x_{i+1,j,k}} - q_{y_{i,j+1,k}} A_{y_{i,j+1,k}} - q_{z_{i,j,k+1}} A_{z_{i,j,k+1}} \tag{5}$$

For this study, the fluxes are discretized using a first-order approximation in space, e.g.,

$$q_{x_{i,j,k}} \cong -\kappa \frac{T_{i,j,k} - T_{i-1,j,k}}{\Delta x_{i,j,k}} \tag{6}$$

For the surface cell ($i=1$), the surface flux is approximated as

$$q_{s_{1,j,k}} \cong -\kappa \frac{T_{1,j,k} - T_{s_{j,k}}}{0.5\Delta x_{1,j,k}} \tag{7}$$

The temporal discretization is approximated with a first order explicit formation,

$$\frac{\partial T_{i,j,k}}{\partial t} \cong \frac{T_{i,j,k_n} - T_{i,j,k_{n-1}}}{\Delta t} \tag{8}$$

While other researchers have improved accuracy and processing time requirements by using higher order discretizations and more stable implicit formulations (e.g., alternating direction implicit method used by Ling et al. [24]), the present algorithm was sufficiently stable to produce results in a reasonable timeframe for this study. The size of elements in the $y$ and $z$-directions corresponded to the size of IR camera data pixels (roughly $0.5 \times 0.5$ mm$^2$). Grid refinement below 0.5 mm was not attempted since the surface temperature data were not available in a finer resolution. The effect of a coarser spatial resolution on the accuracy of the technique is addressed later. The rough surface topology necessitated a variable $x$-dimension for the 3D cells, though the $\Delta x$ cell size was held to no larger than 16% of 0.5 mm. For this size grid, stability was ensured using a time step of 0.0625 s or smaller. Since the IR surface temperature data were acquired in

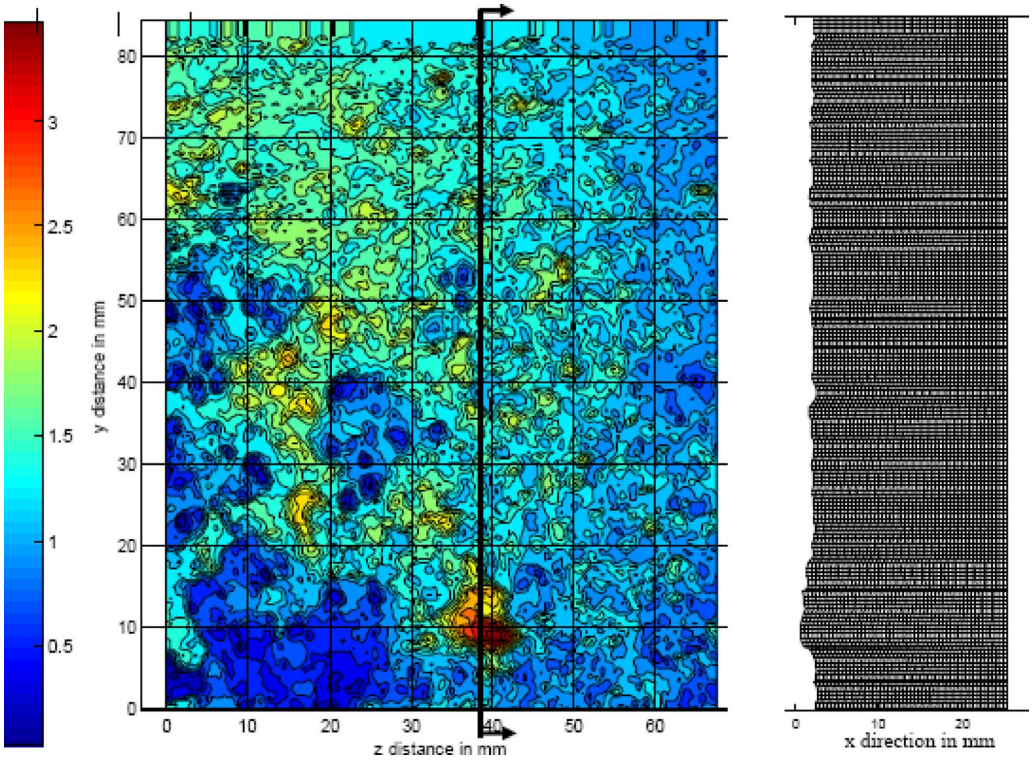


**Fig. 1 Rough surface topology showing slice of finite volume grid taken at $z=38$ mm**

1 s intervals, the $T_s(y,z,t)$ maps were linearly interpolated in time to provide data at the smaller time step necessary for stability. The thickness of the roughness panel was 25.4 mm at its thickest point. It was fabricated from acrylic using a computer numerically controlled (CNC) mill, as discussed by Bons et al. [25]. The roughness topology was measured using a contact surface profilometer. The scaled surface was then milled with a conical countersink tool that matched the 90 deg cone shape of the profilometer stylus. The thermophysical properties, thermal conductivity ($\kappa$), and thermal diffusivity ($\alpha=\kappa/\rho c_p$) for the acrylic panel material were determined experimentally by Thermal Properties Research Laboratory at Purdue University using a transient heat transfer technique. The measurements yielded the following values: $\kappa=0.196$ W/m K $\pm 6\%$ and $c_p=1330$ J/kg K $\pm 3\%$. The plastic density is 1188 kg/m$^3$ $\pm 2\%$.

Due to the low thermal diffusivity of the acrylic, test times shorter than 5 min yield a Fourier number ($\mathrm{Fo}=\alpha t/l^2$) less than 1/16, which is the semi-infinite limit. This confirmed the use of the semi-infinite conduction assumption in the 1D data processing method. Thus, the back panel and sides of the 3D finite-volume domain were prescribed with an adiabatic boundary condition. The present formulation did not account for property variations with temperature, though this refinement could be added through Eqs. (5)–(7). Before evaluating the heat transfer on the rough plate, a smooth test plate of comparable thickness and material was installed for validation of the two processing techniques. The area-averaged smooth plate St value was found to be within 1% of a standard correlation. Repeatability was within $\pm 3\%$ and bias uncertainty was estimated at $\pm 0.00015$ for the smooth plate measurement of $\mathrm{St}_o=0.00228$ at $\mathrm{Re}_L=750{,}000$.

## Results and Discussion

The importance of lateral conduction can be illustrated by comparing the predicted $q_s(t)$ history for a 3D finite volume analysis with that obtained using the 1D technique. Figure 2 shows $T_s(y,z)$ and $T_s(y,t)$ data taken on the roughness panel shown in Fig. 1 using a FLIR Thermacam SC 3000 IR camera. Figure 2(*a*) is the surface temperature map taken at $t=50$ s. The panel was subjected to an instantaneous hot gas flow $[(T_\infty - T_{\mathrm{init}}) \cong 23$ K] at a time of $t=3$ s, as shown in the time history plot (Fig. 2(*b*)). The flow direction was in the negative $y$-direction and the boundary layer was tripped turbulent, with a flow Reynolds number of 750,000 at the roughness panel center. The boundary layer momentum thickness at the roughness panel was approximately 30% smaller than the maximum peak to valley height of the roughness (3.5 mm).

The IR camera has a sensitivity of 0.03°C (at 30°C) and was focused on a 67 mm(cross stream) $\times$ 83 mm(streamwise) field of view. During testing, Bons et al. [25] discovered that the infrared measurement was sensitive to the temperature of the surfaces surrounding the roughness panel. This occurred because some of the radiation that was incident on the camera originated from the wind tunnel enclosure and was reflected off the roughness panel. The magnitude of this component of radiation varied as a function of the tunnel wall temperature. The FLIR software accounts for this by allowing the user to specify the ambient enclosure temperature. Since the heat transfer test was transient, this input was adjusted in postprocessing to track the time-varying tunnel wall temperature. Also, six 50 $\mu$m bead diameter thermocouples were flush mounted to the acrylic panel to verify the IR surface temperature measurement. This allowed calibration of the camera to within $\pm 0.3$°C of the initial surface temperature ($T_{\mathrm{init}}$).

As expected, Figs. 2(*a*) and 2(*b*) show hot and cold spots at locations corresponding to peaks and valleys (respectively) on the surface topology map in Fig. 1. The roughness peaks exhibit a faster temperature response due to elevated convective heat transfer from the hot gas flow and higher air temperatures further from the wall in the thermal boundary layer. Figures 3(*a*) and 3(*b*) show time averaged $q_s(y,z)$ over the period $80<t<100$ s calculated using the 1D and 3D methods. The figures show that the local $q_s$ peaks are more pronounced in the 3D result compared with the 1D analysis. This finding can be understood by revisiting the finite

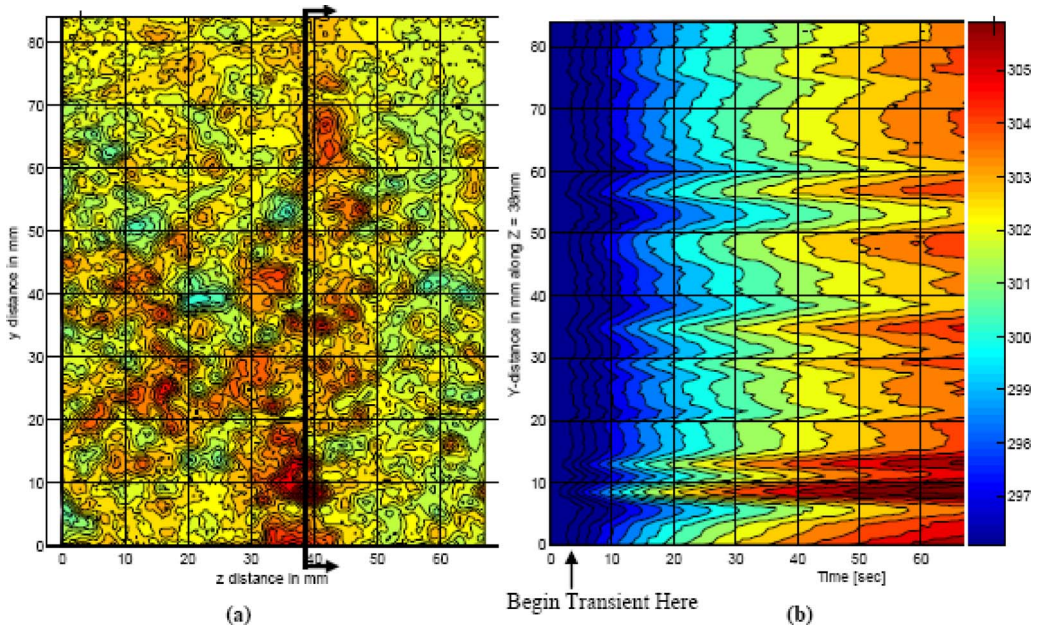


**Fig. 2 Surface temperature maps for rough surface measured with IR camera: (*a*) $T_s(y,z)$ at $t=50$ s and (*b*) $T_s(y,t)$ at $z=38$ mm; temperatures in kelvins**

volume grid shown in Fig. 1. In the 3D analysis, a local surface hot spot (e.g., due to a roughness peak) will create a higher temperature ($T_{1,j,k}$) cell just beneath the surface. This will in turn establish gradients for lateral heat flow to the cooler neighboring ($j\pm1,k\pm1$) cells. By conservation of energy, these lateral conduction losses must be offset by higher $q_s$ to the surface hot spot. The 1D heat flow model does not include these lateral "losses" and thus underpredicts the surface heat flux to the hot spots for the same surface temperature history. Explained another way, to create the same surface temperature history at a localized hot spot, a 3D conduction model must impose a larger surface heat flux since a fraction of the heat absorbed by the solid surface is conducted laterally compared with the 1D model where the only available path for heat flow from the surface is directly into the solid. This effect is only slightly subdued by the physical isolation of the peaks, which curtails the lateral conduction somewhat ($<5\%$) compared with a flat surface with the same local hot spot. A similar analysis shows the opposite trend for cold spots, for which the 1D analysis overpredicts the $q_s$. For a clearer quantitative comparison, Fig. 4 plots a line of surface heat flux taken from both contour maps in Fig. 3 (at $z=38$ mm). The 3D prediction of $q_s$ shows a peak-to-valley variation that is four to five times that of the 1D method (e.g., from $5<y<10$ mm).

The surface heat flux data from both the 1D and 3D calculation

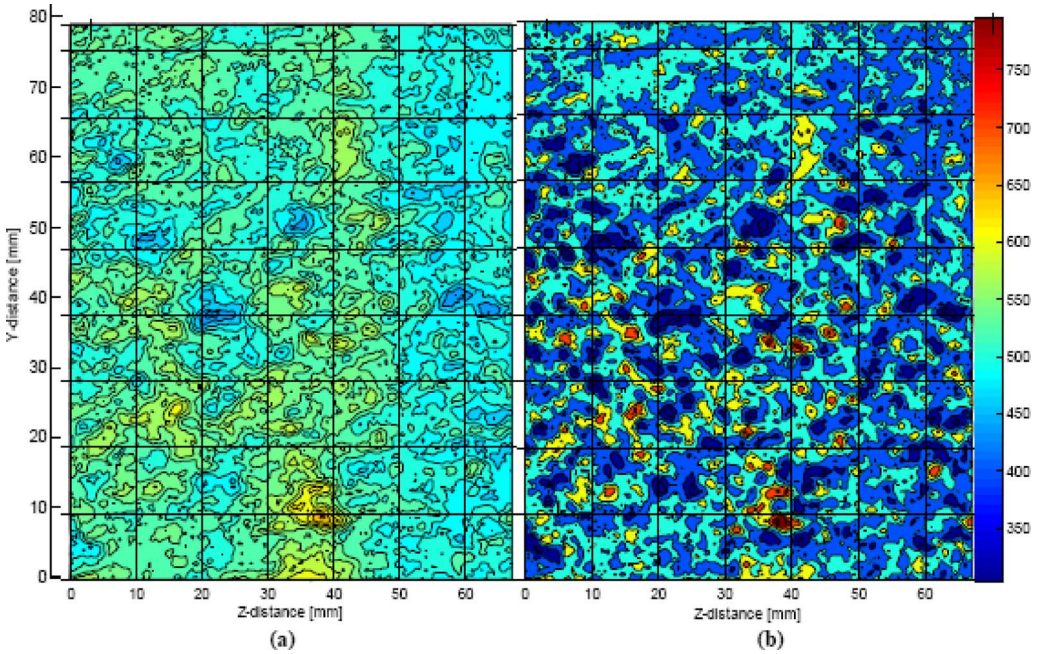


**Fig. 3 Time-averaged ($80<t<100$ s) surface heat flux maps, $q_s(y,z)$, from (*a*) 1D method and (*b*) 3D method for rough surface**

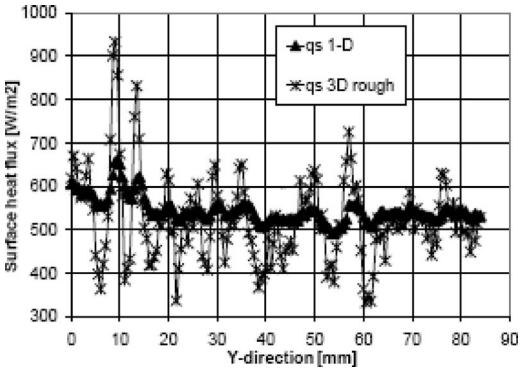


**Fig. 4 Time-averaged ($80<t<100$ s) surface heat flux, $q_s(y)$, from 1D method and 3D method for rough surface ($z=38$ mm)**

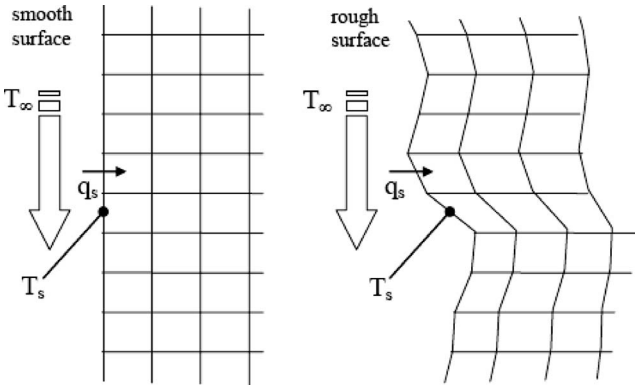


**Fig. 6 Schematic showing section of 3D finite volume grid for smooth versus rough surface**

methods are area averaged and plotted versus time in Fig. 5. (For consistency, area-averages are computed using the rough topology for the 3D method and the flat planform area for the 1D method.) Note that the area-averaged surface heat flux for the 3D method is reduced from the value predicted by the 1D method. This result is unexpected since conservation of energy would seem to suggest that the area-averaging should even out the spatial variations in $q_s$ due to lateral conduction. However, the conservation of energy applies to the actual heat transfer, $Q$, rather than the heat transfer per unit area (flux), $q_s$. When accounting for the irregular surface topology in the 3D analysis, the $T_s(y,z,t)$ history is imposed over a larger surface area than in the 1D case (see schematic in Fig. 6). This contributes to a higher initial heat load ($Q=qA$) into each of the surface cells. This additional $Q$ must still be conducted into the solid with the same thermal properties ($\alpha$) as the 1D method. Consequently, the additional $Q$ builds up in the first few cells near the surface and the rough surface finite-volume calculates a lower area-averaged $q_s(t)$ than the 1D model using the same $T_s(t)$ data. In essence, the temperature of the first few layers of cells increases more rapidly due to the larger net $Q$ in the rough surface model. Thus, it would take an even more rapid transient $T(t)$ rise to yield the same area-averaged $q_s$ prediction for the rough surface as for the smooth surface.

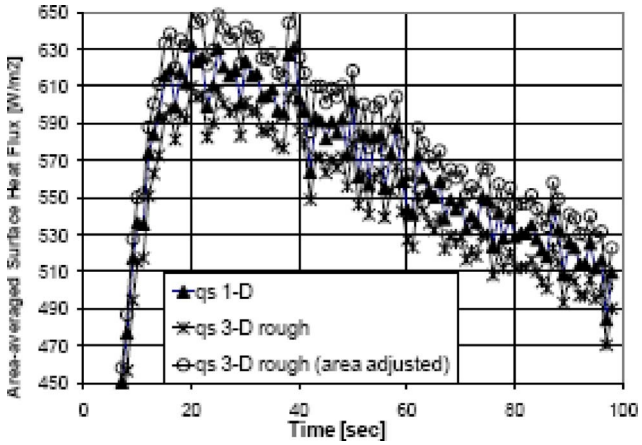


**Fig. 5 Area-averaged surface heat flux history from 1D method, 3D method for rough surface, and "area-adjusted" 3D method for rough surface**

If the transient IR technique is used to obtain an area-averaged Stanton number for a rough surface to be compared with a corresponding smooth surface, the result in Fig. 5 must be interpreted carefully to make an accurate comparison. From an engineering perspective, the parameter of interest is usually the rate at which heat penetrates down into the solid rather than the "per unit area" heat transfer at the surface. Unfortunately, Stanton number is based on the latter $[\mathrm{St}=q_s/\rho c_p U_\infty(T_\infty-T_s)]$. Thus, the area-averaged St result from the transient 3D conduction model should be multiplied by the ratio of wetted-to-planform surface area ($S_{\mathrm{wet}}/S_{\mathrm{flat}}$) to accurately account for the rate of heat transfer to the solid. For the rough surface representation employed in this study ($S_{\mathrm{wet}}/S_{\mathrm{flat}}=1.063$), the difference is shown in Fig. 5 and in Table 1. The "area-adjusted" St value predicts approximately 60% more heat transfer augmentation than does the unadjusted 3D result for the rough surface compared with the smooth St value of 0.00228 for this Reynolds number (columns 2 and 3).

Since the area-adjusted Stanton number for the rough surface in Table 1 is a function of the $S_{\mathrm{wet}}/S_{\mathrm{flat}}$ ratio, the result depends on the spatial resolution of the surface roughness topology. The roughness panel employed in this study was milled from an acrylic sheet using a CNC mill with a data resolution of 0.4 mm in both the $y$ and $z$ surface coordinates. This is very close to the 0.5 mm spatial resolution of the IR camera used for the heat transfer

**Table 1 Area-averaged Stanton numbers for various models. Data from three different roughness spatial resolutions (0.5 mm, 1 mm, and 2 mm). Time averaged data from $80<t<100$ s.**

| Roughness grid spatial resolution | 0.5 mm (matches IR camera) | 0.5 mm (matches IR camera) | 1 mm | 1 mm | 2 mm | 2 mm |
|---|---|---|---|---|---|---|
| | Area-averaged Stanton number | % St increase from smooth plate St | Area-averaged Stanton number | % St increase from smooth plate St | Area-averaged Stanton number | % St increase from smooth plate St |
| Smooth wall result (Bons et al. [21]) | 0.00228 | 0 | 0.00228 | 0 | 0.00228 | 0 |
| Rough surface, 1D | 0.00265 | 16.0% | 0.00265 | 16.2% | 0.00265 | 16.2% |
| Rough surface, 3D | 0.00256 | 12.5% | 0.00261 | 14.5% | 0.00263 | 15.4% |
| Rough surface, 3D area adjusted | 0.00274 | 20.0% | 0.00269 | 18.0% | 0.00267 | 17.1% |

measurement. To produce the topology map shown in Fig. 1, the raw height data used by the CNC mill were resampled at a 0.5 mm resolution before being used in the finite-volume calculation. Thus the IR and surface topology maps are perfectly matched. If, however, the surface roughness data were on a coarser spatial grid than the IR camera resolution, the surface data could be interpolated to match the IR camera resolution. Of course, the interpolation process may not account for the true wetted surface area and could lose some of the accuracy of the local heat transfer spatial variation. To demonstrate the magnitude of the effect of this interpolation process, the 0.5 mm resolution surface height data were resampled at 1 mm and again at 2 mm spatial resolution. In each case, the coarse grid was then linearly interpolated back to the 0.5 mm spatial grid to match the IR camera resolution. Doing so reduced the wetted surface area from $S_{\text{wet}}/S_{\text{flat}}=1.063$ for the original (0.5 mm resolution) surface to $S_{\text{wet}}/S_{\text{flat}}=1.033$ and 1.015 for the 1 mm and 2 mm resolution surfaces, respectively. The corresponding area-averaged results for Stanton number are shown in Table 1. As the wetted surface area decreases, both the "rough surface 3D" and the "rough surface 3D area-adjusted" results converge to the "rough surface 1D" values. This is as expected since the process of linearly interpolating from a coarser and coarser mesh eventually approaches the smooth surface limit. Once the surface roughness has been smoothed out, accounting for lateral conduction does not change the area-averaged St from the 1D case. Lateral conduction alone redistributes energy but does not increase the area-averaged heat transfer.

For the data shown in Table 1, the spatial resolution of the roughness topology is equal to or coarser than the IR camera spatial resolution. It is perhaps more common that the IR spatial resolution would be coarser than the surface topology variations. In this case, the IR camera will register a single average temperature for a region that may, in fact, be represented by multiple contiguous cell-faces in a finite volume representation. Because of the lack of adequate spatial resolution in the temperature map, the 3D transient technique will be subject to the same "smoothing" error that occurred from the coarser roughness height representations evaluated in Table 1 (i.e., the area-averaged St will be underpredicted). Linearly interpolating the temperature data onto a finer grid to correct for this will recover some but not all of the lost measurement fidelity.

One additional roughness feature that must be considered when performing an optical surface temperature evaluation such as this is the surface angularity. When imaging a radiating surface at an angle other than normal ($\theta=0$), it must be ensured that the radiosity is independent of direction (i.e., that the radiation obeys Lambert's law). Lambert's law is derived for diffuse "gray" surfaces but holds reasonably well for "real" surfaces up to a $\theta$ angle of 60 deg. Beyond this, the directional emittance drops off appreciably [14]. Thus, optical surface heat flux measurement techniques are not suitable for rough surfaces with high surface angularity. For the surface used in this study, the maximum surface angularity was 62 deg with a mean surface angle of 10.2 deg. Also, a high surface emissivity is desirable since this reduces the percentage of surface radiation that is due to reflections from neighboring surface cells. The emissivity for the acrylic surface in this study was 0.9, though this drops considerably at high angles compounding the surface angularity problem. Lower emissivity surfaces combined with high surface angularity will tend to smear out spatial temperature variations due to reflected radiation sensed by the IR camera.

Though the 3D finite volume technique coupled with the transient IR method provides greater measurement accuracy, it does so at significant computational cost. Due to the smaller time step required for stability in the present implementation, the finite-volume method increases the computational time by a factor of over 500. Also, the 1D method requires no detailed knowledge of surface topology, while the 3D finite-volume method must have an accurate surface topology that is correctly positioned relative to the IR camera image. This added cost and complexity may not be warranted for the modest increase in accuracy for the area-averaged St measurements shown in Table 1. However, if accurate spatial resolution of St (or $q_s$) is desired, the data shown in Figs. 3 and 4 leave little doubt that the 1D approximation method is not suitable for rough surfaces.

## Summary and Conclusions

The effect of lateral conduction on convective heat transfer predictions using the transient infrared technique over a rough surface is evaluated. Comparisons are made between a full 3D finite volume analysis and a simpler 1D transient conduction model. The randomly rough surface is a scaled model of actual surface deposits generated in a gas turbine flowfield. The surface temperature time history was measured with a high resolution infrared camera during an impulsively started hot gas flow over the rough test plate at a flow Reynolds number of 750,000. The boundary layer was turbulent with the peak roughness elements protruding just above the boundary layer momentum thickness. Based on the analysis, the following conclusions are made.

1. The 1D model is not suitable for measurements of local surface heat flux (or St) around roughness elements. Neglecting lateral conduction can lead to a factor of 5 underestimate of the peak-to-valley variation of surface heat flux over the rough surface.
2. Care must be taken in making area-averaged St measurements of rough surfaces using optical methods. The wetted-to-flat surface area ratio ($S_{\text{wet}}/S_{\text{flat}}$) must be multiplied by the resultant area-averaged St from the 3D model in order to properly account for the heat transfer augmentation due to roughness. If not, the error in predicted augmentation could exceed 50%. It is inaccurate to simply multiply the area-averaged St result from a 1D analysis by the wetted-to-flat surface area ratio. This correction must only be performed with the 3D model result. This conclusion is valid for both transient and steady-state measurement techniques.
3. For accurate surface heat flux prediction using the 3D finite volume model, the spatial resolution of surface temperature should match that of the surface topology. If not, temperature smoothing and loss of wetted area can result in inaccurate predictions.
4. Surface angularity of the roughness elements must not exceed 60 deg in order to assume a diffuse radiosity independent of direction and to limit temperature smoothing due to roughness element cross-radiation.

In summary, transient St measurement over rough surfaces must be performed with significant care in order to produce accurate measurements of both local and area-averaged heat transfers.

## Acknowledgment

The author would like to acknowledge several students who assisted in the collection of these data: James Wammack, Jared Crosby, and Daniel Fletcher. Dr. Brent Webb and Dr. Thomas Fletcher (both at Brigham Young University) contributed substantially to the analysis portion of this document. Their comments and encouragement are gratefully acknowledged.

**Nomenclature**

$A$ = finite volume cell surface area
Fo = Fourier number ($\alpha t/l^2$)
$L$ = distance from the wind tunnel leading edge to the center of the roughness panel
$Q$ = heat flux
$\text{Re}_L$ = Reynolds number ($U_\infty L/\nu$)
$S$ = roughness panel surface area
St = Stanton Number, $h_c/(\rho c_p U_\infty)$
$T$ = temperature

$U$ = velocity
$V$ = cell volume
$c_p$ = specific heat at constant pressure
$dt$ = time step
$h_c$ = convective heat transfer coefficient
$l$ = panel thickness
$q$ = heat flux per unit area
$t$ = time
$x$ = direction into solid from the surface
$y$ = upstream direction along the surface
$z$ = cross stream direction along the surface
$\alpha$ = thermal diffusivity $(\kappa/\rho c_p)$
$\Delta x$ = cell dimension in the $x$-direction
$\Delta t$ = time step
$\kappa$ = thermal conductivity
$\eta_{fc}$ = film cooling effectiveness
$\nu$ = kinematic viscosity
$\theta$ = local surface angularity
$\rho$ = density
$\tau$ = dummy time integration variable

**Subscripts**

coolant = coolant property
flat = planform (flat) surface area
fluid = fluid property
$i$ = summation index
$i$ = $x$ direction cell index
init = initial condition ($t=0$)
$j$ = $y$ direction cell index
$k$ = $z$ direction cell index
$n$ = summation limit
$n$ = time index
$s$ = solid surface adjacent to the fluid
$s$, cond = conductive surface heat flux
$s$, conv = convective surface heat flux
$s$, rad = radiative surface heat flux
wet = wetted surface area
$\infty$ = freestream value

## References


[1] Hosni, M. H., Coleman, H. W., and Taylor, R. P., 1991, "Heat Transfer Measurements and Calculations in Transitionally Rough Flow," ASME J. Turbomach., **113**, pp. 404–411.
[2] Chen, P. H., and Goldstein, R. J., 1991, "Convective Transport Phenomena on the Suction Surface of a Turbine Blade Including the Influence of Secondary Flows Near the Endwall," ASME Paper No. 91-GT-35.
[3] Gao, Z., Wright, L. M., and Han, J.-C., 2005, "Assessment of Steady State PSP and Transient IR Measurement Techniques for Leading Edge Film Cooling," Paper No. IMECE2005-80146.
[4] Powell, O. A., and Bons, J. P., 2001, "Heat Transfer to the Inclined Trailing Wall of an Open Cavity," J. Thermophys. Heat Transfer, **15**(3), pp. 293–301.
[5] Roger, M., 2007, "A Periodic Transient Method for High-Resolution Heat Transfer Measurement on Two-Dimensional Curved Surfaces," ASME J. Heat Transfer, **129**, pp. 1638–1654.
[6] Bunker, R. S., 2004, "Latticework (Vortex) Cooling Effectiveness Part I: Stationary Channel Experiments," ASME Paper No. GT-2004-54157.
[7] Nasir, H., Ekkad, S. V., Bunker, R. S., and Prakash, C., 2004, "Effects of Tip Gap Film Injection From Plain and Squealer Blade Tips," ASME Paper No. GT-2004-53455.
[8] Ou, S., and Rivir, R. B., 2006, "Shaped Hole Film Cooling With Pulsed Secondary Flow," ASME Paper No. GT–2006-90272.
[9] Nirmalan, N. V., Bunker, R. S., and Hedlund, C. R., 2003, "The Measurement of Full-Surface Internal Heat Transfer Coefficients for Turbine Airfoils Using a Non-Destructive Thermal Inertia Technique," ASME J. Turbomach., **125**, pp. 83–89.
[10] Walker, D. G., Scott, E. P., and Nowak, R. J., 2000, "Estimation Methods for Two-Dimensional Conduction Effects of Shock-Shock Heat Fluxes," J. Thermophys. Heat Transfer, **14**(4), pp. 553–539.
[11] Lin, M., and Wang, T., 2000, "A Transient Liquid Crystal Method Using Hue Angle and a 3D Inverse Transient Conduction Scheme," ASME Paper No. 2000-GT-0231.
[12] Bogard, D. G., Schmidt, D. L., and Tabbita, M., 1998, "Characterization and Laboratory Simulation of Turbine Airfoil Surface Roughness and Associated Heat Transfer," ASME J. Turbomach., **120**(2), pp. 337–342.
[13] Hosni, M. H., Coleman, H. W., and Taylor, R. P., 1991, "Measurements and Calculations of Rough-Wall Heat Transfer in the Turbulent Boundary Layer," Int. J. Heat Mass Transfer, **34**(4/5), pp. 1067–1082.
[14] Mills, A. F., 1992, *Heat Transfer*, 1st ed., Irwin, Homewood, IL.
[15] Kakac, S., and Yener, Y., 1992, *Heat Conduction*, 1st ed., Taylor & Francis, London.
[16] Cook, W. J., and Felderman, E. J., 1966, "Reduction of Data From Thin-Film Heat-Transfer Gages: A Concise Numerical Technique," AIAA J., **4**, pp. 561–562.
[17] Schultz, D. L., and Jones, T. V., 1973, "Heat-Transfer Measurements in Short-Duration Hypersonic Facilities," NATO Advisory Group for Aerospace Research and Development No. 165.
[18] Licu, D. N., Findlay, M. J., Gartshore, I. S., and Salcudean, M., 2000, "Transient Heat Transfer Measurements Using a Single Wide-Band Liquid Crystal Test," ASME J. Turbomach., **122**, pp. 546–552.
[19] Guo, S. M., Lai, C. C., Jones, T. V., Oldfield, M. L. G., Lock, G. D., and Rawlinson, A. J., 2000, "Influence of Surface Roughness on Heat Transfer and Effectiveness for a Fully Film Cooled Nozzle Guide Vane Measured by Wide Band Liquid Crystals and Direct Heat Flux Gages," ASME J. Turbomach., **122**, pp. 709–716.
[20] Barigozzi, G., Franchini, G., and Perdichizzi, A., 2007, "End-Wall Film Cooling Through Fan-Shaped Holes With Different Area Ratios," ASME J. Turbomach., **129**, pp. 212–220.
[21] Lu, Y., Dhungel, A., Ekkad, S. V., and Bunker, R. S., 2007, "Film Cooling Measurements for Cratered Cylindrical Inclined Holes," ASME Paper No. GT-2007-27386.
[22] Brauckmann, D., and von Wolfersdorf, J., 2005, "Application of Steady State and Transient IR-Thermography Measurements to Film Cooling Experiments for a Row of Shaped Holes," ASME Paper No. GT-2005-68035.
[23] Baldauf, S., Schulz, A., and Wittig, S., 2001, "High-Resolution Measurements of Local Effectiveness From Discrete Hole Film Cooling," ASME J. Turbomach., **123**, pp. 758–765.
[24] Ling, J. P. C. W., Ireland, P. T., and Turner, L., 2004, "A Technique for Processing Transient Heat Transfer, Liquid Crystal Experiments in the Presence of Lateral Conduction," ASME J. Turbomach., **126**, pp. 247–258.
[25] Bons, J. P., Wammack, J. E., Crosby, J., Fletcher, D. H., and Fletcher, T. H., 2008, "Evolution of Surface Deposits on a High Pressure Turbine Blade, Part II: Convective Heat Transfer," ASME J. Turbomach., **130**, p. 021021.
[26] Bons, J. P., Taylor, R., McClain, S., and Rivir, R. B., 2001, "The Many Faces of Turbine Surface Roughness," ASME J. Turbomach., **123**(4), pp. 739–748.

# Transient Method for Convective Heat Transfer Measurement With Lateral Conduction—Part II: Application to an Isolated Spherical Roughness Element

**J. Bons**
Professor
Ohio State University,
2300 West Case Road,
Columbus, OH 43235

**Daniel Fletcher**
Boeing Company,
100 North Riverside,
Chicago, IL 60606-1596

**Brad Borchert**
Brigham Young University,
Provo, UT 84602

*The effect of lateral conduction on convective heat transfer measurements using a transient infrared technique over an isolated spherical roughness element (bump) is evaluated. Comparisons are made between a full 3D finite-volume analysis and a simpler 1D transient conduction model. The surface temperature history was measured with a high resolution infrared camera during an impulsively started hot-gas flow at a flow Reynolds number of 860,000. The boundary layer was turbulent with the bump heights equivalent to 0.75, 1.5, and 3 times the boundary layer momentum thickness. When considering transient conduction effects only in the bump wake, the 1D approximate method underestimates the actual Stanton number estimated with the 3D model. This discrepancy is only 10% for a 75% change in St number occurring over a surface distance of 10 mm (the half-width of the wake). When the actual bump topology is accounted for in estimating the Stanton number on the bump itself with the 3D analysis technique, the increased surface area of the finite-volume cells on the protruding bump actually decreases the predicted value of St locally. The net result is that the two effects can cancel each other, and in some cases the 1D approximate technique can provide a reasonably accurate estimate of the surface heat transfer without the added complexity of the 3D finite-volume method. For the case of the largest bump tested, with maximum surface angularity exceeding 60 deg, the correction for 3D topology yields a 1D St estimate that is within 20–30% of the 3D estimate over much of the bump surface. These observed effects are valid for transient measurement techniques while the opposite is true for steady-state measurement techniques.* [DOI: 10.1115/1.2976785]

*Keywords: transient heat transfer measurement, bump roughness*

## 1 Introduction/Background

Understanding the effect of surface roughness on fluid flow and heat transfer is critical for a multitude of engineering devices. Environmental factors such as icing on airfoils, sand erosion in helicopter engines, deposits in industrial piping and pumps, and coating removal (spallation) in gas turbines can produce unacceptable performance loss and accelerated maintenance intervals. For nearly a century, roughness models have been employed in laboratory testing to study the effect of operationally induced surface roughness. For example, sand, powders, and screens have been used to simulate rough (as manufactured) surfaces in piping, pumps, and turbines [1–3]. Other researchers have used distributed cylinders [4,5], spherical segments [6–8], cones [9,10], and pedestals [11] to represent icing, salt deposits, or surface erosion. As outlined in the companion (Part I) paper [12], optical methods are often employed to nonintrusively measure heat transfer augmentation for rough surfaces. The increased spatial resolution afforded by optical methods necessitates careful treatment of surface nonuniformities, particularly for the case of transient optical measurements. The companion paper outlines a method of accounting for three-dimensional conduction and rough surface effects in the determination of local surface heat flux from transient optical surface temperature measurements. The purpose of this Part II study is to provide a well-defined test case for evaluating the relative importance of the two effects addressed in the companion paper, i.e., lateral conduction and rough surfaces. An isolated spherical bump mounted to a smooth-wall was employed since it is a canonical three-dimensional structure that has been studied by many others [6–8,13,14] and thus provides a good test case for this refined transient infrared (IR) procedure.

## 2 Analytical Development

The full analytical development of the transient IR method is included in the Part I paper. As a brief summary, the traditional 1D transient method uses Duhamel's superposition method to calculate the surface heat flux for a specified surface temperature history. It assumes that the test article is a semi-infinite solid at constant temperature at the start of the transient. As indicated by its moniker, the 1D method neglects lateral conduction, instead treating the surface temperature history imaged on each pixel of the IR camera as an isolated 1D heat conduction normal to the surface being imaged. This assumption permits rapid postprocessing of even the most dense IR camera pixel arrays since the analytical solution involves only a simple summation of the temperature step responses. The 3D method introduced in Part I discretizes the solid domain using a finite-volume method. The surface heat flux distribution (and eventually Stanton number) is determined from the surface temperature history using a three-dimensional unsteady conduction finite-volume algorithm with time-varying

Contributed by the Heat Transfer Division of ASME for publication in the JOURNAL OF HEAT TRANSFER. Manuscript received October 10, 2007; final manuscript received May 19, 2008; published online October 15, 2008. Review conducted by Gautam Biswas.

  

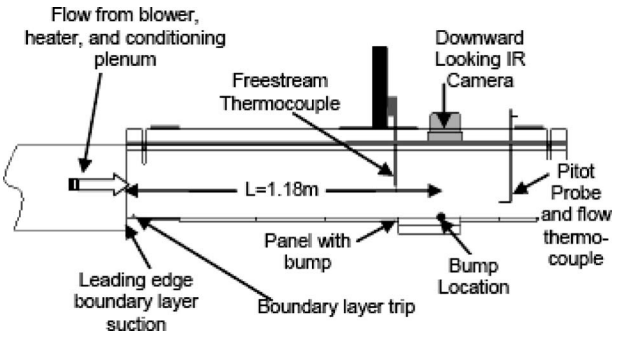


**Fig. 1 Facility used for bump study**

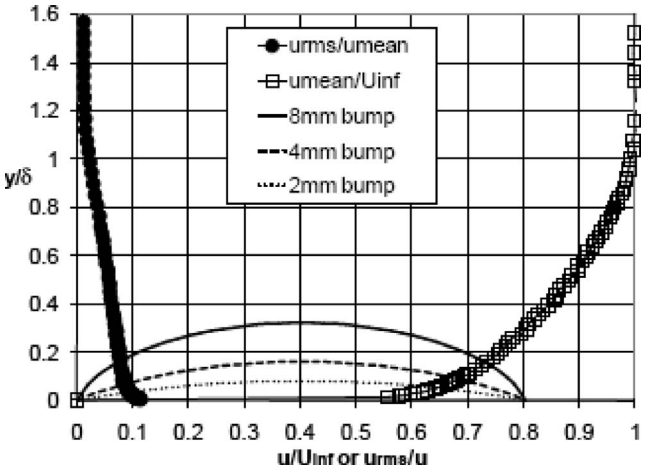


**Fig. 2 Velocity and turbulence profiles relative to bump height**

boundary conditions. The time-varying surface heat flux is calculated from the surface normal temperature gradient in the solid. The finite-volume implementation employed for this spherical bump study uses the same nominal 0.5 mm cell dimensions, matching the spatial resolution of the IR camera. The same grid generation algorithm, discretization scheme, and time stepping procedures are employed in both Part I and Part II studies.

## 3 Experimental Facility

A schematic of the research facility used for this study is shown in Fig. 1. The open loop wind tunnel uses a main-flow blower to provide a nominal mass flow of 2 kg/s to the test section. A heat exchanger at the main-flow blower discharge can be used to vary the flow temperature from 20°C to 50°C. Flow conditioning downstream of the heat exchanger yields 2D flow uniformity of ±0.4% in velocity and ±1°C over the center 0.18 m of the test section span. The freestream turbulence level in the wind tunnel is 0.7%. At 1.52 m from the conditioning plenum exit, a knife-edge boundary layer bleed with suction removes the bottom 2.7 cm of the growing boundary layer. The top wall of this final section pivots about its forward end in order to adjust the pressure gradient in the tunnel. For the tests presented here, the wall was adjusted to produce zero freestream acceleration over the test panel. At 2.5 cm from the boundary layer suction point, a 2 mm diameter cylinder spans the test section to trip the boundary layer to turbulent. The bump under study is located 1.18 m from the boundary layer suction point, as shown in the figure.

Three different sized spherical segments ("bumps") were milled into three separate 2.54 cm thick acrylic panels with the same thermal properties as the panels used in Part I: $k=0.196$ W/m K ± 6% and $c_p=1330$ J/kg K ± 3%. The plastic density is 1188 kg/m$^3$ ± 2%. To study the effect of increasing surface angularity on the transient IR measurement technique, the bumps were milled with constant base diameter (20 mm) but with varying heights: 2 mm, 4 mm, and 8 mm. The corresponding sphere radii are shown in Table 1 along with the maximum surface angularity at the edge of the bump. The maximum angularity of the 8 mm bump just exceeds the upper limit of the hemispherical emittance criterion (~60 deg) established in Part I.

**Table 1 Bump geometry**

| Bump height ($k$) (mm) | Bump base diameter (mm) | Sphere radius (mm) | Maximum surface angularity (deg) |
|---|---|---|---|
| 2 | 20 | 26 | 22 |
| 4 | 20 | 14.4 | 44 |
| 8 | 20 | 10.25 | 73 |

Freeestream flow velocity was measured using a Pitot-static probe with a colocated flow thermocouple with 0.13 mm bead diameter for flow temperature measurement. The two instruments are positioned at midspan just outside the boundary layer and downstream of the test panel during transient testing. A second thermocouple was located upstream of the test panel and farther away from the wall in the freestream, as shown in Fig. 1. Uncertainty in the velocity measurement was within ±1.5% at flow rates of interest.

A boundary layer Pitot probe with a colocated 0.13 mm bead diameter flow thermocouple was used to determine the boundary layer mean velocity and the thermal profiles at the bump location. Figure 2 shows the mean boundary layer profile relative to the three bump heights ($k/\delta$ is shown to scale where $\delta \cong 24$ mm). A turbulence ($u_{\text{rms}}/u_{\text{mean}}$) profile measured with a hot-wire anemometer is also shown. The boundary layer momentum thickness of this turbulent boundary layer is approximately 2.7 mm at the bump location (measured without the bump installed). The shape factor is 1.35, with a variability of ±0.01 over the center 80 mm of the wind tunnel. The maximum bump height is roughly three times the momentum thickness. All three bumps are concentrated in a region of steep velocity (and thermal) gradients as well as elevated turbulence levels.

For the heat transfer measurements, a FLIR Thermacam SC 3000 infrared camera system is mounted with the lens fit into a hole in the acrylic ceiling of the tunnel. The camera has a sensitivity of 0.03°C (at 30°C) and allows frame rates of approximately 1 Hz with 240×320 pixels. The test procedure is as follows. The entire test section was maintained at room temperature for several hours before testing. Using the main-flow heat exchanger, a hot-gas air flow (50°C) was then diverted instantaneously through the tunnel from an adjacent duct. The time-varying freestream velocity and temperature, as well as the average surface temperature (with the IR camera), were monitored for a period of 4 min. The analysis technique accounts for the variable freestream velocity and temperature, as described in the Part I paper [12]. The radiative heat flux from the test plate to the surrounding tunnel walls was always less than 1% of the calculated convective heat flux. The smooth-plate area-averaged St value was found to be within 3% of a standard correlation. Repeatability was within ±5% and bias uncertainty was estimated at ±0.00015 for the flat-plate measurement of $\text{St}_{\text{flat}}=0.00225$ at $\text{Re}_L=860{,}000$.

## 4 Results and Discussion

Figure 3 shows a typical temperature pattern measured by the IR camera for the 8 mm bump during the hot flow transient. The

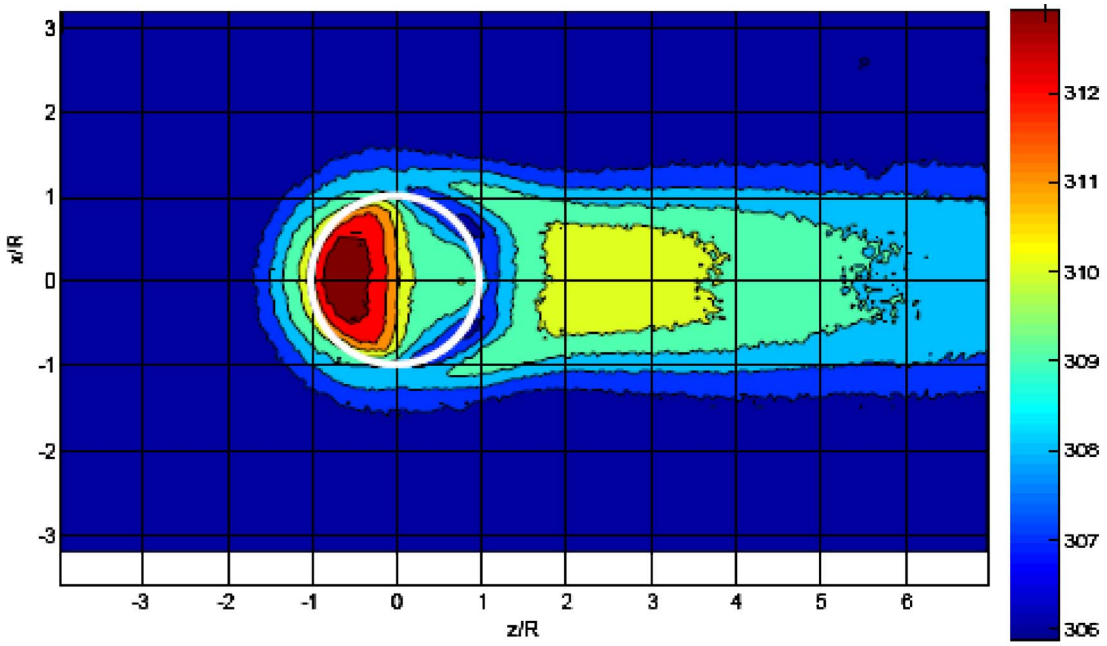


**Fig. 3 Surface temperature map for 8 mm bump measured with IR camera ($t$=50 s)**

flow is from left to right. The position of the bump is noted on the temperature map with the white circle. The plot axes are normalized by the bump base radius $R=10$ mm and centered on the bump. Note the high temperature at the bump leading edge followed by low temperatures on the trailing edge. Also, the bump wake shows elevated temperature levels relative to the unperturbed flow at the top and bottom of the image. When the full time series of temperature maps (e.g., Fig. 3) is evaluated using the 1D superposition technique, the Stanton number distribution shown in Fig. 4($a$) is produced. Processing the same data set with the 3D finite-volume technique yields a slightly different St map [Fig. 4($b$)]. Note the background value of Stanton number outside the bump-affected region in Fig. 4 closely approximates the flat-plate correlation value of 0.00225. This "unperturbed" St value was used to normalize the data field in the discussion that follows.

To more effectively evaluate the relative importance of lateral conduction and surface curvature effects on heat transfer calculations using the transient IR technique, St maps (e.g., Fig. 4) for each bump height were further interrogated as follows. First, each St map was normalized by the average unperturbed Stanton value at the upper and lower edges of the IR viewing window. This normalization eliminated the measurement uncertainty related to the plastic properties and allowed direct comparison with previous work by Henry et al. [8]. The normalized St data for all three bumps were then plotted along the streamwise bump line of symmetry ($x/R=0$) and along a spanwise line through the wake ($z/R=2$). The wake line of data is in a region of high temperature gradients without surface curvature while the line of symmetry ($x/R=0$) has both strong temperature gradients and regions of maximum surface curvature. Figure 5 shows the normalized St data along the symmetry line. Each bump test was conducted at least twice, thus the data in Fig. 5 represent the average of multiple tests. The results from both the 3D finite-volume analysis and the 1D approximate technique are shown for comparison. Figure 5 also contains experimental data from Ref. [8] for a similar spherical bump configuration ($k/R=0.92$ for Ref. [8] versus $k/R=0.8$ for the 8 mm bump in the present study) immersed in a turbulent boundary layer ($k/\delta \cong 0.4$ and $\mathrm{Re}_L \cong 500{,}000$ for Ref. [8] versus $k/\delta \cong 0.33$ and $\mathrm{Re}_L \cong 860{,}000$ for the 8 mm bump).

Because of the comparable flow conditions, the data of Henry et al. [8] exhibit strong similarities with the 8 mm bump data. The upstream effect begins at $z/R=-2$ and the augmented heat transfer levels in the wake are nearly matched. Both data sets also show the peak heat transfer on the leading edge at $z/R=-0.5$, with a dip in heat transfer on the leeward side of the bump. The two data sets do not agree on the peak augmentation level ($\mathrm{St}/\mathrm{St}_{\mathrm{flat}}=2.7$ for the present study versus 2.1 from Ref. [8]). This discrepancy may be due to the different experimental methods employed. Henry et al. [8] used a steady-state IR camera measurement of the surface temperature to calculate the heat transfer augmentation due to the bump. By irradiating the surface with a constant heat flux source (heat lamps) and neglecting radiation losses and conduction within the bump, the authors concluded that the perturbed-to-unperturbed heat transfer coefficient ratio ($\mathrm{St}/\mathrm{St}_{\mathrm{flat}}$) was approximately equal to the temperature ratio $(T_{\mathrm{flat}}\text{-}T_{\mathrm{inf}})/(T\text{-}T_{\mathrm{inf}})$ (where $T$ is the local surface temperature and $T_{\mathrm{flat}}$ is the unperturbed surface temperature to the side of the bump).

McClain et al. [13] re-evaluated the assumptions invoked by Henry et al. [8] and used a 2D boundary layer code with a discrete-element model for the extended-surface (bump) to show that conduction within the bump has a non-negligible effect on the $\mathrm{St}/\mathrm{St}_{\mathrm{flat}}$ values calculated by Henry et al. [8] The model results of McClain et al. [13] shown in Fig. 5 exhibit twice the peak heat transfer augmentation of the estimate of Henry et al. [8] by accounting for this (and other) corrections. Because the model of McClain et al. [13] is only 2D, it does not account for St variations around the bump, thus it erroneously produces a symmetric distribution about $z/R=0$. The 3D finite-volume transient IR method used to process the IR data in the present study properly accounts for conduction inside the bump and thus calculates a similarly higher $\mathrm{St}/\mathrm{St}_{\mathrm{flat}}$ ratio than that reported by Henry et al. [8]. Since the bump dimensions and flow conditions used in these two separate studies are not identical, it is not expected that the calculation of McClain et al. [13] should match the present data exactly. However, upon further analysis, two of the assumptions made by McClain et al. [13] are likely to contribute to the overprediction shown in Fig. 5. First, McClain et al. [13] assumed that the momentum in the incident turbulent boundary layer is redirected around the bump but not over it. The local Nusselt number value for a given elevation on the bump is then calculated from the equivalent Reynolds number $[\mathrm{Re}_D=D(y)u(y)/v]$ at the corre-

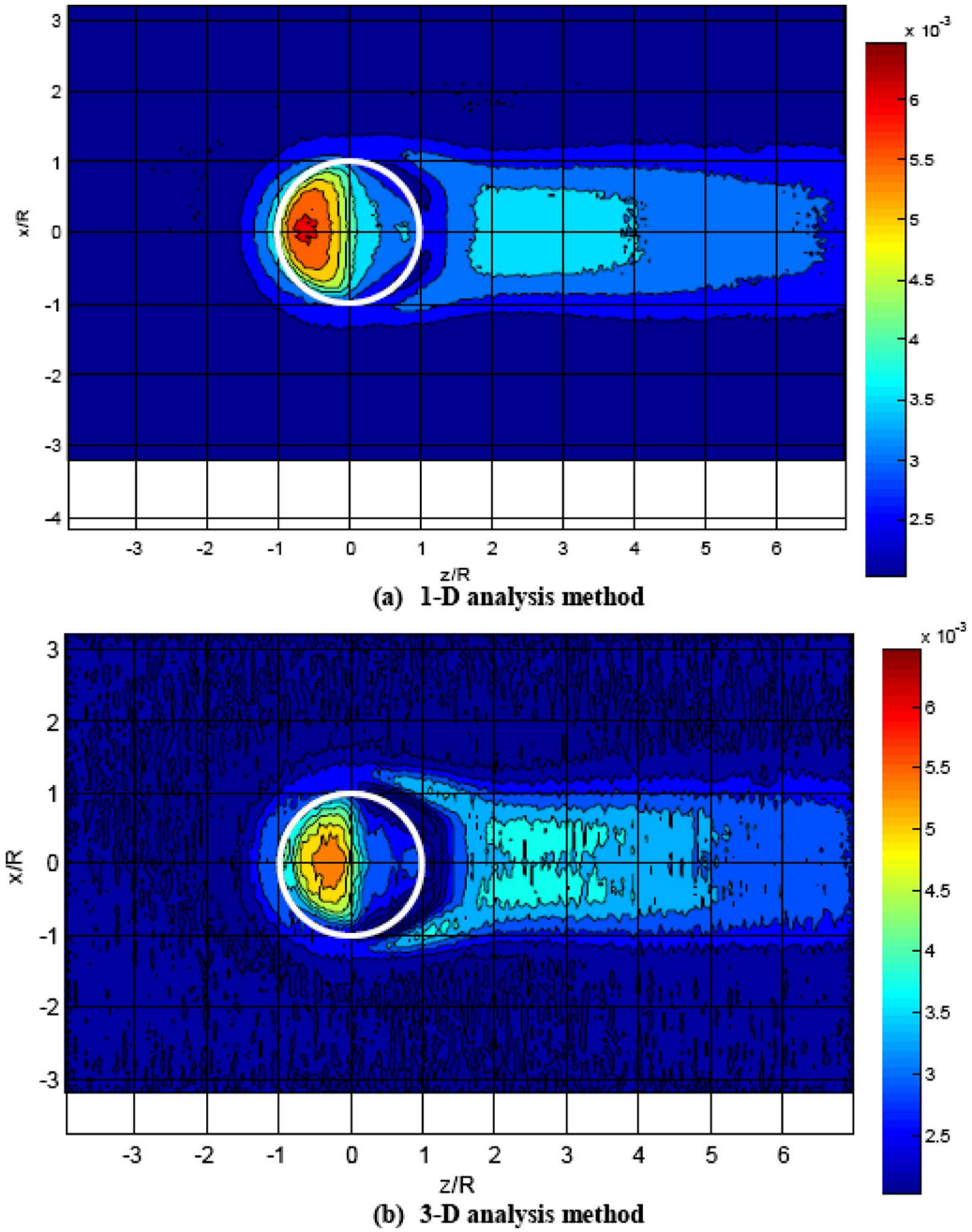


**Fig. 4 Time-averaged (80<$t$<100 s) St maps for 8 mm bump**

sponding height ($y$) on the bump. If properly accounted for, the flow over the bump would tend to reduce the local $Re_D$ at a given elevation due to the three-dimensional relieving effect and thus decrease the predicted $Nu(y)$ (and subsequently $St/St_{flat}$) from the values shown in Fig. 5. Second, McClain et al. [13] approximated the bump as an extended-surface and thus treated only temperature gradients in the wall normal ($y$) direction. This artificially constrains conduction within the bump to occur in the $y$ direction only, creating a greater resistance to heat flow than what actually occurs in the bump. Because the bump is relatively squat ($k/R<1$) compared with a typical extended-surface cooling fin, the heat flow is more three-dimensional and the bump can accommodate more heat flow than a narrow fin. Relaxing this assumption would also reduce the $St/St_{flat}$ predicted by McClain et al. [13] in Fig. 5.

Referring to the 3D method centerline data in Fig. 5, the heat transfer behavior on the leading (windward) half of the bump shows a monotonic (though not linear) increase in St with bump height. Both the heat transfer peak at $z/R=-0.5$ and the upstream influence ($-2<z/R<-1$) increase as the bump height increases from 2 mm to 4 mm to 8 mm. The leeward side of the bump is a region of diffusing flow with potentially separated or stagnant fluid that exhibits a significantly reduced heat transfer compared with the windward surface. For the 2 mm bump, the heat transfer near the trailing edge interface with the smooth-plate is nearly 40% lower than for the unperturbed region ($St/St_{flat}=0.6$). As the bump height is increased to 4 mm and then 8 mm, it is likely that unsteady shedding of vortices in the wake of the bump (the effective Reynolds number $Re_D$ based on the 20 mm bump base diameter is approximately 10,000) is responsible for an increase in

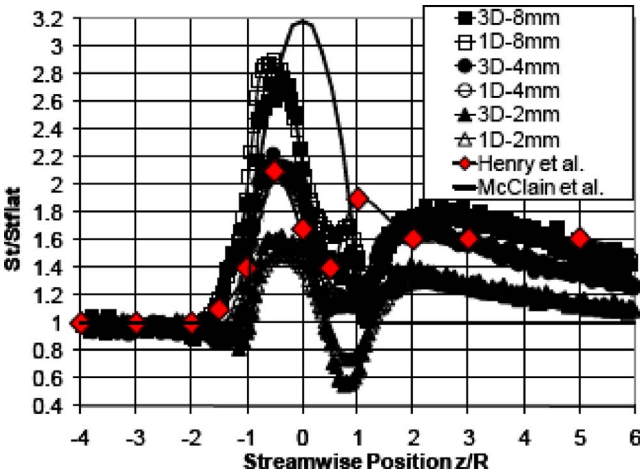


**Fig. 5 Time-averaged (80<*t*<100 s) Stanton number ratio along the bump centerline (*x*/*R*=0) for all three configurations: 3D and 1D method results shown. Also, data from Henry et al. [8] and 2D computation from McClain et al. [13].**

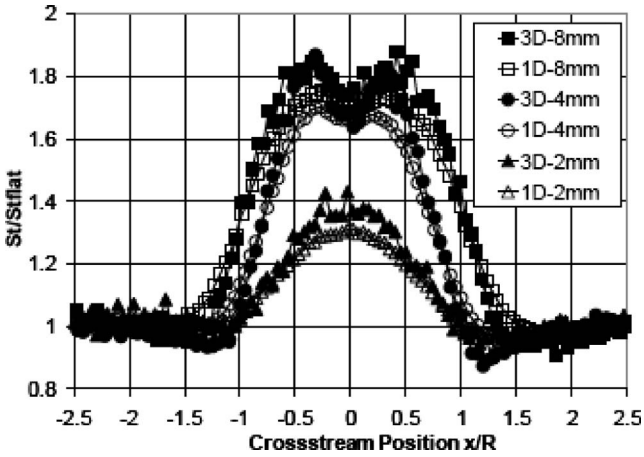


**Fig. 6 Time-averaged (80<*t*<100 s) Stanton number ratio across bump wake (*z*/*R*=2) for all three configurations: 3D and 1D method results shown**

$St/St_{flat}$ above unity. The 8 mm bump leeward heat transfer actually shows a local peak at $z/R=0.8$ before $St/St_{flat}$ drops just below unity immediately after the bump trailing edge. Also, the peak wake augmentation location migrates downstream between the 4 mm and 8 mm data ($z/R=2$–2.5)—indicating a later reattachment point for the separated flow with the larger bump height.

Comparing the 3D and the 1D method results presented in Fig. 5, the 1D analysis deviates from the more accurate 3D analysis primarily in the vicinity of the bump itself. In the bump wake ($z/R>1$), the 1D method underestimates the $St/St_{flat}$ ratio only near the peak of the curves where the temperature gradients are most severe. On the bump itself, the 1D analysis underestimates St at the leading edge peak for the 2 mm bump yet overestimates St in the same region for the 8 mm bump. The leeward drop in St is underestimated by the 1D method for both the 2 mm and 8 mm cases. Curiously, the 4 mm case appears to display no significant difference between the two analysis methods—seemingly rendering the more time-intensive 3D method completely unnecessary. This apparently random variation in the error between the 1D and the 3D methods actually signals the strong interplay between the temperature gradient and the surface angularity effects on the 3D transient conduction analysis. This is easier to see when evaluating the difference between the two analysis methods in a region where only temperature gradients are present, i.e., the bump wake.

Figure 6 shows the heat transfer augmentation ratio ($St/St_{flat}$) for both the 3D and 1D analysis methods along a cross-stream line through the bump wake, one diameter downstream of the bump center ($z/R=2$). The abrupt change in the peak level of heat transfer augmentation between a bump height of 2 mm and 4 mm clearly signals a change in flow behavior. The 2 mm bump resides in the lower 10% of the boundary layer thickness, and the wake is due to incomplete diffusion of the flow as it expands to fill the void behind the leeward face of the bump. The peak heat transfer for the 2 mm bump is at the centerline ($x/R=0$), indicating the region of maximum separation extent before reattachment. By contrast, both the 4 mm and 8 mm bump data exhibit a double peak in heat transfer about the bump centerline. This suggests the existence of secondary flow structures such as horseshoe vortices and/or unsteady vortex shedding such as what occurs behind a cylindrical obstruction protruding from the wall [15].

In all three cases shown in Fig. 6, the 1D approximate method underestimates the peak heat transfer augmentation by 5–10% in regions of steep temperature gradients. The reason for this error was identified in the Part I paper [12]. Essentially, a local surface hot spot (e.g., due to a wake unsteadiness) will create a higher temperature in the cell just beneath the surface. In the 3D analysis, this will in turn establish gradients for lateral heat flow to the cooler neighboring $(j\pm1,k\pm1)$ cells. By conservation of energy, these lateral conduction losses must be offset by higher $q_s$ from the surface (to maintain the higher temperature of the hot spot). Thus, accounting for the lateral conduction produces a higher local St estimate. The 1D heat flow model does not include these lateral "losses" and thus underpredicts the surface heat flux to the hot spots for the same surface temperature history. This effect only occurs in regions where the local St gradient is changing rapidly with $x$ (or $z$). For such cases, the $\partial^2T/\partial x^2$ and $\partial^2T/\partial z^2$ terms neglected in the 1D transient conduction analysis presented in the Part I companion paper are significant enough to warrant consideration. As a rule of thumb, for both the 4 mm and 8 mm bumps, a 75% change in St predicted by the 1D method over one bump radius (10 mm) produces a 10% maximum error between the 1D approximate technique and the more complex 3D analysis. The 2 mm data suggest that with only half of that St increase (30%), the maximum error is roughly halved as well (5%).

When the lateral conduction and the curved bump surface are both properly accounted for in the transient IR analysis, the two effects on St estimation are competing. In regions of steep temperature (heat transfer) gradients, such as the bump leading edge, the 1D analysis would be expected to underestimate the local St as it did in the bump wake (Fig. 6). However, accounting for the protrusion from the surface has the effect of isolating the finite-volume cells that are located in the bump. With a more constrained lateral conduction path, the effect of lateral conduction is muted. In addition, when accounting for the curved surface topology, the surface temperature history is imposed over a larger surface area than in the flat-surface 1D analysis. This contributes to a higher initial heat load ($Q=qA$) into each of the surface cells on the bump. This additional $Q$ must be conducted into the solid with the same thermal properties ($\alpha$) as the 1D method. Consequently, the additional $Q$ gets restrained in the first few cells near the surface and, the 3D finite-volume method calculates a lower $q_s$ than the approximate 1D model using the same $T_s$ data. In essence, the temperature of the first few layers of cells in the bump increases more rapidly due to the larger net $Q$ in the 3D model. Thus, it would take an even more rapid transient $T(t)$ increase on the curved bump to yield the same $q_s$ prediction as for the flat-surface 1D analysis.

This effect is illustrated in Fig. 7, which includes a 3D finite-volume calculation result obtained using a completely flat-surface (i.e., neglecting the surface curvature of the bump altogether) compared with the 8 mm results repeated from Fig. 5. As ex-

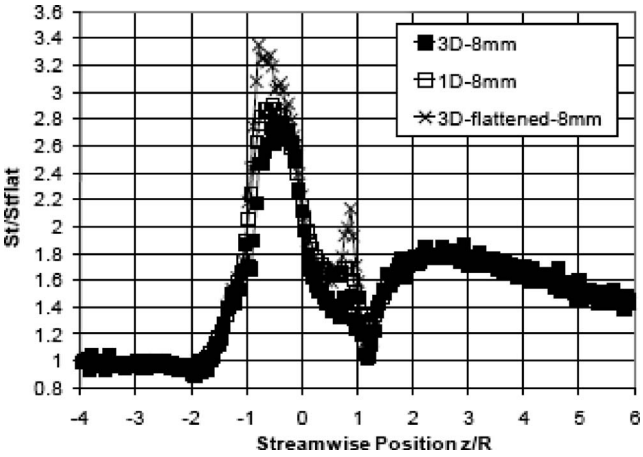


**Fig. 7 Time-averaged ($80 < t < 100$ s) Stanton number ratio along the bump centerline ($x/R=0$) for 8 mm bump: 1D method results compared with 3D with and without accounting for bump curvature**

pected, since this "flattened" calculation only accounts for lateral conduction effects, it estimates a higher peak $St/St_{flat}$ ratio compared with the 1D approximate technique (similar to the wake result in Fig. 6). The "error" (i.e., the difference between the approximate 1D result and the flattened 3D result) is as high as 40% in the region $-1 < z/R < -0.5$ where the temperature map (Fig. 3) shows the steepest gradients. When the bump curvature is accounted for, the result is a dramatic drop in the estimated St in regions of high surface angularity (i.e., $-1 < z/R < -0.5$). For the 8 mm bump, the effect is large enough to drop from the flattened 3D St result to below the 1D method result. Revisiting the data in Fig. 5, it appears that the surface angularity has little effect for the 2 mm bump whereas at 4 mm, the angularity effect almost exactly cancels the thermal gradient effect. This makes the 1D method result for the 4 mm bump appear to be reasonably accurate over much of the bump topography. Because of this conflict between these two effects, it is difficult to identify a precise quantitative criterion for use of the 1D approximate method. For the case of an isolated bump with 8 mm height and 10 mm base radius (with maximum surface angularity greater than 60 deg), the 1D method yields errors on the order of 20–30% over much of the bump surface. In the opinion of these authors, errors of this magnitude warrant the added time and complexity of a full 3D analysis. The errors for the smaller bump heights would be considered acceptable and the much faster (greater than two orders of magnitude) processing time is welcome.

Though all of the preceding discussion focused on the discrepancies between the two processing techniques at local peaks in heat transfer, errors of similar magnitude (but opposite sign) are evident at low points in the St data for Figs. 5–7. Also, with reference to the discussion in the Part I companion paper regarding the appropriate "area-adjusted" St augmentation for rough surfaces, the heat transfer augmentation provided by the 8 mm bump is 16% if the transient temperature data is processed using the 1D approximate method compared with 24% using the more accurate 3D finite-volume processing method. This augmentation value is obtained by multiplying the area-averaged St by the wetted-to-planform surface area and comparing it to the unperturbed St.

A final observation regards differences between the lateral conduction correction for transient and steady-state IR techniques. As noted in Fig. 5, when McClain et al. [13] accounted for lateral conduction effects on the bump in the study of Henry et al. [8], the predicted convective heat transfer was higher. This result is opposite to that shown for the present transient IR study, where the 8 mm bump heat transfer prediction is lower when accounting for 3D conduction effects. An evaluation of this apparent contradiction requires a careful analysis of the two competing effects already outlined in this paper. For example, when considering surface temperature gradients on a flat-surface, the transient method yielded a higher heat transfer estimate for a 3D analysis compared with a 1D analysis (Fig. 6). This is because the surface heat flux at a local hot spot is not conducted exclusively normal to the surface—some fraction being conducted laterally. Thus, the transient 3D conduction analysis predicts a higher surface heat flux to account for both the lateral and the normal conductions. In a steady-state experiment with a uniform surface heat flux boundary condition, the opposite is true. Henry et al. [8] produced a uniform surface heat flux input using heat lamps above their test plate. In their subsequent analysis, they assumed that the input radiative heat flux was exactly equal to the convective heat flux from the surface into the constant temperature fluid flow. Thus, accounting for lateral conduction losses from a local hot spot would reduce the predicted convective heat transfer since convection and conduction must sum to equal the input radiation.

When the 3D bump surface is considered in the transient technique, the added surface area and the relative isolation of the extended-surface result in an accumulation of energy in the surface protrusion. Thus, the transient 3D analysis would require a more aggressive temperature history on the bump to yield the same surface heat flux prediction as a transient 1D analysis. Again, in a steady-state experiment the opposite is true. McClain showed that in steady-state mode the isolation of the bump yields a reduced conduction correction in the extended-surface and consequently a higher predicted convective heat transfer when accounting for 3D effects. For the 8 mm bump in the present transient IR study, the bump effect dominates the temperature gradient effect, and the 3D St prediction on the bump is lower than the 1D prediction. Since both effects are opposite in the steady-state experiment of Henry et al. [8], the conduction correction of McClain et al. [13] produces a higher convective heat transfer estimate on the bump compared with the estimate of Henry et al. [8] (Fig. 5). This highlights the importance of accounting for 3D conduction effects for *both* transient and steady-state techniques if accurate spatial resolution of heat transfer measurements near complex three-dimensional geometries is desired (e.g., near film cooling holes [16]).

## 5 Summary and Conclusions

The effect of lateral conduction on convective heat transfer predictions using the transient infrared technique over a spherical bump is evaluated. Comparisons are made between a full 3D finite-volume analysis and a simpler 1D transient conduction model. Based on the analysis, the following conclusions are made.

1. When considering only transient conduction effects in the bump wake, the 1D approximate method underestimates the actual peak Stanton number calculated using the more accurate 3D model by only 10% for a 75% change in St number occurring over a surface distance of 10 mm (the half-width of the bump wake).
2. When the surface curvature of the bump is accounted for in estimating the Stanton number on the bump itself with the 3D analysis technique, the increased surface area of the finite-volume cells on the protruding bump actually decreases the predicted St locally. The net result being that the two effects can cancel each other, and in some cases the 1D approximate technique can provide a reasonably accurate estimate of the surface heat transfer without the added complexity of the 3D finite-volume method. Because of the nonlinear interaction between these two effects, it is difficult to establish precise quantitative criteria for the accurate use of the simpler 1D analysis technique on arbitrary three-dimensional surface features. For the case of the 8 mm bump, with maximum surface angularity exceeding 60 deg, the 1D St estimate is within 20–30% of the 3D estimate over

much of the bump surface. For the much more irregular roughness surface studied in the Part I companion paper, the 1D estimate was up to 40% lower than the 3D estimate on the most abrupt roughness peaks.

3. The above observations for the transient IR technique are opposite those found when accounting for 3D conduction effects using a steady-state IR measurement technique. In that case, temperature gradients on a flat-surface reduce the predicted convective heat transfer, and extended-surfaces (bumps) increase the predicted convective heat transfer.

## Acknowledgment

The authors would like to acknowledge the able assistance of Nathan Rhead in acquiring the data and conducting numerous tests, and the expert design and machining accomplished by Ken Forster in support of this research.

## Nomenclature

$A$ = finite-volume cell surface area
$D$ = diameter
$L$ = distance from the wind tunnel leading edge to bump center
$Q$ = heat flux
$R$ = bump base radius
$\mathrm{Re}_L$ = Reynolds number ($U_\infty L/\upsilon$)
St = Stanton Number, $h_c/(\rho c_p U_\infty)$
$T$ = temperature
$U$ = velocity
$c_p$ = specific heat at constant pressure
$h_c$ = convective heat transfer coefficient
$k$ = bump height
$q$ = heat flux per unit area
$t$ = time
$u$ = streamwise velocity
$x$ = cross-stream direction along surface
$y$ = surface normal direction
$z$ = streamwise direction along surface
$\delta$ = boundary layer thickness
$\kappa$ = thermal conductivity
$\upsilon$ = kinematic viscosity
$\rho$ = density

### Subscripts

flat = unperturbed (smooth-wall) value
inf or $\infty$ = freesteam value
mean = average value
rms = root mean square
$s$ = solid surface adjacent to fluid

## References

[1] Nikuradse, J., 1933, "Laws for Flows in Rough Pipes," *VDI-Forchungsheft 361, Series B*, Vol. 4 (English Translation NACA, TM-1292, 1950).
[2] Bammert, K., and Sandstede, H., 1980, "Measurements of the Boundary Layer Development Along a Turbine Blade With Rough Surfaces," ASME J. Eng. Power, **102**, pp. 978–983.
[3] Turner, A., Tarada, F., and Bayley, F., 1985, "Effects of Surface Roughness on Heat Transfer to Gas Turbine Blades," Paper No. AGARD-CP-390, p. 9.
[4] Goldstein, R., Eckert, E., Chiang, H., and Elovic, E., 1985, "Effect of Surface Roughness on Film Cooling Performance," ASME J. Eng. Gas Turbines Power, **107**, pp. 111–116.
[5] Pinson, M. W., and Wang, T., 1997, "Effects of Leading Edge Roughness on Fluid Flow and Heat Transfer in the Transitional Boundary Layer Over a Flat Plate," Int. J. Heat Mass Transfer, **40**(12), pp. 2813–2823.
[6] Taylor, R. P., Scaggs, W. F., and Coleman, H. W., 1988, "Measurement and Prediction of the Effects of Nonuniform Surface Roughness on Turbulent Flow Friction Coefficients," ASME J. Fluids Eng., **110**, pp. 380–384.
[7] Hosni, M. H., Coleman, H. W., and Taylor, R. P., 1991, "Measurements and Calculations of Rough-Wall Heat Transfer in the Turbulent Boundary Layer," Int. J. Heat Mass Transfer, **34**(4/5), pp. 1067–1082.
[8] Henry, R. C., Hansman, R. J., and Breuer, K. S., 1995, "Heat Transfer Variation on Protuberances and Surface Roughness Elements," J. Thermophys. Heat Transfer, **9**(1), pp. 175–180.
[9] Scaggs, W. F., Taylor, R. P., and Coleman, H. W., 1988, "Measurement and Prediction of Rough Wall Effects on Friction Factor: Uniform Roughness Results," ASME J. Fluids Eng., **110**, pp. 385–391.
[10] Bogard, D. G., Schmidt, D. L., and Tabbita, M., 1998, "Characterization and Laboratory Simulation of Turbine Airfoil Surface Roughness and Associated Heat Transfer," J. Turbomach., **120**(2), pp. 337–342.
[11] Barlow, D. N., and Kim, Y. W., 1995, "Effect of Surface Roughness on Local Heat Transfer and Film Cooling Effectiveness," presented at the ASME International Gas Turbine Exposition in Houston, Houston, Texas, Jun., ASME, Paper No. 95-GT-14.
[12] Bons, J. P., 2009, "Transient Method for Convective Heat Transfer Measurement With Lateral Conduction—Part I: Application to a Deposit-Roughened Gas Turbine Surface," ASME J. Heat Transfer, **131**(1), p. 011301.
[13] McClain, S. T., Vargas, M., Kreeger, R. E., and Tsao, J.-C., 2007, "Heat Transfer From Protuberances," J. Thermophys. Heat Transfer, **21**(2), pp. 337–345.
[14] Coleman, H. W., Moffat, R. J., and Kays, W. M., 1981, "Heat Transfer in the Accelerated Fully Rough Turbulent Boundary Layer," ASME J. Heat Transfer, **103**, pp. 153–158.
[15] Sabatino, D. R., and Smith, C. R., 2007, "Boundary Layer Influence on the Unsteady Horseshoe Vortex Flow and Surface Heat Transfer," ASME Paper No. GT2007-27633.
[16] Waye, S. K., and Bogard, D. G., 2007, "High-Resolution Film Cooling Effectiveness Measurements of Axial Holes Embedded in a Transverse Trench With Various Trench Configurations," ASME J. Turbomach., **129**, pp. 294–302.

# Simple Explicit Equations for Transient Heat Conduction in Finite Solids

**A. G. Ostrogorsky**
Department of Mechanical Aerospace and Nuclear Engineering,
and Department of Materials Science and Engineering,
Rensselaer Polytechnic Institute,
Troy, NY 12211

*Based on the one-term Fourier series solution, a simple equation is derived for low Biot number transient conduction in plates, cylinders, and spheres. In the $0<Bi<0.3$ range, the solution gives approximately three times less error than the lumped capacity solution. For asymptotically low values of Bi, it approaches the lumped capacity solution. A set of equations valid for $0<Bi<1$ is developed next. These equations are more involved but give approximately ten times lower error than the lumped capacity solution. Finally, a set of broad-range correlations is presented, covering the $0<Bi<\infty$ range with less than 1% error.* [DOI: 10.1115/1.2977540]

*Keywords: transient, conduction, diffusion, Fourier series, eigenvalues*

## 1 Introduction

In many important heat and mass transfer problems, the surface of finite solids is exposed to the surroundings at a uniform temperature and concentration, respectively. The early engineering problems included burning of bricks, steaming of wood, and vulcanization of rubber. In most problems, the heat transfer coefficient $h$ ($W/m^2 K$) and the related Biot number

$$\mathrm{Bi} = \frac{hL}{k} = \text{finite}$$

are finite and can be assumed to be uniform. In the Biot number, $k$ (W/m K) is the thermal conductivity and $L$ is the characteristic length.

The solutions to the transient conduction in large plates, long cylinders, and spheres with symmetric convection boundary conditions are known since 1822 [1]. The solution is comprised of Fourier infinite series, which are difficult to evaluate, although the series converge rapidly. For

$$\mathrm{Fo} \equiv \frac{\alpha t}{L^2} > 0.2$$

where Fo is the Fourier number, $\alpha$ ($m^2/s$) is thermal diffusivity, $t$ (s) is time, only one term is needed. The key obstacle to using the Fourier's solutions are the eigenvalues. For finite Bi, the boundary condition of the third kind yields transcendental implicit eigenvalue equations that have to be solved numerically or graphically. Therefore, in most heat transfer textbooks, eigenvalues are tabulated as a function of Bi.

Because of the importance of the problem, a number of charts have been developed to provide a graphical solution of the Fourier equations. In 1947 Heisler [2] published a set of semilog charts, valid for $0.2 \leqslant \mathrm{Fo} < \infty$, which has been reproduced in most heat transfer textbooks and has been widely used by students and practitioners.

Empirical correlations are usually more accurate than the semilog charts and are more convenient for use in design and analysis than tabulations and complex analytical results [3]. Several explicit approximations of the transcendental eigenvalue equations have been proposed. Luikov [4] established that a plot of $\ln[\mu_1(\mathrm{Bi}\to\infty)/\mu_1(\mathrm{Bi})-1]$ versus $\log(\mathrm{Bi})$ yields nearly a straight line, giving the following approximation:

$$\mu_1 = \mu_{1,\infty}\left[\frac{1}{1+A/\mathrm{Bi}^k}\right]^{1/2} \tag{1}$$

where $\mu_{1,\infty}$ are the asymptotic values for $\mathrm{Bi}\to\infty$, $\mu_{1,\infty}=\pi/2$ for the plate, $\mu_{1,\infty}=2.4048$ for cylinder, and $\mu_{1,\infty}=\pi$ for the sphere. By fitting the straight line to the exact values, he obtained the following constants: (i) $A=2.24$ and $k=1.02$ for plates (ii) $A=2.45$ and $k=1.04$ for cylinders, and (iii) $A=2.7$ and $k=1.07$ for spheres. Beck et al. [5] provided an accurate yet more involved approximation for $\mu_1$, valid for flat plates and $\mathrm{Bi}<2$. Yovanovich [6] used the general expression of Churchill and Usagi [3],

$$Y = (1+Z^n)^{1/n} \tag{2}$$

with

$$Y \equiv \frac{y(z)}{y(z\to 0)}$$

$$Z \equiv \frac{y(z\to\infty)}{y(z\to 0)}$$

for correlating functions $y(z)$ that have asymptotically small and large values of the independent variable $z$. Yovanovich obtained

$$\mu_1 = \frac{\mu_{1,\infty}}{\left[1+\left(\frac{\mu_{1,\infty}}{\mu_{1,0}}\right)^n\right]^{1/n}} \tag{3}$$

where $\mu_{1,0}$ is the asymptotic value of the first eigenvalues for $\mathrm{Bi}\to 0$, $\mu_{1,0}=\sqrt{\mathrm{Bi}}$ for plates, $\mu_{1,0}=\sqrt{2\mathrm{Bi}}$ for cylinders, and $\mu_{1,0}=\sqrt{3\mathrm{Bi}}$ for spheres. The constant $n$ was determined by fitting the above equation to the exact eigenvalues. Yovanovich determined $n=2.139$ for plates, $n=2.238$ for cylinders, and $n=2.314$ for spheres. Recently, Ostrogorsky and Mikic [7] used the successive substitution method to derive a set of explicit expressions for $\mu_1$ for plates, cylinders, and spheres valid for $0<\mathrm{Bi}<\infty$.

For $\mathrm{Bi}\ll 1$, temperature gradients within solids are considered negligible, so that the lumped capacity solution provides an explicit expression for transient temperature,

Contributed by the Heat Transfer Division of ASME for publication in the JOURNAL OF HEAT TRANSFER. Manuscript received December 7, 2007; final manuscript received June 10, 2008; published online October 17, 2008. Review conducted by A. Haji-Sheikh.

  

$$\frac{T-T_f}{T_i-T_f}=\frac{\theta(t)}{\theta_i}=e^{-(hA/\rho cV)t}=e^{-(hL/k)(\alpha t/L)(A/V)}=e^{-\mathrm{Bi}(\alpha t/L)(A/V)}$$

where $T_i$ is the initial temperature and $T_f$ is the temperature of the surrounding fluid. The transient temperature $\theta(t)/\theta_i$ is function of Fo and Bi. $A/V$ is the surface to volume ratio of the solid. For a $2L$ plate, the surface to volume ratio is $A/V=1/L$, resulting in

$$\frac{\theta(t)}{\theta_i}=e^{-\mathrm{BiFo}} \tag{4}$$

For a long cylinder having radius $R$, $A/V=2/R$, yielding

$$\frac{\theta(t)}{\theta_i}=e^{-2\mathrm{BiFo}} \tag{5}$$

For a sphere having radius $R$,

$$\frac{\theta(t)}{\theta_i}=e^{-3\mathrm{BiFo}} \tag{6}$$

since $A/V=3/R$. Incropera and De Witt [8] advised that the error associated with using the lumped capacitance model is small for $\mathrm{Bi}<0.1$.

Here, we convert the one-term Fourier series solutions into a set of approximate explicit equations, which provide the transient temperature profiles in plates, cylinders, and spheres. The transient temperature profiles can be evaluated without the use of numerical procedures. We derive

(a) a low Biot number approximation, which is almost as simple as the lumped capacity solution yet accounts for spatial variation and thus is more accurate
(b) a more complex broad-range approximation valid for $\mathrm{Fo}>0.2$ and $0<\mathrm{Bi}<\infty$

We will consider only one-dimensional transients since the multidimensional problems can be readily split into one-dimensional ones using the separation of variables.

## 2 Low Biot Number Solution

**2.1 Large Plate With $2L$ Thickness.** The mathematical formulation of the problem is

$$\frac{1}{\alpha}\frac{\partial\theta}{\partial t}=\frac{\partial^2\theta}{\partial x^2}$$

where $\theta=T-T_f$. The boundary conditions are

$$\mathrm{BC}(1):-k\frac{\partial\theta(L,t)}{\partial x}=h\theta(L,t)$$

$$\mathrm{BC}(2):\frac{\partial\theta(0,t)}{\partial x}=0$$

The initial condition is

$$\mathrm{IC}:\theta(x,0)=\theta_i$$

Fourier's infinite series solution is

$$\frac{\theta(t,x)}{\theta_i}=2\sum_{n=1}^{\infty}\frac{\sin\mu_n}{\mu_n+\sin\mu_n\cos\mu_n}\cos(\mu_n\xi)e^{-\mu_n{}^2\mathrm{Fo}} \tag{7}$$

where $\xi=x/L$ and $\mu_n=\lambda_n L$ is a product of the eigenvalues $\lambda_n$ and the plate thickness, defined by the transcendental equation,

$$\mu_n\tan\mu_n=\mathrm{Bi} \tag{8}$$

However, for $\mathrm{Fo}\geqslant 0.2$ [2] Eq. (7) may be approximated by one term. Hence,

$$\mu_1\tan\mu_1=\mathrm{Bi} \tag{9}$$

and

$$\frac{\theta(t,x)}{\theta_i}=2\frac{\sin\mu_1}{\mu_1+\sin\mu_1\cos\mu_1}\cos\left(\mu_1\frac{x}{L}\right)e^{-\mu_1{}^2\mathrm{Fo}} \tag{10}$$

or

$$\frac{\theta(t,x)}{\theta_i}=B_{\mathrm{plate}}\cos\left(\mu_1\frac{x}{L}\right)e^{-\mu_1{}^2\mathrm{Fo}} \tag{11}$$

where $B_{\mathrm{plate}}$ is the Fourier coefficient,

$$B_{\mathrm{plate}}=2\frac{\sin\mu_1}{\mu_1+\sin\mu_1\cos\mu_1} \tag{12}$$

For $\mathrm{Fo}=0.25$, the error is approximately 1%, depending on Bi and $x/L$. The key obstacle to getting $\theta(t,x)/\theta_i$ is $\mu_1$, which accounts for the boundary conditions and thus contains the Biot number. Equation (9) is an implicit transcendental equation whose solution requires iterations.

*2.1.1 Transient Temperature $\theta(t,x)/\theta_i$ in a $2L$ Plate.* An explicit form of Eq. (9) can be obtained by expanding the tangent,

$$\tan(\mu_1)=\mu_1+\frac{\mu_1{}^3}{3}+\frac{2\mu_1{}^5}{15}+\cdots$$

and, for small $\mu_1$,

$$\tan(\mu_1)=\mu_1 \tag{13}$$

For small $\mu_1$, Eqs. (13) and (9) yield [4]

$$\mu_1=\sqrt{\mathrm{Bi}} \tag{14}$$

Because of Eq. (13), the error in Eq. (14) grows with Bi to 1.65% for $\mathrm{Bi}=0.1$ and to 4.98% for $\mathrm{Bi}=0.3$. Next we simplify the $B_{\mathrm{plate}}$ by expanding sin and cos for small values of $x$ [9],

$$\sin(x)=x-\frac{x^3}{3!}+\frac{x^5}{5!}-\cdots \tag{15}$$

$$\cos(x)=1-\frac{x^2}{2!}+\frac{x^4}{4!}\cdots \tag{16}$$

Equation (12) is approximated as

$$B_{\mathrm{plate}}\approx\frac{1}{1-\mathrm{Bi}/4}$$

Since for small $\varepsilon$,

$$\frac{1}{1-\varepsilon}\approx 1+\varepsilon \tag{17}$$

one gets

$$B_{\mathrm{plate}}\approx 1+\frac{\mathrm{Bi}}{4} \tag{18}$$

and

$$\frac{\theta(t,x)}{\theta_i}=\left(1+\frac{\mathrm{Bi}}{4}\right)\cos\left(\mu_1\frac{x}{L}\right)e^{-\mu_1{}^2\mathrm{Fo}} \tag{19}$$

Now using Eq. (14) gives

$$\frac{\theta(t,x)}{\theta_i}=\left(1+\frac{\mathrm{Bi}}{4}\right)\cos\left(\sqrt{\mathrm{Bi}}\frac{x}{L}\right)e^{-\mathrm{BiFo}} \tag{20}$$

Finally using Eq. (16) again,

$$\frac{\theta(t,x)}{\theta_i}=\left(1+\frac{\mathrm{Bi}}{4}\right)\left[1-\frac{\mathrm{Bi}}{2}\left(\frac{x}{L}\right)^2\right]e^{-\mathrm{BiFo}} \tag{21}$$

one gets an explicit equation, nearly as simple as the lumped system equation.

Figure 1(*a*) shows the transient temperature calculated using Eqs. (20) and (21) together with the the exact Fourier series solution and the lumped capacity model (Eq. (4)). Equations (20) and

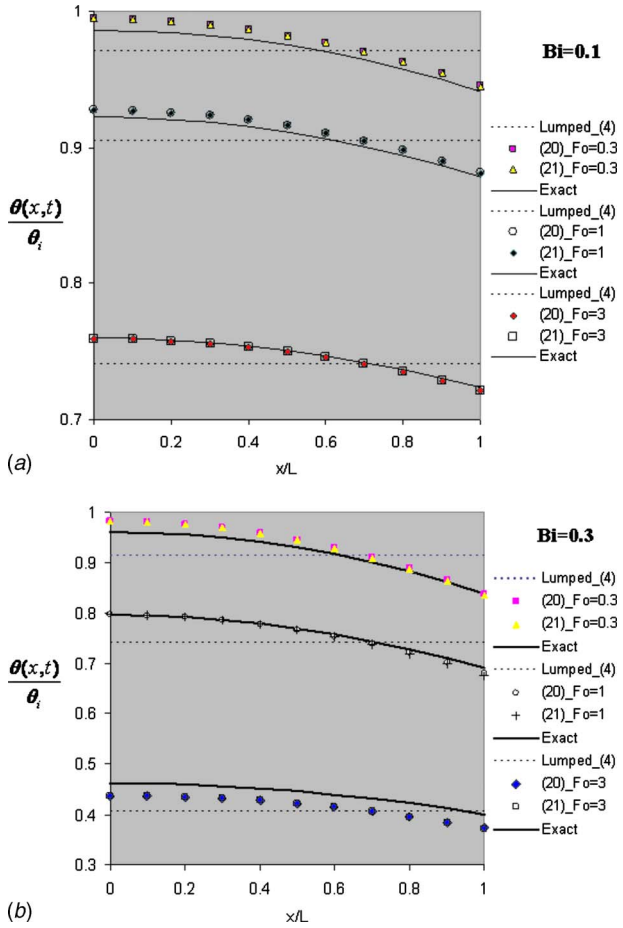


**Fig. 1 Transient temperature $\theta(x,t)/\theta_i$ in 2$L$ plates calculated using Eqs. (20) and (21) together with the exact five-term Fourier series solution (full lines) and the lumped capacity solution (Eq. (4)), dashed lines. (*a*) Bi=0.1. (*b*) Bi=0.3.**

(21) overlap, giving a less than 0.86% $\theta_i$ error for Bi=0.1.

Figure 1(*b*), shows $\theta(x,t)/\theta_i$ calculated for Bi=0.3, which is at the border of the low Bi number approximation. The highest error is less than 2.88% $\theta_i$ (for Fo=3 at the centerline). The lumped capacity solution provides the highest error of 7.6% $\theta_i$. Since there is no notable difference in accuracy between Eqs. (20) and (21), the simpler Eq. (21) should be used.

*2.1.2 Total Energy Released $Q(t)/Q_0$ From a Plate.* The total energy content of the plate that can be removed by heat transfer into the surroundings at $T_f$ is

$$Q_0 = AL\rho c(T_i - T_f) \tag{22}$$

Spatial integration of the temperature profile over the volume defines the energy that remains in the solid that can be removed by heat transfer. Then, the exact solution for the dimensionless heat loss $Q(t)/Q_0$ is obtained as:

$$\frac{Q(t)}{Q_0} = 1 - n\int_0^1 \frac{\theta(u,t)}{\theta_i} u^{n-1} du \tag{23}$$

In the above, $u$ is a dimensionless spatial coordinate ($x/L$ for slab, $r/R$ for cylinder and sphere) and $n$ is 1 for slab, 2 for cylinder, and 3 for sphere. For a 2$L$ plate, the result of the integration is

$$\frac{Q(t)}{Q_o} = 1 - 2\sum_0^n \frac{\sin^2(\mu_n)}{\mu_n(\mu_n + \sin\mu_n\cos\mu_n)} e^{-\mu_n{}^2\mathrm{Fo}} \tag{24}$$

Equation (24) decays rapidly with time, so that one term can be used for Fo$>$0.2 [2]. In contrast, the published solution for the dimensionless heat loss $Q(t)/Q_0$ [8,10,11]

$$\frac{Q(t)}{Q_0} = 2\sum_{n=1}^{\infty} \frac{\sin^2(\mu_n)}{\mu_n(\mu_n + \sin\mu_n\cos\mu_n)}(1 - e^{-\mu_n{}^2\mathrm{Fo}}) \tag{25}$$

yields an erroneous one-term approximation if Bi$\gg$0 (even though Fo$>$0.2). For Bi$>$0, Eq. (24) is equal to Eq. (25) only in the infinite series form. The one-term approximation of Eq. (24) is

$$\frac{Q(t)}{Q_0} = 1 - 2\frac{\sin^2\mu_1}{\mu_1(\mu_1 + \sin\mu_1\cos\mu_1)} e^{-\mu_1{}^2\mathrm{Fo}}$$

or

$$\frac{Q(t)}{Q_0} = 1 - C_{\mathrm{plate}} e^{-\mu_1{}^2\mathrm{Fo}} \tag{26}$$

where

$$C_{\mathrm{plate}} = 2\frac{\sin^2\mu_1}{\mu_1(\mu_1 + \sin\mu_1\cos\mu_1)} \tag{27}$$

Since $\sin\sqrt{\mathrm{Bi}} \approx \sqrt{\mathrm{Bi}}$ and $\cos\sqrt{\mathrm{Bi}} \approx 1$,

$$C_{\mathrm{plate}} \approx 1$$

$C_{\mathrm{plate}}$ has a narrow span between the two asymptotic limits: $C_{\mathrm{plate}}(\mathrm{Bi}\to 0)=1$ and $C_{\mathrm{plate}}(\mathrm{Bi}\to\infty)=0.8106$. Therefore, at Bi=0.3, $C_{\mathrm{plate}}$ is equal to 0.99827, bringing a less than 0.2% error into

$$\frac{Q(t)}{Q_0} = 1 - e^{-\mathrm{BiFo}} \tag{28}$$

**2.2 Long Cylinder With Radius *R*.** Using $\theta(r,t)=T(r,t)-T_i$ and $\theta_f=T_f-T_i$, the mathematical formulation of the problem is

$$\frac{1}{\alpha}\frac{\partial\theta}{\partial t} = \frac{1}{r}\frac{\partial}{\partial r}\left(r\frac{\partial\theta}{\partial r}\right) \tag{29}$$

with

$$\frac{\partial\theta(t,0)}{\partial r} = 0$$

$$-k\left.\frac{\partial\theta(t,r)}{\partial r}\right|_{r=R} = h\theta_S$$

$$\theta(0,r) = \theta_i$$

The temperature field in the infinite cylinder is

$$\frac{\theta(t,r)}{\theta_i} = 2\sum_{n=1}^{\infty} \frac{\mathrm{Bi}}{(\mu_n{}^2 + \mathrm{Bi}^2)} \frac{J_0\left(\mu_n\frac{r}{R}\right)}{J_0(\mu_n)} e^{-\mu_n{}^2\mathrm{Fo}} \tag{30}$$

where $\mathrm{Fo}=\alpha t/R^2$, $\mathrm{Bi}=hR/k$ and, $\mu_n=\lambda_n R$ are roots of the transcendental equation,

$$\mu_n J_1(\mu_n) - \mathrm{Bi}J_0(\mu_n) = 0$$

The one-term approximation of Eq. (30) is

$$\frac{\theta(t,r)}{\theta_i} = 2\frac{\mathrm{Bi}}{(\mu_1^2 + \mathrm{Bi}^2)} \frac{J_0\left(\mu_1\frac{r}{R}\right)}{J_0(\mu_1)} e^{-\mu_1{}^2\mathrm{Fo}} \tag{31}$$

or

$$\frac{\theta(t,r)}{\theta_i} = B_{\text{cylinder}} J_0\left(\mu_1 \frac{r}{R}\right) e^{-\mu_1^2 \text{Fo}} \tag{32}$$

where

$$B_{\text{cylinder}} = \frac{2\text{Bi}}{(\mu_1^2 + \text{Bi}^2) J_0(\mu_1)} \tag{33}$$

and

$$\mu_1 J_1(\mu_1) = J_0(\mu_1)\text{Bi} \tag{34}$$

*2.2.1 Transient Temperature in 2R Cylinders.* For small values of $\mu_1$ and Bi,

$$J_0(\mu_1) = 1 - \frac{(\mu_1/2)^2}{(1!)^2} + \frac{(\mu_1/2)^4}{(2!)^2} - \cdots = 1 - \frac{\mu_1^2}{4} + \frac{\mu_1^4}{64} - \cdots \tag{35}$$

$$J_1(\mu_1) = \frac{\mu_1}{2} - \left(\frac{\mu_1/2}{1!2!}\right)^3 + \left(\frac{\mu_1/2}{2!3!}\right)^5 \cdots = \frac{\mu_1}{2} - \frac{\mu_1^3}{16} + \frac{\mu_1^5}{386} - \cdots \tag{36}$$

Using the first terms of Eqs. (35) and (36) and in Eq. (34) gives the expression [4]

$$\mu_1 = \sqrt{2\text{Bi}} \tag{37}$$

Now using Eq. (37) in Eq. (33) yields

$$B_{\text{cylinder}} = \frac{1}{1 - \text{Bi}/2} \approx 1 + \frac{\text{Bi}}{2} \tag{38}$$

A comparison to the exact solution shows that the approximation used for the plates,

$$B_{\text{cylinder}} \approx 1 + \frac{\text{Bi}}{4} \tag{39}$$

is more precise. At Bi=0.3, Eq. (39) gives $B_{\text{cylinder}}=1.0750$, while the exact value is 1.0711. Thus,

$$\frac{\theta(t,r)}{\theta_i} = \left(1 + \frac{\text{Bi}}{4}\right) J_0\left(\mu_1 \frac{r}{R}\right) e^{-\mu_1^2 \text{Fo}} \tag{40}$$

and using Eq. (37),

$$\frac{\theta(t,r)}{\theta_i} = \left(1 + \frac{\text{Bi}}{4}\right) J_0\left(\sqrt{2\text{Bi}} \frac{r}{R}\right) e^{-2\text{BiFo}} \tag{41}$$

Using the two-term approximation of $J_0(\mu_1)$ gives

$$\frac{\theta(t,r)}{\theta_i} = \left(1 + \frac{\text{Bi}}{4}\right)\left[1 - \frac{\text{Bi}}{2}\left(\frac{r}{R}\right)^2\right] e^{-2\text{BiFo}} \tag{42}$$

Figure 2 shows Eqs. (41) and (42) plotted along with the exact solution (full lines) and the lumped capacity solution (dashed lines). Since the two-term approximation of $J_0(\mu_1)$ is precise, Eqs. (41) and (42) overlap. Hence, the simpler Eq. (42) should be used. For (a) Bi=0.1 (Fig. 2(*a*)), the error in Eq. (42) is below 0.88% $\theta_i$. For Bi=0.3 (Fig. 2(*b*)), the highest error for Eq. (42) is 2.95% $\theta_i$ compared to the 6.9% $\theta_i$ error for the lumped capacity.

*2.2.2 Total Energy Released $Q(t)/Q_0$ From Cylinders.* The dimensionless heat loss from cylinders is obtained by substituting the temperature profile (30) into Eq. (23), setting $u=r/R$ and $n=2$ and integrating. The result of this integration is

$$\frac{Q(t)}{Q_0} = 1 - 4\sum_{n=1}^{\infty} \frac{\text{Bi}^2}{\mu_n^2(\mu_n^2 + \text{Bi}^2)} e^{-\mu_n^2 \text{Fo}} \tag{43}$$

where

$$Q_0 = R^2 \pi L \rho c (T_i - T_f)$$

The one-term approximation of Eq. (43) is

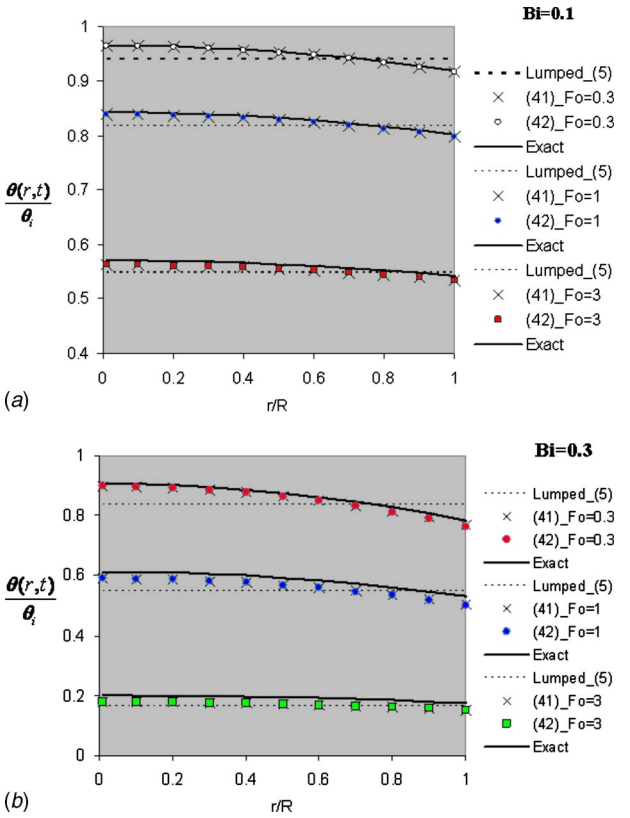


**Fig. 2 Transient temperature $\theta(r,t)/\theta_i$ in cylinders calculated using Eqs. (41) and (42), along with the exact five-term Fourier series solution (full lines) and the lumped capacity solution (Eq. (5)), dashed lines. (*a*) Bi=0.1 (*b*) Bi=0.3.**

$$\frac{Q(t)}{Q_0} = 1 - 4\frac{\text{Bi}^2}{\mu_1^2(\mu_1^2 + \text{Bi}^2)} e^{-\mu_1^2 \text{Fo}} \tag{44}$$

or

$$\frac{Q(t)}{Q_0} = 1 - C_{\text{cylinder}} e^{-\mu_1^2 \text{Fo}}$$

where

$$C_{\text{cylinder}} \approx 1$$

For example, for Bi=0.3, $C_{\text{cylinder}}=0.9952$. For small Bi, using $\mu_1=\sqrt{2\text{Bi}}$

$$\frac{Q(t)}{Q_0} = 1 - e^{-2\text{BiFo}} \tag{45}$$

The error grows with Bi. For $0<\text{Bi}<0.3$, the error is less than 2% $Q_0$.

**2.3 Sphere With Radius *R*.** The mathematical formulation is

$$\frac{1}{\alpha}\frac{\partial \theta}{\partial t} = \frac{1}{r^2}\frac{\partial}{\partial r}\left(r^2 \frac{\partial \theta}{\partial r}\right) \tag{46}$$

with

$$\frac{\partial \theta(t,0)}{\partial r} = 0$$

$$-k \left.\frac{\partial \theta(t,r)}{\partial r}\right|_{r=R} = h\theta_S$$

and

$$\theta(0,r) = \theta_i$$

The transient temperature field in the sphere is

$$\frac{\theta(t,r)}{\theta_i} = 2\sum_{n=1}^{\infty}\left(\frac{\sin\mu_n - \mu_n\cos\mu_n}{\mu_n - \sin\mu_n\cos\mu_n}\right)\frac{\sin\left(\mu_n\frac{r}{R}\right)}{\mu_n\frac{r}{R}}e^{-\mu_n{}^2\mathrm{Fo}} \quad (47)$$

where the eigenvalues $\mu_n = \lambda_n R$ are defined by

$$\mu_n\cot\mu_n = 1 - \mathrm{Bi}$$

The one-term approximation of Eq. (47) is

$$\frac{\theta(t,r)}{\theta_i} = 2\frac{\sin\mu_1 - \mu_1\cos\mu_1}{\mu_1 - \sin\mu_1\cos\mu_1}\frac{\sin\left(\mu_1\frac{r}{R}\right)}{\mu_1\frac{r}{R}}e^{-\mu_1{}^2\mathrm{Fo}} \quad (48)$$

or

$$\frac{\theta(t,r)}{\theta_i} = B_{\mathrm{sphere}}\sin\left(\mu_1\frac{r}{R}\right)\frac{R}{\mu_1 r}e^{-\mu_1{}^2\mathrm{Fo}} \quad (49)$$

where

$$B_{\mathrm{sphere}} = 2\frac{\sin\mu_1 - \mu_1\cos\mu_1}{\mu_1 - \sin\mu_1\cos\mu_1} \quad (50)$$

and

$$\mu_1\cot\mu_1 = 1 - \mathrm{Bi} \quad (51)$$

*2.3.1 Transient Temperature in Spheres*. For small values of $\mu_1$ and Bi,

$$\cot\mu_1 = \frac{1}{\mu_1} - \frac{\mu_1}{3} - \frac{\mu_1{}^3}{45} - \cdots \approx \frac{1}{\mu_1} - \frac{\mu_1}{3} \quad (52)$$

Combining Eqs. (51) and (52) provides a simple approximation for $\mu_1$ [4],

$$\mu_1 = \sqrt{3\mathrm{Bi}} \quad (53)$$

Using small number expansions for sin and cos, one gets $B_{\mathrm{sphere}} \approx 1$. However, the approximation used for plates provides an accurate approximation,

$$B_{\mathrm{sphere}} \approx B_{\mathrm{plate}} \approx 1 + \frac{\mathrm{Bi}}{4}$$

giving for Bi=0.1 $B_{\mathrm{sphere}}$=1.0250, while the exact value is 1.0298. Therefore,

$$\frac{\theta(t,r)}{\theta_i} = \left(1 + \frac{\mathrm{Bi}}{4}\right)\frac{R}{\sqrt{3\mathrm{Bi}}\cdot r}\sin\left(\sqrt{3\mathrm{Bi}}\frac{r}{R}\right)e^{-\mu_1{}^2\mathrm{Fo}} \quad (54)$$

Equation (54) is further simplified by using a two-term approximation for sin,

$$\frac{\theta(t,r)}{\theta_i} = \left(1 + \frac{\mathrm{Bi}}{4}\right)\left[1 - \frac{\mathrm{Bi}}{2}\left(\frac{r}{R}\right)^2\right]e^{-3\mathrm{BiFo}} \quad (55)$$

Figure 3 shows the transient temperature calculated using Eq. (55) along with the exact solution (full lines) and the lumped capacity solution (dashed lines). For Bi=0.1, the error is less than 0.97% $\theta_i$. For Bi=0.3, the error is less than 3.1% $\theta_i$.

*2.3.2 Total Energy Released $Q(t)/Q_0$ From Sphere*. The dimensionless heat loss from spheres is obtained by substituting the temperature profile (47) into Eq. (17), setting $u = r/R$ and $n=3$ and integrating. The result of this integration is

**Table 1 Low Bi solution (LBi) for Bi<1/3**

| | $\theta(t,x)/\theta_i$ (Eq. No.) | $Q(t)/Q_0$ (Eq. No.) |
|---|---|---|
| Plate | $\left(1+\frac{\mathrm{Bi}}{4}\right)\left[1-\frac{\mathrm{Bi}}{2}\left(\frac{x}{L}\right)^2\right]e^{-\mathrm{BiFo}}$ (21) | $1-e^{-\mathrm{BiFo}}$ (28) |
| Cylinder | $\left(1+\frac{\mathrm{Bi}}{4}\right)\left[1-\frac{\mathrm{Bi}}{2}\left(\frac{r}{R}\right)^2\right]e^{-2\mathrm{BiFo}}$ (42) | $1-e^{-2\mathrm{BiFo}}$ (45) |
| Sphere | $\left(1+\frac{\mathrm{Bi}}{4}\right)\left[1-\frac{\mathrm{Bi}}{2}\left(\frac{r}{R}\right)^2\right]e^{-3\mathrm{BiFo}}$ (55) | $1-e^{-3\mathrm{BiFo}}$ (60) |

$$\frac{Q(t)}{Q_0} = 1 - 6\sum_{n=1}^{\infty}\frac{1}{\mu_n{}^3}\frac{(\sin\mu_n - \mu_n\cos\mu_n)^2}{\mu_n - \sin\mu_n\cos\mu_n}e^{-\mu_n{}^2\mathrm{Fo}} \quad (56)$$

where

$$Q_0 = \tfrac{4}{3}R^3\pi\rho c(T_i - T_f) \quad (57)$$

The one-term approximation of Eq. (56) is

$$\frac{Q(t)}{Q_0} = 1 - 6\frac{1}{\mu_1{}^3}\frac{(\sin\mu_1 - \mu_1\cos\mu_1)^2}{\mu_1 - \sin\mu_1\cos\mu_1}e^{-\mu_1{}^2\mathrm{Fo}} \quad (58)$$

or

$$\frac{Q(t)}{Q_0} = 1 - C_{\mathrm{sphere}}e^{-\mu_1{}^2\mathrm{Fo}} \quad (59)$$

where

$$C_{\mathrm{sphere}} \approx 1$$

For example, for Bi=0.3, $C_{\mathrm{sphere}}$=0.9985. Replacing $C_{\mathrm{sphere}}=1$ and $\mu_1 = \sqrt{3\mathrm{Bi}}$ in Eq. (59) gives

$$\frac{Q(t)}{Q_0} = 1 - e^{-3\mathrm{BiFo}} \quad (60)$$

**2.4 Summary.** The equations for transient temperature $\theta(\xi,t)$ and heat released $Q(t)/Q_0$, derived in Sec. 2, are listed in Table 1.

*2.4.1 Low Biot Number Solution (LBi)*. The lumped capacity solution is normally used up to Bi=0.1 [8,10], where it gives ~3% $\theta_i$ error or up to Bi=1/6 [12], where it gives ~5% $\theta_i$ error (see Figs. 1–3 and Table 3). This is justified since in many cases one does not know the convection coefficient better than ±10%.

The low Biot number solution presented herein accounts for nonzero gradients within the solid. Based on Figs. 1–3 and Tables 1–3,

- it is more precise than the lumped capacity solution by a factor of ~3,
- it can be used up to Bi~1/3, where it gives ~3% error, and
- it has a general form valid for plates, cylinders, and spheres,

$$\frac{\theta(t,\xi)}{\theta_i} = \left(1 + \frac{\mathrm{Bi}}{4}\right)\left[1 - \frac{\mathrm{Bi}}{2}\xi^2\right]e^{-n\mathrm{BiFo}} = B\cdot F\cdot e^{-n\mathrm{BiFo}} \quad (61)$$

where $n=1$ for plates, $n=2$ for cylinders, and $n=3$ for spheres. Equation (61) is almost as simple as the lumped capacity solution. For Bi→0, $B$ and $F$ asymptotically approach 1, reducing Eq. (61) to the lumped capacity model. Therefore, one could consider the lumped capacity solution to be a limiting case of the low Biot number solution presented herein.

The coefficient $F$ accounts for the spatial variation of temperature. Surprisingly, the two-term approximation,

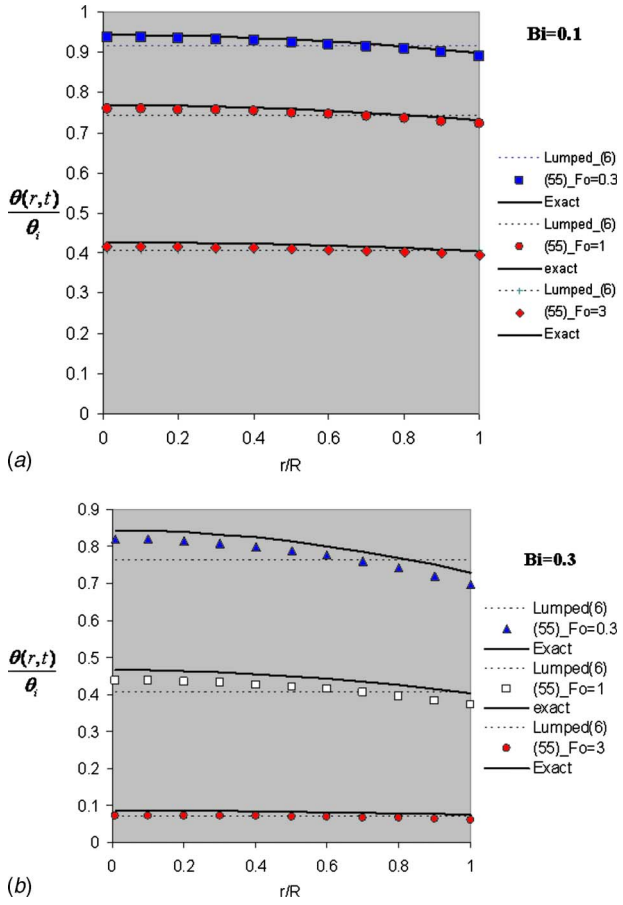


**Fig. 3 Transient temperature $\theta(r,t)/\theta_i$ in spheres calculated using Eq. (55) along with the exact five term Fourier series solution (full lines) and the lumped capacity solution (Eq. (6)), dashed lines. (*a*) Bi=0.1. (*b*) Bi=0.3.**

**Table 2 Extended low Bi solution (ELBi) for Bi<2**

| | $\mu_1$ | $\theta(t,x)/\theta_i$ |
|---|---|---|
| Plate | $\sqrt{\frac{\mathrm{Bi}}{1+\mathrm{Bi}/3}}$ | $\left(1+\frac{\mathrm{Bi}}{7}\right)\cos\left(\mu_1\frac{x}{L}\right)e^{-\mu_1{}^2\mathrm{Fo}}$ |
| Cylinder | $\sqrt{\frac{2\mathrm{Bi}}{1+\mathrm{Bi}/4}}$ | $\left(1+\frac{\mathrm{Bi}}{4}\right)J_0\left(\mu_1\frac{r}{R}\right)e^{-\mu_1{}^2\mathrm{Fo}}$ |
| Sphere | $\sqrt{\frac{3\mathrm{Bi}}{1+\mathrm{Bi}/5}}$ | $\left(1+\frac{\mathrm{Bi}}{3.5}\right)\frac{R}{\mu_1 r}\sin\left(\mu_1\frac{r}{R}\right)e^{-\mu_1{}^2\mathrm{Fo}}$ |

$$\cos(\sqrt{\mathrm{Bi}_1}\xi)\approx J_0(\sqrt{2\mathrm{Bi}}\xi)\approx\frac{\sin(\sqrt{3\mathrm{Bi}}\xi)}{\sqrt{3\mathrm{Bi}}\xi}\equiv F=1-\frac{\mathrm{Bi}}{2}\xi^2 \quad (62)$$

gives the same result in all three geometries. Furthermore, the Fourier coefficients $B$ in the three geometries are well approximated with a single expression,

$$B_{\mathrm{plate}}\approx B_{\mathrm{cylinder}}\approx B_{\mathrm{sphere}}\equiv B=1+\mathrm{Bi}/4 \quad (63)$$

Fine-tuning the constant in the denominator to fit Eqs. (12), (33), and (50), respectively, gives

$$B_{\mathrm{plate}}=1+\mathrm{Bi}/7$$

$$B_{\mathrm{cylinder}}=1+\mathrm{Bi}/4.5$$

$$B_{\mathrm{sphere}}=1+\mathrm{Bi}/3.5 \quad (64)$$

However, using the above coefficients instead of $B=1+\mathrm{Bi}/4$ will not give a clear improvement of Eq. (61) because the error in $\mu_1$ is dominant.

*2.4.2 Extended Low Biot Number Approximation (ELBi).* For $0<\mathrm{Bi}<2$, the simplest approximation for the first eigenvalue in plates, cylinders, and spheres is given in Ref. [7],

$$\mu_{1,\mathrm{plate}}{}^2=\frac{\mathrm{Bi}}{1+\mathrm{Bi}/3}$$

$$\mu_{1,\mathrm{cylinder}}{}^2=\frac{2\mathrm{Bi}}{1+\mathrm{Bi}/4}$$

$$\mu_{1,\mathrm{sphere}}{}^2=\frac{3\mathrm{Bi}}{1+\mathrm{Bi}/5} \quad (65)$$

Using Eqs. (64) and (65) in Eqs. (11), (32), and (49) gives a set of extended low Biot number approximations listed in Table 2 for plates, cylinders, and spheres. This set is more precise than the lumped capacity solution by one order of magnitude (Table 3), and can be used up to $\mathrm{Bi}\sim 1$.

## 3 Broad-Range Correlations Valid for $0<\mathrm{Bi}<\infty$

The range of the approximate equations is extended by widening the range of the coefficients and the eigenvalues.

### 3.1 Infinite Plates

*3.1.1 Coefficients $B_{\mathrm{plate}}$ and $C_{\mathrm{plate}}$.* The coefficient $B_{\mathrm{plate}}$ defined by Eq. (12) asymptotically approaches constant values, $B_{\mathrm{plate}}(\mathrm{Bi}\to 0)=1$ and $B_{\mathrm{plate}}(\mathrm{Bi}\to\infty)=1.273$. Hence, expression (2) is constant,

$$Z\equiv\frac{y(z\to\infty)}{y(z\to 0)}=1.273$$

This violates Churchill and Usagi's requirement that "$y(z\to 0)$ and $y(z\to\infty)$ cannot be both constant" [3]. However, the difference

**Table 3 Error % $\theta_i$ in LBi and ELBi solutions (see Tables 1 and 2) and in the lumped capacity solution**

| | Plate | | | Cylinder | | | Sphere | | |
|---|---|---|---|---|---|---|---|---|---|
| | Lumped Eq. (4) | LBi | ELBi | Lumped Eq. (5) | LBi | ELBi | Lumped Eq. (6) | LBi | ELBi |
| Bi=0.03 | −0.95 | −0.27 | 0.09 | 0.74 | 0.12 | −0.1 | 0.89 | 0.25 | 0.04 |
| Bi=0.1 | −2.98 | −0.86 | 0.03 | 2.4 | 0.88 | −0.38 | 2.9 | 0.97 | 0.11 |
| Bi=0.3 | −7.67 | 2.9 | 0.45 | 6.9 | 2.9 | −0.40 | 8.0 | 3.1 | 0.20 |
| Bi=1/2 | −11.0 | 4.8 | −0.40 | 9.2 | 5.3 | −0.87 | 12.3 | 6.2 | 0.22 |
| Bi=2/3 | −12.9 | 5.3 | −0.87 | 12.4 | 8.6 | −3.4 | 15.3 | 8.7 | 0.23 |
| Bi=1 | | | −2.1 | | | −2.3 | | | 0.27 |
| Bi=2 | | | −6.9 | | | −5.5 | | | 0.61 |

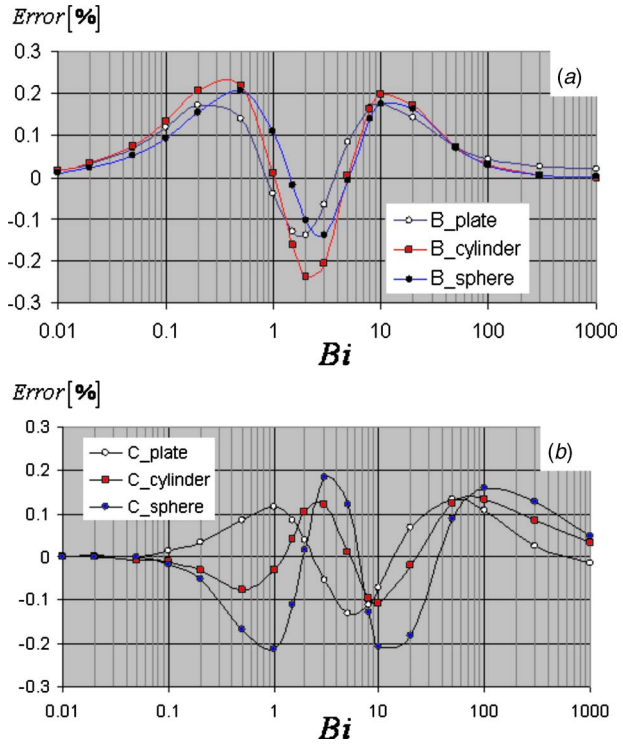


**Fig. 4 Error: (*a*) B coefficients, error (%) = $(B_{exact} - B_{approx})/B_{exact} \times 100\%$; (*b*) Coefficients, error (%) = $(C_{exact} - C_{approx})/C_{exact} \times 100\%$**

$B_{plate} - B_{plate}(0)$ is subject to a simple approximation,

$$B_{plate} - 1 = 0.273 \frac{1}{1 + 1/\mathrm{Bi}}$$

which holds both limits and gives less than 2% error. To further reduce the error, we employ a more complex approximation,

$$B_{plate} - 1 = 0.273 \frac{1}{(1 + K/\mathrm{Bi}^n)^{1/n}} \tag{66}$$

which also holds both limits. To minimize error in the $0.1 < \mathrm{Bi} < 10$ range, the constants are adjusted to $n = 1.5$ and $K = 2.42$,

$$B_{plate} = 1 + 0.273 \frac{1}{(1 + 2.45/\mathrm{Bi}^{1.5})^{2/3}} \tag{67}$$

Figure 4(*a*) shows the error in the Fourier constants for transient temperature in plates, cylinders, and spheres. Equation (67) gives less than 0.16% for $0 < \mathrm{Bi} < \infty$. Note that Eq. (67) has the form of Eq. (2), yet the constant, $1.801^{1.5} = 2.45$, does not seem to be related to the limits (zero or 0.273). Combining Eqs. (67) and (11) gives the transient temperature,

$$\frac{\theta(t,x)}{\theta_i} = \left[1 + \frac{0.273}{(1 + 2.42/\mathrm{Bi}^{1.5})^{2/3}}\right] \cos\left(\mu_1 \frac{x}{L}\right) e^{-\mu_1^2 \mathrm{Fo}} \tag{68}$$

The Fourier coefficient $C_{plate}$ for transient heat loss defined by Eq. (27) also approaches asymptotically constant values for small and large values of Bi. The coefficient decreases from $C_{plate}(\mathrm{Bi} \to 0) = 1$ to $C_{plate}(\mathrm{Bi} \to \infty) = 0.8106$. The expression $Z$ is again constant,

$$Z \equiv \frac{y(z \to 0)}{y(z \to \infty)} = 1.234$$

so that Eq. (2) cannot be readily implemented. Instead, the difference $C_{plate}(0) - C_{plate}$ is subject to a simple approximation,

$$1 - C_{plate} = 0.189 \frac{1}{1 + 6/\mathrm{Bi}}$$

which holds both limits and gives less than 1.5% error. The form of approximation (66) with one exponent $n$ did not reduce the error sufficiently. However,

$$1 - C_{plate} = 0.189 \frac{1}{1 + K/\mathrm{Bi}^m} \tag{69}$$

with $K = 9.5$ and $m = 1.25$ gives less than 0.5% error. Then, introducing the second independent exponent

$$1 - C_{plate} = 0.189 \frac{1}{(1 + 3.8/\mathrm{Bi}^{1.116})^{1.613}} \tag{70}$$

gives less than 0.14% error in the $0 < \mathrm{Bi} < \infty$ range (Fig. 4(*b*)). Equation (70) can be written in the form of Churchill and Usagi's Eq. (2),

$$C_{plate} = 1 - 0.189 \frac{1}{[1 + (8.61/\mathrm{Bi}^{1.8})^{0.62}]^{1/0.62}} \tag{71}$$

Yet, it is hard to relate 8.613 and $\mathrm{Bi}^{1.8}$ to the asymptotic behavior of $(1 - C_{plate})$ at either limit. Combining Eqs. (71) and (26) gives the dimensionless heat loss $Q(t)/Q_0$, valid in the $0 < \mathrm{Bi} < \infty$ range.

$$\frac{Q(t)}{Q_0} = 1 - \left[1 - 0.189 \frac{1}{(1 + 3.8/\mathrm{Bi}^{1.116})^{1.62}}\right] e^{-\mu_1^2 \mathrm{Fo}} \tag{72}$$

*3.1.2 First Eigenvalue for Plates* $\mu_1$. For $\mathrm{Bi} < 0.1$, Eq. (14) provides the simplest approximation for $\mu_1$. This can be seen in Fig. 5, which shows the error $\mu_{exact} - \mu_{approx} = \Delta\mu_1$. For $0 < \mathrm{Bi} < \infty$, the first eigenvalue can be approximated as [7]

$$\mu_1(\mathrm{Bi}) = \sqrt{\frac{\mathrm{Bi}}{1 + \mathrm{Bi}\left(\frac{2}{\pi}\right)^2}} = \frac{\pi/2}{\sqrt{1 + 2.4674/\mathrm{Bi}}} \tag{73}$$

Approximation (73) is precise at both limits (error <1% for $\mathrm{Bi} < 0.5$ and $\mathrm{Bi} > 25$) but gives $\Delta\mu_1 = 0.029$ (or $\Delta\mu_1/\mu_1 \times 100\% = 2.29\%$) error at $\mathrm{Bi} \approx 4$, see Fig. 5(*a*)). For most applications this is acceptable because

- interpolating between the 1/Bi lines in the Heisler charts should result in a higher error;
- most correlations for convective heat transfer coefficient $h$, have uncertainty of about ±10%, which causes uncertainty in Bi and $\mu_1$.

At Bi=4, Eq. (73) gives a maximum error $\mu_{1,approx} = 1.2354$ instead of $\mu_{1,exact} = 1.2646$, a $\Delta\mu_1 = 0.029$ error. Using $\mu_1 = 1.235$ in Eq. (9), one gets Bi=3.543, so that the error introduced by Eq. (73) is equivalent to making a $(4 - 3.543)/4 \times 100 = 11.4\%$ error in $h$ or Bi. Yet, Eq. (73) is considerably improved by adjusting the constant and the exponent,

$$\mu_1(\mathrm{Bi}) = \frac{\pi/2}{\sqrt{1 + 2.3/\mathrm{Bi}^{1.035}}} \tag{74}$$

Equation (74) gives error $\Delta\mu_1 = 0.0044$ at $\mathrm{Bi} \approx 1$ where $\mu_{exact} \approx 0.85$ (or ≈0.5% error). It has the same form as the Luikov's equation but contains different constants. Luikov's Eq. (1) is significantly less accurate in the $0.1 < \mathrm{Bi} < 5$ range. It is more accurate for $\mathrm{Bi} < 0.05$ where $\mu_1 = \sqrt{\mathrm{Bi}}$ is yet more precise. The approximation proposed by Yovanovich [6],

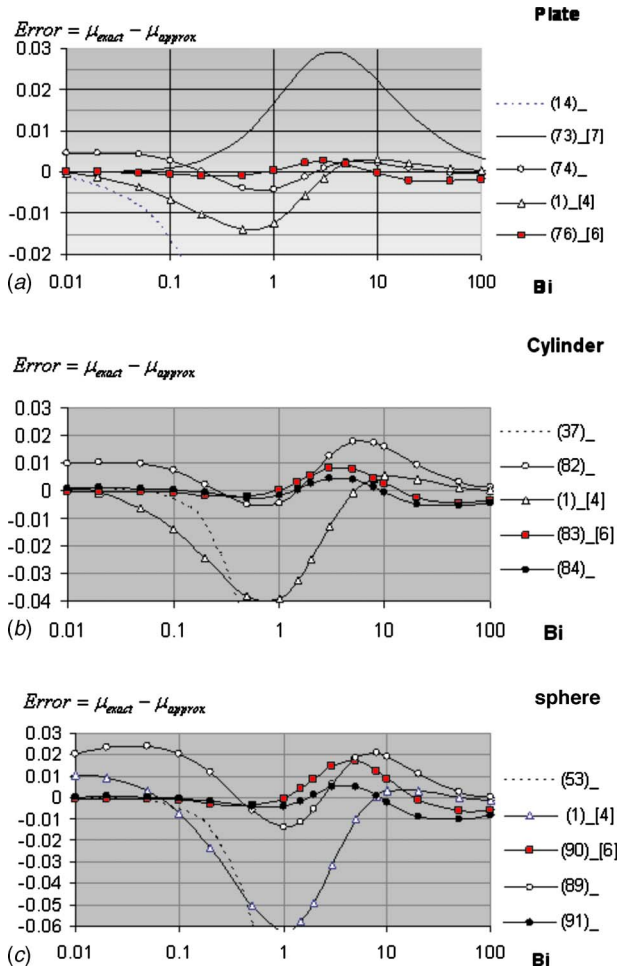


**Fig. 5 Error= $\mu_{exact}-\mu_{approx}=\Delta\mu_1$ as a function of the Biot number for (*a*) plate, (*b*) cylinder, and (*c*) sphere**

$$\mu_1(\mathrm{Bi})=\frac{\pi/2}{\left[1+\left(\frac{\pi/2}{\sqrt{\mathrm{Bi}}}\right)^{2.139}\right]^{1/2.139}} \tag{75}$$

is the most accurate approximation for $0.01<\mathrm{Bi}<2$ (Fig. 5(*a*)). The maximum error is $\Delta\mu_1=0.0026$ at $\mathrm{Bi}\approx 3$ where $\mu_{exact}\approx 1.2$ (or $\approx 0.22\%$ error). However, it is more complex than Eq. (14) or (74). Equation (75) can be further simplified as

$$\mu_1(\mathrm{Bi})=\frac{\pi/2}{(1+2.62/\mathrm{Bi}^{1.07})^{0.468}} \tag{76}$$

How much accuracy in $\mu_1$ is needed? In calculating $\theta(\xi,t)/\theta_i$, the main source of error is the uncertainty in the heat transfer coefficient $h$. Therefore, one can expect typically $\pm 10\%$ error in the Biot number. However, the relation between Bi and $\mu_1$ is exceedingly nonlinear. For example, using Bi=1.1 instead of $\mathrm{Bi}_{exact}=1$ due to 10% error in $h$ will result in error $\Delta\mu_1=0.89035-0.86033=0.03002$. Using Eq. (74) will give approximately ten times less error (see Fig. 5(*a*)). Yet, using Bi=110 instead of $\mathrm{Bi}_{exact}=100$ will give $\sim 30$ times lower error in the eigenvalue, $\Delta\mu_1=1.55665-1.55525=0.0014$. Based on the above, one could conclude that for $\mathrm{Bi}\gg 1$, the correlations need to provide $\mu_1$ with four digits of accuracy, or the error in $h$ will be augmented. However, for $\mathrm{Bi}\gg 1$, the resistance within the solid controls the transient, and a relatively large error in $h$ (or Bi) will cause a small error in $\mu_1$ and $\theta(\xi,t)/\theta_i$.

### 3.2 Cylinders

*3.2.1 Coefficients $B_{cylinder}$ and $C_{cylinder}$.* The coefficient $B_{cylinder}$ asymptotically approaches $B_{cylinder}(\mathrm{Bi}\to 0)=1$ and $B_{cylinder}(\mathrm{Bi}\to\infty)=1.602$. The simple approximation,

$$B_{cylinder}-1=\frac{0.602}{1+2/\mathrm{Bi}} \tag{77}$$

holds both limits and gives less than 2% error. As for $B_{plate}$, we explore the more complex approximation, which holds both limits,

$$B_{cylinder}-1=\frac{0.602}{(1+K/\mathrm{Bi}^n)^{1/n}}$$

Adjusting the constants $K$ and $n$ brings the error down to less than 0.23% (see Fig. 4(*a*)),

$$B_{cylinder}=1+\frac{0.602}{(1+4.8/\mathrm{Bi}^{1.64})^{1/1.64}} \tag{78}$$

Combining Eqs. (78) and (32) gives

$$\frac{\theta(t,r)}{\theta_i}=\left[1+\frac{0.602}{(1+4.8/\mathrm{Bi}^{1.64})^{0.61}}\right]J_0\left(\mu_1\frac{r}{R}\right)e^{-\mu_1{}^2\mathrm{Fo}} \tag{79}$$

The Fourier coefficient $C_{cylinder}$ for the dimensionless heat loss asymptotically approaches 1 for $\mathrm{Bi}\to 0$ and $C_{cylinder}=0.6917$ for $\mathrm{Bi}\to\infty$. Again, the difference $C_{cylinder}(0)-C_{cylinder}$ is subject to a simple approximation,

$$1-C_{cylinder}=\frac{0.3083}{1+7/\mathrm{Bi}}$$

which holds both limits and gives less than 2.5% error. As for $C_{plate}$, we assume

$$1-C_{cylinder}=\frac{0.3083}{(1+K/\mathrm{Bi}^m)^n} \tag{80}$$

Adjusting the exponents to $K=2.58$, $m=1.08$, and $n=2.35$ gives less than 0.12% error in the $0<\mathrm{Bi}<\infty$ range (see Fig. 4(*b*)). Using Eq. (80) in Eq. (44) provides an explicit expression for $Q(t)/Q_0$ valid for $0<\mathrm{Bi}<\infty$,

$$\frac{Q(t)}{Q_0}=1-\left[1-\frac{0.308}{(1+2.58/\mathrm{Bi}^{1.08})^{2.35}}\right]e^{-\mu_1{}^2\mathrm{Fo}} \tag{81}$$

*3.2.2 First Eigenvalue for Cylinders $\mu_1$.* For $\mathrm{Bi}<0.1$, Eq. (37) provides the simplest and yet very accurate approximation. For $0.1<\mathrm{Bi}<\infty$, the approximation based on Refs. [4,7]

$$\mu_1(\mathrm{Bi})=\frac{2.4048}{\sqrt{1+2.62/\mathrm{Bi}^{1.05}}} \tag{82}$$

yields sufficient accuracy, provided that the constants are adjusted to minimize the error. It can be seen in Fig. 5(*b*) that Eq. (82) is more precise than Eq. (1) with $A=2.45$ and $k=1.04$, except for $\mathrm{Bi}<0.07$. The approximation proposed by Yovanovich [6],

$$\mu_1(\mathrm{Bi})=\frac{2.4048}{\left[1+\left(\frac{2.4048}{\sqrt{2\mathrm{Bi}}}\right)^{2.238}\right]^{1/2.238}}=\frac{2.4048}{\left(1+\frac{3.005}{\mathrm{Bi}^{1.119}}\right)^{0.4468}} \tag{83}$$

yields the maximum error of $\Delta\mu_1=0.0082$ at $\mathrm{Bi}\approx 3$ where $\mu_{exact}=1.8$ (or 0.46% error). By further simplifying Eq. (83) and adjusting the constants,

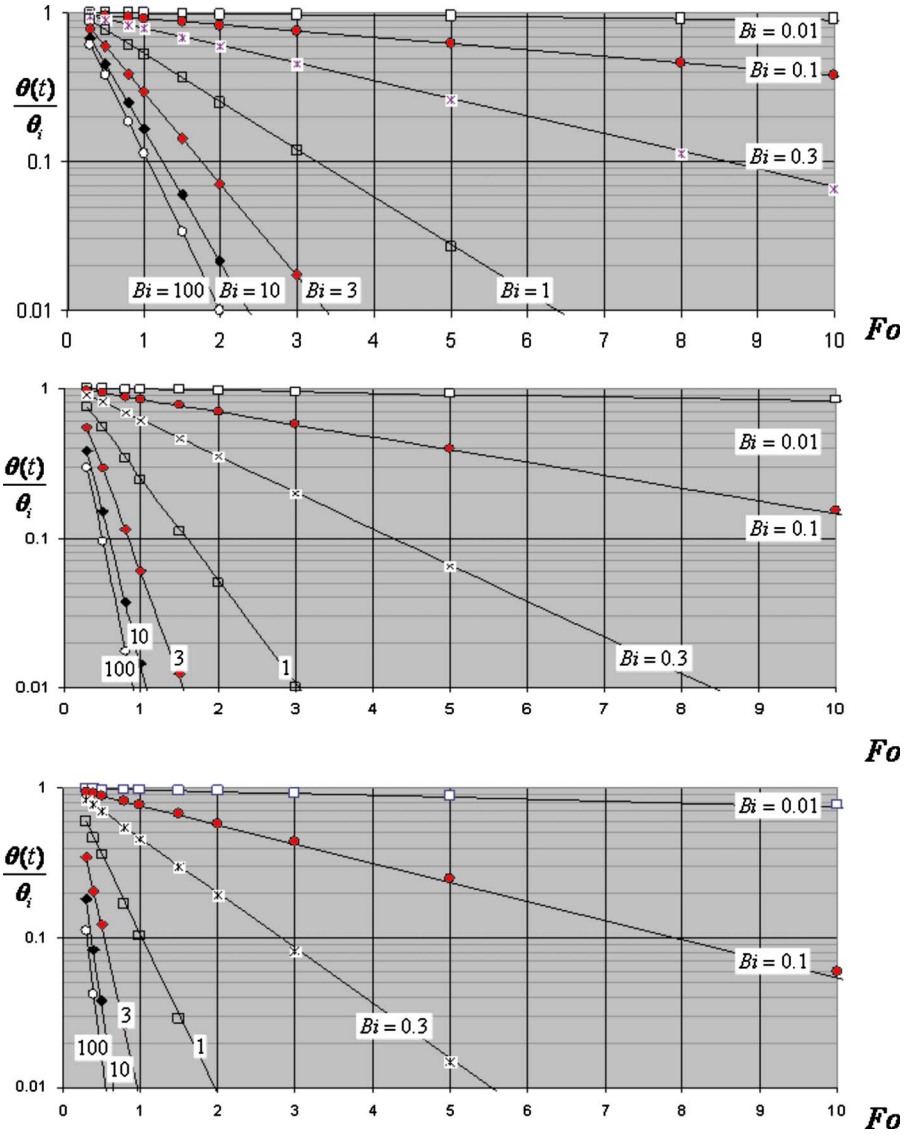


**Fig. 6 Transient temperature $\theta(t)/\theta_i$ (at $\xi=0$), calculated using equations listed in Tables 4 and 5 (symbols). The full lines are the exact Fourier series solution. (*a*) Plate, (*b*) cylinder, and (*c*) sphere.**

$$\mu_1(\mathrm{Bi}) = \frac{2.4048}{(1+3.28/\mathrm{Bi}^{1.125})^{0.446}} \tag{84}$$

the error is reduced to 0.00455 also at $\mathrm{Bi}\approx 3$ (or $\approx 0.25\%$ error) (see Fig. 5(*b*)). However for $\mathrm{Bi}>10$, the error is slightly increased.

### 3.3 Spheres

*3.3.1 Coefficients $B_{\mathrm{sphere}}$ and $C_{\mathrm{sphere}}$.* The coefficient $B_{\mathrm{sphere}}$ has asymptotic values: $B_{\mathrm{sphere}}(\mathrm{Bi}\to 0)=1$ and $B_{\mathrm{sphere}}(\mathrm{Bi}\to\infty)=2$. As for plates and cylinders, the approximation

$$B_{\mathrm{sphere}} - 1 = \frac{1}{(1+K/\mathrm{Bi}^n)^{1/n}} \tag{85}$$

holds both limits. Adjusting the constant to $K=8.87$ and the exponents to $n=1.76$ gives less than 0.21% error in the $0<\mathrm{Bi}<\infty$ range (Fig. 4(*a*)). The transient temperature in spheres is obtained by substituting Eq. (85) into Eq. (49),

$$\frac{\theta(t,r)}{\theta_i} = \left[1+\frac{1}{(1+8.87/\mathrm{Bi}^{1.76})^{0.568}}\right]\frac{R}{\mu_1 r}\sin\left(\frac{\mu_1 r}{R}\right)e^{-\mu_1^2\mathrm{Fo}} \tag{86}$$

The Fourier coefficient $C_{\mathrm{sphere}}$ for the heat loss asymptotically approaches $C_{\mathrm{sphere}}(\mathrm{Bi}\to 0)=1$ and $C_{\mathrm{sphere}}(\mathrm{Bi}\to\infty)=0.392$. The approximation

$$1 - C_{\mathrm{sphere}} = \frac{0.392}{1+7.7/\mathrm{Bi}}$$

holds both limits but gives less than 3.5% error. Adjusting the constant and the exponents as in Eq. (70) for the plate gives

$$1 - C_{\mathrm{sphere}} = \frac{0.392}{(1+2.36/\mathrm{Bi}^{1.09})^{2.85}} \tag{87}$$

Approximation (87) yields less than 0.21% error in the $0<\mathrm{Bi}<\infty$ range (Fig. 4(*b*)). Then using Eq. (87) with Eq. (59) gives

**Table 4 Approximate equations valid for $0<\mathrm{Bi}<\infty$. For Fo $>0.5$ and Fo$>0.3$, the error is less than 0.2% and 0.6%, respectively**

| | | |
|---|---|---|
| Plate | $\frac{\theta(t,x)}{\theta_i}=\left[1+\frac{0.273}{(1+2.42/\mathrm{Bi}^{1.5})^{2/3}}\right]\cos\left(\mu_1\frac{x}{L}\right)e^{-\mu_1^2\mathrm{Fo}}$ | (68) |
| | $\frac{Q(t)}{Q_0}=1-\left[1-0.189\frac{1}{(1+3.8/\mathrm{Bi}^{1.116})^{1.62}}\right]e^{-\mu_1^2\mathrm{Fo}}$ | (72) |
| Cylinder | $\frac{\theta(t,r)}{\theta_i}=\left[1+\frac{0.602}{(1+4.8/\mathrm{Bi}^{1.64})^{0.61}}\right]J_0\left(\mu_1\frac{r}{R}\right)e^{-\mu_1^2\mathrm{Fo}}$ | (79) |
| | $\frac{Q(t)}{Q_0}=1-\left[1-\frac{0.308}{(1+2.58/\mathrm{Bi}^{1.08})^{2.35}}\right]e^{-\mu_1^2\mathrm{Fo}}$ | (81) |
| Sphere | $\frac{\theta(t,r)}{\theta_i}=\left[1+\left(1+\frac{8.87}{\mathrm{Bi}^{1.76}}\right)^{-0.568}\right]\frac{R}{\mu_1 r}\sin\left(\frac{\mu_1 r}{R}\right)e^{-\mu_1^2\mathrm{Fo}}$ | (86) |
| | $\frac{Q_{\mathrm{sphere}}(t)}{Q_0}=1-\left[1-\frac{0.392}{(1+2.36/\mathrm{Bi}^{1.09})^{2.85}}\right]e^{-\mu_1^2\mathrm{Fo}}$ | (88) |

$$\frac{Q(t)}{Q_0}=1-\left[1-\frac{0.392}{(1+2.36/\mathrm{Bi}^{1.09})^{2.85}}\right]e^{-\mu_1^2\mathrm{Fo}} \tag{88}$$

*3.3.2 First Eigenvalue for Spheres* $\mu_1$. For $\mathrm{Bi}<0.1$, Eq. (53) provides the simplest and yet very accurate approximation. For $0.1<\mathrm{Bi}<\infty$, the approximation based on Refs. [4,7] with adjusted constants,

$$\mu_1(\mathrm{Bi})=\frac{\pi}{\sqrt{1+2.93/\mathrm{Bi}^{1.08}}} \tag{89}$$

yields sufficient accuracy (see Fig. 5(*c*)). Luikov's Eq. (1) with $A=2.7$ and $k=1.07$ for spheres is less accurate than Eq. (89), except for $\mathrm{Bi}<0.2$. The approximation proposed by Yovanovich [6],

$$\mu_1(\mathrm{Bi})=\frac{\pi}{\left[1+\left(\frac{\pi}{\sqrt{3\mathrm{Bi}}}\right)^{2.314}\right]^{1/2.314}}=\frac{\pi}{\left(1+\frac{3.9662}{\mathrm{Bi}^{1.157}}\right)^{0.43215}} \tag{90}$$

yields maximum error of $\Delta\mu_1=0.0180$ at $\mathrm{Bi}\approx 4$, where $\mu_{\mathrm{exact}}\approx 2.45$ (or 0.71% error). The constants and the exponents can be further adjusted,

$$\mu_1(\mathrm{Bi})=\frac{\pi}{(1+4.1/\mathrm{Bi}^{1.18})^{0.4238}} \tag{91}$$

to give less than $\Delta\mu_1=0.051$ or 0.21% error.

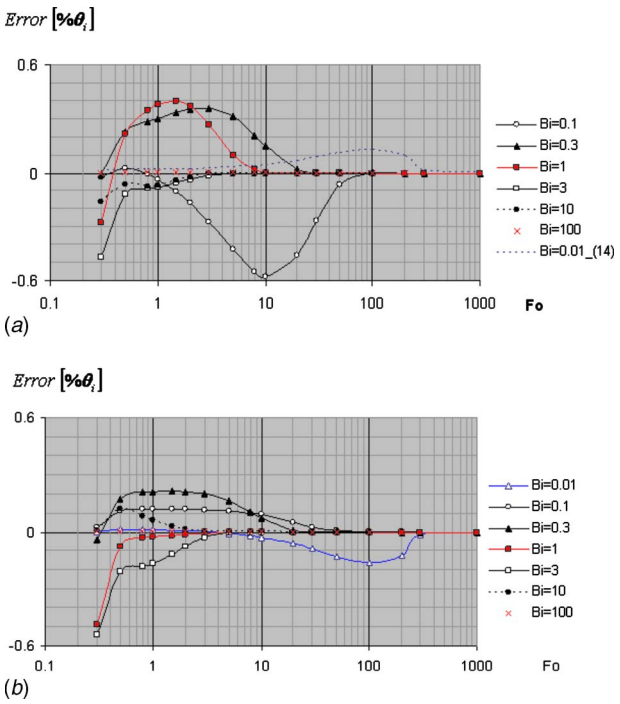


**Fig. 7 Error in midplane temperature, error (%)$=(\theta_{\mathrm{exact}}-\theta_{\mathrm{approx}})/\theta_i\times 100\%$, for 2*L* plates as a function of Bi and Fo, calculated using equations listed in Table 4, with correlations for $\mu_1$ listed in (*a*) Table 5 and (*b*) Table 6.**

## 3.4 Results for the Broad-Range Correlations

Figure 6 shows the transient temperature $\theta(t)/\theta_i$ at $\xi=0$, plotted in the format of the Heisler charts [2]. The exact Fourier series solution is given by the full lines. The approximate solutions were calculated using (i) the correlations listed in Table 4 (ii) the eigenvalues given in Table 5. The error in $\theta(t)/\theta_i$ is well below 1%. This level of precision cannot be obtained from the Heisler charts or by interpolating the tabulated values for $\mu_1$. Since the log-linear charts do not provide a sufficient resolution, the error in midplane temperature for a 2*L* plate is shown in Fig. 7. For $\mathrm{Bi}>10$, the error is particularly low ($>0.1\%$) because conduction within the solid (not convection at the boundary) controls the transient.

## 4 Conclusions and Recommendations

The *low Biot number solution* (LBi, Table 1) is approximately three times more accurate than the lumped capacity solution. It is recommended for the $0.03<\mathrm{Bi}<0.3$ range, where the error of the lumped capacity solution is considerable (see Table 3). *The extended low Biot number solution* (ELBi, Table 2) is approximately ten times more accurate than the lumped capacity solution but is

**Table 5 Explicit correlations for the first eigenvalue: simpler option**

| | $\mathrm{Bi}\leqslant 0.1$ | $\mathrm{Bi}>0.1$ |
|---|---|---|
| Plate | $\sqrt{\mathrm{Bi}}$ | $\mu_1=\frac{\pi/2}{\sqrt{1+2.3/\mathrm{Bi}^{1.035}}}$ (74) |
| Cylinder | $\sqrt{2\mathrm{Bi}}$ | $\mu_1=\frac{2.4048}{\sqrt{1+2.62/\mathrm{Bi}^{1.05}}}$ (82) |
| Sphere | $\sqrt{3\mathrm{Bi}}$ | $\mu_1=\frac{\pi}{\sqrt{1+2.93/\mathrm{Bi}^{1.08}}}$ (89) |

**Table 6 Explicit correlations for the first eigenvalues: the general option**

| | $0<\mathrm{Bi}<\infty$ |
|---|---|
| Plate | $\mu_1=\frac{\pi/2}{(1+2.62/\mathrm{Bi}^{1.07})^{0.468}}$ (76) |
| Cylinder | $\mu_1=\frac{2.4048}{(1+3.28/\mathrm{Bi}^{1.125})^{0.446}}$ (84) |
| Sphere | $\mu_1=\frac{\pi}{(1+4.1/\mathrm{Bi}^{1.18})^{0.4238}}$ (91) |

more complicated. It is most useful in the $0.1 < \mathrm{Bi} < 1$ range. *The broad-range correlations* (Table 4 with Table 5 and 6) yield less that 1% $\theta_i$ error in the entire $0 < \mathrm{Bi} < \infty$ range (for $\mathrm{Fo} \geq 0.3$). For $\mathrm{Fo} > 0.5$, the error is typically less than 0.2% $\theta_i$.


## Acknowledgment

Professor B. B. Mikic of Massachusetts Institute of Technology provided valuable ideas and advice throughout this project.


## Nomenclature

$A$ = area
$B$ = Fourier coefficient for transient temperature
$C$ = Fourier coefficient for heat loss
$F$ = orthogonal function
$A/V$ = surface to volume ratio
$\alpha$ = thermal diffusivity
$c$ = specific heat
$L$ = characteristic length
$R$ = radius of cylinder or sphere
$k$ = thermal conductivity
$h$ = heat transfer coefficient
$T$ = temperature
$T_i$ = initial temperature
$T_f$ = fluid temperature
$Q(t)$ = heat loss
$Q_0$ = total energy content
$\rho$ = density
$\mu_n$ = $n$th root of eigenvalue equation
$\mu_{1,\infty}$ = the first eigenvalue for $\mathrm{Bi} \to \infty$
$\mu_{1,0}$ = the first eigenvalue for $\mathrm{Bi} \to 0$
$\lambda_n$ = $n$th eigenvalue

### Dimensionless Parameters

$\mathrm{Bi}$ = $hL/k$
$\mathrm{Fo}$ = $\alpha t/L^2$
$\xi$ = $x/L$ or $r/R$

## References


[1] Fourier, J. B. J., 2003, "Theorie analytic da la chaleur," *The Analytical Theory of Heat*, Dover, New York.
[2] Heisler, M. P., 1947, "Temperature Charts for Induction and Constant-Temperature Heating," Trans. ASME, **69**, pp. 227–236.
[3] Churchill, S. W., and Usagi, R., 1972, "A General Expression for the Correlation of Rates of Transfer and Other Phenomena," AIChE J., **18**, pp. 1121–1128.
[4] Luikov, A. V., 1968, *Analytical Heat Diffusion Theory*, Academic, New York.
[5] Beck, J. V., Cole, K. D., Haji-Sheikh, A., and Litouhi, B., 1992, *Heat Conduction Using Green's Functions*, Hemisphere, Washington, DC, p. 496.
[6] Yovanovich, M. M., 1996, National Heat Transfer Conference, Houston, TX, Aug. 3–6, Paper No. AIAA-96–3968.
[7] Ostrogorsky, A. G., and Mikic, B. B., 2008, J. Cryst. Growth, **310**, pp. 2691–2696.
[8] Incropera, F. P., and De Witt, D. P., 1990, *Introduction to Heat Transfer*, 2nd ed., Willey, New York.
[9] Mikic, B. B., 2007/2008, private communication.
[10] Arpaci, V., 1966, *Conduction Heat Transfer*, Addison-Wesley, Reading, MA.
[11] Kakac, S., 1993, *Heat Conduction*, 3rd ed., Taylor & Fancis, London.
[12] Rohsenow, W. M., and Choi, H. Y., 1961, *Heat Mass and Momentum Transfer*, Prentice-Hall, Englewood Cliffs, NJ.

# Analytical Solution to Transient Asymmetric Heat Conduction in a Multilayer Annulus

**Prashant K. Jain**[1]
**Suneet Singh**
**Rizwan-uddin**

Department of Nuclear, Plasma and Radiological Engineering,
University of Illinois at Urbana–Champaign,
216 Talbot Lab,
104 South Wright Street,
Urbana, IL 61801

*In this paper, we present an analytical double-series solution for the time-dependent asymmetric heat conduction in a multilayer annulus. In general, analytical solutions in multidimensional Cartesian or cylindrical $(r,z)$ coordinates suffer from existence of imaginary eigenvalues and thus may lead to numerical difficulties in computing analytical solution. In contrast, the proposed analytical solution in polar coordinates (2D cylindrical) is "free" from such imaginary eigenvalues. Real eigenvalues are obtained by virtue of precluded explicit dependence of transverse (radial) eigenvalues on those in the other direction.* [DOI: 10.1115/1.2977553]

*Keywords: heat conduction, layered annulus, analytical method*

## 1 Introduction

In modern engineering applications, multilayer components are extensively used due to the added advantage of combining physical, mechanical, and thermal properties of different materials. Many of these applications require a detailed knowledge of transient temperature and heat-flux distribution within the component layers. Both analytical and numerical techniques may be used to solve such problems. Nonetheless, numerical solutions are preferred and prevalent in practice, due to either unavailability or higher mathematical complexity of the corresponding exact solutions. Rather limited use of analytical solutions should not diminish their merit over numerical ones; since exact solutions, if available, provide an insight into the governing physics of the problem, which is typically missing in any numerical solution. Moreover, analyzing closed-form solutions to obtain optimal design options for any particular application of interest is relatively simpler. In addition, exact solutions find their applications in validating and comparing various numerical algorithms to help improve computational efficiency of computer codes that currently rely on numerical techniques.

Although multilayer heat conduction problems have been studied in great detail and various solution methods—including *orthogonal and quasiorthogonal expansion technique, Laplace transform method, Green's function approach, finite integral transform technique* [1–11]—are readily available; there is a continued need to develop and explore novel methods to solve problems for which exact solutions still do not exist. One such problem is to determine exact unsteady temperature distribution in polar coordinates $(r,\theta)$ with multiple layers in the radial direction.

Salt [12,13] addressed time-dependent heat conduction problem by orthogonal expansion technique, in a two-dimensional composite slab (Cartesian geometry) with no internal heat source, subjected to homogenous boundary conditions. Later, Mikhailov and Ozisik [14] solved the 3D transient conduction problem in a Cartesian nonhomogenous finite medium. More recently, Haji-Sheikh and Beck [15] applied Green's function approach to develop transient temperature solutions in a 3D Cartesian two-layer orthotropic medium including the effects of contact resistance. Lu et al. [5] developed a novel method by combining Laplace transform method and *separation of variables method* to solve multidimensional transient heat conduction problem in a rectangular and cylindrical multilayer slab with time-dependent periodic boundary condition. The treatment in the cylindrical coordinates is, however, restricted to the $r-z$ coordinates. *Eigenfunction expansion method* is applied by de Monte [16] to solve the unsteady heat conduction problem in a two-dimensional two-layer isotropic slab subjected to homogenous boundary conditions. Feng-Bin Yeh [17] applied the method of separation of variables to solve plasma heating of a one-dimensional two-layer composite slab with layers in imperfect thermal contact.

The brief review of relevant literature is by no means exhaustive. However, a literature survey showed that the analytical solution for unsteady temperature distribution in a multilayer annular geometry has not yet been developed. Recently, an exact solution based on the separation of variables method is developed by Singh et al. [18] for multilayer heat conduction in polar coordinates. However, that exact solution is applicable only to domains with pie slice geometry ($\phi<2\pi$, where $\phi$ is the angle subtended by the layers). Numerous applications involving multilayer cylindrical geometry require evaluation of temperature distribution in complete disk-type (i.e., $\phi=2\pi$) layers. One typical example is a nuclear fuel rod, which consists of concentric layers of different materials and often subjected to asymmetric boundary conditions. Moreover, several other applications including multilayer insulation materials, double heat-flux conductimeter, typical laser absorption calorimetry experiments, cryogenic systems, and other cylindrical building structures would benefit from such analytical solutions. This paper extends the solution approach developed by Singh et al. [18] for such applications and presents an analytical double-series solution for the time-dependent asymmetric heat conduction in a multilayer annulus. Solution is valid for any combinations of time-independent, inhomogeneous boundary conditions at the inner and outer radii of the domain. The results for an illustrative problem involving a three-layer annulus subjected to asymmetric heat-flux are also presented.

## 2 Mathematical Formulation

Consider an $n$-layer annulus ($r_0 \leqslant r \leqslant r_n$), as shown schematically in Fig. 1. All the layers are assumed to be isotropic in thermal properties and are in perfect thermal contact. Let $k_i$ and $\alpha_i$ be the temperature independent thermal conductivity and thermal diffusivity of the $i$th layer. At $t=0$, each $i$th layer is at a specified temperature $f_i(r,\theta)$ and time-independent heat sources $g_i(r,\theta)$ are switched on for $t>0$. Both the inner ($i=1$, $r=r_0$) as well as the

[1]Corresponding author.

Contributed by the Heat Transfer Division of ASME for publication in the JOURNAL OF HEAT TRANSFER. Manuscript received February 12, 2008; final manuscript received April 21, 2008; published online October 20, 2008. Review conducted by Peter Vadasz.

  

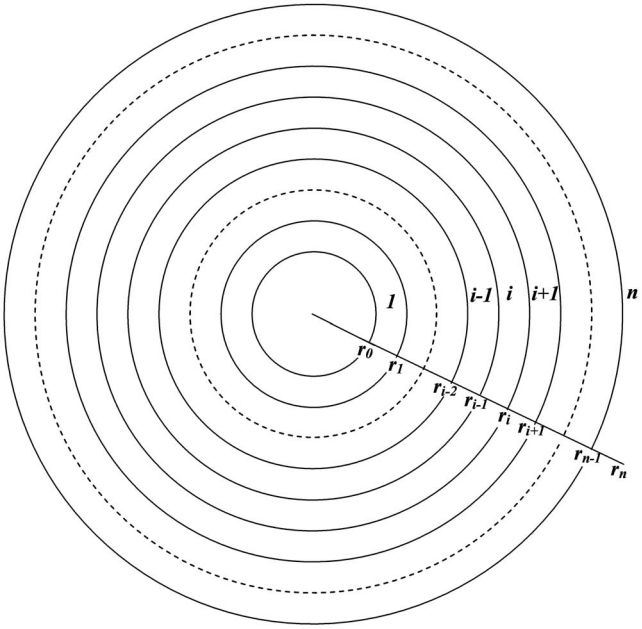


**Fig. 1 Schematic of an *n*-layer annulus. *i*th layer has an inner and outer radii equal to $r_{i-1}$ and $r_i$, respectively.**

outer ($i=n$, $r=r_n$) surfaces of the annulus may be subjected to any combination of temperature and heat-flux boundary conditions. (Since perfect thermal contact between the adjacent layers is seldom observed in real materials, dealing with imperfect contact would require explicit modeling of the thermal resistance at the layer interfaces [11,17,19]. For such cases, the temperature at the contact interfaces will not be continuous.)

Under these assumptions, the governing heat conduction equation along with the boundary and initial conditions are as follows. Governing equation (for $r_{i-1} \leq r \leq r_i$, $0 \leq \theta \leq 2\pi$, and $t>0$, where $i=1,2,\ldots,n$):

$$\frac{1}{\alpha_i}\frac{\partial T_i}{\partial t}(r,\theta,t) = \frac{1}{r}\frac{\partial}{\partial r}\left(r\frac{\partial T_i}{\partial r}(r,\theta,t)\right) + \frac{1}{r^2}\frac{\partial^2 T_i}{\partial \theta^2}(r,\theta,t) + \frac{g_i(r,\theta)}{k_i} \tag{1}$$

Boundary conditions:

- Inner surface of the first layer (for $0 \leq \theta \leq 2\pi$ and $t>0$)

$$A_{\text{in}}\frac{\partial T_1}{\partial r}(r_0,\theta,t) + B_{\text{in}}T_1(r_0,\theta,t) = C_{\text{in}}(\theta) \tag{2}$$

- Outer surface of the $n$th layer (for $0 \leq \theta \leq 2\pi$ and $t>0$)

$$A_{\text{out}}\frac{\partial T_n}{\partial r}(r_n,\theta,t) + B_{\text{out}}T_n(r_n,\theta,t) = C_{\text{out}}(\theta) \tag{3}$$

- Periodic boundary conditions (for $r_{i-1} \leq r \leq r_i$ and $t>0$, where $i=1,2,\ldots,n$)

$$T_i(r,\theta=0,t) = T_i(r,\theta=2\pi,t) \tag{4}$$

$$\frac{\partial T_i}{\partial \theta}(r,\theta=0,t) = \frac{\partial T_i}{\partial \theta}(r,\theta=2\pi,t) \tag{5}$$

- Interface of the $(i-1)$st and the $i$th layer (for $0 \leq \theta \leq 2\pi$ and $t>0$, where $i=2,\ldots,n$)

$$T_i(r_{i-1},\theta,t) = T_{i-1}(r_{i-1},\theta,t) \tag{6}$$

$$k_i\frac{\partial T_i}{\partial r}(r_{i-1},\theta,t) = k_{i-1}\frac{\partial T_{i-1}}{\partial r}(r_{i-1},\theta,t) \tag{7}$$

Initial condition (for $r_{i-1} \leq r \leq r_i$ and $0 \leq \theta \leq 2\pi$, where $i=1,2,\ldots,n$):

$$T_i(r,\theta,t=0) = f_i(r,\theta) \tag{8}$$

Boundary conditions either of the first, second, or third kind may be imposed at $r=r_0$ and $r=r_n$ by choosing the appropriate coefficients in Eqs. (2) and (3). However, the case in which $B_{\text{in}}$ and $B_{\text{out}}$ are simultaneously zero is not considered. In addition, asymmetric boundary conditions can be applied by choosing $\theta$-dependent $C_{\text{in}}$ and $C_{\text{out}}$. Furthermore, multiple layers with zero inner radius ($r_0=0$) can be simulated by assigning zero values to constants $B_{\text{in}}$ and $C_{\text{in}}$ in Eq. (2). It should be noted that the formulation presented in this paper only applies toward time-independent boundary conditions and/or source terms due to the limitation of the separation of variables method. This solution methodology cannot be extended to include the effects of time-dependence in boundary conditions and/or sources. Such problems can be solved analytically using the finite integral transform technique [20,21].

## 3 Solution Methodology

In order to apply the separation of variables method, which is only applicable to homogenous problems, the nonhomogenous problem has to be split [21] into: (1) homogenous transient problem, and (2) nonhomogenous steady-state problem. This is accomplished by splitting $T_i(r,\theta,t)$ in the governing Eqs. (1)–(8) as $\bar{T}_i(r,\theta,t)+T_{\text{ss},i}(r,\theta)$, where $\bar{T}_i(r,\theta,t)$ is the "complementary" transient part and $T_{\text{ss},i}(r,\theta)$ is the steady-state part of the solution.

**3.1 Homogenous Transient Problem.** Homogenized complementary transient equations corresponding to Eqs. (1)–(8) are as follows.

Governing equation (for $r_{i-1} \leq r \leq r_i$, $0 \leq \theta \leq 2\pi$ and $t>0$, where $i=1,2,\ldots,n$):

$$\frac{1}{\alpha_i}\frac{\partial \bar{T}_i}{\partial t}(r,\theta,t) = \frac{1}{r}\frac{\partial}{\partial r}\left(r\frac{\partial \bar{T}_i}{\partial r}(r,\theta,t)\right) + \frac{1}{r^2}\frac{\partial^2 \bar{T}_i}{\partial \theta^2}(r,\theta,t) \tag{9}$$

Boundary conditions:

- Inner surface of the first layer (for $0 \leq \theta \leq 2\pi$ and $t>0$)

$$A_{\text{in}}\frac{\partial \bar{T}_1}{\partial r}(r_0,\theta,t) + B_{\text{in}}\bar{T}_1(r_0,\theta,t) = 0 \tag{10}$$

- Outer surface of the $n$th layer (for $0 \leq \theta \leq 2\pi$ and $t>0$)

$$A_{\text{out}}\frac{\partial \bar{T}_n}{\partial r}(r_n,\theta,t) + B_{\text{out}}\bar{T}_n(r_n,\theta,t) = 0 \tag{11}$$

- Periodic boundary conditions (for $r_{i-1} \leq r \leq r_i$ and $t>0$, where $i=1,2,\ldots,n$)

$$\bar{T}_i(r,\theta=0,t) = \bar{T}_i(r,\theta=2\pi,t) \tag{12}$$

$$\frac{\partial \bar{T}_i}{\partial \theta}(r,\theta=0,t) = \frac{\partial \bar{T}_i}{\partial \theta}(r,\theta=2\pi,t) \tag{13}$$

- Interface of the $(i-1)$st and the $i$th layer (for $0 \leq \theta \leq 2\pi$ and $t>0$ where $i=2,\ldots,n$)

$$\bar{T}_i(r_{i-1},\theta,t) = \bar{T}_{i-1}(r_{i-1},\theta,t) \tag{14}$$

$$k_i \frac{\partial \bar{T}_i}{\partial r}(r_{i-1},\theta,t) = k_{i-1} \frac{\partial \bar{T}_{i-1}}{\partial r}(r_{i-1},\theta,t) \tag{15}$$

Initial condition (for $r_{i-1} \leqslant r \leqslant r_i$ and $0 \leqslant \theta \leqslant 2\pi$, where $i = 1,2,\ldots,n$):

$$\bar{T}_i(r,\theta,t=0) = f_i(r,\theta) - T_{\mathrm{ss},i}(r,\theta) \tag{16}$$

**3.2 Inhomogeneous Steady-State Problem.** Inhomogeneous steady-state equations corresponding to Eqs. (1)–(8) are as follows. Governing equation (for $r_{i-1} \leqslant r \leqslant r_i$ and $0 \leqslant \theta \leqslant 2\pi$, where $i = 1,2,\ldots,n$):

$$\frac{1}{r}\frac{\partial}{\partial r}\left(r\frac{\partial T_{\mathrm{ss},i}}{\partial r}(r,\theta)\right) + \frac{1}{r^2}\frac{\partial^2 T_{\mathrm{ss},i}}{\partial \theta^2}(r,\theta) + \frac{g_i(r,\theta)}{k_i} = 0,$$
$$r_{i-1} \leqslant r \leqslant r_i,\ 1 \leqslant i \leqslant n \tag{17}$$

Boundary conditions:

- Inner surface of the first layer (for $0 \leqslant \theta \leqslant 2\pi$)

$$A_{\mathrm{in}}\frac{\partial T_{\mathrm{ss},1}}{\partial r}(r_0,\theta) + B_{\mathrm{in}}T_{\mathrm{ss},1}(r_0,\theta) = C_{\mathrm{in}}(\theta) \tag{18}$$

- Outer surface of the $n$th layer (for $0 \leqslant \theta \leqslant 2\pi$)

$$A_{\mathrm{out}}\frac{\partial T_{\mathrm{ss},n}}{\partial r}(r_n,\theta) + B_{\mathrm{out}}T_{\mathrm{ss},n}(r_n,\theta) = C_{\mathrm{out}}(\theta) \tag{19}$$

- Periodic boundary conditions (for $r_{i-1} \leqslant r \leqslant r_i$, where $i = 1,2,\ldots,n$)

$$T_{\mathrm{ss},i}(r,\theta=0) = T_{\mathrm{ss},i}(r,\theta=2\pi) \tag{20}$$

$$\frac{\partial T_{\mathrm{ss},i}}{\partial \theta}(r,\theta=0) = \frac{\partial T_{\mathrm{ss},i}}{\partial \theta}(r,\theta=2\pi) \tag{21}$$

- Interface of the $(i-1)$st and the $i^{\mathrm{th}}$ layer (for $0 \leqslant \theta \leqslant 2\pi$, where $i = 2,\ldots,n$)

$$T_{\mathrm{ss},i}(r_{i-1},\theta) = T_{\mathrm{ss},i-1}(r_{i-1},\theta) \tag{22}$$

$$k_i\frac{\partial T_{\mathrm{ss},i}}{\partial r}(r_{i-1},\theta) = k_{i-1}\frac{\partial T_{\mathrm{ss},i-1}}{\partial r}(r_{i-1},\theta) \tag{23}$$

## 4 Solution to the Homogenous Transient Problem

**4.1 Separation of Variables.** Substituting the product form

$$\bar{T}_i(r,\theta,t) = R_i(r)\Theta(\theta)\Gamma_i(t) \tag{24}$$

in Eq. (9) and applying separation of variables yield the following ordinary differential equations (ODEs).

$$\frac{1}{r}\frac{d}{dr}\left(r\frac{dR_i(r)}{dr}\right) + \left(\lambda_i^2 - \frac{m^2}{r^2}\right)R_i(r) = 0 \quad \text{in } r_{i-1} \leqslant r \leqslant r_i,$$
$$\text{where } i = 1,2,\ldots,n \tag{25}$$

$$\frac{d^2\Theta(\theta)}{d\theta^2} + m^2\Theta(\theta) = 0 \quad \text{in } 0 \leqslant \theta \leqslant 2\pi \tag{26}$$

$$\frac{1}{\alpha_i}\frac{d\Gamma_i(t)}{dt} + \lambda_i^2\Gamma_i(t) = 0 \quad \text{for } t > 0, \quad \text{where } i = 1,2,\ldots,n \tag{27}$$

where $\lambda_i^2$ are constants of separation.

**4.2 General Solution.** In view of the ODEs listed above, a general solution for Eq. (9) may be realized as

$$\bar{T}_i(r,\theta,t) = \sum_{p=1}^{\infty} D_{0p}e^{-\alpha_i\lambda_{i0p}^2 t}R_{i0p}(\lambda_{i0p}r) + \sum_{m=1}^{\infty}\sum_{p=1}^{\infty} D_{\mathrm{mp}}e^{-\alpha_i\lambda_{\mathrm{imp}}^2 t}R_{\mathrm{imp}}(\lambda_{\mathrm{imp}}r)\cos(m\theta) + \sum_{m=1}^{\infty}\sum_{p=1}^{\infty} E_{\mathrm{mp}}e^{-\alpha_i\lambda_{\mathrm{imp}}^2 t}R_{\mathrm{imp}}(\lambda_{\mathrm{imp}}r)\sin(m\theta) \tag{28}$$

where continuity of the heat-flux at the layer interfaces requires the following relationship between the $i$th $\lambda_{\mathrm{imp}}$ and $\lambda_{1\mathrm{mp}}$ to hold [15,16,21,22],

$$\lambda_{\mathrm{imp}} = \lambda_{1\mathrm{mp}}\sqrt{\alpha_1/\alpha_i} \quad i = 1,2,\ldots,n \tag{29}$$

The radial (transverse) eigenfunction, $R_{\mathrm{imp}}(\lambda_{\mathrm{imp}}r)$ in Eq. (28) is

$$R_{\mathrm{imp}}(\lambda_{\mathrm{imp}}r) = a_{\mathrm{imp}}J_m(\lambda_{\mathrm{imp}}r) + b_{\mathrm{imp}}Y_m(\lambda_{\mathrm{imp}}r) \tag{30}$$

and the corresponding orthogonality condition is [18]

$$\sum_{i=1}^{n}\frac{k_i}{\alpha_i}\int_{r_{i-1}}^{r_i} rR_{\mathrm{imp}}(\lambda_{\mathrm{imp}}r)R_{\mathrm{imq}}(\lambda_{\mathrm{imq}}r)dr = \begin{cases} 0 & \text{if } p \neq q \\ N_{\mathrm{rmp}} & \text{if } p = q \end{cases} \tag{31}$$

where $J_m$ and $Y_m$ are Bessel functions of the first and second kind of order $m$, respectively. $N_{\mathrm{rmp}}$ is normalization integral in the $r$-direction.

For the angular eigenfunctions $\Theta_m(\theta)$—formed via combination of constant $\sin(m\theta)$ and $\cos(m\theta)$—the standard orthogonality condition is valid [21].

**4.3 Radial (Transverse) Eigencondition.** Application of the boundary conditions (Eqs. (10) and (11)) and interface conditions (Eqs. (14) and (15)) to the transverse eigenfunction $R_{\mathrm{imp}}(\lambda_{\mathrm{imp}}r)$ yields a $(2n \times 2n)$ matrix for each integer value of $m$. Transverse eigencondition is obtained by setting the determinant of this matrix equal to zero. Roots of which, in turn, yield the infinite number of eigenvalues $\lambda_{1\mathrm{mp}}$ corresponding to the first layer for each integer value of $m$.

**4.4 Determination of Coefficients $a_{\mathrm{imp}}$ and $b_{\mathrm{imp}}$.** Coefficients $a_{\mathrm{imp}}$ and $b_{\mathrm{imp}}$ in the radial eigenfunction $R_{\mathrm{imp}}(\lambda_{\mathrm{imp}}r)$ (see Eq. (30)) are evaluated from the following recurrence relationship, obtained from the $i$th interface condition, valid for $i \in (1,n-1)$:

$$\begin{pmatrix} a_{i+1,\mathrm{mp}} \\ b_{i+1,\mathrm{mp}} \end{pmatrix} = \begin{pmatrix} J_m(\lambda_{i+1,\mathrm{mp}}r_i) & Y_m(\lambda_{i+1,\mathrm{mp}}r_i) \\ k_{i+1}J_m'(\lambda_{i+1,\mathrm{mp}}r_i) & k_{i+1}Y_m'(\lambda_{i+1,\mathrm{mp}}r_i) \end{pmatrix}^{-1} \times \begin{pmatrix} J_m(\lambda_{\mathrm{imp}}r_i) & Y_m(\lambda_{\mathrm{imp}}r_i) \\ k_iJ_m'(\lambda_{\mathrm{imp}}r_i) & k_iY_m'(\lambda_{\mathrm{imp}}r_i) \end{pmatrix}\begin{pmatrix} a_{\mathrm{imp}} \\ b_{\mathrm{imp}} \end{pmatrix} \tag{32}$$

where $b_{1\mathrm{mp}} = -(C_{1\mathrm{in}}/C_{2\mathrm{in}})a_{1\mathrm{mp}}$, and $a_{1\mathrm{mp}}$ is arbitrary.

**4.5 Determination of Coefficients $D_{0p}$, $D_{\mathrm{mp}}$, and $E_{\mathrm{mp}}$.** Coefficients $D_{0p}$, $D_{\mathrm{mp}}$, and $E_{\mathrm{mp}}$ in Eq. (28) are evaluated by applying the initial condition (Eq. (16)) and then making use of the orthogonality conditions in the radial and angular directions, as follows

$$D_{0p} = \frac{1}{2\pi N_{r0p}}\sum_{i=1}^{n}\frac{k_i}{\alpha_i}\int_0^{2\pi}\int_{r_{i-1}}^{r_i} rR_{i0p}(\lambda_{i0p}r)\bar{T}_i(r,\theta,t=0)drd\theta \tag{33}$$

$$D_{\mathrm{mp}} = \frac{1}{\pi N_{\mathrm{rmp}}}\sum_{i=1}^{n}\frac{k_i}{\alpha_i}\int_0^{2\pi}\int_{r_{i-1}}^{r_i} rR_{\mathrm{imp}}(\lambda_{\mathrm{imp}}r)\cos(m\theta) \times \bar{T}_i(r,\theta,t=0)drd\theta \tag{34}$$

$$E_{\mathrm{mp}} = \frac{1}{\pi N_{\mathrm{rmp}}} \sum_{i=1}^{n} \frac{k_i}{\alpha_i} \int_0^{2\pi} \int_{r_{i-1}}^{r_i} r R_{\mathrm{imp}}(\lambda_{\mathrm{imp}} r) \sin(m\theta) \bar{T}_i(r,\theta,t=0) dr d\theta \tag{35}$$

## 5 Absence of imaginary Radial Eigenvalues

In general, transverse eigenvalues for multilayer time-dependent heat conduction problems in Cartesian coordinates may be imaginary [16]. Same is true for 2D $(r,z)$ cylindrical coordinates. The eigenvalues are imaginary due to the explicit dependence of the transverse eigenvalues on those in the remaining direction(s). For example, in a two-layer homogenous heat conduction problem with layers in the $x$-direction, the general solution in the $i$th layer is [15,16]

$$T_i(x,y,t) = \sum_{m=1}^{\infty} \sum_{p=1}^{\infty} Z_{\mathrm{mp}} e^{-\alpha_i(\nu_{\mathrm{imp}}^2 + \eta_m^2)t} X_{\mathrm{imp}}(\nu_{\mathrm{imp}} x) Y_m(\eta_m y) \tag{36}$$

where $\nu_{\mathrm{imp}}$ and $\eta_m$ are eigenvalues in the $x$- and $y$-directions, respectively; and $X_{\mathrm{imp}}$ $(\nu_{\mathrm{imp}} x)$ and $Y_m(\eta_m y)$ are the corresponding eigenfunctions.

For heat-flux to be continuous at the interface $\forall t$

$$\alpha_1(\nu_{1\mathrm{mp}}^2 + \eta_m^2) = \alpha_2(\nu_{2\mathrm{mp}}^2 + \eta_m^2) \tag{37}$$

which implies

$$\nu_{2\mathrm{mp}} = \sqrt{\frac{\alpha_1}{\alpha_2}\nu_{1\mathrm{mp}}^2 + \left(\frac{\alpha_1}{\alpha_2} - 1\right)\eta_m^2} \tag{38}$$

Clearly, the relationship above may result in either real or imaginary transverse eigenvalues [13,15,16].

However, in the present case, similar considerations led to Eq. (29), which is similar to what has been established for 1D multilayer time-dependent problems and eliminates the possibility of imaginary eigenvalues. Moreover, physical considerations dictate that eigenvalues should be real (both in the present and the corresponding 1D case) because imaginary eigenvalues will result in exponentially growing temperatures. In contrast, the solution given in Eq. (36) can have a physically realizable solution even in the case where eigenvalues in one of the directions are imaginary.

It should be noted that, though there is no explicit dependence between radial and angular eigenvalues, the order of the Bessel functions constituting radial eigenfunctions is determined by the angular eigenvalues. Hence, the radial eigenvalues *implicitly* depend on the angular eigenvalues. Moreover, unlike in Cartesian coordinates, this implicit dependence does not vanish even if $\alpha_1 = \alpha_i (i \neq 1)$. In fact, it exists even for single-layer problems.

## 6 Solution to the Inhomogeneous Steady-State Problem

The inhomogeneous steady-state problem is solved using the eigenfunction expansion method. The steady-state temperature distribution, governed by Eq. (17), may be written as a generalized Fourier series in terms of angular eigenfunctions,

$$T_{\mathrm{ss},i}(r,\theta) = \hat{T}_{i0}(r) + \sum_{m=1}^{\infty} \hat{T}_{c,\mathrm{im}}(r)\cos(m\theta) + \sum_{m=1}^{\infty} \hat{T}_{s,\mathrm{im}}(r)\sin(m\theta), \quad r_{i-1} \leqslant r \leqslant r_i, \quad 1 \leqslant i \leqslant n \tag{39}$$

Substituting Eq. (39) in Eq. (17) leads to the following ODEs:

$$\frac{1}{r}\frac{d}{dr}\left(r\frac{d\hat{T}_{c,\mathrm{im}}(r)}{dr}\right) - \frac{m^2}{r^2}\hat{T}_{c,\mathrm{im}}(r) + \frac{\hat{g}_{c,\mathrm{im}}(r)}{k_i} = 0 \tag{40}$$

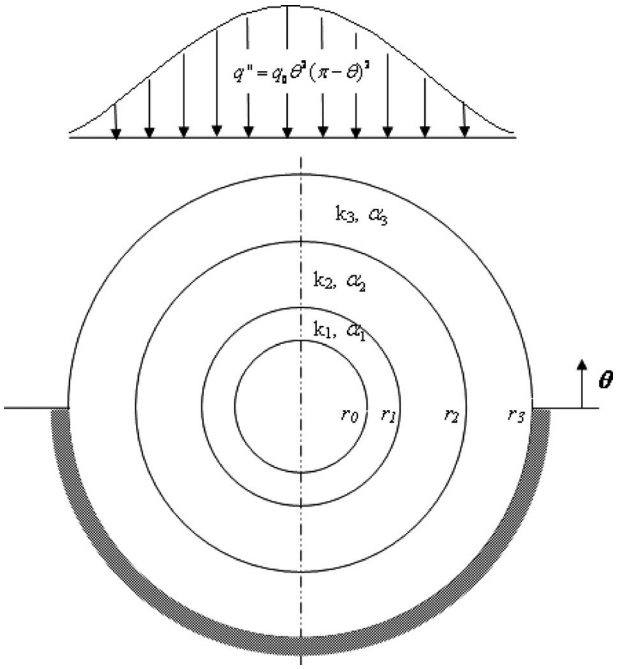


**Fig. 2 Asymmetric heat conduction in a three-layer annulus. Each layer has a different thermal conductivity ($k_i$) and thermal diffusivity ($\alpha_i$). The lower-half of the annulus ($\pi \leqslant \theta \leqslant 2\pi$) is kept insulated, while the upper-half ($0 \leqslant \theta \leqslant \pi$) is subjected to a $\theta$-dependent *incoming* heat-flux.**

$$\frac{1}{r}\frac{d}{dr}\left(r\frac{d\hat{T}_{s,\mathrm{im}}(r)}{dr}\right) - \frac{m^2}{r^2}\hat{T}_{s,\mathrm{im}}(r) + \frac{\hat{g}_{s,\mathrm{im}}(r)}{k_i} = 0 \tag{41}$$

$$\frac{1}{r}\frac{d}{dr}\left(r\frac{d\hat{T}_{i0}(r)}{dr}\right) + \frac{\hat{g}_{i0}(r)}{k_i} = 0 \tag{42}$$

where the source term $g_i(r,\theta)$ is expanded in a generalized Fourier series as

$$g_i(r,\theta) = \hat{g}_{i0}(r) + \sum_{m=1}^{\infty} \hat{g}_{c,\mathrm{im}}(r)\cos(m\theta) + \sum_{m=1}^{\infty} \hat{g}_{s,\mathrm{im}}(r)\sin(m\theta) \tag{43}$$

and

$$\hat{g}_{c,\mathrm{im}}(r) \equiv \frac{1}{\pi}\int_0^{2\pi} g_i(r,\theta)\cos(m\theta)d\theta \tag{44}$$

$$\hat{g}_{s,\mathrm{im}}(r) \equiv \frac{1}{\pi}\int_0^{2\pi} g_i(r,\theta)\sin(m\theta)d\theta \tag{45}$$

$$\hat{g}_{i0}(r) \equiv \frac{1}{2\pi}\int_0^{2\pi} g_i(r,\theta)d\theta \tag{46}$$

Similarly, $C_{\mathrm{in}}(\theta)$ and $C_{\mathrm{out}}(\theta)$ in Eqs. (18) and (19) may be expanded in a generalized Fourier series to yield boundary conditions for ODEs in Eqs. (40)–(42).

Solutions for the Euler equations, Eqs. (40) and (41) are given by

$$\hat{T}_{c,\mathrm{im}}(r) = A_{c,i}r^m + B_{c,i}r^{-m} + f_{\mathrm{pc}}(r) \tag{47}$$

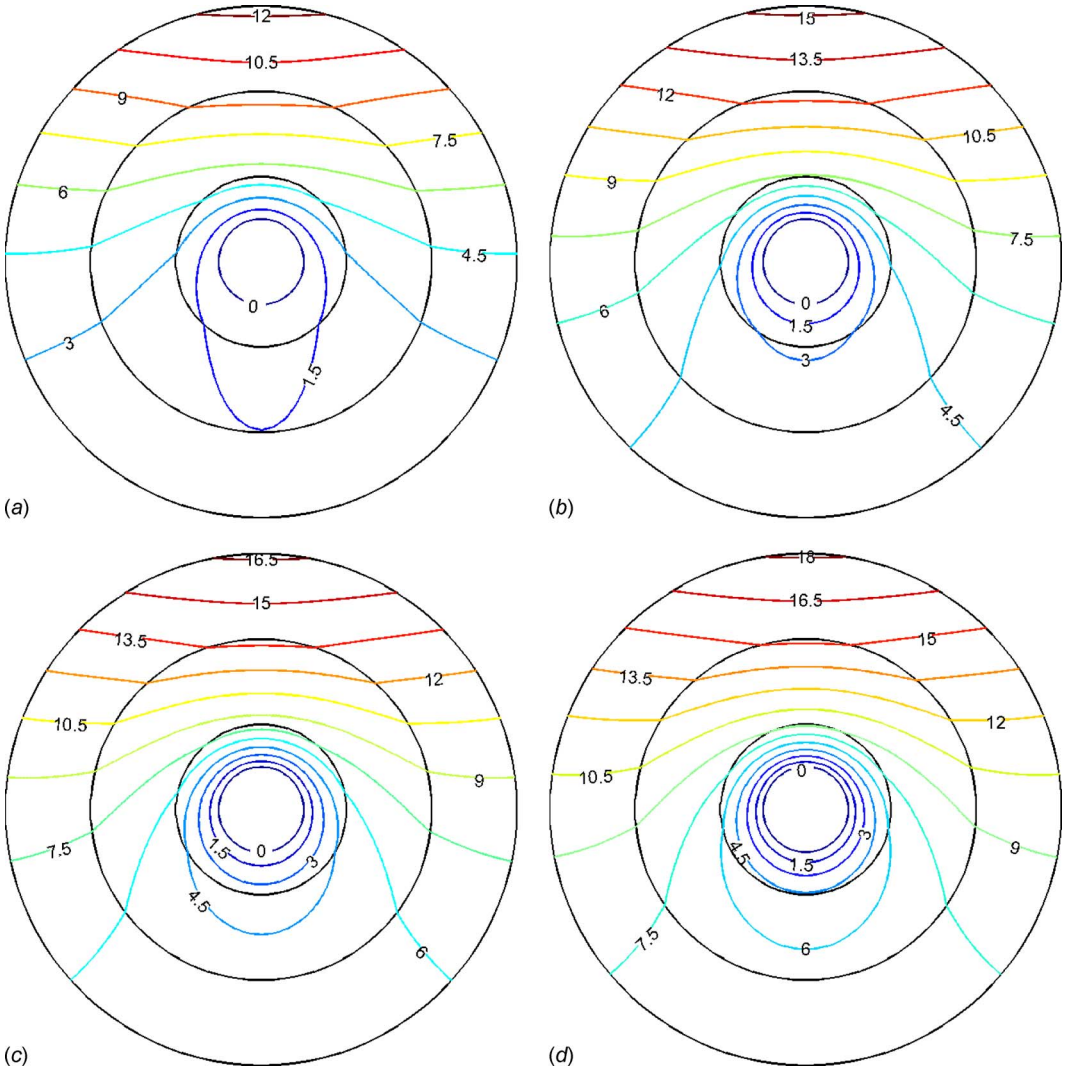


**Fig. 3 Transient isotherms in three-layer annulus: (*a*) $t=5$, (*b*) $t=10$, (*c*) $t=15$, and (*d*) steady state**

$$\hat{T}_{s,\mathrm{im}}(r) = A_{s,i}r^{m} + B_{s,i}r^{-m} + f_{\mathrm{ps}}(r) \tag{48}$$

where $f_{\mathrm{pc}}(r)$ and $f_{\mathrm{ps}}(r)$ are particular integrals, which can be evaluated by the application of method of variation of parameters or method of undetermined coefficients. The constants $A_{c,i}$, $A_{s,i}$, $B_{c,i}$, and $B_{s,i}$ may be evaluated using boundary and interface conditions for $\hat{T}_{c,\mathrm{im}}(r)$ and $\hat{T}_{s,\mathrm{im}}(r)$. Once $\hat{g}_{i0}(r)$ are evaluated, the solution for $\hat{T}_{i0}(r)$ is straightforward.

## 7 Illustrative Example and Results

A three-layer annulus ($r_0 \leqslant r \leqslant r_3$, $0 \leqslant \theta \leqslant 2\pi$; see Fig. 2) is initially at a uniform zero temperature. For time $t>0$, $\theta$-dependent heat flux given by

$$q''(r=r_3,\theta) = \begin{bmatrix} q_0\theta^2(\pi-\theta)^2, & 0 \leqslant \theta \leqslant \pi \\ 0, & \pi \leqslant \theta \leqslant 2\pi \end{bmatrix} \tag{49}$$

is applied at the outer surface ($r=r_3$) while the inner surface ($r=r_0$) is maintained isothermal at zero temperature. This leads to the coefficients $A_{\mathrm{in}}=0$, $B_{\mathrm{in}}=1$, $A_{\mathrm{out}}=k_3$, $B_{\mathrm{out}}=0$, $C_{\mathrm{in}}(\theta)=0$, and $C_{\mathrm{out}}(\theta)=q''(r_3,\theta)$ in the respective boundary condition equations. There is no volumetric heat generation in any of the layers, i.e., $g_i(r,\theta)=0$.

Parameter values used in this problem are $k_2/k_1=2$, $k_3/k_1=4$, $\alpha_2/\alpha_1=4$, $\alpha_3/\alpha_1=9$, $r_1/r_0=2$, $r_2/r_0=4$, and $r_3/r_0=6$. These have been arbitrarily chosen and do not, in any way, simplify the solution.

It should be noted that, in the results that follow, $r$, $t$, and $T_i(r,\theta,t)$ are in the units of $r_0$, $r_0^2/\alpha_1$, and, $q_0 r_0/k_1$, respectively.

For this particular problem, the infinite series solution for the complementary transient temperature $\bar{T}_i(r,\theta,t)$ is truncated at $p=P$ and $m=M$ leading to

$$\begin{aligned}\bar{T}_i(r,\theta,t) = &\sum_{p=1}^{P} D_{0p}e^{-\alpha_i\lambda_{i0p}^2 t}R_{i0p}(\lambda_{i0p}r) \\ &+ \sum_{m=1}^{M}\sum_{p=1}^{P} D_{\mathrm{mp}}e^{-\alpha_i\lambda_{\mathrm{imp}}^2 t}R_{\mathrm{imp}}(\lambda_{\mathrm{imp}}r)\cos(m\theta) \\ &+ \sum_{m=1}^{M}\sum_{p=1}^{P} E_{\mathrm{mp}}e^{-\alpha_i\lambda_{\mathrm{imp}}^2 t}R_{\mathrm{imp}}(\lambda_{\mathrm{imp}}r)\sin(m\theta) \\ &- \varepsilon_i(r,\theta,t;M,P)\end{aligned} \tag{50}$$

where $\varepsilon_i(r,\theta,t;M,P)$ is the truncation error. Since $\lambda_{1\mathrm{mp}}$ increases with increasing $m$ and $p$, it is obvious that for a given $M$ and $P$,

maximum truncation error occurs at $t=0$. Moreover, since $\bar{T}_i(r,\theta,t=0)=-T_{ss,i}(r,\theta)$, therefore

$$\varepsilon_i(r,\theta,t=0;M,P)=T_{ss,i}(r,\theta)+\sum_{p=1}^{P}D_{0p}R_{i0p}(\lambda_{i0p}r)+\sum_{m=1}^{M}\sum_{p=1}^{P}D_{mp}R_{imp}(\lambda_{imp}r)\cos(m\theta)+\sum_{m=1}^{M}\sum_{p=1}^{P}E_{mp}R_{imp}(\lambda_{imp}r)\sin(m\theta) \quad (51)$$

However, $T_{ss,i}(r,\theta)$ is also evaluated as a series solution (see Eq. (39)) and hence, the above equation can be written as

$$\varepsilon_i(r,\theta,t=0;M,P)=\left(\hat{T}_{i0}(r)+\sum_{m=1}^{M_{ss}}\hat{T}_{c,im}(r)\cos(m\theta)+\sum_{m=1}^{M_{ss}}\hat{T}_{s,im}(r)\sin(m\theta)+\varepsilon_{ss,i}(r,\theta,M_{ss})\right)+\sum_{p=1}^{P}D_{0p}R_{i0p}(\lambda_{i0p}r)+\sum_{m=1}^{M}\sum_{p=1}^{P}D_{mp}R_{imp}(\lambda_{imp}r)\cos(m\theta)+\sum_{m=1}^{M}\sum_{p=1}^{P}E_{mp}R_{imp}(\lambda_{imp}r)\sin(m\theta) \quad (52)$$

A good estimate of $\varepsilon_i(r,\theta,t=0;M,P)$ may be obtained only if $\varepsilon_{ss,i}(r,\theta;M_{ss})\ll\varepsilon_i(r,\theta,t=0;M,P)$. The above requirement may be fulfilled by including, not surprisingly, a large number of terms in the steady-state series solution so as to minimize the steady-state truncation error. The maximum difference between the steady-state temperatures obtained with $M_{ss}=45$ and $M_{ss}=50$ is found to be of the order of $10^{-5}$, therefore, this series is truncated at $M_{ss}=50$.

The maximum percent error defined as $\max(\varepsilon(r,\theta,t=0))/(T_{ss,\max}-T_{ss,\min})$ is evaluated for various values of $M$ and $P$. For $M=P=6$, 8, and 10, the error is 2.25%, 1.69%, and 1.36%, respectively.

Isotherms in the three-layer annulus are shown for different $t$ values in Fig. 3. At any time $t$, maximum and minimum temperatures are observed on the outer edge of the annulus ($r=r_3$) at angular locations $\theta=\pi/2$ and $3\pi/2$, respectively. Temperature kinks (or discontinuity in temperature slopes) are clearly visible in the isotherms indicating different thermal properties of the three layers. Additionally, radial temperature variations at distinct angular positions are shown in Fig. 4. At any given $(r,t)$, maximum and minimum temperatures are observed at $\theta=\pi/2$ and $3\pi/2$, respectively, as expected, since the *incoming* heat-flux is symmetric in $0\leqslant\theta\leqslant\pi$ and has a maxima at $\theta=\pi/2$. The results shown in Figs. 3 and 4 are obtained with $M=P=10$.

## 8 Conclusions

In this paper, an analytical solution to the asymmetric transient heat conduction in a layered annulus is presented. Each layer can have spatially varying but time-independent volumetric heat source. Inhomogeneous boundary condition of the first, second, or the third kind can be applied in the radial direction. The proposed solution is also applicable to the layered-structures with inner radius $r_0=0$.

It is noted that the solution of the multilayer two-dimensional heat conduction problem in polar coordinates is not analogous to the corresponding problem in multidimensional Cartesian coordinates (or 2D cylindrical $r-z$ coordinates). In polar coordinates, dependence of the eigenvalues in the transverse direction on those in the other direction is not explicit. The absence of explicit dependence leads to a complete solution, which does not have imaginary transverse eigenvalues. Numerical evaluation of the

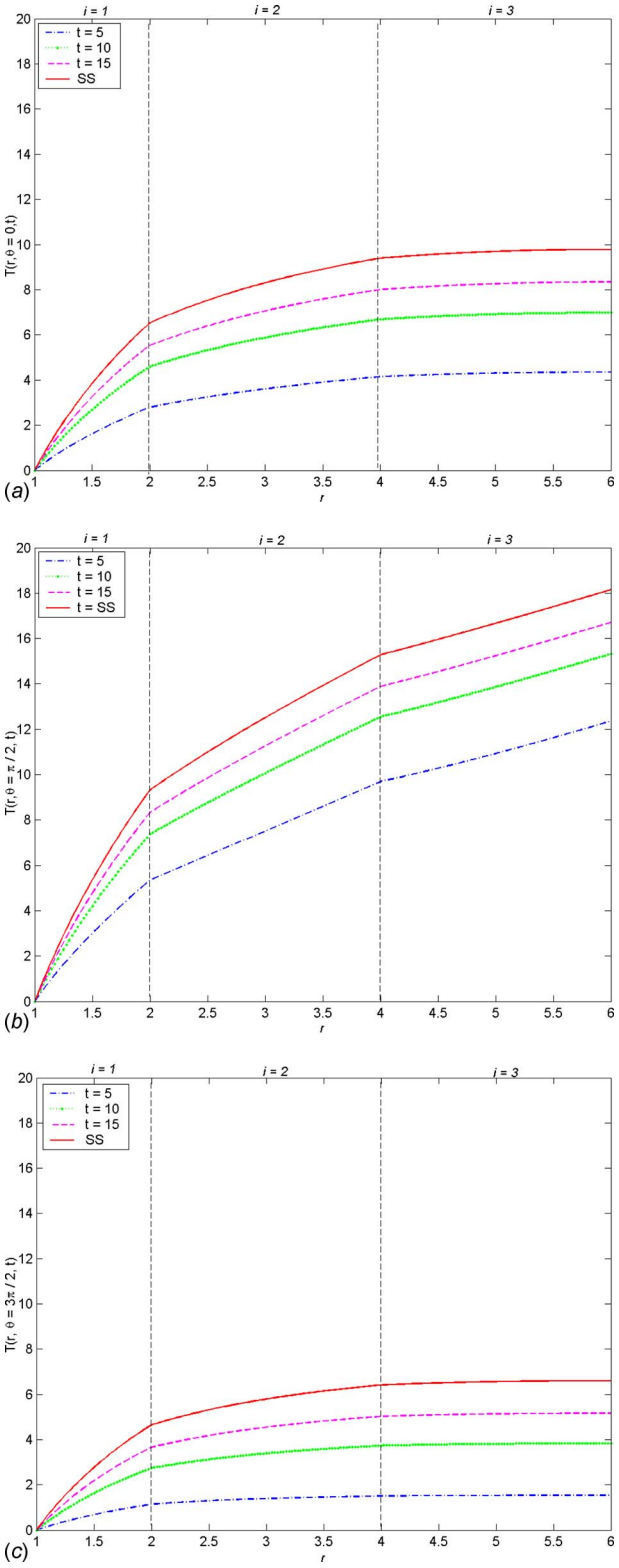


**Fig. 4 Transient temperature variation in the radial direction at (*a*) $\theta=0$, (*b*) $\theta=\pi/2$, and (*c*) $\theta=3\pi/2$**

double-series solution shows that a reasonable number of terms are sufficient to obtain results with acceptable errors for engineering applications.

## References


[1] Mulholland, G. P., and Cobble, M. H., 1972, "Diffusion Through Composite Media," Int. J. Heat Mass Transfer, **15**, pp. 147–160.

[2] Mikhailov, M. D., Ozisik, M. N., and Vulchanov, N. L., 1983, "Diffusion in Composite Layers With Automatic Solution of the Eigenvalue Problem," Int. J. Heat Mass Transfer, **26**(8), pp. 1131–1141.

[3] Desai, A., Geer, J., and Sammakia, B., 2006, "Models of Steady Heat Conduction in Multiple Cylindrical Domains," ASME J. Electron. Packag., **128**, pp. 10–17.

[4] Bulavin, P. E., and Kascheev, V. M., 1965, "Solution of the Non-Homogeneous Heat Conduction Equation for Multilayered Bodies," Int. Chem. Eng., **1**, pp. 112–115.

[5] Lu, X., Tervola, P., and Viljanen, M., 2006, "Transient Analytical Solution to Heat Conduction in Composite Circular Cylinder," Int. J. Heat Mass Transfer, **49**, pp. 341–348.

[6] Shupikov, A. N., Smetankina, N. V., and Svet, Y. V., 2007, "Nonstationary Heat Conduction in Complex-Shape Laminated Plates," ASME J. Heat Transfer, **129**, pp. 335–341.

[7] Geer, J., Desai, A., and Sammakia, B., 2007, "Heat Conduction in Multilayered Rectangular Domains," ASME J. Electron. Packag., **129**, pp. 440–451.

[8] Huang, S. C., and Chang, Y. P., 1980, "Heat Conduction in Unsteady, Periodic and Steady States in Laminated Composites," ASME J. Heat Transfer, **102**, pp. 742–748.

[9] Siegel, R., 1999, "Transient Thermal Analysis of Parallel Translucent Layers by Using Green's Functions," J. Thermophys. Heat Transfer, **13**(1), pp. 10–17.

[10] Haji-Sheikh, A., and Beck, J. V., 1990, "Green's Function Partitioning in Galerkin-Base Integral Solution of the Diffusion Equation," ASME J. Heat Transfer, **112**, pp. 28–34.

[11] Yener, Y., and Ozisik, M. N., 1974, "On the Solution of Unsteady Heat Conduction in Multi-Region Finite Media With Time-Dependent Heat Transfer Coefficient," *Proceedings of the Fifth International Heat Transfer Conference*, JSME, Tokyo, Japan, Sep. 3–7, pp. 188–192.

[12] Salt, H., 1983, "Transient Heat Conduction in a Two-Dimensional Composite Slab. I. Theoretical Development of Temperatures Modes," Int. J. Heat Mass Transfer, **26**(11), pp. 1611–1616.

[13] Salt, H., 1983, "Transient Heat Conduction in a Two-Dimensional Composite Slab. II. Physical Interpretation of Temperatures Modes," Int. J. Heat Mass Transfer, **26**(11), pp. 1617–1623.

[14] Mikhailov, M. D., and Ozisik, M. N., 1986, "Transient Conduction in a Three-Dimensional Composite Slab," Int. J. Heat Mass Transfer, **29**(2), pp. 340–342.

[15] Haji-Sheikh, A., and Beck, J. V., 2002, "Temperature Solution in Multi-Dimensional Multi-Layer Bodies," Int. J. Heat Mass Transfer, **45**(9), pp. 1865–1877.

[16] de Monte, F., 2003, "Unsteady heat Conduction in Two-Dimensional Two Slab-Shaped Regions. Exact Closed-Form Solution and Results," Int. J. Heat Mass Transfer, **46**(8), pp. 1455–1469.

[17] Yeh, F.-B., 2007, "Prediction of the Transient and Steady Temperature Distributions in a Two-Layer Composite Slab in Contact With a Plasma: Exact Closed-Form Solutions," J. Phys. D: Appl. Phys., **40**, pp. 3633–3643.

[18] Singh, S., Jain, P. K., and Rizwan-uddin, 2008, "Analytical Solution to Transient Heat Conduction in Polar Coordinates With Multiple Layers in Radial Direction," Int. J. Therm. Sci., **47**, pp. 261–273.

[19] Yuen, W. Y. D., 1994, "Transient Temperature Distribution in a Multilayer Medium Subject to Radiative Surface Cooling," Appl. Math. Model., **18**, pp. 93–100.

[20] Singh, S., Jain, P. K., and Rizwan-uddin, 2007, "Finite Integral Transform Technique to Solve Asymmetric Heat Conduction in a Multilayer Annulus With Time-Dependent Boundary Conditions," submitted.

[21] Ozisik, M. N., 1993, *Heat Conduction*, 2nd ed., Wiley and Sons, New York.

[22] de Monte, F., 2002, "An Analytic Approach to the Unsteady Heat Conduction Processes in One-Dimensional Composite Media," Int. J. Heat Mass Transfer, **45**(6), pp. 1333–1343.

# The Effect of Pore Size on the Heat Transfer Between a Heated Finned Surface and a Saturated Porous Plate

**M. J. Schertzer**

**D. Ewing**[1]

**C. Y. Ching**[2]
e-mail: chingcy@mcmaster.ca

Department of Mechanical Engineering,
McMaster University,
1280 Main Street West,
Hamilton, ON, L86 4L7, Canada

**J. S. Chang**
Department of Engineering Physics,
McMaster University,
1280 Main Street West,
Hamilton, ON, L86 4L7, Canada

*An investigation was performed to examine the effect that the pore size in a porous plate had on the heat transfer between a heated finned surface and a saturated porous plate at different gap distances between the surfaces. Experiments were performed for a porous plate with a nominal pore size of 50 $\mu$m and the results were compared with previous results for a pore size of 200 $\mu$m (Schertzer et al., 2006, "The Effect of Gap Distance on the Heat Transfer Performance Between a Finned Surface and a Saturated Porous Plate," Int. J. Heat. Mass Transfer, **4**, pp. 4200–4208). The plate with the smaller pore size performed better at small and intermediate gaps but not at large gaps. The maximum heat transfer coefficient was similar for both plates when compared in terms of the ratio between the gap distance and the pore size. However, the temperature distributions on the heated foil and their evolution with heat flux were dissimilar when compared in terms of the gap distance or the gap to pore ratio, suggesting that the boiling dynamics within the gap does not scale with either parameters.* [DOI: 10.1115/1.2977595]

*Keywords: boiling, porous structure, two-phase heat transfer, capillary evaporator*

## Introduction

Increasing heat flux requirements and thermal constraints in a range of applications have increased the demand for highly effective heat transport systems [1–3], including passive two phase heat transfer devices such as heat pipes and capillary pumped loops. In capillary pumped loops, the heat transferred to a saturated porous plate through a series of heated fins evaporates a working fluid. The resulting vapor escapes to vapor grooves between the heated fins and is carried to the condenser section before being recirculated back to the evaporator [4]. It has been argued that the boiling process below the fin can limit the wicking of fluid within the porous structure and lead to failure at high heat fluxes [5–9]. As a result, a number of models have been developed to predict the heat transfer performance of a capillary evaporator, including models that did [7–9] and did not [5,6] consider vapor penetration within the wick itself. The models that considered vapor penetration into the wick predict that this would eventually lead to a decrease in the performance of the evaporator. Experimental studies have observed the formation of a two phase liquid-vapor region within the porous structure when the heated fin was in direct contact with the wick [10–12]. In these cases, the heat transfer performance initially increased with the heat flux before reaching a maximum and then decreased with a further increase in heat flux.

The models for the capillary evaporator predicted that the heat transfer performance of the device could be improved by reducing the pore size in the wick, which increases the maximum capillary pressure and thus should delay vapor penetration [5,11]. Experiments to evaluate the effect of pore size on the heat transfer performance of a capillary evaporator were performed for bead packed beds with particle diameters between 0.55 mm and 1.99 mm (or nominal pore sizes between 194 $\mu$m and 702 $\mu$m) [11]. The results showed that the maximum heat flux increased when the particle size was reduced in all cases. However, the maximum heat transfer coefficient did not increase in all cases, instead decreasing when the particle size decreased from 1.09 mm to 0.55 mm. Liao and Zhao argued that the permeability of the porous structure was lower for the smallest particle size, which increased the viscous losses and limited the flow of the working fluid through the wick, thereby affecting the rewetting of the heated surface.

Figus et al. [13] proposed that introducing a small gap between the heated fins and the porous structure in a capillary evaporator could allow vapor to escape to the vapor channels more easily, reducing the vapor penetration into the wick. Model predictions [13] suggested that gap distances as small as 10 $\mu$m could be sufficient to improve the heat transfer performance, but experimental studies with porous structures with pore radii of 20 $\mu$m and 200 $\mu$m indicated larger optimum gap distances of 100 $\mu$m and 500 $\mu$m, respectively [14,15]. This suggests that the optimum gap distance may be a function of the pore radius, but these experiments were performed for different configurations, thus making it difficult to compare the results. In particular, Platel et al. [14] considered a coaxial evaporator, while Schertzer et al. [15] considered the heat transfer between a finned foil and a porous plate that allowed measurements of the transient temperature of the heated surface. Schertzer et al. [15] found evidence that vapor periodically built up beneath the heated surface before escaping to the vapor grooves for small gap distances. This vapor buildup appeared to be less prominent as the gap distance increased, indicating that the vapor escaped more easily as suggested by Figus et al. [13]. The performance of the evaporator initially increased with gap distance but remained relatively unchanged for gap distances between 500 $\mu$m and 900 $\mu$m. Similar measurements have not been performed for porous plates with other pore sizes, so it is not yet clear how the optimum gap distance would depend on the pore size.

The objective of this investigation was to characterize the effect

[1]Present address: Department of Mechanical and Materials Engineering, Queen's University.

[2]Corresponding author.

Contributed by the Heat Transfer Division of ASME for publication in the JOURNAL OF HEAT TRANSFER. Manuscript received November 30, 2007; final manuscript received April 29, 2008; published online October 17, 2008. Review conducted by Peter Vadasz.

  

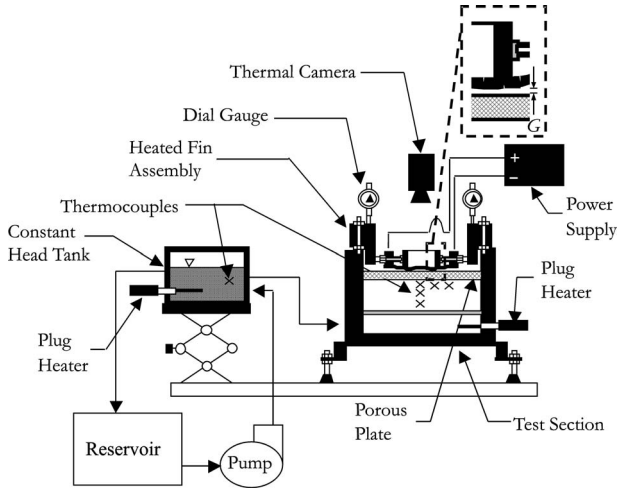


**Fig. 1 Schematic of the experimental facility**

that the pore size had on the heat transfer between a heated finned surface and a saturated porous plate. This was done by repeating the experiments outlined in Schertzer et al. [15] for a porous plate with a pore radius of 50 $\mu$m and comparing these results to those for the 200 $\mu$m pore size [15]. The experimental methodology is described in the next section followed by the experimental results and the conclusions of the investigation.

## 2 Experimental Facility

The experimental facility used in this investigation, shown in Fig. 1, was the same as that used in Schertzer et al. [15]. The facility consisted of a main test section that contained the porous plate and the heated surface, a constant head tank that supplied preheated working fluid to the test section, and a system reservoir. Distilled water from the system reservoir was constantly pumped into the constant head tank and allowed to overflow back into the reservoir in a controlled manner to maintain the height of the fluid in the constant head tank. The height of the water in the constant head tank was maintained at a level corresponding to the upper surface of the porous plate in the main test section. The water in the constant head tank was preheated to 60°C using a 1 kW plug heater that was turned on and off using a proportional-integral-derivative (PID) controller with input from a T-type thermocouple located in the tank. The water from the constant head tank entered a small reservoir on the bottom of the main test section, where it was heated to 75°C using two 100 W plug heaters that were turned on and off using a PID controller. The input in this case was the average from five T-type thermocouples placed at various heights in the main test section. The change in the volume of the working fluid within the system was measured to within $\pm 2$ mL using a graduated cylinder mounted on the system reservoir.

The experiments were performed here for a 12 mm thick porous alumina plate ($Al_2O_3$) with a reported porosity ($\Phi$) of 50% and a nominal pore radius ($R_P$) of 50 $\mu$m. Typical scanning electron microscope (SEM) images of the two porous plates are shown in Fig. 2 to illustrate the pore size and distribution. The plate was heated from above using a 25 $\mu$m thick stainless steel resistive foil that was attached to a machined Teflon block with five 80 mm long fins, as shown in Fig. 2. The stainless steel foil had a nominal width of 60 mm but much of the central section was cut away, leaving three 80 mm long strips that matched the three central fins of the Teflon block. The gap between the strips was 10 mm and the middle strip on the foil had a width of 10.0 mm, while the two adjacent strips had widths of 10.5 mm so that the largest heat flux would occur on the central strip. The two outermost fins of the Teflon block acted to contain the vapor flow from beneath the two outer heated fins. Slots that were 5 mm wide were machined through the center of the three central fins attached to the heated foil to allow optical access to the foil surface. The temperature distribution on the upper surface of the visible portion of the central strip of the foil was measured using a high-speed infrared camera. The visible portion of the foil was painted with flat black paint that had an emissivity ($\varepsilon$) of $0.96 \pm 0.01$ [16] to facilitate these measurements.

The ends of the stainless steel foil were attached to large copper electrodes and were resistively heated using a dc power supply with a maximum current output of 200 A. The copper electrodes were mounted on rails using Teflon bearings that allowed the foil to be tensioned by adjusting stainless steel screws that butted up against the Teflon block. This entire heated finned assembly was mounted on a separate set of rails that could be used to adjust the vertical gap distance between the heated surface and the porous plate (Fig. 3). The vertical gap distance was measured on either end of the evaporator section using dial gauges with an accuracy of $\pm 12.0$ $\mu$m.

At steady state, the electric heating in the stainless steel foil was transferred to the working fluid or lost to the ambient by convection or radiation. The heating in the thin strips was estimated using a resistance network, while the latent heat transfer to the water was determined using the mass flow rate from the main reservoir. These estimates were found to agree to within $\pm 5\%$ in all experiments, suggesting that the electrical heating in the thin strips could be used to determine the heat flux transferred to the fluid. The sum of the radiation and convection losses from the exposed portion of the foil was estimated to be approximately 1.2 kW/m$^2$.

The temperature distribution on the visible portion of the foil

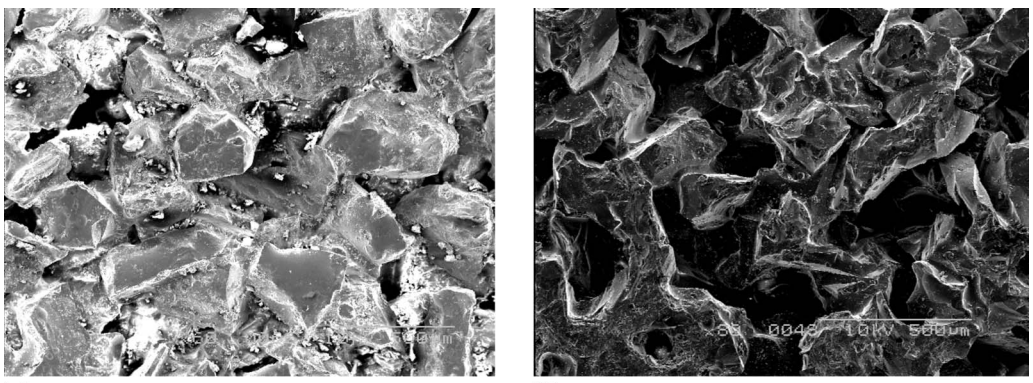

(*a*) (*b*)

**Fig. 2 SEM images of the surface of the porous plate with a pore size of (*a*) 50 $\mu$m and (*b*) 200 $\mu$m. A length of 500 $\mu$m is shown on both images.**

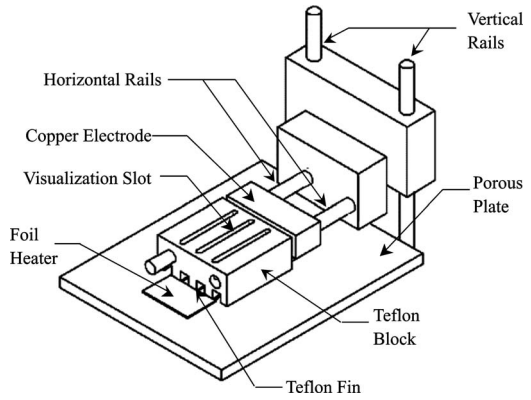


**Fig. 3 Detailed sketch of the heated fin assembly. The second copper electrode and a portion of the horizontal rails have been removed for clarity.**

beneath the center fin was measured with the high-speed infrared camera at a resolution of 0.5 mm/pixel and an accuracy of 1.0 °C. The temperature distributions for each case were recorded at both 2 frames/s and 60 frames/s, for a total of 220 frames. The measurements were taken after a minimum of 10 min of operation in order to allow the average foil temperature to come to a steady state. The average foil temperature and probability density functions (PDFs) of the temperature on the heated foil were determined from the measurements recorded at 2 frames/s, while the high frequency measurements were used to examine the boiling dynamics beneath the foil. The experimental uncertainties in the measurements for this investigation are given in Table 1, further details of which can be found in Schertzer et al. [15].

## 3 Results and Discussion

The change in the averaged temperature on the visible portion of the heated foil and the heat transfer coefficient with heat flux for $R_P$=50 $\mu$m and 200 $\mu$m [15] plates are presented in Fig. 4 for selected gap distances. In all cases, the applied heat flux was increased until a local maximum in the average heat transfer coefficient was observed. When the heat flux was increased further, the average temperature of the heated foil became unstable. The maximum heat transfer with a stable temperature increased with the gap distance for the range of gap distances studied here, consistent with previous results [13–15]. The change in the heat transfer performance with a gap can be attributed to a change in the boiling dynamics below the heated surface. Schertzer et al. [15] showed that at relatively small gap distances, vapor built up periodically beneath the heated surface before being exhausted to the vapor grooves. For larger gap distances, the vapor did not appear to build up below the fin, but instead seemed to escape to the vapor grooves relatively easily, resulting in an increase in the heat transfer performance.

The change in the average temperature with heat flux was similar for the zero gap case for both plates; however, there was a significant difference in the performance for gap distances of 300 $\mu$m or greater. The maximum stable heat flux at a gap distance of 300 $\mu$m was 160 kW/m$^2$ for the $R_P$=50 $\mu$m plate, but

**Table 1 Experimental uncertainty**

| Measurement | Expt. uncertainty |
|---|---|
| Gap distance ($G$) | ±50 $\mu$m |
| Mass flow rate ($\dot{m}$) | ±4% |
| Heat flux ($q''$) | ±5% |
| Instantaneous foil temperature ($T_{sur}$) | ±1 °C |

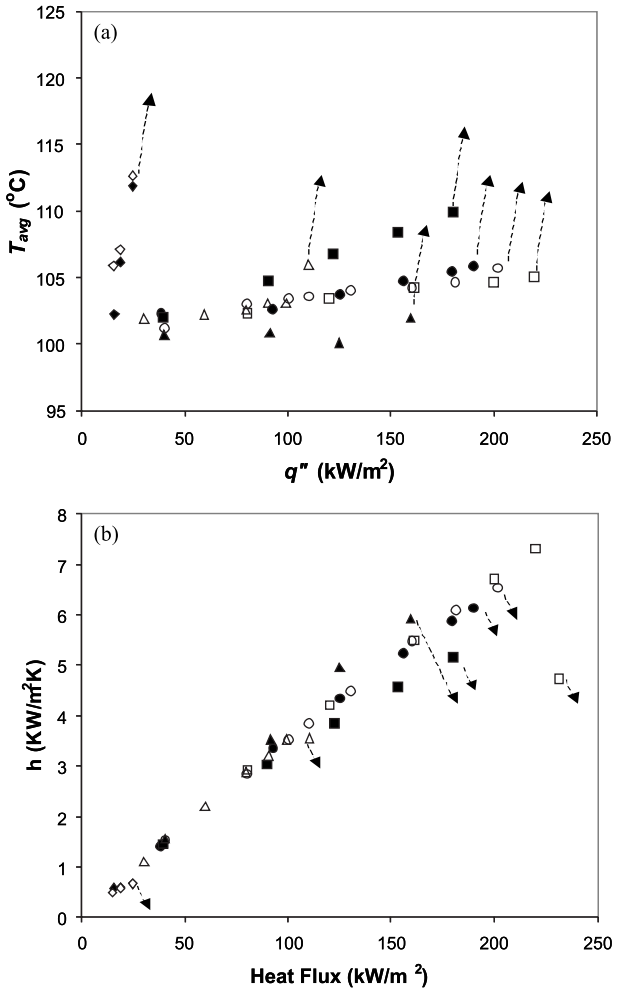


**Fig. 4 Change in (*a*) the average foil temperature and (*b*) the average heat transfer coefficient as a function of heat flux for gap distances of ◇ ◆ $G$=0 $\mu$m, ▲ △ $G$=300 $\mu$m ● ○ $G$=500 $\mu$m, and ■ □ $G$=900 $\mu$m. The solid symbols are for the $R_P$=50 $\mu$m plate, and the open symbols are for the $R_P$=200 $\mu$m plate [15].**

only 110 kW/m$^2$ for the $R_P$=200 $\mu$m plate. This is consistent with the model predictions [5,11], which suggest that a reduction in the pore size improves the performance of the evaporator. Somewhat surprisingly, the maximum heat flux for the $R_P$=200 $\mu$m plate was 230 kW/m$^2$ at a gap distance of 900 $\mu$m and only 180 kW/m$^2$ for the $R_P$=50 $\mu$m plate. For gap distances greater than 500 $\mu$m, the average foil temperature at a given heat flux increased with the gap size for the $R_P$=50 $\mu$m plate, unlike the $R_P$=200 $\mu$m plate where the change in the average foil temperature with heat flux was relatively independent of the gap size at large gap distances [15]. This transition appears to occur at a gap distance of approximately 500 $\mu$m where the performance of both plates was similar.

The change in the averaged foil temperature with heat flux at gap distances between 0 $\mu$m and 300 $\mu$m is shown in more details in Fig. 5. The results show that the maximum stable heat flux was similar for both plates at gap distances of 0 $\mu$m and 100 $\mu$m. However, the average foil temperature was lower for the $R_P$=50 $\mu$m plate at low heat fluxes, suggesting that the reduction in pore size does increase the performance of the evaporator at low heat fluxes. The results at the higher heat fluxes are similar for both pore plates at these gap distances, suggesting that the failure mechanism at small gaps may not be strongly dependent on the pore size as predicted in the models [5,11]. The average tempera-

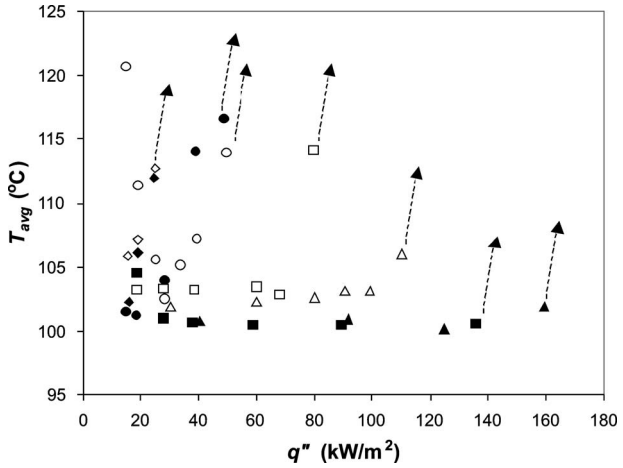


**Fig. 5 Change in the average foil temperature as a function of heat flux for gap distances of ◇ ◆ $G$=0 $\mu$m, ● ○ $G$=100 $\mu$m, ■ □ $G$=200 $\mu$m, and ▲ △ 300 $\mu$m. The solid symbols are for the $R_P$=50 $\mu$m plate, and the open symbols are for the $R_P$ =200 $\mu$m plate [15].**

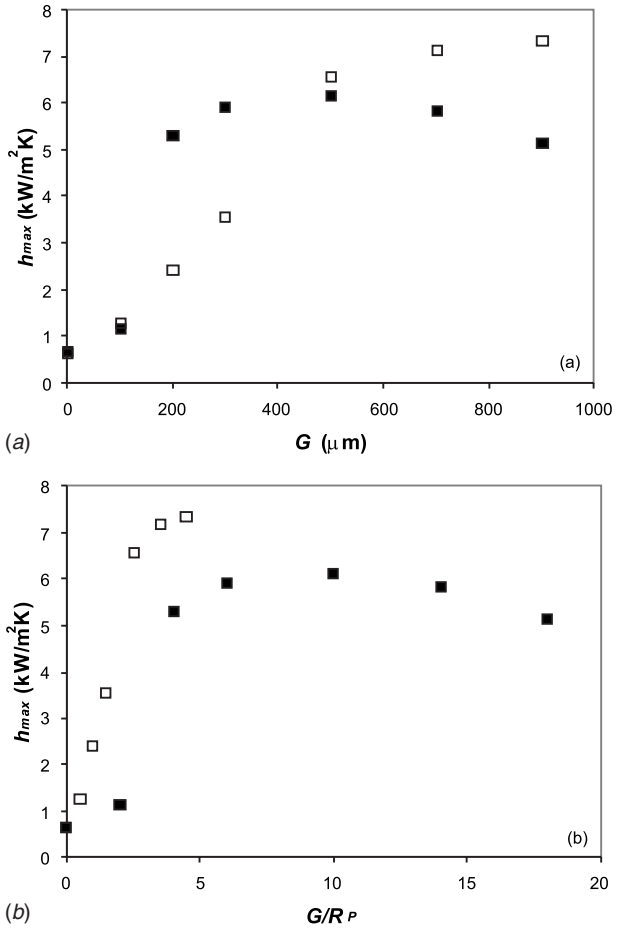


**Fig. 6 Change in the maximum heat transfer coefficient as a function of (*a*) gap distance and (*b*) the ratio of the gap distance to pore radius for ■ the $R_P$=50 $\mu$m plate and □ the $R_P$ =200 $\mu$m plate.**

ture on the foil at gap distances of 200 $\mu$m and 300 $\mu$m is again lower for the $R_P$=50 $\mu$m plate at lower heat fluxes. The maximum heat flux for the $R_P$=50 $\mu$m plate was substantially greater than that for the $R_P$=200 $\mu$m plate at these gap distances, suggesting that the failure mechanism in these cases depends on the pore size, unlike at the smaller gap distances.

The change in the maximum heat transfer coefficient with gap distance for both plates is shown in Fig. 6. The heat transfer coefficient here is based on the difference between the average temperature on the foil and the temperature of the subcooled liquid beneath the porous media [17]. The trends were similar for heat transfer coefficients based on the saturation temperature of the liquid, but the magnitudes were significantly larger when the average temperatures were close to the saturation temperature. The maximum heat transfer coefficient for the two porous plates was similar for gap distances of 0 $\mu$m and 100 $\mu$m. The maximum heat transfer coefficient for the $R_P$=50 $\mu$m plate was 118% and 66% larger for gap distances of 200 $\mu$m and 300 $\mu$m, respectively; but, they were between 6% and 30% lower for gap distances between 500 $\mu$m and 900 $\mu$m. The largest heat transfer coefficient for both plates occurred for a gap distance approximately 3 to 5 times greater than the pore radius (Fig. 6(*b*)), consistent with the previous results for a coaxial evaporator with a 20 $\mu$m pore radius [14]. The maximum heat transfer coefficient was between 25% and 75% larger for the $R_P$=200 mm plate at all gap distances to pore size ratios with the difference becoming smaller at larger gaps to pore ratios. This suggests that the performance of the $R_P$=50 $\mu$m plate may be superior between 100 $\mu$m and 500 $\mu$m because these distances were closer to the optimum gap distance to pore size ratio.

**3.1 Temperature Distributions on the Heated Surface.** The time averaged data suggest that there are potentially three modes of behavior, which are dependent on both the gap distance and the pore radius. This is examined further using transients of the temperature distribution measured on the foil and the PDFs of these temperatures. The typical sequences of the instantaneous temperature distributions of the heated foil in direct contact with the $R_P$ =50 $\mu$m plate at a heat flux of 15 kW/m$^2$ after it had reached steady state operation are presented in Fig. 7. There is evidence of high temperature regions that increase in size and then disappear, suggesting that vapor regions grow beneath the heated foil until the vapor can escape to the vapor grooves similar to the results for the 200 $\mu$m pore radius [15]. The temperature distributions in both cases were two-dimensional and transient, suggesting that a steady state model for the vapor distribution in the porous plate and the gap may not accurately predict the phenomenon.

The results for the two plates with different pore radii can be compared using the PDFs of the foil temperature shown in Fig. 8. The results for the $R_P$=200 $\mu$m plate were not considered in Ref. [15]. The PDFs here are determined from the temperatures on the visible portion of the foil. The PDFs of the foil temperature for the $R_P$=50 $\mu$m plate are bimodal, with one peak near the saturation

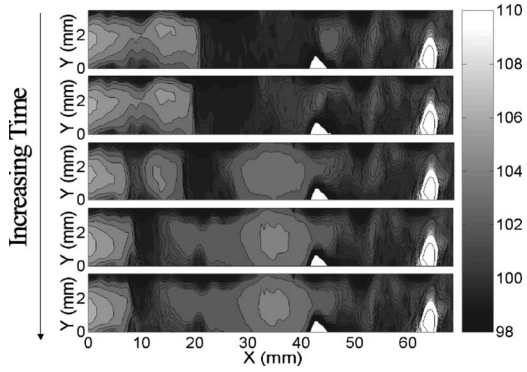


**Fig. 7 Typical transients of the instantaneous temperature (°C) distribution on the heated foil for the $R_P$=50 $\mu$m plate with G=0 $\mu$m at a heat flux of 15 kW/m$^2$. These images were recorded 17 ms apart.**

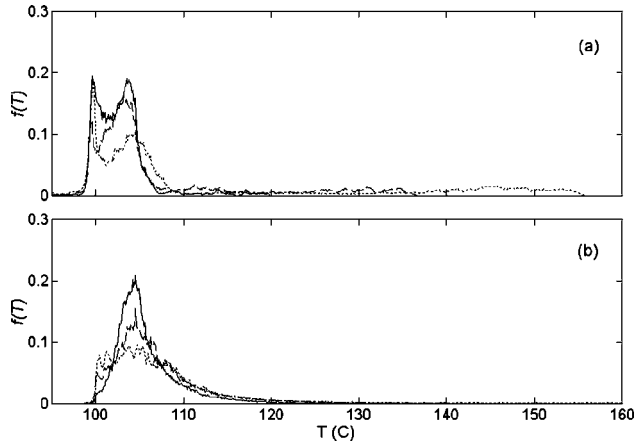


**Fig. 8 Time and space averaged probability density functions of the temperature on the foil surface for (*a*) the $R_P$=50 $\mu$m plate and (*b*) the $R_P$=200 $\mu$m plate with $G$=0 $\mu$m at $q''$= — 15, — 20 and ··· 25 kW/m$^2$.**

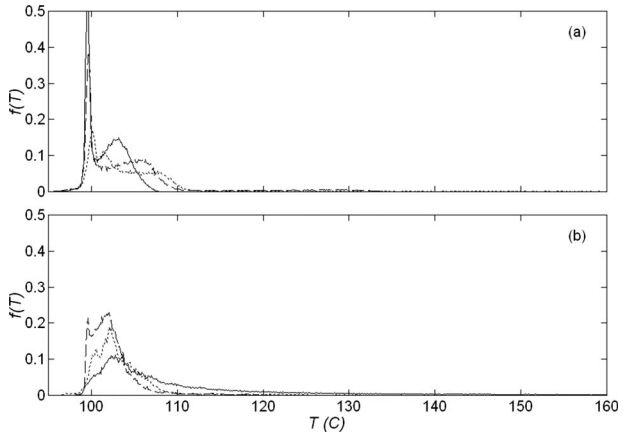


**Fig. 9 Time and space averaged probability density functions of the temperature on the foil surface for (*a*) the $R_P$=50 $\mu$m plate and (*b*) the $R_P$=200 $\mu$m plate with $G$=100 $\mu$m at $q''$= — 20, —30 and ··· 50 kW/m$^2$.**

temperature and a second peak at higher temperatures. In contrast, the PDFs of the temperature on the foil for the $R_P$=200 $\mu$m plate have a single peak near 105 °C. The bimodal distribution for the smaller pore radius shows that a significant portion of the foil operates near the saturation temperature even at high heat fluxes. Despite this increase in performance at low and moderate heat fluxes, the foil temperature becomes unstable at the same heat flux as the $R_P$=200 $\mu$m plate. This suggests that the failure mode at small gap distances is a local phenomenon and that the maximum heat flux is more dependent on the gap distance than the pore radius in these cases.

The PDFs of the foil temperature for the 100 $\mu$m gap are shown in Fig. 9. The PDFs are again bimodal for the $R_P$ =50 $\mu$m plate at low heat fluxes. Here, the temperature of the second peak initially increased with heat flux more than in the zero gap case. At 50 kW/m$^2$, the secondary maximum shifted to a lower temperature, but there is also a longer tail in the distribution. These changes seem to be due, in part, to the fact that the maximum heat flux is significantly higher than that observed in the zero gap case. The PDF for the $R_P$=200 $\mu$m plate has a single peak at low heat fluxes that sharpens and shifts to lower temperatures when the heat flux was increased from 20 kW/m$^2$ to 30 kW/m$^2$, resulting in the nonmonotonic behavior that was previously observed by Schertzer et al. [15]. This was not observed for the smaller pore radius.

The high temperatures in these PDFs correspond to local high temperature regions such as those observed in Fig. 7 that persist and increase in temperature at high heat fluxes. The maximum temperature of these regions tends to be greater for the larger pore radius at the same heat flux. The results for gap distances of 0 $\mu$m and 100 $\mu$m show evidence of very high temperatures even as a portion of the foil remained at the saturation temperature, suggesting that failure of the evaporator at smaller gaps is a local phenomenon. The high temperature tails on the PDFs appear at similar heat fluxes for both plates when $G$=0 $\mu$m and 100 $\mu$m. This could explain why the failure of the evaporator at small gap distances does not appear to be dependent on pore radius, despite the apparent differences in the boiling dynamics.

The results at the larger gap distances were first considered in terms of the ratio of the gap distance to the pore size. The change in the PDFs of the foil temperature for gap to pore ratios between 2 and 6, where the maximum heat transfer coefficient was observed to follow a similar trend for both plates, is presented in Fig. 10. While the gap to pore ratios for the two porous plates presented in the figure are not the same, the results are still revealing. In particular, the PDFs of the foil temperature for the $R_P$ =50 $\mu$m plate were bimodal in all cases, while those for the $R_P$ =200 $\mu$m plate have a single peak. In the PDFs for the $R_P$ =50 $\mu$m plate, the low temperature peak was more substantial at higher gap to pore ratios for a given heat flux, suggesting that the vapor beneath the fin escapes more easily at larger gap to pore ratios. At higher heat fluxes, the low temperature peak broadened, while the higher temperature peak became more substantial and extended to higher temperatures. The bimodal nature of the PDFs for the $R_P$=50 $\mu$m plate shows that a significant portion of the foil exists at the saturation temperature even at the highest heat fluxes examined here. This again suggests that the failure of the evaporator is a local phenomenon. The peaks in the PDFs for the $R_P$=200 $\mu$m plate broaden and shift to higher temperatures as the heat flux increases with few measurements near the saturation temperature even at moderate heat fluxes. Thus, the mechanism responsible for cooling the heated surface is less effective for the $R_P$=200 $\mu$m plate. The difference in the PDFs and the change in these functions with heat flux indicates that the boiling dynamics within the gap differ for the two porous plates despite the similarity in the change in the maximum heat transfer coefficient at similar gap to pore ratios.

A comparison of the PDFs of the foil temperature for the two plates in terms of gap distance is shown in Fig. 11. The PDFs for the larger pore radius all have a single peak that tends to broaden and shift to higher temperatures with increased heat flux for a given gap distance. The change in the distribution with heat flux is similar at different gap distances, suggesting that the heat transfer mechanism is likely similar for large and intermediate gap distances. The PDFs for the $R_P$=50 $\mu$m plate at gap distances of 300 $\mu$m and 500 $\mu$m are bimodal, but at gap distances above 500 $\mu$m (i.e., 900 $\mu$m), the PDFs have a single peak that shifts to higher temperatures at higher heat fluxes. This suggests that there is a change in the boiling dynamics for the $R_P$=50 $\mu$m plate at large gap distances that were not seen for the $R_P$=200 $\mu$m plate [15]. For example, at a gap distance of 900 $\mu$m, the majority of the foil is above 105 °C at 180 kW/m$^2$ and only a small portion of the foil is near the saturation temperature. This shift in the PDF at high heat fluxes is larger than that observed for the $R_P$=200 $\mu$m plate at the same gap distance. Typical transient temperature distributions for the $R_P$=50 $\mu$m plate at gaps distances of 300 $\mu$m and 900 $\mu$m are presented in Fig. 12. The results for the 300 $\mu$m gap show that a significant portion of the foil is near the saturation temperature with small high temperature regions that appear and disappear on the foil. However, at the gap distance of 900 $\mu$m, the

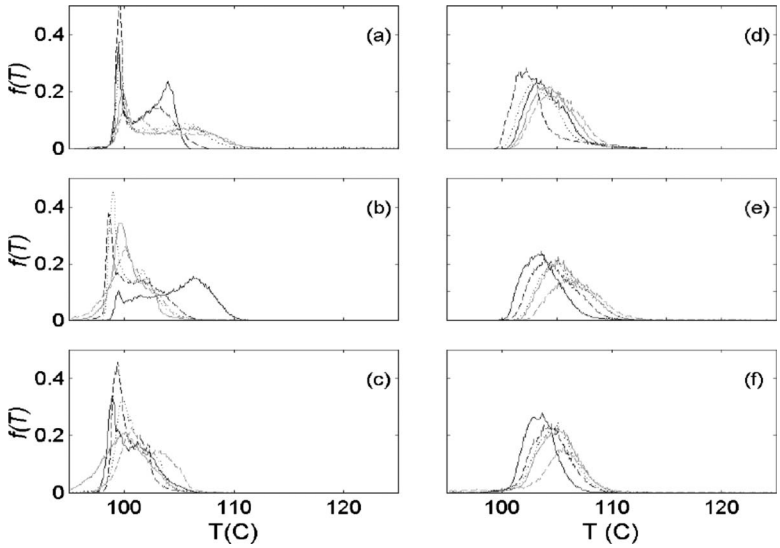


**Fig. 10 Time and space averaged probability density functions for the $R_P$ =50 $\mu$m plate (left) and the $R_P$=200 $\mu$m plate (right). The results for gap to pore ratio of (*a*) 2 for $q''$= — 15 kW/m$^2$, – – 20 kW/m$^2$, ··· 30 kW/m$^2$, — 40 kW/m$^2$, and – – 50 kW/m$^2$, (*b*) 4 for $q''$= — 20 kW/m$^2$, – – 30 kW/m$^2$, ··· 40 kW/m$^2$, — 90 kW/m$^2$, and – – 135 kW/m$^2$, (*c*) 6 for $q''$= — 40 kW/m$^2$, – – 60 kW/m$^2$, ··· 90 kW/m$^2$, — 125 kW/m$^2$, and – – 160 kW/m$^2$, (*d*) 2.5 for $q''$= — 60 kW/m$^2$, – – 80 kW/m$^2$, ··· 130 kW/m$^2$, — 180 kW/m$^2$, and – – 200 kW/m$^2$ (*e*) 3.5 for $q''$= — 120 kW/m$^2$, – – 160 kW/m$^2$, ··· 200 kW/m$^2$, — 220 kW/m$^2$, and – – 240 kW/m$^2$, and (*f*) 4.5 for $q''$= — 100 kW/m$^2$, – – 120 kW/m$^2$, ··· 200 kW/m$^2$, — 220 kW/m$^2$, and – – 230 kW/m$^2$.**

majority of the foil is above the saturation temperature, which is similar to the results for large gaps with the $R_P$=200 $\mu$m plate [15]. The high temperature regions in this case are transient, suggesting the presence of a two-phase flow below the foil. Thus, the results show that the boiling dynamics within the gap for the two plates become similar for gaps greater than 500 $\mu$m, though the performance is a function of the pore radius with the $R_P$ =50 $\mu$m plate having a poorer performance.

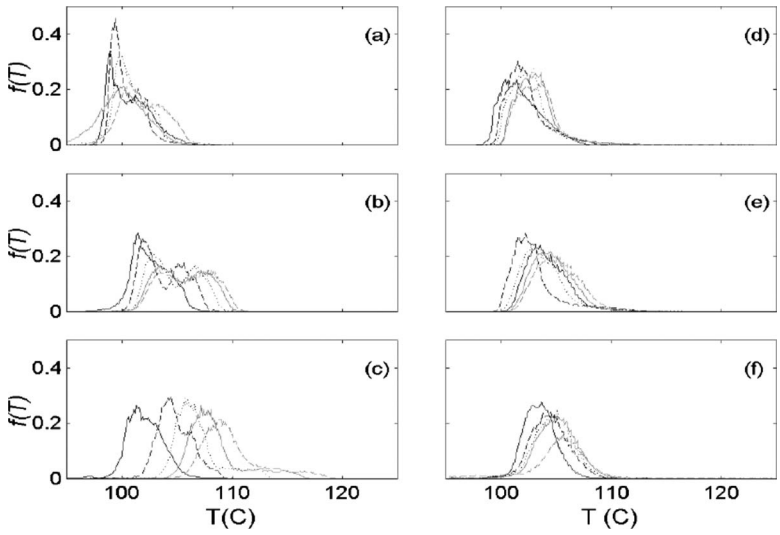


**Fig. 11 Time and space averaged probability density functions for the $R_P$ =500 $\mu$m plate (left) and the $R_P$=200 $\mu$m plate (right). The results for (*a*) $G$ =300 $\mu$m $q''$= — 40 kW/m$^2$, – – 60 kW/m$^2$, ··· 90 kW/m$^2$, — 125 kW/m$^2$, and – – 160 kW/m$^2$ (*b*) $G$=500 $\mu$m for $q''$= — 90 kW/m$^2$, – – 120 kW/m$^2$, ··· 150 kW/m$^2$, — 180 kW/m$^2$, and – – 190 kW/m$^2$, (*c*) $G$=900 $\mu$m for $q''$= — 40 kW/m$^2$, – – 90 kW/m$^2$, ··· 120 kW/m$^2$, — 150 kW/m$^2$, and – – 180 kW/m$^2$, (*d*) $G$=300 $\mu$m for $q''$= — 30 kW/m$^2$, – – 60 kW/m$^2$, ··· 80 kW/m$^2$, — 100 kW/m$^2$, and – – 110 kW/m$^2$, (*e*) $G$=500 $\mu$m for $q''$= — 60 kW/m$^2$, — 80 kW/m$^2$, ··· 130 kW/m$^2$, — 180 kW/m$^2$, and – –200 kW/m$^2$ and (*f*) $G$ =900 $\mu$m for $q''$= — 100 kW/m$^2$, – – 120 kW/m$^2$, ··· 200 kW/m$^2$, — 220 kW/m$^2$, and – – 230 kW/m$^2$.**

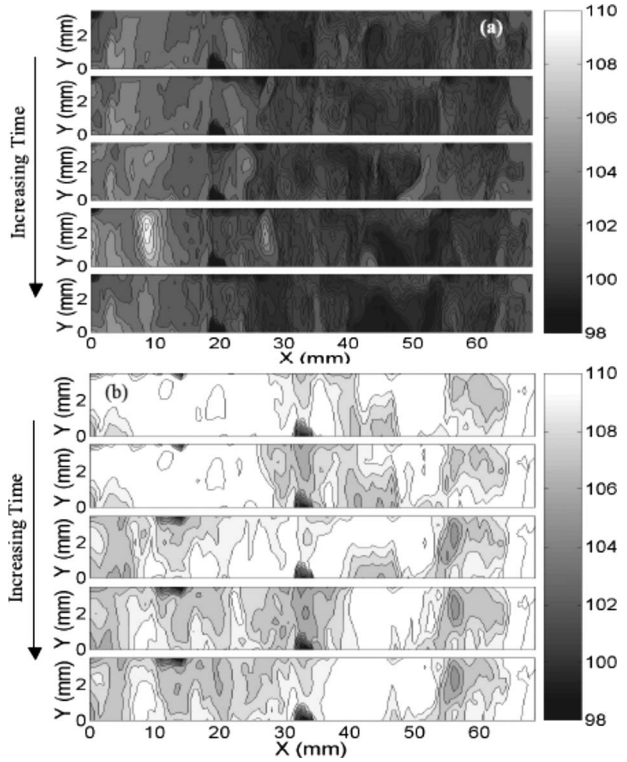


**Fig. 12 Typical transients of the instantaneous temperature (°C) distribution on the heated foil for the $R_P$=50 $\mu$m plate when (*a*) G=300 and $q''$=160 kW/m$^2$ and when (*b*) G=900 $\mu$m and $q''$=180 kW/m$^2$. The images were recorded 17 ms apart.**

## 4 Conclusions

An experimental investigation was performed to examine the effect that pore size had on the heat transfer between a heated finned surface and a saturated porous plate when a gap was and was not present between the two surfaces. Experiments were performed using a porous plate with nominal pore size of 50 $\mu$m for gap distances from 0 $\mu$m to 900 $\mu$m and compared to previous results for a pore size of 200 $\mu$m [15]. The results show that the boiling dynamics within the gap are different at small, intermediate, and large gap distances. The transition between these operating regimes is dependent on the pore size, with the smaller pore sized plate having a better performance at small and intermediate gaps but a lower performance at larger gaps. The maximum heat transfer coefficient depends on the ratio between the gap distance and the pore radius, with an optimum performance at a gap distance that was 3 to 5 times the nominal pore radius. The temperature distributions on the heated surface and their evolution with heat flux were significantly different for the two plates, and do not appear to be dependent on either the gap distance or the ratio between the gap distance and the pore radius. This indicates that the boiling dynamics within the gap do not scale with the ratio between the gap distance and the pore radius.

## Acknowledgment

The support of the Canadian Space Agency, Ontario Centres of Excellence and Acrolab Ltd is gratefully acknowledged. The first author acknowledges the financial support from the National Sciences and Engineering Research Council (NSERC) of Canada through a PGSA scholarship. The authors acknowledge the contributions of Mr. M. Khammar, who first developed the experimental facility, for this research work.

## Nomenclature

$G$ = gap distance between the heated surface and the porous plate (m)
$h$ = average heat transfer coefficient (W/m$^2$ K)
$\dot{m}$ = mass flow rate of water (kg/s)
$q''$ = heat flux (W/m$^2$)
$R_P$ = nominal pore radius within the porous plate (m)
$t$ = time (s)
$T$ = temperature (°C)
$w$ = spanwise position from the center of the heated foil (m)
$\varepsilon$ = emissivity
$\Phi$ = porosity of the porous plate
$f(T)$ = probability density function of the temperature on the surface of the heated foil (1/°C)

### Subscripts

av = average
max = maximum
$W$ = wick
$P$ = pore
sur = heated surface

## References

[1] Butler, D., 1999, "Overview of CPL and LHP Applications on NASA Missions, Space Technology and Applications International Forum," AIP Conf. Proc., **458**, pp. 792–798.
[2] Chen, P., and Lin, W., 2001, "The Application of Capillary Pumped Loop for Cooling of Electronic Components," Appl. Therm. Eng., **21**, pp. 1739–1754.
[3] Liepmann, D., 2001, "Design and Fabrication of a Micro-CPL for Chip-Level Cooling," *Proceedings of the 2001 ASME International Mechanical Engineering Congress and Exposition*, New York, Nov. 11–16, pp. 1–4.
[4] Ku, J., 1999, "Operating Characteristics of Loop Heat pipes," SAE Technical Paper 1999-01-2007 *29th International Conference on Environmental System*, Denver, CO, Jul. 12–15, pp. 1–16.
[5] Cao, Y., and Faghri, A., 1994, "Conjugate Analysis of a Flat-Plate Type Evaporator for Capillary Pumped Loops With Three-Dimensional Vapour Flow in the Groove," Int. J. Heat Mass Transfer, **37**, pp. 401–109.
[6] Cao, Y., and Faghri, A., 1994, "Analytical Solutions of Flow and Heat Transfer in a Porous Structure With Partial Heating and Evaporation on the Upper Surface," Int. J. Heat Mass Transfer, **37**, pp. 1525–1533.
[7] Embacher, E., and Wulz, H. G., 1990, "Capillary Pumped Loops for Space Applications: Experimental and Theoretical Studies on the Performance of Capillary Evaporator Designs," *Proceedings of AIAA/ASME Fifth Joint Thermophysics and Heat Transfer Conference*, Seattle, WA, Jun. 18–20, AIAA-90-1739.
[8] Khrustalev, D., and Faghri, A., 1995, "Heat Transfer in the Inverted Meniscus Type Evaporator at High Heat Fluxes," Int. J. Heat Mass Transfer, **38**, pp. 3091–3101.
[9] Demidov, A. S., and Yatsenko, E. S., 1994, "Investigation of Heat and Mass Transfer in the Evaporation Zone of a Heat Pipe Operating by the 'Inverted Meniscus' Principle," Int. J. Heat Mass Transfer, **37**, pp. 2155–2163.
[10] Zhao, T. S., and Liao, Q., 2000, "A Visual Study of Phase-Change Heat Transfer in a two Dimensional Porous Structure With a Partial Heating Boundary," Int. J. Heat Mass Transfer, **43**, pp. 1089–1102.
[11] Liao, Q., and Zhao, T. S., 1999, "Evaporative Heat Transfer in a Capillary Structure Heated by a Grooved Block," J. Thermophys. Heat Transfer, **13**, pp. 126–133.
[12] Zhao, T. S., and Liao, Q., 2000, "On Capillary-Driven Flow and Phase-Change Heat Transfer in a Porous Structure Heated by a Finned Surface: Measurements and Modeling," Int. J. Heat Mass Transfer, **43**, pp. 1141–1155.
[13] Figus, C., Bories, S., and Prat, M., 1996, "Investigation and Analysis of a Porous Evaporator for a Capillary Pumped Loop," Engineering Systems Design and Analysis, ASME, Petroleum Division (Publication) PD, **78**(6), pp. 99–106.
[14] Platel, V., Fudym, O., Butto, C., and Briend, P., 1996, "Heat Transfer Coefficient at Vaporization Interface of a Two Phase Capillary Pump," Rev. Gen. Therm., **35**, pp. 592–598.
[15] Schertzer, M. J., Ewing, D., and Ching, C. Y., 2006, "The Effect of Gap Distance on the Heat Transfer Performance Between a Finned Surface and a Saturated Porous Plate," Int. J. Heat Mass Transfer, **49**, pp. 4200–4208.
[16] Gao, N., Sun, H., and Ewing, D., 2003, "Heat Transfer to Impinging Round Jets With Triangular Tabs," Int. J. Heat Mass Transfer, **46**, pp. 2557–2569.
[17] Hasan, A., Roy, R. P., and Kalra, S. P., 1990, "Experiments on Subcooled Flow Boiling Heat Transfer in a Vertical Annular Channel," Int. J. Heat Mass Transfer, **33**, pp. 2285–2293.

# Convective Condensation of Vapor in Laminar Flow in a Vertical Parallel Plate Channel in the Presence of a High-Concentration Noncondensable Gas

**V. Dharma Rao**[1]
Department of Chemical Engineering,
College of Engineering,
Andhra University,
Visakhapatnam 530003, India
e-mail: vdharmarao@yahoo.com

**V. Murali Krishna**
Department of Mechanical Engineering,
Vignans Engineering College,
Vadlamudi,
Guntur 522213, India
e-mail: murvmk@yahoo.co.in

**P. K. Sarma**
Director
R & D,
GITAM,
Rishikonda,
Visakhapatnam 530045, India
e-mail: sarmapk@yahoo.com

**K. V. Sharma**
Centre for Energy Studies,
JNTU College of Engineering,
Kukatpally,
Hyderabad 500085, India
e-mail: kvsharmajntu@yahoo.com

*The problem of laminar film condensation of a vapor from vapor-gas mixture in laminar flow in a vertical parallel plate channel is formulated theoretically. The flowing gas-vapor mixture contains a noncondensable gas in high concentration. An example of this case is the flow of humid air, in which air is present in high concentration. Vapor condenses at the dew point temperature corresponding to mass fraction of vapor in the gas-vapor mixture and the total pressure. The rate of condensation is controlled by the diffusion of the vapor through the noncondensable gas film. Thus the problem of convective condensation is treated as a combined problem of heat and mass transfer. The problem is governed by the mass, momentum and energy balance equations for the vapor-gas mixture flowing in a channel, and the diffusion equation for the vapor species. The flow of the falling film of condensate is governed by the momentum and energy balance equations for the condensate film. The boundary conditions for the gas phase and the condensate film are considered. The temperature at the gas-to-liquid interface is estimated by making use of the equations of heat and mass balance at the interface. The local condensation Nusselt number, condensation Reynolds number, and temperature at the gas-to-liquid interface are estimated from the numerical results for different values of the system parameters at the channel inlet, such as relative humidity, temperature of vapor-gas mixture, gas phase Reynolds number, and total pressure. The condensation heat transfer coefficients computed from the present theory are compared with the experimental data available in literature, and the agreement is found to be good. The present work is an extension of the earlier work, in which the problem of in-duct condensation of humid air in turbulent flow was solved theoretically. Humid air is considered as the gas-vapor mixture, since various physical and thermal properties have to be specified during the analysis.* [DOI: 10.1115/1.2993541]

*Keywords: high-concentration noncondensable gas, in-tube condensation, laminar flow in a channel, two-phase flow*

## 1 Introduction

Condensation of water vapor in the presence of a high-concentration noncondensable gas takes place in air cleaning and conditioning systems, humidity control systems, atmospheric condensers, refrigeration engineering, and also heat exchangers with narrow channels. In air-conditioning equipment the air flows in between parallel plate channels, which are at a low temperature due to their contact with the cold pipe carrying the refrigerant. When the water vapor in the vapor-air mixture is cooled below its dew point temperature, it undergoes condensation on the plates of the channel and flows down in the form of a film. The total heat flux from water vapor-air mixture to the plate is the sum of convection spent on cooling the vapor-gas mixture in the boundary layer and the latent heat spent on vapor condensation. Hence the process of condensation of water vapor from vapor-air mixture is governed by the convection through the vapor boundary layer and the diffusion of vapor to the surface followed by its condensation. The problem of condensation of water vapor from vapor-air mixture needs a combined solution of mass, momentum and energy balances, and the diffusion equation. If the plates of the channel are below the freezing temperature of water, then the condensate on the plate surface freezes and forms ice or frost. In the present analysis the plates of the channel are maintained above the freezing temperature of water, thus precluding the possibility for frost formation.

The problem in the present investigation relates to the case of condensation of vapor in the presence of a high percentage of noncondensable gas. A popular example of this case is condensation of water vapor from humid air, which contains air in high concentration. Lebedev et al. [1] performed a combined experimental study of heat and mass transfer in condensation of vapor from humid air on a flat plate in longitudinal flow in an asymmetrically cooled slot. They observed an increase in condensation heat transfer with an increase in the relative humidity of the air. Recently Dharma Rao et al. [2] tackled theoretically the problem of condensation of water vapor from humid air flowing in a duct

[1]Author to whom correspondence should be addressed.

Contributed by the Heat Transfer Division of ASME for publication in the JOURNAL OF HEAT TRANSFER. Manuscript received November 27, 2007; final manuscript received July 7, 2008; published online October 21, 2008. Review conducted by Louis C. Chow.

  

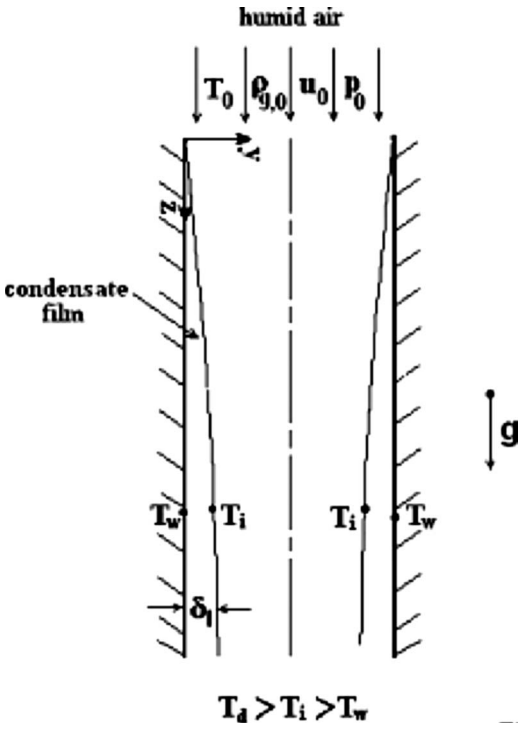


**Fig. 1 Physical model and configuration**

in turbulent flow. They obtained local and average values of the condensation Nusselt number, condensation Reynolds number, gas-liquid interface temperature, and pressure drop from the numerical results for different values of the system parameters at the inlet, such as relative humidity, temperature of air, gas phase Reynolds number, and total pressure. Hence, in view of its importance, the same problem is solved presently for the case of laminar flow of humid air in a parallel plate channel. The condensate film on the wall of the channel is assumed to be a thin film in laminar flow. The condensation rates are obtained by a conjugate analysis of the problem of forced convection of the humid air in the channel with the Nusselt's analysis of condensation for the condensate film. A detailed review of contemporary literature on this topic was presented by Dharma Rao et al. in Ref. [2].

The present problem is different from the problem of condensation of steam from a steam-air mixture, which contains air in low concentration. The reasons, due to which the problems of high and low concentrations are different, are listed below.

(1) Humid air flows in the case of high concentration [2,3] while steam flows in the case of low concentration of noncondensable gas [4–6].
(2) The temperature of vapor-gas mixture is nearer to room temperature in the case of high concentration while it is nearer to the saturation temperature of vapor in the case of low concentration.
(3) The controlling parameter in the case of high concentration is the humidity or mass fraction of water vapor in the gas-vapor mixture, while it is the mass fraction of noncondensable gas in the gas-vapor mixture in the case of low concentration.

## 2 Physical Model and Formulation

The physical model under consideration is shown in Fig. 1. Humid air flows down in a vertical parallel plate channel of width $W$ and length $L$ in laminar forced flow. The coordinates along and normal to the channel wall are $z$ and $y$, respectively, and the corresponding velocity components are $u$ and $v$. The breadth of the channel is assumed to be large in comparison with its width, and the flow is assumed to be two dimensional. The water vapor-air mixture enters with a Reynolds number $\mathrm{Re}_{g,0}$, temperature $T_0$, total pressure $P_0$, and relative humidity $R_{H,0}$. The temperature on both the plates is maintained at a uniform value, $T_w$, and $T_w < T_0$. The partial pressure of water vapor at the inlet is $p_{v,0}$, where $p_{v,0}=(R_{H,0})(p^*_{v,0})$. $p^*_{v,0}$ is the saturation vapor pressure of water at temperature $T_0$. The vapor-air mixture is cooled to its dew point temperature, $T_d$, causing condensation of water vapor. The temperature on the plate of the channel, $T_w$, is below the dew point temperature, $T_d$, for $0 \le z \le L$. The inlet temperature of air $T_0$ may be either equal to or greater than $T_d$. The vapor condensing at the dew point temperature diffuses on to the surface of the channel through the air film. The thickness of the condensate layer is $\delta_l$ on each plate. The flow of the condensate film is assumed to be laminar and the flow of the condensate is caused by gravity and the shear force acting on the film surface by the flowing gas. Since the rate of condensation is expected to be low, the condensate film is assumed to be thin. The temperature on the free surface of the condensate is $T_i$, which is less than dew point temperature, $T_d$. Thus $T_d < T_i < T_w$. $T_i$ is an unknown temperature, which is to be evaluated by a trial-and-error procedure. In formulating the problem of condensation of vapor from the flowing air-vapor mixture, it is assumed that the flow is steady and laminar in both gas and liquid phases, the gas-to-liquid interface is smooth, and the vapor-air mixture is treated as an ideal gas mixture. The total pressure, $P$, is assumed to be constant across the channel, i.e., $\partial P/\partial y=0$; however, $P$ varies in the $z$-direction due to friction loss, momentum change, and hydrostatic pressure loss. Humid air is considered as the gas-vapor mixture, since various physical and thermal properties have to be specified during the analysis. The procedures and equations to evaluate saturation vapor pressure of water, dew point temperature, density of gas-vapor mixture, various physical and thermal properties of the gas-vapor mixture, etc., are given in Ref. [2]. The correlation equations used to evaluate saturation vapor pressure, dew point temperature, and latent heat of condensation of vapor are obtained with the help of the data book prepared by Schmidt and Grigull [7]. The data obtained from correlation equations are compared with the data in Ref. [7] and the maximum deviation found to be $\pm 0.4\%$ over the temperature range from 5°C to 40°C, which is the operating range of temperature in our numerical results.

**2.1 Governing Equations for Gas Phase.** The mass, momentum and energy balance equations for the gas phase, and the diffusion equation for the vapor species are written as follows. The density of the gas phase, $\rho_g$, is assumed to be a function of $z$ alone.

For mass balance,

$$\frac{\partial u}{\partial z} + \frac{\partial v}{\partial y} + \frac{u}{\rho_g}\frac{d\rho_g}{dz} = 0 \tag{1}$$

For momentum balance,

$$u\frac{\partial u}{\partial z} + v\frac{\partial u}{\partial y} = g - \frac{1}{\rho_g}\frac{\partial P}{\partial z} + \nu_g\frac{\partial^2 u}{\partial y^2} \tag{2}$$

For energy balance,

$$u\frac{\partial T}{\partial z} + v\frac{\partial T}{\partial y} = \frac{\nu_g}{\mathrm{Pr}_g}\frac{\partial^2 T}{\partial y^2} \tag{3}$$

For diffusion,

$$u\frac{\partial \rho_v}{\partial z} + v\frac{\partial \rho_v}{\partial y} - u\frac{\rho_v}{\rho_g}\frac{d\rho_g}{dz} = D_{\mathrm{va}}\frac{\partial^2 \rho_v}{\partial y^2} \tag{4}$$

The governing momentum and energy balance equations for condensate film are given in Ref. [2].

**2.2 Boundary Conditions.** The boundary conditions for the governing equations for the gas phase ($\delta_l \le y \le W - \delta_l$) and condensate film ($0 \le y \le \delta_l$) are as follows. $\delta_l$ is the thickness of the condensate film.

For $z=0$, i.e., at the inlet of the channel,

$$u = u_0, \quad v = 0, \quad T = T_0, \quad \rho_g = \rho_{g,0}, \quad \rho_v = \rho_{v,0} \quad \text{for} \quad 0 \le y \le W \tag{5}$$

For $z>0$, the conditions at the channel walls, i.e., at $y=0$ and $y=W$, are as follows:

$$u = 0, \quad v = 0, \quad T = T_w = \text{const} \tag{6}$$

The conditions at the center line of wall, i.e., at $y=W/2$, are as follows:

$$\frac{\partial u}{dy} = 0, \quad v = 0, \quad \frac{\partial T}{\partial y} = 0, \quad \frac{\partial \rho_v}{\partial y} = 0 \tag{7}$$

The conditions at the gas-to-liquid interface i.e., at $y=\delta_l$ and $y=(W-\delta_l)$, are as follows:

$$u = u_i, \quad T = T_i, \quad \rho_v = \rho_{v,i} \tag{8}$$

The subscript $i$ refers to the gas-to-liquid interface.

**2.3 Condensate Film Equations.** The procedures to evaluate the thickness of the condensate film and the interface temperature are explained in Ref. [2]; hence, those details are omitted here.

The mass balance at the interface is given by the following equation:

$$\frac{d\dot{m}_l}{dz} = \frac{D_{\text{va}}}{1 - (C_{v,i}/\bar{C}_i)} \frac{\partial \rho_v}{\partial y} \tag{9}$$

where

$$\frac{C_{v,i}}{\bar{C}_i} = \frac{\rho_{v,i} R_v T_i}{18P}$$

Heat transfer from the vapor-gas mixture to the liquid film at the interface comprises two components, namely, the sensible heat by convection and the latent heat released by the condensing vapor. Then the heat flux at the gas-to-liquid interface can be written as follows:

$$q_{l,i} = q_{g,i} + \lambda_i \frac{d\dot{m}_l}{dz} \tag{10}$$

where $q_{l,i}$=total heat flux received by the condensate film$= -k_l(\partial T/\partial y)|_l$, $q_{g,i}$=heat flux transferred by convection from the gas$=-k_g(\partial T/\partial y)|_g$, and $\lambda_i$=latent heat of condensation of vapor at temperature, $T_i$.

The expression for condensate film thickness, $\delta_l$, is given as follows:

$$\delta_l = \left[ \frac{2\nu_l \dot{m}_l}{\mu_g} \frac{1}{(\partial u/\partial y)|_g} \frac{(1-F)}{(1+F/3)} \right]^{1/2} \tag{11}$$

where $F = g(\rho_l - \rho_v)\delta_l^2 / 2\mu_l u_i$. Equation (11) may be simplified by setting $F$ equal to zero, which amounts to assuming linear velocity profile in condensate film [2]. The temperature at the gas-to-liquid interface, $T_i$, is given by the following equation:

$$T_i = T_w + \delta_l \left[ \frac{k_g}{k_l} \frac{\partial T}{\partial y}\bigg|_g + \frac{\lambda_i}{k_l} \frac{d\dot{m}_l}{dz} \right] \tag{12}$$

**2.4 Normalized Equations for Gas Phase and Condensate Film.** The constitutive equations are put in the normalized form making use of the following dimensionless variables and parameters:

$$u^+ = u/u_0, \quad v^+ = v\text{Re}_g/u_0, \quad T^+ = (T - T_w)/(T_0 - T_w), \quad \rho_g^+ = \rho_g/\rho_{g,0}$$

$$\rho_v^+ = \rho_v/\rho_{v,0}, \quad z^+ = z/W\text{Re}, \quad y^+ = y/W, \quad \delta^+ = \delta/W, \quad \rho_{g,v}^+ = \rho_g/\rho_{v,0}$$

$$k^+ = k_g/k_l, \quad \mu^+ = \mu_g/\mu_l, \quad \nu^+ = \nu_g/\nu_l, \quad \lambda_i^+ = \lambda_i/\lambda_0, \quad \text{Re}_g = u_0 W/\nu_g$$

$$\text{Sc}_g = \nu_g/D_{\text{va}}, \quad \text{Re}_l = 4\dot{m}_l/\mu_l, \quad P^+ = (P - P_0)/\rho_{g,0}u_0^2, \quad \text{Ar} = gW^3/\upsilon_g^2 \tag{13}$$

**2.5 Normalized Gas Phase Equations.** The normalized equations for gas phase, i.e., Eqs. (1)–(4), are written as follows.

For continuity equation,

$$\frac{\partial u^+}{\partial z^+} + \frac{\partial v^+}{\partial y^+} + \frac{u^+}{\rho_g^+} \frac{\partial \rho_g^+}{\partial z^+} = 0 \tag{14}$$

For momentum equation,

$$u^+ \frac{\partial u^+}{\partial z^+} + v^+ \frac{\partial u^+}{\partial y^+} = -\frac{1}{\rho_g^+} \frac{\partial P^+}{\partial z^+} + \frac{\partial^2 u^+}{\partial y^{+2}} + \frac{\text{Ar}}{\text{Re}_g} \tag{15}$$

For energy equation,

$$u^+ \frac{\partial T^+}{\partial z^+} + v^+ \frac{\partial T^+}{\partial y^+} = \frac{1}{\text{Pr}_g} \frac{\partial^2 T^+}{\partial y^{+2}} \tag{16}$$

For diffusion equation,

$$u^+ \frac{\partial \rho_v^+}{\partial z^+} + v^+ \frac{\partial \rho_v^+}{\partial y^+} - u^+ \frac{\rho_v^+}{\rho_g^+} \frac{\partial \rho_g^+}{\partial z^+} = \frac{1}{\text{Sc}_g} \frac{\partial^2 \rho_v^+}{\partial y^{+2}} \tag{17}$$

where

$$\text{Re}_g = \text{Re}_{g,0} \frac{\rho_g^+}{\mu_g^+}, \quad \text{Pr}_g = \text{Pr}_{g,0} \frac{\mu_g^+ C_{pg}^+}{k_g^+}, \quad \text{and} \quad \text{Sc}_g = \text{Sc}_{g,0} \frac{\mu_g^+}{\rho_g^+ D_{\text{va}}^+} \tag{18}$$

**2.6 Normalized Condensate Film Equations.** The normalized form of mass balance equation at the interface, i.e., Eq. (9), is written as follows:

$$\frac{d\text{Re}_l}{dz^+} = \frac{4\mu^+}{\text{Sc}_g} \frac{\text{Re}_g}{\rho_{g,v}^+} \frac{\partial \rho_v^+/\partial y^+}{1 - (C_{v,i}/\bar{C}_i)} \tag{19}$$

where

$$\frac{C_{v,i}}{\bar{C}_i} = \left( \frac{p_{v,0}}{T_0} \right) \left( \frac{\beta T_i^+ + 1}{P} \right) \rho_{v,i}^+$$

The dimensionless condensate film thickness, ($\delta_l^+$), which is obtained from Eq. (11), is given by the following equation:

$$\delta_l^+ = \left( \frac{\text{Re}_l}{2\nu^+ \mu^+ \text{Re}_g} \frac{1}{\partial u^+/\partial y^+|_g} \frac{(1-F)}{(1+F/3)} \right)^{1/2} \tag{20}$$

Hence Eq. (20) may be simplified to the form shown below, by assuming linear velocity profile, viz., by setting $F$ equal to zero, as stated earlier.

$$\delta_l^+ = \left( \frac{\text{Re}_l}{2\nu^+ \mu^+ \text{Re}_g} \frac{1}{\partial u^+/\partial y^+|_g} \right)^{1/2} \tag{21}$$

Thus either Eq. (20) or Eq. (21) may be used to compute the value of $\delta_l^+$. From Eq. (12), the normalized temperature at the gas-to-liquid interface, $T_i^+$, is given by the following equation:

$$T_i^+ = \delta_l^+ \left[ k^+ \frac{\partial T^+}{\partial y^+}\bigg|_g + \frac{\text{Pr}_l}{4S} \frac{\lambda_i^+}{\text{Re}_g} \frac{d\text{Re}_l}{dz^+} \right] \tag{22}$$

**2.7 Nusselt and Sherwood Numbers.** The local condensation Nusselt number, $\text{Nu}_{l,z}$, is computed from the following equation:

$$\mathrm{Nu}_{l,z} = \frac{T_i^+}{\delta_l^+ T_{\mathrm{av}}^+} = \frac{1}{T_{\mathrm{av}}^+}\left[k^+ \left.\frac{\partial T^+}{\partial y^+}\right|_g + \frac{\mathrm{Pr}_l}{4S}\frac{\lambda_i^+}{\mathrm{Re}_g}\frac{d\,\mathrm{Re}_l}{dz^+}\right] \tag{23}$$

The local convection Nusselt number ($\mathrm{Nu}_{g,z}$) and Sherwood number ($\mathrm{Sh}_{g,z}$) are computed from the following equations:

$$\mathrm{Nu}_{g,z} = \frac{1}{T_{\mathrm{av}}^+}\left.\frac{\partial T^+}{\partial y^+}\right|_{g,y^+=\delta_l^+} \tag{24}$$

$$\mathrm{Sh}_{g,z} = \frac{1}{\rho_{v,\mathrm{av}}^+}\left.\frac{\partial \rho_v^+}{\partial y^+}\right|_{y^+=\delta_l^+} \tag{25}$$

## 3 Method of Solution

The gas phase, viz., the mixture of noncondensable gas and condensable vapor, occupies the width of the channel completely at the inlet. As the gas-vapor mixture moves forward in the $z$-direction the condensate forms and the portion of the width occupied by the gas phase decreases in proportion to the thickness of the condensate layer. In conventional moving boundary problems involving phase change such as condensation or solidification, the identification of the moving front is required in terms of the grid number. However, this procedure is more often used, for example, in the problem of solidification of a moving warm liquid, where the thickness of the solidified mass is comparable in magnitude to the thickness of the liquid flowing.

A combination of finite-difference and integral methods is used in solving the equations of the gas phase and condensate film, respectively. In the present case of condensation of vapor from a mixture containing gas in high concentration this conventional procedure is not used for the following two reasons. The thickness of the condensate layer is by far less compared with the width of the channel. The thickness of the condensate film is the highest at the end of the channel where it is about one-hundredth of the channel width. The continuity and momentum and energy balance equations for the gas phase are solved by applying pressure correction method to provide the necessary inputs to the velocity and temperature derivative in Eqs. (20) and (22). The increase in the condensate Reynolds number ($\mathrm{Re}_l$) for an increment ($\Delta z^+$) is calculated from Eq. (19).

*Pressure correction.* The local pressure gradient must be specified to calculate the velocity field from the momentum balance equation [8]. An equation is obtained to calculate the local pressure gradient using a procedure, which is described below. The derivative $(\partial u/\partial z)$ is eliminated from the momentum balance equation with the help of the continuity equation. The resulting equation is integrated partially with respect to $y$ to yield the following equation in normalized form. Utilizing the fact that $\delta_l^+$ is by far less than unity, the following equation is obtained:

$$\frac{1}{2\rho_g^+}\frac{\partial P^+}{\partial z^+} = \int_0^{0.5} u^+\frac{\partial v^+}{\partial y^+}dy^+ + \frac{1}{\rho_g^+}\frac{\partial \rho_g^+}{\partial z^+}\int_0^{0.5} u^{+2}dy^+ - \int_0^{0.5} v^+\frac{\partial u^+}{\partial y^+}dy^+ - \left.\frac{\partial u^+}{\partial y^+}\right|_{y^+=0} + \frac{\mathrm{Ar}_0}{2\mathrm{Re}_{g,0}} \tag{26}$$

Equation (26) is used to calculate $(\partial P^+/\partial z^+)$ at any $z^+$ for $z^+ > 0$. The pressure gradient at the inlet, i.e., at $z^+ = 0$, is calculated from the following equation:

$$\frac{1}{\rho_g^+}\frac{\partial P^+}{\partial z^+} = -\left.\frac{\partial u^+}{\partial y^+}\right|_{y^+=0} \tag{27}$$

The method of solution of the normalized mass, momentum and energy balance equations, and the diffusion equation is as follows. The values of $P_0$, $T_0$, $R_{H,0}$, and $\mathrm{Re}_{g,0}$ at the inlet, i.e., at $z=0$, are specified. The system parameters are $\mathrm{Re}_g$, $\mathrm{Pr}_g$, $\mathrm{Pr}_l$, $S$, and $\mathrm{Sc}_g$. The grid independence and convergence tests at each increment in the downstream distance were conducted on the magnitudes of all velocities and temperatures and particularly on the central line velocity and temperature. The independence of the numerical results on the gird size $\Delta y^+$ has been tested by increasing the number of grids in the $y$-direction and a value of 200 grids is arrived at in this process. $\Delta z^+$ is chosen such that $\Delta z^+ \le [(\Delta y^+)^2 L/W\mathrm{Re}_{g,0}]$. Oosthuizen and Naylor [9] solved the problem of forced flow in a parallel plate channel using an explicit numerical method. They took the value of $\Delta z^+$ based on the criterion that $\Delta z^+ \le (\Delta y^{+2} L/W\mathrm{Re}_{g,0})$. Since we solved the problem by using an implicit method, we could choose a larger value of $\Delta z^+$ than that in an explicit method. However, we used the same value of $\Delta z^+$ as in the explicit method, which is given by the inequality given above. The solution is started at the inlet, i.e., at $z^+ = 0$. An initial guess value for the pressure gradient $(dP^+/dz^+)$ is calculated from Eq. (27). The momentum balance equation, i.e., Eq. (15), is solved by an implicit finite-difference scheme with an upwind differencing scheme for the first derivatives in the $y$-direction. The tridiagonal matrix is solved by Thomas algorithm to get the $u^+$-velocity field at $z^+ = \Delta z^+$. An improved value of $(dP^+/dz^+)$ is calculated using the derived equation, i.e., Eq. (26). The momentum balance equation is solved again during the same $\Delta z^+$ interval using the calculated value of $(dP^+/dz^+)$ to get improved values of the velocity field. This procedure is repeated until a converged value of $(dP^+/dz^+)$ is obtained.

The normalized energy balance and diffusion equations, i.e., Eqs. (16) and (17), are also numerically solved to obtain $T^+$ and $\rho_v^+$ over an increment of $\Delta z^+$ by an implicit finite-difference method with the aid of Thomas algorithm. The values of $v^+$ at all the grid points for $\delta_l^+ \le y^+ \le 0.5$ are calculated using the normalized equation of continuity, i.e., Eq. (14). The converged values of $u^+$ at $z^+ = \Delta z^+$ become the inputs for the solution of the momentum balance equation for the next increment in $\Delta z^+$. The converged value of $(dP^+/dz^+)$ becomes the initial guess value for the second step of $\Delta z^+$. Thus the numerical solution is continued to compute $u^+$, $T^+$, $\rho_v^+$, and $v^+$ at each increment of $\Delta z^+$ until $z^+$ becomes equal to $L^+$. The procedure to calculate $(\partial \rho_g/\partial z)$, $\delta_l^+$, and $T_i^+$ is explained in Ref. [2]. $\mathrm{Nu}_{l,z}$, $\mathrm{Nu}_{g,z}$, and $\mathrm{Sh}_{g,z}$ are calculated from Eqs. (23)–(25), respectively.

## 4 Results and Discussion

The present theoretical work is validated with the experimental data of Lebedev et al. [1], who conducted experiments in a rectangular duct to study the heat and mass transfer in the condensation of vapor from humid air in a preturbulent flow. The experimental setup of Lebedev et al. [1] consists of a rectangular duct, which is 0.02 m wide, 0.15 m high, and 0.6 m long. They obtained experimental data for condensation heat transfer coefficients at two different velocities at the inlet, viz., $u_0 = 1.4$ m/s ($\mathrm{Re}_{g,0} = 1480$) and $u_0 = 0.7$ m/s ($\mathrm{Re}_{g,0} = 740$), which are shown in Fig. 2. The mass flow rates of vapor and air per unit width of the channel corresponding to $\mathrm{Re}_{g,0} = 1480$ are $1.806 \times 10^{-4}$ and 0.0294 kg/m s, respectively. Numerical results are obtained from the present work for local condensation heat transfer coefficient, $h_{l,z}$, for the same conditions of inlet velocity ($u_0$), gas inlet temperature ($T_0$), and total pressure of gas-vapor mixture at the inlet ($P_0$) as those of Lebedev et al. [1]. The other data used are as follows: $L = 0.6$ m, $W = 0.02$ m, and $T_w = 5\,^\circ\mathrm{C}$. The local condensation heat transfer coefficients computed at the middle of the test section are shown in Fig. 2, which show satisfactory agreement with the experimental data of Lebedev et al. [1].

The input system parameters of the present study are the $R_{H,0}$, the relative humidity of the air entering the channel, $\mathrm{Re}_{g,0}$, the gas phase Reynolds number at the channel inlet, $T_0$, the temperature of the air at the channel inlet, and $P_0$, the total pressure of the air in the channel at the inlet. The numerical results are obtained for the chosen common parameters of constant wall temperature, $T_w = 5\,^\circ\mathrm{C}$, the length of the channel, $L = 1$ m, and the channel width,

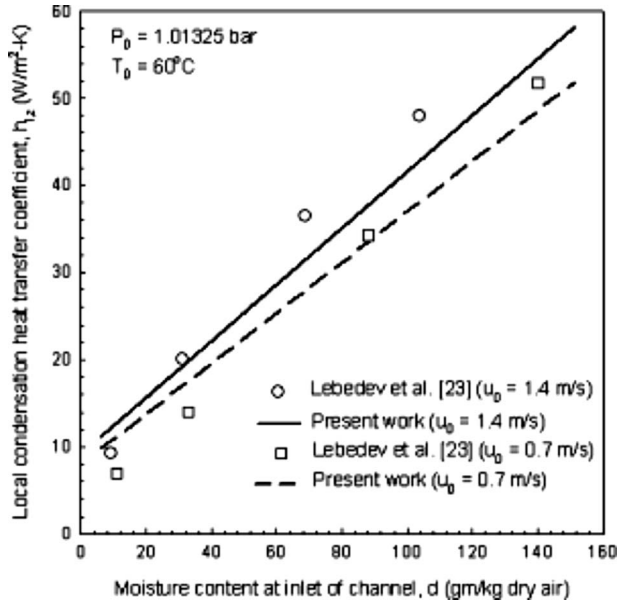


**Fig. 2 Comparison of $h_{l,z}$ of the present work with experimental data**

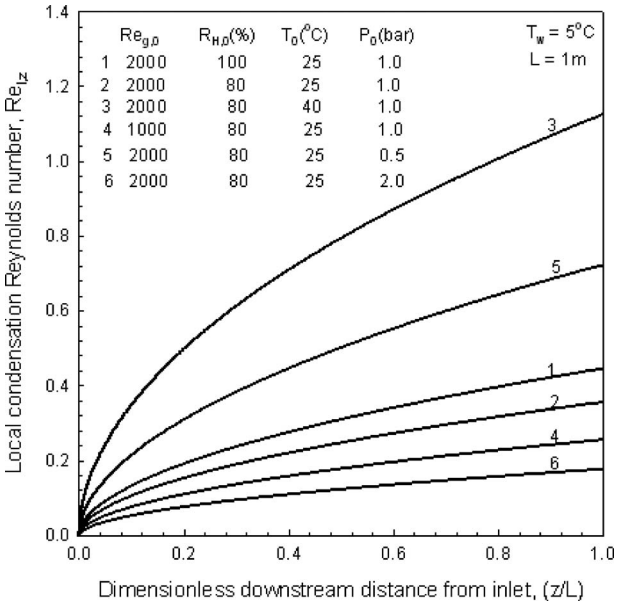


**Fig. 4 Variation of $Re_{l,z}$ with $T_0$, $Re_{g,0}$, $P_0$, and $R_{H,0}$**

$W=0.025$ m. From the numerical results the local values of Nusselt number, condensation Reynolds number, and gas-liquid interface temperature are estimated for different values of the system parameters. In forced convection condensation, the total heat transferred to the wall is the sum of the heat transferred by convection through the gas film and the latent heat of condensation of vapor. The condensation Nusselt number reported in this work is calculated from the total heat transfer rate. The local condensation Nusselt numbers, $Nu_{l,z}$, are shown plotted in Fig. 3 as a function of dimensionless downstream distance, $z/L$. Curves 1 and 2 of Fig. 3 show the effect of $R_{H,0}$ on $Nu_{l,z}$ for prescribed values of $P_0$, $T_0$, and $Re_{g,0}$. A comparison of curves 1 and 2 shows a decrease in local condensation Nusselt number with a decrease in the value of $R_{H,0}$, due to an increase in the percentage of noncondensable gas in the vapor-air mixture at the inlet and a consequent decrease in the vapor content of the mixture. Curves 2 and 3 of Fig. 3 show the effect of $T_0$ at fixed $R_{H,0}$, $P_0$, and $Re_{g,0}$ on the local condensation Nusselt number, $Nu_{l,z}$. The saturation vapor pressure increases with an increase in $T_0$, resulting in an increase in the humidity of water vapor in the gas phase. The heat transfer by convection also increases due to an increase in the temperature difference between the vapor-gas mixture core and the wall with an increase in $T_0$. Hence $Nu_{l,z}$ increases with an increase in $(T_0)$, due to increase in the total heat transfer to the condensate film. The heat and mass transfer during condensation of vapor from vapor-air mixture is also controlled by flow hydrodynamics. As the gas phase Reynolds number at the inlet, $Re_{g,0}$, increases, the flow rate of vapor increases due to increase in the flow rate of vapor-gas mixture. The higher the flow velocity, the higher the heat transferred to the condensate film. Curves 4 and 2 of Fig. 3 illustrate the same trend that the local condensation Nusselt number increases with an increase in $Re_{g,0}$ at fixed values of $R_{H,0}$, $P_0$, and $T_0$. Curves 6, 2, and 5 of Fig. 3 show an increase in the value of $Nu_{l,z}$, as $P_0$ is decreased for a fixed value of $R_{H,0}$, $T_0$, and $Re_{g,0}$. The property mostly affected by the pressure is the mixture density, $\rho_g$. The $\rho_g$ increases with an increase in $P_0$ due to the increase in the saturation temperature. The gas phase Nusselt number $(h_g W/k_l)$, which represents the convection part of the total heat transfer, is shown plotted by the dashed line in Fig. 3. Curves 8 and 7 of Fig. 3 show that the gas phase Nusselt number $(h_g W/k_l)$ increases with an increase in $Re_{g,0}$. However, the variation of gas phase Nusselt number $(Nu_{g,z})$ with $R_{H,0}$, $T_0$, and $P_0$ is not significant.

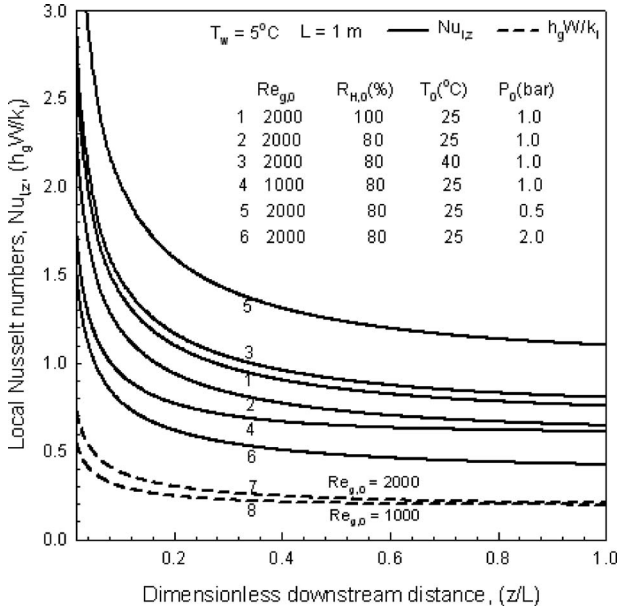


**Fig. 3 Effect of $T_0$, $Re_{g,0}$, $P_0$, and $R_{H,0}$ on local Nusselt numbers**

The effects of the system parameters $R_{H,0}$, $Re_{g,0}$, $T_0$, and $P_0$ on the local condensation Reynolds number, $Re_{l,z}$, are shown plotted in Fig. 4 as a function of the downstream distance, $(z/L)$. An increase in $R_{H,0}$ (curves 2 and 1), $T_0$ (curves 2 and 3), and $Re_{g,0}$ (curves 4 and 2) the local condensate Reynolds number, $Re_{l,z}$, increases due to increase in vapor density of the mixture toward the condensation surface. The $Re_{l,z}$ increases with a decrease in total pressure at the inlet, $P_0$ (curves 6, 2, and 5) due to decrease in saturation temperature and the resulting decrease in density of mixture.

Figure 5 shows the effect of the system parameters on the gas-to-liquid interface temperature, $T_i$, as a function of downstream distance. $T_i$, the temperature on the free surface of the condensate film, increases along the downstream distance due to the transfer

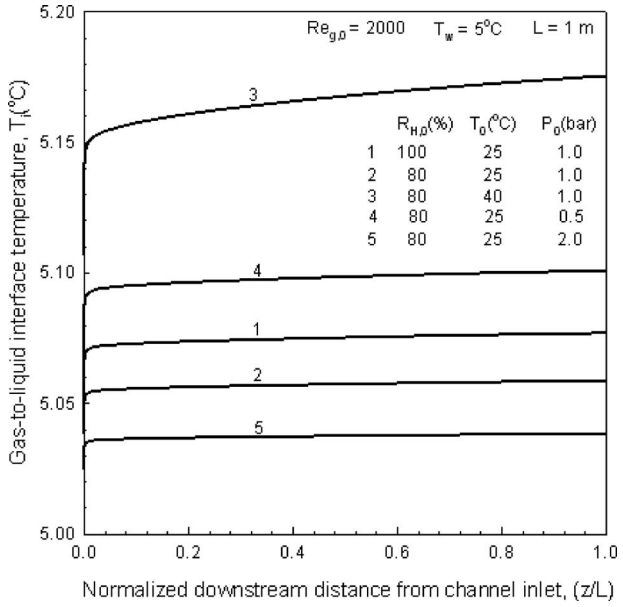


**Fig. 5 Effect of $T_0$, $P_0$, and $R_{H,0}$ on gas-to-liquid interface temperature**

of convection and latent heat to the condensate film from the gas phase and the condensing vapor. Curves 2 and 1 of Fig. 5 show an increase in $T_i$ with an increase in $R_{H,0}$, which is due to an increase in the latent heat released to the condensate film. Curves 2, 4, and 5 of the same figure show the variation of $T_i$ with $P_0$. The $T_i$ decreases with an increase in $P_0$, due to decrease in heat transfer to the condensate film as explained earlier. Curves 2 and 3 of Fig. 5 show the variation of $T_i$ with $T_0$. The $T_i$ increases with an increase in $T_0$, due to an increase in convection and condensation heat transfer to the condensate film. The effect of the convection heat transfer is not significant in comparison with the latent heat transfer. So the effect of $\mathrm{Re}_{g,0}$ on $T_i$ is almost negligible since the variation of magnitudes of $\mathrm{Re}_{g,0}$ in laminar flow is not high.

## 5 Conclusions

A theoretical model is formulated for the case of laminar film condensation of water vapor from a mixture of vapor and high-concentration noncondensable gas flowing in a vertical parallel plate channel under laminar forced flow.

Numerical results are obtained for different values of system parameters controlling the process, such as $T_0$, $\mathrm{Re}_{g,0}$, $R_{H,0}$, and $P_0$.

From the numerical results the local Nusselt number, condensation Reynolds number, and gas-liquid interface temperature are estimated.

The numerical results of the present theoretical study agree satisfactorily with the experimental data available in literature.

## Nomenclature

$\mathrm{Ar}_0$ = Archimedes number, $gW^3/\nu_{g,0}^2$
$C_p$ = specific heat at constant pressure
$C_{p,g}^+$ = normalized gas specific heat at constant pressure, $(C_{p,g}/C_{p,g,0})$
$d$ = moisture content
$d_e$ = equivalent diameter
$D_{\mathrm{va}}$ = mass diffusion coefficient of water vapor in air
$D_{\mathrm{va}}^+$ = normalized mass diffusion coefficient, $(D_{\mathrm{va}}/D_{\mathrm{va},0})$
$F$ = term defined in Eq. (11)
$g$ = gravitational acceleration
$k$ = thermal conductivity
$k^+$ = gas-to-liquid thermal conductivity ratio, $(k_g/k_l)$
$k_g^+$ = normalized gas thermal conductivity, $(k_g/k_{g,0})$
$L$ = length of the channel
$L^+$ = normalized length of the channel, $(L/W\,\mathrm{Re}_{g,0})$
$\dot{m}$ = condensate mass flux
$\mathrm{Nu}_l$ = condensation Nusselt number, $(h_l W/k_l)$
$\mathrm{Nu}_g$ = convection Nusselt number, $(h_g W/k_g)$
$P$ = total pressure
Pr = Prandtl number, $(\mu C_p/k)$
$p$ = partial pressure
$\mathrm{Re}_{g,0}$ = gas phase Reynolds number at inlet, $(\rho_{g,0}u_0 W/\mu_{g,0})$
$\mathrm{Re}_l$ = condensation Reynolds number, $(4\dot{m}_l/\mu_l)$
$R_H$ = relative humidity, $(p_v/p_v^*)$
$R$ = gas constant
$q$ = heat flux
$S$ = subcooling parameter, $(C_{p,l}(T_0-T_w)/\lambda_0)$
Sc = Schmidt number, $(\mu_g/\rho_g D_{\mathrm{va}})$
Sh = Sherwood number, $(h_D W/D_{\mathrm{va}})$
$T$ = temperature of gas-vapor mixture
$T^+$ = normalized temperature, $(T-T_w)/(T_0-T_w)$
$u$ = component of air velocity in the $z$-direction
$u^+$ = normalized $u$-velocity, $(u/u_0)$
$v$ = component of air velocity in the $y$-direction
$v^+$ = normalized $v$-velocity, $(v\mathrm{Re}_g/u_0)$
$W$ = width of the channel
$y^+$ = normalized distance in the $y$-direction, $(y/W)$
$z$ = downstream distance
$z^+$ = normalized distance in the $z$-direction, $(z/W\mathrm{Re}_g)$

### Greek Symbols

$\beta$ = temperature ratio parameter, $(T_0-T_w)/T_w$
$\delta_l$ = thickness of the condensate film
$\delta^+$ = normalized boundary layer thickness, $(\delta/W)$
$\lambda$ = latent heat of condensation
$\lambda^+$ = normalized latent heat of condensation, $(\lambda/\lambda_0)$
$\mu$ = dynamic viscosity
$\mu^+$ = gas-to-liquid viscosity ratio, $(\mu_g/\mu_l)$
$\mu_g^+$ = normalized gas viscosity, $(\mu_g/\mu_{g,0})$
$\nu$ = kinematic viscosity, $(\mu/\rho)$
$\rho$ = density
$\rho_g^+$ = normalized gas density, $(\rho_g/\rho_{g,0})$
$\rho_v^+$ = normalized vapor density, $(\rho_v/\rho_{v,0})$
$\rho_{g,v}^+$ = density ratio parameter, $(\rho_g/\rho_{v,0})$
$\tau$ = shear stress

### Subscripts

0 = inlet
$a$ = air species
$c$ = concentration
$d$ = dew point
$e$ = exit, i.e., at $z=L$
$g$ = gas phase, i.e., air-water vapor mixture
$i$ = gas-to-liquid interface
$l$ = liquid (condensate)
$v$ = water vapor
$w$ = wall

## References

[1] Lebedev, P. D., Baklastov, A. M., and Sergazin, Zh. F., 1969, "Aerodynamics, Heat and Mass Transfer in Vapor Condensation From Humid Air on a Flat Plate in a Longitudinal Flow in Asymmetrically Cooled Slot," Int. J. Heat Mass Transfer, **12**, pp. 833–841.
[2] Dharma Rao, V., Murali Krishna, V., Sharma, K. V., and Sarma, P. K., 2007,

"A Theoretical Study on Convective Condensation of Water Vapor From Humid Air in Turbulent Flow in a Vertical Duct," ASME J. Heat Transfer, **129**, pp. 1627–1637.
[3] Dharma Rao, V., Murali Krishna, V., Sharma, K. V., and Mohan Rao, P. V. J., 2008, "Convective Condensation of Vapor in the Presence of a Non-Condensable Gas of High Concentration in Laminar Flow in a Vertical Pipe," Int. J. Heat Mass Transfer, available online June 2, 2008.
[4] Wang, C. Y., and Tu, C. J., 1988, "Effects of Non-Condensable Gas on Laminar Film Condensation in a Vertical Tube," Int. J. Heat Mass Transfer, **31**, pp. 2339–2345.
[5] Siow, E. C., Ormiston, S. J., and Soliman, H. M., 2004, "A Two-Phase Model for Laminar Film Condensation From Steam-Air Mixtures in Vertical Parallel-Plate Channels," Heat Mass Transfer, **40**, pp. 365–375.
[6] Oh, S., and Revankar, S. T., 2006, "Experimental and Theoretical Investigation of Film Condensation With Non-Condensable Gas," Int. J. Heat Mass Transfer, **49**, pp. 2523–2534.
[7] Schmidt, E., 1982, *Properties of Water and Steam in SI Units*, U. Grigull, ed., Springer-Verlag, New York.
[8] Patankar, S. V., 1980, *Numerical Heat Transfer and Fluid Flow*, Hemisphere, Washington, DC, pp. 113–134.
[9] Oosthuizen, P. H., and Naylor. D., 1999, *Introduction to Convective Heat Transfer Analysis*, McGraw-Hill, New York, pp. 212–218.

# Effect of Longitudinal Minigrooves on Flow Stability and Wave Characteristics of Falling Liquid Films

**Klaus Helbig**

**Ralph Nasarek**

**Tatiana Gambaryan-Roisman**

**Peter Stephan**

Chair of Technical Thermodynamics,
Technische Universität Darmstadt,
Petersenstrasse 30,
64287 Darmstadt, Germany

*Falling liquid films are used in many industrial apparatuses. In many cases the film flow along a wall with topography is considered advantageous for intensification of the heat and mass transport. One of the promising types of the wall topography for the heat transfer intensification is comprised of minigrooves aligned along the main flow direction. The wall topography affects the development of wavy patterns on the liquid-gas interface. Linear stability analysis of the falling film flow based on the long-wave theory predicts that longitudinal grooves lead to the decrease in the disturbance growth rate and therefore stabilize the film. The linear stability analysis also predicts that the frequency of the fastest growing disturbance mode and the wave propagation velocity decrease on a wall with longitudinal minigrooves in comparison with a smooth wall. In the present work the effect of the longitudinal minigrooves on the falling film flow is studied experimentally. We use the shadow method and the confocal chromatic sensoring technique to study the wavy structure of falling films on smooth walls and on walls with longitudinal minigrooves. The measured film thickness profiles are used to quantify the effect of the wall topography on wave characteristics. The experimental results confirm the theoretical predictions.* [DOI: 10.1115/1.2993539]

*Keywords: falling films, wall topography, interfacial waves, film stability*

## 1 Introduction

Falling liquid films are used in many industrial applications, including evaporation [1,2], condensation [3,4], and adsorption [5]. The advantages of falling films include high heat and mass transfer rates at low film flow rates and short contact time between the process fluid and the wall. The transport heat and mass transport mechanisms in falling films are coupled with the film hydrodynamics [6–13].

Falling films on vertical and inclined walls are unstable to long-wave disturbances [14,15]. Smooth films flowing down inclined walls are stable if the flow rate, or the film Reynolds number, lies below a certain critical value. In contrast, the films on vertical walls are unstable at an arbitrarily small Reynolds number. The long-wave instability leads to development of waves. The amplitude and shape of the waves depend on the liquid flow rate (or the Reynolds number), the kind of the liquid, and the distance from the film distributor [9,16,17].

The hydrodynamics of wavy laminar and turbulent films has been a focus of numerous studies over several decades [6,7,9,10,12,13,16–18].

Telles and Dukler [6] have analyzed the time-varying thickness of the falling film by electrical conductivity measurements. The measurements have been performed in the range of the film Reynolds number Re from 900/4 to 6000/4 with and without countercurrent gas flow. It has been found that the film thickness variation is random in character. Methods of extracting statistically meaningful information about the waves behavior have been suggested.

Karimi and Kawaji [18] have used a laser-induced photochromic tracer technique to investigate the instantaneous velocity profile and film thickness in a thin, wavy falling liquid film in a vertical tube for $1408/4 < \mathrm{Re} < 6549/4$ with and without an interfacial shear. Their experiments revealed the occurrence of circulatory motions under large waves, which may significantly affect the transport phenomena for wavy films.

Adomeit and Renz [9] have experimentally investigated the flow and three-dimensional structure of the liquid-gas interface in laminar wavy films for $108 < \mathrm{Re} < 800$. At $\mathrm{Re} \sim 120$ most of the waves had the U- or W-shapes and were comparable in size. At $\mathrm{Re} \sim 300$ most of the waves had elongated shapes, and the wave collisions occurred more frequently. At $\mathrm{Re} \sim 800$ the wave interactions lead to formation of turbulent spots.

Lel et al. [10] have measured the thickness evolution of wavy films of silicone oils on vertical and inclined plates simultaneously by the confocal chromatic sensoring technique (CHR) and fluorescence intensity technique. The authors have investigated the average film thickness and the wave propagation velocity for $2 < \mathrm{Re} < 700$.

Nosoka and Miyara [17] have studied the development of excited waves on a water film flowing down a glass plate in the range $15 < \mathrm{Re} < 75$. The authors have registered the shadow images of the falling film and investigated the scenarios of the wave evolution.

When the liquid film is used in cooling apparatuses or in evaporators, it is often advantageous to create the film on a microstructured wall instead of a smooth one. A promising type of the wall topography for the falling film apparatuses is comprised of micro- or minigrooves oriented along the main flow direction [13,19,20].

The wall topography affects the falling film stability. Our linear stability analysis in the framework of the long-wave theory [21] has shown that the longitudinal grooves lead to the decrease in the disturbance growth rate and therefore stabilize the film flow [19].

Contributed by the Heat Transfer Division of ASME for publication in the JOURNAL OF HEAT TRANSFER. Manuscript received October 7, 2007; final manuscript received May 5, 2008; published online October 14, 2008. Review conducted by Satish G. Kandlikar. Paper presented at the 5th International Conference on Nanochannels, Microchannels, and Minichannels (ICNMM2007), Puebla, Mexico, June 18–20, 2007.

  

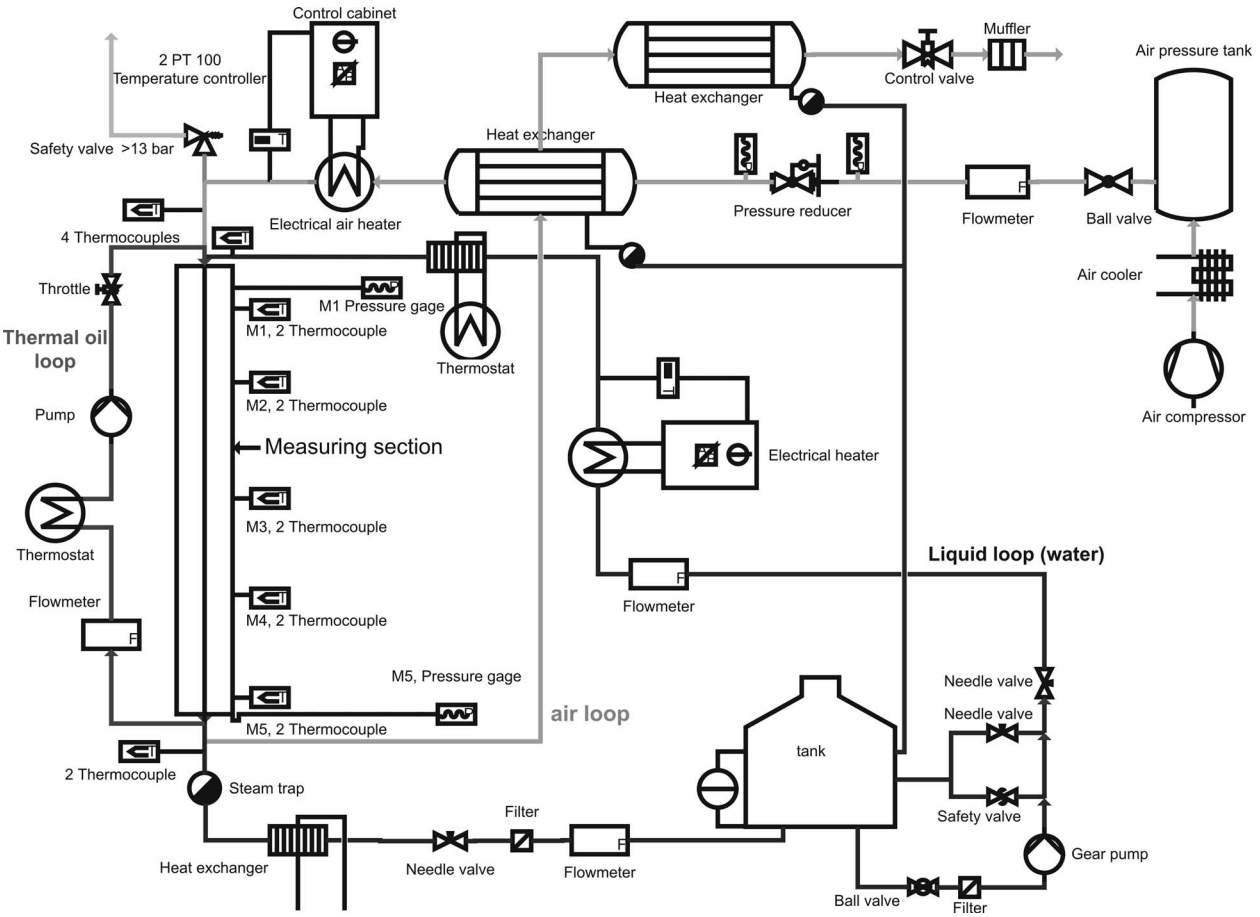


**Fig. 1 Experimental setup**

It has been also found that longitudinal grooves lead to the increase in the wavelength of the fastest growing disturbance and to the decrease in the wave propagation velocity.

Most of the studies dealing with a problem of film flow over topography are devoted to wall structures with periodical or single corrugations in the main flow direction [22,23]. Only a few experimental works are devoted to the hydrodynamics of falling films on walls with longitudinal topographical features. Lozano Avilés et al. [12] have used a high frequency impedance needle probe to measure the thickness of an evaporating film of water–ethylene glycol mixture on a smooth plate and on a plate with longitudinal fins separated from each other by a distance of 2.4 mm. The authors have shown that longitudinal fins lead to increase in the film thickness at the wave crests and to increase in the dominant wavelength. The wave propagation velocity on a structured plate was lower than that on a smooth plate. The experimental results of Ref. [12] agree qualitatively with our theoretical predictions.

A similar structured plate has been used for investigation of the film rupture on a heated wall [24]. It has been found that the longitudinal wall topography leads to increase in the heat flux at which film rupture occurs. Moreover, the wall topography prevents the spreading of the dry patch over the entire plate surface and therefore increases the wall heat flux corresponding to the heat transfer crisis.

The analysis of current literature shows that no comprehensive experimental data quantifying the influence of the longitudinal wall topography on the characteristics of interfacial waves have been reported until now.

The present paper aimed at experimental investigation of the effect of longitudinal minigrooves on the film dynamics and on the wavy patterns on a surface of a film flowing down a vertical wall. The wave characteristics (frequency, propagation velocity, and area of the liquid-gas interface) are determined from the film thickness measurements, and their dependence on the Reynolds number and on the wall topography is analyzed. We compare the experimental findings with theoretical predictions based on the long-wave analysis.

## 2 Experimental Apparatus and Procedure

**2.1 Experimental Setup.** Figure 1 shows a flowchart of the experimental setup for investigation of falling and gas flow-driven liquid films. The setup consists of three main loops: a test liquid loop, an oil loop, and an air loop. The air and oil loops have not been used for the experiments reported in this paper. The test liquid (water) is supplied from a storage tank by a gear pump. The liquid enters the test section and flows downwards in a ring-shaped channel on the outside surface of the evaporator tube with an outer diameter of $d_{\text{tube}}=25$ mm (see Fig. 2(*a*)). The outer circumference of the channel is made of four quartz glass tubes with an inside diameter of $d_{\text{glass}}=56$ mm. The film thickness, the gas and liquid temperatures, and the pressure can be measured at five different positions along the tube separated from each other by a distance of 0.320 m. The highest and the lowest measurement positions are located at distances $l_1=0.02$ m and $l_5=1.3$ m from the film distributor, respectively.

The investigated copper test surfaces are shown in Fig. 2. Figure 2(*a*) depicts a smooth surface on the left side and a structured surface on the right side. The geometry of the structured test surface is illustrated in Fig. 2(*b*).

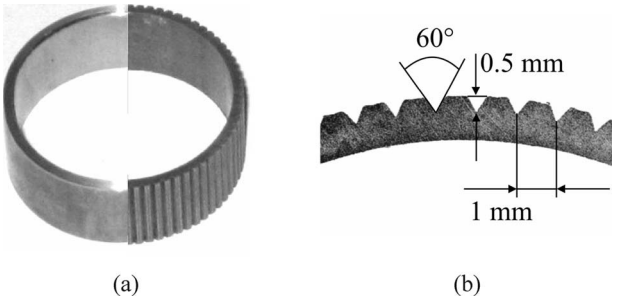


**Fig. 2 (*a*) Smooth and structured evaporator tubes; (*b*) structure geometry**

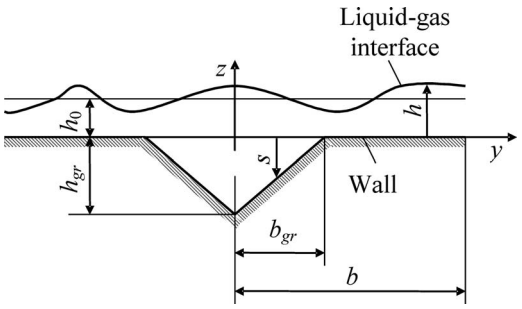


**Fig. 4 Geometry of the minigroove**

**2.2 Film Thickness Measurement.** Figure 3 illustrates an arrangement for simultaneous measurement of the film thickness using the CHR and the shadow method.

The shadow method is based on a shadow cast video recording of the falling film by a high-speed complementary metal-oxide semiconductor (CMOS) camera [13,16]. First, a reference picture of the dry tube is taken. After that the shadow of the water film flowing along the tube is recorded by the camera with a rate of 1000 frames/s. The film thickness distribution in each frame is determined using image analysis. The measurement error of the shadow method is 10 $\mu$m.

To validate the results obtained from the shadow method, we have compared them with the CHR based on chromatic longitudinal aberration of special optical probe [10,13]. This technique has a measurement error of less than 5 $\mu$m.

The CHR method can be used for pointwise film thickness measurements, whereas the shadow method allows the measurement of the film profile over a certain tube portion, which is necessary for determination of the wave propagation velocity and the wavelength.

**2.3 Evaluation of Wave Parameters.** The wave parameters have been determined from the images of the film profile collected using the shadow method.

In a wide range of the Reynolds numbers the wavy pattern is comprised of isolated waves of large amplitude accompanied by small-amplitude capillary waves. The film between the large-amplitude waves, or the basis film, is relatively smooth. We have developed an algorithm for automatic detection of isolated waves from the $h$ (film thickness) versus $t$ (time) curves. We define the beginning of each wave as an instant, at which the function $h^{-1}dh/dt$ exceeds a certain threshold value. It means that the propagation of wave through the given measurement point manifests itself by a fast rate of film thickness increase starting from a small value. The end of a wave has been set at a point where the film thickness is smaller than the time-averaged film thickness. The results of this algorithm have been compared with the manual wave counting showing a perfect agreement.

The wave propagation velocity for each wave has been determined by cross correlating the functions $h(t)$ taken at a distance of $\Delta s$ from each other. The time shift $\Delta t$ corresponding to the peak of the cross-correlation function has been calculated for each single wave, and the wave propagation velocity has been calculated as $v_w=\Delta s/\Delta t$. Averaging the velocities of the single waves brings forth the average wave velocity. The wave frequency $f_w$ has been determined by dividing the number of detected waves through the time of measurement.

The shadow method captures the projection of the liquid-gas interface on the vertical plane, $h(x)$. We have defined an interface projection arc length $\Gamma$ in the following form:

$$\Gamma = (x_2 - x_1)^{-1} \int_{x_1}^{x_2} (h_x^2 + 1)^{1/2} dx \tag{1}$$

where $x_1$ and $x_2$ denote the beginning and the end of the measurement section and the subscript $x$ denotes a particular $x$-derivative. This parameter correlates with the area of the liquid-gas interface and is thus important for the interfacial transport.

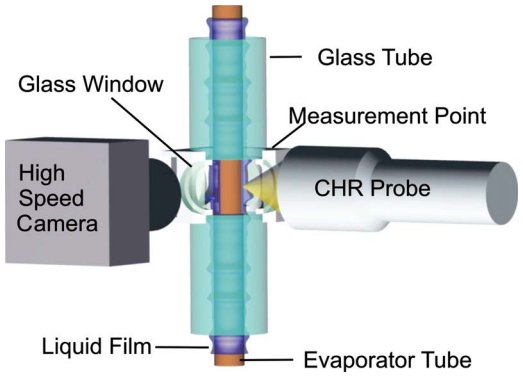


**Fig. 3 Arrangement for the simultaneous film thickness measurements by the CHR method and the shadow method**

## 3 Theoretical and Numerical Investigations

We assume that the liquid film fully covers the wall, which corresponds to the experimental observations in the studied range of the mass flow rates.

Figure 4 depicts a cross section of a groove. The wall topography is given by a function $z=s(y)$, whereas the liquid-gas interface is described by a function $z=h(x,y,t)$.

The film hydrodynamics is governed by the Navier–Stokes equations and the continuity equation. The no-penetration and no-slip conditions for the velocity field are posed at $z=s(y)$. The conditions of continuity of the normal and the tangential stresses (dynamic boundary conditions), as well as the kinematic boundary condition, are posed at $z=h(x,y,t)$.

The solution of the nonstationary three-dimensional system of Navier–Stokes equations in a system with moving boundaries is still a challenge. Until now only the results of two-dimensional simulations of development of waves on falling films on smooth walls have been reported [17,25]. In the following sections 3.1 and 3.2 we consider the velocity field in the undisturbed film and perform a linear stability analysis in the framework of the long-wave approximation.

**3.1 Velocity Field in Undisturbed Laminar Film.** The aim of this section is the determination of the relationship between the liquid mass flow rate and the film thickness for the structured wall. The results of this section will be used for comparison with experimentally determined average film thickness at different Reynolds numbers.

Assume that the flow is stationary and laminar, and the liquid-gas interface is undisturbed ($h=h_0$=const). The velocity field is

fully developed. Then the Navier–Stokes equations are reduced to a two-dimensional Poisson equation for the $x$-component of the velocity, $u$, as follows:

$$\nu\left(\frac{\partial^2 u}{\partial y^2}+\frac{\partial^2 u}{\partial z^2}\right)=-g \tag{2}$$

where $g$ is the gravitational acceleration and $\nu$ denotes the kinematic viscosity of the liquid. Other velocity components are zero. This equation has been solved numerically for different values of $h_0$ (see Fig. 4). The volumetric liquid flow rate has been calculated by integrating the velocity over the film cross section.

**3.2 Linear Long-Wave Stability Analysis.** The waviness of the liquid-gas interface detected in the experiment results from the long-wave instability pertinent to falling films [14,15]. The wave characteristics (frequency, propagation speed, and wavelength) in the wave formation region are determined by the fastest growing disturbance mode, which can be calculated from the linear stability analysis. As the disturbances grow, the nonlinear effects become increasingly important.

The falling film stability analysis at arbitrary Reynolds numbers has to be performed by solution of the Orr–Sommerfeld equations [14,15]. The solution of these equations for complicated geometries (represented, for example, by the wall topography) is connected with numerical difficulties.

For the Reynolds numbers up to 10 the film dynamics can be modeled in the framework of the long-wave theory [21]. This theory is applicable in the cases where the characteristic film thickness is much smaller than the characteristic wavelength of the film thickness variation. With the long-wave approximation, the Navier–Stokes equations reduce to a single partial differential equation describing the evolution of the interface.

Consider an undisturbed falling film with the interface position at $z=h_0$, or, in dimensionless form, $Z=H_0=h_0/h_N$, where the Nusselt film thickness for a falling film on a smooth wall has been chosen as a linear scale. This thickness can be determined from the following relation [3]:

$$h_N=(3\ \mathrm{Re}\ \nu^2/g)^{1/3},\quad \mathrm{Re}=\dot{m}/\Pi\mu \tag{3}$$

where Re denotes the Reynolds number, $\mu$ is the dynamic viscosity of the liquid, $\dot{m}$ is the liquid mass flow rate, and $\Pi$ is the width of the film, which in the case of a film flowing along a tube wall is equal to the circumference: $\Pi=\pi d_{\mathrm{tube}}$.

We assume the following form of the perturbed interface position:

$$H(X,Y,\tau)=H_0+\delta_0\varphi(Y)\exp[iK(X-V_w\tau)+\Omega\tau] \tag{4}$$

where $\tau=t\sigma/(3h_N\mu)$ is the dimensionless time, $K$ is a dimensionless disturbance wave number, $V_w$ is the dimensionless wave propagation velocity, $\Omega$ is a dimensionless disturbance growth rate, $\delta_0$ is a small parameter, and $\varphi(Y)$ is an unknown amplitude function. If $\Omega$ is negative, the disturbance decays with time, and if it is positive, the disturbance grows exponentially, and the flow is unstable.

Substituting expression (4) into a long-wave evolution equation accounting for the wall topography [19], we arrive at the following relation:

$$(\xi^3\varphi_{YYY})_Y-2K^2\xi^3\varphi_{YY}-3K^2\xi^2\xi_Y\varphi_Y+\left[K^4\xi^3+K^2\frac{9}{40\ \mathrm{We}}\xi^6+K\frac{3}{\mathrm{Re\ We}}\xi^2-\left(1+iK\frac{5}{8\ \mathrm{Re\ We}}\xi^4\right)(\Omega-iKV_w)\right]\varphi=0 \tag{5}$$

where $\xi(Y)=H_0-S(Y)$, $S(Y)$ is the dimensionless wall topography, and We is the Weber number as follows:

$$\mathrm{We}=\frac{\sigma}{\rho\bar{u}^2h_N},\quad \bar{u}=\frac{\mathrm{Re}\ \nu}{h_N} \tag{6}$$

Herein $\sigma$ denotes the surface tension and $\rho$ denotes the liquid density.

Equation (5) together with appropriate boundary conditions constitutes an eigenvalue problem for determination of the disturbance growth rate $\Omega$, the disturbance propagation speed $V_w$, and the frequency $F_w=V_wK/(2\pi)$ as a function of the wave number, physical parameters of the system, and the wall topography $S(Y)$.

## 4 Results and Discussion

In this section the results of the comparison between two measurement techniques for determination of the film thickness are presented. After that the measured film characteristics are reported for the smooth and the structured tube. The results of the theoretical/numerical analysis are presented.

**4.1 Comparison Between Two Methods of Film Thickness Measurement.** The simultaneous film thickness measurement by the shadow method and the CHR method at the same location has been achieved using the arrangement shown in Fig. 3 and simultaneous triggering of both systems. Our earlier studies have shown that the $h(t)$ curves obtained by both methods are very close to each other [13]. We have computed cross-correlation between the $h(t)$ signals obtained by simultaneous measurement by the shadow method and the CHR method. The resulting extremely high cross-correlation coefficient (98%) is a clear indication of a good agreement between the two measurement methods.

We have performed 40 simultaneous measurements of the film thickness using both measurement systems at Re=250 and $l_5=1.3$ m. Each of these measurements has been taken during 8.2 s with a rate of 1000 data points per second. The values of the average film thickness $\bar{h}$ have been distributed according to the Gaussian normal distribution function with a mean value of $\bar{\bar{h}}=331.47$ $\mu$m for the CHR method and $\bar{\bar{h}}=334.20$ $\mu$m for the shadow method. The deviation between these two values is less than 1%, which is within the measurement error of the CHR method.

The performed statistical analysis of both measurement systems has shown that the agreement between them is excellent. The results of this section provide a justification for using the shadow method for the film thickness measurement.

**4.2 Average Film Thickness.** All the film thickness measurements discussed in this paper have been taken at atmospheric pressure and at a temperature of 20°C.

To verify the uniformity of the film distribution around the tube the film thickness has been measured at four positions around the tube at $l_1=0.02$ m, directly under the film distributor. The film thickness varies up to 30% of the average film thickness depending on the flow length and the Reynolds number. However, this variation decreases downwards.

Figure 5 shows the average film thickness measured using the shadow method at $l_2=0.34$ m and $l_5=1.3$ m versus the Reynolds number. The experimental data are compared with the Nusselt solution for the smooth walls (dashed line) and with our numerical simulations for the structured walls, as described in Sec. 3.1 (solid line). A good agreement between the experimental data and the theoretical predictions has been found.

For most of the presented regimes the average film thickness slightly decreases with the distance from the film distributor. However, in the case of the smooth wall surface in the range of the Reynolds numbers $180<\mathrm{Re}<280$, an opposite trend has been observed. This can be explained by the slight nonuniformity of the film distribution around the tube perimeter.

In the range $\mathrm{Re}<200$ the film thicknesses measured at $l_5=1.3$ m are lower than the predicted values. This can be attributed

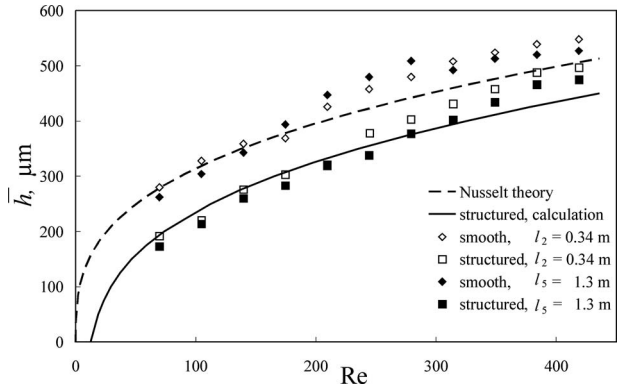


**Fig. 5 Average film thickness (shadow method and numerical calculations)**

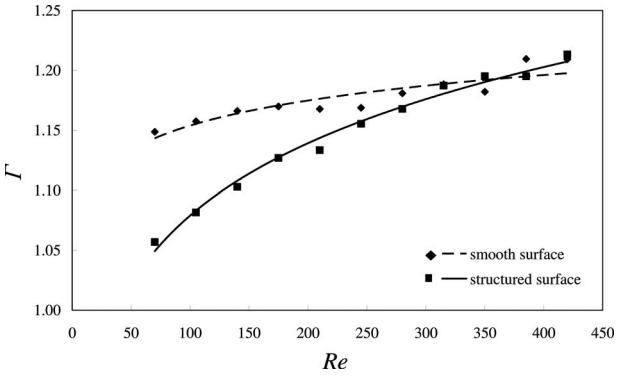


**Fig. 7 Interface arc length for the structured and smooth surfaces ($l_4$=1 m)**

to the film waviness. In the presence of waves on a laminar film the average film thickness is smaller than the thickness of a smooth film at the same value of the Reynolds number. This small discrepancy does not take place for $l_2$=0.34 m, where the liquid-gas interface is smooth. In the range of higher Reynolds numbers (Re > 300) the measured average film thicknesses exceed the predicted values. In this range of Reynolds numbers the transition to turbulence starts. We suggest that the film thickness behavior at high Reynolds numbers can be attributed to the turbulent fluctuations of the velocity.

**4.3 Wave Characteristics.** The results presented in Figs. 6 and 7 have been obtained by processing the data collected using the shadow method. The results depicted in Figs. 8 and 9 have been obtained using the CHR method.

Figure 6 shows the average wave propagation velocities on the smooth and structured surfaces versus the Reynolds number. The measurements were performed at a distance of $l_4$=1.00 m from the film distributor. It is clearly seen that the waves on the structured surfaces propagate more slowly than on the smooth surfaces, which agrees well with the experimental results reported in Ref. [12] and with the theoretical predictions [19].

The interface arc length for the structured and smooth surfaces (Eq. (1)) is presented in Fig. 7. The interface arc length is equal to unity for a smooth liquid-gas interface and higher than unity for a wavy interface. The results presented in Fig. 7 show that at moderate Reynolds numbers the arc length of the film on a structured surface is smaller than that on a smooth surface, which can be attributed to the flow stabilization due to the wall topography. With increasing Reynolds number the arc length increases for both kinds of the wall surface, and the difference between the smooth and the structured surface decreases. This happens because the stabilizing effect of the wall topography becomes weaker as the film thickness increases.

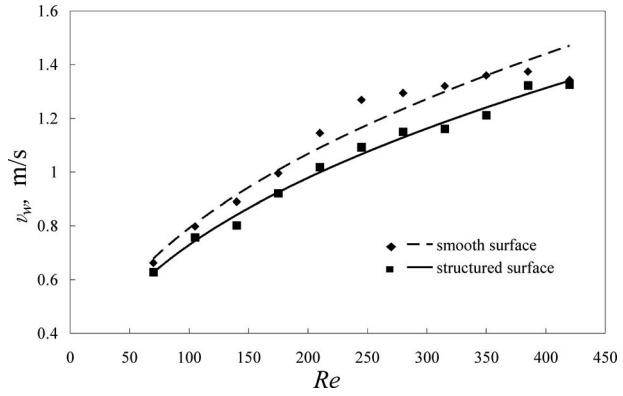


**Fig. 6 Wave propagation velocities on smooth and structured surfaces ($l_4$=1 m)**

Figure 8 depicts the time evolution of the film thickness $h(t)$ at Re=30 and $l_5$=1.30 m for the smooth and structured wall surfaces. The number of waves on a film falling down the structured surface is much smaller than on a film falling down the smooth surface. Therefore, the characteristic wave frequency is significantly lower on a structured surface. This result is in qualitative agreement with the data collected by Lozano Avilés et al. [12] on evaporating water–ethylene glycol mixture film flowing down a plate with longitudinal fins (see Fig. 7 in Ref. [12]). However, no direct comparison between the results reported in Ref. [12] and our work can be done. Since the measurements described in Ref. [12] have been performed on an evaporating mixture of two fluids, the film dynamics reported in Ref. [12] can be significantly affected by solutocapillarity, thermocapillarity, and evaporative mass loss, whereas our experiments have been performed with pure water at isothermal conditions.

The average wave frequencies computed on the basis of the number of detected waves per unit time are depicted in Fig. 9 versus the Reynolds number for the smooth surface and for the surface with minigrooves. The effect of the wall topography is to reduce the wave frequency $f_w$. The influence of the topography is significant for small values of the Reynolds number, where the film thickness over the minigroove crest is significantly smaller than the groove depth. The effect of the wall topography reduces with increase in the Reynolds number. At Re ~ 60 no difference between the two types of surfaces can be detected. At larger values of the Reynolds number the wave frequencies corresponding to the grooved wall decrease again. The ratio between the wave frequencies at the structured and smooth surfaces tends to unity with increase in Re.

The analysis of the wave characteristics has revealed several trends. First, the liquid-gas interface of a film falling down a structured wall is smoother than the interface of a film falling down a smooth surface. Second, the wave propagation velocity on a structured surface is lower than that on a smooth surface. Third, the wave frequency on a structured surface is lower than that on a smooth surface. In Sec. 4.4 we explain these trends on the basis of the results of the linear stability analysis.

**4.4 Film Stability.** The following results are not intended to provide quantitative agreement with the measured wave characteristics. Due to the limitations of the long-wave theory our analysis is applicable for much larger groove angles (or much smaller values of $h_{gr}/b$) than those studied experimentally, and for smaller Reynolds numbers. Moreover, the wavelengths, the wave propagation velocities, and the wave frequencies, corresponding to the fastest growing wave predicted by the linear theory, are measur-

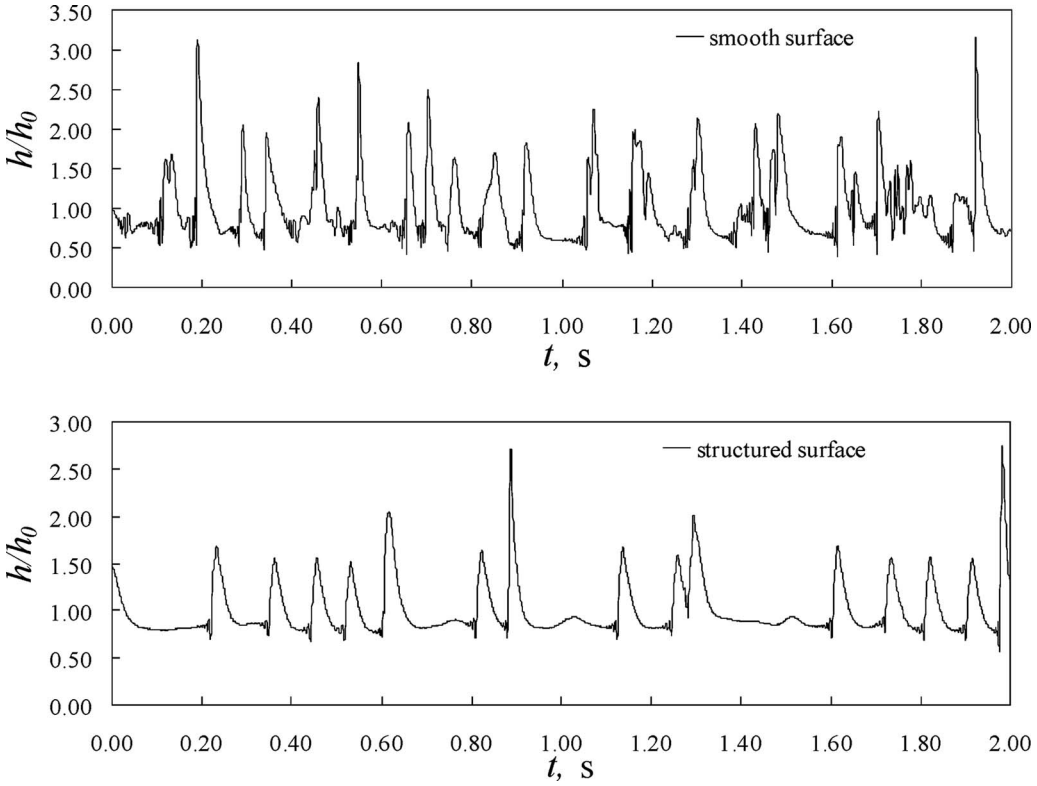


**Fig. 8 Evolution of film thickness at the smooth and structured surfaces (Re=30 and $l_5$=1.30 m)**

able only in the region of wave formation [16]. In spite of that we show that the long-wave stability analysis can capture all the most important effects induced by the wall topography.

Figure 10 illustrates the dimensionless disturbance growth rate on the smooth and on the structured surface as a function of the disturbance wave number. The computations have been performed for $h_{gr}$=50 $\mu$m, $b_{gr}$=288.7 $\mu$m, and $b$=500 $\mu$m (see Fig. 4), i.e., all the groove dimensions except for the groove depth correspond to the tube used in experiments. The corners at the groove trough ($y$=0) and at $y=b_{gr}$ have been smoothed by replacing the line segments adjacent to the corners with arcs. This is needed to comply with the requirements of the long-wave theory. On the other hand, it is evident that the corners in the grooves machined in a metal plate are never sharp. The computations have been performed for two different values of the film thickness over the groove crest (corresponding to $h_0/b$=0.15 and $h_0/b$=0.2). The solid lines depict the disturbance growth rate for the structured wall and the dashed lines depict the disturbance growth rate for the smooth wall. It is seen that the wall structure leads to the decrease in the disturbance growth rate, which is in agreement with our earlier results for longitudinal grooves with sinusoidal cross section [19]. This stabilization effect is responsible for the reduction of the liquid-gas interface area on the structured wall, which has been observed in experiments (see Fig. 7). The wave propagation velocity reduces on the structured wall by a factor of 1.23 for $h_0/b$=0.15 and by a factor of 1.17 for $h_0/b$=0.2, which is in good agreement with the results presented in Fig. 6.

Figure 11 illustrates the effect of the wall topography on the dominant wave frequency. The dominant wave frequency has been calculated as $f_w=kv_w/(2\pi)$, where the wave number $k$ and the wave propagation velocity $v_w$ have been evaluated at the

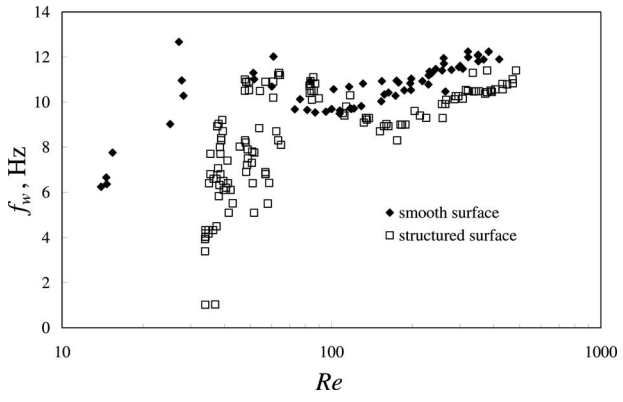


**Fig. 9 Average wave frequencies for the smooth and structured surfaces ($l_5$=1.30 m)**

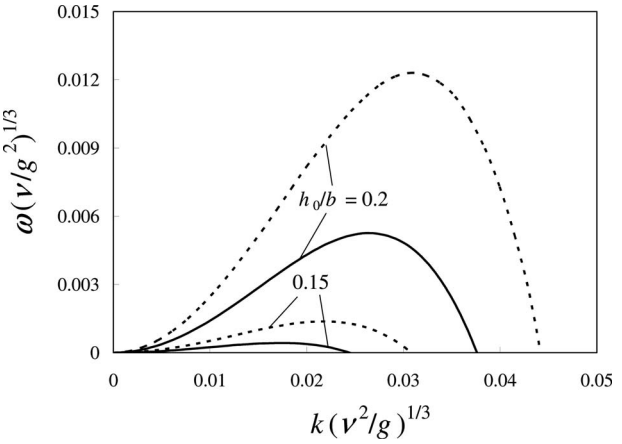


**Fig. 10 Scaled disturbance growth rate versus the scaled disturbance wave number. (Solid lines) Structured wall. (Dashed lines) Smooth wall.**

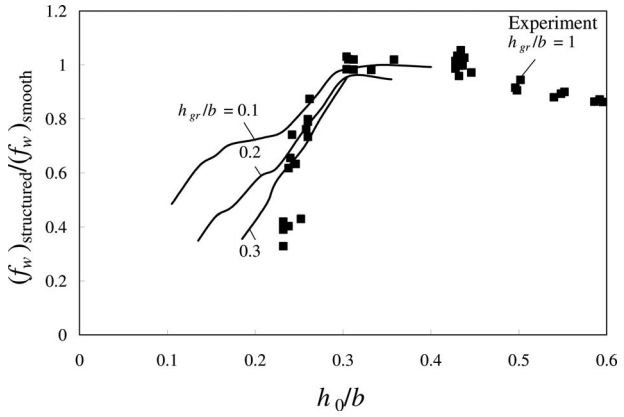


**Fig. 11 Frequencies of the fastest growing waves: the ratio between the wave frequencies on the structured and smooth surfaces. The experimental data are taken from Fig. 9.**

maximal of the function $\omega(k)$ (maximum linear growth rate). The ratio of the dominant wave frequencies between the structured and the smooth wall has been compared with the experimental data presented in Fig. 9 (see full squares in Fig. 11). Since the long-wave approximation does not allow to simulate the wall structures with $h_{gr}/b=1$ (corresponding to the real experiment), we have performed three series of computations with $h_{gr}/b=0.1$, 0.2, and 0.3, respectively, with an expectation to find at least a qualitative agreement between our simulations and the experimental trend. Surprisingly, not only qualitative but also quantitative agreement with the experimental results has been achieved (see Fig. 11). Our theory has accurately predicted the value of the film thickness at which the ratio of dominant wave frequencies on structured and smooth wall surfaces achieves a maximum (this film thickness corresponds to $h_0/b=0.3$). For this film thickness the dominant wave frequencies for both types of wall are equal to each other. Our theory has also accurately predicted the behavior of the frequency ratio for $0.26<h_0/b<0.3$. In order to predict the behavior of the dominant wave frequency at $h_0/b>0.35$ and at $h_0/b<0.26$, the stability analysis should be performed using the Orr–Sommerfeld equations, and the limitations of the long-wave theory should be relaxed.

## 5 Conclusions

An experimental setup for investigation of the hydrodynamics and heat transfer in thin liquid gravity- and shear-driven liquid films has been developed. The evolution of the falling film thickness has been measured using the shadow method, as well as using the CHR method, based on chromatic longitudinal aberration of an optical probe. The agreement between the two measurement techniques is very good.

The measured average film thickness agrees very well with the theoretical predictions both for the smooth and structured wall surfaces. The small deviations between the measurement results and the theoretical predictions can be attributed to the film waviness (at $\mathrm{Re}<150$) and to the transition to turbulence (at $\mathrm{Re}>300$).

A digital image processing has been applied to the images produced by the shadow method for determination of the wave propagation velocity, the wave frequency, and the arc length of the liquid-gas interface.

Comparison between the wave parameters of the films on structured and smooth surfaces showed that the films on the structured surface are characterized by slower waves with lower frequency. Furthermore, the surface area of the liquid-gas interface on the structured wall is smaller than that on the smooth wall. The difference in the surface area is significant at moderate Reynolds numbers ($\mathrm{Re}<200$).

A linear stability analysis has been performed for the isothermal falling films on smooth walls and on the walls with triangular minigrooves. It has been found that the linear disturbance growth rate is lower on the structured walls than on the smooth walls. This explains the experimental finding that the liquid-gas interface is smoother and less wavy on the structured walls. It has been also found that the frequency and the propagation speed of the fastest growing wave are lower on the structured wall than on the smooth wall. This trend agrees very well with the experimental observations both qualitatively and quantitatively.

The present study can become an important step toward understanding and designing the wall structures for controlling the wavy patterns in falling liquid films.

Further studies will be aimed at the investigation of different mechanisms contributing to the heat transfer enhancement on structured surfaces, including the film waviness, the thin film evaporation in the vicinity of the triple line, and the thermocapillary convection.

## Acknowledgment

The authors wish to acknowledge the support of the German Science Foundation (DFG) through the collaborative research center SFB 568 Program and through the Emmy Noether Program.

### Nomenclature

$b$ = half-period of the structure, m
$b_{\mathrm{gr}}$ = half of the groove width, m
$d_{\mathrm{tube}}$ = tube diameter, m
$f_w$ = wave frequency, Hz
$F_w$ = dimensionless wave frequency
$g$ = gravity acceleration, $\mathrm{m/s^2}$
$h$ = film thickness over the structure crest, m
$\bar{h}$ = average film thickness over the structure crest, m
$H$ = dimensionless film thickness above the structure crest
$h_0$ = undisturbed film thickness above the structure crest, m
$H_0$ = dimensionless undisturbed film thickness above the structure crest
$h_{\mathrm{gr}}$ = groove height, m
$k$ = disturbance wave number, 1/m
$K$ = dimensionless disturbance wave number
$\dot{m}$ = mass flow rate, kg/s
Re = Reynolds number, dimensionless
$s$ = wall topography function, m
$S$ = dimensionless wall topography function
$\Delta s$ = distance, m
$\Delta t$ = time shift, s
$v_w$ = velocity of the wave propagation, m/s
$V_w$ = dimensionless velocity of the wave propagation
We = Weber number, dimensionless

### Greek Symbols

$\Gamma$ = arc length of the liquid-gas interface, dimensionless
$\rho$ = density of the test liquid, $\mathrm{kg/m^3}$
$\nu$ = kinematic viscosity of the test liquid, $\mathrm{m^2/s}$
$\mu$ = dynamic viscosity of the test liquid, kg/m s
$\Pi$ = film width, m
$\sigma$ = surface tension, N/m
$\omega$ = disturbance growth rate, 1/s
$\Omega$ = dimensionless disturbance growth rate

## References

[1] Chun, K. R., and Seban, R. A., 1971, "Heat Transfer to Evaporating Liquid Films," ASME J. Heat Transfer, **93**, pp. 391–396.
[2] Shmerler, J. A., and Mudawar, I., 1988, "Local Evaporative Heat Transfer

Coefficient in Turbulent Free–Falling Liquid Films," Int. J. Heat Mass Transfer, **31**(4), pp. 731–742.
[3] Nusselt, W., 1916, "Die Oberflächenkondensation des Wasserdampfes," Z. Ver. Dtsch. Ing., **60**, pp. 541–546 and 569–575.
[4] Aktershev, S. P., and Alekseenko, S. V., 2005, "Influence of Condensation on the Stability of a Liquid Film Moving Under the Effect of Gravity and Turbulent Vapor Flow," Int. J. Heat Mass Transfer, **48**, pp. 1039–1052.
[5] Killion, J. D., and Garimella, S., 2004, "Simulation of Pendant Droplets and Falling Films in Horizontal Tube Absorbers," ASME J. Heat Transfer, **126**(6), pp. 1003–1013.
[6] Telles, A. S., and Dukler, A. E., 1970, "Statistical Characteristics of Thin, Vertical, Wavy Liquid Films," Ind. Eng. Chem. Fundam., **9**(3), pp. 412–421.
[7] Shmerler, J. A., and Mudawar, I., 1988, "Local Heat Transfer Coefficient in Wavy Free-Falling Turbulent Liquid Films Undergoing Uniform Sensible Heating," Int. J. Heat Mass Transfer, **31**(1), pp. 67–77.
[8] Alhusseini, A. A., Tuzla, K., and Chen, J. C., 1998, "Falling Film Evaporation of Single Component Liquids," Int. J. Heat Mass Transfer, **41**(12), pp. 1623–1632.
[9] Adomeit, P., and Renz, U., 2000, "Hydrodynamics of Three-Dimensional Waves in Laminar Falling Films," Int. J. Multiphase Flow, **26**, pp. 1183–1208.
[10] Lel, V. V., Al-Sibai, F., Leefken, A., and Renz, U., 2005, "Local Thickness and Wave Velocity Measurement of Wavy Films With a Chromatic Confocal Imaging Method and a Fluorescence Intensity Technique," Exp. Fluids, **39**, pp. 856–864.
[11] Miyara, A., Nosoko, T., and Nagata, T., 2002, "Enhancement of Heat and Mass Transfer by Waves on Falling Liquid Films," Proceedings of the 12th International Heat Transfer Conference, Grenoble, France, Aug. 18–23, pp. 591–596.
[12] Lozano Avilés, M., Maun, A. H., Iversen, V., Auracher, H., and Wozny, G., 2005, "High Frequency Needle Probes for Time- and Space-Characteristic Measurements of Falling Films on Smooth and Enhanced Surfaces," Proceedings of the Sixth World Conference on Experimental Heat Transfer, Fluid Mechanics, and Thermodynamics, Matsushima, Miyagi, Japan, Apr. 17–21, Paper No. 7-b-9.
[13] Helbig, K., Alexeev, A., Gambaryan-Roisman, T., and Stephan, P., 2005, "Evaporating of Falling and Shear-Driven Thin Films on Smooth and Grooved Surfaces," Flow, Turbul. Combust., **75**, pp. 85–104.
[14] Yih, C.-S., 1955, "Stability of Parallel Laminar Flow With a Free Surface," Q. Appl. Math., **13**, pp. 434–439.
[15] Yih, C.-S., 1963, "Stability of Liquid Flow Down an Inclined Plane," Phys. Fluids, **6**(3), pp. 321–334.
[16] Alekseenko, S. V., Nakoryakov, V. E., and Pokusaev, B. G., 1994, *Wave Flow of Liquid Films*, Begell House, New York.
[17] Nosoko, T., and Miyara, A., 2004, "The Evolution and Subsequent Dynamics of Waves on a Vertically Falling Liquid Film," Phys. Fluids, **16**, pp. 1118–1126.
[18] Karimi, G., and Kawaji, M., 1999, "Flow Characteristics and Circulatory Motion in Wavy Falling Films With and Without Counter-Current Gas Flow," Int. J. Multiphase Flow, **25**, pp. 1305–1319.
[19] Gambaryan-Roisman, T., and Stephan, P., 2003, "Analysis of Falling Film Evaporation on Grooved Surfaces," J. Enhanced Heat Transfer, **10**(4), pp. 445–457.
[20] Alexeev, A., Gambaryan-Roisman, T., and Stephan, P., 2005, "Marangoni Convection and Heat Transfer in Thin Liquid Films on Heated Walls With Topography: Experiments and Numerical Study," Phys. Fluids, **17**, 062106.
[21] Oron, A., Davis, S. H., and Bankoff, S. G., 1997, "Long-Scale Evolution of Thin Liquid Films," Rev. Mod. Phys., **69**, pp. 931–980.
[22] Vlachogiannis, M., and Bontozoglou, V., 2001, "Experiments on Laminar Film Flow Along a Periodic Wall," J. Fluid Mech., **457**, pp. 133–156.
[23] Gramlich, C. M., Kalliadasis, S., Homsy, G. M., and Messer, C., 2002, "Optimal Leveling of Flow Over One-Dimensional Topography by Marangoni Stresses," Phys. Fluids, **14**(6), pp. 1841–1850.
[24] Zaitzsev, D. V., Lozano Aviles, M., Auracher, H., and Kabov, O., 2007, "Rupture of a Subcooled Liquid Film Falling Down a Heated Grooved Surface," Microgravity Sci. Technol., **XIX**(3/4), pp. 71–74.
[25] Gao, D., Morley, N. B., and Dhir, V., 2003, "Numerical Simulation of Wavy Falling Film Flow Using VOF Method," J. Comput. Phys., **192**, pp. 624–642.

# Numerical Investigation of Electrohydrodynamic-Conduction Pumping of Liquid Film in the Presence of Evaporation

**Miad Yazdani**
e-mail: myazdan1@iit.edu

**Jamal Seyed-Yagoobi**
e-mail: yagoobi@iit.edu

Two-Phase Flow and Heat Transfer Enhancement Laboratory,
Mechanical, Materials and Aerospace Engineering Department,
Illinois Institute of Technology,
Chicago, IL 60616

*Electrohydrodynamic (EHD) conduction pumping is associated with the heterocharge layers of finite thickness in the vicinity of the electrodes, generated by the process of dissociation of the neutral electrolytic species and the recombination of the generated ions. This paper numerically investigates the EHD-conduction pumping of a liquid film in the presence of evaporation. The flow system comprises a liquid film flowing over a two-dimensional flat plate. The vapor phase above the flat plate is extended far beyond the interface. The channel is separated into four different sections: the entrance, electrode, evaporation, and downstream sections. The entrance, electrode, and downstream regions are adiabatic while a constant heat flux is applied in the evaporation section. The concept of EHD-conduction pumping of liquid film in the presence of phase change is numerically demonstrated in this paper. The resultant heat transfer due to conduction pumping is evaluated as well. The results for heat transfer coefficient along the channel indicate considerable improvement of heat transfer coefficient compared with the pressure-driven counterpart.* [DOI: 10.1115/1.2993542]

*Keywords: EHD-conduction, liquid film, evaporation*

## 1 Introduction

Pumping of liquid films is encountered in a wide range of physical and technological applications. Utilization of electrohydrodynamic (EHD) mechanisms to induce fluid motion in liquids is known as an effective approach for situations where special requirements and restrictions are imposed, while enhanced heat transfer and mass transport are required. The implementation of the EHD phenomena to heat transfer and mass transport introduces complex interactions among interdependent variables. The EHD pumping relies on the generated electric body force within a dielectric liquid primarily due to the presence of net charge density. There are three kinds of EHD pumping mechanisms utilizing the Coulomb force: ion-drag pumping requiring direct injection of free charges into the liquid and is not desirable due to degradation of the liquid properties, induction pumping based on charges induced in a liquid due to a gradient or discontinuity of the electric conductivity, and conduction pumping based on nonequilibrium behavior of dissociation of the neutral electric species and recombination of charges at the vicinity of electrodes [1]. The conduction term here represents a mechanism for electric current flow in which charged carriers are produced not by injection from electrodes but by dissociation of molecules within the liquid. The EHD-conduction pumping of dielectric liquids has been studied recently only by a few researchers [2–7].

The liquid film flows driven by EHD induction pumping have been extensively studied by a few researchers as well. Wawzyniak and Seyed-Yagoobi [8] developed an analytical model to study the EHD induction pumping of a stratified liquid/vapor medium in a horizontal channel. Brand and Seyed-Yagoobi [9] extended this model to different electrode configurations to investigate the effect of the various electrode geometries on the pump performance. In the extension of their work, Aldini and Seyed-Yagoobi [10] presented theoretical analysis of EHD induction pumping of liquid film in a vertical annular configuration. Brand and Seyed-Yagoobi [11] carried out an experimental study of the EHD induction pumping of a dielectric microcondensation film, in an external horizontal configuration.

This study extends the work of Yazdani and Seyed-Yagoobi [12] by fundamentally illustrating the electrically driven liquid film flow based on the conduction phenomenon in the presence of liquid film evaporation. The presence of liquid evaporation complicates the problem in hand due to the changes in the liquid film thickness along the heated plate. The effects of primary dimensionless numbers on the evolution of the liquid/vapor interface profile and resultant heat transfer performance are investigated in this paper.

## 2 Theoretical Model

The solution domain is presented in Fig. 1. The vapor phase above the interface is extended two orders of magnitude larger than the liquid film thickness at the entrance. Additionally, the downstream region is extended adiabatically to allow fully developed conditions for the liquid film at the outlet. The length of this adiabatic region, however, is determined based on the generated net flow rate for each operating condition. The theoretical model presented below incorporates the following assumptions.

1. Flow is steady and laminar.
2. The numerical domain is two dimensional.
3. There is no volumetric electric charge in the vapor phase.
4. Mobility and diffusion coefficients for the positive and negative ions are the same.
5. Charge injection is absent.

**2.1 Dimensionless Governing Equations.** The liquid and vapor phases satisfy the continuity via a single equation, Eq. (1).

Contributed by the Heat Transfer Division of ASME for publication in the JOURNAL OF HEAT TRANSFER. Manuscript received October 15, 2007; final manuscript received August 7, 2008; published online October 22, 2008. Review conducted by Anthony M. Jacobi. Paper presented at the 2007 ASME-JSME Thermal Engineering Conference and Summer Heat Transfer Conference (HT2007), Vancouver, BC, Canada, July 8–12, 2007.

  

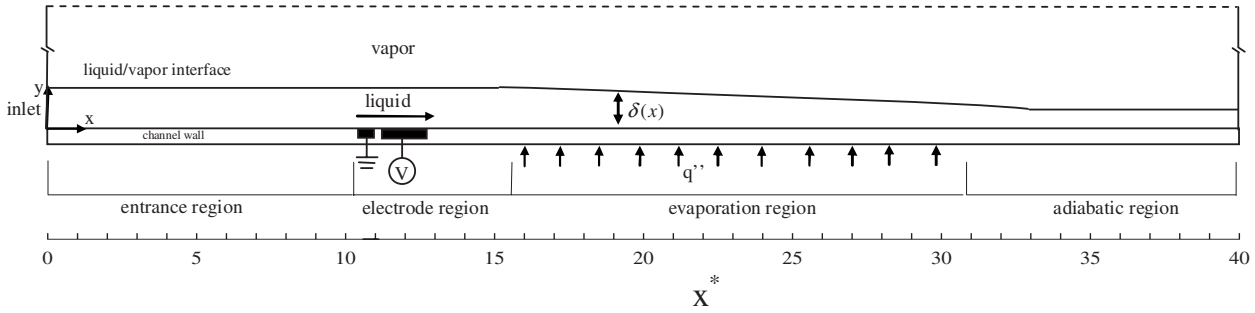


**Fig. 1 Schematic of 2D solution domain (not to scale). The interface profile presented is merely for illustration purposes.**

However, an additional equation is required to represent the changes in the interface profile due to liquid evaporation as discussed in Sec. 2.2.

$$\nabla^* \cdot \mathbf{U}^* = 0 \tag{1}$$

The dimensionless momentum and energy equations in the liquid phase account for the presence of electric body force and Joule heating, respectively, and are as follows:

$$(\mathbf{U}_l^* \cdot \nabla^*)\mathbf{U}_l^* = -\left(\frac{1}{\mathrm{Re}_{\mathrm{EHD}}}\right)^2 \nabla^* P_l^* + \frac{1}{\mathrm{Re}_{\mathrm{EHD}}} \nabla^{*2} \mathbf{U}_l^* + M_0^2 C_0 (p^* - n^*)\mathbf{E}^* \tag{2}$$

$$(\mathbf{U}_l^* \cdot \nabla^*)(T_l^*) = \frac{1}{\mathrm{Pe}_l} \nabla^{*2} T_l^* + J_e^* \tag{3}$$

The last term on the right hand side of Eq. (2) represents the electric body force density, which is the source of the pumping of the liquid film. The last term on the right hand side of Eq. (3) is the dimensionless form of Joule heating, which is defined as

$$J_e^* = J_e \left(\frac{c_{\mathrm{pl}} d^2}{\mathrm{Pe}_l k_l u_e^2}\right) \tag{4}$$

where

$$J_e = \int_{\forall} \sigma E^2 d\forall \tag{5}$$

The electric body force vanishes in the absence of electric charge within the vapor phase. Therefore, vapor motion is solely induced due to the shear stress along the interface. In addition, one can assume negligible contribution of the Joule heating within the vapor phase. Thus, the temperature distribution inside the vapor phase is only the consequence of heat diffusion across the interface, which is expected to have a small effect on the temperature variation of the vapor phase. The dimensionless momentum and energy equations for the vapor phase reduce to the following equations:

$$(\mathbf{U}_v^* \cdot \nabla^*)\mathbf{U}_v^* = -\left(\frac{1}{\mathrm{Re}_{\mathrm{EHD}}}\right)^2 \frac{\rho_l}{\rho_v} \nabla^* P_v^* + \frac{1}{\mathrm{Re}_{\mathrm{EHD}}} \frac{\nu_v}{\nu_l} \nabla^{*2} \mathbf{U}_v^* \tag{6}$$

$$(\mathbf{U}_v^* \cdot \nabla^*)(T_v^*) = \frac{1}{\mathrm{Pe}_l} \frac{\gamma_v}{\gamma_l} \nabla^{*2} T_v^* \tag{7}$$

To account for the effects of surface tension along the interface, the Young–Laplace equation is assumed to be valid, which in dimensionless form reduces to

$$\left(\frac{1}{\mathrm{Re}_{\mathrm{EHD}}}\right)^2 \nabla^* P_v^* = \left(\frac{1}{\mathrm{Re}_{\mathrm{EHD}}}\right)^2 \nabla^* P_l^* - \frac{1}{\mathrm{Fr}_e^2}\left[\nabla^* \delta^* - \frac{1}{\mathrm{Bo}} \nabla^* (\nabla^* \cdot \mathbf{n})\right] \tag{8}$$

where $\mathbf{n}$ is the unit vector normal to the interface and in general form is defined as

$$\mathbf{n} = \frac{\left(\frac{\partial \delta}{\partial x}, \frac{\partial \delta}{\partial y}\right)}{\sqrt{\left(\frac{\partial \delta}{\partial x}\right)^2 + \left(\frac{\partial \delta}{\partial y}\right)^2}} \tag{9}$$

The dimensionless static pressure is as expressed in Table 1. Bo and $\mathrm{Fr}_e$, respectively, are Bond and Froude numbers and are defined as

$$\mathrm{Bo} = \frac{g(\rho_l - \rho_v)d^2}{\sigma} \tag{10}$$

$$\mathrm{Fr}_e = \frac{u_e}{\sqrt{\frac{\rho_l - \rho_v}{\rho_l} g d}} \tag{11}$$

Here, $\sigma$ represents the liquid surface tension. The shear stress induced by the Marangoni effect is of negligible significance due to the slight variation in the interface temperature. In addition, the effects of Maxwell's stresses are neglected due to the small values of electric field along the interface.

The electric body force and the Joule heating are the results of applied electric field. These terms require the solution of the following Maxwell's and charge conservation relations within the liquid film.

$$\mathbf{E}^* = -\nabla^* \phi^* \tag{12}$$

**Table 1 Dimensionless parameters for governing equations**

| Parameter | Dimensionless parameter | Normalization factor |
|---|---|---|
| Charge density | $p^*$, $n^*$ | $n_{\mathrm{eq}}$ |
| Electric field | $\mathbf{E}^*$ | $V/d$ |
| Electric potential | $\phi^*$ | $V$ |
| Gradient operator | $\nabla^*$ | $d$ |
| Pressure | $P^*$ | $\mu_l^2/\rho_l d^2$ |
| Temperature | $T^*$ | $u_e^2/c_{pl}$ |
| Velocity field | $\mathbf{U}^*$ | $u_e$ |
| Heat flux | $q^*$ | $\sigma_l V^2/d$ |
| Spatial coordinates | $x^*$, $y^*$ | $d$ |

**Table 2 Summary of electrostatic and flow boundary conditions for the liquid film**

| Electrodes | | Channel | | |
|---|---|---|---|---|
| HV | Ground | Wall | Inlet/outlet | Interface |
| $u_y^*=u_x^*=0$ | $u_y^*=u_x^*=0$ | $u_y^*=u_x^*=0$ | $\left.\frac{\partial u_x^*}{\partial x^*}\right\vert=0$, $u_y^*=0$ | $\mu_l \left.\frac{\partial u_x^*}{\partial y^*}\right\vert_l=\mu_v \left.\frac{\partial u_x^*}{\partial y^*}\right\vert v$ |
| $\phi^*=1$ | $\phi^*=0$ | $\frac{\partial \phi^*}{\partial y^*}=0$ | $\frac{\partial \phi^*}{\partial x^*}=0$ | $\mathbf{n}\cdot\nabla\phi^*=0$ |
| $p^*=0$, $\frac{\partial n^*}{\partial y^*}=0$ | $n^*=0$, $\frac{\partial p^*}{\partial y^*}=0$ | $\frac{\partial (p^*,n^*)}{\partial y^*}=0$ | $\frac{\partial (p^*,n^*)}{\partial x^*}=0$ | $\mathbf{n}\cdot\nabla(p^*,n^*)=0$ |
| $\frac{\partial T^*}{\partial y^*}=0$ | $\frac{\partial T^*}{\partial y^*}=0$ | $\frac{\partial T^*}{\partial y^*}=0$ | $T^*\vert_{\text{in}}=T^*_{\text{sat}}$ | $T_l^*=T_v^*$ |
| | | $\left.\frac{\partial T^*}{\partial y^*}\right\vert_{\text{a}}=q^*$ | $\left.\frac{\partial T^*}{\partial x^*}\right\vert_{\text{out}}=0$ | $(\mathbf{n}\cdot\nabla kT^*)_l=(\mathbf{n}\cdot\nabla kT^*)_v$ |

[a]This boundary condition corresponds to the heat flux applied to the evaporation section of the channel wall.

$$\nabla^*\cdot\mathbf{E}^*=C_0(p^*-n^*) \tag{13}$$

The charge conservation equations for the positive and negative charges, respectively, are as follows:

$$\nabla^*\cdot[p^*(\mathbf{E}^*+\mathbf{U}^*)-\alpha\nabla^*p^*]=2C_0(F(\omega)-p^*n^*) \tag{14}$$

$$-\nabla^*\cdot[n^*(\mathbf{E}^*-\mathbf{U}^*)+\alpha\nabla^*n^*]=2C_0(F(\omega)-p^*n^*) \tag{15}$$

The definition of dimensionless parameters appearing in the above equations are

$$\mathrm{Re}_{\mathrm{EHD}}=\frac{u_e d}{\nu_l}=\frac{b_l V}{\nu_l},\quad \mathrm{Pe}_l=\mathrm{Re}_{\mathrm{EHD}}\mathrm{Pr}_l,\quad M_0=\sqrt{\frac{\epsilon_l}{\rho_l b_l^2}}$$

$$C_0=\frac{n_{\mathrm{eq}}d^2}{\epsilon_l V}=\frac{\sigma_l d^2}{2b_l\epsilon_l V}=\frac{1}{2N_{\mathrm{un}}},\quad \alpha=\frac{D_l}{b_l V}=\frac{k_B T}{eV} \tag{16}$$

The charge concentration at equilibrium $n_{\mathrm{eq}}$ is defined as $n_{\mathrm{eq}}=\sigma_l/2b_l$. $M_0$ is identified as the mobility ratio [13] and $N_{\mathrm{un}}=\epsilon u_e/\sigma d$ is expressed as the convection-conduction ratio [14]. Table 1 summarizes the definitions of the dimensionless variables for governing differential equations. The boundary conditions for the liquid phase are presented in Table 2.

For the vapor phase, the no slip boundary condition is applied for the upper wall, which is located far beyond the interface. Furthermore, the continuity of shear stress and zero-gradient boundary conditions are applied for the interface and inlet/outlet boundaries of the vapor phase, respectively.

**2.2 Interface Tracking Strategy.** In the present study, the volume of fluid (VOF) method [15,16] is modified to represent the heat and mass exchange across the interface. The advantage of the VOF method is its relatively easy programming with common finite difference discretization methods while it provides precise measurement of the interface profile under various operating conditions. The modified volume of fluid formulation is given as follows:

$$\dot{m}_{\mathrm{vap}}=\rho_l(\mathbf{U}_l-\mathbf{V}_f)\cdot\mathbf{n}=\rho_v(\mathbf{U}_v-\mathbf{V}_f)\cdot\mathbf{n} \tag{17}$$

$$\dot{m}_{\mathrm{vap}}h_{lv}-\dot{q}=0 \tag{18}$$

where $\dot{m}_{\mathrm{vap}}$ is the interphase mass flux, $h_{lv}$ is the latent heat, and $\dot{q}$ stands for the rate of heat release at the interface. $\mathbf{V}_f$ is the front velocity and represents the momentum transfer across the interface due to evaporation. The reader is referred to the review by Lakehal et al. [17] for the complete set of equations. Therefore, the continuity equation across the interface must reflect the interphase liquid mass transfer due to evaporation.

$$\frac{\partial}{\partial t}(\chi_l\rho_l)+\nabla\cdot(\chi_l\rho_l\mathbf{U})=-\rho_l(\mathbf{U}-\mathbf{V}_f)\cdot\nabla\chi_l \tag{19}$$

Here $\chi_l$ represents the volume of the liquid phase. This equation can be split into the pure mass continuity equation, Eq. (1), and a complementary equation, which characterizes the topological representation of the interface. In the case of evaporation, this equation can be reduced to

$$\frac{\partial\chi_l}{\partial t}+\mathbf{U}\cdot\nabla\chi_l=-\frac{1}{\rho_l}\int_0^x\dot{m}_{\mathrm{vap}}\delta(\mathbf{x}-\mathbf{x}_f)ds \tag{20}$$

$\dot{m}_{\mathrm{vap}}$ can be replaced by the rate of heat transfer through Eq. (18). For the steady flow, the first term on the left hand side vanishes and the following equation for the volume of the fluid can be obtained:

$$\mathbf{U}\cdot\nabla\chi_l=-\frac{1}{\rho_l h_{lv}}\int_0^x\mathbf{q}_{\mathrm{int}}\cdot\mathbf{n}\,\delta(\mathbf{x}-\mathbf{x}_f)ds \tag{21}$$

The rate of heat transfer across the interface $\mathbf{q}_{\mathrm{int}}\cdot\mathbf{n}=\dot{q}$ is the jump of energy and is determined upon the solution of energy equations (3) and (7).

## 3 Numerical Technique

The governing equations are solved in both liquid and vapor phases with the assumption that there is no charge in the vapor medium. The discretization equations are solved iteratively by the line-by-line application of the tridiagonal matrix algorithm. The central difference scheme is applied to the Gauss law while upwind scheme, based on the electric field and flow directions, is applied to the charge conservation equations. The Eulerian-based interface tracking is utilized, which fixes the grid independence of the interface motion. The interface profile is implicitly updated in every iteration on the balance of mass and energy at each longitudinal cross section, as governed by Eq. (21). The updated value of the energy jump across the interface in this equation is provided from the solution of the energy equation. The convergence criteria of $|(\psi_{i+1}-\psi_i)/\psi_i|<10^{-6}$ is applied for all involved parameters. An adaptive function is defined to dynamically refine the grid as the solution proceeds. The adaption scheme is based on the maximum velocity gradient for the elements and refines the grid elements whose velocity gradient in the streamwise direction is more than a

**Table 3 Comparison of current numerical model predictions against experimental results of Ref. [18] for falling vertical liquid film evaporation**

| Expt. data[a] | | | Current model predictions | | |
|---|---|---|---|---|---|
| $\delta$(mm) | $\mathrm{Re}=\frac{4\Gamma}{\mu}$ | $h_x\left(\frac{\nu^2}{k^3 g}\right)^{1/3}$ | $\delta$(mm) | $\mathrm{Re}=\frac{4\Gamma}{\mu}$ | $h_x\left(\frac{\nu^2}{k^3 g}\right)^{1/3}$ |
| 0.28 | $3\times10^3$ | 0.23 | 0.273 | $2.85\times10^3$ | 0.235 |
| 0.30 | $4\times10^3$ | 0.28 | 0.303 | $3.91\times10^3$ | 0.228 |
| 0.35 | $6\times10^3$ | 0.20 | 0.350 | $6.02\times10^3$ | 0.193 |
| 0.37 | $7\times10^3$ | 0.19 | 0.372 | $7.23\times10^3$ | 0.188 |

[a]Reference [18].

predefined threshold. The adaption function does not apply across the interface because it requires a fixed number of elements to accurately identify the interface profile. The numerical code has been validated against the available limited experimental data [18] for the heat transfer rate of evaporating liquid films falling along the vertical plate. The comparison is limited to the laminar liquid film evaporation of distilled water (Pr=5.1) with a constant heat flux along the wall ($q''=14.49$ kW) and is tabulated in Table 3.

## 4 Results and Discussions

The reference values selected to calculate the dimensionless parameters correspond to the properties of refrigerant R-123 as the working fluid, and they are provided in Table 4. Note that the results in this section represent the pumping of the liquid film by only one electrode pair utilized in the upstream region of the evaporation section. This is to fundamentally illustrate the electrically driven liquid film flow in the presence of evaporation and not necessarily to achieve optimum pumping performance. The effects of heat flux along with the primary dimensionless parameters on heat transfer performance are investigated in this section. The values of the dimensionless numbers for the base case are presented in Table 5. These values correspond to the fluid properties given in Table 4 and applied voltage of 10 kV. For the base case, the initial film thickness and applied heat flux in the evaporation region of the channel wall are set to $d=6$ mm and $q''=20$ kW/m$^2$ ($q^*=6300$), respectively. Furthermore, the base case corresponds to the electrode design and the selected spacing described before.

**Table 4 Properties of working fluid R-123**

| Property | Value | Ref. |
|---|---|---|
| Electrical permittivity (F/m) | $42.43\times10^{-12}$ | [19] |
| Electrical conductivity (S/m) | $4.7\times10^{-11}$ | [19] |
| Density (kg/m$^3$) | 1452 | [20] |
| Mobility (m$^2$/V s) | $3.894\times10^{-8}$ | [21][a] |
| Molecular viscosity (Pa s) | $4.087\times10^{-4}$ | [20] |
| $T_{sat}$ at one bar (K) | 300 | - |
| Thermal conductivity (W/m K) | $66.8\times10^{-3}$ | [20] |
| Specific heat (kJ/kg K) | 0.99 | [20] |
| Surface tension (N/m) | $6.9\times10^{-3}$ | [20] |

[a]Based on Walden's rule.

**Table 5 Numerical values of dimensionless numbers for the base case**

| Dimensionless No. | Numerical value |
|---|---|
| $\mathrm{Re}_{EHD}$ | 1380 |
| $\mathrm{Pe}_l$ | 8300 |
| $C_0$ | 0.0512 |
| $M_0$ | 4.39 |
| $\mathrm{Fr}_e$ | 0.27 |
| Bo | 72 |

The resultant liquid/vapor interface profile and corresponding streamlines in the presence of phase change are illustrated in Fig. 2. For unidirectional flow such as pressure-driven flows, one should expect the gradual decrease in liquid film thickness at any specific heat flux as the flow proceeds downstream of the evaporation section. Here, however, while the liquid film thickness is decreased in overall development along the channel, the liquid/vapor interface encounters local bumps, especially close to the electrode region. The local thickening of the liquid film is attributed to the local flow circulations generated by the local electric body forces, as depicted in Fig. 2. Figures 3–5 illustrate the distributions of electric field, net charge density, and electric body force, respectively. As shown in Fig. 3, the interelectrode region is characterized by high intensity of electric field in both directions resulting in significant values of electric body force in this region (Fig. 5). In addition, Fig. 4 shows that the net electric charges are limited to the small region within the vicinity of the two electrodes. This confirms the assumption of zero charge flux across the liquid/vapor interface along with zero value of charge density within the vapor phase. The electric body force distributions in streamwise and spanwise directions are presented in Figs. 5(*a*) and 5(*b*), respectively. As a result of this electric body force distribution, the liquid is carried from the narrower ground electrode toward the wider high voltage (HV) electrode. The flow is also associated with local circulations, primarily due to the spanwise component of the electric body force along with the opposing streamwise forces mainly acting on the right hand side of the electrodes. The cross-sectional velocity profiles at the middle of

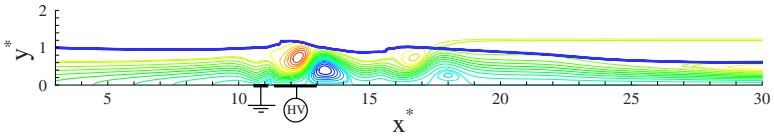


**Fig. 2 Liquid film interface profile and corresponding streamlines**

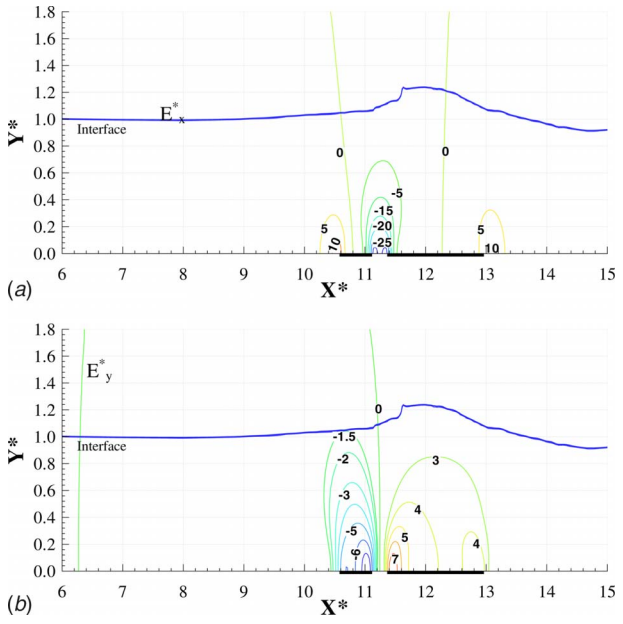


**Fig. 3 Dimensionless contours of electric field: (*a*) streamwise direction, $E_x^*$, and (*b*) spanwise direction, $E_y^*$**

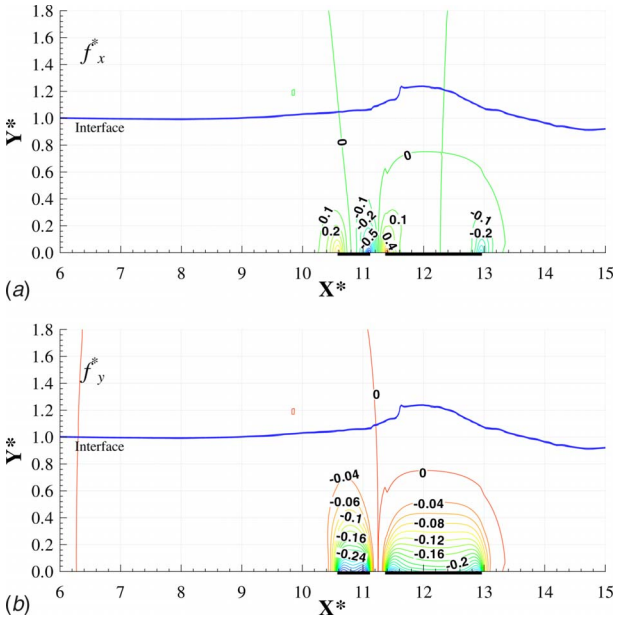


**Fig. 5 Dimensionless contours of electric body force: (*a*) streamwise direction, $f_{ex}^*$, and (*b*) spanwise direction, $f_{ey}^*$**

the interelectrode region, as shown in Fig. 6, illustrate the circulatory flow in those regions. Note that the flow direction is not influenced by the polarity of the electrodes.

Sectional heat transfer analysis for the EHD-conduction driven liquid film flow is provided and compared with that of the conventional pressure-driven flow in Fig. 7. In the pressure-driven flow, the electric body force in Eq. (2) is replaced by a favorable constant pressure gradient, which provides the driving force. Its value is chosen to provide the same volumetric flow rate at the channel inlet as that produced by the corresponding conduction driven flow. However, the liquid film driven by conventional pressure gradients is not quite feasible since in practice the pressure-driven mechanism pumps the liquid phase and the vapor phase simultaneously and thus, it does not quite apply to the case stated above. Note that the major motivation of this study is to demonstrate the feasibility of pumping of liquid film by means of the EHD-conduction mechanism in the presence of evaporation and not necessarily to achieve the optimum enhancement in heat transfer. The local heat transfer coefficient and local Nusselt number within the evaporation section are defined with respect to the applied heat flux along the channel wall as follows:

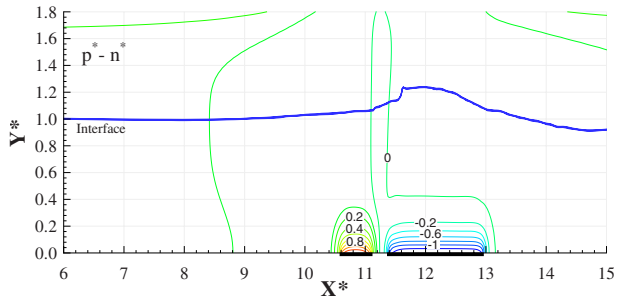


**Fig. 4 Dimensionless contours of net charge density, $p^*-n^*$**

$$h_l = \frac{q_s''}{T_w - T_{\text{sat}}}, \quad \text{Nu}_x = \frac{h_l x}{k_l} \tag{22}$$

Additionally, to evaluate the overall heat transfer performance, the average heat transfer coefficient and Nusselt number are defined as follows:

$$\bar{h}_l = \frac{1}{x}\int_{x_0}^{x} h_l dx, \quad \text{average Nu}_x = \frac{\bar{h}_l \Delta x}{k_l}, \quad \Delta x = x - x_0 \tag{23}$$

The integration is performed only in the evaporation section to merely evaluate the heat transfer performance in this region while the results are presented with $x^*$ defined from the channel inlet. The heat transfer coefficient tends to be very large near the initiation point of the heat flux due to the least temperature increase. However, the finite value of heat transfer coefficient in this region is because of the heat diffusion toward the upstream region, prior to the evaporation section. While in early stages of evaporation, the pressure-driven flow shows better heat transfer performance compared with the EHD-conduction driven counterpart; the eventual increase of the Nusselt number in the downstream region is

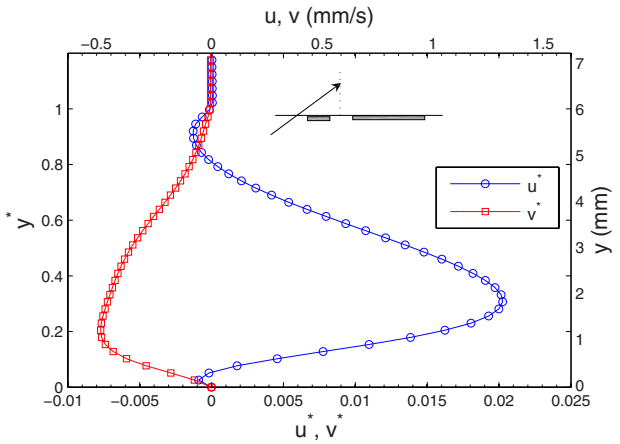


**Fig. 6 Streamwise and spanwise velocity profiles at $x^*$ =11.1($x$=66.6 mm)**

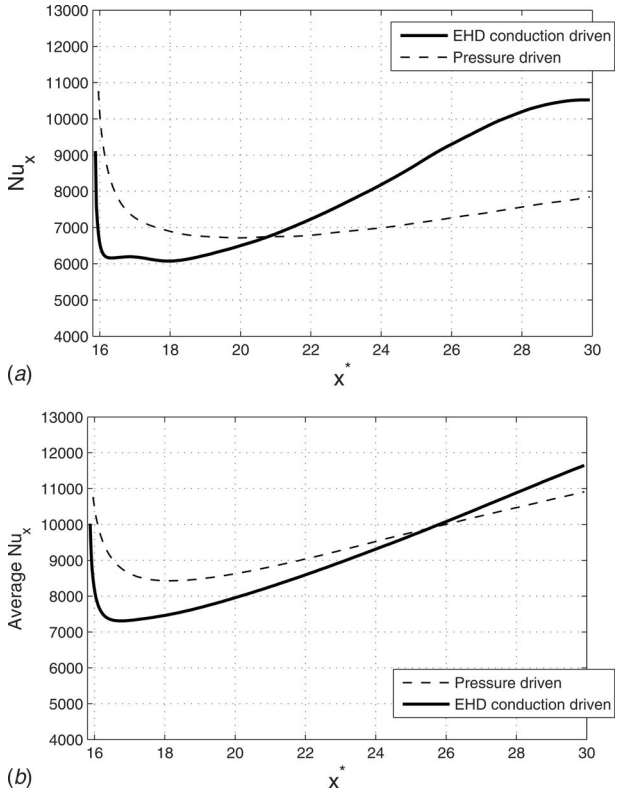


**Fig. 7 Local and average Nusselt numbers along the dimensionless channel length in the evaporation section for EHD-conduction induced and pressure-driven flows**

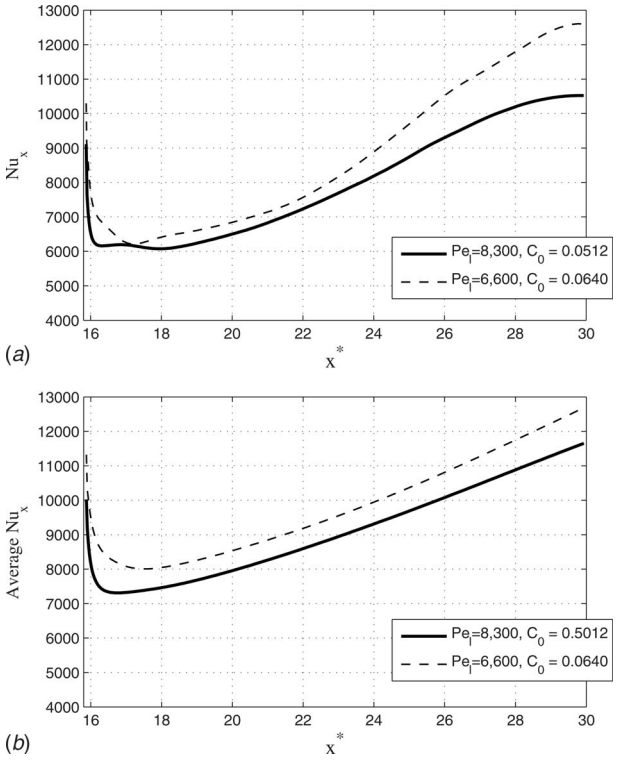


**Fig. 8 Local and average Nusselt numbers along the dimensionless channel length in the evaporation section for EHD-conduction induced flow at two levels of $Pe_l$ and $C_0$ with $M_0$ fixed**

considerably higher for the EHD-driven flow resulting in better overall heat transfer performance for the latter case, as observed in Fig. 7(*b*). The lower minimum value of the local Nusselt number for the EHD-conduction generated flow is attributed to the local liquid film thickening, which adversely influences the heat transfer across the liquid film. The eventual increase in the local Nusselt number is due to the liquid film suppression as the flow proceeds along the channel. However, local flow circulations in the EHD-conduction driven flow improve the rate of heat transfer across the liquid film, which in turn increases the rate of liquid evaporation. Much higher heat transfer enhancement can be simply achieved by using additional electrode pairs.

To understand how the evaporation heat transfer varies with the controlling parameters, one needs to explore the effects of primary dimensionless parameters on the local heat transfer performance. Equations (2)–(15) suggest $Pe_l$, $C_0$, and $M_0$ as the essential dimensionless numbers for the EHD-conduction pumping. The fourth dimensionless number $Re_{EHD}$ has been embedded in the definition of the Peclet number. The charge diffusion constant $\alpha$ has negligible effect, and the changes in $Fr_e$ and Bo mainly influence the interface primarily in the region close to the electrodes with minor effect on the overall flow field and heat transfer characteristics (i.e., the influence of these parameters on the overall heat transfer was not beyond 2% under all the operating conditions considered in this study). The effects of $Pe_l(=Re_{EHD}Pr_l)$, $C_0$, and $M_0$ on the evaporation heat transfer performance along the heated part of the wall are presented in Figs. 8–12. Figures 8 and 9 primarily reflect the effects of applied potential as it appears in the definition of $Re_{EHD}$ and $C_0$ and are associated with no changes in the mobility ratio $M_0$ since all fluid properties were kept constant. Additionally, Fig. 10 is the mere representation of the role of geometric length scale (i.e., $d$, the initial liquid film thickness) as it only appears in the definition of $C_0$ (see Eq. (16)).

As observed in Fig. 8, large values of the Peclet number and $C_0^{-1}$, which essentially occur at higher applied voltages, are associated with the suppression of heat conduction across the liquid film compared with convection heat transfer along the channel, as governed by Eq. (3). Furthermore, larger applied voltages yield in the increase in liquid film mass flow rate and thus decrease the rate of evaporation. Consequently, lower rate of evaporation and smaller values of local and average Nusselt numbers are expected with large values of the Peclet number and $C_0^{-1}$, as confirmed by Fig. 8. Notice that $Pe_l=8$ and 300 and $Pe_l=6$ and 600 correspond to the applied voltages of $V=10$ kV and $V=8$ kV, respectively. Figure 9 illustrates the variation in the average Nusselt number calculated along the heated part of the channel and liquid film thickness at the outlet (equal to the liquid film thickness at the exit of evaporation section) with $Pe_l$ and $C_0^{-1}$. The applied voltage is varied within the range of 2–18 kV with the maximum field intensity maintained far below the dc breakdown limit of Ref. [22].

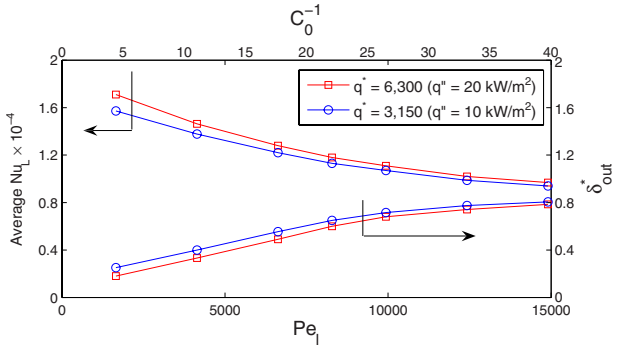


**Fig. 9 Variation in average Nusselt number along the evaporation section and dimensionless liquid film thickness at the channel outlet as a function of $Pe_l$ and $C_0^{-1}$**

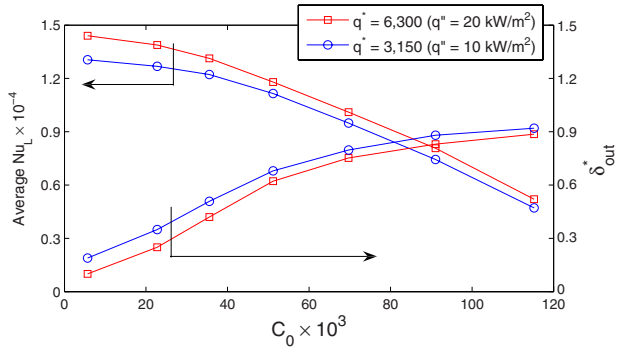


**Fig. 10 Variation in average Nusselt number along the evaporation section and dimensionless liquid film thickness at the channel outlet as a function of $C_0$ with $Pe_l$ and $M_0$ kept constant**

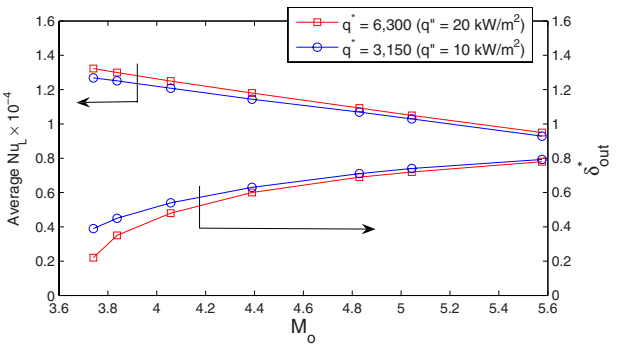


**Fig. 12 Variation in average Nusselt number along the evaporation section and dimensionless liquid film thickness at the channel outlet as a function of $M_0$**

As stated above, the average Nusselt number decreases with an increase in $Pe_l$ and $C_0^{-1}$, which is associated with an increase in outlet liquid film thickness due to the drop in the evaporation rate. At higher heat flux, one should expect an increase in the Nusselt number and a reduction in outlet flow rate with the difference eventually diminished as the applied voltage increases.

The effect of $C_0$ on the average Nusselt number and liquid film height at the channel outlet is presented in Fig. 10 with other dimensionless numbers kept constant. The change in $C_0$ with other dimensionless numbers fixed is feasible simply by changing the characteristic length scale $d$. The average Nusselt number along the evaporation section decreases due to the increase in the liquid film height. The range of $C_0$ presented in the figures corresponds to the initial liquid film thickness varying from 2 mm to 9 mm (with electrodes dimensionless design characteristics fixed). Note that the local Nusselt number dependency on $C_0$ is identical to the trend depicted in Fig. 8.

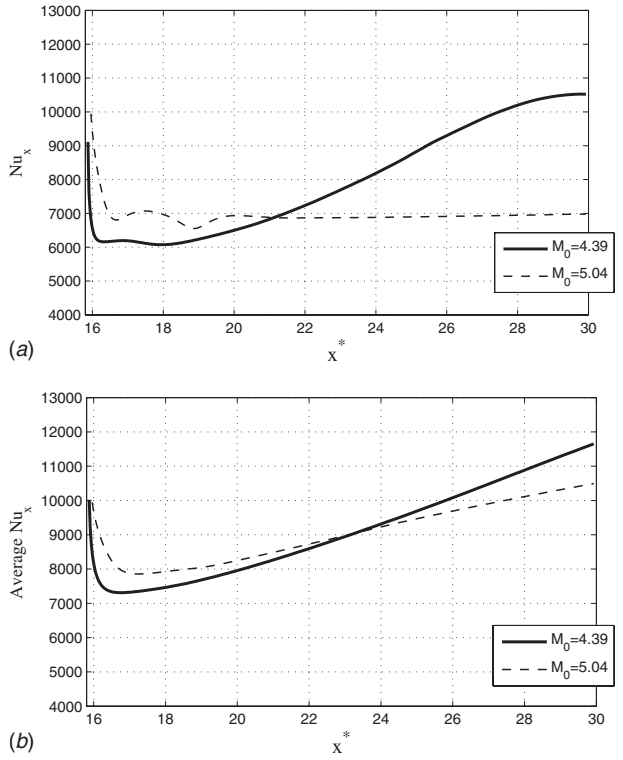


**Fig. 11 Local and average Nusselt numbers along the dimensionless channel length in the evaporation section for EHD-conduction induced flow at two levels of $M_0$**

Figure 11 illustrates the distribution of local and average Nusselt numbers along the evaporation section at two levels of $M_0$. Similarly, Fig. 12 shows the average Nusselt number and the liquid film height at the channel outlet over the variety of mobility coefficients $M_0$. As stated previously, changing $M_0$ merely represents the effect of working fluid properties on the EHD-conduction liquid film pumping and is solely associated with the variation in electric body force intensity. However, a change in $M_0$ value alters the other two dimensionless numbers $Pe_l$ and $C_0$ unless this change is made through the variation in working fluid density. Therefore, Figs. 11 and 12 demonstrate the role of liquid density on the heat and mass transfer characteristics of liquid film evaporation. At early stages of evaporation, the Nusselt number is higher for larger values of $M_0$, primarily due to the higher generated circulatory flow in this region. The Nusselt number eventually degrades further downstream of the evaporation section due to the increase in the liquid film flow rate.

## 5 Conclusions

The EHD-conduction pumping of laminar liquid film in the presence of evaporation was numerically investigated. The numerical results showed good agreement with available experimental data for laminar falling liquid film evaporation. The liquid/vapor interface in the EHD-conduction induced flow encountered local bumps, which are attributed to the generated circulations in the interelectrode region. The electric field, net electric charges, and electric body force distributions within the electrode region were presented to fundamentally illustrate the concept. The EHD-conduction induced flow showed better overall heat transfer performance compared with the pressure-driven counterpart, primarily because of the local flow circulations. The effects of primary dimensionless parameters on the heat transfer characteristics were also studied. A low value of the Peclet number resulted in a higher rate of liquid evaporation because of the dominance of heat conduction across the liquid film. The larger value of $C_0$ as well as the smaller value of $M_0$ was associated with a higher overall heat transfer rate, which primarily corresponds to the lower rate of generated liquid film flow.


## Acknowledgment

The work was financially supported by the NASA Microgravity Fluid Physics Program.


## Nomenclature

$b$ = charge mobility
Bo = Bond number, $\mathrm{Bo}=g(\rho_l-\rho_v)d^2/\sigma$
$C_0$ = EHD dimensionless number, $C_0=\sigma_l d^2/2b_l\epsilon_l V$
$c_p$ = constant pressure specific heat
$D$ = charge diffusion constant

$d$ = initial liquid film thickness
$e$ = electron charge
$\mathbf{E}$ = electric field vector
$F(\omega)$ = $I_1(2\omega)/\omega$
$\mathrm{Fr}_e$ = Froude number, $\mathrm{Fr}_e = u_e/\sqrt{(\rho_l - \rho_v)/\rho_l g d}$
$g$ = gravity acceleration, $g = 9.8\ \mathrm{m/s^2}$
$h_{lv}$ = latent heat
$k$ = thermal conductivity
$k_B$ = Boltzmann universal constant
$k_D$ = rate of dissociation in the absence of electric field
$k_d$ = rate of dissociation in the presence of electric field, $k_d = k_D F(\omega)$
$k_R$ = rate of recombination in the absence and presence of electric field
$M_0$ = mobility ratio, $M_0 = \sqrt{\epsilon_l/\rho_l b_l^2}$
$\dot{m}_{\mathrm{vap}}$ = interphase mass flux due to evaporation
$n$ = negative charge density
$\mathbf{n}$ = unit vector normal to the interface
$P$ = pressure
$p$ = positive charge density
Pe = Peclet number, $\mathrm{Pe} = \mathrm{Re}_{\mathrm{EHD}}\mathrm{Pr}$
Pr = Prandtl number, $\mathrm{Pr} = \nu/\gamma$
$Q$ = volumetric flow rate
$\dot{q}$ = jump of energy across the liquid/vapor interface
Re = Reynolds number defined for falling film evaporation, $\mathrm{Re} = 4\Gamma/\mu$
$\mathrm{Re}_{\mathrm{EHD}}$ = film Reynolds number, $\mathrm{Re}_{\mathrm{EHD}} = u_e d/\nu_l$
$T$ = absolute temperature
$\mathbf{t}$ = unit vector tangent to the interface
$\mathbf{U}$ = velocity vector
$u_e$ = EHD reference velocity corresponding to the mobility limit, $u_e = b_l V/d$
$u_x$ = $x$-component of fluid velocity
$u_y$ = $y$-component of fluid velocity
$V$ = applied electric potential
$\mathbf{V}_f$ = front velocity
$x$ = streamwise coordinate
$x_0$ = streamwise start point of evaporation section
$y$ = spanwise coordinate
$\alpha$ = nondimensionalized charge diffusion constant
$\delta$ = local film thickness
$\epsilon$ = absolute electric permittivity
$\Gamma$ = mass flow rate for falling film evaporation, $\Gamma = (\rho g/\nu)(\delta^3/3)$
$\gamma$ = thermal diffusivity
$\chi$ = volume of fluid
$\mu$ = dynamic viscosity of fluid
$\nu$ = kinematic viscosity of fluid
$\omega$ = dissociation rate coefficient, $\omega = [e^3|E|/4\pi\epsilon_l k_B^2 T_{\mathrm{sat}}]^{1/2}$
$\rho$ = mass density
$\sigma$ = electric conductivity or surface tension of fluid
$\phi$ = potential field

eq = equilibrium
in = channel inlet
out = channel outlet
$l$ = liquid
$v$ = vapor
$*$ = dimensionless variable

## References


[1] Seyed-Yagoobi, J., 2005, "Electrohydrodynamic Pumping of Dielectric Liquids," J. Electrost., **63**, pp. 861–869.
[2] Jeong, S. I., and Seyed-Yagoobi, J., 2002, "Experimental Study of Electrohydrodynamic Pumping Through Conduction Phenomenon," J. Electrost., **56**, pp. 123–133.
[3] Atten, P., and Seyed-Yagoobi, J., 2003, "Electrohydrodynamically Induced Dielectric Liquid Flow Through Pure Conduction in Point/Plane Geometry," IEEE Trans. Dielectr. Electr. Insul., **10**, pp. 27–33.
[4] Feng, J., and Seyed-Yagoobi, J., 2004, "Understanding of Electrohydrodynamic Conduction Pumping Phenomenon," Phys. Fluids, **16**, pp. 2432–2441.
[5] Hanaoka, R., and Takata, S., 2002, "Properties of Liquid Jet Induced by Electrohydrodynamic Pumping in Dielectric Liquids," Electr. Eng. Jpn., **138**, pp. 1–9.
[6] Hanaoka, R., and Nakamich, H., 2006, "Distinctive Flow Properties of Liquid Jet Generated by EHD Pump and Conical Nozzle," Electr. Eng. Jpn., **154**, pp. 9–19.
[7] Yazdani, M., and Seyed-Yagoobi, J., 2006, "Electrohydrodynamic Conduction Pumping of Dielectric Liquids in Annular Configuration," Proceedings of the IMECE06.
[8] Wawzyniak, M., and Seyed-Yagoobi, J., 1999, "An Analytical Study of Electrohydrodynamics Induction Pumping of a Stratified Liquid/Vapor Medium," IEEE Trans. Ind. Appl., **35**, pp. 231–239.
[9] Brand, K., and Seyed-Yagoobi, J., 2002, "Effect of Electrode Configuration on Electrohydrodynamic Induction Pumping of a Stratified Liquid/Vapor Medium," IEEE Trans. Ind. Appl., **38**, pp. 389–400.
[10] Aldini, S., and Seyed-Yagoobi, J., 2005, "Stability of Electrohydrodynamic Induction Pumping of Liquid Film in Vertical Annular Configuration," IEEE Trans. Ind. Appl., **41**, pp. 1522–1530.
[11] Brand, K., and Seyed-Yagoobi, J., 2003, "Experimental Study of Electrohydrodynamic Induction Pumping of a Dielectric Micro Liquid Film in External Horizontal Condensation Process," ASME J. Heat Transfer, **125**, pp. 1096–1105.
[12] Yazdani, M., and Seyed-Yagoobi, J., 2006, "Electrically Induced Dielectric Liquid Film Flow Based on Electric Conduction Phenomenon," M.S. thesis, Illinois Institute of Technology, Chicago, IL.
[13] Atten, P., 1996, "Electrohydrodynamic Instability and Motion Induced by Injected Space Charges in Insulating Liquids," IEEE Trans. Dielectr. Electr. Insul., **3**, pp. 1–17.
[14] Crowley, J. M., 1995, *Handbook of Electrostatic Processes*, Marcel Dekker, New York.
[15] Hirt, C., and Nichols, B. D., 1981, "Volume of Fluid (VOF) Method for the Dynamics of Free Boundaries," J. Comput. Phys., **39**, pp. 201–212.
[16] Kothe, D. B., Rider, W. J., Mosso, S. J., Brock, J. I., and Hochstein, J. S., 1996, "Volume Tracking of Interfaces Having Surface Tension in Two and Three Dimensions," AIAA Paper No. 96-0859.
[17] Lakehal, D., Meier, M., and Fulgosi, M., 2002, "Interface Tracking Towards the Direct Simulation of Heat and Mass Transfer in Multiphase Flows," Int. J. Heat Fluid Flow, **23**, pp. 242–247.
[18] Chun, K., and Seban, R., 1971, "Heat Transfer to Evaporating Liquid Films," ASME J. Heat Transfer, **93**, pp. 391–396.
[19] Bryan, J. E., 1998, "Fundamental Study of Electrohydrodynamically Enhanced Convective and Nucleate Boiling Heat Transfer," Ph.D. thesis, Department of Mechanical Engineering, Texas A&M University, College Station, TX.
[20] ASHRAE, 2001, *Handbook of Fundamentals*, American Society of Heating, Refrigerating and Air Conditioning Engineers, Atlanta, GA.
[21] Adamczewski, I., 1969, *Ionization, Conductivity, and Breakdown in Dielectric Liquids*, Taylor & Francis, London, UK.
[22] Crowley, J. M., and Wright, G. S., 1990, "Selecting a Working Fluid to Increase the Efficiency and Flow Rate of an EHD Pump," IEEE Trans. Ind. Appl., **26**, pp. 42–49.

# A Method for Determining the Heat Transfer Properties of Foam-Fins

**Robert J. Moffat**
e-mail: rmoffat@stanford.edu

**John K. Eaton**
e-mail: eaton@vonkarman.stanford.edu

**Andrew Onstad**
e-mail: aonstad@stanford.edu

Department of Mechanical Engineering,
Stanford University,
450 Serra Mall,
Stanford, CA 94305

*Metallic and graphitic open-cell foams are being used or proposed as extended surfaces (fins) in heat sinks for electronic cooling and compact heat exchangers for aircraft applications. Three parameters must be known to calculate the heat transfer performance of a foam-fin: the product $h_m A_c^*$ as a function of flow-rate (the convective conductance per unit volume), the product $k_s A_k^*$ (the effective conductive conductance as a fin), and $R_{bond}$ (the effective thermal resistance between the foam and the surface to which it is attached). This paper describes a new test method, which, in conjunction with an older well established type of test, allows all three parameters to be measured using one specimen.* [DOI: 10.1115/1.2977599]

*Keywords: porous fins, experimental heat transfer, metal foam, electronics cooling, compact heat exchangers*

## Introduction

Metallic and graphitic foams are commercially available, and they appear to have attractive properties for heat transfer applications. The foam provides an extended surface with high surface area and complex flow paths. The combination is expected to yield low resistance to convective heat transfer. Foams may also be structurally more stable than thin sheet-metal fins and may offer other manufacturing advantages.

If metallic and graphitic foams are to be widely used, their characteristics must be made available to potential users in terms that fit into current design methods, and there must be a way to evaluate the bond resistance between the foam and the primary surface.

The classical approach to presenting heat transfer data is to give the friction factor and Colburn modulus ($StPr^{2/3}$) as functions of Reynolds number. These parameters can only be calculated if the geometry of the surfaces is known in detail, and the resulting correlations are only useful for congruent geometries.

When dealing with foams it is convenient, and useful for design purposes, to keep $h_m A_c^*$ (the convective conductance per unit volume) together as a parameter and present it as a function of the mass velocity approaching the foam.

There are well-known transient tests [1,2] that can be used to directly measure the number of transfer units (NTU) of the specimen ($h_m A_c^* / \dot{m} c_p$) and the flow is known from the test conditions. The parameter $k_s A_k^*$ (the effective conductive conductance as a fin) is not a function of the flow-rate and can be presented as a property of the foam.

The thermal resistance between the foam and its substrate ($R_{\text{bond}}$) is determined by the manufacturing assembly process. While $R_{\text{bond}}$ is not a property of the foam itself, it is extremely important in that it may be the controlling factor in limiting the actual heat transfer from the foam to its substrate.

Some investigators have relied on porosity and area density values provided by the foam supplier and reported friction factor and Colburn modulus (e.g., Kim et al. [3]) accordingly, but the supplied values provided by some have been questioned by others. The fact is that locally (i.e., within a single system, a single paper, or a single study) it does not matter how one partitions the $h_m A_c^*$ product. The problem begins when one tries to compare $h_m$ values from one program with values from another program. It introduces less chance for misinterpretation to simply keep the parameter as an entity.

Other researchers have avoided the issue by reporting the "heat transfer coefficient" based on the area of contact between the fin and the wall (e.g., Boomsma et al. [4] and Haack et al. [5] for metal foams, and Klett and McMillan [6] for graphitic foams). These works treated the metal foam as a heat transfer augmentation device. In their experiments, each foam specimen was mounted on a base consisting of an instrumented heated block. The heat transfer rate resulting from this "one-heated-wall" test was described in terms of the "footprint" heat transfer coefficient. While undeniably useful in describing the heat transfer from a particular specimen, this approach yields almost no insight into how to make better use of the foam from which the specimen was made. The results apply only for the one specimen size tested and with the foam bonded to the primary surface in one way.

It would be helpful, for designers in the field, to have a test method for foams that would deliver all of the required parameters needed in current design methods.

Roughly speaking, there are three approaches to the design of a heat exchanger, each with its own set of requirements.

1. The classic method is to use effectiveness/NTU correlations or log-mean temperature difference (LMTD) factors specific to the flow arrangement, as presented by Kays and London [7]. These methods require $h_m A_c^*$ as a function of flow-rate $k_s A_k^*$ and $R_{\text{bond}}$. (Note that it is never necessary to know the separate values of $h_m$ and $A_c^*$, or of $k_s$ and $A_k^{**}$ although, in fact, they are usually tabulated separately.)
2. Alternatively, one can execute finite-difference or finite-element calculations, modeling the structure of the heat exchanger. This method also requires $h_m A_c^*$ as a function of flow-rate, $k_s A_k^*$, and $R_{\text{bond}}$.
3. Finally, one could execute a conjugate numerical solution, simultaneously calculating the temperature field in the fluid and the solid. This method requires an acceptable geometric model and a highly refined computational grid. At high Reynolds numbers, it also requires a turbulence model capable

Contributed by the Heat Transfer Division of ASME for publication in the JOURNAL OF HEAT TRANSFER. Manuscript received October 30, 2007; final manuscript received June 13, 2008; published online October 22, 2008. Review conducted by Jamal Seyed-Yagoobi. Paper presented at the 2006 ASME International Mechanical Engineering Congress (IMECE2006), Chicago, IL, Nov. 5–10, 2006.

  

of accurately handling separated and reattaching flows, a major challenge for existing Reynolds averaged models.

The NTU correlation method and the LMTD method are both well accepted for estimating heat exchanger performance. The principle descriptor of the heat exchanger that is needed in both approaches is the (UA) product—the inverse of the total thermal resistance between the two fluids. The method was originally developed for situations in which the axial conduction was low compared to the heat transfer to the fluid, and a correction factor was applied when axial conduction was felt to be too large to ignore but still small. Both metallic and graphitic foams tend to have significant axial conduction, and these methods, while surely useful for preliminary design studies, will probably not play a major role in the final design of foam-based heat exchangers.

Computational fluid dynamics (CFD) computations require detailed modeling of the geometry and sufficient resolution in the grid to resolve the boundary layers on the individual elements well enough to calculate the heat transfer. To support this approach, one must be able to describe the geometry of the solid material in the foam in considerable detail. Foam exchangers present a large range of scales, from the full size of the exchanger to the boundary layer on the smallest filament of solid. This range of scales makes it unlikely that fully resolved CFD calculations will be routinely used to design heat exchangers, even allowing for automatic grid generation and parallel processing.

It appears, to the present authors, that the most practical design method for foam-based heat exchanger design is to use a finite difference/finite-element solver method with experimentally determined parameters to describe the foam.

There have been, however, some very interesting publications on the modeling issue and the axial conduction issue. Krishnan et al. [8] have shown recent results achieved by modeling an investment-cast metal foam based on a body-centered cubic array of spheres with a sphere in the center, as well. The solid metal occupies the space not filled by the spheres. The resulting images look remarkably similar to the scanning electron microscope (SEM) images of real foams. Although this work is promising, the routine use of a full CFD solution does not seem practical at present.

Al-Bakhit and Fakheri [9] described a hybrid CFD approach in which the CFD code is used to solve the flow field only once and without considering properties variation due to heat transfer. That solution is then "frozen" and handed off to a conjugate heat transfer solver.

Calmidi and Mahajan [10] used a geometric model of the foam lattice with a Nusselt number correlation for cylinders in cross-flow, modified to account for noncircular cross sections. They used a two-temperature model, solving separately for the fluid and the solid temperature fields and linking the two through the heat transfer term. Two "adjustable constants" were tuned by comparison with early experiments and then applied without further adjustment to four different foams, each over a ten-fold range of Reynolds numbers. The agreement between the predictions and the data was very good. Their experiments were, again, of the "footprint $h$" type, and included the bond resistance as part of the thermal resistance represented by $1/hA$.

Most of the work reviewed falls into one of two categories: programs aimed at measuring the footprint heat transfer of a manufactured part or efforts at modeling the heat transfer from generic foams using idealized geometries. These are worthy objectives. It is important to get the modeling work started early. Modeling complex geometries is not easy, and it will take creative and diligent effort to develop good modeling methods but in the meantime, it is important to be able to design foam-based heat exchangers with confidence.

The footprint $h$ data now in the literature allow designers to incorporate those foams that have been tested. But there is a weakness in that approach: all of the design aspects of the test sample are incorporated into the one answer—the value of the footprint $h$. The data do not allow a heat exchanger designer to investigate alternatives such as changing the height of the foam-fin changing the method of attaching the foam to the wall, or to optimize a design for a given application.

There seems to be a definite need for a method of testing foams that separately identifies the convective and the conductive attributes of the foam in an operationally useful manner and allows the bond resistance to be measured under convective boundary conditions.

## Objective of the Present Work

The objective of the present paper is to describe a new experimental method for measuring the three parameters that describe the heat transfer behavior of a foam-fin: $h_m A_c^*$ as a function of flow-rate, $k_s A_k^*$, and $R_{\text{bond}}$.

The same parameter set supports the NTU correlation method, the log-mean temperature difference method, and the finite-difference/finite-element method of designing heat exchangers.

## Overview of the Proposed Method

Two tests are needed: one to determine the convective heat transfer properties of the foam, isolated from the wall, and one to determine the behavior of the foam as a fin connected to the wall. The two tests are used together to extract the parameters needed to describe the foam-fin.

The specimens used should be "thin" in the streamwise direction but thick enough to be representative of the bulk foam. The flow approaching the specimen is assumed to be uniform in velocity and in temperature.

The steps are as follows:

1. Measure the NTU of the sample using any appropriate method. We suggest a transient test, either a "single-blow transient" or a "periodic" test, as described later in this paper.
2. Calculate the effectiveness of the sample as a heat exchanger using $\xi = 1 - e^{(-\text{NTU})}$. (This assumes a uniform surface temperature in the streamwise direction within the control volume at each $y$-elevation.)
3. Extract the $h_m A_c^*$ product as a function of flow from the known NTU and the flow-rate.
4. Measure the air temperature distribution just downstream of the sample with a known heat rate delivered to the sample from one wall. The unheated end of the sample should be either adiabatic or at air temperature.
5. Plot $\ln(T_{\text{out}} - T_{\text{in}})$ versus $y$ (distance from the heated wall) and examine the curve. If it is reasonably linear, find the value of $M$ from the slope of the least-squares best linear fit to the data, using Eq. (13). If the curve is not linear, examine the sample and the flow field for evidence of nonuniformity.
6. Extrapolate the curve to $y=0$ and determine the air-out temperature at $y=0$. Find the corresponding value of $T_o$, the effective temperature of the solid material at $y=0$, using Eq. (2) and the effectiveness.
7. Extract $k_s A_k^*$ from $M$, $\xi$, and the flow-rate.
8. Calculate $R_{\text{bond}}$ from the heat rate and the difference between $T_{\text{wall}}$ and $T_o$.

Both the single-blow transient test and the cyclic input test have been used for many years to measure the heat transfer properties of porous media and candidate heat exchanger cores. In both of these tests, a sample of the porous medium or heat exchanger core is inserted into a small wind-tunnel lined with a good insulator (e.g., balsa wood), thermally isolated from the wall of the apparatus and sealed to the walls to eliminate leakage. In a perfect world, the specimen would exchange heat only with the air-flow. The air temperatures are measured just upstream and just down-

stream of the specimen using an array of very fine thermocouples (50–100 $\mu$m diameter) or resistance temperature detectors.

Typically, a rapid response electric heater upstream of the specimen initiates either a step increase in the air temperature entering the specimen (single-blow transient) or a steady sinusoidal variation with time (cyclic input method). The NTU of the specimen is then determined from the exit temperature response curve by one of several methods if the single-blow transient method is used or from the amplitude reduction and phase shift of the exit trace relative to the inlet trace if the cyclic input method is used.

The basic theory for the single-blow transient test was developed analytically in 1929 by Schumann [11]. The method was originally limited to specimens with negligible axial conduction. Subsequent work has expanded the utility of the method by introducing corrections for axial conduction. Mullison and Loehrke [12] greatly extended the usefulness of the single-blow transient method by comparing the experimentally measured output trace with the trace generated by a finite-difference program using an assumed value of $h$. The assumed value of $h$ is varied until the experimental curve is matched within a specified tolerance. Their method accommodates variable properties and axial conduction and does not require a "step" increase in air temperature. It requires only that the inlet temperature be known as a function of time.

Blanchet [2] has applied the general concept of the Mullison and Loehrke to the cyclic variation method, again with excellent results.

The output of either test is an estimate of the NTU of the sample. For the geometries being considered here, the NTU expression can be written as

$$\mathrm{NTU} = \frac{h_m A_c}{\dot{m} C_p} \tag{1}$$

Since the flow-rate and fluid properties are known, the product $h_m A_c$ can be found from the NTU.

The second part of the test program is a new type of one heated wall test that resembles the situation used in many of the references cited here to measure the footprint $h$, except that the new test derives its principal output from the shape of the temperature distribution in the air leaving the sample.

The unheated end of the foam could be insulated or the flow-rate could be chosen so that the ligaments of the foam farthest from the heated wall reach fluid temperature. For the first case, the fin has an adiabatic tip, while for the latter condition, the fin would be considered "infinitely long." In either case, the analysis proceeds as follows.

## Analysis

The foam is modeled as a porous fin, perpendicular to the heated wall, as shown in Fig. 1.

The control volume encloses the full width of the porous fin $W$, the full length of the sample in the flow direction $\Delta x$, and is of small (almost, but not quite, differential) height $dy$. Radiation is ignored, as is conduction in the fluid, and all solid and fluid properties are considered constant. The control volume begins just upstream of the inlet face of the foam and ends just downstream of the exit face of the foam. Fluid enters the control volume at $T_{\mathrm{in}}$ and leaves it at $T_{\mathrm{out}}$, both of which may vary in the $y$-direction. The spanwise averaged temperature of the solid is treated as a smooth, continuous function of distance in the $y$-direction and is denoted by $T_s$.

The rate of heat transfer from the solid to the fluid inside the control volume is described using heat exchanger concepts. The temperature of the fluid leaving the control volume depends on its inlet temperature, the average temperature of the solid material within the control volume, and the heat exchange effectiveness of the control volume. For the present situation,

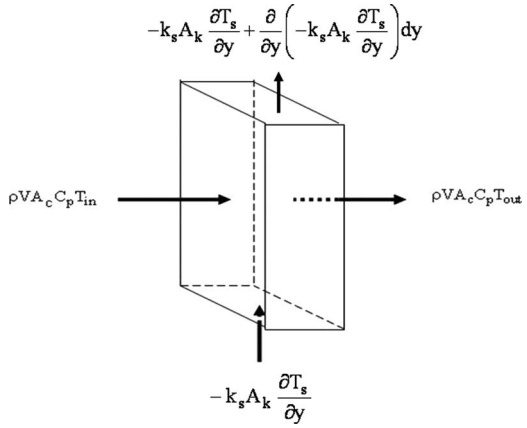


**Fig. 1 A control volume for the porous fin analysis**

$$\frac{(T_{\mathrm{out}} - T_{\mathrm{in}})}{(T_s - T_{\mathrm{in}})} = \xi \tag{2}$$

An energy balance incorporating this description of the heat transfer rate equation yields a differential equation describing the temperature distribution in a porous fin.

$$\frac{d^2 T_s}{dy^2} - \frac{\rho V C_p W}{k_s A_k}(T_{\mathrm{out}} - T_{\mathrm{in}}) = 0 \tag{3}$$

$$\frac{d^2 T_s}{dy^2} - \xi\frac{\rho V C_p W}{k_s A_k}(T_s - T_{\mathrm{in}}) = 0 \tag{4}$$

Equation (4) follows from Eq. (3) using the definition of heat exchanger effectiveness.

Assuming that the solid within each control volume is essentially uniform in temperature in the streamwise direction, the situation is classically described as a two-fluid exchanger with $C_{\min}/C_{\max}=0$ (i.e., one "fluid" (the solid) acts as though it had an infinite capacity rate in that its temperature does not change in the flow direction in response to heat transfer from the fluid. This results in a particularly simple expression for the effectiveness of the exchanger.

$$\xi = 1 - e^{(-\mathrm{NTU})} \tag{5}$$

The control volume is considered to be "small" in the flow direction but not differentially small. Logically, to be representative, it should be at least one "pore diameter" in height, length, and width.

This analysis differs from the conventional treatment of a fin in the way the heat transfer between the solid and the fluid is described.

Porous fin:

$$q = \rho V C_p W \xi (T_s - T_{\mathrm{in}}) dy \tag{6}$$

Solid fin:

$$q = h_\infty p (T_s - T_{\mathrm{in}}) dy \tag{7}$$

The new formulation acknowledges that the air temperature changes within the control volume, and this variation significantly affects the heat transfer from the fin: At low flow-rates the heat transfer from the fin to the air may be limited by the capacity rate of the flow through the fin, not by the heat transfer coefficient.

In the limit for low NTU (high flow-rates), Eqs. (6) and (7) are identical. This can be seen by examining the first few terms of the series expansion for $e^{(-\mathrm{NTU})}$.

To investigate this approach to modeling porous fins, Eq. (4) was used to numerically calculate the temperature distribution in

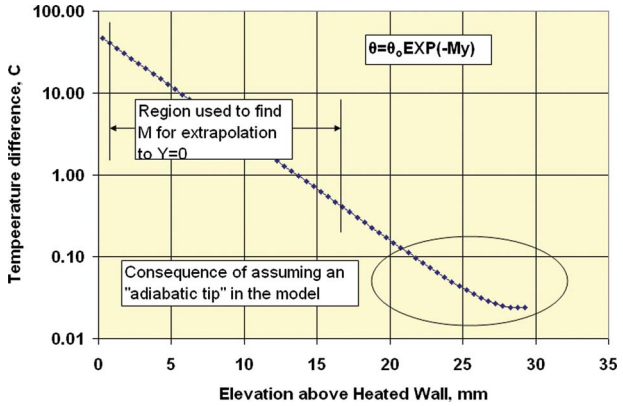


**Fig. 2 A semilog plot of ($T_{air,out} - T_{air,in}$) can be used to measure *M* if the inlet air is uniform**

the solid material of a porous fin with heat transfer, and then Eq. (10) was used to predict the air temperature rise across the fin. The results are shown in Fig. 2.

Note that "height" in Fig. 2 is measured from the top surface of the bond layer, not from the heated wall beneath the bond layer. The "region used to find *M* for extrapolation to the wall" was taken to begin some small distance above the bond layer to acknowledge the realities of measurement in the lab. The "toe" on the curve reflects the enforcement of adiabaticity at the tip.

A slice 2.5 mm thick in the flow direction was used for these calculations, with the foam properties estimated from Boomsma et al. [4]. The representative values of the heat transfer coefficient were extracted from correlations based on tests of woven wire screen matrices (Kays and London [7]). Diffusive mixing in the *y*-direction was not considered and may be a factor near the wall where there is high curvature in the temperature distribution.

The temperature distribution in an infinitely long fin is given by Eq. (8), with *M* as a constant determined by the heat exchanger aspects of the porous fin. The straight line portion in Fig. 2 follows that distribution.

$$\frac{(T_s - T_{in})}{(T_o - T_{in})} = e^{-My} \tag{8}$$

Note that the temperature at the base of the fin, $T_o$, is defined as the temperature of the fin where it attaches to the top surface of the bond layer, not the temperature of the heated wall below the bond layer. The temperature difference across the bond layer depends on the heat flow into the fin and the thermal resistance of the bond layer.

Equation 8 is expressed in terms of solid temperature—the temperature of the ligaments of the foam—but that temperature cannot be directly measured without a great deal of effort. It is relatively easy, however, to measure the temperature of the air leaving the foam-fin. The solid temperature distribution can then be inferred from the air temperature distribution.

If the foam is uniform and the flow is uniform, then the effectiveness $\xi$ is uniform over all the differential control volumes. In that case, the temperature of the air leaving the porous fin maps the solid temperature $T_s$ with a scale factor $\xi$, as can be seen from

$$T_{out} = T_{in} + \xi(T_s - T_{in}) \tag{9}$$

$$T_{out} = T_{in} + \xi(T_o - T_{in})e^{-My} \tag{10}$$

If $T_{in}$ is uniform, then plotting ($T_{out}$-$T_{in}$) versus *y* in semilog coordinates will yield a straight line if the coefficient *M* is truly constant.

Note that Fig. 2 was generated from "pseudodata" for air-out temperature. Those data were created by numerically solving for the temperature distribution in a porous fin with an adiabatic tip, assuming *M* to be constant, and then calculating the resulting air-out temperature distribution assuming uniform effectiveness. Figure 2 is illustrative of the linearity expected but it does not establish that real data will be so well behaved. In general, there will be scatter in the temperature data, especially near the free-end of the fin, where the temperature differences are small.

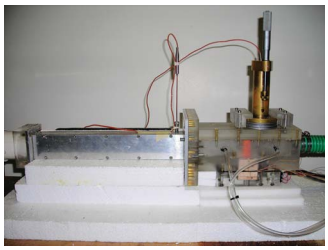

**Fig. 3 The test section**

The value of *M* should be determined from the "best fit" straight line through the measured data in the linear region. It is not necessary to know $T_o$ or $\xi$ to do this, as can be seen from the following.

$$(T_{out} - T_{in})_1 = \xi(T_o - T_{in})e^{-My_1} \tag{11}$$

$$(T_{out} - T_{in})_2 = \xi(T_o - T_{in})e^{-My_2} \tag{12}$$

$$\ln\left[\frac{(T_{out} - T_{in})_1}{(T_{out} - T_{in})_2}\right] = M(y_2 - y_1) \tag{13}$$

This method of data analysis serves two purposes: (1) It displays whether or not there is a constant *M* that describes the behavior of the porous fin, and (2) it gives the best estimate of the value of *M* based on the entire data set. If the data lie along a straight line, that confirms the validity of the method. If the data do not lie along a straight line, either the sample or the flow (or both) may be nonuniform. It would be possible to estimate the slope by using only two data points, rather than a "best fit straight line," but the "plot and fit" method is recommended because it offers an opportunity to confirm the validity of the data or to deny it.

At this point, two of the three parameters needed for design are in hand: the NTU per unit volume of the foam and the value of *M*. It remains only to estimate the effective value of the thermal resistance of the bond layer, as defined by

$$R_{bond} = \frac{(T_{wall} - T_o)}{q}$$

The temperature of the heated wall under the bond layer $T_{wall}$ is available from the data as is the heat flow delivered to the base of the fin. The base temperature of the foam-fin $T_o$, where it attaches to the upper surface of the bond layer, can be estimated from the air temperature distribution. The air-out temperature at the effective base of the fin can be found by extrapolating the semilog plot of ($T_{out}$–$T_{in}$) versus *y* to *y*=0. Knowing the air-out temperature, the air-in temperature, and the effectiveness $\xi$, we can estimate the metal temperature at the effective base of the fin $T_o$. Thus, by combining the data from these two tests, we can extract the three parameters needed to describe the heat transfer behavior of a foam-fin.

## Experimental Results

Figure 3 shows the test section used for these experiments.

Air enters from the left, from a filtered, temperature stabilized, pressure regulated laboratory air supply. The aluminum portion of the test section contains metal screens to ensure uniform flow and

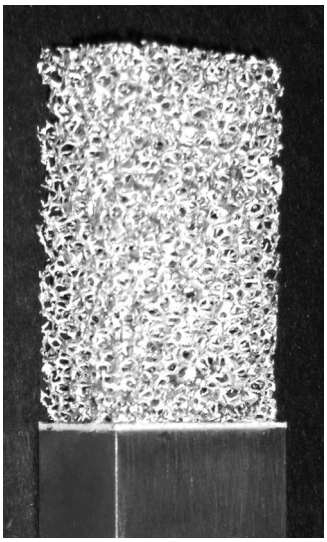

**Fig. 4 A typical test specimen mounted using 1 mm of high conductivity cement**

thermocouples to measure air temperature and wall temperature. The Plexiglas portion of the test section is smoothly faired into the aluminum portion.

A typical aluminum foam specimen is shown in Fig. 4 attached to its heater base using a 1.0 mm thick layer of high conductivity silver-filled epoxy cement. This provides a simple, highly repeatable attachment that is acceptable for the present tests. The value of the bond resistance does not affect the measurement of $M$ as long as the temperature profile extends far enough into the fin that its slope, in semilog coordinates, can be accurately measured.

The foam block is cut to fill the flow channel within a few thousands of an inch. The foam specimen and the heater block are assembled in a fixture that ensures that the same volume of epoxy is used on each sample. The epoxy is cured at high temperature in an oven. The temperature of the heater block is measured with three $K$-type thermocouples. Foil-type heaters are attached to the upstream and downstream faces of the heater block, and the block is surrounded by 0.5 in. thick balsa wood insulation. Thermocouples embedded in the balsa wood allow estimation of the heat losses. At low flow-rates, the conduction loss through the insulation is about 5% of the input power; at high flows, about 2%.

The specimen and heater assembles are mounted to the bottom surface of the flow channel. The specimen fills the channel from top to bottom and from side to side. Wall static pressure is measured upstream and downstream of the specimen. A probe traverse driven by a stepper-motor is mounted downstream of the specimen, on the centerline. The traverse uses an "L-shaped" thermocouple probe that extends the junction upstream to within 3 mm of the back face of the specimen. The probe can be traversed from bottom to top of the channel, aligned with the flow or yawed as much as $\pm 8$ mm off the centerline without exceeding the probe's yaw tolerance for constant recovery factor. Velocity traverses in the vertical direction are typically taken on the centerline and at $\pm 4$ mm and $\pm 8$ mm.

Graphitic, aluminum, and copper foams have been tested using the same apparatus and the same technique. Representative data from tests of a copper-alloy foam specimen are shown in Fig. 5, in Cartesian coordinates, and Fig. 6 in semilog coordinates. These data are all from the same foam specimen tested at three flow-rates. Similar results have been obtained from aluminum foams.

The objective of showing these figures is to confirm that the theoretical basis for this new approach is valid, not to document the behavior of these specific foams. The appearance of a straight line in the semilog representation of the data confirms that the underlying concept of this new experimental method is sound.

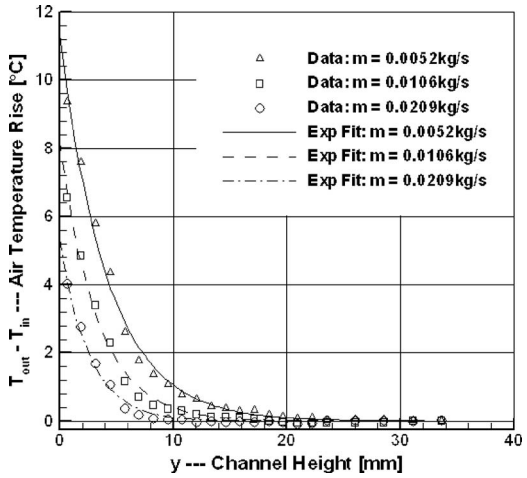


**Fig. 5 Exit temperature distributions from a typical specimen—Cartesian coordinates**

## Discussion

The temperature distribution downstream of an ideal uniform foam would yield a straight line when plotted in semilog coordinates. Tests on real foams have shown deviations: sometimes abrupt changes in level, sometimes abrupt changes in slope. We believe that these small-scale deviations from the ideal straight line provide valuable diagnostic information about nonuniformities in the foam.

The value of $M$ for a given foam changes with flow-rate, reflecting the variation of the heat transfer coefficient with velocity. A change in slope (a change in the value of $M$) within a traverse suggests that the specimen may not be uniform. This could be either a change in the local $hA_c$ product or a change in the local flow. An abrupt step down in level, within a traverse, suggests that there may be a discontinuity in the effective conduction parameter ($kA_k^*$). For example, in Fig. 6, there appears to be a step down in the data at $y=6$ mm at the highest flow-rate 0.0209 kg/s and also a change in slope (a change in $M$). Based on other diagnostic tests on this specimen, we believe this indicates a discontinuity within

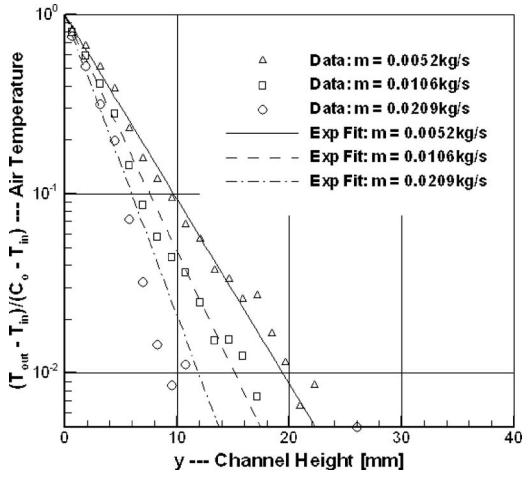


**Fig. 6 Exit temperature distributions from a typical specimen—semilog coordinates**

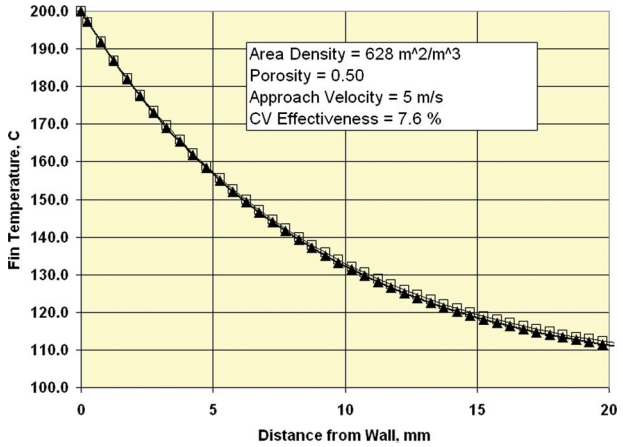


**Fig. 7 The temperature distribution in a low-effectiveness foam-fin**

the foam, either of porosity (which affects the local velocity through the foam) or of conductivity (such as a "slip-plane" within the foam).

Thus, although we do not yet know how to unambiguously describe the hydraulic radius, porosity, and area density of a foam, we can describe its heat transfer behavior as a function of flow and examine a specimen for uniformity in a useful manner.

The porous fin analysis presented here yields a different temperature distribution for a porous fin than would the classical "isolated solid fin" analysis for the same values of $h$ and $A_c$. The difference arises from the fact that the air temperature changes within the porous fin.

It is important to note that different definitions of $h$ are used in the porous fin analysis and the solid fin analysis. In the case of the solid fin, $h$ is defined using the external flow definition of the temperature difference (surface temperature minus the fluid temperature far from the surface—a constant), denoted by $h_\infty$. For the porous fin, $h$ is defined using the internal flow definition (surface temperature minus the local bulk mean temperature of the fluid—a function of $x$), denoted by $h_m$. When the effectiveness of the control volume is small, the fluid temperature does not change much within the control volume, and the two analyses produce very similar results, as shown in Fig. 7 for a case where $\xi = 7.6\%$.

The difference becomes larger as the effectiveness rises, as shown in Fig. 8 for a case with effectiveness of 95%. Such high

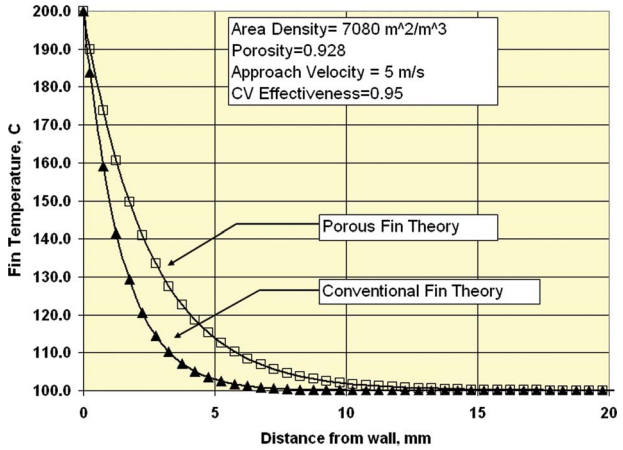


**Fig. 8 The temperature distribution in a high-effectiveness foam-fin**

values of effectiveness are easily attained using modern metallic or graphitic foams, since their area densities are very high.

The temperature distribution in the fin controls the heat transfer from the fin. The porous fin model predicts significantly lower heat transfer rates than the solid fin model for the same $hA_c$ and the same $k_sA_k$. This is consistent with the fact that the heat exchanger model of the porous fin's convective process allows the air temperature to change within the fin, thus reducing the driving potential for heat transfer whereas the solid fin model uses the same air temperature to drive all of the heat transfer from the area $A_c$.

This latter observation has significant implications regarding the attainable heat rate using a porous fin. The behavior of a full-scale heat exchanger using porous fins can be calculated as a sequence of thin slices with the exit temperature from the $n$th slice being the inlet temperature for the $(n+1)$th slice.

## Conclusions

1. The heat transfer performance of a foam-fin can be calculated if three parameters are known: the product $h_mA_c^*$ (the convective conductance per unit volume) as a function of flow-rate, the product $k_sA_k^*$ (the effective conductive conductance as a fin), and $R_{\text{bond}}$ the effective thermal resistance between the foam and the surface to which it is attached.
2. This paper presents a new method for measuring the heat transfer properties of foam materials that combines a classical single-blow transient test (or a cyclic test), long used to measure the heat transfer properties of compact heat exchanger surfaces, with a new type of one-heated-wall test. In this new test, the exit air temperature distribution (downstream of the porous fin) is measured, as well as the base heat transfer rate. The air temperature distribution is used to determine the porous fin parameter $M$, which contains the ratio of the convective to the conductive parameters of the fin.

   The convective parameter can be extracted from the NTU of the specimen, which can be measured using a conventional single-blow transient or cyclic test. With $M$ and NTU known, the third parameter—the thermal resistance of the bond at the wall—can be estimated.
3. The new one-heated-wall test arose from the hypothesis that the temperature distribution in the air leaving a porous fin would map the metal temperature of the fin, assuming a uniform flow and a uniform foam. The experimental results presented here support this hypothesis.
4. Analytically, the porous fin is treated as a heat exchanger, not as an isolated object in an infinite flow field. This approach acknowledges the fact that the air temperature changes inside the porous fin.
5. The heat transfer from a porous fin is determined by its effectiveness as a heat exchanger, not simply by its $hA_c$ product. Thus, the heat transfer may be limited by the capacity rate of the perfusing flow regardless of the value of $hA_c$.
6. The porous fin model yields a different temperature distribution than the traditional solid fin model, for the same $hA_c$ and $k_sA_k$, and predicts a lower heat transfer rate. This has implications for the design of heat exchangers using foam-fins.

## Nomenclature

$A_c$ = effective area for convective heat transfer within the control volume, $m^2$

$A_c^*$ = effective area for convective heat transfer per unit volume, (the area density) $m^2/m^3$

$A_k$ = effective area for conductive heat transfer perpendicular to the heated wall, $m^2$

$A_k^*$ = effective area for conductive heat transfer per unit plan-form area (width times flow length), $m^2/m^2$

$(C_{min}/C_{max})$ = ratio of thermal capacity rates of the two fluids, a parameter in heat exchanger theory, dimensionless

$C_p$ = specific heat of the fluid, J/kg K

$h$ = generic symbol for a heat transfer coefficient, $W/m^2$ K

$h_m$ = heat transfer coefficient based on the difference between the bulk mean temperature of the fluid, the solid temperature, and the wetted area, $W/m^2$ K

$h_\infty$ = heat transfer coefficient based on fluid temperature far from the surface, the solid temperature, and the wetted area, $W/m^2$ K; used only in Eq. (7).

$h_m A_c^*$ = parameter controlling convective heat transfer per unit volume between the fluid and the solid, $W/m^3$ K

$k_s A_k^*$ = parameter controlling conductive heat transfer perpendicular to the heated wall, W/m K

$k_s$ = thermal conductivity of the solid, W/m K

$\dot{m}$ = mass flow-rate of fluid, kg/s

$M$ = fin parameter for a porous fin, $m^{-1}$; $M=\sqrt{\xi(\rho V C_p W/k_s A_k)}$

$p$ = perimeter of a solid fin, m. Used in Eq. (7).

$q$ = convective heat transfer rate between the solid and the fluid in a porous fin, W; used in Eqs. (6) and (7)

$R_{bond}$ = effective thermal resistance between the foam-fin and the heated wall, $K/(W/m^2)$

$T_{in}$ = temperature of fluid entering the control volume, K

$T_{out}$ = temperature of fluid leaving the control volume, K

$T_s$ = temperature of the solid in the control volume, K

$T_o$ = temperature of the solid material of the foam at the plane defining the effective base of the fin, (i.e., at the upper surface of the bond layer), K

$T_{wall}$ = temperature of the wall to which the foam is bonded, K

$V$ = velocity of the fluid approaching the front face of the foam, m/s

$W$ = width of the control volume, perpendicular to the flow and parallel to the heated wall, m

$y$ = distance from the heated wall, m

$\Delta x$ = length of the control volume in the flow direction, m

$\Delta y$ = height of the control volume, perpendicular to the heated wall, m

$\rho$ = density of the fluid, $kg/m^3$

$\xi$ = effectiveness, $(Q_{actual}/Q_{max})$ for the same initial states and flow-rates, dimensionless

## References


[1] Kays, W. M., and London, A. L., 1964, *Compact Heat Exchangers*, 2nd ed., McGraw-Hill, New York, p. 135.

[2] Blanchett, S., "The Periodic Technique for Measuring Convective Transport and Flow Friction Characteristics of Catalytic Reactors," Vehicle Thermal Management Systems 3 (VTMS-3), SAE International Technical Paper Series No. 971808.

[3] Kim, S. Y., Paek, J. W., and Kang, B. H., 2000, "Flow and Heat Transfer Correlations for Porous Fin in a Plate-Fin Heat Exchanger," ASME J. Heat Transfer, **122**(3), pp. 572–578.

[4] Boomsma, K., Poulikakos, D., and Zwick, F., 2003, "Metal Foams as Compact High Performance Heat Exchangers," Mech. Mater., **35**, 1161–1176 (and online at www.sciencedirect.com).

[5] Haack, D. P., Butcher, K. R., Kim, T., and Lu, T. J. "Novel Lightweight Metal Foam Heat Exchangers," Porvair Fuel Cell Technology, Inc., 700 Shepherd St., Hendersonville, NC 28792. (Also: www.porvairmetalfoam.com/papers.)

[6] Klett, J., and McMillan, A., "Modeling Convective Heat Transfer With Graphitic Foams," Oak Ridge National Laboratory, Oak Ridge, TN 37831. (Also see: www.poco.com/us/thermal/foam.asp?lang=1000.)

[7] Kays, W. M., and London, A. L., 1964, "Compact Heat Exchangers." McGraw-Hill, New York.

[8] Krishnan, S., Murthy, J. Y., and Garimella, S., 2005, "Direct Simulation of Transport in Open-Cell Metal Foams," ASME Paper No. IMECE2005-81309.

[9] Al-Bakhit, H., and Fakheri, A., 2005, "A Hybrid Approach for Full Numerical Simulation of Heat Exchangers," ASME Paper No. HT2005-72745.

[10] Calmidi, V. V., and Mahajan, R. L., 2000, "Forced Convection in High Porosity Metal Foams," ASME J. Heat Transfer, **122** pp. 557–565.

[11] Schumann, T. E. W., 1929, "Heat Transfer: A Liquid Flowing Through a Porous Prism," J. Franklin Inst., **208**(3), pp. 405–416.

[12] Mullison, R. S., and Loehrke, R. I., 1986, "A Transient Heat Exchanger Evaluation Test for Arbitrary Fluid Inlet Temperature Variation and Longitudinal Core Conduction," ASME Trans. J. Heat Transfer, **108**(2), pp. 370–376.

# Oscillation Effect of Impingement Surface on Two-Dimensional Impingement Heat Transfer

**Koichi Ichimiya**
Interdisciplinary Graduate School of Medicine and Engineering,
Mechanical Systems Engineering Division,
University of Yamanashi,
Takeda-4, Kofu,
Yamanashi 400-8511, Japan
e-mail: ichimiya@yamanashi.ac.jp

**Yutaka Yoshida**
Tokyo Electric Co. Ltd.,
25-Shintomi, Futtsu,
Chiba 293-0011, Japan

*This paper describes the oscillation effect of impingement surface on two-dimensional impingement heat transfer with confined wall. The local temperature distribution on an impingement surface was measured using a thermosensitive liquid crystal sheet and an image processor. Experiments were conducted by using air as a working fluid. Experimental conditions were as follows: Reynolds number $Re=1000–10,000$, dimensionless distance between nozzle and impingement surface $h/B=1.0–4.0$, frequency $f=0–100$ Hz, and amplitudes $a=0.5$ mm and 1.0 mm. The local Nusselt number was improved for the comparatively low Reynolds number and low frequency and was depressed for high frequency. In the case of heat transfer enhancement, vortices on the impingement surface were renewed frequently, and on the other hand, in the case of heat transfer depression, thermal boundary layer thickness increased in appearance by the vibration of the impingement surface.* [DOI: 10.1115/1.2955474]

*Keywords: forced convection, impingement heat transfer, slit-nozzle, oscillation, thermosensitive liquid crystal, experiment*

## Introduction

The impinging jet is utilized as a conventional method to enhance the heat transfer [1,2] and the mass transfer [3,4]. The increase in the flow directional and normal gradients of the velocity and turbulence intensity near the heat transfer surface (the impingement surface) contributes to the heat transfer improvement. We consider the cooling of the heat engine by the impinging jet. The heat engine surface vibrates due to the thermodynamic and hydrodynamic states of the gas or steam cycle at operation. Therefore, we should study basically the impingement heat transfer with and without the vibration. In the case of heat transfer enhancement of gas flow by oscillation, the oscillation of the working fluid [5–7] and heat transfer surface [8,9] are expected. Fand et al. [5] achieved the experiment on the interaction between sound and free convection around the circumference of a heated horizontal cylinder. The results show that a relatively large percentage increase in the heat transfer coefficient on the upper portion of the cylinder is caused by the oscillating vortex flow, which is characteristic of thermoacoustic streaming. Davis and Richardson [6] considered natural convection around a horizontal circular isothermal cylinder in conjunction with a transverse standing sound field propagated in the vertical or the horizontal direction. According to the results, horizontal oscillations increase heat transfer at the bottom of a cylinder, and vertical oscillations decrease the local heat transfer because of the generation of the reverse flow. Gospinath and Harder [7] studied experimentally on the convective heat transfer from a cylinder in an intense acoustic field. Two distinct flow regimes were identified. The first regime is the laminar attached flow regime, which shows the square root dependence of the Nusselt number on the appropriate Reynolds number. The second regime is an unstable regime in which vortex shedding is prevalent and contributes to a higher heat transfer rate. Davidson [8] obtained theoretical results for heat transfer from a circular cylinder oscillating in an unbounded viscous fluid, which is otherwise at rest. An interesting feature of the flow is that the tangential velocity is not zero at the axis of oscillation and fluid will be ejected along the axis in the form of a jet. Heat carried over the surface of the cylinder will be swept away along the axis of oscillation. Momose et al. [9] investigated numerically the influence of horizontal vibration on heat transfer from a horizontal cylinder. Results indicate that for low frequency vibration the local heat transfer rate depends on the inner vortex flow and on the other hand, for high frequency vibration, it depends on the outer vortex flow. The heat transfer characteristics by the combination of the oscillation and the impinging jet are needed to be examined experimentally. Liu and Sullivan [10] investigated experimentally the flow structure and heat transfer in a circular impinging jet excited by a loudspeaker with low nozzle-to-plate spacing. The random vertical structure in the wall-jet region enhances the local heat transfer when the forcing near the subharmonic of the natural frequency stable vortex pairing is promoted. The strong large scale well organized vortices induce the unsteady separation of the wall boundary layer and lead to local heat transfer reduction. Gau et al. [11] experimented on the impingement cooling flow structure and wall heat transfer under the acoustic excitation at both inherent and noninherent frequencies. The acoustic excitation can make the unstable wave, the vortex formation, and its subsequent pairing process. At inherent frequencies, the most unstable wave can be amplified, which increases the turbulent intensity and enhances the heat transfer. At noninherent frequencies, the situation was inverse. Poh et al. [12] performed numerically on the effect of flow pulsations on time-averaged Nusselt number under a laminar impinging jet. They found that the onset of separation at the wall-jet region of pulsating impinging jet is associated with the point of constant Nusselt number wave form during the oscillation cycle, and within one oscillation; large vortices existing during the minimum velocity state are broken into two smaller vortices. Those references are on the oscillation of working fluid in the impinging jet. We should examine experimentally and basically the effect of oscillation of the impingement surface on the impingement heat transfer.

In the present study, it is examined experimentally how the heat transfer characteristics of an air jet from a slit-type nozzle change with and without oscillation of the impingement surface. The impingement surface temperature was measured by the relationship

Contributed by the Heat Transfer Division of ASME for publication in the JOURNAL OF HEAT TRANSFER. Manuscript received October 1, 2007; final manuscript received January 27, 2008; published online October 16, 2008. Review conducted by Bengt Sunden. Paper presented at the The Sixth Wold Conference on Experimental Heat Transfer, Fluid Dynamics and Thermodynamics, 2005.

  

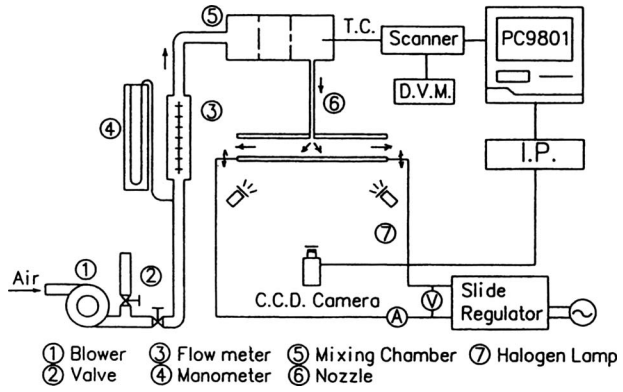


**Fig. 1 Schematic of experimental apparatus**

between the color distribution on a thermosensitive liquid crystal sheet and the temperature. The heat transfer corresponded to the flow, which was measured by a hot wire anemometer and was visualized by the smoke inserting method.

## Experimental Apparatus

The experimental apparatus is shown schematically in Fig. 1. The apparatus is divided into four partial fractions, namely, the flow delivery system, the impingement section, the temperature measurement system, and the oscillation generation system. The air, as a working fluid, was driven to the nozzle by a blower, through a flow meter and a mixing chamber. The developing portion with more than 50 times the length of the nozzle width was set, and the velocity distribution at the nozzle exit (10 mm width and 180 mm breath) was almost fully developed. After air impinged on the flat heat transfer oscillated surface (impingement surface), its flow direction changed to the horizontal direction and it was released to the atmosphere. The impingement section (heat transfer portion) is composed of a stainless foil and a thermosensitive liquid crystal adhered on a transparent acrylic plate whose size is $400\times400\times10$ mm$^3$. The stainless steel foil (impingement surface) was heated electrically and almost uniformly. The thermosensitive liquid crystal was illuminated by four halogen lamps with infrared absorption filters. The color image on the liquid crystal was converted into an electrical signal by a charge coupled device (CCD) camera with optical filters (red, green, and blue). The relationship between color brightness and temperature was calibrated in advance by the regression equation method.

The oscillation apparatus is presented in Fig. 2. The heated portion is supported by four arms of a table set on an oscillator. The oscillation is vertically transformed to the heat transfer surface with an amplitude of 1 mm. The frequency was controlled by a pulse oscillator. The displacement was regulated by a power amplifier and the displacement was recognized by a piezotype pickup and a cap-type charger. Since the output of the piezotype pickup monitor was presented by an acceleration, the oscillation was caught by integrating it two times.

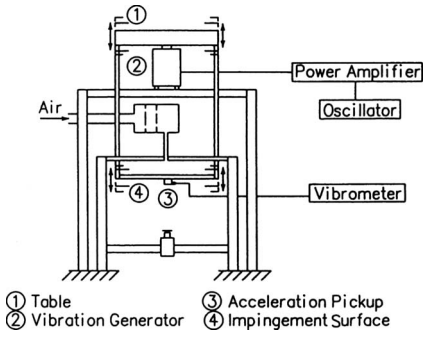


**Fig. 2 Vibration system**

**Table 1 Experimental conditions**

| | |
|---|---|
| Re | 1000, 2000, 4000, 6000, 8000, 10,000 |
| $h$ (mm) | 10, 20, 40 |
| $H=h/B$ | 1.0, 2.0, 4.0 |
| $a$ (mm) | 0.5, 1.0 |
| $f$ (Hz) | 0, 10, 20, 40, 60, 100 |

## Experimental Procedure

After the geometric conditions, which are a 10 mm nozzle width and the space between the nozzle and the impingement surface $h$ were fixed, air flow rate was controlled. Additionally, the impingement surface temperature was corrected within the thermosensitive region of the liquid crystal by controlling the electric power and the air temperature. The impingement heat transfer experiment without oscillation was performed in advance and in the next stage, the frequency and amplitude of the oscillation were fixed within experimental conditions (Table 1). Dependence of air temperature and pressure was considered in the flow rate measurement. The color distribution of the thermosensitive liquid crystal on the impingement surface was captured as the light brightness of red, green, and blue and was converted to the temperature by using the regression equation showing the relation between the relative brightness and the temperature. The local heat flux was corrected by numerically solving the three-dimensional thermal conduction for each pixel ($0.4\times0.4$ mm$^2$, 0.5 mm thick) in the acrylic plate and the stainless steel foil. The local heat transfer coefficient $\alpha$ and local Nusselt number Nu were obtained by using net heat flux $q_{\text{net}}$

$$\alpha = q_{\text{net}}/(T_w - T_o) \tag{1}$$

$$\text{Nu} = \alpha \cdot 2B/\lambda \tag{2}$$

The uncertainty of the local Nusselt number was estimated by ANSI/ASME PTC [13]. The main sources of errors in the local Nusselt number were the evaluation of the temperature, the heat flux, the thermal conductivity of fluid, and the nozzle width. In the procedure, the partial derivative of Nu (for instance, $\partial\text{Nu}/\partial T$) by

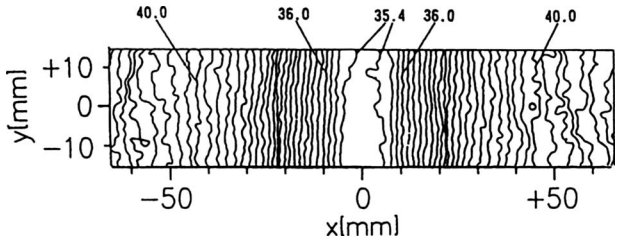


**Fig. 3 Isothermal lines (°C) (Re=1000, $H$=1.0, and $f$=0 Hz)**

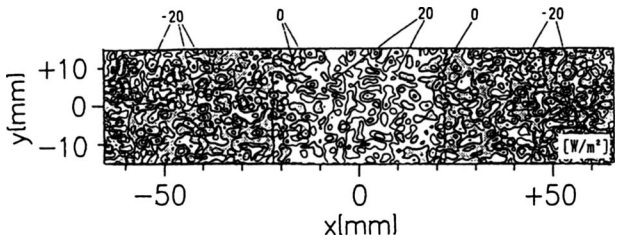


**Fig. 4 Corrected heat flux (Re=1000, $H$=1.0, and $f$=0 Hz)**

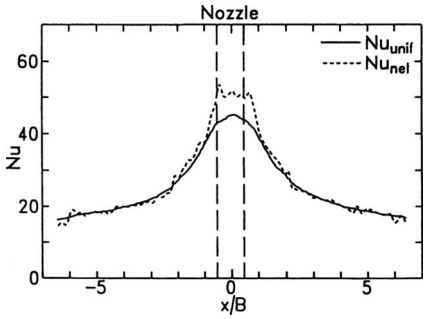


**Fig. 5 Nusselt number along the flow direction (Re=1000, $H$ =1.0, and $f$=0 Hz)**

the main source was operated by the finite difference. As a result, a 95% relative coverage of uncertainty was about 4.4%.

The velocity and turbulence intensity across the section were measured by a hot wire anemometer. The flow was visualized by a smoke inserting method [14].

Experimental conditions are listed in Table 1. The Reynolds number is based on the velocity at the nozzle exit.

## Results and Discussions

**Heat Transfer Characteristics.** The isothermal line on the impingement surface without oscillation is shown in Fig. 3 for Re =1000 and $H$=1.0. The position $x$=0 mm in the figure denotes the center of the nozzle. According to the figure, the isothermal lines are almost parallel and the line space changes with the flow direction. The temperature is the lowest at the air impinging point and the temperature gradient is the highest where the flow direction changes horizontally. Figure 4 presents the corrected heat flux considered in the three-dimensional heat flow by thermal conduction in an acrylic plate and a stainless steel foil. The white portion means positive values, namely, heat inflow into one pixel and the gray portion means negative values, namely, heat outflow from one pixel. The dark solid lines represent the corrected heat flux =0 and the heat flux step=20 W/m$^2$. Heat inflow appears around $x \cong 0$ mm and heat outflow appears downstream from $x \cong 20$ mm. In this case, the uniform heat flux without correction was $q_{\text{unif}}$ =198 W/m$^2$.

Figure 5 indicates the effect of the heat flux correction on the Nusselt number. This Nusselt number was averaged along the width, namely,

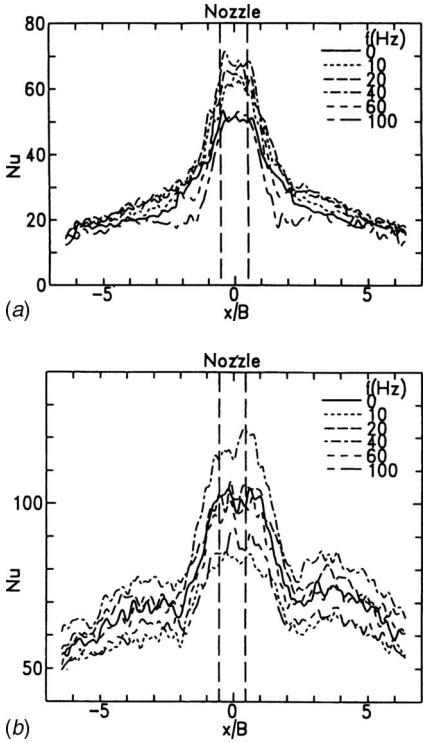


**Fig. 6 Nusselt number ($H$=1.0 and $a$=1.0 mm): (*a*) Re=1000; (*b*) Re=10,000**

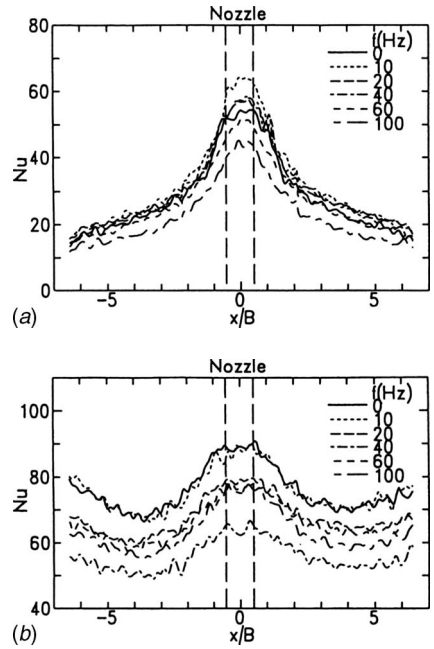


**Fig. 7 Nusselt number ($H$=4.0 and $a$=1.0 mm): (*a*) Re=1000; (*b*) Re=10,000**

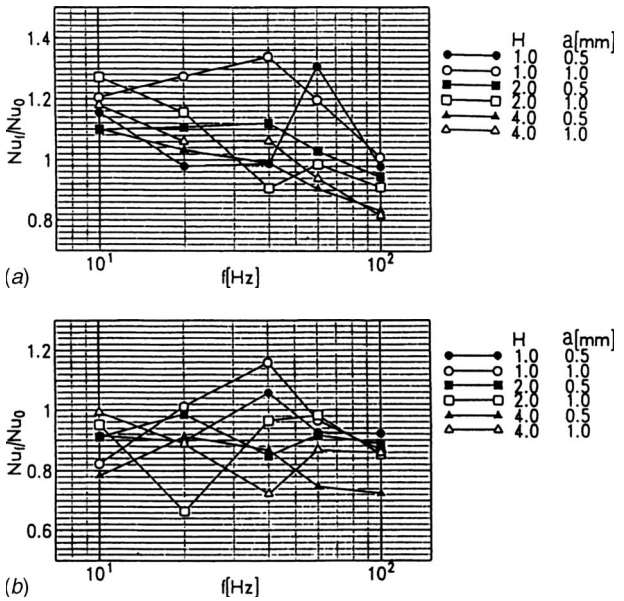


**Fig. 8 Nusselt number ratio beneath the nozzle $Nu_f/Nu_o$: (*a*) Re=1000; (*b*) Re=10,000**

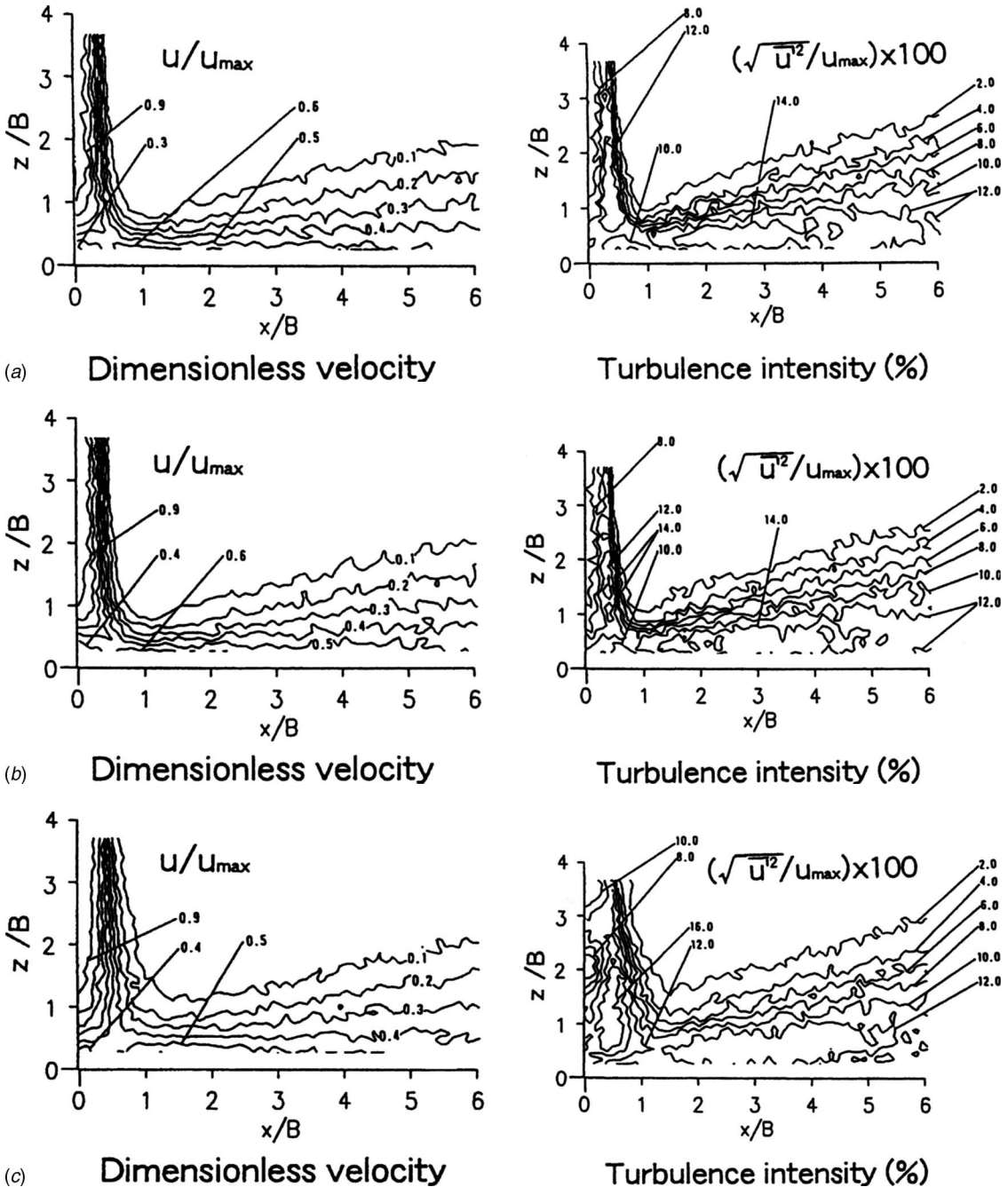


**Fig. 9 Dimensionless velocity and turbulence intensity ($H$=4.0, $a$=1.0, and Re=2000): (*a*) $f$=0 Hz; (*b*) $f$ =10 Hz; (c) $f$=100 Hz**

$$\mathrm{Nu} = \sum_{j=1}^{n} \mathrm{Nu}j/n$$

where Nu$j$ is local Nusselt number and $n$ is the number of pixel along the width, and was denoted along the dimensionless length $x/B$. The dotted and solid lines show the Nusselt number with and without heat flux correction, $\mathrm{Nu}_{\mathrm{unif}}$ and $\mathrm{Nu}_{\mathrm{net}}$, respectively. The peak values are improved by the heat flux correction and the maximum difference between them is 18%. These values agree with the numerical values [15] within 5%.

In the next stage, the heat transfer characteristics with oscillation are presented. Figures 6 and 7 show the longitudinal distribution of the Nusselt number averaged along the width for $H$ =1.0 and 4.0, respectively. Figures 6(*a*) and 6(*b*) are for the space between the nozzle and the impingement surface $H$=1.0, the Reynolds number based on nozzle width, Re=1000 and 10,000, and the amplitude $a$=1 mm. The parameter is the frequency, and the two vertical dotted lines are the nozzle width. According to Fig. 6(*a*), the Nusselt numbers within the nozzle width are 20.6%, 27.5%, and 34.0% higher for $f$=10 Hz, 20 Hz, and 40 Hz than those without oscillation, respectively. However, the Nusselt number decreases for $f$=60 Hz and is less than that without oscillation for $f$=100 Hz. The reduction rate is remarkable within $x/B=\pm 3$. For Re=10,000 (Fig. 6(*b*)), the Nusselt number at $f$=10 Hz is lower in the whole area at $f$=10 Hz than that without oscillation and increases with an increase in frequency. It approaches 1.2 times of Nu without oscillation at $f$=40 Hz. After that, it tends to reduce with frequency. For Re=1000 and $H$=4.0 (Fig. 7(*a*)), the

heat transfer is slightly improved in the range of $f=10-40$ Hz. However, it reduces in the whole region for more than $H=60$ Hz. For Re=10,000 and $H=4.0$ (Fig. 7($b$)), the heat transfer is depressed in the whole heated surface with an increase in frequency. These results indicate that both the enhancement and the depression of heat transfer by oscillation appear and depend on the geometrical size, the Reynolds number, and the frequency. Consequently, heat transfer is enhanced in the narrow space between the nozzle and the impingement surface, and in the low Reynolds number and low frequency, but is depressed in the high frequency. For a wide space, heat transfer is depressed in the whole frequency. The effect of oscillation exists particularly beneath the nozzle for low Reynolds numbers and expands to the whole area for high Reynolds numbers.

In order to evaluate the Nusselt number with and without oscillation, the local Nusselt number was averaged in the region of $-0.5 \leqslant x/B \leqslant 0.5$ (beneath the nozzle) and in Figs. 8($a$) and 8($b$), the ratio of the Nusselt number with and without oscillation $\mathrm{Nu}_f/\mathrm{Nu}_o$ is presented for the abscissa, frequency $f$ as a parameter of the dimensionless space $H$. The white signals are for amplitude $a=1.0$ mm and the dark signs are for $a=0.5$ mm. For Re=1000 (Fig. 8($a$)), heat transfer enhancement approaches 1.3 at a low frequency. However, for Re=10,000 (Fig. 8($b$)), the ratio $\mathrm{Nu}_f/\mathrm{Nu}_o$ is less than 1.0 and heat transfer is depressed. It takes a peak value at a certain frequency in Figs. 8($a$) and 8($b$). This tendency cannot be seen clearly in another Reynolds number and should be examined in detail in the near future.

**Flow Field.** Flow measurements give us the qualitative mechanism of heat transfer enhancement and depression. Figures 9($a$)–9($c$) indicate the dimensionless velocity and the turbulence intensity with and without oscillation for $H=4.0$ and Re=2000. In the case without oscillation, the turbulence intensity is from 8% to 12% perpendicular to the flow direction and approaches 14% from $x/B=1.5-4$ near the impingement surface. As shown in Fig. 9($b$) ($f=10$ Hz and $a=1.0$ mm), the turbulence intensity constructs the closed regions of 10%, 12%, and 14%. The area of 14% expands from $x/B=1.3-5$ and contributes to the heat transfer improvement. With an increase in frequency, the jet area from the nozzle exit expands horizontally and the maximum turbulence intensity approaches 16%. However, the turbulence intensity near the improvement surface is 12% at most, and the heat transfer is depressed due to the increase in thermal boundary layer thickness.

Figures 10($a$)–10($c$) show the power spectrum of velocity fluctuation based on Fig. 9. The sampling frequency is 20 kHz, the sampling time is 100 ms, and the sampling number is 10 at one measuring point. In Fig. 10($a$), the power spectrum takes a peak around $f=50$ Hz, as a background. When the peak is emphasized by oscillation $f=10$ Hz, as shown in Fig. 10($b$), heat transfer is improved. On the other hand, when a peak is weakened by oscillation $f=100$ Hz, as shown in Fig. 10($c$), heat transfer is depressed.

Flow fields at the heat transfer enhancement and depression were visualized by a smoke inserting method and a video equipment in Figs. 11($a$) and 11($b$). Flow models corresponding to Figs. 11($a$) and 11($b$) were expressed in Figs. 12($a$) and 12($b$), respectively. In the video picture of Fig. 11($a$), the jet from the nozzle is contracted and the flow along the impingement surface is undulated (top and bottom). The flow model is represented in Fig. 12($a$). Strictly speaking, after the jet from the nozzle impinged to the flat surface with oscillation, vortices are generated on both the right and left hand sides of the jet and flow downstream with growing up. The renewal of these vortices on the impingement surface contributes to the heat transfer enhancement. The renewal is due to the propagation of oscillated pressure to the nozzle and the jet of oscillated air from the nozzle. The pitch and size of the vortices become narrow and small with an increase in frequency, respectively. For high frequency, after the jet from the nozzle expands to both sides, the stilled layer is produced on the impingement surface, as shown in Figs. 11($b$) and 12($b$). The thermal boundary layer increases along the flow direction without undulation. In this circumstance, the heat transfer is depressed.

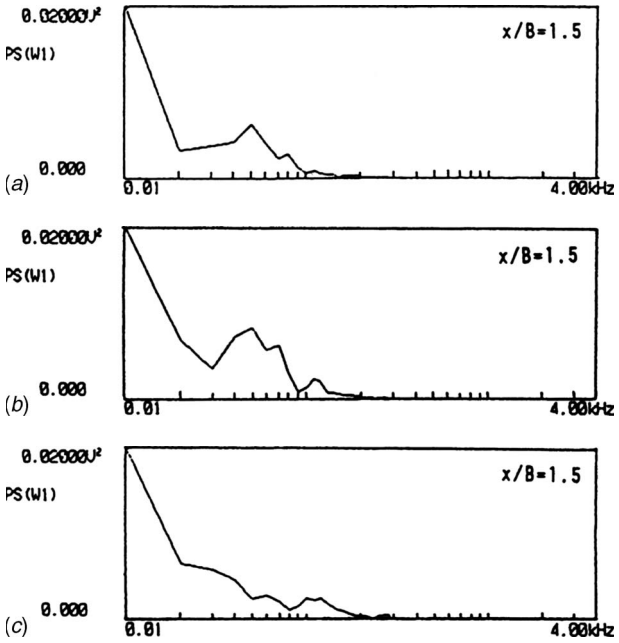


**Fig. 10 Power spectrum ($H=4.0$, $a=1.0$ mm, and Re=2000): ($a$) $f=0$ Hz; ($b$) $f=10$ Hz; ($c$) $f=100$ Hz**

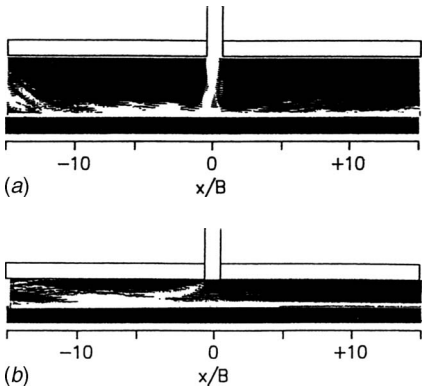


**Fig. 11 Flow visualization: ($a$) heat transfer improvement ($H=4.0$, $a=1.0$ mm, $f=10$ Hz, and Re=500); ($b$) heat transfer depression ($H=2.0$, $a=1.0$ mm, $f=60$ Hz, and Re=500)**

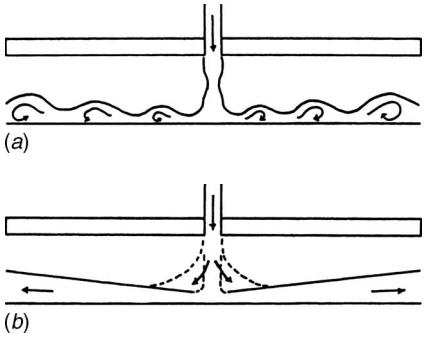


**Fig. 12 Flow model: ($a$) heat transfer improvement; ($b$) heat transfer depression**

## Conclusions

The effect of oscillation of impingement surface on two-dimensional impinging jet from slit-type nozzle was examined experimentally by using thermosensitive liquid crystal, hot wire anemometer, and smoke inserting method for dimensionless space $H=1-4$, Reynolds number $\mathrm{Re}=1000-10{,}000$, frequency $f=0-100$ Hz, and amplitudes $a=0.5$ mm and 1.0 mm. Both heat transfer enhancement and depression can appear due to oscillation. In the case of $H\cong 1$, heat transfer is enhanced for low frequencies at low Reynolds numbers, and in the case of wide space between the nozzle and the impingement surface it tends to be depressed for high Reynolds numbers. In the flow field at the heat transfer improvement, vortices are generated on both sides of the jet on the impingement surface, and the turbulence intensity increases by the renewal of these vortices. At heat transfer depression, the thermal boundary layer thickness on the impingement surface increases along the flow direction due to the high frequency oscillation. The average Nusselt number beneath the nozzle approaches 1.3 times of that without oscillation within the present experimental conditions.

## Nomenclature

- $a$ = amplitude (mm)
- $B$ = nozzle width (mm)
- $f$ = frequency (Hz)
- $h$ = distance between nozzle and impingement surface (mm)
- $H$ = dimensionless distance between nozzle and impingement surface ($h/B$)
- $\mathrm{Nu}$ = Nusselt number (refer to Eq. (2))
- $\mathrm{Nu}_f$ = average Nusselt number with oscillation beneath the nozzle
- $\mathrm{Nu}_{\mathrm{net}}$ = Nusselt number based on heat flux correction (Fig. 5)
- $\mathrm{Nu}_o$ = Nusselt number without oscillation beneath the nozzle
- $\mathrm{Nu}_{\mathrm{unif}}$ = Nusselt number without heat flux correction (Fig. 5)
- $q_{\mathrm{net}}$ = net heat flux ($\mathrm{W/m^2}$)
- $\mathrm{Re}$ = Reynolds number at nozzle exit ($U_o \cdot 2B/\nu$)
- $T_o$ = fluid temperature at nozzle exit (°C or K)
- $T_w$ = impingement surface temperature (°C or K)
- $U_o$ = average velocity at nozzle exit (m/s)
- $x$ = distance from the center of the nozzle (mm)
- $z$ = distance perpendicular to the impingement surface (mm)
- $\alpha$ = heat transfer coefficient (refer to Eq. (1))
- $\lambda$ = thermal conductivity of fluid (W/(mK))
- $\nu$ = kinematic viscosity of fluid ($\mathrm{m^2/s}$)

## References


[1] Viskanta, R., 1993, "Heat Transfer to Impinging Isothermal Gas and Flame Jets," Exp. Therm. Fluid Sci., **6**, pp. 111–134.

[2] Jambunathan, K., Lai, E., Moss, M. A., and Button, B. L., 1992, "A Review of Heat Transfer Data for Single Circular Jet Impingement," Int. J. Heat Fluid Flow, **13**, pp. 106–115.

[3] Loo, E., and Mujumdar, A. S., 1984, "A Simulation Model for Combined Impingement and Through Drying Using Superheated Steam as the Drying Medium," *Drying '84*, A. S. Mujumdar, ed., Hemisphere, New York, pp. 264–280.

[4] Martin, H., 1977, "Heat and Mass Transfer Between Impinging Gas Jets and Solid Surfaces," Adv. Heat Transfer, **13**, pp. 1–27.

[5] Fand, R. M., Roos, J., Cheng, J., and Kaye, J., 1962, "The Local Heat Transfer Coefficient Around a Heated Horizontal Cylinder in an Intense Sound Field," ASME Trans. J. Heat Transfer, **84**, pp. 245–250.

[6] Davis, G. D., and Richarson, P. D., 1973, "Natural Convection in a Sound Field Giving Large Streaming Reynolds Numbers," Int. J. Heat Mass Transfer, **16**, pp. 1245–1265.

[7] Gospinath, A., and Harder, D. R., 2000, "An Experimental Study of Heat Transfer From a Cylinder in Low-Amplitude Zero-Mean Oscillatory Flows," Int. J. Heat Mass Transfer, **43**, pp. 505–520.

[8] Davidson, B. J., 1973, "Heat Transfer From a Vibrating Circular Cylinder," Int. J. Heat Mass Transfer, **16**, pp. 1703–1727.

[9] Momose, K., Setokawa, H., Asami, T., and Hosokawa, Y., 1999, "Local Characteristics of Heat Transfer From a Vibrating Cylinder," JSME, **58**, pp. 3437–3444.

[10] Liu, T., and Sullivan, J. P., 1996, "Heat Transfer and Flow Structures in an Excited Circular Impinging Jet," Int. J. Heat Mass Transfer, **39**, pp. 3695–3706.

[11] Gau, C., Sheu, W. Y., and Shen, C. H., 1997, "Impingement Cooling Flow and Heat Transfer Under Acoustic Excitation," ASME Trans. J. Heat Transfer, **119**, pp. 810–817.

[12] Poh, H. J., Kumar, K., and Mujundar, A. S., 2005, "Heat Transfer From a Pulsed Laminar Impinging Jet," Int. Commun. Heat Mass Transfer, **32**, pp. 1317–1324.

[13] ANSI/ASME PTC 19-1, 1985, "Supplement to Performance Test Coded, Instrument and Apparatus, Part 1: Measurement Uncertainty," ASME, New York, pp. 169–185.

[14] T. Asanuma, ed., 1977, *Handbook of Flow Visualization*, Asakura, Tokyo, pp. 169–185.

[15] Ichimiya, K., and Hosaka, H., 1992, "Experimental Study of Heat Transfer Characteristics Due to Confined Impinging Two-Dimensional Jets," Exp. Therm. Fluid Sci., **5**, pp. 803–807.

# The Flow of Non-Newtonian Fluids on a Flat Plate With a Uniform Heat Flux

**M. M. Molla**
Department of Mechanical Engineering,
University of Glasgow,
Glasgow G12 8QQ, UK

**L. S. Yao**
Department of Mechanical and Aerospace Engineering,
Arizona State University,
Tempe, AZ 85287

*Forced convective heat transfer of non-Newtonian fluids on a flat plate with the heating condition of uniform surface heat flux has been investigated using a modified power-law viscosity model. This model does not restrain physically unrealistic limits; consequently, no irremovable singularities are introduced into a boundary-layer formulation for power-law non-Newtonian fluids. Therefore, the boundary-layer equations can be solved by marching from leading edge to downstream as any Newtonian fluids. For shear-thinning and shear-thickening fluids, non-Newtonian effects are illustrated via velocity and temperature distributions, shear stresses, and local temperature distribution. Most significant effects occur near the leading edge, gradually tailing off far downstream where the variation in shear stresses becomes smaller.* [DOI: 10.1115/1.2977610]

*Keywords: boundary layer, non-Newtonian fluids, modified power law*

## 1 Introduction

The interest in heat transfer problems involving power-law non-Newtonian fluids has grown in the past half century. A sequence of excellent lectures on non-Newtonian fluids was given by Hinch [1]. It appears that the paper of Acrivos [2], a frequently cited paper, was the first to consider boundary-layer flows for such fluids. Since then, a large number of papers have been published due to their wide relevance in chemicals, foods, polymers, molten plastics, and petroleum production, and other natural phenomena. A complete survey of this literature is impractical since Ref. [2] is one of the most cited references in engineering literature. However, a few items are listed here to provide starting points for a broader literature search [3–10].

Two common mistakes often appear in papers studying boundary layers of power-law non-Newtonian fluids. The first is that few authors recognize that the power law introduces a length scale into boundary-layer formulations; consequently, boundary-layer problems with power-law non-Newtonian fluids cannot have simple self-similar solutions. It is nevertheless a convenient practice to ignore the dependence of boundary-layer solutions on the streamwise coordinate. It has been demonstrated in Refs. [11,12] that such a self-similar solution is actually only valid at the leading edge of the boundary layer. The similarity solution is a natural upstream condition, which is needed to integrate boundary-layer equations along the streamwise direction from the leading edge.

The second concern is related to the unrealistic physical result, introduced by the traditional power-law correlation, that viscosity either vanishes or becomes infinite in the limit of large or small shear rates, respectively. This usually occurs at the leading edge of a flat plate or along the outer edge of boundary layers where the boundary layer matches with the outer inviscid flow. Thus, power-law correlations introduce nonremovable singularities into boundary-layer formulations for an infinite or zero viscosity. A brief discussion of the singularity associated with a sharp leading edge of boundary layers is provided in Ref. [13]. Without recognizing the cause of such unrealistic conditions, a false-starting process has been used to integrate boundary-layer equations slightly downstream from the leading edge to avoid the leading-edge region; sometimes complex multilayer structures have been introduced to overcome mathematical difficulties in order to obtain solutions of a nonphysical formulation [9,10].

The recently proposed modified power-law correlation is sketched for various power indices $n$ in Fig. 1. It is clear that the new correlation does not contain the physically unrealistic limits of zero and infinite viscosities displayed by traditional power-law correlations [1]. The modified power law, in fact, fits data better [13,14]. The constants in the proposed model are fixed with available measurements and are described in detail in Ref. [11]. The boundary-layer formulation on a flat plate is described and numerically solved in Ref. [11], and the associated heat transfer for two different heating conditions is reported in Ref. [12] for a shear thinning fluid. In this investigation, the behaviors of both shear-thinning and shear-thickening fluids are studied by choosing the power-law index as $n$ (=0.6, 0.8, 1, 1.2, 1.4) in order to fully demonstrate the impact of these non-Newtonian fluids.

## 2 Formulation of Problem

A steady laminar boundary layer of a non-Newtonian fluid on a semi-infinite flat plate with uniform heat flux has been studied. The viscosity depends on shear rate and is correlated by a modified power law. We consider shear-thinning and shear-thickening situations of non-Newtonian fluids. It is assumed that a surface heat flux $q_w$ is applied to the plate; $T_\infty$ is the ambient temperature of the fluid. The coordinate system is shown in Fig. 2.

The boundary-layer equations for the flow and heat transfer are

$$\frac{\partial \bar{u}}{\partial \bar{x}} + \frac{\partial \bar{v}}{\partial \bar{y}} = 0 \tag{1}$$

$$\bar{u}\frac{\partial \bar{u}}{\partial \bar{x}} + \bar{v}\frac{\partial \bar{u}}{\partial \bar{y}} = \frac{\partial}{\partial \bar{y}}\left(\nu \frac{\partial \bar{u}}{\partial \bar{y}}\right) \tag{2}$$

$$\bar{u}\frac{\partial T}{\partial \bar{x}} + \bar{v}\frac{\partial T}{\partial \bar{y}} = \alpha \frac{\partial^2 T}{\partial \bar{y}^2} \tag{3}$$

where $(\bar{u}, \bar{v})$ are velocity components along the $(\bar{x}, \bar{y})$ axes, $T$ is the temperature, and $\alpha$ is the thermal diffusivity of the fluid. The viscosity is correlated by a modified power law, which is

Contributed by the Heat Transfer Division of ASME for publication in the JOURNAL OF HEAT TRANSFER. Manuscript received October 24, 2007; final manuscript received June 17, 2008; published online October 17, 2008. Review conducted by Yogesh Jaluria.

  

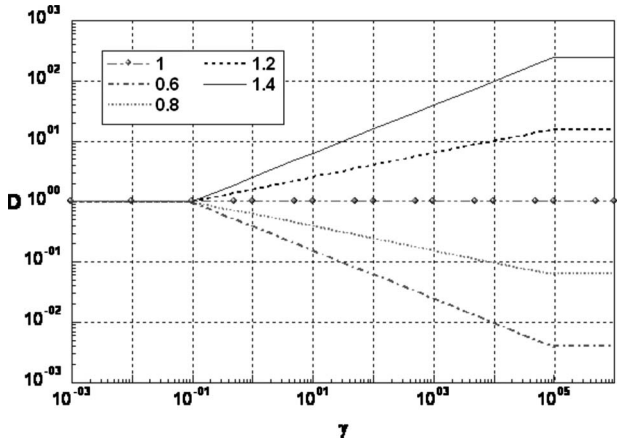


**Fig. 1 Modified power-law correlation**

$$\nu = \frac{K}{\rho}\left|\frac{\partial \bar{u}}{\partial \bar{y}}\right|^{n-1} \quad \text{for } \bar{\gamma}_1 \leqslant \left|\frac{\partial \bar{u}}{\partial \bar{y}}\right| \leqslant \bar{\gamma}_2 \tag{4}$$

The constants $\bar{\gamma}_1$ and $\bar{\gamma}_2$ are two "threshold" shear rates, $\rho$ is the density of the fluid, and $K$ is a dimensional constant, whose dimension depends on the power-law index $n$. The values of these constants can be determined by matching with measurements. Outside of the above range, viscosity is assumed constant; its value can be fixed with data given in Fig. 1.

The boundary conditions for the present problem are

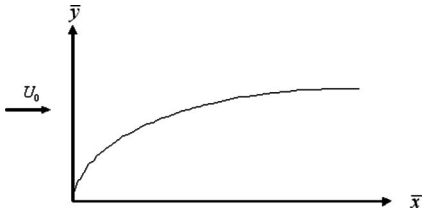


**Fig. 2 Coordinates**

$$\bar{u} = \bar{v} = 0, \quad -k\frac{\partial T}{\partial \bar{y}} = q_w \quad \text{at } \bar{y} = 0 \tag{5a}$$

$$\bar{u} \to U_0, \quad T \to T_\infty \quad \text{as } \bar{y} \to \infty \tag{5b}$$

The required upstream conditions will be provided later. We now introduce the following nondimensional transformations:

$$\xi = x = \frac{\bar{x}}{l}, \quad \eta = \frac{\bar{y}}{l}\left(\frac{U_0}{2\bar{x}\nu_1}\right)^{1/2}, \quad U = \frac{\bar{u}}{U_0}, \quad V = \bar{v}\left(\frac{2\bar{x}}{U_0\nu_1}\right)^{1/2}$$
$$\theta = (T - T_\infty)\frac{q_w}{k}\left(\frac{\nu_1 l}{U_0}\right)^{1/2}, \quad \mathrm{Re} = \frac{U_0 l}{\nu_1}, \quad D = \frac{\nu}{\nu_1} \tag{6}$$

where $\nu_1$ is the reference viscosity, $\theta$ is the dimensionless temperature of the fluid, and Re is the Reynolds number. The variable viscosity,

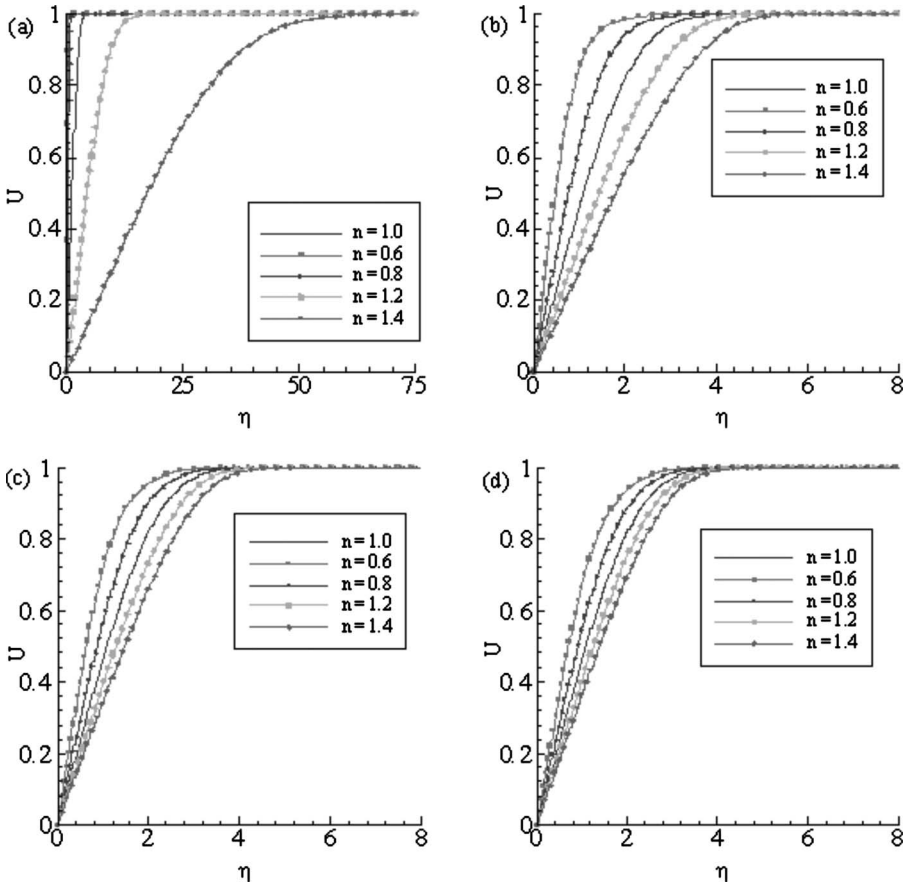


**Fig. 3 Velocity distribution at (*a*) $\xi$=0.0, (*b*) $\xi$=0.1075, (*c*) $\xi$=1.0102, and (*d*) $\xi$=2.0139**

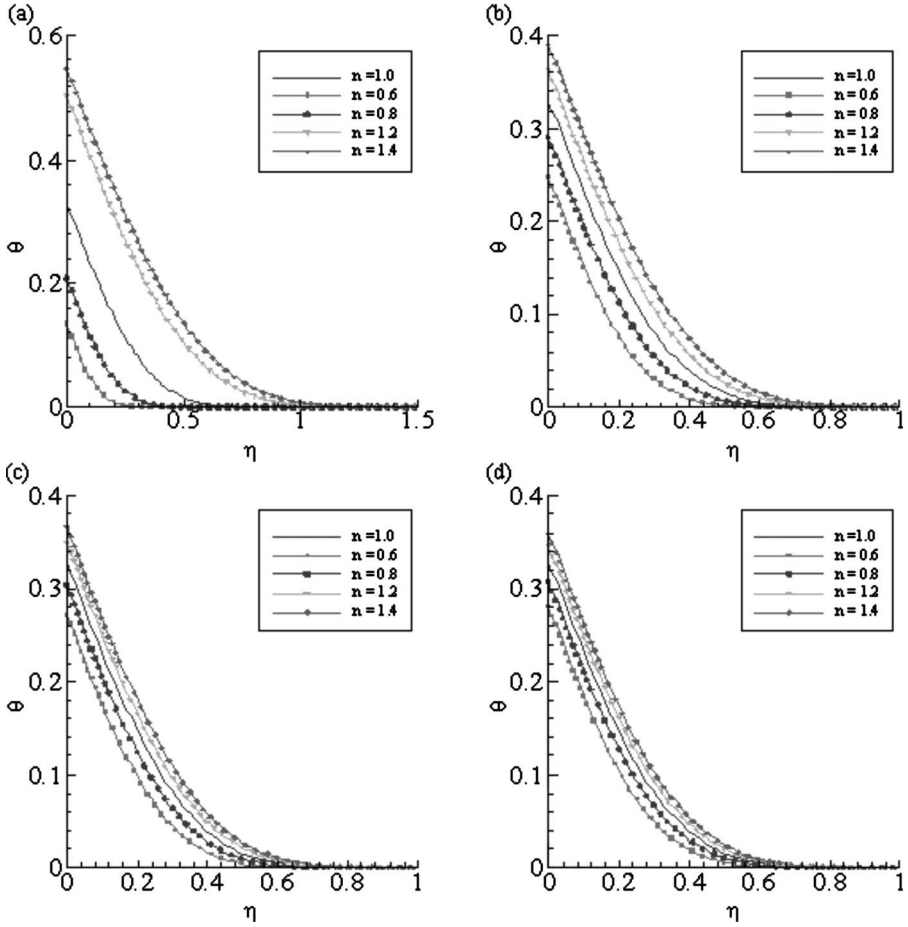


**Fig. 4 Temperature distribution at (*a*) $\xi$=0.0, (*b*) $\xi$=0.1075, (*c*) $\xi$=1.0102, and (*d*) $\xi$ =2.0139 while Pr=100**

$$D = \frac{K}{\rho \nu_1}\left(\frac{U_0^3}{l\nu_1}\right)^{(n-1)/2}\left|\frac{\partial u}{\partial y}\right|^{n-1} = C\left|\frac{\partial u}{\partial y}\right|^{n-1} \tag{7a}$$

becomes

$$D = \begin{cases} 1, & |\gamma| \leqslant \gamma_1 \\ |\gamma|^{n-1}, & \gamma_1 \leqslant |\gamma| \leqslant \gamma_2 \\ 0.5, & |\gamma| \geqslant \gamma_2 \end{cases} \quad \text{where } \gamma = \frac{\partial u}{\partial y} \tag{7b}$$

Then, the length scale associated with the non-Newtonian power law [12] is

$$l = C^{2/(1-n)}\left[\left(\frac{K}{\rho}\right)^2 1/\upsilon_1^{(n+1)}\right]^{1/(n-1)} U_0^3 \tag{7c}$$

Because of this length scale, the current problem does not have a self-similar solution. Substituting variables (6) into Eqs. (1)–(4) leads to the following equations:

$$(2\xi)\frac{\partial U}{\partial \xi} - \eta\frac{\partial U}{\partial \eta} + \frac{\partial V}{\partial \eta} = 0 \tag{8}$$

$$(2\xi)U\frac{\partial U}{\partial \xi} + (V - \eta U)\frac{\partial U}{\partial \eta} = \frac{\partial}{\partial \eta}\left[D\frac{\partial U}{\partial \eta}\right] \tag{9}$$

$$(2\xi)U\frac{\partial \theta}{\partial \xi} + (V - \eta U)\frac{\partial \theta}{\partial \eta} + U\theta = \frac{1}{\mathrm{Pr}}\frac{\partial^2 \theta}{\partial \eta^2} \tag{10}$$

and

$$\gamma = (2\xi)^{-1/2}\frac{\partial U}{\partial \eta} \tag{11}$$

$$D = \begin{cases} 1, & |\gamma| \leqslant \gamma_1 \\ \left|\dfrac{\gamma}{\gamma_1}\right|^{n-1}, & \gamma_1 \leqslant |\gamma| \leqslant \gamma_2 \\ \left|\dfrac{\gamma_2}{\gamma_1}\right|^{n-1}, & |\gamma| \geqslant \gamma_2 \end{cases} \tag{12}$$

Correlation (12) is almost identical to the one proposed in Ref. [12]. Equations (8) and (9) can be solved by marching downstream, with the upstream condition satisfying the following differential equations:

$$-\eta\frac{\partial U}{\partial \eta} + \frac{\partial V}{\partial \eta} = 0 \tag{13}$$

$$(V - \eta U)\frac{\partial U}{\partial \eta} = \frac{\partial}{\partial \eta}\left[D\frac{\partial U}{\partial \eta}\right] \tag{14}$$

$$(V - \eta U)\frac{\partial \theta}{\partial \eta} + U\theta = \frac{1}{\mathrm{Pr}}\frac{\partial^2 \theta}{\partial \eta^2} \tag{15}$$

which are the limits of Eqs. (13)–(15) as $\xi \to 0$. The corresponding boundary conditions are

$$U = V = 0, \quad \frac{\partial \theta}{\partial \eta} = -1 \quad \text{at } \eta = 0 \tag{16a}$$

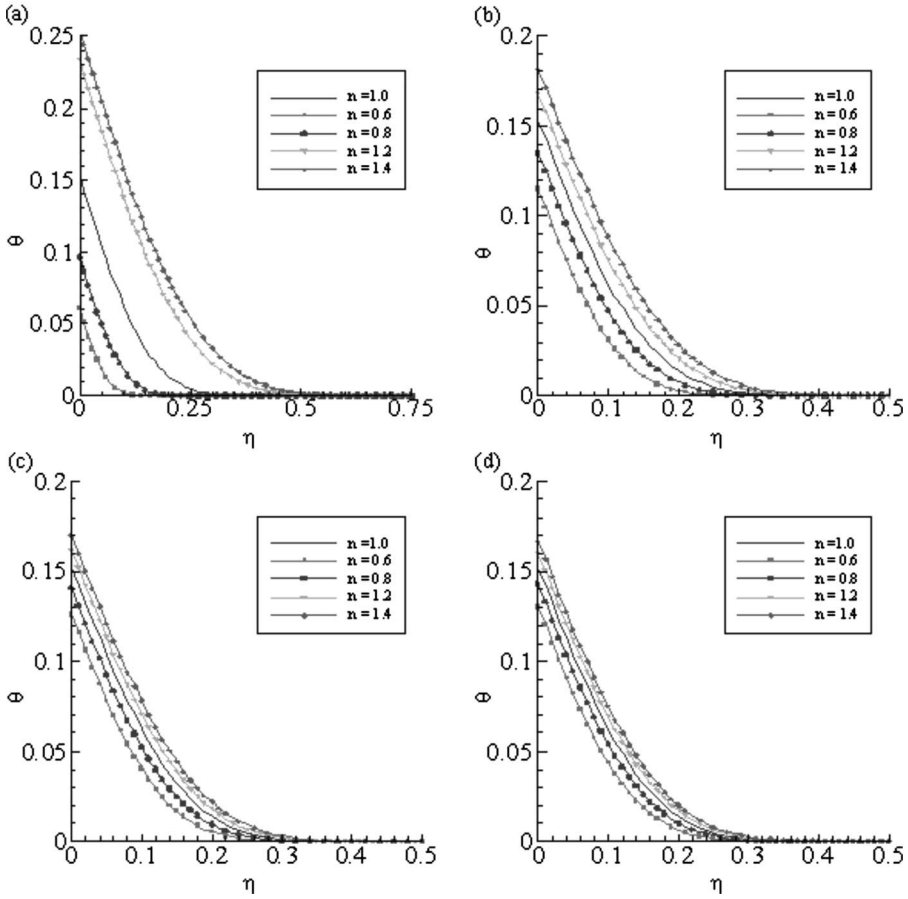


**Fig. 5 Temperature distribution at (*a*) $\xi=0.0$, (*b*) $\xi=0.1075$, (*c*) $\xi=1.0102$, and (*d*) $\xi=2.0139$ while Pr=1000.**

$$U \to 1, \quad \theta \to 0 \quad \text{as } \eta \to \infty \tag{16b}$$

Equations (8)–(10) and (13)–(15) are discretized by a central-difference scheme for the diffusion term and a backward-difference scheme for the convection terms; hence, the truncation errors are $O(\Delta\xi)$. Finally we get an implicit tridiagonal algebraic system of equations, which can be solved by a double-sweep technique. The normal velocity is directly solved from the continuity equation. The computation is started from $\xi=0$, and the solution of Eqs. (13)–(15) is the upstream condition for marching downstream to $\xi=100$. After several test runs, converged results are obtained by using $\Delta\xi=2\times10^{-9}$ and $\Delta\eta=0.001$ near the leading edge, say, $\xi=0.0-10^{-5}$; afterward $\Delta\xi$ is gradually increased to $\Delta\xi=0.01$.

In practical applications, the physical quantities of principal interest are the skin-friction coefficient $C_f$ and the local surface temperature distribution $\tau_w$, which are

$$C_f(2\xi)^{1/2} = \left[D\frac{\partial U}{\partial \eta}\right]_{\eta=0} \tag{17}$$

$$\tau_w = \theta(\xi,0) \tag{18}$$

## 3 Results and Discussion

The numerical results are presented for the non-Newtonian power-law fluids of shear-thinning ($n<1$) and shear-thickening ($n>1$) cases along with the Newtonian fluid ($n=1$). For a large Prandtl number, the velocity and temperature distributions are given in Figs. 3–5; the skin-friction coefficient $C_f(2\xi)^{1/2}$ and the local surface temperature distribution $\theta(\xi,0)$ appear in Figs. 6–8 for different values of the power-law index $n$ (=0.6, 0.8, 1.0, 1.2, 1.4). The singularity mentioned earlier has been successfully removed by using the modified power-law correlation. Since the shear tress at the leading edge is inversely proportional to $\sqrt{2\xi}$, $D=(\gamma_2/\gamma_1)^{n-1}$ at the leading edge.

The velocity distributions as a function of $\eta$ at selected $\xi$ locations for the power-law index $n$ are shown in Figs. 3(*a*)–3(*d*). In Fig. 3(*a*), it is seen that for the shear-thinning fluids $n$ (=0.6, 0.8), the velocity accelerates quickly, owing to the decreased influence of viscosity near the leading edge. Since the actual Reynolds number is larger for a bigger $n$, the boundary layer is thinner. For the shear-thickening fluids $n$ (=1.2, 1.4), the velocity decreases due to the increase in the effects of viscosity, and the boundary layer is thicker near the leading edge. In the downstream region, the velocity distribution gradually approaches the velocity distribution of the Newtonian fluid ($n=1$), as seen in Figs. 3(*b*)–3(*d*). This means that for the shear-thinning case, the effect of viscosity increases while it decreases for the shear-thickening fluid. The distribution of shear stresses gradually smooths out, and so does that of viscosities. It should be mentioned that the boundary-layer thickness for $n=1.4$ at $\xi=0$ is approximately 75 but quickly drops below 10 before $\xi=0.1$. This is because $n=1.4$ is a rather extreme case, with the viscosity at $\xi=0$ about 15 times larger than that for $n=1.2$. As soon as the fluid flows past the leading edge, the viscosity quickly drops, the local Reynolds number increases, and the boundary layer becomes thinner.

Figures 4 and 5 show the temperature distribution for Pr=100 and 1000, respectively. For both values of Prandtl number, the values of the wall temperature for a shear-thinning fluid are less than those for shear-thickening fluids. At the leading edge the wall

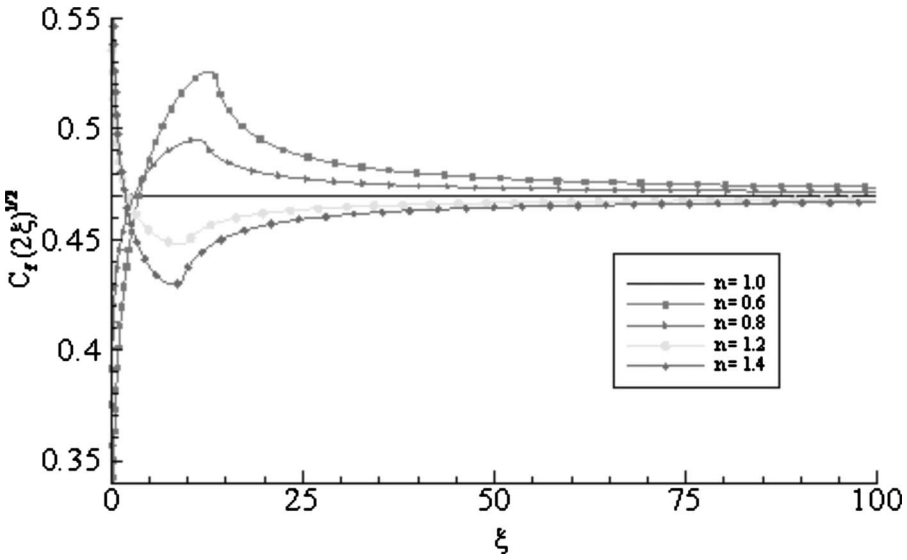


**Fig. 6 Distribution of shear stress**

temperature is relatively small for a shear-thinning fluid as compared to a shear-thickening fluid. In the downstream region the wall temperature increases for $n$ (=0.6,0.8) and decreases for $n$ (=1.2,1.4) owing to the opposite viscous effect for the shear-thinning and shear-thickening fluids. Here it is notable that for Pr=1000 the thermal boundary-layer thickness is approximately half of that for Pr=100. For large values of Pr, corresponding to materials that are lightly conducting thermally, an increase in Pr corresponds to a decrease in thermal conductivity. Then, for any point on the wall, heat is not able to conduct more easily into the fluid as Pr increases, and therefore the thermal boundary layer becomes thinner.

The effect of the power-law index on the variation in skin-friction coefficient $C_f(2\xi)^{1/2}$ is shown in Fig. 6. For the shear-thinning case, the wall shear stress increases up to $\xi \approx 12.5$ and then gradually decreases and asymptotically approaches the value for a Newtonian fluid ($n=1$). Similarly, for a shear-thickening fluid, the wall shear stress decreases up to $\xi \approx 10$ and then asymptotically approaches the wall shear of a Newtonian fluid. From this figure, we can say that the extreme variation in $C_f(2\xi)^{1/2}$ for the shear-thinning and shear-thickening cases happens near the leading edge and are due to the effect of the non-Newtonian variable viscosity. In a run up to $\xi=8000$, the difference in the wall shear stress between a non-Newtonian fluid and a Newtonian fluid became extremely small but still nonzero. This is a result of the inherent nonlinearity associated with a non-Newtonian fluid.

The local temperature distributions are plotted in Figs. 7 and 8 for Pr=100 and 1000, respectively. The minimum surface temperature $\theta(\xi,0)$ occurs at the leading edge for the shear-thinning fluid, which are 0.13391 for Pr=100 and 0.06088 for Pr=1000 at the case of $n=0.6$. On the other hand, for the shear-thickening case, the maximum value of $\theta(\xi,0)$ at $\xi=0$ for Pr=100 is 0.55001 and that for Pr=1000 is 0.25397 while $n=1.4$. Hence, at $\xi=0$ the local temperature decreases by 54.53% for $n=0.6$ and by 53.84% for $n=1.4$ as Pr increases from 100 to 1000. Downstream from the leading edge, the surface temperature increases for shear-thinning cases ($n=0.6,0.8$) and decreases for shear-thickening cases ($n=1.2,1.4$). They asymptotically approach the surface temperature

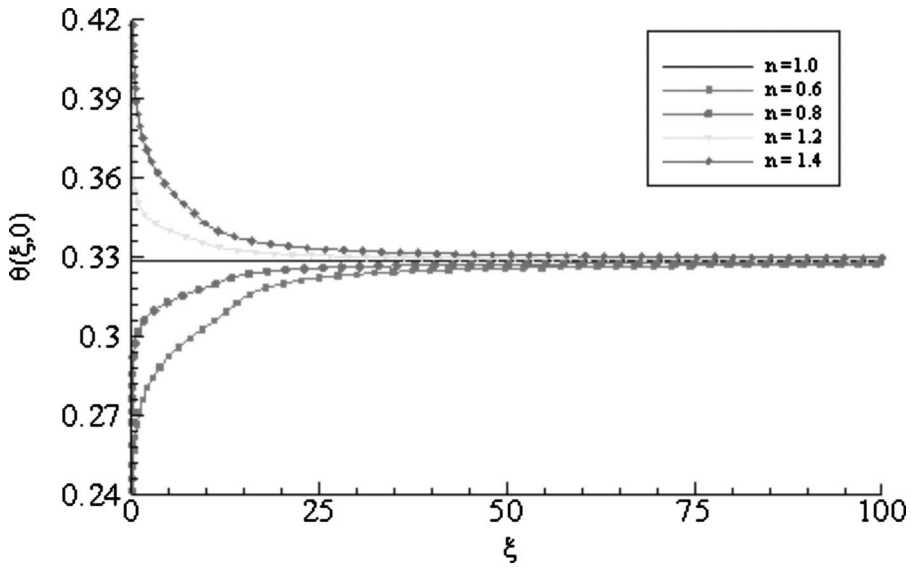


**Fig. 7 Distribution of local surface temperature for Pr=100**

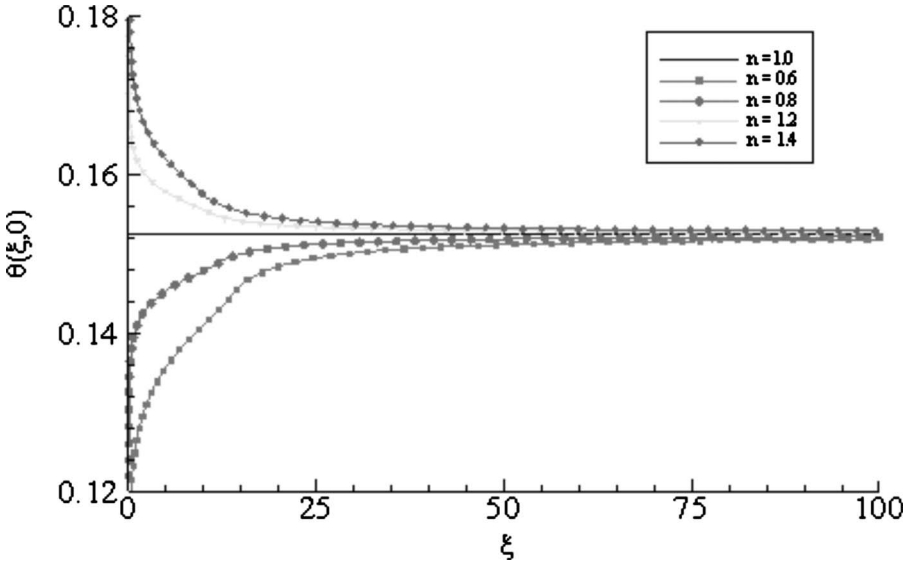


**Fig. 8 Distribution of Nusselt number for Pr=1000**

of an associated Newtonian fluid. It is worthy to note that the solution of a Newtonian fluid depends on $\eta$ and not on $\xi$, a similarity solution.

## 4 Conclusions

The proposed modified power-law correlation agrees well with the actual measurement of non-Newtonian fluids; consequently it is a physically realistic model. The problems associated with the nonremoval singularity introduced by the traditional power-law correlations do not exist for the modified power-law correlation proposed in this paper. The model of modified power law for non-Newtonian fluids can be used to investigate the heat transfer problems associated with thin layers where a boundary-layer approximation is valid.

## Nomenclature

$C$ = constant
$C_f$ = dimensionless skin-friction coefficient
$D$ = nondimensional viscosity of the fluid
$K$ = constant for variable viscosity, Eq. (4)
$k$ = thermal conductivity
$l$ = reference length scale of the plate
$n$ = non-Newtonian power-law index
Nu = Nusselt number
$q_w$ = surface heat flux
Re = Reynolds number
$(\bar{u},\bar{v})$ = fluid velocities in the $(\bar{x},\bar{y})$ directions, respectively
$(U,V)$ = dimensionless fluid velocities in the $(\xi,\eta)$ directions, respectively
$U_0$ = freestream velocity
$T$ = dimensional temperature of the fluid
$T_w$ = surface temperature
$T_\infty$ = ambient temperature

### Greek Symbols

$\xi$ = axial direction along the plate
$\eta$ = pseudosimilarity variable
$\gamma$ = shear rate
$\rho$ = fluid density
$\tau_w$ = surface temperature
$\nu$ = viscosity of the non-Newtonian fluid
$\nu_1$ = reference viscosity of the fluid
$\alpha$ = thermal diffusivity
$\theta$ = dimensionless temperature of the fluid

## References

[1] Hinch, J., 2003, "Non-Newtonian Geophysical Fluid Dynamics," 2003 Program in Geophysical Fluid Dynamics, Woods Hole Oceanographic Institution Woods Hole, MA 02543 USA, http://gfd.whoi.edu/proceedings/2003/PDFvol2003.html
[2] Acrivos, A., 1960, "A Theoretical Analysis of Laminar Natural Convection Heat Transfer to Non-Newtonian Fluids," AIChE J., **16**, pp. 584–590.
[3] Emery, A. F., Chi, H. S., and Dale, J. D., 1970, "Free Convection Through Vertical Plane Layers of Non-Newtonian Power Law Fluids," ASME J. Heat Transfer, **93**, pp. 164–171.
[4] Chen, T. V. W., and Wollersheim, D. E., 1973, "Free Convection at a Vertical Plate With Uniform Flux Conditions in Non-Newtonian Power-Law Fluids," ASME J. Heat Transfer, **95**, pp. 123–124.
[5] Shulman, Z. P., Baikov, V. I., and Zaltsgendler, E. A., 1976, "An Approach to Prediction of Free Convection in Non-Newtonian Fluids," Int. J. Heat Mass Transfer, **19**, pp. 1003–1007.
[6] Som, A., and Chen, J. L. S., 1984, "Free Convection of Non-Newtonian Fluids Over Non-Isothermal Two-Dimensional Bodies," Int. J. Heat Mass Transfer, **27**, pp. 791–794.
[7] Haq, S., Kleinstreuer, C., and Mulligan, J. C., 1988, "Transient Free Convection of a Non-Newtonian Fluid Along a Vertical Wall," ASME J. Heat Transfer, **110**, pp. 604–607.
[8] Khan, W. A., Culham, J. R., and Yovanovich, M. M., 2006, "Fluid Flow and Heat Transfer in Power-Law Fluids Across Circular Cylinders: Analytical Study," ASME J. Heat Transfer, **128**, pp. 870–878.
[9] Denier, J. P., and Hewitt, R. E., 2004, "Asymptotic Matching Constraints for a Boundary-Layer Flow of a Power-Law Fluid," J. Fluid Mech., **518**, pp. 261–279.
[10] Denier, J. P., and Dabrowski, P. P., 2004, "On the Boundary-Layer Equations for Power-Law Fluids," Proc. R. Soc. London, Ser. A, **460**, pp. 3143–3158.
[11] Yao, L. S., and Molla, M. M., 2008, "Flow of a Non-Newtonian Fluid on a Flat Plate: I. Boundary Layer," J. Thermophys. Heat Transfer, in press.
[12] Molla, M. M., and Yao, L. S., 2008, "Flow of a Non-Newtonian Fluid on a Flat Plate: II. Heat Transfer," J. Thermophys. Heat Transfer, in press.
[13] Yao, L. S., and Molla, M. M., 2008, "Forced Convection of a Non-Newtonian Fluid on a Heated Flat Plate," Int. J. Heat Mass Transfer, in press.
[14] Molla, M. M., and Yao, L. S., 2008, "Non-Newtonian Natural Convection Along a Vertical Heated Wavy Surface Using a Modified Power-law Viscosity Model," ASME J. Heat Transfer, in press.

# Forced Convection Flow in a Wavy Channel With a Linearly Increasing Waviness at the Entrance Region

**Esam M. Alawadhi**
Department of Mechanical Engineering,
Kuwait University,
P.O. Box 5969,
Safat, 13060, Kuwait
e-mail: esam@kuc01.kuniv.edu.kw

*This research studies the fluid flow and heat transfer in a wavy channel with a linearly increasing waviness at the entrance region. The considered model consists of a channel formed by two wavy plates described by a sinusoidal profile and maintained at a uniform temperature. The finite element method is utilized to solve the problem. Reynolds numbers are considered in the range of* $125 < Re < 1000$ *to avoid unsteady flow, and* $Pr = 0.7$*. The global objective of this research is to reduce the pressure drop in the wavy channel due to the developing flow at the entrance region. The effect of the Reynolds number, length of the increasing waviness region, waviness of the wavy wall on the hydrodynamics, and thermal characteristics of the channel is investigated. The result indicates that the linearly increasing waviness at the entrance region significantly reduces the pressure drop in the channel on the other hand, the thermal characteristics of the wavy wall are nearly unaffected.* [DOI: 10.1115/1.2977554]

*Keywords: wavy channel, forced convection, entrance region*

## 1 Introduction

The wavy channel is typically employed in compact heat exchangers for enhancing heat transfer [1]. The geometrical complexity of this channel significantly affects the flow pattern and also the heat transfer. The heat transfer enhancement in this heat exchanger is due to three mechanisms. Firstly, the wavy channel interrupts the development of the hydrodynamics and thermal boundary layers. Secondly, the wavy walls introduce some form of mixing into the flow, which reduces the temperature gradient near the wall and increases the heat transfer. Thirdly, the corrugations of the wall increase the heat transfer surface area. Various wall geometries have been investigated in literature, such as corrugated, arc-shaped, and sinusoidal in two- or three-dimensional spaces.

Many numerical and experimental studies are available in literature on the fluid flow and heat transfer in the wavy channels. The numerical analysis of forced convection in a sinusoidal curved channel was solved using the spline alternating-direction implicit method by Wang and Chen [2]. Their results show that amplitudes of the Nusselt number and skin-friction coefficient are increased with the Reynolds number and waviness of the wall. Sinusoidal and arc-shaped configurations were numerically studied by Bahaidarah et al. [3], and they reported an 80% heat transfer enhancement in some case studies. Experimental work on heat transfer enhancement in sinusoidal wavy passages was reported by Rush et al. [4]. The onset of macroscopic mixing is directly linked to a significant increase in local heat transfer. The effect of the hydrodynamics condition on the heat transfer enhancement was presented by Gradeck et al. [5], and they pointed out a strong relationship between the wall velocity gradient and the Nusselt number. Experimental and numerical analyses were performed by Nishimura and Matsune [6] to study the effect of the fluid dynamics behavior for unsteady flow. The frequency of the fluid flow enhances the heat and mass flow at low Reynolds numbers. Guzman and Amon [7] studied the transition from laminar to chaotic flow in wavy channels through the use of the spectral element method. Stalio and Piller [8] presented the heat transfer enhancement in a wavy channel in an anticipated transition to unsteady. The effect of the three-dimensional hydrodynamics wavy channel on heat transfer enhancement was presented by Sawyers et al. [9] using numerical and analytical techniques. Fabbri [10] maximizes the heat transfer in a corrugated channel by optimizing the corrugation profile. However, the results indicate that the wall profile can only maximize the heat transfer when the Reynolds and Prandtl numbers are not too low. Separation characteristics inside a channel with a wavy surface were determined numerically by Mahmud et al. [11], and separations were strongly dependent on the surface waviness and aspect ratio. Lin et al. [12] presented a dimensional analysis for heat transfer characteristics in corrugated channels using the Buckingham Pi theorem. The results show that the local Nusselt number is affected primarily by the Reynolds number, the hydraulic diameter, and the corrugated angle.

In all the above works, the heat removal from the channel is significantly improved when a wavy channel is introduced instead of a straight one. However, a high pressure drop across the wavy channel is associated with these structures [13]. As a result, the overall performance of the thermal system is degraded because a larger mechanical pumping power is required. The pressure drop in the wavy channel is not only due to the geometry of the wall, but also due to the flow development at the entrance region. The flow development at the entrance region contributes most of the pressure drop in a wavy channel if the length of the channel is short, and the wall skin-friction at the entrance region is higher than at the fully developed region [14].

To tackle this disadvantage, this research presents a technique to reduce the pressure drop in a wavy channel by introducing a linearly increasing waviness region at the entrance. The pressure drop, the distribution of skin-friction, and the Nusselt number at the wavy surface are presented for the different Reynolds numbers, the waviness, and the length of the linearly increasing waviness region. The cost for manufacturing the proposed geometry should not be more than the cost of manufacturing a typical corrugated plate because the same technique can be used. Corrugated

Contributed by the Heat Transfer Division of ASME for publication in the JOURNAL OF HEAT TRANSFER. Manuscript received February 13, 2008; final manuscript received June 14, 2008; published online October 20, 2008. Review conducted by Gautam Biswas.

  

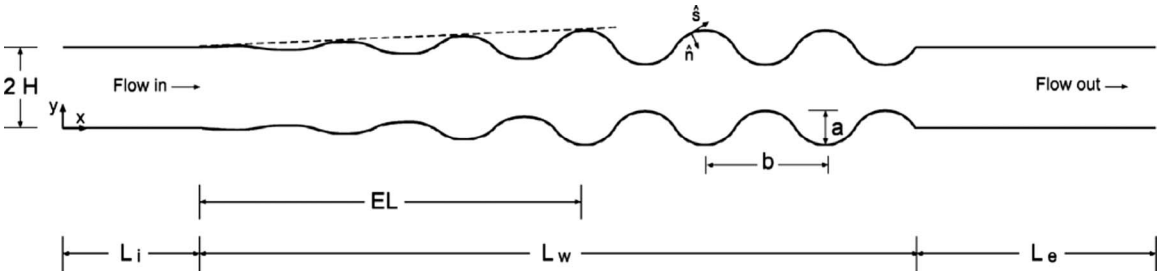


**Fig. 1 Schematic of the wavy channel configuration with the entrance showing the definition of important geometric parameters**

roll forming machines are used. The roll forming process consists of passing a continuous ribbon of structural steel through a series of rollers, which plastically deform the plate until the required shape is achieved.

## 2 Model Description and Solution Method

Figure 1 shows a schematic of the wavy channel configuration and the definition of important geometric parameters. The model is composed of two corrugated plates described by a sinusoidal function, and they are spaced with a distance $2H$. The total length of the channel is $L$. The walls start to wave at a distance $L_i$ from the channel's inlet, and ends at a distance $L_e$ from the exit. The horizontal length of the wavy section of the channel is equal to $L_w$. The waviness of the wall is $a$, while the wavelength is $b$. There is symmetry in the problem because the channel has periodic converging-diverging cross sections. Only the lower half of the geometry is considered in the analyses. The wavy section of the channel is composed of two regions. In the first region, the waviness of the wavy wall is increasing linearly for a distance $EL$. In the second region, the waviness is constant and the structure is periodic for a distance $L_w-LE$. The mathematical expressions of the wavy wall for the first and second regions are given as, respectively

$$y(x) = -\frac{a}{2}\sin\left(\frac{\pi}{b}x\right)(Ax + B) \tag{1a}$$

$$y(x) = -\frac{a}{2}\sin\left(\frac{\pi}{b}x\right) \tag{1b}$$

where $A=-aL_i/EL$ and $B=-a/EL$.

**2.1 Governing Equations.** Based on the characteristic scales of the half separation distance between the wavy walls ($H$), average inlet velocity ($u_i$), temperature difference ($T_w-T_i$), and $\rho u_i^2$, the dimensionless variables are defined as follows:

$$U = \frac{u}{u_i}, \quad v = \frac{v}{u_i}, \quad X = \frac{x}{H}, \quad Y = \frac{y}{H}, \quad P^* = \frac{P}{\rho u_i^2}, \quad \theta = \frac{T - T_i}{T_w - T_i}$$

The two basic dimensionless groups describing the problem are the Reynolds (Re) and Prandtl (Pr) numbers, and they are defined as, respectively

$$\mathrm{Re} = \frac{\rho u_i H}{\mu}, \quad \mathrm{Pr} = \frac{\mu C_p}{k}$$

Considering the above dimensionless variables and groups, the dimensionless governing equations for a steady laminar forced convection flow in a wavy channel are as follows:

Continuity equation:

$$\frac{\partial U}{\partial X} + \frac{\partial V}{\partial Y} = 0 \tag{2}$$

$X$- and $Y$-momentum equations:

$$U\frac{\partial U}{\partial X} + V\frac{\partial U}{\partial Y} = -\frac{\partial P^*}{\partial X} + \frac{1}{\mathrm{Re}}\left(\frac{\partial^2 U}{\partial X^2} + \frac{\partial^2 U}{\partial Y^2}\right) \tag{3}$$

$$U\frac{\partial V}{\partial X} + V\frac{\partial V}{\partial Y} = -\frac{\partial P^*}{\partial Y} + \frac{1}{\mathrm{Re}}\left(\frac{\partial^2 V}{\partial X^2} + \frac{\partial^2 V}{\partial Y^2}\right) \tag{4}$$

Energy equation:

$$U\frac{\partial \theta}{\partial X} + V\frac{\partial \theta}{\partial Y} = \frac{1}{\mathrm{RePr}}\left(\frac{\partial^2 \theta}{\partial X^2} + \frac{\partial^2 \theta}{\partial Y^2}\right) \tag{5}$$

The spaces are normalized based on the half separation distance between wavy walls ($H$). The dimensionless half height and total length of the channel are $H^*=1$ and $L^*=L/H$, respectively. The waviness and wavelength are given in dimensionless form as $a^*=a/H$ and $b^*=b/H$, respectively. Due to the elliptic nature of the governing equations, the boundary conditions along the entire domain must be specified for all field variables. The dimensionless boundary conditions are described in the following mathematical form:

1. at the inlet $(X=0, 0\le Y\le 1): U=\frac{3}{2}y(2-y^2),\ V=0,\ \theta=0,$
2. at the exit $(X=L^*, 0\le Y\le 1): \partial U/\partial X=0,\ V=0,\ \partial\theta/\partial X=0,$
3. at the bottom wall $(0\le X\le L_i^*, Y=0): U=V=\theta=0,\ (L_i^*\le X < L_i^*+EL^*, Y=-(a^*/2)\sin((\pi/b^*)X)): U=V=0,\ \theta=1,$ $(L_i^*+EL^*\le X<L_W^*,\ Y=-(a^*/2)\sin((\pi/b^*)X)(A^*X+B^*)): U=V=0,\ \theta=1,$ and $(L_i^*+L_W^*\le X\le L^*, Y=0): U=V=\theta=0,$ and
4. at the symmetry $(0\le X\le L^*, Y=1): V=0,\ \partial\theta/\partial Y=0$

The local Nusselt number $(\mathrm{Nu})_s$ along the wavy wall is used to describe the heat flow out of the wall and to evaluate the thermal effect of the wavy wall. $(\mathrm{Nu})_s$ is defined as

$$(\mathrm{Nu})_s = -\frac{1}{\theta_s}\frac{\partial \theta}{\partial \hat{n}} \tag{6}$$

where $\hat{n}$ is the normal coordinate to the surface and $\theta_s$ is the dimensionless temperature at the wall surface. The temperature gradient at the wavy wall is defined as

$$\frac{\partial \theta}{\partial \hat{n}} = \sqrt{\left(\frac{\partial \theta}{\partial X}\right)^2 + \left(\frac{\partial \theta}{\partial Y}\right)^2} \tag{7}$$

The average Nusselt number $(\mathrm{Nu})_{\mathrm{ave}}$ for the wavy wall is expressed as

$$(\mathrm{Nu})_{\mathrm{ave}} = \frac{1}{d}\int_0^d (\mathrm{Nu})_s d\hat{s} \tag{8}$$

where $\hat{s}$ is the dimensionless coordinate along the surface of the wavy wall and $d$ is the length of the wavy wall. The local skin-friction coefficient at the wavy wall is obtained using the following expression:

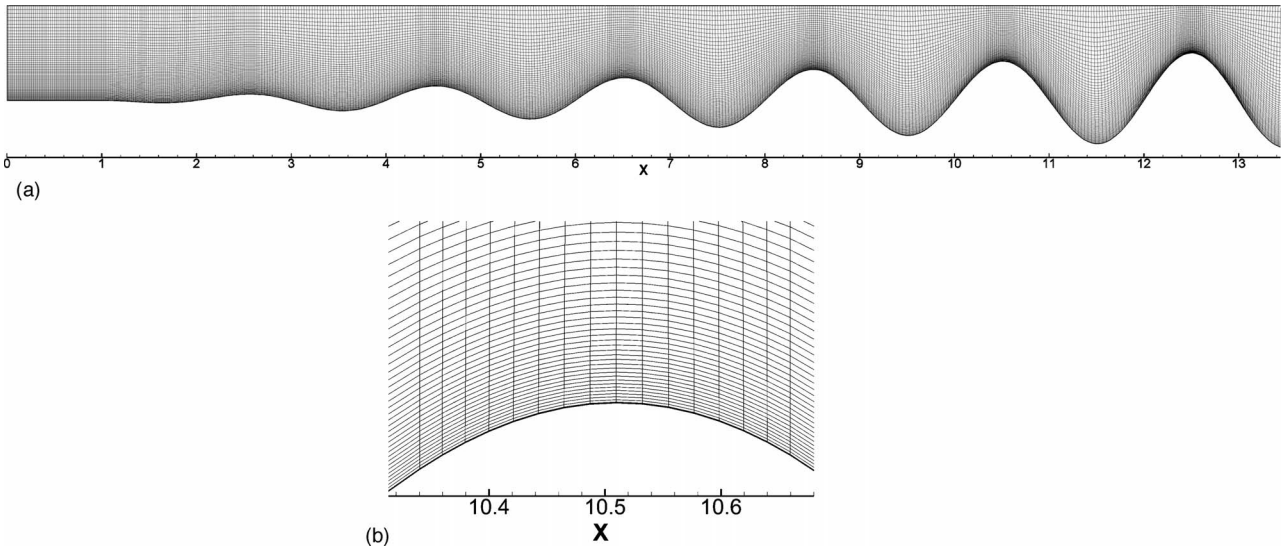


**Fig. 2 Finite element mesh at (*a*) the entrance region, for $EL^*=11.5$ and $a^*=0.5$ and (*b*) a close up view of the wavy wall**

$$C_f = \frac{1}{\mathrm{Re}}\left(\frac{\partial U}{\partial Y} + \frac{\partial V}{\partial X}\right) \tag{9}$$

The pressure drop enhancement percentage of the wavy channel is evaluated by comparing the pressure drop of the wavy channel with the wavy entrance region to the one without the wavy entrance region ($EL^*=0$). The pressure drop enhancement percentage is defined by

$$(\Delta P^*)_{\mathrm{Enh}} = \frac{\Delta P^*}{(\Delta P^*)_{EL=0}} \times 100 \tag{10}$$

where $(\Delta P^*)_{EL=0}$ is pressure drop for a channel without the wavy entrance region.

**2.2 Finite Element Method.** The dimensionless governing equations and boundary conditions are solved using the finite element method. Four node quadrilateral elements were used to mesh the computational domain. Figure 2(*a*) shows the mesh at the entrance region of the channel, and Fig. 2(*b*) shows a close up view at the wavy wall. The mesh consists of 74,400 elements and 75,701 nodes. The elements are concentrated in the region near the wavy wall to accurately capture the local skin-friction and Nusselt numbers. Mesh independent results were confirmed by testing the mesh density in the domain. The number of elements is increased by 10% and 20%. The results indicate that the difference between the models was less than 2.3%, and therefore, the original model was adopted for the numerical simulations. It was also ensured that the channel exit length ($L_e^*$) is long enough so that imposed exit conditions have no effect on the solution. The tridiagonal matrix algorithm (TDMA) iterative solver [15] was used to solve a set of discretized equations for velocity components, while the preconditional conjugate residual (PCR) solver [16] was used to solve for the pressure. The preconditional generalized minimum residual (PGMR) solver was employed to solve a set of discretized equations for energy. The PGMR solver was used for the energy equation because the TDMA solver was ineffective to solve the energy equation. A relaxation factor of 0.5 was specified for all field variables. The problem was solved, and the following condition was used to declare convergence:

$$\frac{1}{\left(\sum_{j=1}^{N} \Pi_j^{m+1}\right)} \sqrt{\sum_{j=1}^{N} (\Pi_j^{m+1} - \Pi_j^{m})^2} \leqslant 10^{-6} \tag{11}$$

where the superscript $m$ refers to the iteration number, the subscript $j$ refers to the node number, $\Pi$ refers to the field variable, and $N$ refers to the maximum node number. Decreasing the value of convergence criteria below $10^{-6}$ does not contribute any significant changes to the results. The convergence monitor represents the sum of the changes of a variable calculated from the results between the current $(m+1)$th iteration and previous $m$th iteration divided by the sum of the current values.

**2.3 Numerical Validation.** The present finite element model was validated against the previously published results of Wang and Chen [2]. They calculated the local Nusselt number along the wavy surface. Their model is similar to the present model, but water was used as a working fluid. Figure 3 shows the local Nusselt number distribution along the wavy wall of the present and the results in Ref. [2]. The results are for $a^*=0.2$, $b^*=2$, $\mathrm{Re}=500$, and $\mathrm{Pr}=6.93$. As shown, a good agreement between the two models is obtained.

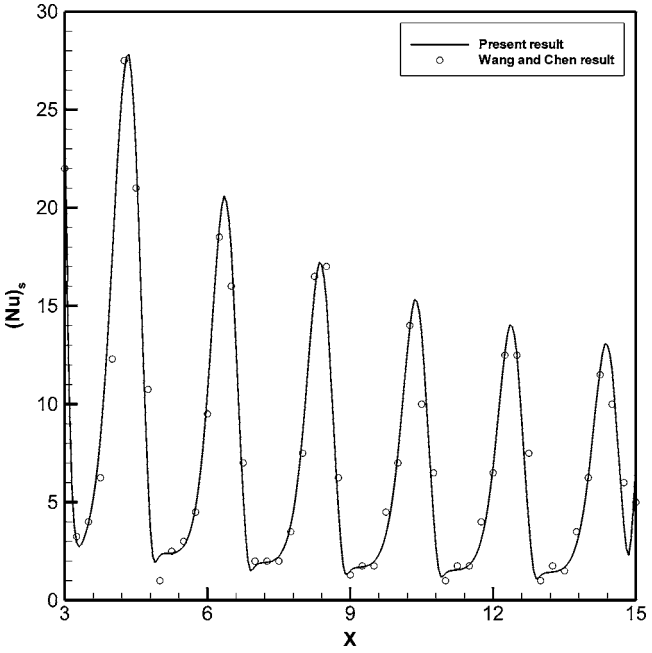


**Fig. 3 Distribution of the local Nusselt number along the wavy wall of the present study and of Wang and Chen's result [2]**

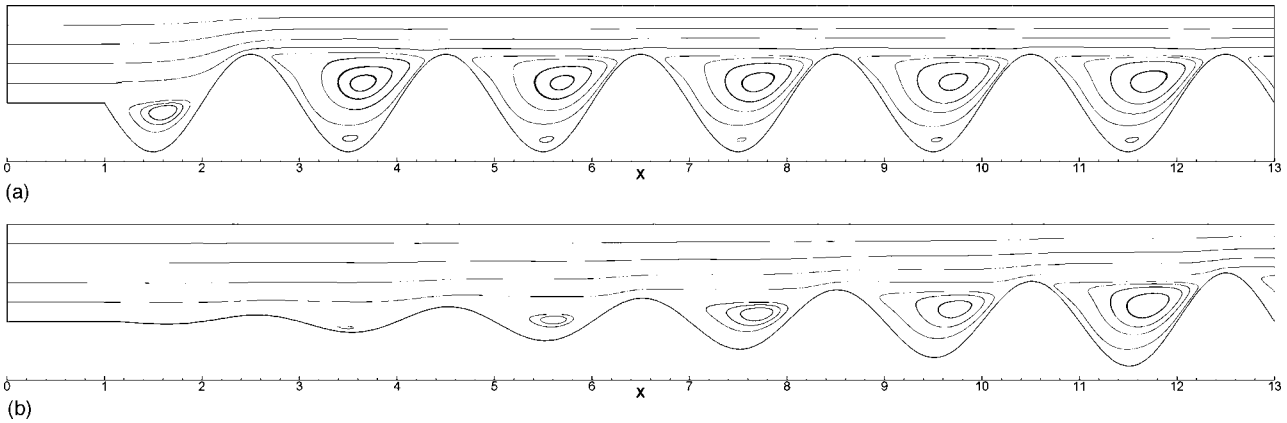


**Fig. 4 Effect of the entrance on streamlines for $a^*=0.5$, Re=500, and (*a*) $EL^*=0$ and (*b*) $EL^*=11.5$**

## 3 Results and Discussion

The effect of introducing the linearly increasing waviness region at the entrance on the hydrodynamics and thermal characteristics of the wavy channel is presented. The results are compared to a wavy channel without the wavy entrance region to study its effect. Air is used as the working fluid, Pr=0.7, and Reynolds numbers of 125–1000 are selected to maintain the laminar flow condition. A transitional flow in a wavy channel is observed at Re=1500 [4]. Air enters the channel with a temperature of $\theta_i=0$, and the wavy wall is maintained at a temperature of $\theta_w=1$. The channel's height and width, including the wavy, upstream, and downstream lengths, are $H^*=1$, $L^*=32$, $L^*_w=26$, $L^*_t=1$, and $L^*_e=5$, respectively. For $1<X<EL^*$, the waviness of the wall is increasing linearly, and for $EL^*<X<27$, the waviness is constant. Different values of $EL^*$ are selected for this study, $EL^*=0$, 5.5, 11.5, and 25.5. For $EL^*=25.5$, the waviness is increasing linearly in the entire length of the wavy section of the channel. As a special case, a wavy channel with $EL^*=0$ is for the channel without a linearly increasing waviness region. The waviness of the wavy wall is examined as a design parameter, and the examined waviness are $a^*=0.125$, 0.25, and 0.5. The wavelength is maintained constant at $b^*=2$.

**3.1 Hydrodynamics Results.** The effect of introducing a linearly increasing waviness region at the entrance of the wavy wall on the flow streamlines is presented. Figures 4(*a*) and 4(*b*) show the streamlines for $a^*=0.5$, Re=500, and $EL^*=0$ and 11.5, respectively. These figures show only the entrance region of the channel, $0<X<13$. Flow enters the channel from the left open side and exits from the right open side. The flow pattern, including the speed of the axial core flow and the recirculating flow in the diverged regions of the channel, has an important influence on the pressure drop in the channel. Figure 4(*a*) shows that a large portion of streamlines is detached from the wavy wall, showing the several separation and reattachment points. The boundary layer separates from the wall at the diverged sections and reattacheds at the converged sections. The recirculating flow completely fills the diverged regions of the channel, reducing the width of the channel for the axial core flow by half. The expansion of the channel cross section and the resulting deceleration of the fluid creates a pressure gradient that opposes the fluid motion. On the other hand, for the wavy wall with the wavy entrance region, Fig. 4(*b*) indicates that the size of the recirculating flow is gradually increasing in the axial direction, and that most of the wavy wall are directly imposed on the axial core flow, reducing the pressure drop and the thermal resistance in the channel.

Figure 5(*a*) shows the distribution of the local skin-friction coefficient for $a^*=0.5$, Re=500, and $EL^*=0$, 5.5, 11.5, and 25.5. For $EL^*=0$, the skin-friction coefficient distribution has the highest magnitude on the first wave, then decreases to eventually reach the periodic condition, but the skin-friction behaves differently when the wavy entrance region is introduced. For $EL^*=5.5$, the skin-friction increases with the waviness of the wall to reach its maximum value at $X=6.5$, then it decreases and becomes constant at the periodic section. With $EL^*=11.5$, the maximum skin-friction is shifted to X=12.5. Figure 5(*a*) indicates that the average skin-friction is significantly decreased when the wavy entrance region is introduced. The effect of the Reynolds number on the distribution of the local skin-friction coefficient is presented in Fig. 5(*b*), and the results are for $EL^*=11.5$, $a^*=0.5$, and Re =125, 250, 500, and 1000. The figure indicates that the skin-friction increases from the first wave for all Re values and has the highest magnitude on the sixth wave. As the Reynolds number increases the amplitudes of skin-friction are also increased at all locations.

The pressure drop across the wavy section of the channel is determined for all examined cases. Figure 6(*a*) shows the pressure drop enhancement, $(\Delta P^*)_{\text{Enh}}$ for Re=500, $a^*=0.5$, and $EL^*=5.5$, 11.5, and 25.5. For the highest examined wavy entrance region length, $EL^*=25.5$, the wavy entrance region is capable of reducing the pressure drop by about 50% at Re=125, and 25% at Re =1000. For $EL^*=11.5$, the wavy entrance region is capable of reducing the pressure drop by about 20% at Re=125 and 11% at Re=1000. The effect of the waviness of the wavy channel is also examined as a design parameter. Figure 6(*b*) shows the pressure drop across the wavy channel with $EL^*=0$ and 11.5, Re=500, and $a^*=0.125$, 0.25, and 0.5. A decrease in the waviness would result in a decrease in the recirculation size and strength because of the smoothness of the wall curvature. As shown, the wavy entrance region is more effective in reducing the pressure drop at high waviness values. With $a^*=0.125$, the wavy entrance region is completely ineffective in reducing the pressure drop. As $a^*$ is increased from $a^*=0.125$ to 0.25 and 0.5, the effectiveness of the wavy entrance region becomes more evident.

**3.2 Thermal Results.** Dimensionless temperature contours for $a^*=0.5$, Re=500, and $EL^*=0$ and 11.5 are shown in Figs. 7(*a*) and 7(*b*), respectively. For $EL^*=0$, Fig. 7(*b*), almost the entire wavy wall is exposed to the relatively low velocity of the recirculation flow in the diverged regions and away from the high velocity of the axial core flow. Additionally, the heat flow out of the wall is captured by the recirculating flow, which increases the fluid temperature. The high temperature of the recirculating flow increases the thermal resistance between the flow and the wall that reduces the heat flow out of the wall. When the wavy entrance region is introduced to the wavy channel, Fig. 7(*b*), the tempera-

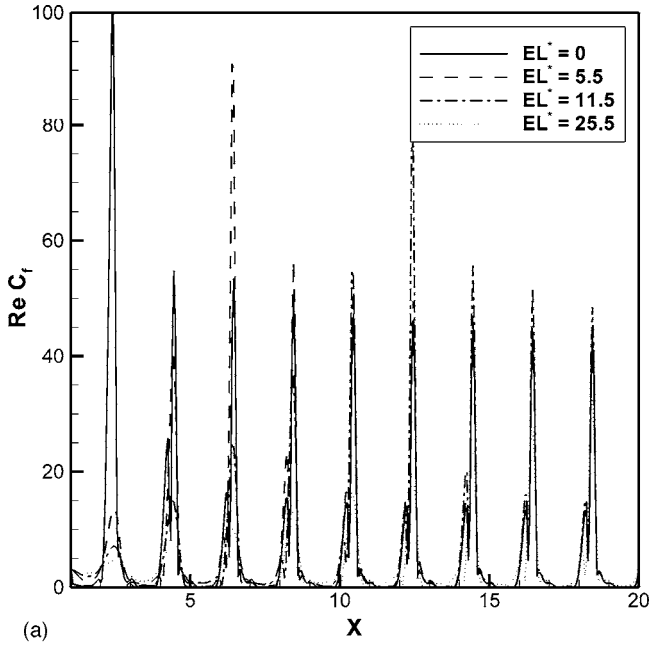


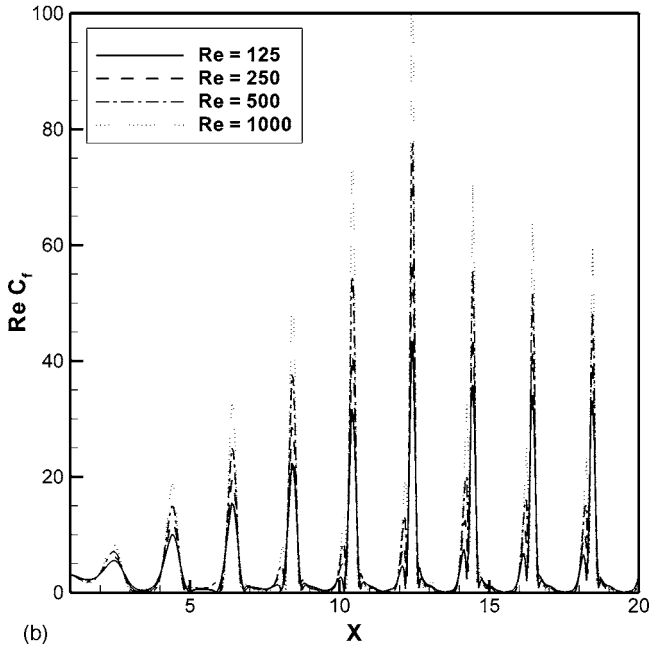


**Fig. 5 (*a*) Distribution of the local skin-friction coefficient for $a^*=0.5$ and Re=500 and (*b*) distribution of the local skin-friction coefficient for $a^*=0.5$ and $EL^*=11.5$**

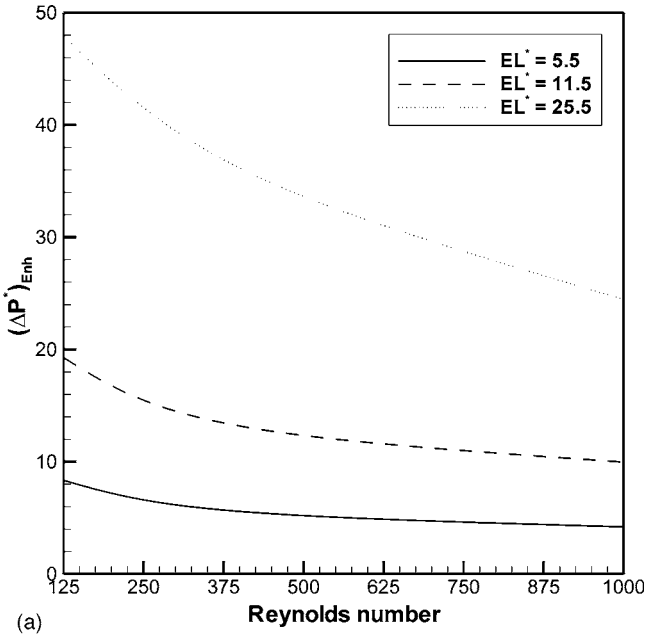


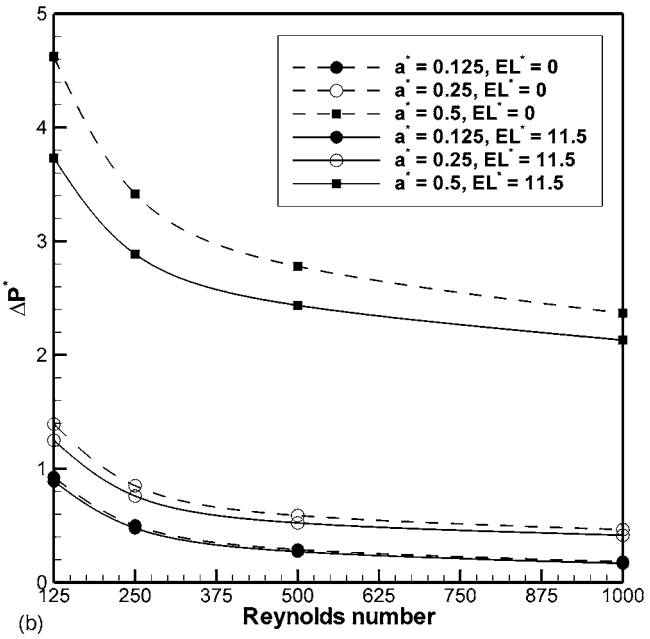


**Fig. 6 (*a*) The effect of the Reynolds number on the pressure drop enhancement across the wavy channel and (*b*) the effect of the Reynolds number on the pressure drop across the wavy channel**

ture of the fluid in the channel is significantly decreased. With this design, the wavy wall is exposed more to the high velocity of the axial core flow, increasing the heat flow out of the wall. Figure 7(*b*) shows that higher value isotherms penetrate farther downstream, indicating that the colder fluid is getting closer to the wavy wall.

Figure 8(*a*) shows the effect of Re on the distribution of the local Nusselt number along the wavy wall for $a^*=0.5$ and $EL^*=11.5$. The general behavior of the $(\mathrm{Nu})_s$ is similar to the skin-fiction. The $(\mathrm{Nu})_s$ is extremely high at $X=1$ because the temperature difference between the wall and bulk flow is at the maximum. For $X>1$, the $(\mathrm{Nu})_s$ increases for all Re values and has the highest magnitude on the sixth wave, at $X=12.5$. Then, it decreases and becomes constant at the periodic section. As the Reynolds number increases the amplitudes of $(\mathrm{Nu})_s$ are also increased at all locations. Figure 8(*b*) shows the effect of introducing the wavy entrance region on the average Nusselt number for $a^*=0.25$ and $EL^*=5.5$, 11.5, and 25.5. As expected, increasing the Reynolds number increases the $(\mathrm{Nu})_{\mathrm{ave}}$ for all examined cases. The concept of the wavy entrance region has not only a positive effect on the pressure drop, but also on the average Nusselt number. The $(\mathrm{Nu})_{\mathrm{ave}}$ is increased as the magnitude of $EL^*$ is increased from zero. For $EL^*>0$, most of the wavy wall at the entrance are directly imposed on the axial core flow and away from the recirculating flow, reducing thermal resistance in the channel and promoting heat transfer. However, the noticed heat transfer enhancement is not significant.

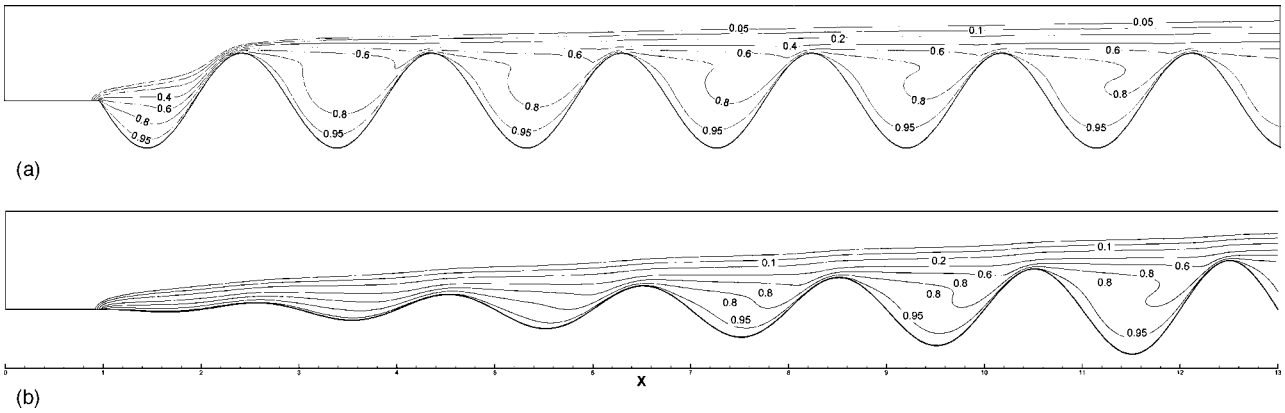


**Fig. 7 Effect of the entrance on isotherms for $a^*=0.5$, Re=500, and (*a*) $EL^*=0$ and (*b*) $EL^*=11.5$**

## 4 Conclusion

Results of the fluid flow and heat transfer in a wavy channel with a linearly increasing waviness at the entrance region is presented. The aim of the wavy entrance region is to reduce the pressure drop in the wavy channel. The considered geometry consists of a channel formed by two wavy plates described by a sinusoidal profile and maintained at a uniform temperature and solved numerically. The result indicates that the linearly increasing waviness at the entrance significantly reduces the pressure drop in the channel, and increasing its length reduces the pressure drop more. The effectiveness of the linearly increasing waviness is more significant at high waviness values and at a low Reynolds number flow. On the other hand, the linearly increasing waviness slightly increases the average Nusselt number. With the wavy entrance region, the wavy wall is exposed to the high velocity of the axial core flow more increasing the heat flow out of the wall. However, the heat transfer enhancement is not significant.

## Nomenclature

$A$ = constant in Eq. (1*a*)
$a$ = waviness of the wavy wall, m
$B$ = constant in Eq. (1*a*)
$b$ = wavelength of the channel, m
$C_p$ = specific heat, kJ/kg °C
$C_f$ = skin-friction coefficient
$d$ = surface length of the wavy wall, m
$EL$ = length of the increasing waviness region, m
$H$ = half separation distance between wavy walls, m
$k$ = thermal conductivity, W/m °C
$L$ = total length of the channel, m
$L_e$ = downstream length, m
$L_i$ = upstream length, m
$L_w$ = horizontal length of wavy wall, m
$N$ = maximum node number
$\hat{n}$ = dimensionless coordinate normal to the surface
$P$ = pressure, $N/m^2$
Pr = Prandtl number
Re = Reynolds number
$\hat{S}$ = dimensionless coordinate along to the surface
$T$ = temperature, °C
$u_i$ = average inlet velocity, m/s
$U$, $u$ = dimensional and dimensionless $x$-velocity component, m/s
$V$, $v$ = dimensionless and dimensional $y$-velocity component, m/s

**Greek**

$\Pi$ = general field variable

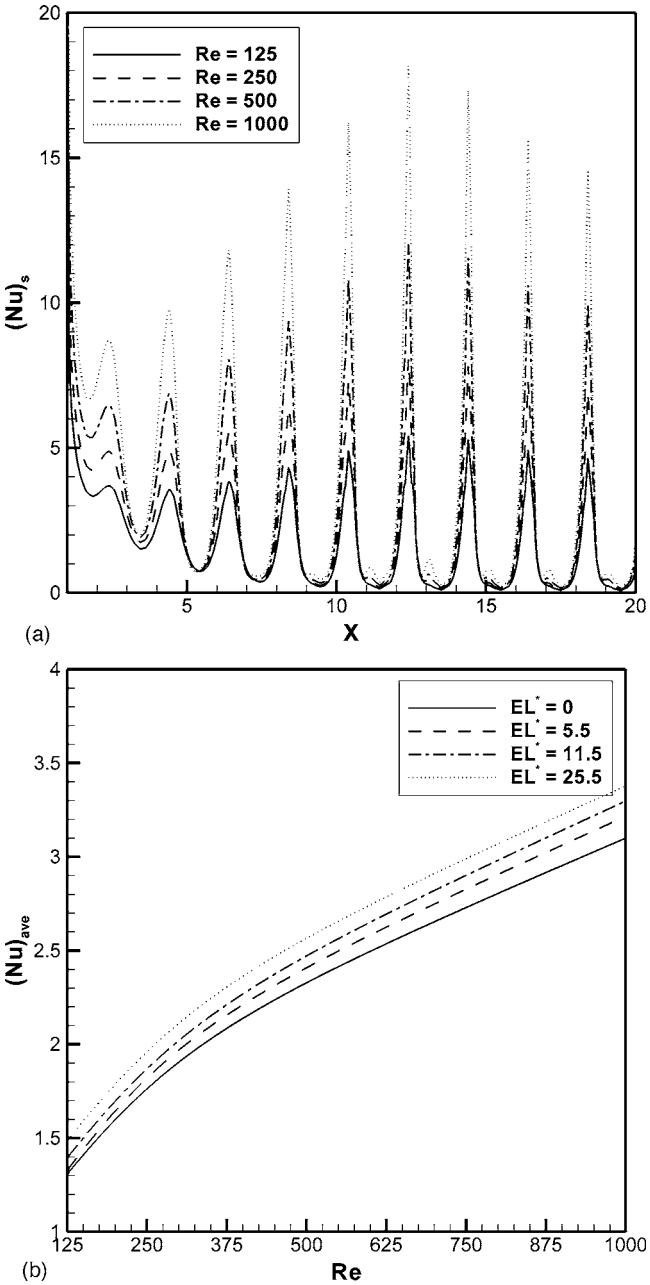


**Fig. 8 (*a*) Distribution of the local Nusselt number for $a^*=0.5$ and $EL^*=11.5$ and (*b*) the effect of the Reynolds number on the average Nusselt number**

$\theta$ = dimensionless temperature
$\mu$ = viscosity, $N/m^2$ s
$\rho$ = density, $kg/m^3$

**Subscripts**

ave = average
$i$ = inlet
$j$ = node number
$s$ = local
$w$ = wall

**Superscripts**

$m$ = iteration number
$*$ = dimensionless quantity

## References


[1] Jacobi, A., and Shah, R., 1998, "Air-Side Flow and Heat Transfer in Compact Heat Exchanger: A Discussion of Enhancement," Heat Transfer Eng., **19**, pp. 29–41.

[2] Wang, C., and Chen, C., 2002, "Forced Convection in a Wavy-Wall Channel," Int. J. Heat Mass Transfer, **45**, pp. 2587–2595.

[3] Bahaidarah, H., Anand, N., and Chen, H., 2005, "Numerical Study of Heat and Momentum Transfer in Channels With Wavy Walls," Numer. Heat Transfer, Part A, **47**, pp. 417–439.

[4] Rush, T., Newell, T., and Jacobi, A., 1999, "An Experimental Study of Flow and Heat Transfer in Sinusoidal Wavy Passages," Int. J. Heat Mass Transfer, **42**, pp. 1541–1553.

[5] Gradeck, M., Hoareau, B., and Lebouche, M., 2005, "Local Analysis of Heat Transfer Inside Corrugated Channel," Int. J. Heat Mass Transfer, **48**, pp. 1909–1915.

[6] Nishimura, T., and Matsune, S., 1996, "Mass Transfer Enhancement in a Sinusoidal Wavy Channel for Pulsatile Flow," Heat Mass Transfer, **32**, pp. 65–72.

[7] Guzman, A., and Amon, C., 2006, "Dynamical Flow Characterization of Transitional and Chaotic Regimes in Converging-Diverging Channels," J. Fluid Mech., **321**, pp. 25–57.

[8] Stalio, E., and Piller, M., 2007, "Direct Numerical Simulation of Heat Transfer in Converging-Diverging Wavy Channels," ASME J. Heat Transfer, **129**, pp. 769–777.

[9] Sawyers, D., Sen, M., and Chang, H., 1998, "Heat Transfer Enhancement in Three-Dimensional Corrugated Channel Flow," Int. J. Heat Mass Transfer, **41**, pp. 3559–3573.

[10] Fabbri, G., 2000, "Heat Transfer Optimization in Corrugated Wall Channels," Int. J. Heat Mass Transfer, **43**, pp. 4299–4310.

[11] Mahmud, S., Islam, A., and Mamun, M., 2002, "Separation Characteristics of Fluid Flow Inside Two Parallel Plates With Wavy Surface," Int. J. Eng. Sci., **40**, pp. 1495–1509.

[12] Lin, J., Huang, C., and Su, C., 2007, "Dimensional Analysis for the Heat Transfer Characteristics in the Corrugated Channels of Plate Heat Exchangers," Int. Commun. Heat Mass Transfer, **34**, pp. 304–312.

[13] Metwally, H., and Manglik, R., 2004, "Enhanced Heat Transfer Due to Curvature-Induced Lateral Vortices in Laminar Flow in Sinusoidal Corrugated-Plate Channels," Int. J. Heat Mass Transfer, **47**, pp. 2283–2293.

[14] Mohamed, N., Khedidja, B., Belkacem, Z., and Michel, D., 2005, "Numerical Study of Laminar Forced Convection in Entrance Region of a Wavy Wall Channel," Numer. Heat Transfer, Part A, **53**, pp. 35–52.

[15] Patankar, S., 1980, *Numerical Heat Transfer and Fluid Flow*, Hemisphere, New York.

[16] Brooks, A., and Hughes, T., 1982, "Streamline Upwind/Petrov–Galerkin Formulation for Convection Dominated Flow With Particular Emphasis on the Incompressible Navier–Stokes Equation," Comput. Methods Appl. Mech. Eng., **32**, pp. 199–259.

# The Heat/Mass Transfer Analogy for a Simulated Turbine Endwall With Fillets

**S. Han**
Korea Institute of Machinery and Materials,
Daejeon 305-343, Korea
e-mail: sjhan@kimm.re.kr

**R. J. Goldstein**[1]
Heat Transfer Laboratory,
Department of Mechanical Engineering,
University of Minnesota,
Minneapolis, MN 55455
e-mail: rjg@me.umn.edu

*Mass transfer measurements are employed as alternative methods for heat transfer measurement because of the difficulty of heat transfer measurements in thin boundary layers, complicated secondary flows, and large thermal gradients. Even though mass transfer experiments are fast and show detailed local measurement data, the conversion of mass transfer results to heat transfer data requires the heat/mass transfer analogy factors in detail. Therefore, the usefulness of mass transfer data depends on finding a simple analogy factor. The heat/mass transfer analogy on a simulated turbine endwall with fillets is evaluated in the present paper. Since the heat/mass transfer analogy factor may not be always the same, the heat/mass transfer analogy should be verified for other different geometries and experimental conditions. To utilize the heat/mass transfer analogy fully, it is necessary to check that the presence of different aerodynamic conditions caused by the fillets affects the heat/mass transfer analogy on a simulated turbine endwall with fillets. To compare heat transfer data and mass transfer data, heat transfer measurements on the endwall with fillets are conducted with a thermal boundary layer measurement technique and mass transfer measurements employing naphthalene sublimation technique on the endwall with the fillets are extracted from literature with equivalent experimental conditions and a similar geometry. As expected by heat transfer and mass transfer equations, the heat/mass transfer analogy factor is applied and shows a good agreement between heat transfer and mass transfer results on the endwall with the fillets from the leading edge to the trailing edge.* [DOI: 10.1115/1.2969756]

*Keywords: heat/mass transfer analogy, thermal boundary layer, constant wall temperature, turbine endwall, turbine blade, fillet, gas turbine*

## Introduction

Compared with mass transfer experiments with equivalent experimental conditions, heat transfer experiments with a constant temperature condition are often difficult, expensive, and sensitive to conduction and radiation errors so that mass transfer experiments have been used to get heat transfer results instead. Mass transfer experiments can get local results, are fast, and free of conduction and radiation errors, which always occur in heat transfer experiments. However, it requires heat/mass transfer analogy factors in detail for equivalent experimental conditions and a geometry to convert mass transfer results to heat transfer data with confidence. There are a couple of methods to evaluate heat/mass transfer analogy factors, but the best way to evaluate them is to conduct heat transfer and mass transfer experiments in a given geometry with equivalent experimental conditions. However, the difficulty of maintaining equivalent experimental conditions in heat transfer makes researchers to find other alternatives.

Lewis [1] investigated heat transfer and mass transfer, respectively, and showed that the heat transfer results can be accurately related to the mass transfer results using universal velocity profiles in a turbulent boundary layer. Endwall heat transfer coefficient distributions were measured by Blair [2] in a large scale turbine cascade. Local heat transfer coefficients were measured using about 150 heaters covering the test section from the leading edge to the trailing edge. The heat transfer results are evaluated to measure the power input of each heater to maintain a constant temperature on the endwall. He showed that endwall heat transfer is strongly influenced by the existence of the large vortex located in the corner between the endwall and the suction surfaces. Local heat transfer measurement on the endwall and blade surfaces was conducted by Granziani et al. [3]. They measured the power input to each heater and calculated the heat transfer coefficients. They found that the secondary flow strongly affects the heat transfer on the endwall and the pressure surface of the blade, but does not influence the heat transfer on the pressure surface. They also found that the inlet boundary layer thickness on the endwall has a significant effect on the endwall and suction surface heat transfer. Chen and Goldstein [4] suggested using the Colburn relation $\mathrm{Nu}/\mathrm{Sh}=(\mathrm{Pr}/\mathrm{Sc})^n$, $n=1/3$ to get an analogy factor. The naphthalene sublimation technique and the heat/mass transfer analogy with a constant heat flux boundary condition were extensively reviewed by Goldstein and Cho [5]. They recommended $n=1/3$ for a laminar flow and $n=0.14$ for wake regions in a Colburn type relation. Eckert et al. [6] indicated three methods of applying the extended heat/mass transfer analogy: The first is deduced from the Navier–Stokes equation for a constant property fluid, the second is obtained from empirical expressions of heat transfer and mass transfer equations for a specified flow, and the third involves the assumption that local Nusselt numbers are proportional to the local Sherwood numbers with the averaged analogy factor $\overline{\mathrm{Nu}}/\overline{(\mathrm{Sh})}$. They compared experimental heat transfer and mass transfer results with the heat/mass transfer analogy for laminar, turbulent, and three-dimensional flow. However, comparison across different studies is difficult due to the different geometric and experimental conditions. Local and average mass transfer rates from a rectangular cylinder were measured by Yoo et al. [7]. Comparison between the mass transfer results and the heat transfer results with a

[1]Corresponding author.

Contributed by the Heat Transfer Division of ASME for publication in the JOURNAL OF HEAT TRANSFER. Manuscript received June 29, 2007; final manuscript received May 8, 2008; published online October 14, 2008. Review conducted by Bengt Sunden.

  

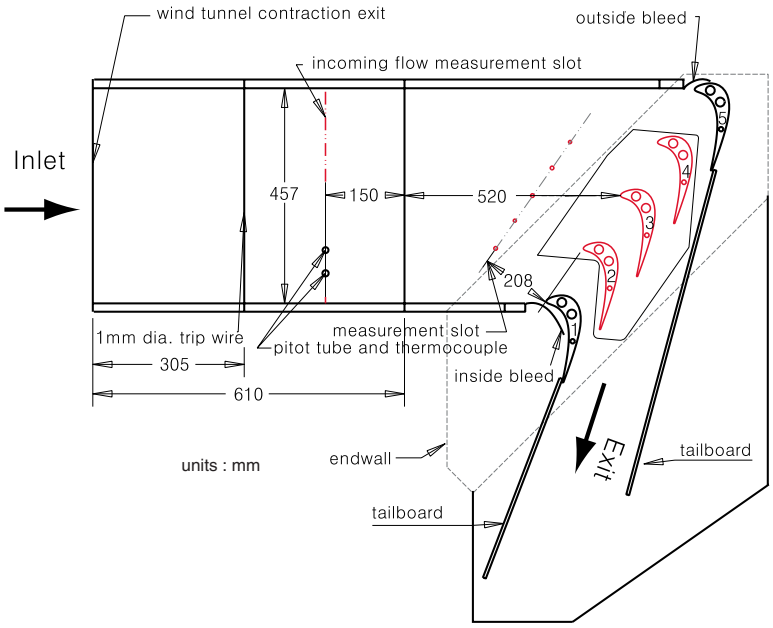


**Fig. 1 Test section for the heat and mass transfer experiments**

constant heat flux condition was reported by them. It was concluded that the discrepancy between the heat and mass transfer results comes from the difference in the boundary condition, the effect of $n$ in the Colburn relation, and the conduction error in the heat transfer and mechanical erosion in mass transfer. Han and Goldstein [8] investigated a heat/mass transfer analogy on a simulated turbine endwall with a constant temperature condition and a constant concentration condition. On the endwall, the heat/mass transfer analogy in a fully developed boundary layer is valid with Colburn relation $\mathrm{Nu}/\mathrm{Sh}=(\mathrm{Pr}/\mathrm{Sc})^n$, $n=0.5$. Han and Goldstein [9] conducted heat/mass transfer experiment on a simulated turbine blade to investigate the heat/mass transfer analogy. They found that the heat/mass transfer analogy changes along the pressure surface and suction surface unlike the heat/mass transfer analogy on the endwall. It is concluded that flows near a blade surface, developing from laminar to turbulence, affect the heat/mass transfer analogy factors.

Since the heat/mass transfer analogy factor may not be always the same, the analogy should be verified for other geometries and experimental conditions. To reduce aerodynamic loss in gas tribunes, fillets have recently been added to blade leading edges. Heat(mass) transfer measurements are conducted to find the heat transfer performance with fillets (Han and Goldstein [10]). To utilize the heat/mass transfer analogy fully, it is necessary to check how the aerodynamic conditions caused by the fillets affect the heat/mass transfer analogy on a simulated turbine endwall with fillets. The present paper investigates to extend the validity of the heat/mass transfer analogy and determines the analogy factors on a simulated turbine endwall with fillets through heat transfer and mass transfer experiments.

## Heat/Mass Transfer Analogy

The heat/mass transfer analogy is derived from the conservation equations of momentum, energy, and concentration of a constant property fluid by Nusselt [11] and Schmidt [12]. Mass transfer results with equivalent experimental conditions can be converted to heat transfer data by the heat/mass transfer analogy and vice versa. The heat/mass transfer conversion is possible due to the similarity of the equations governing heat transfer and mass transfer.

The nondimensional heat transfer equation

$$\frac{D\theta}{D\tau}=\frac{1}{\mathrm{RePr}}\frac{\partial}{\partial\hat{x}_i}\left(\left(1+\frac{\varepsilon}{\nu}\frac{\mathrm{Pr}}{\mathrm{Pr}_t}\right)\frac{\partial\theta}{\partial\hat{x}_i}\right) \tag{1}$$

and the nondimensional mass transfer equation

$$\frac{Dm}{D\tau}=\frac{1}{\mathrm{ReSc}}\frac{\partial}{\partial\hat{x}_i}\left(\left(1+\frac{\varepsilon}{\nu}\frac{\mathrm{Sc}}{\mathrm{Sc}_t}\right)\frac{\partial m}{\partial\hat{x}_i}\right) \tag{2}$$

are very similar in the format. Hence, if the boundary conditions for heat transfer and mass transfer are equivalent for a given geometry, if Pr is equal to $\mathrm{Sc}_t$, and $\mathrm{Pr}_t$ is equal to Sc, then $\theta$ in Eq. (1) and $m$ in Eq. (2) have the same solution. It should, however, be pointed that the Prandtl number in a heat transfer experiment is typically different from the Schmidt number in a mass transfer experiment. Therefore, simple relations for the case of unequal Prandtl and Schmidt numbers are prerequisite to use the heat/mass transfer analogy easily.

The Nusselt (Nu) and Sherwood (Sh) numbers are a function of the Prandtl and Schmidt numbers, respectively, in addition to the Reynolds number and the geometry. Their local values can be described as

$$\mathrm{Nu}=f(\mathrm{Re},\mathrm{Pr},\hat{x}_i),\quad \mathrm{Sh}=f(\mathrm{Re},\mathrm{Sc},\hat{x}_i) \tag{3}$$

For an example, the relation of Eq. (4) is used for obtaining the Nusselt and Sherwood numbers in the laminar flow on a flat plate.

$$\mathrm{Nu}=C_1\mathrm{Re}^m\mathrm{Pr}^n,\quad \mathrm{Sh}=C_1\mathrm{Re}^m\mathrm{Sc}^n \tag{4}$$

However, the Prandtl number of air in the region studied is $\approx$0.7 while the Schmidt number of naphthalene (in air) is $\approx$2.28. This means that a conversion factor is required to obtain Nu from Sh and vice versa.

$$\mathrm{Nu}=F\cdot\mathrm{Sh} \tag{5}$$

Thus, for the same Reynolds number, the analogy factor for a flat plate can be expressed as

$$F=\frac{\mathrm{Nu}}{\mathrm{Sh}}=\left(\frac{\mathrm{Pr}}{\mathrm{Sc}}\right)^n \tag{6}$$

which is called as Colburn relation. The heat/mass transfer analogy is fully described in Eckert et al. [6] and Han and Goldstein [8].

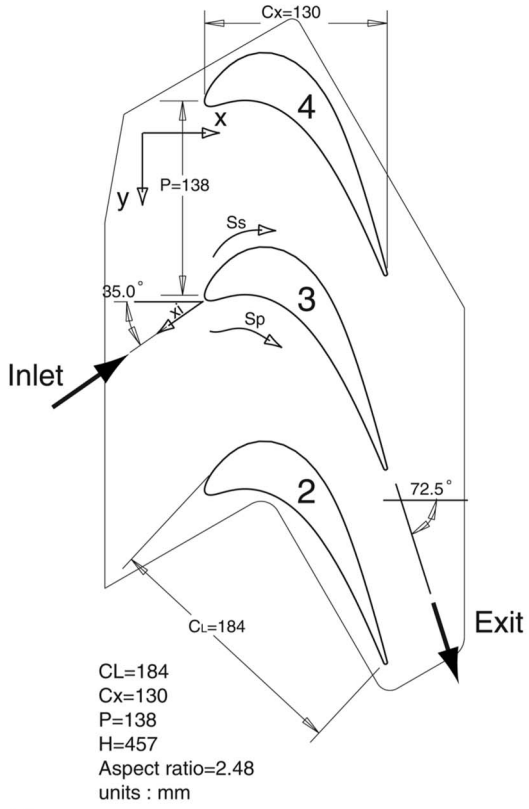


(a)

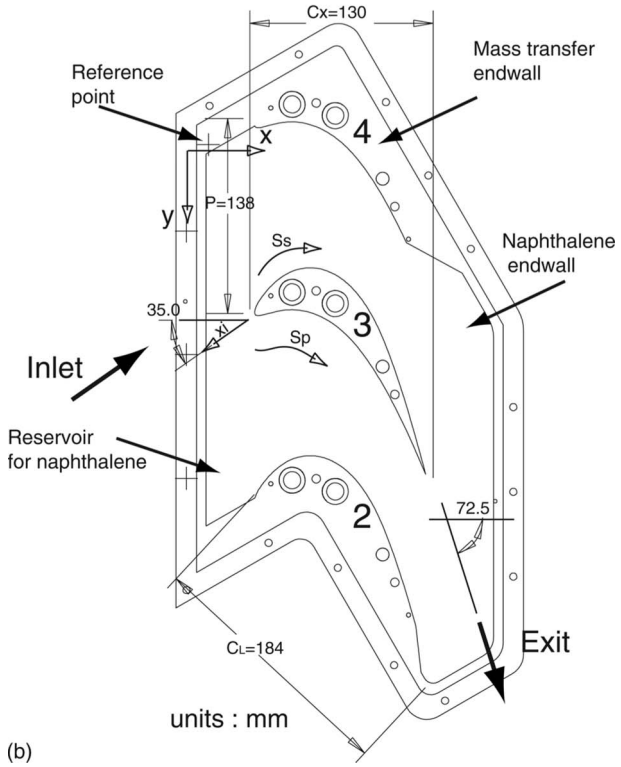


(b)

**Fig. 2 Blade configuration on the heat and mass transfer endwalls**

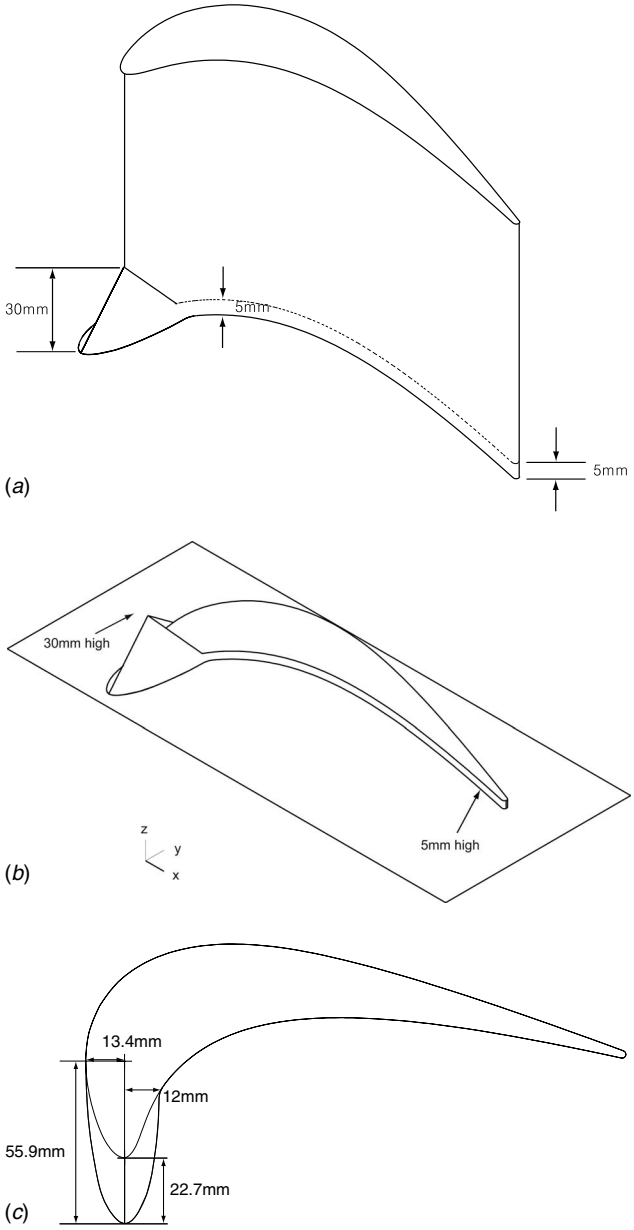


**Fig. 3 The geometry of the blade with the fillet**

## Experimental Apparatus

**Description of the Test Section.** The linear turbine cascade, shown in Fig. 1, consists of five 457 mm long simulated high-performance turbine rotor blades made of aluminum. The test section is connected to the exit of the contraction region of a blowing-type wind tunnel. The bottom endwall has a large opening where the test endwall can be placed. The top endwall has one rectangular window for the insertion of the thermal boundary layer probe and visual observation. The profile of a modern high-performance turbine blade, modified for experimental conditions, is used for the blades in the cascade. The straight section of the tunnel, with a cross section of $457 \times 457$ mm$^2$ and a length of 610 mm, has slots for inserting grid turbulence generators. A 1 mm diameter trip wire is placed near the exit of the contraction section on the bottom endwall (820 mm upstream of the stagnation point of the central blade) to induce a near-fully-developed turbulent boundary layer on the endwall at the inlet to the cascade. The cascade exit flow velocity is calculated using the incoming flow velocity and the area aspect ratio (2.72).

**Fillet.** The design of the fillet is based on the suggestions of Zess and Thole [13]. The elliptical, asymmetric, and sharp slope fillet in Fig. 3 is manufactured in aluminum by a computer numerical control (CNC) machine. The fillet is $7.5\delta_1$ high and $6\delta_1$

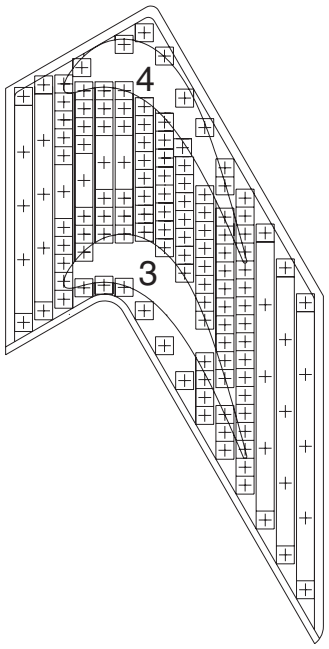


**Fig. 4 Constant temperature endwall with heaters and thermocouple locationsThermal boundary layer probe schematic**

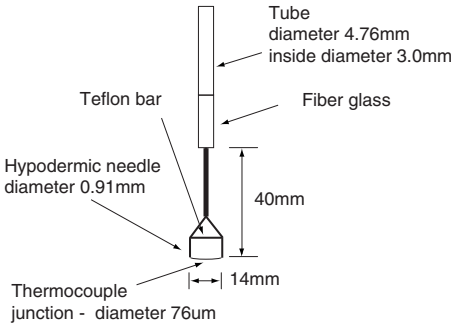


**Fig. 5 Thermal boundary layer probe schematic**

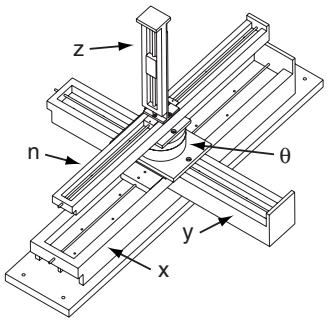


**Fig. 6 Five-axis measurement unit sketch**

long from the stagnation point of a blade. As can be seen, the fillet has a design like a shoe for easy assembly to the blade. It is fixed by mounting-pins and bolts between the blade and the endwall. The fillets sit on the endwall and the blades fit into them like shoes. The fillets are located on blades 2, 3, and 4 to provide periodic flow condition in the blade passage. The fillet was previously used in mass transfer experiments and described in detail by Han and Goldstein [10].

**Constant Temperature Endwall.** The constant temperature endwall has 128 strip heaters and 138 *E*-type thermocouples. Each heater has one *E*-type thermocouple except the $192 \times 12.8$ mm$^2$ heaters, which have three. The locations of the heaters are shown in Fig. 4, with the locations of the thermocouples marked by the plus symbols. The constant temperature endwall only covers one passage between the third and the fourth blade. It consists of an aluminum plate, Kapton strip heaters, an *E*-type thermocouple, a balsa wood insulation, and a phenolic insulated plate. More information is described in Han and Goldstein [14].

**Thermal Boundary Layer Probe.** To measure linear conduction regions of the thermal boundary layers from a wall, a thin thermocouple probe is designed to minimize the effect of flow disturbances and conduction error. According to the suggestion from Blackwell and Moffat [15], a 76 $\mu$m diameter *E*-type thermocouple, which is not relatively sensitive to conduction error, is selected to measure temperatures from a wall. To minimize flow disturbance and conduction error, the junction of the thermocouple is butt-welded by an electrical discharge welding technique. The probes are shown in Fig. 5. The thermocouple supported by two hypodermic needles has an exposed part, which is 14 mm wide and 1 mm high, and has a slight curvature, so that the junction touches the wall first. The endwall probe has a straight shape to make movement easy and guarantee the measurement position. Detailed information is described in Han and Goldstein [14].

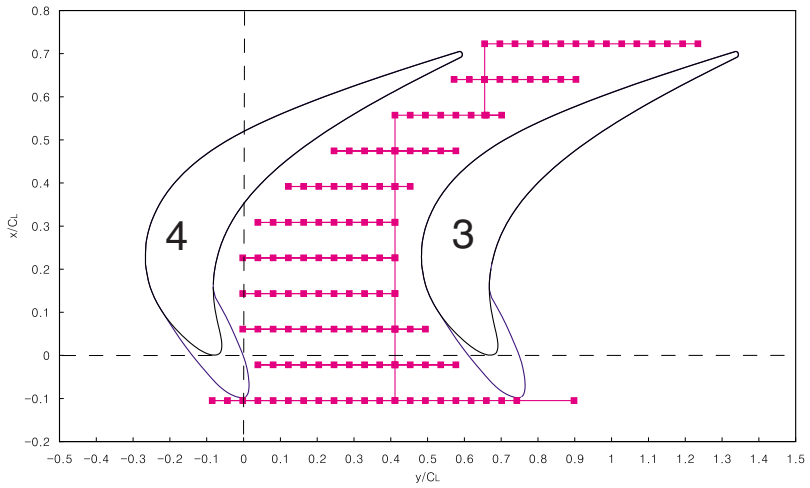


**Fig. 7 Endwall measurement positions for heat transfer experiments with fillets**

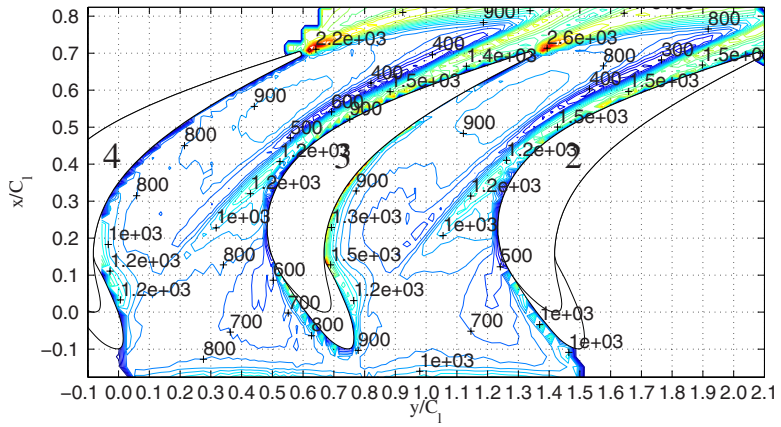


**Fig. 8 Sherwood number contour plot with $Re_{ex}=4.31\times10^5$ and Tu =0.2%, Han and Goldstein [10]**

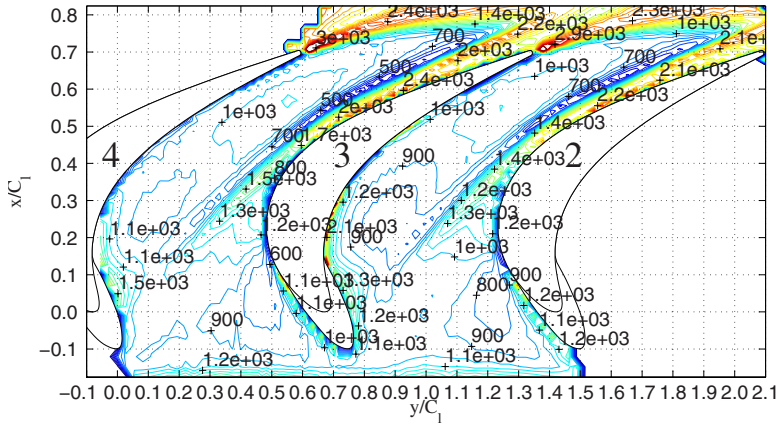


**Fig. 9 Sherwood number contour plot with $Re_{ex}=5.65\times10^5$ and Tu =0.2%, Han and Goldstein [10]**

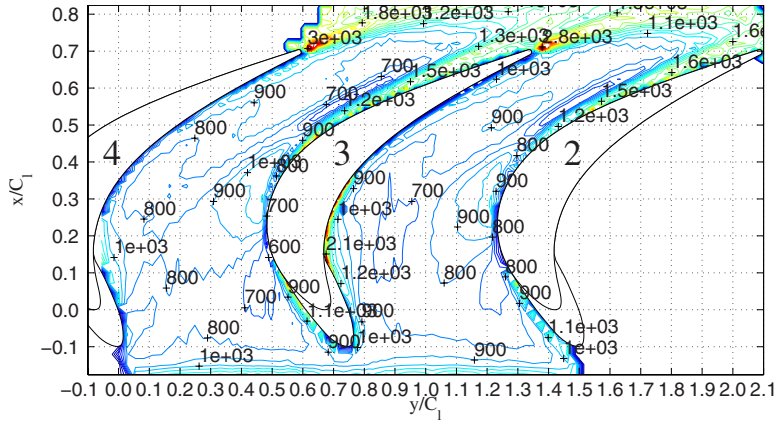


**Fig. 10 Sherwood number contour plot with $Re_{ex}=3.57\times10^5$ and Tu =8.5%, Han and Goldstein [10]**

**Table 1 Mass transfer experimental conditions on the endwall with fillets Han and Goldstein [10]**

| No. | Run No. | Trip wire (mm) | $Re_{ex}$ | $U_{ex}$ (m/s) | Tu (%) |
|---|---|---|---|---|---|
| 1 | F-MT-Run1 | 1.0 | $4.31\times10^5$ | 38.4 | 0.2 |
| 2 | F-MT-Run2 | 1.0 | $5.65\times10^5$ | 49.9 | 0.2 |
| 3 | F-MT-Run3 | 1.0 | $3.57\times10^5$ | 31.8 | 8.5 |
| 4 | F-MT-Run4 | 1.0 | $4.97\times10^5$ | 44.0 | 8.5 |

**Table 2 Heat transfer experimental conditions on the endwall with fillets**

| No. | Run No. | Trip wire (mm) | $Re_{ex}$ | $U_{ex}$ (m/s) | Tu (%) |
|---|---|---|---|---|---|
| 1 | F-HT-Run1 | 1.0 | $2.58\times10^5$ | 22.13 | 0.2 |
| 2 | F-HT-Run2 | 1.0 | $1.89\times10^5$ | 16.36 | 0.2 |
| 3 | F-HT-Run3 | 1.0 | $2.27\times10^5$ | 20.02 | 8.5 |
| 4 | F-HT-Run4 | 1.0 | $1.59\times10^5$ | 14.06 | 8.5 |

**Five-axis Measurement Unit and Computer-Controlled Power Supply.** In the present study, the heat transfer measurements occur near a constant temperature wall between two blades. To guarantee the measurement locations and find the wall with high precision a multiaxis measurement system is built in the Heat Transfer Laboratory of the University of Minnesota, as shown in Fig. 6. It consists of four unislides ($x$, $y$, $z$, and $n$) and one rotating table ($\theta$), a supporter, and a modified five-axis motion controller.

To maintain a constant temperature condition on the wall, the endwall needs one power supply for each heater. Therefore, a computer-controlled power supply with 128 power output channels and proportional and integral (PI) algorithm is designed in the Heat Transfer Laboratory of the University of Minnesota. The measurement and the power control systems are described in Han and Goldstein [14].

**Experimental Procedure.** To investigate the heat/mass transfer analogy on the simulated turbine endwall with the fillets, heat transfer and mass transfer experiments are conducted with equivalent experimental conditions in the similar test setup, respectively.

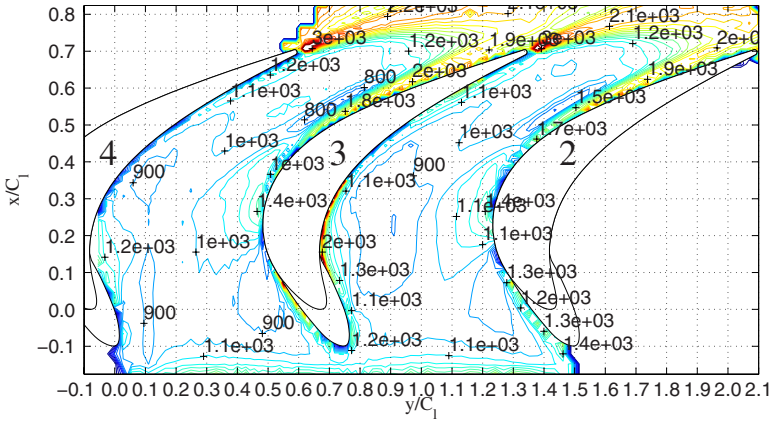


**Fig. 11 Sherwood number contour plot with $Re_{ex}=4.97\times10^5$ and Tu =8.5%, Han and Goldstein [10]**

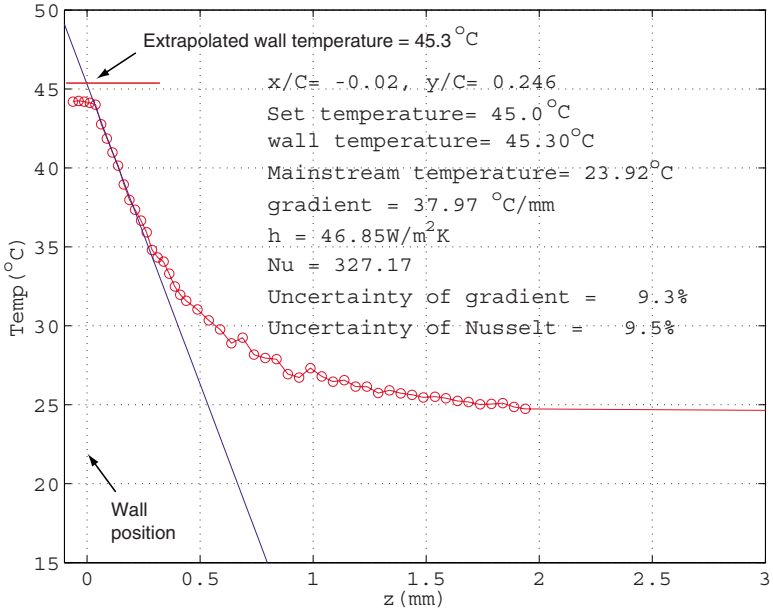


**Fig. 12 Sample thermal boundary layer profile on the endwall**

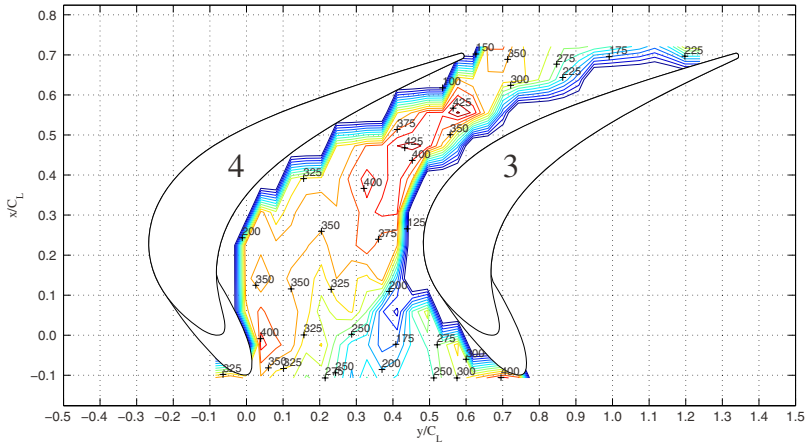


**Fig. 13 Nusselt number contour plot with $Re_{ex}=1.89\times10^5$ and Tu=0.2%**

**Mass Transfer Experiment.** The naphthalene sublimation technique is used to obtain local mass transfer results on the mass transfer endwall with the fillets. The detailed description of this technique is provided by Goldstein and Cho [5].

The test endwall is casted by naphthalene liquid in a casting mold. After the naphthalene surface is solidified and removed from the cast, the test section is scanned first before a wind tunnel experiment. After the wind tunnel experiment, the test section is scanned again and mass transfer results are obtained from a saturation vapor density and experimental period.

The saturation vapor density, $\rho_{v,w}$, is calculated from the perfect gas law equation

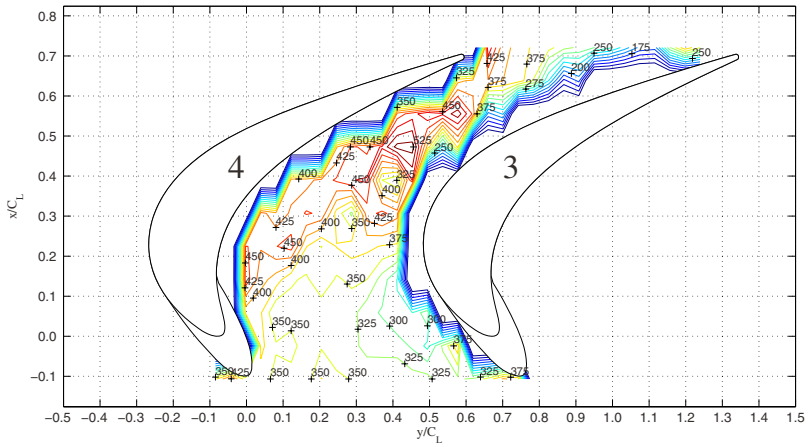


**Fig. 14 Nusselt number contour plot with $Re_{ex}=2.58\times10^5$ and Tu=0.2%**

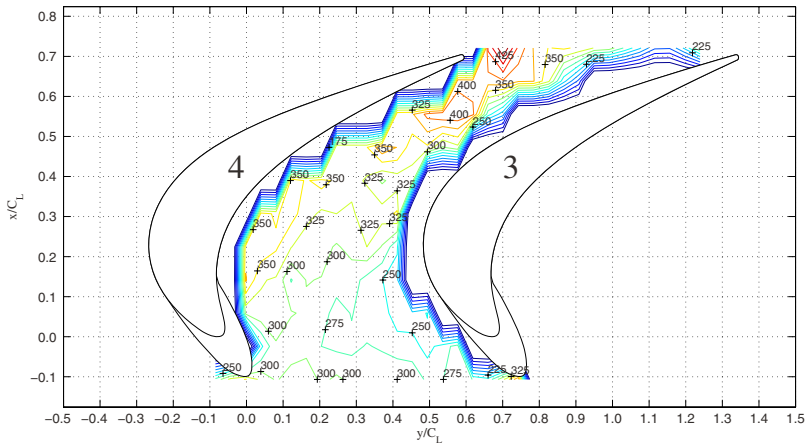


**Fig. 15 Nusselt number contour plot with $Re_{ex}=1.59\times10^5$ and Tu=8.5%**

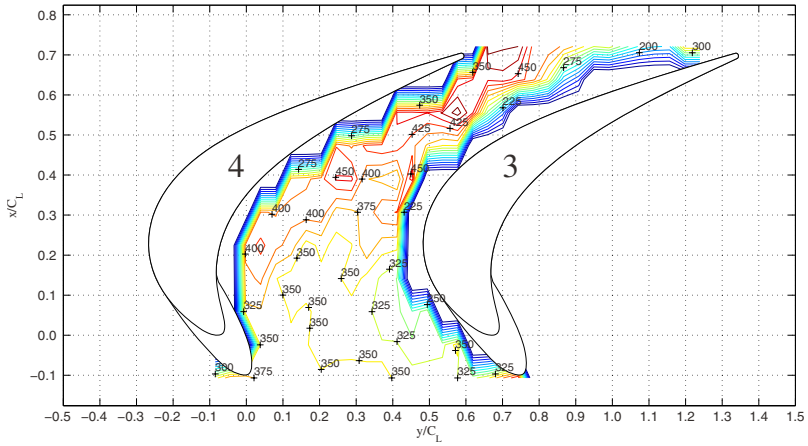


**Fig. 16 Nusselt number contour plot with $Re_{ex}=2.27\times10^5$ and Tu =8.5%**

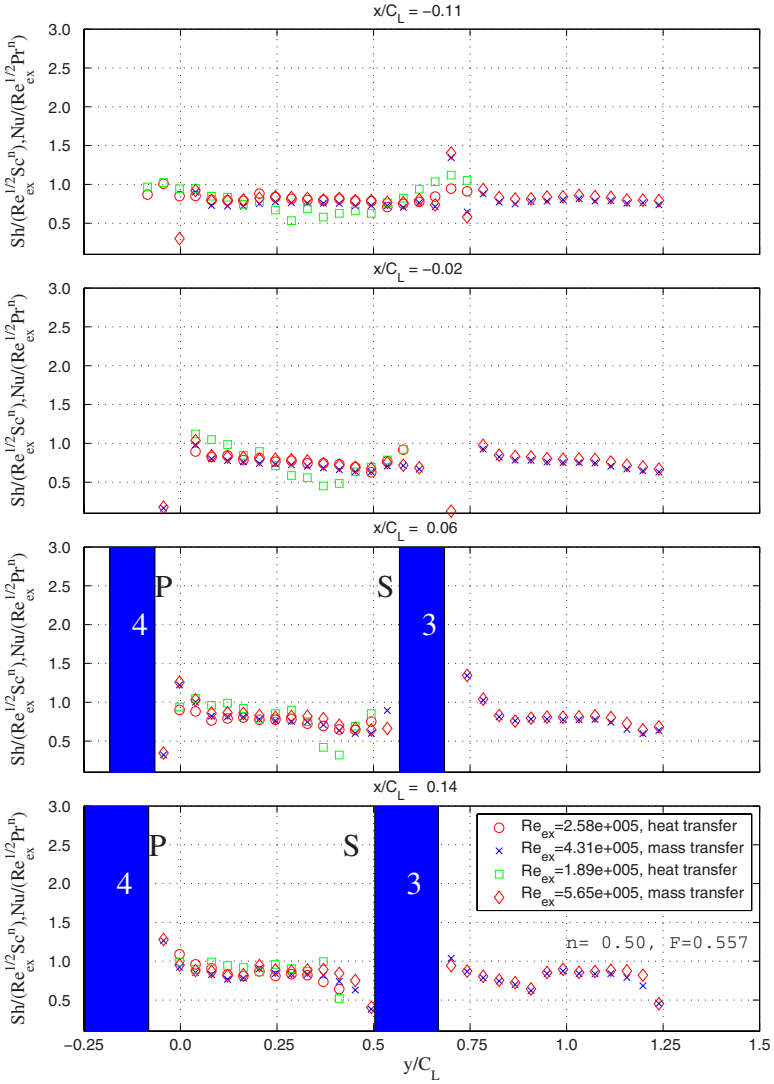


**Fig. 17 Heat and mass transfer analogy plot 1 with $n$=0.5 and Tu =0.2%**

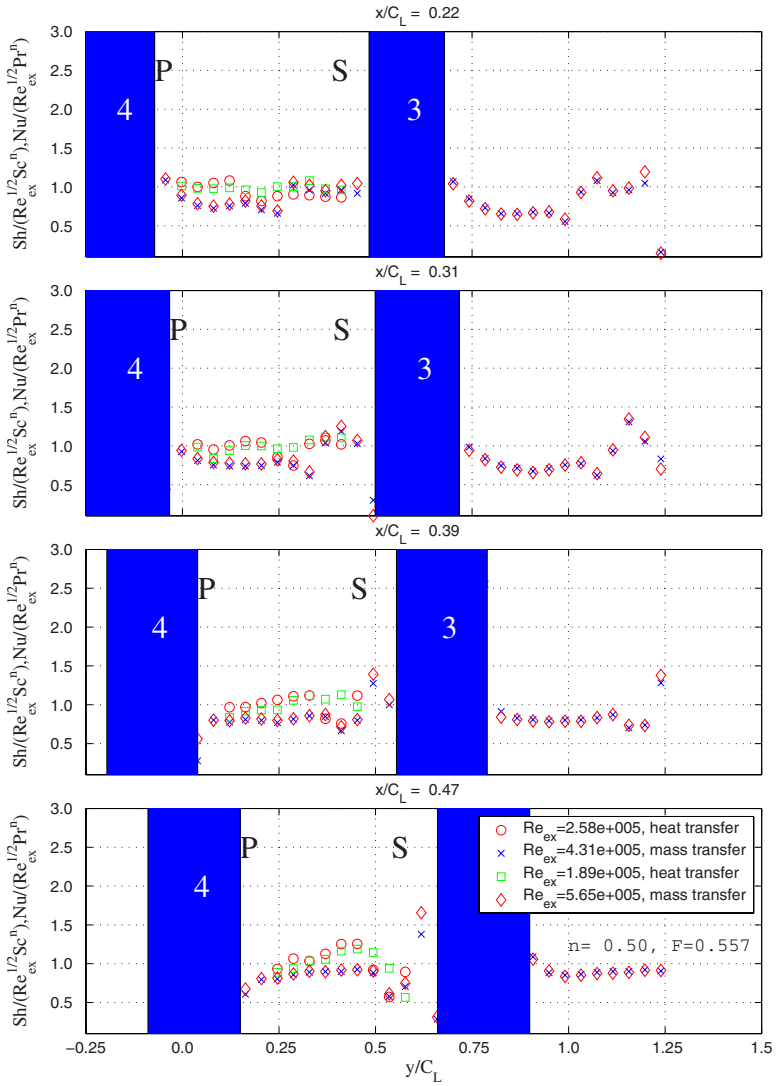


**Fig. 18 Heat and mass transfer analogy plot 2 with $n$=0.5 and Tu =0.2%**

$$\rho_{v,w} = \frac{p_{v,w}}{RT_{n,w}} = \frac{M_{\text{naph}} p_{v,w}}{RT_{n,w}} \tag{7}$$

where $T_{n,w}$ is the surface temperature and $p_{v,w}$ is the saturation vapor pressure. Subsequently, the mass transfer coefficient is determined from

$$h_m = \frac{\dot{m}}{\rho_{v,w} - \rho_{w,\infty}} = \frac{\rho_s \delta t / \delta \tau}{\rho_{v,w}} \tag{8}$$

where $\rho_{v,w}$ is the vapor concentration at a wall and $\rho_{v,\infty}=0$ for the mainstream. The mass diffusion coefficient ($D_{\text{naph}}$), 0.0681 (at 298.16 K), of naphthalene in air is evaluated by averaging two different values from the literatures. From the mass transfer coefficient and diffusion coefficient, the Sherwood number can be expressed as

$$\text{Sh} = \frac{h_m C_l}{D_{\text{naph}}} \tag{9}$$

The uncertainty level of the Sherwood number in the naphthalene sublimation technique using the methodology described in Coleman and Steele [16] is estimated to be approximately 7% at the 95% confidence level ($\pm 2\sigma$). The uncertainty of the mass transfer coefficient, excluding the uncertainty in the diffusion coefficient, is 5.2%, which includes the effects of naphthalene vapor density and saturated vapor pressure.

**Heat Transfer Experiment.** The thermal boundary layer measurement technique is used to measure local heat transfer results on the constant temperature endwall. More information is described in Han and Goldstein [14].

To measure local heat transfer results, the probe is aligned to a reference location by the five-axis measurement system. After the endwall maintains the constant temperature condition, the probe traverses to the measurement location and moves against the wall. After it finds the wall, the temperature measurement starts as it moves away from the wall. When it moves out of a thermal boundary layer and finishes the measurement, it moves to the next location (see Fig. 7) and starts the measurement again.

The heat flux can then be evaluated from the thermal gradient as

$$q_w = -k \frac{\partial T}{\partial n} \tag{10}$$

where $n$ is normal to the surface. Subsequently, the heat transfer coefficient is obtained from the heat flux, wall temperature, and freestream temperature.

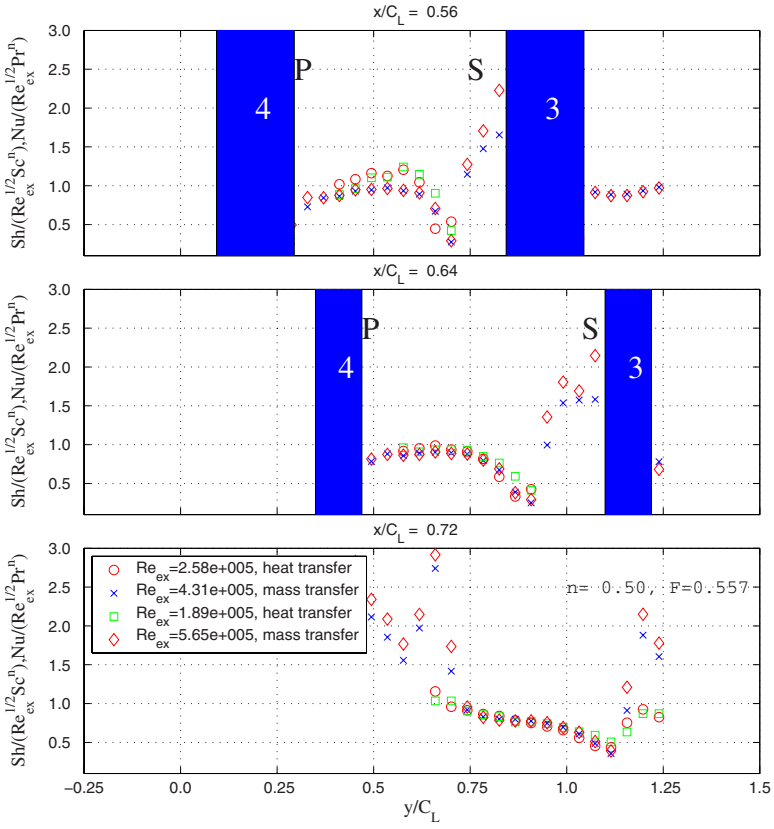


**Fig. 19 Heat and mass transfer analogy plot 3 with $n$=0.5 and Tu =0.2%**

$$h = \frac{q_w}{T_w - T_\infty} = \frac{-k\partial T/\partial n}{T_w - T_\infty} \tag{11}$$

From Eq. (11), the local Nusselt number is expressed as

$$\mathrm{Nu} = \frac{hC_l}{k} = \frac{-C_l\partial T/\partial n}{T_w - T_\infty} \tag{12}$$

## Results and Discussion

In a simulated turbine cascade, four mass transfer experiments and four heat transfer experiments on a simulated turbine endwall with fillets are conducted with equivalent experimental and similar geometrical conditions. Two mass transfer experiments and two heat transfer experiments are conducted with low turbulence intensity (0.2%). Two mass transfer experiments and two heat transfer experiments are conducted with high turbulence intensity (8.5%). The mass transfer data are already published to show the influence of the fillet to reduce secondary flows in Han and Goldstein [10]. The heat transfer data are obtained with enforcing equivalent experimental conditions in the same wind tunnel for the present study.

**Mass Transfer Results on the Endwall With Fillets.** Unlike heat transfer experiments, the mass transfer data are obtained from literature (Han and Goldstein [10]). While Han and Goldstein [10] used the mass transfer data to show the performance of turbine blades between with and without the fillets, their data are here used to investigate the analogy with the heat transfer measurements in the present study due to similar geometrical and equivalent experimental conditions. Contour plots of the mass transfer experiments on the endwall with the fillets are plotted from Figs. 8–11. The detailed experimental conditions are listed in Table 1. The reduced strength of the passage vortex is observed in low turbulence intensity with the fillets. Detailed experimental methods and evaluation of the data are presented in Han and Goldstein [10].

**Heat Transfer Results on the Endwall With Fillets.** The heat transfer experiments are conducted with thermal boundary layer measurement technique. For easy comparison between mass transfer and heat transfer experiments, four experimental conditions are chosen and listed in Table 2. Since the thermal boundary layer measurement technique is sensitive to vibration from high speed flows, low Reynolds numbers are chosen for the heat transfer experiments.

In Fig. 12, one thermal boundary profile from the actual measurement is presented to help understand the thermal boundary measurement technique. Near the wall, the temperature profile has a linear conduction region. Knowing a wall position accurately and using linear square fitting near the wall, the thermal gradient and the wall temperature are calculated. With the extrapolated wall temperature and the thermal gradient, and mainstream temperature, Nusselt number is evaluated with high confidence. In the temperature measurement, the thermal probe moves against the constant temperature wall to guarantee contact between the wall and the probe. The measured data at $z<0$ are obtained when the probe touches the wall and bends against it. The wall position is always monitored and accurately found by the motion controller so that the extrapolated wall temperature (45.3°C) does not show a large difference from the set temperature (45.0°C). The uncertainty of the Nusselt number ranges from 2% to 20% as the flow condition changes. However, an overall 10% uncertainty is obtained on the endwall measurement.

The heat transfer measurements only cover one passage between blades 3 and 4 unlike the mass transfer experiments. 130 locations are selected to measure the heat transfer coefficients

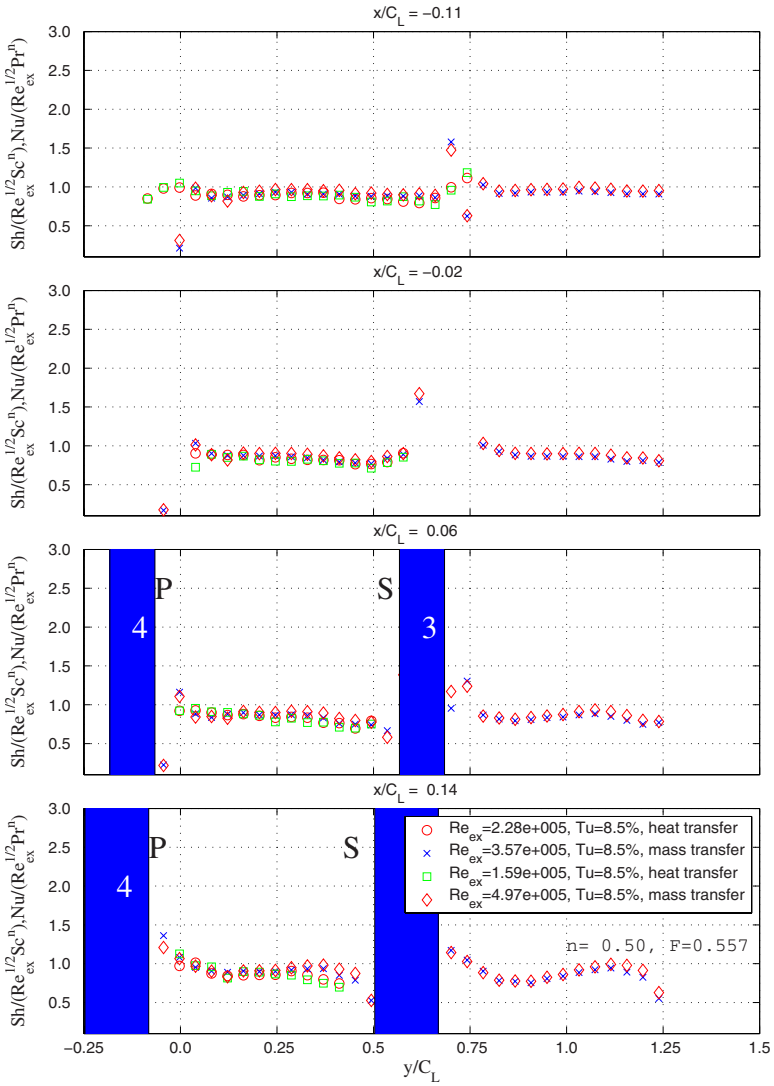


**Fig. 20 Heat and mass transfer analogy plot 1 with $n=0.5$ and Tu =8.5%**

from before a leading edge to after a trailing edge on the endwall (see Fig. 7). At each location, thermal boundary layer profiles like Fig. 12 are measured and evaluated to obtain Nusselt numbers. Like mass transfer measurements, contour plots for each measurement are presented in Figs. 13–16. Comparing the heat transfer contour plots with the mass transfer contour plots, the local heat transfer measurements do not show a complicated secondary flow development in detail. Han and Goldstein [14] conducted the heat transfer measurement on the endwall without the fillets with similar flow conditions ($2.56\times10^5$, Tu=0.2%). In the comparison between heat transfer measurement from Han and Goldstein [14] and Fig. 14, it is observed that the regions of high Nusselt number near the trailing edge are delayed as in the comparison of mass transfer experiments between with and without the fillets from Han and Goldstein [10].

**Heat/Mass Transfer Analogy on the Endwall With Fillets.** Since the analogy factor may not be the same, its evaluation for different geometries and experimental conditions is necessary to utilize the analogy fully.

It is difficult to evaluate the heat/mass transfer measurements in contour plots so that cross-section plots along the streamwise direction are presented in Figs. 17–22 with the analogy.

Complicated expressions for the analogy factor are not convenient for data comparison. Consequently, the Nusselt and Sherwood numbers are expressed using the Prandtl and Schmidt numbers and an exponent $n$, as in Eq. (6). Thus, for the comparison, we assume that the Nusselt number is expressed as

$$\mathrm{Nu} = f(x)\mathrm{Re}_x^m \mathrm{Pr}^n \tag{13}$$

and the Sherwood number is determined from

$$\mathrm{Sh} = f(x)\mathrm{Re}_x^m \mathrm{Sc}^n \tag{14}$$

where $f(x)$ is a function for a certain geometry. The analogy factor is evaluated using Eqs. (13) and (14).

To compare the heat transfer and mass transfer experiments, measurement locations of mass transfer experiments should be aligned on heat transfer measurement locations due to the small number of the heat transfer measurement locations. Therefore, Sherwood numbers from the mass transfer experiments are interpolated to calculate Sherwood numbers at the heat transfer measurement location (see Fig. 7).

The heat/mass transfer results are plotted for low turbulence intensity (see Figs. 17–19) and high turbulence intensity (see Figs. 20–22). In the plots, the blade cross sections are represented by the rectangular bars and the numbers inside the bars mark the blade numbers. The letter "P" means the pressure side and the

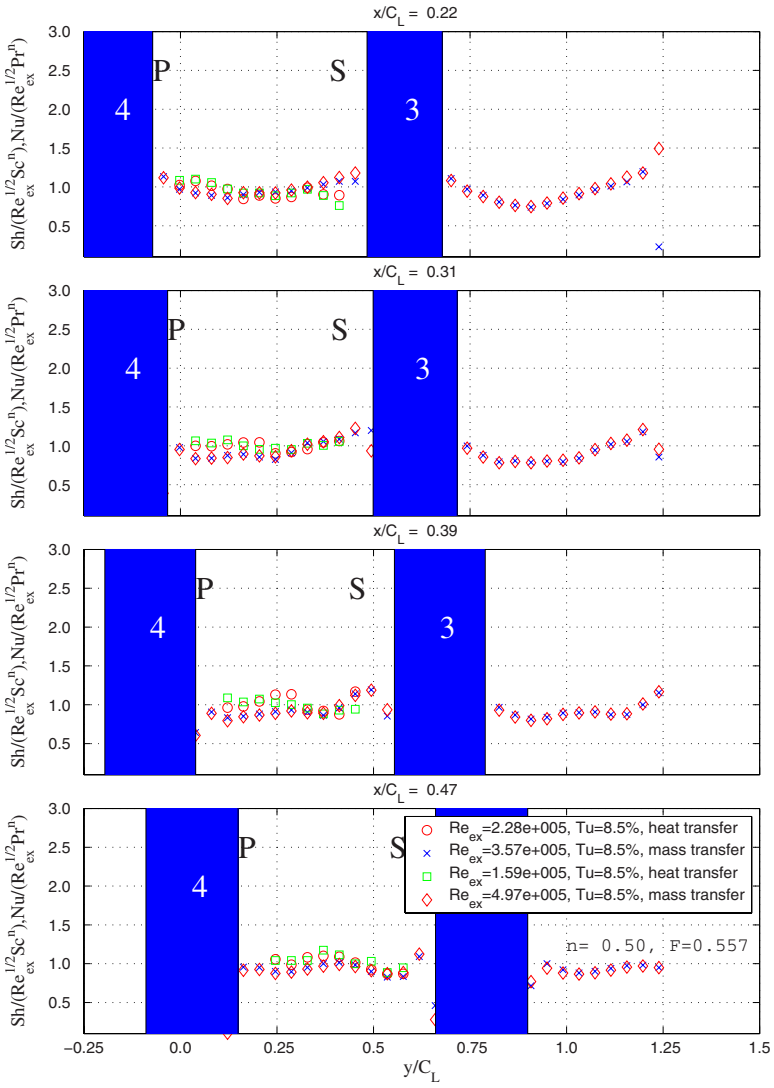


**Fig. 21 Heat and mass transfer analogy plot 2 with $n$=0.5 and Tu =8.5%**

letter "S" means the suction side. Normalized Nusselt numbers are shown between the third and the fourth blade and normalized Sherwood numbers are shown between the third and the fifth blade.

Because of comparing experiments with the different Reynolds numbers, the Nusselt and Sherwood numbers are normalized using $\mathrm{Re}_{ex}^{m}$ with $m=1/2$. The normalized Nusselt and Sherwood numbers are adjusted using $(\mathrm{Pr}/\mathrm{Sc})^{n}$, where Pr=0.707 and Sc =2.28. By varying $n$ from 1/3 to 1.0, $n$=0.5 ($F$=0.557) provides a good agreement between the results of the heat and mass transfer experiments. The boundary layer is fully developed by a 1 mm diameter trip wire so that the fact that $n$=0.5 ($F$=0.557) makes a good agreement between normalized Nusselt and Sherwood numbers agrees with the theoretical results from Goldstein and Cho [5].

For the low turbulence intensity case (F-MT-Run1, F-MT-Run2, F-HT-Run1, and F-HT-Run2), $n$=0.5 ($F$=0.557) provides a good agreement between heat transfer and mass transfer data from the leading edge to the trailing edge. Comparing F-MT-Run1, -Run2 and F-HT-Run1,-Run2, the repeatability of the mass transfer experiments is much better than that of the heat transfer experiments. The heat transfer experiments are affected by mainstream flow more than the mass transfer experiments are. Therefore, mass transfer results show better measurement repeatability. Since the Sherwood number and Nusselt number change significantly along the $y$ axis from $x/C_L$=0.47 to 0.72, it is observed that the heat and mass transfer measurements properly present heat transfer phenomena caused by the secondary flow development.

For the high turbulence intensity case (F-MT-Run3, F-MT-Run4, F-HT-Run3, and F-HT-Run4), $n$=0.5 ($F$=0.557) provides a good agreement from the leading edge to $x/C_L$=0.64. Unlike the low turbulence intensity, the Nusselt and Sherwood numbers do not agree well with $n$=0.5 ($F$=0.557) at $x/C_L$=0.72 except near $y/C_L$=0.75. The discrepancy was observed in Han and Goldstein [8]. This may be due to the vibration and misalignment of the probe in the high turbulence flow. The mass transfer results in the low turbulence intensity flow (see Fig. 19) show no difference from the heat transfer measurement after the trailing edge ($x/C_l$ =0.72), but the mass transfer results in the high turbulence intensity flow (see Fig. 22) differ after the trailing edge ($x/C_l$=0.72). However, the heat transfer results in the low turbulence (see Fig. 19) and high turbulence intensity flows (see Fig. 22) show no difference after the trailing edge ($x/C_l$=0.72). Therefore, the heat transfer results in the high turbulence intensity flow may be not properly evaluated after the trailing edge ($x/C_l$=0.72). Consider-

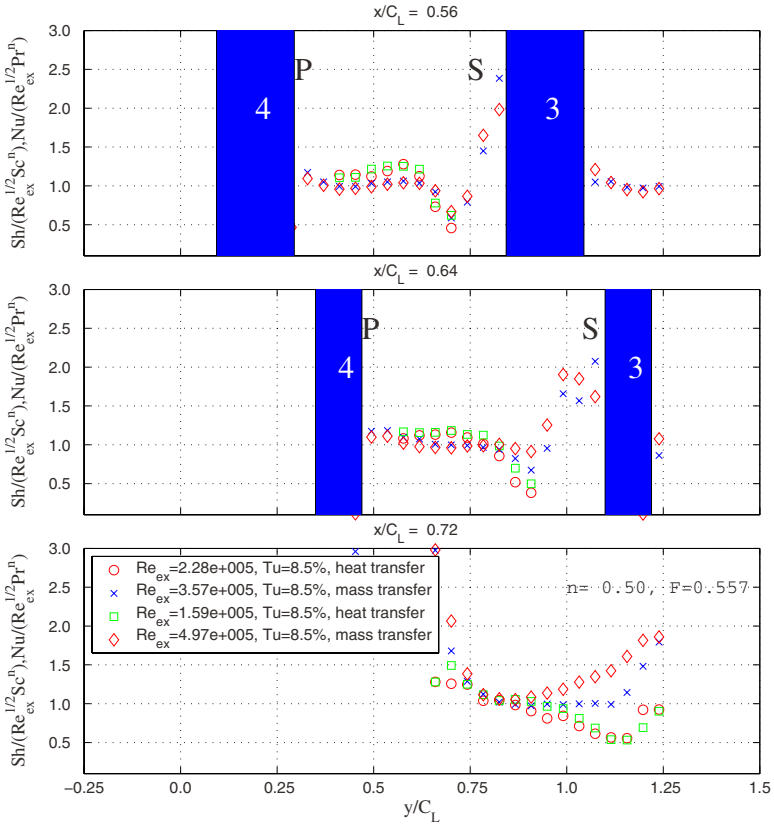


**Fig. 22 Heat and mass transfer analogy plot 3 with $n$=0.5 and Tu=8.5%**

ing this finding, probably $n$=0.5 ($F$=0.557) is still valid at $x/C_L$ =0.72 and the discrepancy occurs due to heat transfer measurement limitations, not to the variation of the analogy factor.

Due to the lack of heat transfer measurement locations near the suction and pressure surface, heat/mass transfer comparison is not provided near the blades. The lack of measurement location can be improved by using a new probe with a small width.

## Summary and Conclusions

The heat/mass transfer analogy is investigated on a simulated turbine endwall with blade fillets. Since the analogy factor is not necessarily the same in all flow conditions, the evaluation of the factor for different geometries and experimental conditions is necessary to utilize the analogy fully. Complicated experimental conditions caused by secondary flows on endwalls with fillets are chosen for the present study. For mass transfer, a naphthalene sublimation technique is used. For heat transfer, the thermal boundary layer probe is employed. The mass transfer results are obtained from Han and Goldstein [10].

An analogy factor of the Colburn relation $\mathrm{Nu}/\mathrm{Sh}=(\mathrm{Pr}/\mathrm{Sc})^n$ is adapted to compare Nusselt and Sherwood numbers with Pr =0.707 and Sc=2.28. In fully developed flows, $n$=0.5 ($F$ =0.557) provides a good agreement between normalized Nusselt and Sherwood numbers from the leading edge to the trailing edge with the blade fillets. In the high turbulence intensity flow, the discrepancy between the normalized Nusselt and Sherwood numbers is observed after the trailing edge, but it is probably due to measurement limitations not to the variation of the analogy factor. It is concluded that $n$=0.5 ($F$=0.557) is still valid for the fully developed flow on the simulated turbine endwall with the blade fillets.

It is believed that the heat transfer results on the endwall after the trailing edge in the high turbulence intensity flow need to be investigated further unlike the mass transfer results.


## Acknowledgment

The authors would like to acknowledge DOE for their support. This research was performed with financial support (02-01-SR096) from the University Turbine System Research Program.


## Nomenclature

$AR$ = inlet/exit area ratio of the cascade, 2.72
$C_l, (C_L)$ = characteristic length, 184 mm in the present study
$c_w$ = local wall concentration
$C_x$ = axial chord length of the blade, 130 mm in the present study
$D_{\mathrm{naph}}$ = mass diffusion coefficient
$F$ = local analogy factor, $F=\mathrm{Nu}/\mathrm{Sh}$
$H$ = height of the blade, 457 mm
$h$ = convective heat transfer coefficient
$h_m$ = convective mass transfer coefficient
$m$ = dimensionless mass fraction
$M_{\mathrm{naph}}$ = molecular mass for naphthalene, $M_{\mathrm{naph}}$=129.17 kg/kmol
$n$ = the distance in the direction normal to the wall
Nu = Nusselt number, $\mathrm{Nu}=h\cdot C_l/k$
$P$ = pitch of the blade, 138 mm
$p$ = static pressure
$p_{v,w}$ = naphthalene vapor pressure at the wall
Pr = Prandtl number, $\mathrm{Pr}=\nu/\alpha$
$\mathrm{Pr}_t$ = turbulent Prandtl number, $\mathrm{Pr}_t=\epsilon/\epsilon_H$
$q_w$ = heat flux from the wall
$R$ = gas constant for naphthalene ($C_{10}H_8$), $R$=0.06487 J/g K
$\bar{R}$ = universal gas constant

$\mathrm{Re}_{ex}$ = exit Reynolds number, $=\rho U_{ex} C_l/\mu$
$S_p$ = curvilinear coordinate on the pressure surface, see Fig. 2
$S_s$ = curvilinear coordinate on the suction surface, see Fig. 2
$\mathrm{Sc}_t$ = turbulent Schmidt number, $\mathrm{Sc}_t = \epsilon/\epsilon_M$
Sc = Schmidt number, $\mathrm{Sc} = \nu/D_{naph}$
Sh = Sherwood number, $\mathrm{Sh} = h_m \cdot C_l/D_{naph}$
St = Stanton number, $\mathrm{St} = \mathrm{Nu}/\mathrm{RePr} = h/\rho c_p U_\infty$
$\mathrm{St}_m$ = mass transfer Stanton number, $\mathrm{St}_m = \mathrm{Sh}/\mathrm{ReSc} = h_m/U_\infty$
$T_{n,w}$ = surface temperature of naphthalene
$T_w$ = local wall temperature
$T_{air}$ = freestream temperature
$T_{aw}$ = adiabatic wall temperature
$T_\infty$ = freestream temperature
Tu = turbulence intensity, $\mathrm{Tu} = \sqrt{\overline{u'^2}}/U_\infty$
$u, v$ = velocity components
$U_\infty$ = mainstream inflow velocity in wind tunnel
$U_{ex}$ = mainstream exit velocity at the exit of the cascade, $AR \cdot U_\infty$
$x$ = coordinate in the blade chord direction
$X_i$ = coordinate along the inflow direction, see Fig. 2
$y$ = coordinate traverse to the blade chord direction
$Z$ = coordinate in the spanwise direction of cascade, $Z=0$ at the tip

**Greek Symbols**

$k$ = thermal conductivity of air
$\nu$ = kinematic viscosity
$\beta_1$ = inlet angle of cascade, 35 deg
$\beta_2$ = outlet angle of cascade, −72.5 deg
$\theta$ = dimensionless temperature difference
$\epsilon$ = turbulent momentum diffusivity
$\epsilon_H$ = turbulent thermal diffusivity
$\rho_{v,w}$ = naphthalene vapor density on the surface
$\rho_s$ = density of solid naphthalene
$\rho_{v,\infty}$ = naphthalene vapor density at infinite or approaching flow
$\delta\tau$ = time duration of data run
$\delta t$ = sublimation depth of naphthalene
$\epsilon_M$ = turbulent mass diffusivity

**Superscripts**

$\hat{}$ = nondimensional parameter

**Subscripts**

atm = atmosphere property
st = static property
$w$ = wall property

## References


[1] Lewis, J. S., 1971, "A Heat/Mass Transfer Analogy Applied to Fully Developed Turbulent Flow in an Annulus," J. Mech. Eng. Sci., **13**(4), pp. 286–292.
[2] Blair, M. F., 1974, "An Experimental Study of Heat Transfer and Film Cooling on Large-Scale Turbine Endwalls," ASME J. Heat Transfer, **96**, pp. 524–529.
[3] Graziani, R. A., Blair, M. F., Taylor, J. R., and Mayle, R. E., 1980, "An Experimental Study of Endwall and Airfoil Surface Heat Transfer in a Large Scale Turbine Blade Cascade," ASME J. Eng. Power, **102**, pp. 257–267.
[4] Chen, P. H., and Goldstein, R. J., 1992, "Convective Transport Phenomena on the Suction Surface of a Turbine Blade Including the Influence of Secondary Flows Near the Endwall," ASME J. Turbomach., **114**, pp. 776–787.
[5] Goldstein, R. J., and Cho, H. H., 1995, "A Review of Mass Transfer Measurements Using Naphthalene Sublimation," Exp. Therm. Fluid Sci., **10**, pp. 416–434.
[6] Eckert, E. R. G., Sakamoto, H., and Simon, T. W., 2001, "The Heat/Mass Transfer Analogy Factor, Nu/Sh, for Boundary Layers on Turbine Blade Profiles," Int. J. Heat Mass Transfer, **44**, pp. 1223–1233.
[7] Yoo, S.-Y., Park, J.-H., Chung, C.-H., and Chung, M.-K., 2003, "An Experimental Study on Heat/Mass Transfer From a Rectangular Cylinder," ASME J. Heat Transfer, **125**, pp. 1163–1169.
[8] Han, S., and Goldstein, R., 2008, "The Heat/Mass Transfer Analogy for a Simulated Turbine Endwall," Int. J. Heat Mass Transfer, **51**(11–12), pp. 3227–3244.
[9] Han, S., and Goldstein, R., 2008, "The Heat/Mass Transfer Analogy for a Simulated Turbine Blade," Int. J. Heat Mass Transfer, **51**(21–22), pp. 5209–5225
[10] Han, S., and Goldstein, R., 2006, "Influence of Blade Leading Edge Geometry on Turbine Endwall Heat(Mass) Transfer," ASME J. Turbomach., **128**, pp. 798–813.
[11] Nusselt, W., 1930, "Wärmeübergang, Diffusion und Verdunstung," Z. Angew. Math. Mech., **2**, pp. 105–121.
[12] Schmidt, E., 1929, "Verdunstung und Wärmeügergang," Gesund.-Ing., **29**, pp. 525–529.
[13] Zess, G. A., and Thole, K. A., 2002, "Computational Design and Experimental Evaluation of Using a Leading Edge Fillet on a Gas Turbine Vane," ASME J. Turbomach., **124**, pp. 167–175.
[14] Han, S., and Goldstein, R., 2007, "Heat Transfer Study in a Linear Turbine Cascade Using a Thermal Boundary Layer Measurement Technique," ASME J. Heat Transfer, **129**, pp. 1384–1394.
[15] Blackwell, B. F., and Moffat, R. J., 1975, "Design and Construction of a Low Velocity Boundary Temperature Probe," ASME J. Heat Transfer, **97**(2), pp. 313–315.
[16] Coleman, H. W., and Steele, W. G., 1999, *Experimentation and Uncertainty Analysis for Engineers*, 2nd ed., Wiley-Interscience, New York.

**Matt Goodro**
Graduate Student
Department of Engineering Science,
Oxford University,
Parks Road,
Oxford OX1 3PJ, UK

**Jongmyung Park**
Korea Institute of Geoscience and Mineral Resources (KIGAM),
30 Gajeong-dong,
Yuseong-gu,
Daejeon, 305-350, Korea

**Phil Ligrani**[1]
Donald Schultz Professor of Turbomachinery
Department of Engineering Science,
Oxford University,
Parks Road,
Oxford OX1 3PJ, UK
e-mail: phil.ligrani@eng.ox.ac.uk

**Mike Fox**
Consulting Engineer

**Hee-Koo Moon**
Heat Transfer Manager

Aero/Thermal and Heat Transfer,
Solar Turbines, Inc.,
2200 Pacific Highway,
P.O. Box 85376,
Mail Zone C-9,
San Diego, CA 92186-5376

# Effect of Temperature Ratio on Jet Array Impingement Heat Transfer

*This paper consider the effects of temperature ratio on the heat transfer from an array of jets impinging on a flat plate. At a constant Reynolds number of 18,000 and a constant Mach number of 0.2, different ratios of target plate temperature to jet temperature are employed. The spacing between holes in the streamwise direction X is 8D, and the spanwise spacing between holes in a given streamwise row Y is also 8D. The target plate is located 3D away from the impingement hole exits. Experimental results show that local, line-averaged, and spatially averaged Nusselt numbers decrease as the $T_{wa}/T_j$ temperature ratio increases. This is believed to be due to the effects of temperature-dependent fluid properties, as they affect local and global turbulent transport in the flow field created by the array of impinging jets. The effect of temperature ratio on crossflow-to-jet mass velocity ratio and discharge coefficients is also examined.*
[DOI: 10.1115/1.2977546]

*Keywords: impingement cooling, internal cooling, turbine cooling, heat transfer augmentation, turbulent heat transfer, variable property effects, temperature ratio effects*

## 1 Introduction

Impingement cooling is a technique for heat management with high effectiveness. It is widely used to remove heat loads resulting from exposure to hot gases or hot liquids on components employed in a variety of applications. Impinging jets are often delivered by orifices, which have been cast or machined into internal structural members to provide maximum heat removal with minimal coolant mass flow rates. For example, when employed for cooling leading edge regions of turbine blades and vanes, the impingement air enters the leading edge cavity from an adjacent cavity through a series of crossover holes on the partition wall between the two cavities. The crossover jets then impinge on the concave leading edge wall and then exit either through film cooling holes or through exit passages, which lead to another part of the airfoil. With this arrangement, spanwise lines of impingement jets are employed, which direct cooling air on high external heat load regions, such as the stagnation region [1]. Impingement cooling is also often used to cool parts of the combustor in gas turbine engines, including combustion chamber liners, transition pieces, and splash plates. In each case, impinging jets are used individually or in arrays [2].

A significant number of papers on impingement cooling are available. Most existing investigations address low Mach number flows with relatively low speeds and low temperature ratios $T_{wa}/T_j$. They consider the effects of changing impingement plate geometric and configuration parameters and physical parameters. Spatially averaged surface heat transfer coefficients beneath an array of impinging jets in low-speed flow for Reynolds numbers from $3\times10^2$ to $3\times10^4$, $X/d$ and $Y/d$ from 3.1 to 12.5, and $Z/d$ from 1.0 to 4.8 were presented by Kercher and Tabakoff [3] who employed plate temperatures of 66 °C and 107 °C with an air temperature of 24 °C. Spent air flow from the impingement array is constrained to exit the flow passage in one direction. These investigators reported that the spatially averaged heat transfer coefficients are dominated by the Reynolds number and streamwise/spanwise hole spacing. They also reported a decrease in heat transfer performance and heat transfer coefficients associated with the increasing crossflow velocity caused by decreasing $Z/d$. Metzger et al. [4] and Chupp et al. [5] considered heat transfer within airfoil leading edge regions. They addressed heat transfer with a semicircular concave region with a line of circular jets impinging on the apex, focusing on the effects of target spacing, hole spacing, and jet Reynolds number. Metzger and Korstad [6] examined the influences of crossflow on a single line of jets, emerging from circular holes and placed on one wall of a channel,

[1]Corresponding author.

Contributed by the Heat Transfer Division of ASME for publication in the JOURNAL OF HEAT TRANSFER. Manuscript received January 4, 2008; final manuscript received May 20, 2008; published online October 21, 2008. Review conducted by Raj M. Manglik. Paper presented at the ASME Turbo Expo 2007: Land, Sea and Air (GT2007), Montreal, QB, Canada, May 14–17, 2007.

  

showing that target spacing, jet Reynolds number, and the relative strengths of the jet flow and crossflows influence heat transfer on the target wall. The jet temperature is the same as the ambient crossflow temperature, and the wall temperature of the test block is about 66°C. Like the investigation of Kercher and Tabakoff [3], Chance [7] also investigated low-speed impingement cooling with spent air constrained to flow out only one side of the flow passage. To study the effect of jet temperature, ratios of impingement to surface absolute temperature of 0.77, 1.27, and 1.54 are employed. Jet temperatures between 32°C and 121°C and wall temperatures between 38°C and 121°C are used. This experiment is limited to a comparison between using impingement jets to heat a surface and using impingement for cooling. Heat transfer values for the impinging hot jets are shown to be about 10% greater than values measured for surface cooling experiments. Static pressure variations with the impingement passage are also described to increase with higher crossflow velocities as $Z/d$ decreases. Optimal values of $Z/d$ are described, which depend on the ratio of the total jet area to the heat transfer area, for best heat transfer enhancement. Also addressed in this investigation are data at Reynolds numbers from $6\times10^3$ to $5\times10^4$, square, equilateral triangle, and rectangular jet arrays, and $Z/d$ values of 2, 3, 4, 6, and 8. Heat transfer characteristics measured on a target surface beneath a two-dimensional array of impinging jets at low-speed flow were also presented in another paper by Metzger et al. [8]. They investigated $Z/d$ values of 1, 2, and 3, $X/d$ and $Y/d$ ranging from 6 to 32, and Reynolds numbers from $5\times10^3$ to $2\times10^4$. The segment surface temperature difference between the maximum power and the zero power about 15–35 K. These investigators indicated that inline jet impingement hole patterns provide better heat transfer than staggered arrangements. A continuation of this investigation is described by Florschuetz et al. [9], wherein Reynolds numbers from $2.5\times10^3$ to $7\times10^4$, inline and staggered hole patterns, $Z/d$ from 1 to 3, $X/d$ from 5 to 15, and $Y/d$ from 4 to 8 are considered. In this investigation, the temperature difference between the impingement surface temperature and the plenum air temperature is normally 15–30 K. As for the previous investigation, impinging air is again constrained to exit in a single direction from the channel formed between the impingement and target plates. Included are data on channel crossflow mass velocity and jet mass velocity (where ratios range from 0 to 0.8), as well as a correlation that gives Nusselt number dependence on these parameters as well as on jet impingement plate geometry, Prandtl number, and Reynolds number. Recent studies by Lee et al. [10], Garimella and Nenaydykh [11], and Shuja et al. [12] addressed the effects of nozzle geometry on heat transfer and fluid flow, while Siba et al. [13] and Chung and Luo [14] showed the effects of turbulent impingement jets. Abdon and Sundén [15] also addressed turbulence in impingement jets using numerical predictions. Tong [16] showed the hydrodynamics and heat transfer of a circular liquid jet through another numeric study. Laschefski et al. [17] performed a numerical investigation of heat transfer by rows of rectangular impinging jets, and Seyedein et al. [18] reported the study of heat transfer from confined multiple turbulent impinging slot jets. Rhee et al. [19] also studied impingement jets in an array, determining local heat transfer, mass transfer, and flow characteristics with effusion holes ejecting spent air.

Another recent study by Obot and Trabold [20] considered different crossflow schemes on impingement heat transfer in low-speed flows. Impingement jet Reynolds numbers from $1\times10^3$ to $2.1\times10^4$, $Z/d$ values from 2 to 16, $X/d$ values of 5 and 10, and $Y/d$ values of 4 and 8 are employed. Also the average temperature difference of the exiting air with power and without power is 25–50 K. According to these investigators, for a given crossflow scheme and constant jet diameter $d$, higher heat transfer coefficients are obtained as the number of jets over a fixed target area increases. Bunker and Metzger [21] presented detailed local heat transfer distributions due to line jet impingement for leading edge regions, both with and without film extraction effects. Fox et al. [22] examined the effects of unsteady vortical structures on the adiabatic wall temperature distribution produced by a single impinging jet. Secondary vortex structures within the jet are described, which alter adiabatic surface temperatures when the target plate is near the jet nozzle (i.e., $Z/d$ of 1, 2, or 4). Also important are self-sustaining acoustic resonance events, which, when present, also alter adiabatic surface temperature distributions. Bailey and Bunker [23] investigated impingement arrays with inline jets in a "square array," with axial and lateral jet spacings of 3, 6, and 9. Reynolds numbers range from $1.4\times10^4$ to $6.5\times10^4$, Mach numbers are relatively low, jet-plate-to-target spacings range from 1.25 to 5.5 impingement hole diameters, and the minimum temperature potential between the wall and plenum temperatures is 18°C. Included are correlations developed from these data, which extend the range of applicability of the correlations presented by Florschuetz et al. [9]. Other recent studies considered the effects of jet impingement on a leading edge/concave wall with roughness [24] and the effects of jets with mist and steam on a concave target surface [25]. Thus, it is evident that aside from a few investigations, most of the impingement data from the open literature are obtained on flat, smooth surfaces and low ratios of the wall absolute temperature to the jet absolute temperature. In another recent investigation, which employs flat target plates, Brevet et al. [26] considered one row of impinging jets in a test section with low-speed flow in which the spent air is again constrained to exit in one direction. Effects of impingement distance, Reynolds number, and spanwise hole spacing on Nusselt number distributions lead to recommendations for optimal $Z/d$ values of 2–5 and optimal spanwise hole spacings of 4–5 hole diameters. Data obtained at Reynolds numbers from $5\times10^3$ to $2\times10^4$, $Z/d$ of 1, 2, 5, and 10, and $X/d$ and $Y/d$ values of 2, 4, 6, and 10 also show that local and spatially averaged Nusselt numbers increase substantially with Reynolds number. For this study, the employed temperature difference between the wall and jet temperatures is 25–65°C. In another study by Brevet et al. [27], recovery factors and Nusselt numbers measured on a flat target surface beneath a single compressible impingement jet are described. Results are given for $Z/d$ ratios from 2 to 10 at different Mach numbers from 0.02 to 0.69. The wall temperature is about 60°C, and the jet total temperature is the same as the ambient temperature. Using different impingement hole plates with different hole diameters from 3 mm to 15 mm, data sets with different Mach numbers and a constant Reynolds number are obtained. Florschuetz and Su [28] investigated the effect of crossflow temperature on heat transfer within an array of impinging jets. The mixed-mean crossflow temperature is varied independently of the jet temperature. This investigation shows that the result is related to the crossflow-to-jet temperature difference influence factor and Nusselt number as functions of jet Reynolds number, crossflow-to-jet mass flux ratio, and geometric parameters.

The present study is unique because it addresses the effect of increasing wall to jet temperature ratio for an array of cool jets impinging on a heated surface with various flow rates of spent air crossflow. Note that no other existing investigation considers the effects of temperature ratio on jet array impingement heat transfer in any depth. The relationship between the degradation of spatially averaged Nusselt number and wall to jet temperature ratio is represented as a correlation. Data are given for six different temperature ratios. As such, the present results represent a new contribution to the archival literature as the effects of temperature ratio on jet array impingement heat transfer are illustrated.

## 2 Experimental Apparatus and Procedures

**2.1 Impingement Flow Facility and Impingement Plate.** Schematic diagrams of the facility used for heat transfer measurements are presented in Figs. 1 and 2 The facility is constructed of 6.1 mm thick ASTM A38 steel plates and A53 Grade B ARW steel piping. The air stream circulates in a closed loop to facilitate

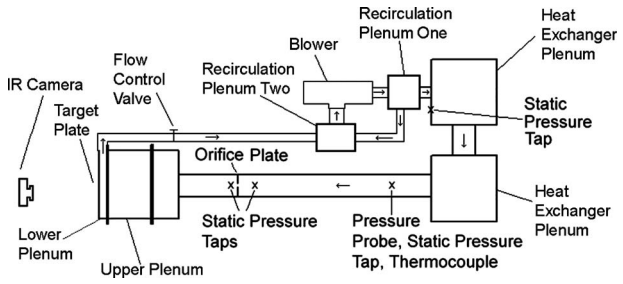


**Fig. 1 Impingement flow facility**

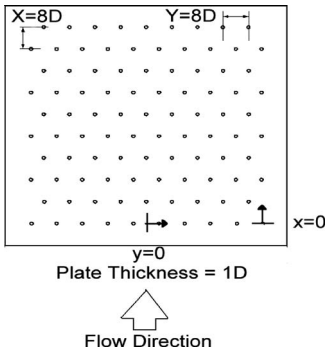


**Fig. 3 Impingement test plate configuration**

impingement air cooling. To achieve the Reynolds number of the present study, a New York Blower Co. 7.5 HP, size 1808 pressure blower is employed. The air mass flow rate provided to the test section is measured (downstream of whichever blower is employed) using an ASME standard orifice plate, flow-mounted calibrated copper-constantan thermocouples, and Validyne DP15 pressure transducers (with diaphragms rated at 13.8 kPa or 34.5 kPa) connected to DP10D carrier demodulators. The blower exits into a series of two plenums arranged in series, where the upstream plenum is 0.63 m in length along each corner, and the downstream plenum dimensions are 0.63 m, 0.77 m, and 0.77 m. A Bonneville crossflow heat exchanger is located within each plenum. As the air exits the heat exchanger and the second plenum, the air passes into a 0.22 m outer diameter pipe, which contains the ASME standard orifice plate employed to measure the air mass flow rate. This pipe then connects to the $0.635 \times 0.635$ m$^2$ side of a plenum. Upon entering this plenum, the air first encounters a flow baffle used to distribute the flow, a honeycomb, and other flow straightening devices. These are followed by the impingement plenum (or upper plenum, located below the honeycomb and flow straightening devices, as shown in Fig. 2) whose dimensions are $0.635 \times 0.635$ m$^2$, and whose height is 0.40 m.

Individual plates with circular sharp-edged holes used to produce the impingement jets are located at the bottom of this plenum, as shown in Fig. 2. The thickness of each impingement plate is 1$D$ or 4.5 mm. The plenum is thus designed so that different impingement plates can be installed at this location. Figure 3 shows that each impingement plate is arranged with ten rows of holes in the streamwise direction, arranged so that holes in adjacent rows are staggered with respect to each other. With this arrangement, either nine or ten holes are located in each streamwise row. The spacing between holes in the streamwise direction $X$ is then 8$D$ or 36.0 mm, and the spanwise spacing between holes in a given streamwise row $Y$ is also 8$D$ or 36.0 mm. The spacing between the hole exit planes and the target plate is denoted $Z$ and is equal to 3$D$. Note that the coordinate system employed is also shown in Fig. 3. The impingement cooling flow, which issues from these holes, is contained within the channel formed by the impingement jet plate and the target surface and is constrained to exit in a single direction, which is denoted here as the x-direction. This channel is called the lower plenum. In the present study, the hole diameter $D$, blower, mass flow rate, and pressure level are employed so that the Mach number is about 0.2 and the Reynolds number is about 17,500

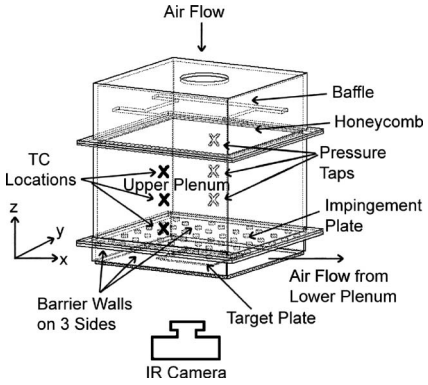


**Fig. 2 Impingement flow facility test section, including impingement plenum, and impingement channel**

In order to obtain different $T_{wa}/T_j$ temperature ratio values, the impingement air is circulated in a closed loop, and cooled to temperatures as low as −80°C using liquid nitrogen in two different Bonneville heat exchangers located two different plenums. In order to avoid formation of frost from water vapor initially contained in the air which passes and circulates in the facility, it is first cooled to a temperature of approximately 0°C for a period of at least one hour. This results in condensation of portions of the water vapor which is initially contained within the air stream. As the facility is cooled to even lower temperatures, this water is then frozen at locations which do not inhibit the passage of the impingement air throughout vital internal components of the facility. This approach serves to dry the air somewhat before air temperatures below 0°C are utilized.

**2.2 Target Plate Test Surfaces for Measurements of Surface Nusselt Numbers.** The entire assembled target plate is 1.57 mm thick and is mounted on the bottom surface of the plenum using gray cloth tape with a solvent containing methyl-ethyl-ketone, tetrahydrofuran, and acetone to seal the edges so that no leaks are present along the flow passage. A mounting frame is also employed to hold the target plate in place and to keep it smooth (without bending or wrinkles) and normal to the impingement jets, as testing is underway. Ten calibrated copper-constantan thermocouples are placed at different streamwise and spanwise locations within the polystyrene target plate so that each senses a different temperature as data are acquired. Each one of these thermocouples is mounted approximately 0.016 cm below the surface adjacent to the air containing the impingement fluid. These provide measurements of local surface temperatures after correction for thermal contact resistance and temperature drop through the 0.016 cm thickness of polystyrene. Thermocouple lead wires are placed in grooves along the polycarbonate and are bonded into place with epoxy having approximately the same thermal conductivity as polystyrene. With this mounting arrangement, there is no indication of the presence of these wires in infrared thermography images and there is no appreciable error caused by the presence of the thermocouples. Each one of these thermocouple wires is then located between the thermofoil heater and the polystyrene portion of the target plate.

Spatially resolved distributions of surface heat transfer coefficients and Nusselt numbers are measured on the polystyrene target plates with heaters and thermocouples attached. The custom-made HK5184R26 thermofoil heaters employed are manufactured by Minco Products Inc. and have a temperature rating of 100°C. The

etched-foil heating element within this device is encased between two layers of DuPont Kapton polyimide films. This heater is located adjacent to the air stream with the impinging air jets to provide a constant surface heat flux boundary condition adjacent to the impingement air stream. Its thermal conductivity is approximately 0.2 W/mK at 20°C. Polystyrene is chosen for the target plate because of its strength and because it does not deform in shape at temperatures as high as 80°C. It is also suitable because of its relatively low thermal conductivity (0.09 W/mK at 20°C), which results in minimal streamwise and spanwise conduction along the test surface. The back side of this polystyrene plate is viewed by the infrared camera as spatially resolved measurements of surface temperature are obtained. Each polystyrene target plate is 1.27 mm thick, and each heater is approximately 0.3 mm thick, giving a total target plate thickness of 1.57 mm. Because of the wear and degradation, which results from exposure to different temperature levels as tests are conducted, these target plates are replaced with all new components after each three or four individual test sequences.

**2.3 Local Impingement Air Pressure and Temperature Measurements.** As shown in Fig. 2, three wall static pressure taps are located on the surface of the upper plenum. Eight wall pressure taps are also located on the surface of the lower plenum for the measurement of local static pressures. As tests are conducted, Validyne Model DP15-46 pressure transducers (with diaphragms rated at 13.8 kPa or 34.5 kPa) driven by DP10D Carrier Demodulators are used to sense pressures from these static pressure tappings. Local airflow recovery temperatures are measured using two calibrated copper-constantan thermocouples located in the central part of the lower plenum and three calibrated copper-constantan thermocouples located in the central part of the upper plenum. In each case, readings from either multiple thermocouples or multiple pressure taps are used to obtain average values of measured quantities for a given plenum. The variations of temperature and wall static pressure, as measured using thermocouples and pressure taps, are typically less than 1%. Voltages from the carrier demodulators and all thermocouples employed in the study are read sequentially using Hewlett-Packard HP44222T and HP44222A relay multiplexer card assemblies, installed in a Hewlett-Packard HP3497A low-speed Data Acquisition/Control Unit. This system provides thermocouple compensation electronically such that voltages for type $T$ copper-constantan thermocouples are given relative to 0°C. The voltage outputs from this unit are acquired by the Dell Precision 530 PC workstation through its USB port, using the LABVIEW 7.0 software and a GPIB-USB-B adaptor made by National Instruments.

Because the overall volume and cross-sectional area of the upper plenum are large compared to the area of the impingement holes, the velocity and Mach number of the air in this plenum are both near zero. As a result, the static pressure measured at the wall static pressure taps is the same as the stagnation pressure and is denoted as $P_{oj}$, the impingement air stagnation pressure. The measured air recovery temperature in the upper plenum is then the same as the upper plenum static temperature and upper plenum stagnation temperature. This resulting value is denoted $T_{oj}$, the impingement stagnation temperature. After measurement of the impingement air volumetric flow rate at the orifice plate, the impingement air mass flux is determined using $\rho_a u_a = \dot{m}/A$.

An iterative procedure is then used to determine the impingement static temperature $T_j$ and the impingement flow Mach number $M_a$. The first step in this procedure is the estimation of the value of $T_j$. The local recovery temperature, which is measured in the lower plenum, is used for this estimation. The impingement static density and spatially averaged impingement jet velocity are then determined using $\rho_a = P_a/RT_j$ and $u_a = \dot{m}/\rho_a A$, respectively, where $\dot{m}$ is the total mass flow rate and $A$ is the combined area, both for all impingement holes. Because the impingement flow vents to the laboratory, the local atmospheric pressure is used for $P_a$. Measurements of lower plenum static pressures using wall pressure taps confirm this approach. Next, the impingement air sonic velocity and Mach number are given by $c_a = (kRT_j)^{1/2}$ and $M_a = u_a/c_a$, respectively. Iterations using these analysis steps are then continued until the impingement static temperature and impingement Mach number are consistent with the isentropic equation given by

$$T_j = T_{oj}/[1 + M_a^2(k-1)/2] \tag{1}$$

With impingement static temperature $T_j$, impingement flow Mach number $M_a$, and other parameters known, the impingement Reynolds number is subsequently given by an equation of the form

$$\mathrm{Re}_j = \rho_a u_a D/\mu \tag{2}$$

A Kiel-type stagnation pressure probe is used to measure the total pressure in the pipe at a position, which is located upstream of the orifice plate employed to measure mass flow rate. A wall pressure tap located on the surface of the pipe and a calibrated copper-constantan thermocouple positioned within the air stream are used to sense static pressure and flow recovery temperature, respectively, at the same streamwise location. Pressures and temperatures measured using the thermocouple, probe, and tap are sensed and processed using the same types of instrumentation mentioned earlier. The velocities deduced from this arrangement are used to provide a cross-check on the velocities deduced from mass flow rates, which are measured using the ASME standard orifice plate.

**2.4 Local Nusselt Number Measurement.** The power to the thermofoil heater, mounted on the target plate, is controlled and regulated using a variac power supply. Energy balances and analysis to determine temperature values on the two surfaces of the target plate then allow determination of the magnitude of the total convective power (due to impingement cooling) for a particular test. To determine the surface heat flux (used to calculate heat transfer coefficients and local Nusselt numbers), the total convective power level, provided by the particular thermofoil heater employed, is divided by the single surface area of this heater, denoted as $A_{\mathrm{ht}}$.

One step in this procedure utilizes a one-dimensional conduction analysis, which is applied between the surface *within* the target plate, where the thermocouples are located (between the heater and the polystyrene target plate), and the ambient air environment behind the target plate. This is used to determine $T_b$, the local temperature on the back surface of the polystyrene target plate, adjacent to the surrounding ambient air environment. Also required for this analysis is $T_{tc}$, the local temperature within the target plate between the heater and the polystyrene plate, which is determined from thermocouple measurements. With these temperatures known, the radiation heat flux and the convection heat flux from the back side of the target plate, $q_{rb}$ and $q_{cb}$, respectively, are determined together using an equation of the form

$$q_{rb} + q_{cb} = h_{\mathrm{loss}}(T_b - T_{\mathrm{ambient}}) \tag{3}$$

where the coefficient, $h_{\mathrm{loss}}$ is taken as a uniform value of 15 W/m$^2$K. The use of a constant heat transfer coefficient for the back side of the heated plate is consistent with Brevet et al. [26]. The value of $h_{\mathrm{loss}}$ used for the present experimental configuration is validated experimentally using the baseline data. $q_{rb}+q_{cb}$ generally amounts to 2–5% of the total heat transfer from the target plate. The radiation heat flux $q_{rf}$ on the front (or impingement side) of the target plate is determined using

$$q_{rf} = \sigma(1/\varepsilon_{\mathrm{inf}} - 1/\varepsilon_f - 1)^{-1}(T_W{}^4 - T_{\mathrm{ambient}}{}^4) \tag{4}$$

where $T_{\mathrm{ambient}}$ is the temperature of the chilled impingement air.

With this approach, the radiation heat flux is determined for an arrangement with multireflection between two infinite plates where each has a uniform temperature. $\varepsilon_f$ and $\varepsilon_{\mathrm{inf}}$ are assumed to be equal to 0.9 for all conditions investigated. This approximate

approach works well since $q_{rf}A_{ht}$ is generally only 3–6% of $Q$, the total amount of power provided to the thermofoil heater. Note that $T_W$, the local target surface temperature on the surface of the heater adjacent impingement air, must be known to determine $q_{rf}$. In order to find these values, a one-dimensional conduction model for the heater is utilized, which includes source generation of thermal energy, to provide a relation between $T_W$, $T_{tc}$, and $q_{cf}$ (the convection heat flux from the front or impingement side of the target plate). Because of the interdependence of $T_W$, $q_{rf}$, and $q_{cf}$, an iterative procedure is required with the one-dimensional analysis to determine these quantities. Also included in the analysis is thermal contact resistance between the internal thermocouples and the adjacent heater. This thermal contact resistance is determined empirically for a similar baseline configuration. This is accomplished using calibrated thermochromic liquid crystals to measure spatially resolved surface temperatures next to the air stream as thermocouples are used to simultaneously measure local temperatures within the test plate.

The convection heat flux from the front side (or impingement side) of the target plate is then given by

$$q_{cf} = Q/A_{ht} - q_{rf} - q_{rb} - q_{cb} \tag{5}$$

The local Nusselt number is then given as

$$\mathrm{Nu} = q_{cf}D/((T_W - T_{oj})\alpha) \tag{6}$$

Spatially resolved distributions of the target test surface temperature $T_W$ are determined using infrared imaging in conjunction with thermocouples, energy balances, digital image processing, and in situ calibration procedures. These are then used to determine spatially resolved surface Nusselt numbers. To accomplish this, the infrared radiation emitted by the heated polycarbonate target plate is captured using a FLIR Systems Inc. ThermoVision® A20M compact temperature measurement IR camera (S/N 22700776), which operates at infrared wavelengths from 7.5 $\mu$m to 13.0 $\mu$m. Temperatures, measured using the calibrated copper-constantan thermocouples distributed within the test surface adjacent to the flow, are used to perform the in situ calibrations simultaneously as the radiation contours from surface temperature variations are recorded.

This is accomplished as the camera views the test surface from behind, as shown in Fig. 2. In general, all ten thermocouple junction locations are present in the infrared field viewed by the camera. The exact spatial and pixel locations of these thermocouple junctions and the coordinates of the field of view are known from calibration maps obtained prior to measurements. During this procedure, the camera is focused and rigidly mounted and oriented relative to the test surface in the same way as when radiation contours are recorded. Thus, each and every acquired infrared image is calibrated in place as it is recorded using the in situ procedures. As this is done, voltages from the thermocouples are acquired using the apparatus mentioned earlier. With these data, gray scale values at the thermocouple locations within digital images from the infrared imaging camera are associated with their corresponding temperatures. A calibration between temperature and gray scale value is developed and used to assign a temperature, $T_W$, to each pixel in the image. This temperature information allows the determination of local Nu values using Eq. (6). Because such calibration data depend strongly on camera adjustment, the same brightness, contrast, and aperture camera settings are used to obtain the experimental data. The in situ calibration approach rigorously and accurately accounts for these variations.

Images from the infrared camera are recorded as an 8 bit gray scale directly into the memory of a Dell Dimension XPS T800r PC computer using a Scion Image Corporation Frame grabber video card, and the SCION IMAGE V.1.9.2 software. One set of 15–20 frames is recorded at a rate of about 1 frame/s. All of the resulting images are then ensemble averaged to obtain the final gray scale data image. The difference in gray scale values between the averaged images is less than 0.5%. This final data set is then imported into MATLAB VERSION 6.1.0.450 (Release 12.1) software to convert each of 256 possible gray scale values to a local Nusselt number at each pixel location using calibration data. Each individual image covers a $256 \times 256$ pixel area. For the experimental configuration used for the present study, this results in a spatial resolution of $0.98 \times 0.98$ mm/pixel. Note that only a portion of the area affected by the impact locations of the impingement jets is viewed using the infrared camera.

**2.5 The Determination of Crossflow Mass Velocity to Jet Mass Velocity Ratio and Discharge Coefficient.** The crossflow-to-jet mass velocity ratio $G_c/G_j$ for all of the data presented, is equivalent at each corresponding $x/D$ location. It is determined by two different methods. The first is directly from experimental data, and the second is from procedures presented by Florschuetz et al. [9]. From the definition of Reynolds number, $G_j$ is given by

$$G_j = (\mathrm{Re}_j \cdot \mu)/D \tag{7}$$

$G_c$ is then defined as $\rho u_c$, the crossflow density multiplied by the crossflow velocity. If the crossflow mass flow rate is $\dot{m}_c = \rho u_c A_{\mathrm{cross}}$, we then have

$$G_c = \dot{m}_c/A_{\mathrm{cross}} \tag{8}$$

Combining Eqs. (7) and (8) then gives

$$\frac{G_c}{G_j} = \frac{\dot{m}_c/A_{\mathrm{cross}}}{(\mathrm{Re}_j \cdot \mu)/D} \tag{9}$$

The crossflow-to-jet mass velocity ratio $G_c/G_j$ is given by Florschuetz et al. [9] as

$$\frac{G_c}{G_j} = \frac{1}{\sqrt{2}C_D} \frac{\sinh \beta\left(x/x_n - \frac{1}{2}\right)}{\cosh \beta(x/x_n)} \tag{10}$$

where $\beta$ is the flow distribution parameter, given by

$$\beta = \frac{C_D\sqrt{2}(\pi/2)}{(y_n/d)(z/d)} \tag{11}$$

Here, $x_n$ is streamwise jet hole spacing, and $x = x_n(i - 1/2)$, $i = 1, 2, 3, \ldots, N_c$. $N_c$ is then the number of spanwise impingement rows in the streamwise direction. The discharge coefficient is subsequently determined using

$$C_D = \rho_a u_a/\rho_i u_i \tag{12}$$

Magnitudes of $C_D$ remain relatively invariant throughout the impingement array because the upstream supply pressure is constant and the exit static pressure is approximately constant. Consequently, an average static pressure value is used at the exits of the impingement holes for the determination of $G_c/G_j$ values at different streamwise locations, which is consistent with the approach employed by Florschuetz et al. [9].

The first step in determining the ideal impingement mass flux $\rho_i u_i$ is the calculation of an ideal impingement Mach number $M_i$ using

$$P_{oj}/P_a = [1 + M_i^2(k-1)/2]^{k/k-1} \tag{13}$$

Here, the local atmospheric pressure is used for the exit static pressure $P_a$ because the impingement flow vents to the laboratory and because the exit static pressure is nearly constant along the impingement array, as mentioned. This is confirmed by measurements of the static pressure distribution in the lower plenum, which are made using an array of wall static pressure taps. As such, $P_a$ is a spatially averaged value at the exits of the impingement holes. Next, the impingement ideal static temperature $T_i$ is determined using $T_{oj}$, the ideal Mach number $M_i$, and the appropriate ideal gas isentropic relationship. Impingement ideal static density is given by $\rho_i = P_a/RT_i$, and impingement ideal velocity is given by $u_i = M_i(kRT_i)^{1/2}$. The actual mass flux $\rho_a u_a$ is determined using the impingement air mass flow rate, which is measured using the ASME standard orifice plate (mentioned earlier), di-

**Table 1 Experimental conditions for the present investigation**

| $T_{wa}/T_j$ | $Re_j$ | Ma | $D$ (mm) | $T_{wa}$ (K) | $T_j$ (K) |
|---|---|---|---|---|---|
| 1.06 | 18,100 | 0.21 | 4.5 | 314.5 | 292.8 |
| 1.25 | 18,100 | 0.20 | 4.5 | 313.0 | 249.0 |
| 1.36 | 18,200 | 0.20 | 4.5 | 319.2 | 232.9 |
| 1.46 | 18,000 | 0.19 | 4.5 | 320.2 | 217.2 |
| 1.58 | 18,100 | 0.19 | 4.5 | 331.5 | 208.2 |
| 1.73 | 17,400 | 0.18 | 4.5 | 348.4 | 201.7 |

vided by the combined area of the impingement holes.

**2.6 Experimental Uncertainty Estimates.** Uncertainty estimates are based on 95% confidence levels and are determined using methods described by Kline and McClintock [29] and Moffat [30]. Uncertainty of temperatures measured with thermocouples is $\pm 0.15°C$. The uncertainty values for spatial and temperature readings achieved with infrared imaging are about 0.1–0.2 mm and 0.4°C, respectively. This magnitude of temperature resolution is due to uncertainty in determining the exact locations of thermocouples with respect to pixel values used for the in situ calibrations. Local Nusselt number uncertainty is then about $\pm 4.8\%$ Note that uncertainties of local Nusselt numbers include the effects of very small amounts of streamwise and spanwise conduction along the test surfaces employed. Reynolds number uncertainty is about $\pm 2.0\%$ for $Re_j$ values of 17,000–20,000.

## 3 Experimental Results and Discussion

Table 1 gives a summary of the experimental conditions employed in the present investigation.

**3.1 Baseline Nusselt Numbers.** Baseline Nusselt numbers are measured using a test plate and flow conditions, which match the ones used by Florschuetz et al. [9] with $Re_j=34{,}500$, Ma approximately equal to 0, and an array of jets with $X=5D$, $Y=4D$, and $Z=3D$. In both cases, the effects of spent air crossflow are considered, and the passage between the impingement and target plates is closed on three sides. Figure 4 shows a comparison of results from the two investigations. Local Nu data for $y/D=4$ and $y/D=8$, line-averaged data, and area-averaged data from the present investigation are presented. Here, line averaging is imposed over $Y/D$ from −8.0 to +8.0. Area-averaged values are determined over $Y/D$ from −8.0 to +8.0 and over $5D$ length segments in the streamwise direction. The present area-averaged data are compared to area-averaged data from Florschuetz et al. [9] in Fig. 4. The good agreement of the area-averaged data from the two sources validates the experimental procedures and apparatus employed in the present study.

Also investigated is the effect of the unheated starting length located upstream of the heated target plate. This is done by adding an extra heater upstream of the heater used on the target plate.

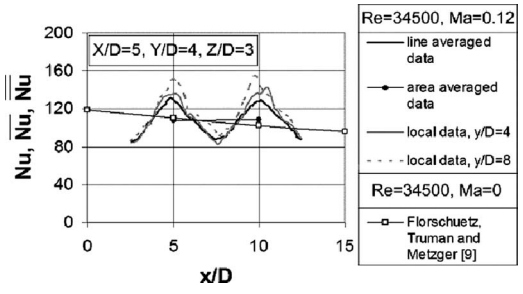


**Fig. 4 Comparison of baseline Nusselt number data with the correlation of Florschuetz et al. [9] for $Re_j=34{,}500$, Ma approximately equal to 0, and an array of jets with $X=5D$, $Y=4D$, and $Z=3D$**

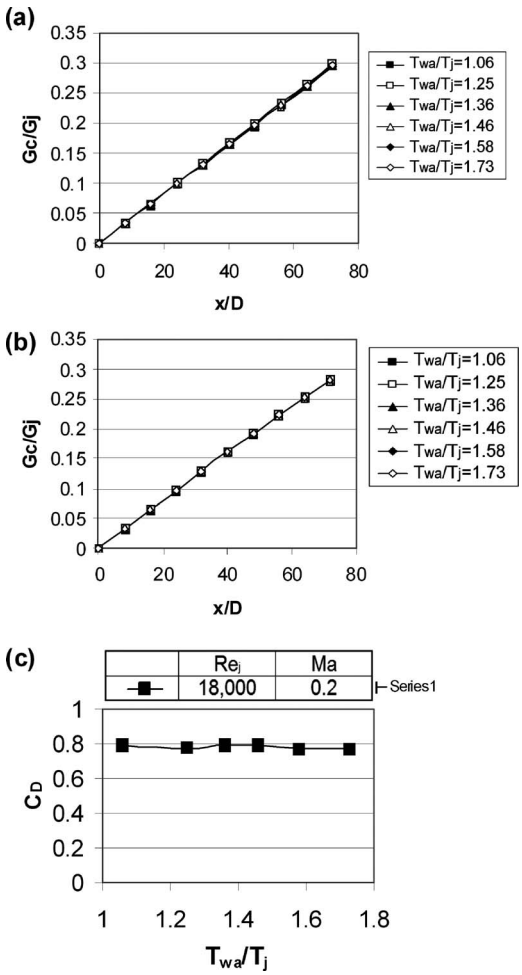


**Fig. 5 (*a*) Crossflow-to-jet mass velocity ratio distribution in the streamwise direction determined experimentally. (*b*) Crossflow-to-jet mass velocity ratio distribution in the streamwise direction predicted using the correlation of Florscheutz et al. [9]. (*c*) Discharge coefficient for $Re_j=18{,}100$, Ma=0.2, and $T_{wa}/T_j=1.06$, 1.25, 1.36, 1.46, 1.58, and 1.73.**

Local and spatially averaged Nusselt numbers are then measured on the target plate, both with and without upstream heating, for $Re_j=34{,}500$ and $M_a=0.12$ with the same impingement hole plate as used for the other baseline data checks. The variation of local and spatially averaged Nusselt numbers between the two tests is only about 2% at most, indicating minimal effect of thermal entry length on impingement heat transfer (for these particular experimental conditions).

**3.2 Crossflow-to-Jet Mass Flux Ratio and Discharge Coefficients.** In many situations, an increase in the mass velocity of the crossflow $G_c$ decreases the effectiveness of the impingement jets; therefore a high value of the crossflow-to-jet mass velocity ratio $G_c/G_j$ is undesirable. Figure 5(*a*) shows the distribution of this quantity as it varies in the streamwise direction determined from experimental data. Figure 5(*b*) presents $G_c/G_j$ valves determined using the correlation of Florschuetz et al. [9]. $G_c/G_j$ values from the two methods show a good agreement with each other at each value of $x/D$ and $T_w/T_j$. Note that $G_c/G_j$ variations with $x/D$ are approximately the same regardless of the value of $T_{wa}/T_j$. In both cases, the ratio of the crossflow-to-jet mass velocity is close to linear and is below 0.3 at the furthest downstream row. Figure 5(*c*) shows that the discharge coefficient remains approximately constant as the temperature ratio changes.

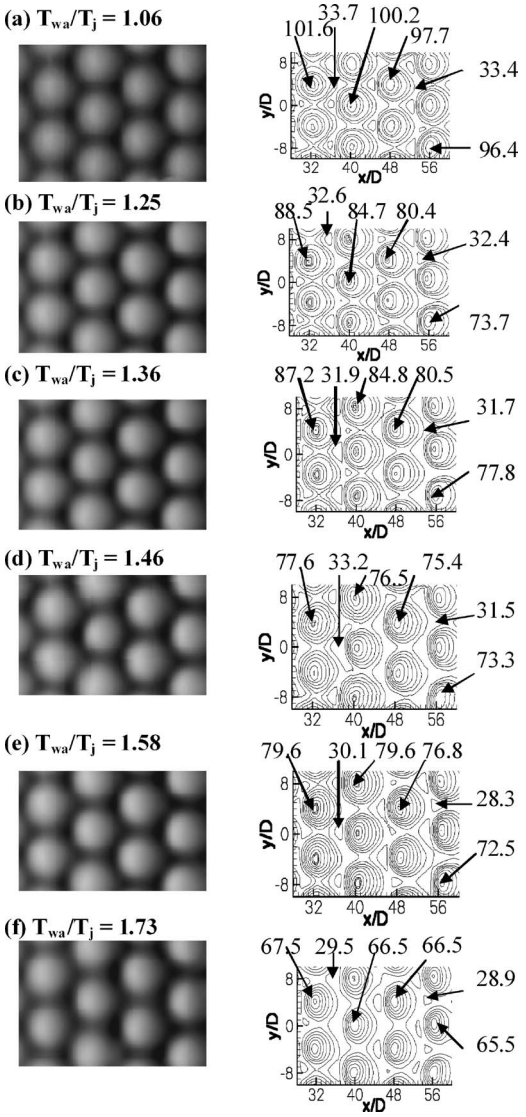


**Fig. 6 Spatially resolved surface Nusselt number distributions for $Re_j$=18,000, Ma=0.2, and $T_{wa}/T_j$=1.06, 1.25, 1.36, 1.46, 1.58, and 1.73**

**3.3 Local surface Nusselt Number and Line-Averaged Nusselt Number Variations With Temperature Ratio.** Figures 6–11 show the effects of the $T_{wa}/T_j$ temperature ratio on local, line-averaged, and spatially averaged Nusselt number data for $Re_j$=18,000 and Ma=0.2. These data at different increasing values of $T_{wa}/T_j$ are obtained by decreasing the impingement jet static temperature $T_j$ and increasing $T_{wa}$, where $T_{wa}$ is the spatially averaged target wall temperature and $T_j$ is the impingement jet static temperature.

Surface Nusselt number distributions are presented in Fig. 6 for Ma=0.20, $Re_j$=18,000, and $T_{wa}/T_j$=1.06, 1.25, 1.36, 1.48, 1.58, and 1.73. Note that regardless of the temperature ratio, the qualitative distributions of the local Nusselt number produced by each impingement jet are similar, with good periodic repeatability in the spanwise direction for each streamwise row of impact locations. Figure 6 also shows that each impingement jet produces only one local maximum value in the Nu distribution on the target surface beneath each jet. Magnitudes of these local maximum values are about the same underneath the different impingement jets for the $T_{wa}/T_j$ values investigated, with minor variations between streamwise rows as $x/D$ increases. These variations with streamwise distance are further illustrated in Fig. 7(*b*) by local

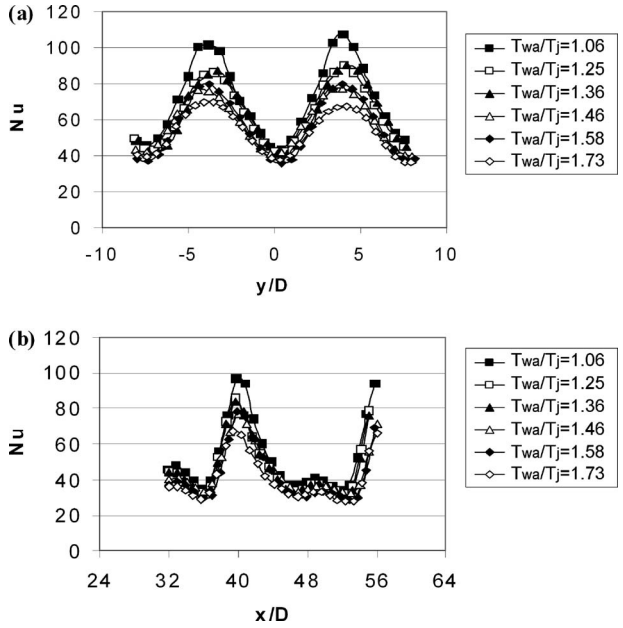


**Fig. 7 Local surface Nusselt number variations for $Re_j$ =18,000, Ma=0.2, and $T_{wa}/T_j$=1.06, 1.25, 1.36, 1.46, 1.58, and 1.73. (*a*) Variations with $y/D$ for $x/D$=32. (*b*) Variations with $x/D$ for $y/D$=8.**

Nusselt number data as it varies with $x/D$ for $y/D$=8. They are due to the increasing effect of hot spent air crossflow, which reduces the effectiveness of the impinging jets. The smaller peak values near $x/D$=32 and $x/D$=48, which are positioned between the larger peak values, are due to local Nusselt number increases

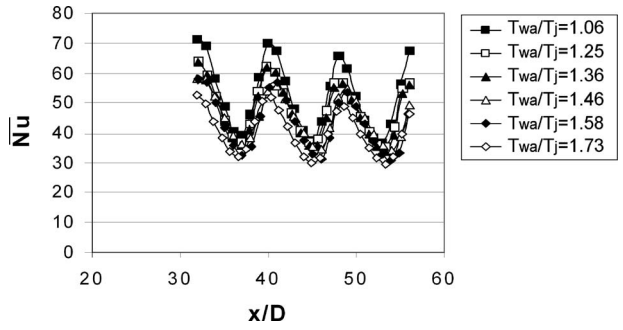


**Fig. 8 Surface Nusselt number variations with $x/D$, which are line averaged over $y/D$ from −8.0 to +8.0 for $Re_j$=18,000, Ma =0.2, and $T_{wa}/T_j$=1.08, 1.25, 1.37, and 1.73**

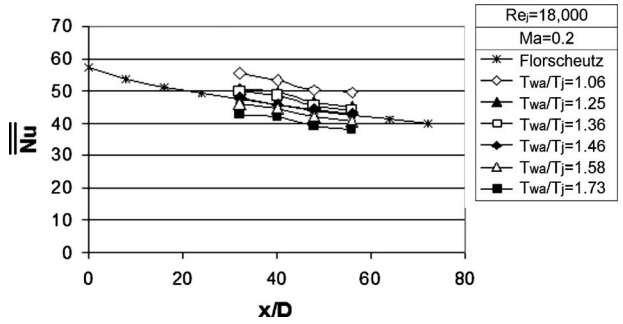


**Fig. 9 Spatially averaged Nusselt numbers as dependent on $x/D$ for $Re_j$=18,000, Ma=0.2, and $T_{wa}/T_j$=1.06, 1.25, 1.36, 1.46, 1.58, and 1.73**

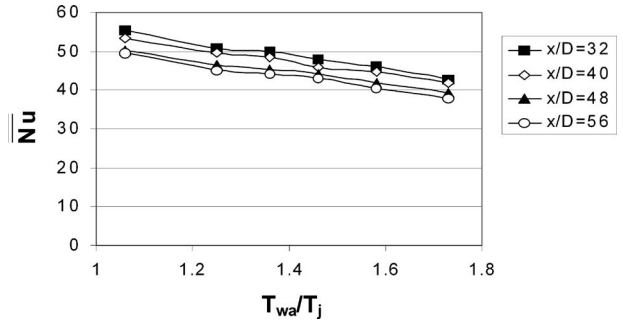


**Fig. 10 Local area-averaged Nusselt numbers as dependent on temperature ratio $T_{wa}/T_j$ for $Re_j$=18,000 and Ma=0.2**

at spanwise locations approximately halfway between the impact points of adjacent impinging jets. Figure 7(*a*) shows spanwise variations in local Nusselt number for each of the $T_{wa}/T_j$ values and $x/D$=32 with the highest Nusselt number values directly under the impingement jets. As seen in Figs. 6 and 7(*b*), Fig. 7(*a*) shows that local Nu values decrease as the temperature ratio increases, with a decrease in peak values as the most noticeable difference. This is because as the temperature ratio increases at the constant Reynolds number, the intensity of the impingement jets decreases due to the decreases in both mass flow rate and volumetric flow rate.

Figure 8 presents Nusselt numbers for the same experimental conditions as they vary with $x/D$, which are line averaged over $y/D$ from −8.0 to +8.0 (which covers two complete spanwise periods of impingement jet array geometry). Here, local maximum values are apparent, spaced approximately 8*D* apart, and due to the impact of impingement jets from each different streamwise row of holes. These local maximum line-averaged Nusselt number values become smaller at successive $x/D$ locations for each value of $T_{wa}/T_j$ temperature ratio due to the increasing crossflow effect. The oscillations inline-averaged Nusselt number are due to the high Nusselt numbers directly under impinging jets and low Nusselt number regions between the jets. In addition to these variations, the $\overline{\mathrm{Nu}}$ data generally decrease with $T_{wa}/T_j$ at each $x/D$ value.

**3.4 Local Area-Averaged Nusselt Number Variations With Temperature Ratio.** Spatially averaged Nusselt numbers are averaged over an area that extends ±4 diameters from the specified $x/D$ location and over $y/D$ data points from −8 to 8. This area thus amounts to two complete spatial periods of impingement jet array geometry. Figure 9 gives spatially averaged Nusselt numbers at different values of $T_{wa}/T_j$, along with values from the correlation of Florscheutz et al. [9]. There are noticeable differences between the present data for $T_{wa}/T_j$=1.06 and the correlation of Florscheutz et al. [9], which is for a temperature ratio

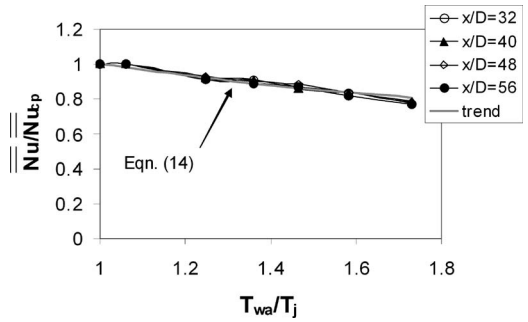


**Fig. 11 Nusselt number ratio data at specific *x/d* locations correlated with respect to temperature ratio, $T_{wa}/T_j$**

$T_{wa}/T_j$ of approximately 1.1. The correlation of Florscheutz et al. is valid for $2500<\mathrm{Re}_j<70{,}000$, $5<x/D<10$, $4<y/D<8$, $1<z/D<3$, and $T_{wa}/T_j\sim1.1$ for a staggered array. While the present case of $\mathrm{Re}_j$=18,000, $z/D$=3, $x/D$=8, and $y/D$=8 falls within the range specified by Florscheutz et al., the results indicate that the appear to be beyond the range of applicability of the correlation of Florscheutz et al. The validity of the results in the present study for temperature ratio ~1 is verified by Park et al. [31]. In both cases, spatially averaged Nusselt number data points are given for $x/D$ of 32, 40, 48, and 56. For each of these streamwise locations, the results in Fig. 9 show that area-averaged Nusselt numbers decrease as the $T_{wa}/T_j$ temperature ratio increases, provided the impingement jet static temperature is held constant.

**3.6 Local Area-Averaged Nusselt Numbers and the Temperature Ratio Correlation Equation.** Figure 10 shows area-averaged Nusselt numbers, for particular $x/D$ values, as they decrease with the $T_{wa}/T_j$ temperature ratio for $\mathrm{Re}_j$=18,000 and Ma=0.2. Here, the local area-averaged Nusselt number value is determined over the area, which extends at $x/D$=32, 40, 48, and 56 over $y/D$ from −8 to 8. The $x/D$ extent for each average is ±4 relative to the calculated value. Note that spatially averaged target surface temperatures $T_{wa}$ are determined over the same spatial surface areas. Nusselt number values then decrease as the $T_{wa}/T_j$ temperature ratio increases, up to 1.73, which evidences some deterioration of impingement cooling performance. This is because the variable property effects degrade local turbulent transport. In addition, the high crossflow temperature relative to jet temperature decreases the effectiveness of the impinging jets and causes area-averaged Nusselt numbers to decrease with $x/D$ at each $T_{wa}/T_j$ temperature ratio value.

Figure 11 shows Nusselt number ratios $\mathrm{Nu}/\mathrm{Nu}_{cp}$ as they depend on temperature ratio $T_{wa}/T_j$ for $\mathrm{Re}_j$=18,000 and Ma=0.2. $\mathrm{Nu}_{cp}$ represents the constant property Nusselt number, a condition corresponding with a temperature ratio, $T_{wa}/T_j$, of approximately 1. In the present study a temperature ratio near 1 (1.06) is used as an approximation for $\mathrm{Nu}_{cp}$. The $\mathrm{Nu}/\mathrm{Nu}_{cp}$ data in Fig. 11 follow the same trend as those in Fig. 10, which shows a decrease in Nusselt number as the $T_{wa}/T_j$ temperature ratio increases from 1.06 to 1.73. The correlation equation, which best represents the data in Fig. 11, is given by

$$\overline{\overline{\mathrm{Nu}}}/\overline{\overline{\mathrm{Nu}}}_{cp}=(T_{wa}/T_j)^{-0.35} \tag{14}$$

This correlation equation is determined for $\mathrm{Re}_j$=18,000, Ma=0.2, $1.06\leq T_{wa}/T_j\leq1.73$, $X/D$=8, $Y/D$=8, $Z/D$=3, and $32\leq x/D\leq56$. However, Eq. (14) is expected to be valid for a wider range of incompressible (or near incompressible) flow conditions, which include $\mathrm{Re}_j$ from near 3,000 to about 30,000, Ma from near 0 to approximately 0.25, and a range of $X/D$ and $Y/D$ values in the vicinity of 8.

The Nusselt number variations, which are observed as either $T_{wa}/T_j$ or $T_w/T_j$ varies, are mostly due to variable property effects. Most important are variations in molecular thermal conductivity, absolute viscosity, and static density with spatial location and time since these change as static temperature varies with spatial location and time. Note that the contributions of specific heat to Nusselt number variations are less important because of its weak dependence on temperature in gas flows. The effects of conductivity, viscosity, and density variations on the local turbulent transport of momentum and heat are complex. For example, turbulent transport is generally mostly a result of mixing, collisions, and interactions of different sizes of turbulent eddies. However, ultimately, as molecular scales are approached, thermal transport is due to conduction between adjacent packets of oscillating fluid. In many cases, such molecular conduction provides some restriction on overall magnitudes of turbulent transport, which can be achieved. Such limitations and the associated phenomena and interactions are especially complex in impingement array flows because they involve such a wide variety of phenomena, including

jet flows, shear layer interactions, stagnation regions, interactions between adjacent impingement jets, wall-jet interactions, three-dimensional boundary layer development, and interactions between impingement jets and these boundary layers.

## 4 Summary and Conclusions

Data are provided as the ratio of impingement target plate temperature to impingement jet temperature is varied at a constant Reynolds number. The spacing between holes in the streamwise direction $X$ is then $8D$, and the spanwise spacing between holes in a given streamwise row $Y$ is also $8D$. The thickness of each impingement plate is $1D$, and the spacing between the hole exit planes and the target plate is denoted as $Z$ and is equal to $3D$. This impingement arrangement is similar to arrangements used in some industrial gas turbine engines, providing results and conclusions applicable to the gas turbine industry.

Local, line-averaged, and spatially averaged Nusselt numbers decrease as the $T_{wa}/T_j$ temperature ratio increases for any particular $x/D$ and $y/D$ location for $\mathrm{Re}_j=18{,}000$ and $\mathrm{Ma}=0.2$. The spatially averaged Nusselt number decrease is especially substantial as the $T_{wa}/T_j$ temperature ratio increases from 1.06 to 1.73, which evidences some deterioration of impingement cooling performance. The area beneath each impingement jet shows a higher rate of heat transfer than the surrounding areas, which do not have the additional heat transfer benefit associated with perpendicular impinging jets. The effect of increasing temperature ratio is more apparent in the regions under the impinging jets where the heat transfer is noticeably reduced, a contrast from the surrounding areas, which show almost no change. This is believed to be due to variable property effects, which degrade local turbulent transport in the impingement flow as $T_{wa}/T_j$ increases. The effect of sequential streamwise rows of impingement jets is increasing amounts of crossflow, which reduce the effectiveness of downstream impingement jets resulting in a progressive decrease in local and line-averaged Nusselt numbers, regardless of the value of the $T_{wa}/T_j$ temperature ratio. The correlation (Eq. (14)), which gives quantitative assessment of the effects of temperature ratio on local area-averaged Nusselt numbers, is expected to be valid for a range of incompressible (or near incompressible) flow conditions: $1.06 \leqslant T_{wa}/T_j \leqslant 1.73$, $Z/D=3$, $32 \leqslant x/D \leqslant 56$, $\mathrm{Re}_j$ from near 3000 to about 30,000, Ma from near 0 to approximately 0.25, and a range of $X/D$ and $Y/D$ values in the vicinity of 8.


## Acknowledgment

The research presented in this paper was sponsored by a Solar Turbine Inc. of San Diego, California, USA.


## Nomenclature

$A$ = impingement hole area
$A_{\mathrm{cross}}$ = exit channel cross-sectional area
$A_{\mathrm{ht}}$ = heat transfer area on the target plate
$c_a$ = impingement air flow sonic velocity
$C_D$ = discharge coefficient
$D$ = diameter of an individual impingement hole
$G_c$ = crossflow mass velocity or crossflow mass flux
$G_j$ = jet mass velocity or jet mass flux
$h_{\mathrm{loss}}$ = heat transfer coefficient to account for convection and radiation losses from the back side of the target plate
$k$ = ratio of specific heats
$\dot{m}$ = impingement air mass flow rate
$\dot{m}_c$ = crossflow air mass flow rate
$M_a$ = impingement air flow Mach number
$M_i$ = impingement air flow ideal Mach number
$\underline{\mathrm{Nu}}$ = local Nusselt number
$\overline{\mathrm{Nu}}$ = line-averaged Nusselt number
$\overline{\overline{\mathrm{Nu}}}$ = spatially averaged Nusselt number
$\overline{\overline{\mathrm{Nu}}}_{\mathrm{cp}}$ = constant property spatially averaged Nusselt number
$P_a$ = impingement air static pressure
$P_{oj}$ = impingement air stagnation pressure
$Q$ = total power provided to the thermofoil heater
$q_{rf}$ = radiation heat flux from the front side (or the impingement side) of the target plate
$q_{rb}$ = radiation heat flux from the back side of the target plate
$q_{cf}$ = convection heat flux from the front side (or impingement side) of the target plate
$q_{cb}$ = convection heat flux from the back side of the target plate
$R$ = ideal gas constant
$\mathrm{Re}_j$ = impingement air flow Reynolds number
$T_{\mathrm{ambient}}$ = ambient static temperature
$T_b$ = local temperature on the back surface of the polystyrene target plate
$T_w$ = local target surface temperature on the surface of the heater adjacent to the impingement air
$T_{wa}$ = spatially averaged target surface temperature on the surface of the heater adjacent to the impingement air
$T_i$ = impingement air ideal static temperature
$T_j$ = impingement air static temperature
$T_{oj}$ = impingement air stagnation temperature
$T_{tc}$ = local thermocouple temperature between the heater and the polystyrene target plate
$u_a$ = impingement air velocity
$u_c$ = crossflow velocity
$u_i$ = impingement air ideal velocity
$x$ = streamwise coordinate
$y$ = spanwise coordinate
$z$ = normal coordinate
$X$ = streamwise distance between centerlines of adjacent impingement holes
$Y$ = spanwise distance between centerlines of adjacent impingement holes
$Z$ = distance between the target plate and impingement hole plate

### Greek Symbols

$\alpha$ = air thermal conductivity
$\beta$ = flow distribution parameter
$\rho_a$ = impingement air static density
$\rho_i$ = impingement air ideal static density
$\mu$ = absolute viscosity
$\sigma$ = Boltzman constant
$\varepsilon_f$ = emissivity of the front surface of the target plate
$\varepsilon_{\mathrm{inf}}$ = emissivity of a plate located opposite to the target plate

## References


[1] Martin, H., 1977, "Heat and Mass Transfer Between Impinging Gas Jets and Solid Surfaces," Adv. Heat Transfer, **13**, pp. 1–60.
[2] Schulz, A., 2001, "Combustor Liner Cooling Technology in Scope of Reduced Pollutant Formation and Rising Thermal Efficiencies," Ann. N.Y. Acad. Sci., **934**, pp. 135–146.
[3] Kercher, D. M., and Tabakoff, W., 1970, "Heat Transfer by a Square Array of Round Air Jets Impinging Perpendicular to a Flat Surface Including the Effect of Spent Air," ASME J. Eng. Power, **92**, pp. 73–82.
[4] Metzger, D. E., Yamashita, T., and Jenkins, C., 1971, "Impingement Cooling of Concave Surfaces With Lines of Circular Air Jets," ASME J. Eng. Power, **91**, pp. 149–158.
[5] Chupp, R., Helms, H., McFadden, P., and Brown, T., 1969, "Evaluation of Internal Heat-Transfer Coefficients for Impingement Cooled Turbine Airfoils," J. Aircr., **6**(3), pp. 203–208.
[6] Metzger, D. E., and Korstad, R., 1972, "Effects of Crossflow on Impingement Heat Transfer," ASME J. Eng. Power, **94**, pp. 35–41.
[7] Chance, J. L., 1974, "Experimental Investigation of Air Impingement Heat

Transfer Under an Array of Round Jets," Tappi J., **57**(6), pp. 108–112.
[8] Metzger, D. E., Florschuetz, L. W., Takeuchi, D. I., Behee, R. D., and Berry, R. A., 1979, "Heat Transfer Characteristics for Inline and Staggered Arrays of Circular Jets With Crossflow of Spent Air," ASME Trans. J. Heat Transfer, **101**, pp. 526–531.
[9] Florschuetz, L. W., Truman, C. R., and Metzger, D. E., 1981, "Streamwise Flow and Heat Transfer Distributions for Jet Array Impingement With Crossflow," ASME Trans. J. Heat Transfer, **103**, pp. 337–342.
[10] Lee, D. H., Song, J., and Jo, M. C., 2004, "The Effects of Nozzle Diameter on Impinging Jet Heat Transfer and Fluid Flow," ASME J. Heat Transfer, **126**(4), pp. 554–557.
[11] Garimella, S. B, and Nenaydykh, B., 1996, "Nozzle-Geometry Effects in Liquid Jet Impingement Heat Transfer," Int. J. Heat Mass Transfer, **39**(14), pp. 2915–2923.
[12] Shuja, S. Z., Yilbas, B. S., and Budair, M. O., 2005, "Influence of Conical and Annular Nozzle Geometric Configurations on Flow and Heat Transfer Characteristics Due to Flow Impingement Onto a Flat Plate," Numer. Heat Transfer, Part A, **48**(9), pp. 917–939.
[13] Siba, E. A., Ganesa-Pillai, M., Harris, K. T., and Haji-Sheikh, A., 2003, "Heat Transfer in a High Turbulence Air Jet Impinging Over a Flat Circular Disk," ASME J. Heat Transfer, **125**(2), pp. 257–265.
[14] Chung, Y. M., and Luo, K. H., 2002, "Unsteady Heat Transfer Analysis of an Impinging Jet," ASME J. Heat Transfer, **124**(6), pp. 1039–1048.
[15] Abdon, A., and Sundén, B., 2001, "Numerical Investigation of Impingement Heat Transfer Using Linear and Non-Linear Two-Equation Turbulence Models," Numer. Heat Transfer, Part A, **40**(6), pp. 563–578.
[16] Tong, A. Y., 2003, "A Numerical Study on the Hydrodynamics and Heat Transfer of a Circular Liquid Jet Impinging Onto a Substrate," Numer. Heat Transfer, Part A, **44**(1), pp. 1–19.
[17] Laschefski, H., Cziesla, T., Biswas, G., and Mitra, N. K., 1996, "Numerical Investigation of Heat Transfer by Rows of Rectangular Impinging Jets," Numer. Heat Transfer, Part A, **30**(1), pp. 87–101.
[18] Seyedein, S. H., Hasan, M., and Mujumdar, A. S., 1995, "Turbulent Flow and Heat Transfer From Confined Multiple Impinging Slot Jets," Numer. Heat Transfer, Part A, **27**(1), pp. 35–51.
[19] Rhee, D. H., Yoon, P. H., and Cho, H. H., 2003, "Local Heat/Mass Transfer and Flow Characteristics of Array Impinging Jets With Effusion Holes Ejecting Spent Air," Int. J. Heat Mass Transfer, **46**(6), pp. 113–125.
[20] Obot, N. T., and Trabold, T. A., 1987, "Impingement Heat Transfer Within Arrays of Circular Jets—Part I: Effects of Minimum, Intermediate, and Complete Crossflow for Small and Large Spacings," ASME Trans. J. Heat Transfer, **109**, pp. 872–879.
[21] Bunker, R., and Metzger, D. E., 1990, "Local Heat Transfer in Internally Cooled Turbine Airfoil Leading Edge Regions—Part I: Impingement Cooling Without Film Extraction," ASME J. Turbomach., **112**, pp. 451–458.
[22] Fox, M. D., Kurosaka, M., Hedges, L., and Hirano, K., 1993, "The Influence of Vortical Structures on the Thermal Fields of Jets," J. Fluid Mech., **255**, pp. 447–472.
[23] Bailey, J. C., and Bunker, R. S., 2002, "Local Heat Transfer and Flow Distributions for Impinging Jet Arrays of Dense and Sparse Extent," ASME Paper No. ASME GT-2002-30473.
[24] Taslim, M. E., Pan, Y., and Bakhtari, K., 2002, "Experimental Racetrack Shaped Jet Impingement on a Roughened Leading-Edge Wall With Film Holes," ASME Paper No. GT-2002-30477.
[25] Li, X., Gaddis, J. L., and Wang, T., 2002, "Mist/Stream Heat Transfer With Jet Impingement Onto a Concave Surface," ASME Paper No. GT-2002-30475.
[26] Brevet, P., Dejeu, C., Dorignac, E., Jolly, M., and Vullierme, J. J., 2002, "Heat Transfer to a Row of Impinging Jets in Consideration of Optimization," Int. J. Heat Mass Transfer, **45**, pp. 4191–4200.
[27] Brevet, P., Dorignac, E., and Vullierme, J. J., 2001, "Mach Number Effect on Jet Impingement Heat Transfer," Ann. N.Y. Acad. Sci., **934**, pp. 409–416.
[28] Florschuetz, L. W., and Su, C. C., 1987, "Effects of Crossflow Temperature on Heat Transfer Within an Array of Impinging Jets," ASME Trans. J. Heat Transfer, **109**, pp. 74–82.
[29] Kline, S. J., and McClintock, F. A., 1953, "Describing Uncertainties in Single Sample Experiments," Mech. Eng. (Am. Soc. Mech. Eng.), **75**, pp. 3–8.
[30] Moffat, R. J., 1988, "Describing the Uncertainties in Experimental Results," Exp. Therm. Fluid Sci., **1**(1), pp. 3–17.
[31] Park, J., Goodro, M., Ligrani, P. M., Fox, M., and Moon, H.-K., 2007, "Separate Effects of Mach Number and Reynolds Number on Jet Array Impingement Heat Transfer," ASME J. Turbomach., **129**, pp. 269–280.

# The Effects of Working Fluid on the Heat Transport Capacity of a Microheat Pipe

**D. Sugumar**
Center for Material and Fiber Innovation,
Deakin University,
Waurn Ponds,
3217 Victoria, Australia
e-mail: sdhar@deakin.edu.au

**Kek-Kiong Tio**
Faculty of Engineering and Technology,
Multimedia University,
Bukit Beruang,
75450 Melaka, Malaysia
e-mail: kktio@mmu.edu.my

*The effects of the thermophysical properties of the working fluid on the performance of a microheat pipe of triangular cross section are investigated. For this purpose, five different working fluids are selected: water, hepthane, ammonia, methanol, and ethanol. For operating temperatures ranging from 20°C to 100°C, it is found that the behavior of the heat transport capacity is dominated by a property of the working fluid, which is equal to the ratio of the surface tension and dynamic viscosity $\sigma/\mu_l$. This property has the same dimension as velocity and can be interpreted as a measure of the working fluid's rate of circulation, which can be provided by capillarity after overcoming the effect of viscosity. Of the five working fluids selected, ammonia is preferable for operating temperatures below 50°C since it yields the highest heat transport capacity; however, water is the preferred working fluid for temperatures above 50°C.* [DOI: 10.1115/1.2977547]

*Keywords: microheat pipes, thermal management, microscale heat transfer, microchannels*

## 1 Introduction

Since it was proposed by Cotter [1] for application in thermal management of microelectronic components and devices, microheat pipes (MHPs) have attracted considerable interests. Currently, the literature consists of a large number of analytical studies and experimental investigations [2–15], as well as numerous reviews, such as those of Peterson [16,17] and the more recent one of Vasiliev [18]. However, there are still many questions, which remain to be addressed, and the purpose of this paper, which is analytical in nature, is to elucidate some of those issues. Specifically, we shall examine the effects of the type of working fluid on the heat transport capacity of a MHP over a range of operating temperatures and identify the thermophysical property of the working fluid, which plays a dominant role in setting the trend of the heat transport capacity. For this purpose, we have selected a MHP of a cross section in the shape of an equilateral triangle. The geometrical parameters of this MHP are listed in Table 1.

In practice, several factors must be considered when we select the most suitable working fluid [19], such as its thermal stability and compatibility with the wall material of the MHP. However, the main objective of this paper is to determine among a given group of different working fluids the one that provides the highest heat transport capacity, but not to actually select the most suitable one. The issue of thermal stability and compatibility is, therefore, of secondary importance and will not be considered further.

In the existing literature, performance studies of MHPs utilize both organic and inorganic working fluids. The commonly used fluids include water [4,11,13], ethanol [5,12], methanol [5,8,12], acetone [9], and pentane [10]. Although these studies offer valuable insights and/or practical results, collectively they do not provide us with a comprehensive picture, in the sense that they do not convey the information that enables us to select the required type of working fluid to maximize the heat transport capacity. To alleviate this deficiency, we shall compare in this paper the heat transport capacities, over a range of operating temperatures of practical interests, of geometrically identical MHPs filled with different working fluids. For this purpose, we have selected five different materials; they are water, ammonia, hepthane, methanol, and ethanol, the thermophysical properties of which are readily available from the monograph of Dunn and Reay [19]. Based on this comparison, we can then determine which working fluid is the most desirable. In this paper, we shall consider horizontal MHPs as well as those that are inclined with respect to the horizontal plane.

In Fig. 1, a schematic is depicted for the MHP studied in this paper. Thermal energy from a heat generating source enters the MHP at its evaporator section and is taken up as the latent heat of evaporation by the working fluid's liquid phase. The vapor that results from this evaporation process then flows toward the adiabatic and condenser sections. Heat transfer does not take place between the microheat pipe and its surroundings in the adiabatic section and, consequently, no phase change occurs. At the condenser section, the vapor condenses and gives up its latent heat, which flows out of the microheat pipe and into its surroundings. By capillary action, the condensate is held in the corner regions and is pumped back to the evaporator section, where the working fluid begins another cycle of phase change and circulation. For a MHP, which is positively oriented with respect to the horizontal plane, such as the one shown in Fig. 1, the liquid flow is also assisted by gravity.

To calculate the fluid flows and heat transfer described above, we shall make use of the one-dimensional model developed by Tio et al. [13]. In this model, the flow channel inside a MHP is assumed to be so small that it can be regarded as a pore of a porous medium. Under this assumption, a one-dimensional MHP model can then be constructed by using Darcy's two-phase equations and Laplace's capillary equation. Other one-dimensional models, which have been developed include, for examples, those of Cotter [1], Longtin et al. [6], Wang et al. [7], and Ha and Peterson [5]. That the model of Tio et al. [13] is selected for our study is primarily due to its simplicity and accuracy. As convincingly shown by the comparison of their results and the experimental data reported by Babin et al. [2] over a range of operating temperatures (Fig. 6, [13]), this porous-medium model does correctly predict the order of magnitude of the heat transport capacity and the trend of its variation with operating temperature. Finally, it should be mentioned that similar order of magnitude and trend

Contributed by the Heat Transfer Division of ASME for publication in the JOURNAL OF HEAT TRANSFER. Manuscript received January 21, 2008; final manuscript received May 15, 2008; published online October 20, 2008. Review conducted by Louis C. Chow.

  

Table 1 Parameters of the equilateral-triangle MHP studied in this paper

| $C_K$ | $s_{cl}$ | $s_{fl}$ | $L$ | $L_a$ | $L_e$ | $L_c$ | $w$ |
|---|---|---|---|---|---|---|---|
| 53.30 | 0.010 | 0.395 | 0.05 m | 0.0246 m | 0.0127 m | 0.0127 m | 0.001 m |

are also predicted by the model of Longtin et al. [6]. However, their model is more complicated than that of Tio et al. [13].

## 2 Analysis

Before we proceed to construct the steady-state mathematical model of the MHP for our study, we state here the assumptions, which are needed to simplify our analysis. First, the thermal energy transported by the MHP enters its evaporator section and leaves its condenser section uniformly over their respective lengths. Furthermore, we are concerned with axial flows only, and the effects of the lateral motion of the liquid and vapor phases are assumed to be negligible. This assumption requires that the axial length scale of the MHP is much greater than that of its cross section, which is practically the case for all microheat pipes. Following the common practice of regarding the microheat pipe as an isothermal device, the condition of temperature uniformity is assumed. Furthermore, it is also assumed that the liquid and vapor phases are saturated at that temperature.

To model the liquid and vapor flows inside a microheat pipe, we make use of the uncoupled one-dimensional two-phase Darcy's equation [20],

$$u_l = -\frac{k_l K}{\mu_l}\left(\frac{dp_l}{dx} + g\rho_l \sin\theta\right) \tag{1}$$

$$u_v = -\frac{k_v K}{\mu_v}\left(\frac{dp_v}{dx} + g\rho_v \sin\theta\right) \tag{2}$$

In these equations, $u_i$, $p_i$, $k_i$, $\rho_i$, and $\mu_i$ represent the velocity, pressure, relative permeability, mass density, and dynamic viscosity of phase $i$, respectively, $K$ is the permeability, $g$ is gravitational acceleration, $x$ is the axial distance from the evaporator end, and $\theta$ (Fig. 1) is the angle of inclination of the MHP. In Eqs. (1) and (2), $u_l$ and $u_v$ are the axial velocities averaged over the cross section of the MHP. The permeability $K$ can be obtained by comparing Darcy's equation with a Poiseuille flow inside the microheat pipe [7]. It is a constant, which depends on the cross-sectional shape and size of the MHP, and is given by

$$K = \frac{2}{C_K} D_h^2 \tag{3}$$

where $C_K$ is a constant, which depends on the cross-sectional shape, and $D_h$ is the hydraulic diameter of the cross section. The values of the constant $C_K$ are provided by Shah and London [21] for various cross-sectional shapes. For equilateral triangles, $C_K = 53.30$ and is tabulated in Table 1 along with the other constants. The relative permeabilities $k_l$ and $k_v$ can be obtained by ignoring the irreducible saturation of the liquid phase [20] and are given by

$$k_l = s^3 \tag{4}$$

$$k_v = (1-s)^3 \tag{5}$$

where $s$ is the volume fraction occupied by the liquid phase.

During steady-state operation of a MHP, there is no accumulation of mass at any cross section. Therefore, the mass-conservation principle can be stated as

$$\dot{m}_l = u_l \rho_l A = -\dot{m} \tag{6}$$

$$\dot{m}_v = u_v \rho_v A = \dot{m} \tag{7}$$

where $\dot{m}_l$ and $\dot{m}_v$ are the mass flow rates of the liquid and vapor phases, respectively, and $A$ is the cross-sectional area of the microheat pipe. Based on the assumption that the heat transfer between the microheat pipe and its surroundings takes place uniformly over the entire length of the evaporator and condenser, the mass flow rate $\dot{m}$ in Eqs. (6) and (7) can be written as

$$\dot{m} = \left(\frac{QL}{h_{fg} L_e}\right)\hat{m} \tag{8}$$

where

$$\hat{m} = \begin{cases} \hat{x}, & \hat{x} \le \dfrac{L_e}{L} \\ \dfrac{L_e}{L}, & \dfrac{L_e}{L} \le \hat{x} \le 1 - \dfrac{L_c}{L} \\ \dfrac{L_e}{L_c}(1-\hat{x}), & 1 - \dfrac{L_c}{L} \le \hat{x} \le 1 \end{cases} \tag{9}$$

$$\hat{x} = \frac{x}{L} \tag{10}$$

Here, $\hat{x}$ is the dimensionless axial distance from the evaporator end. In Eq. (8), $h_{fg}$ is the latent heat of evaporation of the working fluid, and $Q$ is the rate of heat transport by the MHP. The three lengths $L_e$, $L_c$, and $L$, which appear in Eq. (9) are the evaporator length, condenser length, and total length of the MHP, respec-

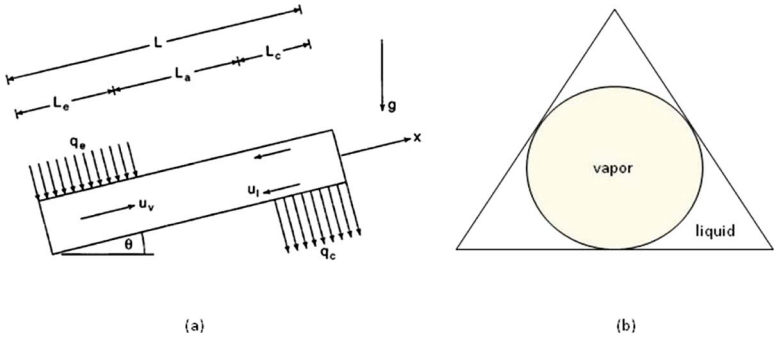


Fig. 1 (*a*) A schematic of an inclined microheat pipe, $\theta$ being the angle of inclination; (*b*) cross-sectional view of a triangular MHP, showing the onset of flooding

tively. Equations (8)–(10) state that the vapor flow rate passing through a cross section of the MHP is equal to the net rate of evaporation over the whole region upstream of the cross section. Since there is no accumulation of mass anywhere inside the microheat pipe during steady-state operation, this vapor flow rate is equal to the liquid flow passing through the same cross section in the opposite direction.

From Eqs. (1), (2), (6), and (7), we obtain

$$\frac{d(p_v - p_l)}{dx} = -\frac{\dot{m}}{AK}\left(\frac{\mu_l}{\rho_l k_l} + \frac{\mu_v}{\rho_v k_v}\right) + (\rho_l - \rho_v) g \sin\theta \tag{11}$$

The pressures of the two phases are related by Laplace's capillary equation,

$$p_v - p_l = \frac{\sigma}{R} \tag{12}$$

where $\sigma$ is the coefficient of surface tension, and $R$ is the radius of curvature of the liquid-vapor interface in a cross section of the microheat pipe. In this paper, it is assumed that this interface consists of circular arcs of the same radius. Therefore, $R$ can be assumed constant throughout a cross section; however, it is allowed to vary from one cross section to another. It should be noted that we have excluded from Eq. (12) the liquid-vapor interface's curvature in the longitudinal plane. This is justified by the fact that the axial length scales of a MHP are usually much larger than those of its cross section. In this paper, it is also assumed that the liquid phase is uniformly distributed among all the corner regions of the cross section, the center region being occupied by the vapor phase. Eliminating the pressures from Eqs. (11) and (12), the following ordinary differential equation for the liquid volume fraction $s$ is obtained:

$$\frac{ds}{d\hat{x}} = \frac{s^{3/2}}{\omega}\left[\mathrm{Ca}\left(\frac{1}{s^3} + \frac{\gamma}{(1-s)^3}\right)\hat{m} - \mathrm{Ga}\sin\theta\right] \tag{13}$$

The capillary number Ca, Gravity number Ga, viscosity ratio $\gamma$, and angular parameter $\omega$ are defined as

$$\mathrm{Ga} = \frac{2gL(\rho_l - \rho_v)(A/N)^{1/2}}{\sigma} \tag{14}$$

$$\mathrm{Ca} = \left(\frac{Q}{\rho_l h_{fg} A (L_e/L)}\right) \Big/ \left(\frac{\sigma K}{2\mu_l L (A)^{1/2}}\right) \tag{15}$$

$$\gamma = \frac{\nu_v}{\nu_l} \tag{16}$$

$$\omega = N^{1/2}\left[\frac{\cos\vartheta\cos(\phi+\vartheta)}{\sin\phi} + (\phi+\vartheta) - \frac{\pi}{2}\right]^{1/2} \tag{17}$$

In Eq. (16), $\nu_i$ is the kinematic viscosity of phase $i$. In Eq. (17), which is valid only for MHPs of cross-sectional shapes in the form of a regular polygon, $N$ is the number of corners of the cross section, and $\phi$ is the half angle of these corners, i.e., $N=3$ and $\phi=\pi/6$ for an equilateral-triangle cross section. In general, the contact angle of the liquid phase and the inner wall of the microheat pipe $\vartheta$ varies throughout the pipe channel. For simplicity, it is assumed to be constant everywhere inside the pipe channel. Furthermore, its value is taken to be zero when actual computations are performed. Thus, unless stated otherwise, the numerical results presented in this paper are valid only for zero contact angles.

For a horizontal microheat pipe ($\theta=0$), we can integrate by numerical quadrature Eq. (13) for a given value of Ca to obtain the axial variation of the liquid volume fraction. For this purpose, we have selected Simpson's rule. For the case in which $\theta \neq 0$, Eq. (13) is a nonlinear ordinary differential equation and its solution must be obtained numerically. In this case, it is integrated using the fourth order Runge-Kutta scheme with a prescribed "initial condition" $s(\hat{x}=0)$. Having determined $s(\hat{x})$, the total mass of the working fluid $M$ inside the MHP can be calculated. In dimensionless form, it is given by

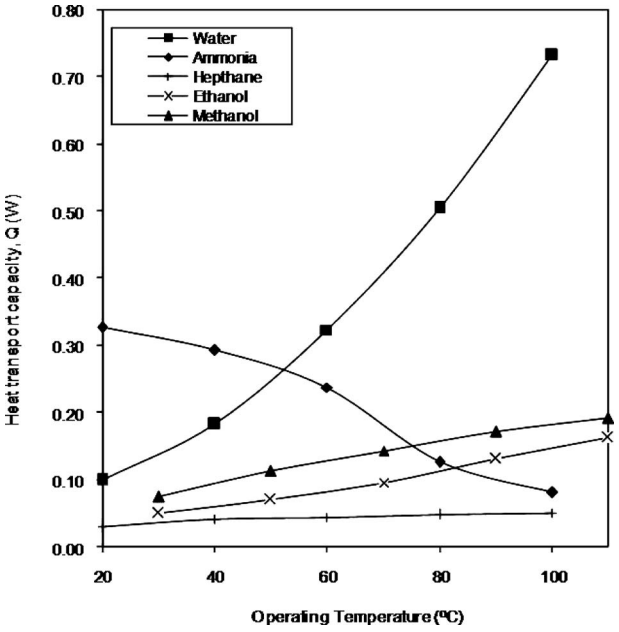


**Fig. 2 Heat transport capacity, as a function of the operating temperature, of the equilateral-triangle MHP in Table 1 optimally filled with different types of working fluid**

$$\hat{M} = \frac{M}{AL\rho_l} = \left(\frac{\rho_v}{\rho_l}\right) + \left[1 - \left(\frac{\rho_v}{\rho_l}\right)\right]\int_0^1 s(\hat{x})\,d\hat{x} \tag{18}$$

For a horizontal microheat pipe ($\theta=0$), the heat transport capacity can be obtained in closed form from Eq. (13). In dimensionless form, it is given by

$$\mathrm{Ca}_{\max} = \frac{2\omega}{\frac{L_e}{L}\left(2 - \frac{Le}{L} - \frac{Lc}{L}\right)}\int_{s_{cl}}^{s_{fl}} \frac{s^{3/2}}{1 + \gamma s^3/(1-s)^3}\,ds \tag{19}$$

The corresponding optimal charge level $\hat{M}_{opt}$ is obtained from Eq. (18) with $s(\hat{x})$ satisfying the simultaneous conditions of $s(0)=s_{cl}$ and $s(1)=s_{fl}$. For an inclined MHP, $\mathrm{Ca}_{\max}$ cannot be obtained in closed form; instead, it must be obtained numerically under the same simultaneous conditions. The integration limit $s_{cl}$ in Eq. (19) corresponds to the first occurrence of dryout at the evaporator end, while $s_{fl}$ corresponds to the onset of flooding at the condenser end. Their values for the case of zero contact angle are tabulated in Table 1. It should be noted that the mathematical condition of $s=0$ at $\hat{x}=0$ is not used to designate the dryout limit. Instead, for safety reasons, the condition of $s=0.01$ at $\hat{x}=0$ is employed to designate the capillary limit [13]. The values of $L_e$, $L_c$, and $L$ are fixed for the MHP studied in this paper. For easy reference, their values are also tabulated in Table 1.

## 3 Discussion

Figure 2 illustrates the heat transport capacity, as a function of the operating temperature, of the MHP in Table 1 filled with different types of working fluid. Here, the microheat pipe is filled with the optimal amount of the working fluid. From Fig. 2, it is

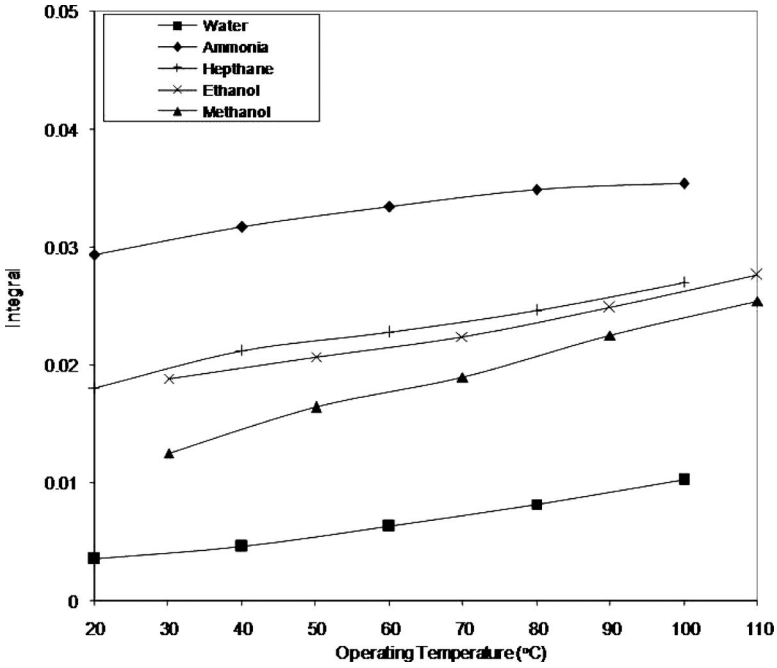


**Fig. 3 The integral in Eq. (20) for different types of working fluid, as a function of their temperature**

observed that the heat transport capacity for each of the five working fluids is, to varying degrees, dependent on the operating temperature of the MHP. Moreover, we also observe that, except for ammonia, the heat transport capacity for the remaining four working fluids increases when the operating temperature is increased. The heat transport capacity for water shows a rapid increase with the operating temperature, from 0.0994 W at 20°C to 0.7329 W at 100°C. The increase in the heat transport capacity for methanol and ethanol is moderate, from 0.0748 W and 0.0495 W at 30°C to 0.1921 W and 0.1632 W at 110°C, respectively. The increase in the heat transport capacity for hepthane is relatively small compared to those for water, ethanol, and methanol over the same range of the operating temperatures. From Fig. 2, it is clearly seen that for operating temperatures below 50°C, it is more advantageous to use ammonia as the working fluid to maximize the heat transport capacity of the MHP. However, water is preferable if the operating temperature is higher than 50°C.

To determine the main reason for the differences in the trends of the heat transport capacities depicted in Fig. 2, we need to see how the heat transport capacity of a MHP depends on its operating temperature through the temperature dependence of the various thermophysical properties of the working fluid. From Eqs. (15) and (19), it is clearly seen that the dependence of the heat transport capacity of a MHP of a cross section in the form of an equilateral triangle on the properties of its working fluid takes the form of

$$Q_{\max} \sim (\rho_l h_{\mathrm{fg}}) \cdot \left(\frac{\sigma}{\mu_l}\right) \cdot \int_{s_{\mathrm{cl}}}^{s_{\mathrm{fl}}} \frac{s^{3/2}}{1+\gamma s^3/(1-s)^3} ds \qquad (20)$$

As noted by Tio et al. [13], the ratio $\sigma/\mu_l$, which has the dimension of velocity, can be interpreted as a measure of the liquid phase velocity and, therefore, a measure of the circulation rate of the working fluid as well. The product $\rho_l h_{\mathrm{fg}}$ is the latent heat of evaporation per unit volume of the liquid phase. The physical significance of the integral in Eq. (20) is not obvious, although it can be traced back to the relative permeabilities given in Eqs. (4) and (5). To have a clearer picture of how these three factors affect the heat transport capacity of an equilateral-triangle MHP as a function of its operating temperature, Figs. 3–5 are plotted. Examination of these figures reveals that of the three factors in Eq. (20), $\sigma/\mu_l$ is dominant. Therefore, it can be concluded that the heat transport capacity of a microheat pipe, as a function of its operating temperature, is largely dependent on its working fluid's circulation effectiveness under the constraint of other factors, such as geometry.

In Fig. 6, we show the optimal charge levels $\hat{M}_{\mathrm{opt}}$ as functions of the operating temperature, associated with the heat transport capacities presented for the five working fluids in Fig. 2. The corresponding mass $M$ of each of the five working fluids is illustrated in Fig. 7. While the charge level $\hat{M}_{\mathrm{opt}}$ for water is always the lowest among the five working fluids, the same cannot be said of its mass $M$. In fact, the required mass for water is the greatest for operating temperatures above 60°C. This observation is, of course, not surprising, if we note that $\hat{M}_{\mathrm{opt}}$ is actually a measure of the relative volume of a working fluid inside a MHP (see the first of Eqs. (18)) and that water has the highest mass density among the five working fluids.

Up to this point, we have confined our discussion to horizontal MHPs only, and the gravity number Ga in Eq. (13) is ignored. In what follows, we shall deal with inclined MHPs, so that the effect of gravity (i.e., the gravity number Ga) must be taken into consideration. As can be seen from Eq. (14), the dependence of Ga on the working fluid's thermophysical properties takes the form of

$$\mathrm{Ga} \sim \frac{(\rho_l - \rho_v)}{\sigma} \qquad (21)$$

Since the thermophysical properties of a working fluid are functions of temperature, any changes in the operating temperature affect the value of Ga. Figure 8 illustrates the relationship of Ga with the operating temperature of a MHP for three different types of working fluid: water, hepthane, and ammonia. We observe from Fig. 8 that, similar to the ratio $\sigma/\mu_l$ depicted in Fig. 4, the Ga for ammonia starts to change rapidly when the temperature is increased to about 60°C.

Figure 9 illustrates the heat transport capacity, as a function of the operating temperature, for various angles of inclination. Here, the MHP in Table 1 is filled optimally with water. We note that the

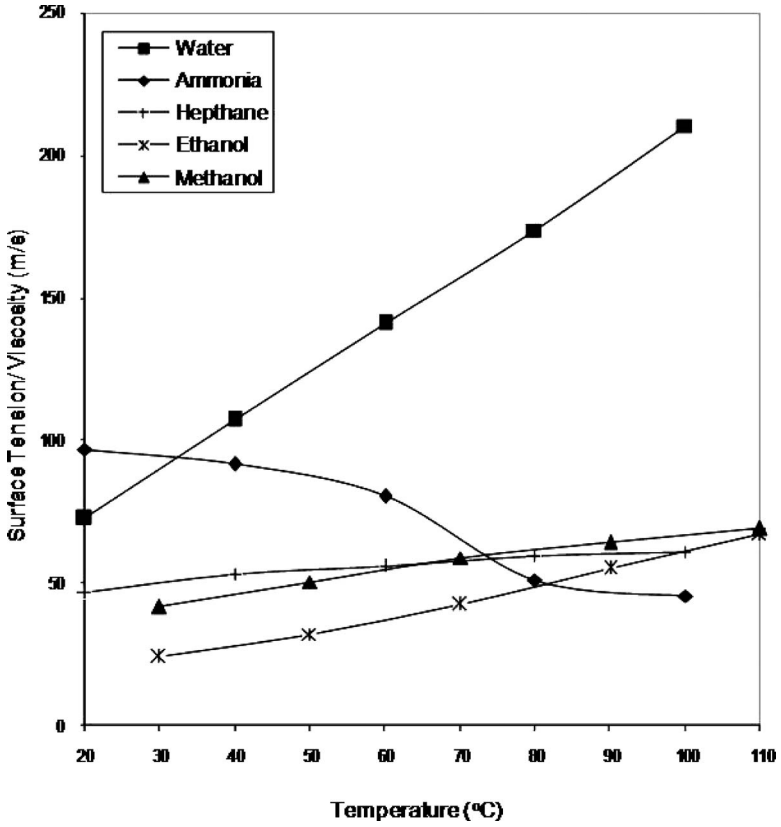


**Fig. 4 Ratio of surface tension and liquid dynamic viscosity of different types of working fluid, as a function of their temperature**

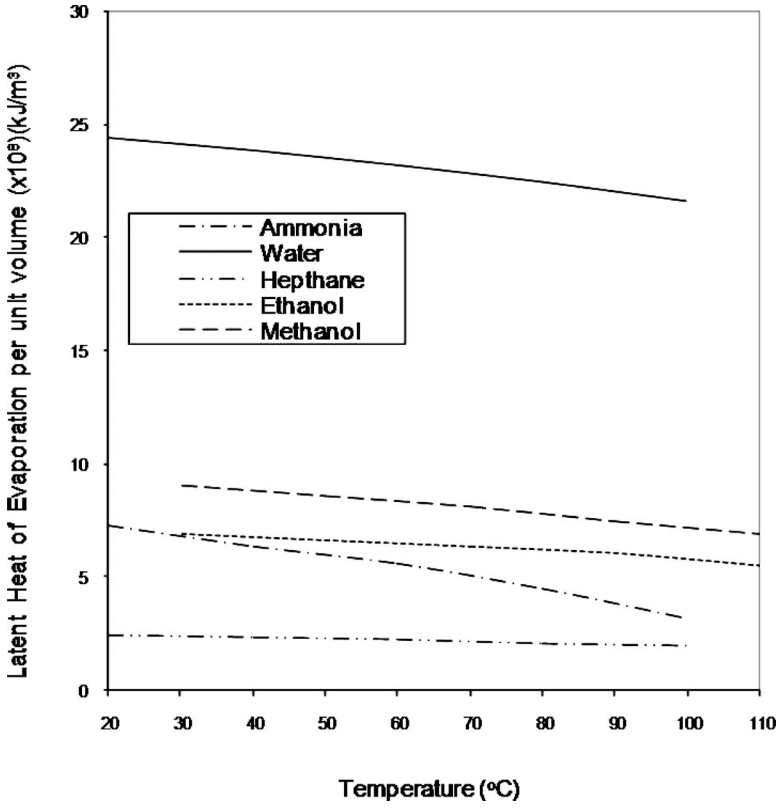


**Fig. 5 Latent heat of evaporation per unit volume for different types of working fluid, as a function of their temperature**

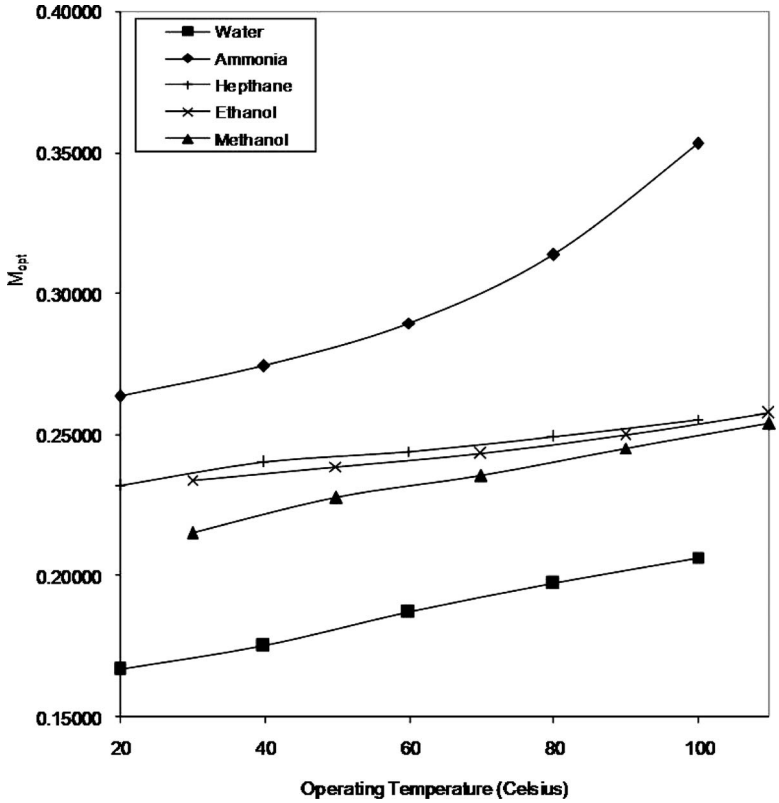


**Fig. 6 Optimal charge level, as a function of the operating temperature, for the equilateral-triangle MHP in Table 1 filled with different types of working fluid**

heat transport capacity of an inclined MHP is also limited by the simultaneous onsets of dryout and flooding. However, unlike a horizontal MHP, the onset of flooding takes place at a finite distance from the condenser end [14]. From Fig. 9, we observe that the heat transport capacity increases with an increase in the operating temperature. For any specific operating temperature, the heat

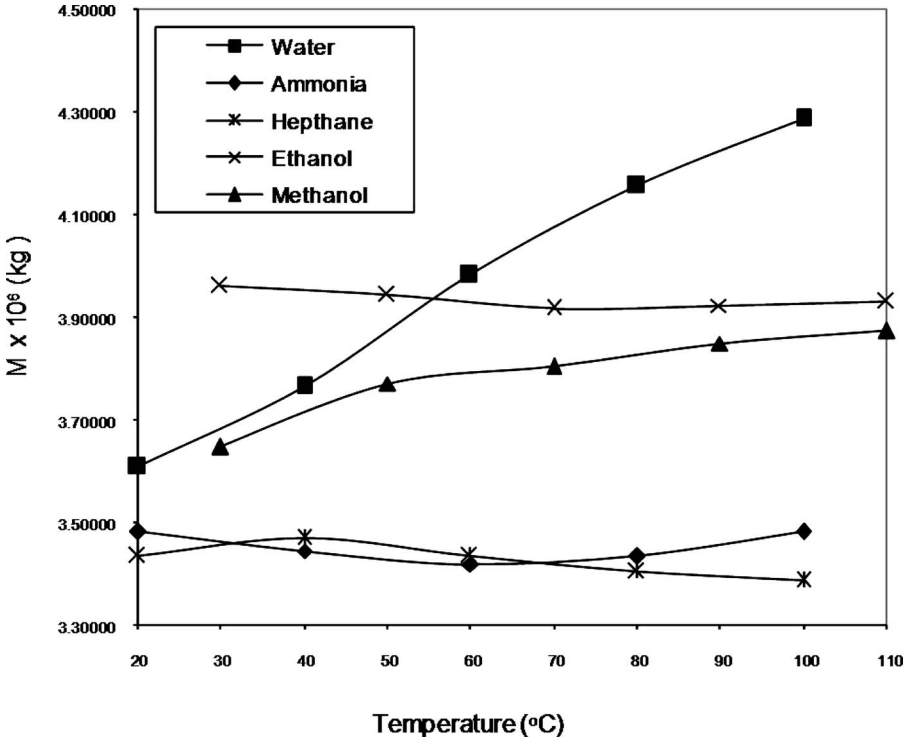


**Fig. 7 Optimal mass of the working fluid, as a function of the operating temperature, for the equilateral-triangle MHP in Table 1 filled with different types of working fluid**

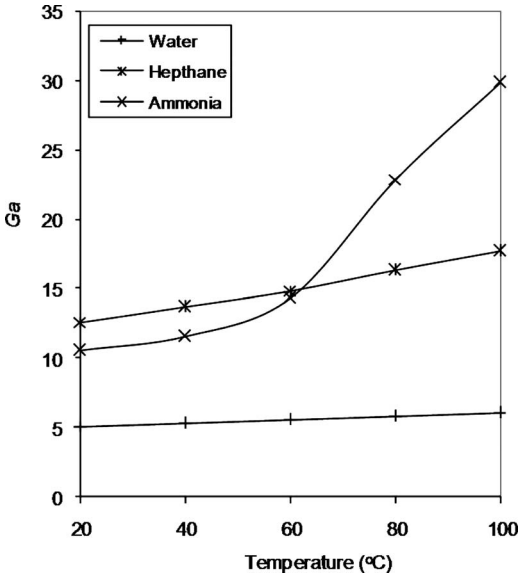


**Fig. 8 Gravity number Ga of different types of working fluid, as a function of the operating temperature.**

transport capacity of the MHP increases when its angle of inclination is increased from 0 deg to 30 deg and 60 deg. When the operating temperature increases, so does the rate of increase in the heat transport capacity with respect to the operating temperature; furthermore, this rate of increase is greater for a larger angle of inclination. These behaviors of the heat transport capacity can be explained as follows. As observed earlier for a horizontal MHP filled with water, its heat transport capacity is largely controlled by the ability of capillarity to circulate its working fluid. For a positively inclined MHP, the circulation rate of the working fluid is enhanced by gravity through Ga and $\theta$ (see Eq. (13)), resulting in a greater heat transport capacity compared to a horizontal MHP at the same operating temperature. As observed previously from Figs. 4 and 8, the pumping ability of capillarity and Ga both increase with the operating temperature. For a fixed angle of inclination $\theta$, the increase in the heat transport capacity with operating temperature is, therefore, contributed by the increase in capillary pumping and by the increase in gravitational effect through Ga. Consequently, the rate of increase in the heat transport capacity (with respect to the operating temperature) of a positively inclined MHP is greater than that of a horizontal MHP, which is solely the result of the increase in capillary strength. Finally, since the effects of Ga become greater as $\theta$ is increased, the rate of increase in the heat transport capacity is greater for a larger $\theta$.

For a MHP optimally filled with hepthane, the heat transport capacity is depicted in Fig. 10 as a function of the operating temperature, the angle of inclination $\theta$ being a parameter. We observe that the general trends of the heat transport capacity with respect to the operating temperature and angle of inclination are similar to those of a water-filled MHP.

Figure 11 shows the heat transport capacity, as a function of the operating temperature of the MHP in Table 1 for the case in which it is tilted with different angles of inclination and filled optimally with ammonia. As expected, the heat transport capacity for a fixed

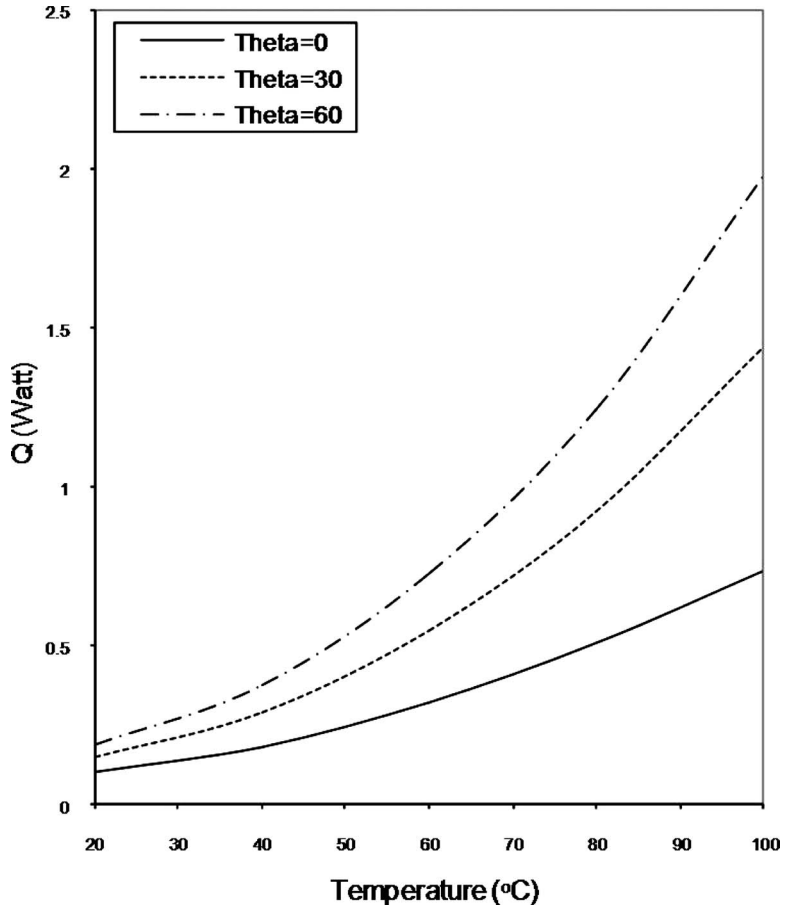


**Fig. 9 Heat transport capacity, as a function of the operating temperature, of the equilateral-triangle MHP in Table 1 for different angles of inclination. Here, the working fluid is water.**

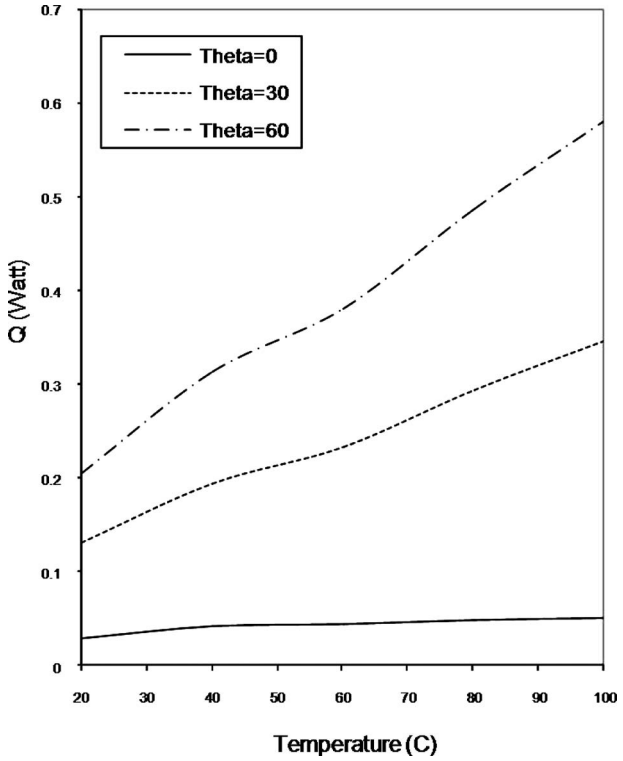


**Fig. 10 Heat transport capacity, as a function of the operating temperature, of the equilateral-triangle MHP in Table 1 for different angles of inclination. Here, the working fluid is hepthane.**

operating temperature becomes greater as the angle of inclination is progressively increased. However, in contrast to the two previous cases for water and hepthane illustrated, respectively, in Figs.

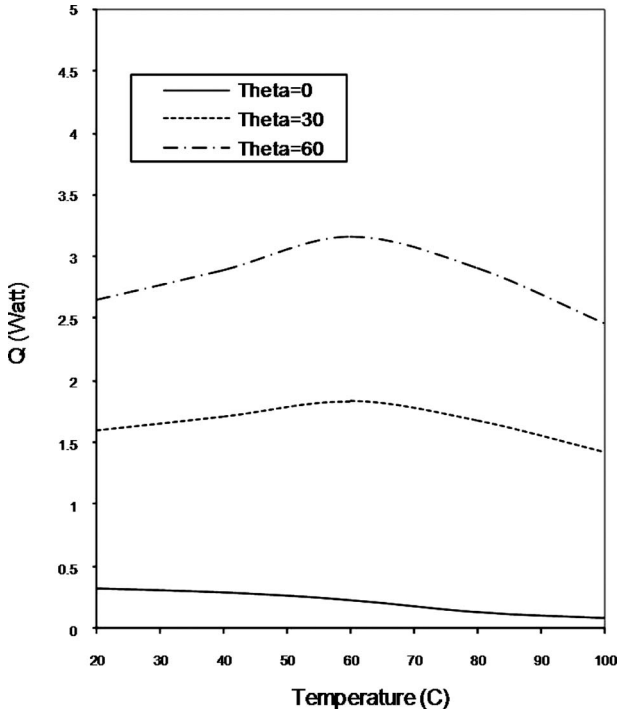


**Fig. 11 Heat transport capacity, as a function of the operating temperature, of the equilateral-triangle MHP in Table 1 for different angles of inclination. Here, the working fluid is ammonia.**

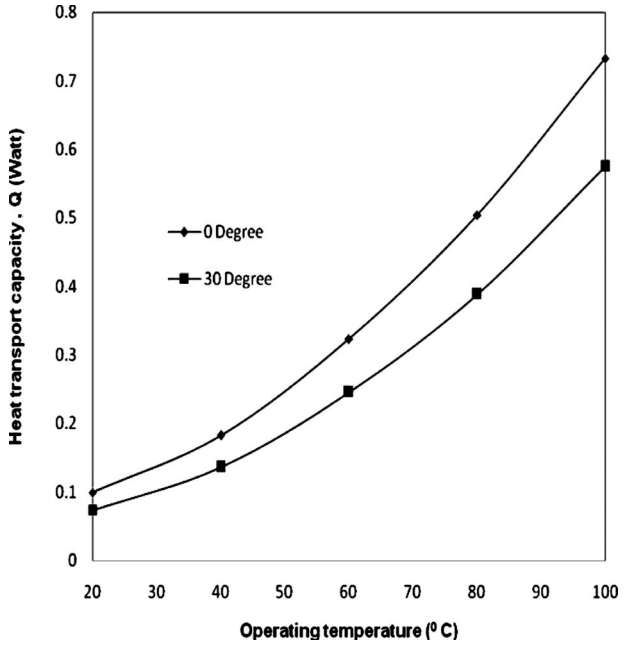


**Fig. 12 Heat transport capacity, as a function of the operating temperature, of the equilateral-triangle MHP in Table 1 for different contact angles. Here, the working fluid is water.**

9 and 10, the heat transport capacity for ammonia does not increase monotonically with the operating temperature but reaches a maximum value at 60°C, at which point it starts to decrease with temperature. Although the heat transport capacity of an ammonia-filled horizontal MHP decreases with the operating temperature, the rate of decrease in capillary strength, as reflected by the ratio $\sigma/\mu_l$ depicted in Fig. 4, is sufficiently moderate for temperatures below 60°C that its negative effects can be rectified by the positive effects of gravity, provided the angle of inclination is sufficiently large. While the rate of increase in Ga with temperature is moderate for temperatures below 60°C (see Fig. 8), it is sufficiently large that the trend of Ga dominates that of the ratio $\sigma/\mu_l$. Consequently, the heat transport capacity for ammonia actually increases with operating temperatures below 60°C, as shown in Fig. 11. For operating temperatures above 60°C, the opposite is true. While Ga increases rapidly with temperature, the ratio $\sigma/\mu_l$ also decreases rapidly. Apparently, the rate of decrease in $\sigma/\mu_l$ is now sufficiently large that it sets the trend, resulting in a heat transport capacity, which decreases with increasing operating temperature, provided that the angle of inclination is not too large.

It should be noted that the results, which we have discussed so far, are obtained under the assumption of a constant contact angle (equal to zero) throughout the flow channel of a MHP. This assumption is, of course, a necessary idealization since the wetting of solid surfaces is a complex phenomenon. Nevertheless, it is still interesting to see how a change in the magnitude of the contact angle, assumed to be uniform throughout the MHP's flow channel, affects its heat transport capacity. For this purpose, we have selected two working fluids: water and ammonia. While an increase in the contact angle from $\vartheta=0$ deg to $\vartheta=30$ deg does not qualitatively change the trend of the MHP's heat transport capacity with respect to its operating temperature, as is clearly seen in Figs. 12 and 13. A closer look at these figures reveals a stark contrast. For a fixed operating temperature, the heat transport capacity of a water-filled MHP decreases, but that of an ammonia-filled MHP actually increases. As first pointed out by Tio et al. [13], the heat transport capacity of a MHP at a given operating temperature increases when the contact angle $\vartheta$ is increased from zero up to a threshold value, beyond which the heat transport capacity de-

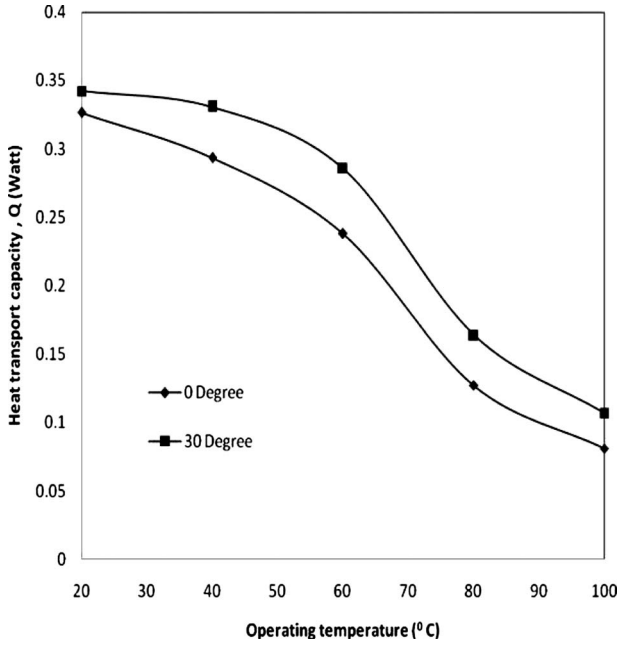


**Fig. 13 Heat transport capacity, as a function of the operating temperature, of the equilateral-triangle MHP in Table 1 for different contact angles. Here, the working fluid is ammonia.**

creases with further increase in $\vartheta$. To see this, we refer to Eq. (19), which gives the dimensionless heat transport capacity $\mathrm{Ca}_{\max}$ as a product of two factors. The first factor, the ratio, can be easily shown to decrease with $\vartheta$. The second, the integral, increases with $\vartheta$ because its upper limit,

$$s_{\mathrm{fl}} = \frac{1}{4\sqrt{3}} \cdot \frac{\omega^2}{\cos^2(\vartheta + \pi/6)} \tag{22}$$

increases with the contact angle. The opposite trends of these two factors then result in a threshold value for the contact angle, at which point the heat transport capacity achieves its maximum. Apparently, by increasing the contact angle from $\vartheta=0$ deg to $\vartheta=30$ deg in Fig. 12, we have crossed its threshold value, so that the heat transport capacity for water actually decreases. On the other hand, the threshold contact angle for ammonia is greater than 30 deg, so that an increase from $\vartheta=0$ deg to $\vartheta=30$ deg yields a higher heat transport capacity, as can be observed from Fig. 13.

## 4 Concluding Remarks

The effects of the thermophysical properties of the working fluid of a microheat pipe on its heat transport capacity have been examined with different types of working fluid. For this purpose, a MHP of cross section in the form of an equilateral triangle is employed. For operating temperatures ranging from 20°C to 100°C, it is observed that the behavior of the heat transport capacity is dominated by a property of the working fluid, which is equal to the ratio of the surface tension and dynamic viscosity $\sigma/\mu_l$. This property has the dimension of velocity and can be interpreted as a measure of the working fluid's rate of circulation, which can be provided by capillarity after overcoming the effect of viscosity. Of the five working fluids selected for this study—water, ammonia, methanol, ethanol, and hepthane—it is found that ammonia yields the highest heat transport capacity for operating temperatures below 50°C. However, water is preferable if the operating temperature is above 50°C.

In this paper, we have also examined the case in which the MHP is inclined with respect to the horizontal plane. For this purpose, three types of working fluid are used: water, hepthane, and ammonia. It is found that the heat transport capacity of the MHP increases when it is positively inclined, the increase in the heat transport capacity being greater for a larger angle of inclination. For water and hepthane, the effect of gravity is found to augment that of capillarity, without altering the general trend of the heat transport capacity with respect to the operating temperature observed in horizontal MHPs. However, for a sufficiently inclined ammonia-filled MHP, gravity may alter the trend of the heat transport capacity. Instead of decreasing with the operating temperature, the heat transport capacity is found to increase with operating temperatures below 60°C.

While we make use of a specific microheat pipe, which is an MHP of cross-sectional shape of an equilateral triangle and geometrical parameters listed in Table 1, when our computations require one, the validity of our conclusion on the dominant role of the ratio $\sigma/\mu_l$ is not limited to this particular MHP. Of the three factors on the right hand side of Eq. (20), only the integral is a function of the shape of the cross section, which can be any regular polygon, through the shape dependent constant $s_{\mathrm{fl}}$. Although the value of this integral depends on what polygon is assumed for the MHP's cross section, its functional dependence on the operating temperature can be seen to be always similar to those depicted in Fig. 3. Thus, our conclusion on the dominant role of the ratio $\sigma/\mu_l$, in setting the trend of the heat transport capacity is valid for all MHPs of cross section in the form of a regular polygon and, one may intuit, MHPs of other cross-sectional shapes as well. Finally, our conclusion on the qualitative effects of the gravity number Ga on the heat transport capacity is also valid for MHPs of arbitrary cross section and axial length scales, for the reason that the arguments leading to this conclusion are independent of geometry.

## Nomenclature

$A$ = cross-sectional area
$C_K$ = constant in Eq. (3)
Ca = capillary number
$\mathrm{Ca}_{\max}$ = dimensionless heat transport capacity
$D_h$ = hydraulic diameter
$g$ = gravitational acceleration
Ga = gravity number
$h_{\mathrm{fg}}$ = latent heat of evaporation
$K$ = permeability
$k$ = relative permeability
$L$ = length of micro heat pipe
$L_a$ = length of adiabatic section
$L_e$ = length of evaporator section
$L_c$ = length of condenser section
$\dot{m}$ = mass flow rate
$\hat{m}$ = as defined in Eq. (9)
$M$ = mass of working fluid
$\hat{M}$ = charge level
$\hat{M}_{\mathrm{opt}}$ = optimal charge level
$N$ = number of corners
$p$ = pressure
$q_c$ = rate of heat flow across a unit length of condenser
$q_e$ = rate of heat flow across a unit length of evaporator
$Q$ = rate of heat transport
$R$ = radius of curvature of liquid-vapor interface
$s$ = volume fraction occupied by liquid phase
$T$ = temperature
$u$ = velocity
$w$ = side of triangle
$x$ = distance from evaporator end
$\hat{x}$ = dimensionless $x$

### Greek Symbols

$\gamma$ = viscosity ratio
$\theta$ = angle of inclination
$\vartheta$ = contact angle
$\mu$ = dynamic viscosity
$\nu$ = kinematic viscosity
$\rho$ = mass density
$\sigma$ = surface tension
$\phi$ = half angle of a corner
$\omega$ = angular parameter defined in Eq. (17)

### Subscripts

cl = capillary limit
fl = onset of flooding
$l$ = liquid
$v$ = vapor

## References


[1] Cotter, T. P., 1984, "Principles and Prospects of Micro Heat Pipes," *Proceedings of the Fifth International Heat Pipe Conference*, Tsukuba, Japan, May 14–18, pp. 328–335.
[2] Babin, B. R., Peterson, G. P., and Wu, D., 1990, "Steady-State Modeling and Testing of a Micro Heat Pipe," ASME J. Heat Transfer, **112**, pp. 595–601.
[3] Peterson, G. P., Duncan, A. B., and Weichold, M. H., 1993, "Experimental Investigation of Micro Heat Pipes Fabricated in Silicon Wafers," ASME J. Heat Transfer, **115**, pp. 751–756.
[4] Khrustalev, D., and Faghri, A., 1998, "Thermal Analysis of a Micro Heat Pipe," ASME J. Heat Transfer, **116**, pp. 189–198.
[5] Ha, J. M., and Peterson, G. P., 1994, "Analytical Prediction of the Axial Dryout Point for Evaporating Liquids in Triangular Microgrooves," ASME J. Heat Transfer, **116**, pp. 498–503.
[6] Longtin, J. P., Badran, B., and Gerner, F. M., 1994, "A One-Dimensional Model of a Micro Heat Pipe During Steady-State Operation," ASME J. Heat Transfer, **116**, pp. 709–715.
[7] Wang, C.-Y., Groll, M., Rosler, S., and Tu, C.-J., 1994, "Porous Medium Model For Two Phase Flow in Mini Channels With Application to Micro Heat Pipes," Heat Recovery Syst. CHP, **14**, pp. 377–389.
[8] Ma, H. B., and Peterson, G. P., 1996, "Experimental Investigation of the Maximum Heat Transport in Triangular Grooves," ASME J. Heat Transfer, **118**, pp. 740–746.
[9] Ha, J. M., and Peterson, G. P., 1996, "The Interline Heat Transfer of Evaporating Thin Films along a Micro Grooved Surface," ASME J. Heat Transfer, **118**, pp. 747–755.
[10] Pratt, D. M., Brown, J. R., and Hallinan, K. P., 1998, "Thermocapillary Effects on the Stability of a Heated, Curved Meniscus," ASME J. Heat Transfer, **120**, pp. 220–226.
[11] Ma, H. B., and Peterson, G. P., 1998, "The Minimum Meniscus Radius and Capillary Heat Transport Limit in Micro Heat Pipes," ASME J. Heat Transfer, **120**, pp. 227–233.
[12] Peterson, G. P., and Ha, J. M., 1998, "Capillary Performance of Evaporating Flow in Micro Grooves, An Approximate Analytical Approach and Experimental Investigation," ASME J. Heat Transfer, **120**, pp. 743–751.
[13] Tio, K.-K., Liu, C. Y., and Toh, K. C., 2000, "Thermal Analysis of Micro Heat Pipes Using a Porous-Medium Model," Heat Mass Transfer, **36**, pp. 21–28.
[14] Sugumar, D., and Tio, K.-K., 2006, "Thermal Analysis of Inclined Micro Heat Pipes," ASME J. Heat Transfer, **128**, pp. 198–202.
[15] Ma, H. B., Lofgreen, K. P., and Peterson, G. P., 2006, "An Experimental Investigation of a High Heat Flux Heat Pipe Heat Sink," ASME J. Electron. Packag., **128**, pp. 18–22.
[16] Peterson, G. P., 1992, "Overview of Micro Heat Pipe Research and Development," Appl. Mech. Rev., **45**, pp. 175–189.
[17] Peterson, G. P., 1996, "Modeling, Fabrication and Testing of Micro Heat Pipes: An Update," Appl. Mech. Rev., **49**, pp. S175–S183.
[18] Vasiliev, L. L., 2008, "Micro and Miniature Heat Pipes—Electronic Component Coolers," Appl. Therm. Eng., **28**, pp. 266–273.
[19] Dunn, P. D., and Reay, D. A., 1994, *Heat Pipes*, 4th ed., Pergamon, New York.
[20] Dullien, F. A. L., 1992, *Porous Media: Fluid Transport and Pore Structure*, 2nd ed., Academic, San Diego, CA.
[21] Shah, R. K., and London, A. L., 1978, *Laminar Flow Forced Convection in Ducts*, Academic, New York.

# Non-Newtonian Natural Convection Along a Vertical Heated Wavy Surface Using a Modified Power-Law Viscosity Model

**M. M. Molla**
Department of Mechanical Engineering,
University of Glasgow,
Glasgow G12 8QQ, UK

**L. S. Yao**
Department of Mechanical and Aerospace Engineering,
Arizona State University,
Tempe, AZ 85287

*Natural convection of non-Newtonian fluids along a vertical wavy surface with uniform surface temperature has been investigated using a modified power-law viscosity model. An important parameter of the problem is the ratio of the length scale introduced by the power-law and the wavelength of the wavy surface. In this model there are no physically unrealistic limits in the boundary-layer formulation for power-law, non-Newtonian fluids. The governing equations are transformed into parabolic coordinates and the singularity of the leading edge removed; hence, the boundary-layer equations can be solved straightforwardly by marching downstream from the leading edge. Numerical results are presented for the case of shear-thinning as well as shear-thickening fluid in terms of the viscosity, velocity, and temperature distribution, and for important physical properties, namely, the wall shear stress and heat transfer rates in terms of the local skin-friction coefficient and the local Nusselt number, respectively. Also results are presented for the variation in surface amplitude and the ratio of length scale to surface wavelength. The numerical results demonstrate that a Newtonian-like solution for natural convection exists near the leading edge where the shear-rate is not large enough to trigger non-Newtonian effects. After the shear-rate increases beyond a threshold value, non-Newtonian effects start to develop.* [DOI: 10.1115/1.2977556]

*Keywords: natural-convection boundary layer, non-Newtonian fluids, modified power law, wavy surface*

## 1 Introduction

The major motivation for studying the dynamics of non-Newtonian power-law fluids is their importance in many practical applications. The interest in heat transfer problems involving power-law, non-Newtonian fluids has grown in the past half century. A sequence of excellent lectures on non-Newtonian fluids was given by Hinch [1]. It appears that Acrivos [2], a frequently cited paper, was the first to consider boundary-layer flows for such fluids. Since then, a large numbers of papers have been published due to their wide relevance in chemicals, foods, polymers, molten plastics and petroleum production, and various natural phenomena. A complete survey of this literature is impractical; however, a few items are listed here to provide starting points for a broader literature search [3–15].

Two common mistakes often appear in papers that study boundary layers of power-law, non-Newtonian fluids. The first is that few authors recognize that their approach introduces a length scale into their formulations; consequently, boundary-layer problems with power-law, non-Newtonian fluids cannot have self-similar solutions. Nevertheless, it is a common practice to ignore the dependence on the streamwise coordinate. It has been demonstrated in Ref. [16] that such a self-similar solution is actually only valid at the leading edge of the boundary layer. The similarity solution is a natural upstream condition, which is needed to integrate boundary-layer equations along the streamwise direction from the leading edge. Here it should be mentioned that normal length and the velocity scale are independent of the surface wavelength. For the Newtonian fluids the axial length scale is the wavelength but it is not true for the non-Newtonian fluids. For this reason there is no similarity solution for any wavy surface of Newtonian or non-Newtonian fluids. However, solution at the leading edge of the wavy surface is the necessary boundary conditions for integrating the other solutions within the boundary layer, which is done successfully by using the modified power-law model.

The second concern is related to the unrealistic physical result, introduced by the traditional power-law correlation, that viscosity either vanishes or becomes infinite in the limits of large or small shear-rates, respectively. This usually occurs at the leading edge of a flat plate or along the outer edge of boundary layers where the boundary layer matches the outer inviscid flow. Thus, power-law correlations introduce nonremovable singularities into boundary-layer formulations for an infinite or zero viscosity. Without recognizing the cause of such unrealistic conditions, a false starting process has been used to integrate boundary-layer equations from slightly downstream of the leading edge in order to avoid the irremovable singularity there [10,11], or sometimes complex multilayer structures have been introduced to overcome mathematical difficulties in order to obtain solutions of a nonphysical formulation [14,15].

The recently proposed modified power-law correlation is sketched for various values of the power index $n$ in Fig. 2. It is clear that the new correlation does not contain the physically unrealistic limits of zero and infinite viscosity displayed by traditional power-law correlations [2]. The modified power-law, in fact, fits data well. The constants in the proposed model can be fixed with available measurements and are described in detail in

Contributed by the Heat Transfer Division of ASME for publication in the JOURNAL OF HEAT TRANSFER. Manuscript received April 4, 2008; final manuscript received June 17, 2008; published online October 21, 2008. Review conducted by Ben Q. Li.

  

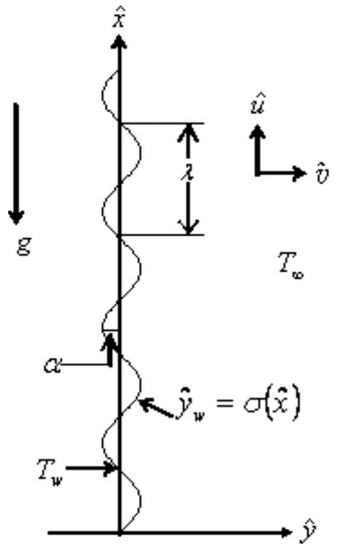


**Fig. 1 Physical model and coordinate system**

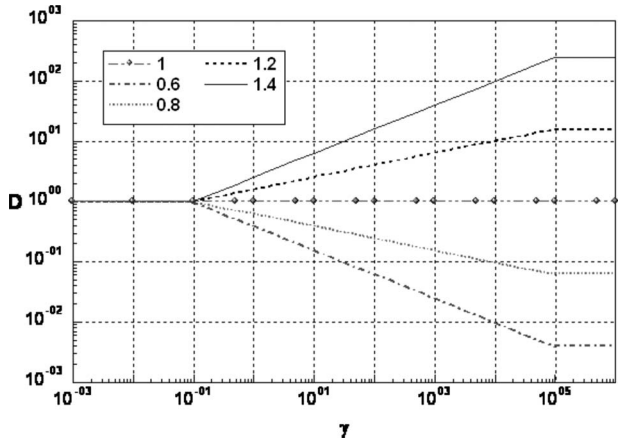


**Fig. 2 Modified power-law correlation for the power-law index $n$ (=0.6, 0.8, 1.0, 1.2, and 1.4) while $\gamma_1=0.1$ and $\gamma_2=10^5$**

Ref. [16]. The boundary-layer formulation on a flat plate is described and numerically solved in Ref. [16], and the associated heat transfer for two different heating conditions is reported in Ref. [17] for a shear-thinning fluid. In Refs. [18,19], this analysis is extended to fluids whose power-law indices are 0.6, 0.8, 1, 1.2, and 1.4 in order to fully demonstrate the effect of non-Newtonian fluids. In this investigation, the behaviors of both shear-thinning and shear-thickening fluids on the natural-convection laminar flow along a vertical wavy surface with uniform surface temperature are studied by choosing the power-law index as $n$ (=0.6,0.8,1,1.2,1.4) in order to fully demonstrate the performance of various non-Newtonian fluids.

## 2 Formulation of Problem

A steady laminar boundary layer of a non-Newtonian fluid along a vertical wavy surface with uniform surface temperature has been studied. The kinematic viscosity $\nu$ depends on shear-rate and is correlated by a modified power-law. We consider shear-thinning and shear-thickening situations of non-Newtonian fluids. Here $T_w$ is the surface temperature and $T_w > T_\infty$, where $T_\infty$ is the ambient temperature of the fluid. The boundary-layer analysis outlined below allows the shape of the wavy surface, $\sigma(\hat{x})$, to be an arbitrary, and first suggested in Refs. [20,21]. In this paper, our detailed numerical computation of a sinusoidal wavy surface has been chosen and described by

$$\hat{y}_w = \sigma(\hat{x}) = \hat{\alpha}\sin\left(\frac{2\pi l}{\lambda}\frac{\hat{x}}{l}\right) \tag{1}$$

where $\hat{\alpha}$ is the amplitude of the waviness, $\lambda$ is the wavelength of the wavy surface, and $l$ is the characteristic length scale of power law, which is defined later. The geometry of the wavy surface and the coordinate system are shown in Fig. 1.

The governing equations for the flow and heat transfer are

$$\frac{\partial \hat{u}}{\partial \hat{x}} + \frac{\partial \hat{v}}{\partial \hat{y}} = 0 \tag{2}$$

$$\hat{u}\frac{\partial \hat{u}}{\partial \hat{x}} + \hat{v}\frac{\partial \hat{u}}{\partial \hat{y}} = -\frac{1}{\rho}\frac{\partial \hat{p}}{\partial \hat{x}} + \nabla\cdot(\nu\nabla\hat{u}) + g\beta(T - T_\infty) \tag{3}$$

$$\hat{u}\frac{\partial \hat{v}}{\partial \hat{x}} + \hat{v}\frac{\partial \hat{v}}{\partial \hat{y}} = -\frac{1}{\rho}\frac{\partial \hat{p}}{\partial \hat{y}} + \nabla\cdot(\nu\nabla\hat{v}) \tag{4}$$

$$\hat{u}\frac{\partial T}{\partial \hat{x}} + \hat{v}\frac{\partial T}{\partial \hat{y}} = \frac{k}{\rho C_p}\nabla^2 T \tag{5}$$

where $(\hat{u},\hat{v})$ are velocity components along the $(\hat{x},\hat{y})$ axes, $T$ is the temperature, $\hat{p}$ is the pressure of the fluid, $g$ is the acceleration due to gravity, $\beta$ is the thermal expansion coefficient, $k$ is the thermal conductivity, and $C_p$ is the specific heat at the constant pressure. The viscosity is correlated by a modified power-law, which is

$$\nu = \frac{K}{\rho}\left|\frac{\partial \hat{u}}{\partial \hat{y}}\right|^{n-1} \quad \text{for } \bar{\gamma}_1 \le \left|\frac{\partial \hat{u}}{\partial \hat{y}}\right| \le \bar{\gamma}_2 \tag{6}$$

The constants $\bar{\gamma}_1$ and $\bar{\gamma}_2$ are threshold shear-rates, $\rho$ is the density of the fluid, and $K$ is a dimensional constant, the dimension of which depends on the power-law index $n$. The values of these constants can be determined by matching with measurements. Outside of the above range, viscosity is assumed constant; its value can be fixed with data given in Fig. 2.

The boundary conditions for the present problem are

$$\hat{u} = 0, \quad \hat{v} = 0, \quad T = T_w \quad \text{at } \hat{y} = \hat{y}_w = \sigma(\hat{x})$$

$$\hat{u} = 0, \quad T = T_\infty, \quad \hat{p} = p_\infty \quad \text{as } \hat{y} \to \infty \tag{7}$$

The required upstream conditions will be provided later. We now introduce the following nondimensional transformations:

$$x = \frac{\hat{x}}{l}, \quad y = \frac{\hat{y} - \sigma(\hat{x})}{l}\mathrm{Gr}^{1/4}, \quad u = \frac{l}{\nu_1}\mathrm{Gr}^{-1/2}\hat{u}$$

$$p = \frac{l^3}{\rho\nu_1^2}\mathrm{Gr}^{-1}\hat{p}, \quad v = \frac{l}{\nu_1}\mathrm{Gr}^{-1/4}(\hat{v} - \sigma_x\hat{u})$$

$$\theta = \frac{T - T_\infty}{T_w - T_\infty}, \quad \sigma_x = \frac{d\hat{\sigma}}{d\hat{x}} = \frac{d\sigma}{dx}, \quad D = \frac{\nu}{\nu_1}$$

$$\mathrm{Gr} = \frac{g\beta\nabla T l^3}{\nu_1^2}, \quad \delta = \frac{l}{\lambda} \tag{8}$$

where $\nu_1$ is the reference viscosity at $\bar{\gamma}_1$, $\theta$ is the dimensionless temperature of the fluid, Gr is the Grashof number, and $\delta$ is the ratio of the length of power law and the surface wavelength. Using Eq. (8) in Eqs. (2)–(5), we get the following nondimensional equations as $\mathrm{Gr}\to\infty$:

$$\frac{\partial u}{\partial x} + \frac{\partial v}{\partial y} = 0 \tag{9}$$

$$u\frac{\partial u}{\partial x}+v\frac{\partial u}{\partial y}=-\frac{\partial p}{\partial x}+\sigma_x \mathrm{Gr}^{1/4}\frac{\partial p}{\partial y}+(1+\sigma_x^2)D\frac{\partial^2 u}{\partial y^2}+(1+\sigma_x^2)\frac{\partial D}{\partial y}\frac{\partial u}{\partial y}+\theta \tag{10}$$

$$\sigma_x\left(u\frac{\partial u}{\partial x}+v\frac{\partial u}{\partial y}\right)+\sigma_{xx}u^2=-\mathrm{Gr}^{1/4}\frac{\partial p}{\partial y}+\sigma_x(1+\sigma_x^2)D\frac{\partial^2 u}{\partial y^2}+\sigma_x(1+\sigma_x^2)\frac{\partial D}{\partial y}\frac{\partial u}{\partial y} \tag{11}$$

$$u\frac{\partial \theta}{\partial x}+v\frac{\partial \theta}{\partial y}=\frac{1}{\mathrm{Pr}}(1+\sigma_x^2)\frac{\partial^2 \theta}{\partial y^2} \tag{12}$$

$$D=\frac{K}{\rho\nu_1}\left(\frac{\nu_1}{l}\mathrm{Gr}^{3/4}\right)^{n-1}\left|\frac{\partial u}{\partial y}\right|^{n-1}=C\left|\frac{\partial u}{\partial y}\right|^{n-1} \tag{13}$$

The length scale associated with the non-Newtonian power-law is

$$l=\left(\frac{C\rho}{K\nu_1^n}\right)^{1/2(n-1)}\frac{1}{\sqrt{g\beta\nabla T}} \tag{14}$$

It can easily be seen that the convection induced by the wavy surface is described by Eqs. (9)–(12). We further notice that Eq. (11) indicates that the pressure gradient along the $y$-direction is of $O(\mathrm{Gr}^{-1/4})$, which implies that lowest order pressure gradient along the $x$-direction can be determined from the inviscid flow solution. However, this pressure gradient is zero since there is no externally induced freestream. On the other hand, Eq. (11) shows that $\mathrm{Gr}^{-1/4}\partial p/\partial y$ is of $O(1)$ and is determined by the left-hand side of this equation. Thus, the elimination of $\partial p/\partial y$ from Eqs. (10) and (11) leads to

$$u\frac{\partial u}{\partial x}+v\frac{\partial u}{\partial y}=(1+\sigma_x^2)\frac{\partial}{\partial y}\left(D\frac{\partial u}{\partial y}\right)-\frac{\sigma_x\sigma_{xx}}{1+\sigma_x^2}u^2+\frac{1}{1+\sigma_x^2}\theta \tag{15}$$

The corresponding boundary conditions are

$$u=v=0,\quad \theta=1\quad \text{at } y=0$$

$$u=0,\quad \theta=0\quad \text{as } y\to\infty \tag{16}$$

Now we introduce the parabolic transformation

$$X=x,\quad Y=\frac{y}{(4x)^{1/4}},\quad U=\frac{u}{(4x)^{1/2}},\quad V=(4x)^{1/4}v \tag{17}$$

Substituting variables (17) into Eqs. (9), (15), (12), and (13) leads to

$$(4X)\frac{\partial U}{\partial X}+2U-Y\frac{\partial U}{\partial Y}+\frac{\partial V}{\partial Y}=0 \tag{18}$$

$$(4X)U\frac{\partial U}{\partial X}+(V-YU)\frac{\partial U}{\partial Y}+\left(2+\frac{4X\sigma_x\sigma_{xx}}{1+\sigma_x^2}\right)U^2=(1+\sigma_x^2)\frac{\partial}{\partial y}\left(D\frac{\partial U}{\partial y}\right)+\frac{1}{1+\sigma_x^2}\theta \tag{19}$$

$$(4X)U\frac{\partial \theta}{\partial X}+(V-YU)\frac{\partial \theta}{\partial Y}=\frac{1}{\mathrm{Pr}}(1+\sigma_x^2)\frac{\partial^2 \theta}{\partial Y^2} \tag{20}$$

and

$$D=\begin{cases}1, & |\gamma|\le\gamma_1\\ \left|\dfrac{\gamma}{\gamma_1}\right|^{n-1}, & \gamma_1\le|\gamma|\le\gamma_2\\ \left|\dfrac{\gamma_2}{\gamma_1}\right|^{n-1}, & |\gamma|\ge\gamma_2\end{cases}\qquad \text{where } \gamma=(4X)^{1/4}\frac{\partial U}{\partial \eta} \tag{21}$$

The correlation (21) is almost identical to the one proposed in Ref. [16]. This correlation shows that, if the shear-rate $|\gamma|$ lies between the threshold shear-rates $\gamma_1$ and $\gamma_2$, the non-Newtonian viscosity, $D$, varies with the power-law of $\gamma$. On the other hand, if the shear-rate $|\gamma|$ does not lie within this range, then the non-Newtonian viscosities are different constants, as shown in Fig. 2. This is a property of many measured viscosities.

Equations (18)–(20) can be solved by marching downstream with the leading-edge condition satisfying the following differential equations, which are the limits of Eqs. (18)–(20) as $X\to 0$.

$$2U-Y\frac{\partial U}{\partial Y}+\frac{\partial V}{\partial Y}=0 \tag{22}$$

$$(V-YU)\frac{\partial U}{\partial Y}+2U^2=(1+\sigma_x^2)\frac{\partial}{\partial Y}\left[D\frac{\partial U}{\partial Y}\right]+\frac{1}{(1+\sigma_x^2)}\theta \tag{23}$$

$$(V-YU)\frac{\partial \theta}{\partial Y}=\frac{1}{\mathrm{Pr}}(1+\sigma_x^2)\frac{\partial^2 \theta}{\partial Y^2} \tag{24}$$

The corresponding boundary conditions are

$$U=V=0,\quad \theta=1\quad \text{at } Y=0 \tag{25a}$$

$$U\to 0,\quad \theta\to 0\quad \text{as } Y\to\infty \tag{25b}$$

Equations (18)–(20) and (22)–(24) are discretized by a central-difference scheme for the diffusion term and a backward-difference scheme for the convection terms. Finally we get an implicit tridiagonal algebraic system of equations, which can be solved by a double-sweep technique. The normal velocity is directly solved from the continuity equation. The computation is started at $X=0$ and marches to downstream to $X=100$. After several test runs, converged results are obtained by using $\Delta X=0.0025$ and $\Delta Y=0.005$.

In practical applications, the physical quantities of principle interest are the local skin-friction coefficient $C_f$ and the local Nusselt number Nu, which are

$$C_f(\mathrm{Gr}/4X)^{1/4}=\sqrt{(1+\sigma_x^2)}\left[D\frac{\partial U}{\partial Y}\right]_{Y=0} \tag{26}$$

$$\mathrm{Nu}(\mathrm{Gr}/4X)^{-1/4}=-\sqrt{(1+\sigma_x^2)}\left(\frac{\partial \theta}{\partial Y}\right)_{Y=0} \tag{27}$$

## 3 Results and Discussion

The numerical results are presented for the non-Newtonian power-law of shear-thinning fluids ($n=0.6,0.8$) and the shear-thickening fluids ($n=1.2,1.4$) along with Newtonian fluid ($n=1.0$) while Prandtl number, $\mathrm{Pr}=100$. Based on the experimental data of Hinch [1] the threshold shears $\gamma_1$ and $\gamma_2$ have been chosen as 0.1 and $10^5$, respectively. The obtained results include the viscosity, velocity, and temperature distribution as well as the wall shear stress in terms of the local skin-friction coefficient, $C_f(\mathrm{Gr}/4X)^{1/4}$ and the rate of heat transfer in terms of the local Nusselt number, $\mathrm{Nu}(\mathrm{Gr}/4X)^{-1/4}$ for the wide range of the power-law index $n$ ($=0.6,0.8,1.0,1.2,1.4$), ratio of the length of power law and the surface wavelength, $\delta$ ($=0.5,1.0,2.0$), and ratio of the amplitude of surface waviness and the wavelength, $\alpha$ ($=0.0,0.1,0.3$).

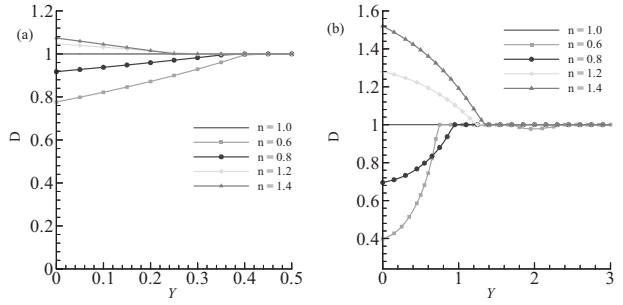


**Fig. 3 Viscosity distribution at (*a*) *X*=1.0 and (*b*) *X*=100 while Pr=100 and $\delta$=1**

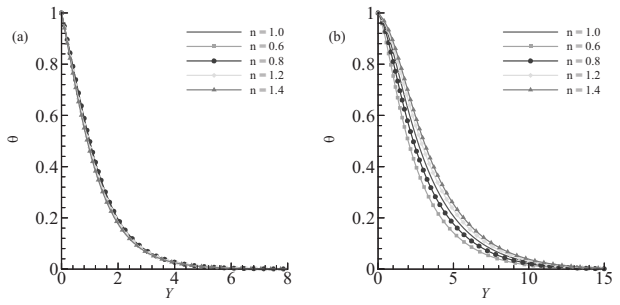


**Fig. 6 Temperature distribution at (*a*) *X*=1.0 and (*b*) *X*=100 while Pr=100, $\alpha$=0.3, and $\delta$=1**

Figures 3(*a*) and 3(*b*) illustrate the viscosity distribution for the different power-law indices $n$ (=0.6, 0.8, 1.0, 1.2, 1.4) for the selected $X$ locations while $\alpha$=0.3 and $\delta$=1.0. Near the leading edge the viscosity is constant, $D$=1.0, which means that there is no non-Newtonian effect near the leading edge due to the small shear-rate. From Fig. 3, it is seen that the non-Newtonian effects activated after the leading edge and exist in the far downstream region. The $U$ and $V$ velocity components are recorded at $X$=1.0 and 100.0 and presented in Figs. 4(*a*) and 4(*b*) and Figs. 5(*a*) and 5(*b*), respectively, for $\alpha$=0.3 and $\delta$=1.0. These figures show that for shear-thinning fluids $n$ (=0.6, 0.8), the velocity increases due to the decrease in viscosities; consequently, the boundary layer becomes thinner. On the other hand, for shear-thickening fluids $n$ (=1.2, 1.4), the velocity decreases and the boundary layer is thickened as the fluid becomes more viscous.

Figures 6(*a*) and 6(*b*) depict the corresponding temperature distributions. At $X$=1.0, the variation in temperature is very small since near the leading edge the non-Newtonian effect is very small, as shown in Fig. 3(*a*). At the downstream region, in the case of shear-thinning fluids, the variation in temperature in the boundary layer is smaller than that of the shear-thickening non-Newtonian fluids and hence the thermal boundary layer becomes thinner for shear-thinning fluids and thicker for shear-thickening fluids.

The velocity distributions at the crest and trough of the wavy surface are presented in Figs. 7(*a*) and 7(*b*) while Pr=100, $n$ =0.6, $\alpha$=0.3, and $\delta$=1.0. At the crest of the wavy surface the velocity is higher than the surface trough region since the wavy surface induces a local approaching and leaving flow slightly downstream of the trough and slightly upstream of the crest of the wavy surface. This agree with the observation of natural convection for Newtonian fluids studied in Ref. [20].

The effect of the ratio of power-law length scale and the surface wavelength $\delta$ (=0.5, 1.0, 2.0) on the local skin-friction coefficient $C_f(\mathrm{Gr}/4X)^{1/4}$ and the local Nusselt number $\mathrm{Nu}(\mathrm{Gr}/4X)^{-1/4}$ are shown in Figs. 8(*a*) and 8(*b*), respectively, while $\alpha$=0.3 and $n$ =0.6 (shear-thinning case). Due to the variation in $\delta$, the period of the wavy surface changes and the corresponding wavelength of the local skin-friction coefficient $C_f(\mathrm{Gr}/4X)^{1/4}$ and the local Nusselt number $\mathrm{Nu}(\mathrm{Gr}/4X)^{1-4}$ changes. For all $\delta$ the wavelength of the local skin-friction coefficient $C_f(\mathrm{Gr}/4X)^{1/4}$ and the local Nusselt number $\mathrm{Nu}(\mathrm{Gr}/4X)^{1/4}$ is half that of the wavy surface. From Fig. 8(*b*), it is observed that for $\delta$=0.5 the amplitude of the local Nusselt number increases while $\delta$=1.0 and 2.0 gradually decrease the amplitude.

Figures 9(*a*) and 9(*b*) depict the local skin-friction coefficient $C_f(\mathrm{Gr}/4X)^{1/4}$ and the local Nusselt number $\mathrm{Nu}(\mathrm{Gr}/4X)^{-1/4}$ for the surface waviness $\alpha$ (=0.0, 0.1, 0.3) while $n$=1.4 (shear-thickening case). From these figures it is found that the skin-friction coefficient and the Nusselt number are smaller than those of the corresponding flat plate. Here it should be mentioned that a roughened surface is much better than the flat plate for designing any heat transfer device since the total rate of heat transfer from the roughened surface is always much larger than that for the flat plate, which is mentioned in Refs. [20–23].

The effect of the non-Newtonian power-law index $n$ (=0.6, 0.8, 1.0, 1.2, 1.4) on the variation in the local skin-friction coefficient $C_f(\mathrm{Gr}/4X)^{1/4}$ and the local Nusselt number $\mathrm{Nu}(\mathrm{Gr}/4X)^{-1/4}$ is il-

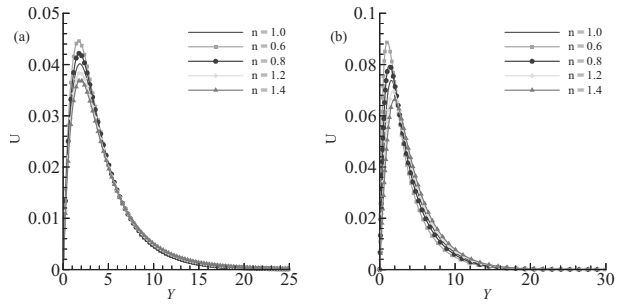


**Fig. 4 Velocity distribution at (*a*) *X*=1.0 and (*b*) *X*=100 while Pr=100 and $\delta$=1**

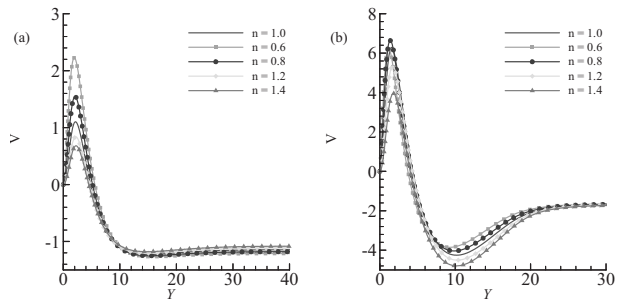


**Fig. 5 Velocity distribution at (*a*) *X*=1.0 and (*b*) *X*=100 while Pr=100, $\alpha$=0.3, and $\delta$=1**

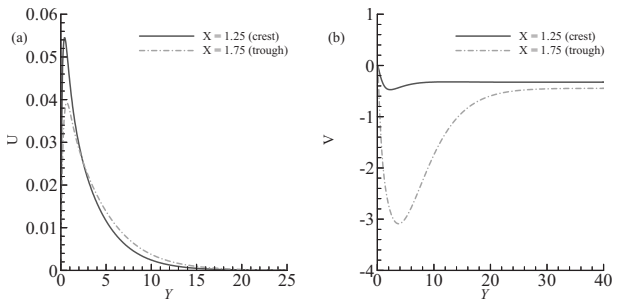


**Fig. 7 Velocity distribution at the crest and trough of the wavy surface while Pr=100, *n*=0.6, $\alpha$=0.3, and $\delta$=1**

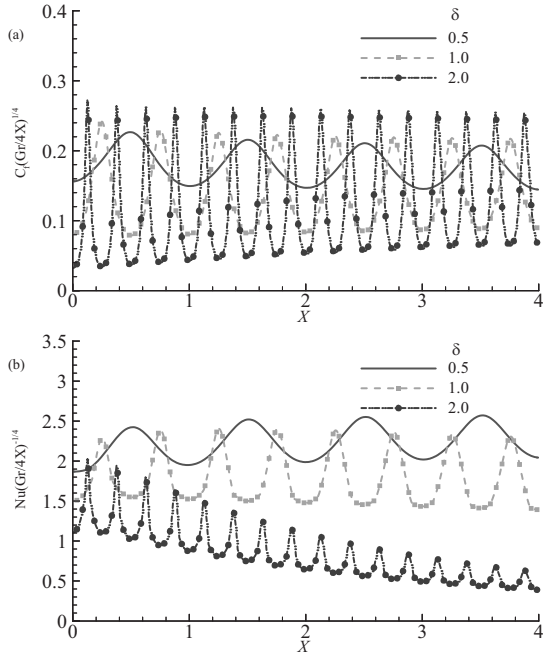


**Fig. 8 (*a*) Skin-friction coefficient and (*b*) Nusselt number for the different $\delta$ while Pr=100, $\alpha$=0.3, and $n$=0.6**

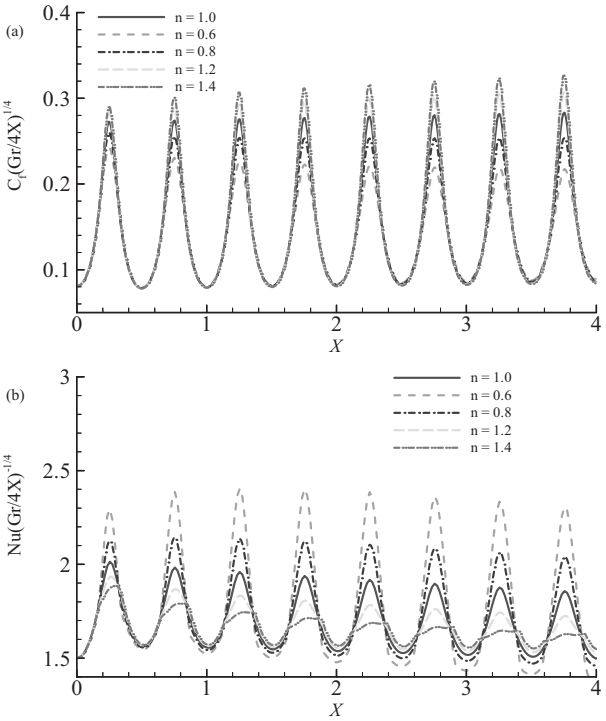


**Fig. 10 (*a*) Skin-friction coefficient, (*b*) Nusselt number, and (*c*) average Nusselt number for the different $n$ while Pr=100, $\alpha$=0.3, and $\delta$=1.0**

lustrated in Figs. 10(*a*) and 10(*b*) for $\alpha$=0.3 and $\delta$=1.0, respectively. The results from these figures clearly show that the local skin-friction coefficient decreases and the local Nusselt number increases for the shear-thinning fluids $n$ (=0.6, 0.8); the opposite phenomena happen for shear-thickening fluids $n$ (=1.2, 1.4).

## 4 Conclusions

The proposed modified power-law correlation fits well with the actual measurement of viscosities for non-Newtonian fluids; consequently it does not contain physically unrealistic limits of zero and infinite viscosity introduced into the boundary-layer formulation by the traditional power-law model. The problems associated with the nonremoval singularity introduced by the traditional power-law correlations do not exist for the modified power-law correlation proposed in this paper. Therefore, the proposed modified power-law correlations can be used to investigate other heat transfer problems for shear-thinning or shear-thickening non-Newtonian fluids in boundary layers. The fundamental mechanism is that the effect of non-Newtonian fluids eventually becomes dominant when shear-rate increases within the threshold shear limits.

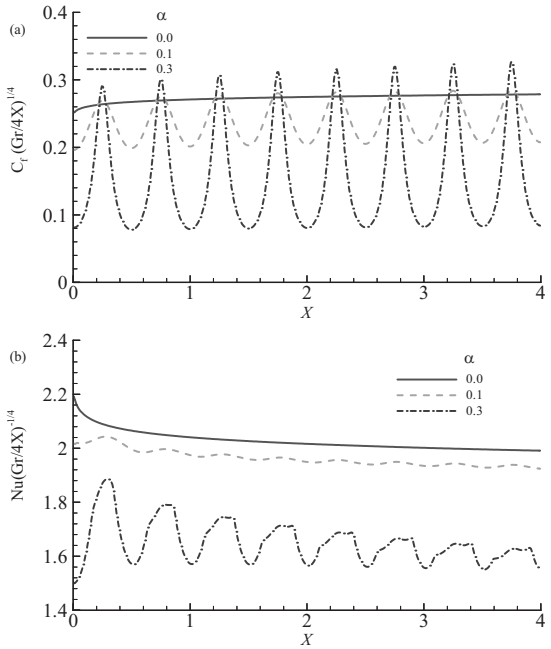


**Fig. 9 (*a*) Skin-friction coefficient and (*b*) Nusselt number for the different $\alpha$ while Pr=100, $\delta$=1.0, and $n$=1.4 (shear-thickening fluid)**

## Nomenclature

$C$ = constant
$C_f$ = dimensionless skin-friction coefficient
$C_p$ = specific heat at constant pressure
$D$ = nondimensional viscosity of the fluid
Gr = Grashof number
$K$ = constant
$k$ = thermal conductivity
$l$ = reference length scale of the plate
$n$ = non-Newtonian power-law index
Nu = Nusselt number
$P$ = pressure of the fluid
$(\hat{u},\hat{v})$ = fluid velocity components in the $(\hat{x},\hat{y})$ directions, respectively
$(U,V)$ = dimensionless fluid velocity components in the $(X,Y)$ directions, respectively
$T$ = dimensional temperature of the fluid
$T_\infty$ = ambient temperature

**Greek**

$\gamma$ = shear-rate
$\rho$ = fluid density
$\nu$ = viscosity of the non-Newtonian fluid
$\nu_1$ = reference viscosity of the fluid

$\alpha$ = amplitude of the wavy surface
$\beta$ = thermal expansion coefficient
$\lambda$ = wavelength of the wavy surface
$\theta$ = dimensionless temperature of the fluid
$\sigma(x)$ = wavy surface defined in Eq. (1)

## References


[1] Hinch, J., 2003, "Non-Newtonian Geophysical Fluid Dynamics," 2003 Program in Geophysical Fluid Dynamics, Woods Hole Oceanographic Institution, Woods Hole, MA.
[2] Acrivos, A., 1960, "A Theoretical Analysis of Laminar Natural Convection Heat Transfer to Non-Newtonian Fluids," AIChE J., **16**, pp. 584–590.
[3] Emery, A. F., Chi, H. S., and Dale, J. D., 1970, "Free Convection Through Vertical Plane Layers of Non-Newtonian Power-Law Fluids," ASME J. Heat Transfer, **93**, pp. 164–171.
[4] Chen, T. V. W., and Wollersheim, D. E., 1973, "Free Convection at a Vertical Plate With Uniform Flux Conditions in Non-Newtonian Power-Law Fluids," ASME J. Heat Transfer, **95**, pp. 123–124.
[5] Dale, J. D., and Emery, A. F., 1972, "The Free Convection of Heat From a Vertical Plate to Several Non-Newtonian Pseudo Plastic Fluids," ASME J. Heat Transfer, **94**, pp. 64–72.
[6] Chen, T. V. W., and Wollersheim, D. E., 1973, "Free Convection at a Vertical Plate With Uniform Flux Conditions in Non-Newtonian Power-Law Fluids," ASME J. Heat Transfer, **95**, pp. 123–124.
[7] Shulman, Z. P., Baikov, V. I., and Zaltsgendler, E. A., 1976, "An Approach to Prediction of Free Convection in Non-Newtonian Fluids," Int. J. Heat Mass Transfer, **19**, pp. 1003–1007.
[8] Som, A., and Chen, J. L. S., 1984, "Free Convection of Non-Newtonian Fluids Over Non-Isothermal Two-Dimensional Bodies," Int. J. Heat Mass Transfer, **27**, pp. 791–794.
[9] Haq, S., Kleinstreuer, C., and Mulligan, J. C., 1988, "Transient Free Convection of a Non-Newtonian Fluid Along a Vertical Wall," ASME J. Heat Transfer, **110**, pp. 604–607.
[10] Huang, M. J., Huang, J. S., Chou, Y. L., and Cheng, C. K., 1989, "Effects of Prandtl Number on Free Convection Heat Transfer From a Vertical Plate to a Non-Newtonian Fluid," ASME J. Heat Transfer, **111**, pp. 189–191.
[11] Huang, M. J., and Chen, C. K., 1990, "Local Similarity Solutions of Free-Convective Heat Transfer From a Vertical Plate to Non-Newtonian Power-Law Fluids," Int. J. Heat Mass Transfer, **33**, pp. 119–125.
[12] Kim, E., 1997, "Natural Convection Along a Wavy Vertical Plate to Non-Newtonian Fluids," Int. J. Heat Mass Transfer, **40**, pp. 3069–3078.
[13] Denier, J. P., and Hewitt, R. E., 2004, "Asymptotic Matching Constraints for a Boundary-Layer Flow of a Power-Law Fluid," J. Fluid Mech., **518**, pp. 261–279.
[14] Khan, W. A., Culham, J. R., and Yovanovich, M. M., 2006, "Fluid Flow and Heat Transfer in Power-Law Fluids Across Circular Cylinders: Analytical Study," ASME J. Heat Transfer, **128**, pp. 870–878.
[15] Denier, J. P., and Dabrowski, P. P., 2004, "On the Boundary-Layer Equations for Power-Law Fluids," Proc. R. Soc. London, Ser. A, **460**, pp. 3143–3158.
[16] Yao, L. S., and Molla, M. M., 2008, "Flow of a Non-Newtonian Fluid on a Flat Plate: I. Boundary Layer," J. Thermophys. Heat Transfer, in press.
[17] Molla, M. M., and Yao, L. S., 2008, "Flow of a Non-Newtonian Fluid on a Flat Plate: II. Heat Transfer," J. Thermophys. Heat Transfer, in press.
[18] Yao, L. S., and Molla, M. M., 2008, "Forced Convection of a Non-Newtonian Fluid on a Heated Flat Plate," Int. J. Heat Mass Transfer, in press.
[19] Molla, M. M., and Yao, L. S., 2008, "The Flow of Non-Newtonian Fluids on a Flat Plate With a Uniform Heat Flux," ASME J. Heat Transfer, in press.
[20] Yao, L. S., 1989, "Natural Convection Along a Vertical Wavy Surface," ASME J. Heat Transfer, **105**, pp. 465–468.
[21] Moulic, S. G., and Yao, L. S., 1989, "Natural Convection Along a Wavy Surface With Uniform Heat Flux," ASME J. Heat Transfer, **111**, pp. 1106–1108.
[22] Yao, L. S., 2006, "Natural Convection Along a Vertical Complex Wavy Surface," Int. J. Heat Mass Transfer, **49**, pp. 281–286.
[23] Molla, M. M., Hossain, M. A., and Yao, L. S., 2007, "Natural Convection Along a Vertical Complex Wavy Surface With Uniform Heat Flux," ASME J. Heat Transfer, **129**, pp. 1403–1407.

# A Vector Form Exchange-Area-Based Method for Computation of Anisotropic Radiative Transfer

**Yu Yan Jiang**
Vehicle Safety Research Center,
Toyota Central R&D Labs., Inc.,
Nagakute, Aichi, 480-1192, Japan
e-mail: e1498@mosk.tytlabs.co.jp

*Exchange-area-based methods (EAMs), such as the zonal method, the combined Monte-Carlo and zonal method, etc., are widely used in the numerical computation of thermal radiative transfer. In view of their inefficiency in treating with the anisotropy of radiation, researchers have been devoted to developing generalized models (GEAMs). In this article a vector form GEAM is proposed, which has concise formulations, and is found to be very efficient for handling the anisotropic scattering and reflection. In the model some vectorlike weighted-summations take account of the directional distribution of radiant energy. The summations give rise to correction coefficients to the radiosities. The heat transfer problem is solved by a coupled computation of the radiosities and the correction coefficients. The model was validated by both a one-dimensional and a three-dimensional benchmark radiation problem. The computational time is decreased to an order of that for computing isotropic radiation by conventional EAM. Such high efficency has never been achieved by the GEAMs proposed to date.* [DOI: 10.1115/1.2994763]

*Keywords: exchange-area, generalized model, zonal method, radiative heat transfer, anisotropic scattering and reflection, two-step method*

## 1 Introduction

The exchange-area-based methods (EAMs) are widely used in the numerical computation of radiative transfer [1,2]. By these methods, the computation includes generally two steps. The first step is to calculate the exchange-area (EA, or say view factor) that measures the exchange relations of radiant energy between every two elements. Many methods can be used to calculate the EA including, e.g., the zonal method [3,4], REM$^2$ [5], and the Monte-Carlo method [6], etc. By the use of the exchange-area the second step is to solve the radiative transfer problem in a certain mathematic scheme that takes into account the effects of particle scattering and wall reflection.

EAMs are widely used partially due to its simplicity. For a medium with constant radiative properties, heat transfer calculation becomes a simple algebraic operation over the elements as soon as EA is known. The disadvantage of EAM are yet multiple, one of which is the difficulty in managing the anisotropy effect in radiation, such as the anisotropic scattering and the nondiffuse wall reflection. For this issue, researchers [7–10] have developed the so-called generalized method (GEAM). However, the models that were proposed suffer from operating either a too large matrix [7,8] or too many equations that need to be solved [9,10] besides the mathematic complexity. In the methods the radiosity emitted from an element is generally taken as a function of the emitting-absorbing counterpart so that it seems unavoidable to solve $L^2$ variables for a system composed of $L$ elements. When deriving the total-exchange-area (TEA) one has to follow the middle processes of anisotropic scattering and reflection by quite complicated mathematics. From an engineering viewpoint it is not practical at all even for the computation to use a moderate-scale mesh.

In the current work we propose a vector form EAM that is based on different mathematics. In the model the radiosity of an emitting element is no longer expressed one by one for every absorbing element, rather it is given by a unique value multiplied by a correction coefficient. The correction coefficient takes account of the directional distribution of the anisotropic radiant energy, which is obtained by some vectorlike summations of incident radiosities. The overall effects of the multiple scattering and reflection processes are approximated by iterative algorithms. In comparison with the aforementioned GEAMs the current model has a concise expression and calls for quite light computation efforts that are comparable to what the computation takes for solving isotropic radiative heat transfer problems.

Section 2 presents the theoretical formulation of the model. Numerical results for benchmark computations are reported in Sec. 3. Comments for the application of the model are given in Sec. 4.

## 2 Theoretical Formulation

Considered is a radiative element of a participating medium, where the radiation intensity $I$ at a position $\boldsymbol{r}$ in a direction $\hat{s}$ can be formulated as

$$\frac{\mathrm{d}I(\boldsymbol{r},\hat{s})}{\mathrm{d}S} = -(\kappa+\sigma_s)I(\boldsymbol{r},\hat{s}) + \kappa I_b(T) + \frac{\sigma_s}{4\pi}\int_{4\pi} I(\boldsymbol{r},\hat{s}')\Phi(\hat{s}\cdot\hat{s}')\mathrm{d}\Omega \tag{1}$$

Equation (1) is the radiative transfer equation (RTE), where $\kappa$ and $\sigma_s$ are the absorption and scattering/reflecting coefficients, respectively. $\Phi(\hat{s}\cdot\hat{s}')$ is a phase function, whereas $\hat{s}'$ denotes an incidence direction. Supposing that a wall surface has an emissivity of $\varepsilon$, and a reflectivity of $\gamma$, in favor of analysis we define an extinction coefficient $\alpha$ and a scattering/reflection albedo $\omega$, i.e., $\alpha=\kappa+\sigma_s$, $\omega=\sigma_s/\alpha$ for medium elements, and $\alpha=\varepsilon+\gamma=1$ and $\omega=\gamma/\alpha$ for surfaces. A system composed of $N$ volume elements and $M$ surfaces is said to have $L$ elements that $L=M+N$. Supposing that the elements are pure-absorbing with equivalent absorptivities of $\alpha_i$ $(i=1,2,\ldots,L)$, one can determine the direct-exchange-area (DEA) $D_{ij}$ $(i,j=1,2,\ldots,L)$. The discussion hereafter focuses on the approaches of radiative transfer computation by use of $D_{ij}$.

Contributed by the Heat Transfer Division of ASME for publication in the JOURNAL OF HEAT TRANSFER. Manuscript received December 12, 2007; final manuscript received August 31, 2008; published online October 16, 2008. Review conducted by Jayathi Murthy.

  

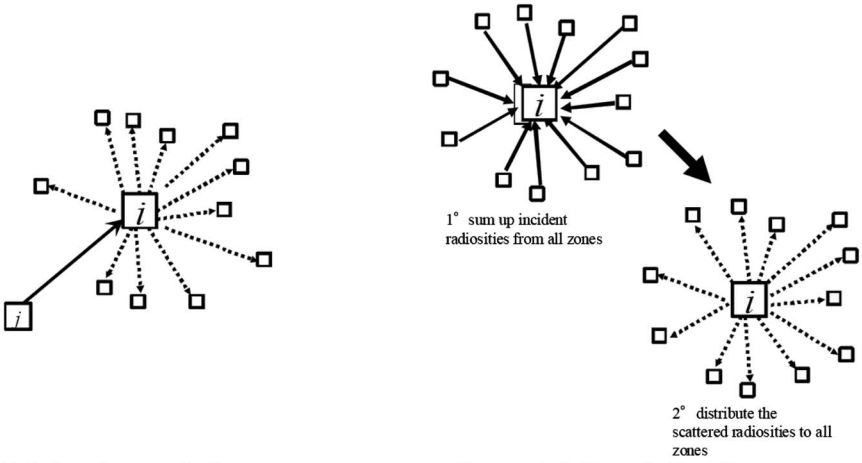


**Fig. 1 Schematics of the concepts for the treatment of anisotropic scattering by GEAM**

**2.1 Brief Review of EAM for Isotropic Radiative Transfer and Old GEAM Models.** Since GEAM inherits the essentials of the conventional EAM [3] regarding the treatment of scattering and reflection, we recount here the formulations of EAM briefly. The gross radiosity $F_iW_i$ of an isotropically scattering/reflecting element $i$ is a sum of self-emission $F_i(1-\omega_i)E_{b,i}$ and the scattered/reflected radiation $\omega_i\sum_{j=1}^{L}D_{ji}W_j$, i.e.,

$$F_iW_i = F_i(1-\omega_i)E_{b,i} + \omega_i\sum_{j=1}^{L} D_{ji}W_j \tag{2}$$

where $F_i$ is related to the element's volume or area, which is $F_i=4\alpha V_i$ for a medium element and $F_i=A_i$ for a surface, $W_i$ is the gross radiosity, and $E_{b,i}$ denotes the black body emissivity that $E_{b,i}=\sigma T_i^4$. Consequently the net heat generation $F_iQ_i$ of the element $i$ can be derived from energy conservation

$$F_iQ_i = F_i(1-\omega_i)E_{b,i} - (1-\omega_i)\sum_{j=1}^{L} D_{ji}W_j \tag{3}$$

If the temperature $T_i$ is given, one can solve Eq. (2) for the gross radiosity $W_i$, so as to obtain the net heat generation $Q_i$ from Eq. (3). If otherwise the radiative equilibrium is assumed, $Q_i$ is given, so that substituting Eq. (3) into Eq. (2) for $E_{b,i}$ yields

$$F_iW_i = F_iQ_i + \sum_{j=1}^{L} D_{ji}W_j \tag{4}$$

One can still solve the unknown temperatures and the heat exchange by using the equation group composed of Eqs. (2) and (4).

One can also deduce TEA from Eq. (2) if it is involved. This is attained by making $E_{b,i_e}=1$ for a specified emissive element $i_e$, and $E_{b,j}=0$ $(j\neq i_e)$ for the others so as to solve Eq. (2) for specific radiosities $W_j(i_e)$. TEA is given by Eq. (5), reading

$$C_{i_e j} = (1-\omega_j)\sum_{k=1}^{L} D_{kj}W_k(i_e) \tag{5}$$

It is needed to solve Eq. (2) for $L$ times to obtain all $C_{ij}$. TEA can also be given explicitly by use of an inverse matrix [4,8], but the computation effort for deriving the inverse matrix are equivalent.

For an anisotropic medium the radiosity varies with the direction that $W_i=W_i(\Phi)$ making its value different for different absorbing elements. The radiosity is taken as a vector function of the emitting-absorbing counterpart in [7–10], so that it is rewritten in discrete form as $W_{ij}$ $(i,j=1,2,\ldots,L)$ for an absorbing element $j$. For example in Ref. [10] Eq. (2) is transformed into

$$F_iW_{ij} = F_i(1-\omega_i)E_{b,i} + \omega_i\sum_{k=1}^{L} D_{ki}W_{ki}\Phi(\hat{s}'_k\cdot\hat{s}_j) \tag{6}$$

It worth mentioning that $W_{ij}$ is a discrete expression of $W_i(\Phi)$ at the direction pointing to the element $j$ rather than the radiosity portion absorbed by it. Here considered is the anisotropy of reflection/scattering and hence the directional variation of $W_i$ arises from the second right hand side (rhs) term only. It is not difficult to include the anisotropy of self-emission if any.

Likewise Eqs. (3) and (4) are transformed into

$$F_iQ_i = F_i(1-\omega_i)E_{b,i} - (1-\omega_i)\sum_{j=1}^{L} D_{ji}W_{ji} \tag{7}$$

$$F_iW_{ij} = F_iQ_i + (1-\omega_i)\sum_{k=1}^{L} D_{ki}W_{ki} + \omega_i\sum_{k=1}^{L} D_{ki}W_{ki}\Phi(\hat{s}'_k\cdot\hat{s}_j) \tag{8}$$

Equations (6)–(8) can be solved without theoretical difficulty (the details can be found in Refs. [9,10]), but problems consist in the computational time. It is noted that the number of the unknown $W_{ij}$ is $L^2$, which makes a program solve the $L$-dimensional-equation-group of Eqs. (6) and (8) $L$ times for the heat transfer calculation, and $L^2$ times for TEA solutions. That means the computational time is $L$-order of that for solving an isotropic radiation problem. This order increases with element number making it prohibitive to compute radiation using even a moderate-scale mesh.

**2.2 A Vector Form GEAM.** On the assessment of the scattering term of an element $i$ in Eq. (1), one straightforward way is that for an incident radiosity from each element $j$ we distribute the scattered radiation to all the $L$ elements in the system (Fig. 1(*a*)). This requests at least $L^2$ times of operations for each element $i$, which gives rise to a quite time-consuming computation. It will be much more efficient if the scattered energy, after a certain kind of summation, could be distributed in a whole way (Fig. 1(*b*)) because this takes only an order of $L$-times operations. In other words, the former method is equivalent to solving for $W_{ij}$ for

every emitting element $i$ and absorbing element $j$ one by one, and the latter is to solve for $W_{ij}$ only once for an emitting element $i$ and distribute the radiosity in an explicit manner.

Note that most of the phase functions of particle scattering and wall refection can be approximated, with very few exceptions, by polynomials of a cosine $\mu=\cos\theta$, where $\theta$ is the angle between the scattering vector $\hat{s}=(s_1,s_2,s_3)$ and the incident vector $\hat{s}'=(s_1',s_2',s_3')$. This includes the linear scattering, the Mie scattering, the Rayleigh scattering, the Delta–Eddington scattering, etc. [11]. Even for the few exceptions the phase functions can also be transformed into a series of $\mu$ by the Taylor or Fourier expansion. As an instance, the exact Mie scattering phase is expressed by an expansion in Legendre polynomials of the first kind, $P_m(\mu)$,

$$\Phi(\mu) = 1 + \sum_{m=1}^{\infty} a_m P_m(\mu) \tag{9}$$

where

$$P_1(\mu) = \mu, \quad P_2(\mu) = (3\mu^2 - 1)/2, \quad P_3(\mu) = (5\mu^3 - 3\mu)/2, \ldots \tag{10}$$

and $a_m$ are constants.

It turns out that in Cartesian coordinates

$$\mu = \hat{s} \cdot \hat{s}' = s_1 s_1' + s_2 s_2' + s_3 s_3' \tag{11}$$

The current model is formulated by use of the single radiosity $W_i$ for an element $i$ being discussed. Of the radiant energy from an element $i$ the portion that is absorbed by $j$ is

$$D_{ij} W_{ij} = D_{ij} W_i f_i(\hat{s}_j) \tag{12}$$

where the coefficient $f_i(\hat{s})$ is a correction to $W_i$ in terms of the anisotropic distribution of the radiosity. The scattered/reflected radiosity into the direction $\hat{s}$ is

$$\begin{aligned} S_i(\hat{s}) &= \sum_{j=1}^{L} D_{ji} W_j f_j(\hat{s}_i) \cdot \Phi(\hat{s} \cdot \hat{s}_j') \\ &= \sum_{j=1}^{L} D_{ji} W_j f_j(\hat{s}_i) \cdot \left[ 1 + \sum_{m=1}^{\infty} a_m P_m(\mu_j) \right] \end{aligned} \tag{13}$$

Substituting Eqs. (10)–(12) into Eq. (13) we arrive at

$$S_i(\hat{s}) = b_0 \Psi_{i,0} + b_1 \sum_{\xi=1}^{3} \Psi_{i,\xi} \cdot s_\xi + b_2 \sum_{\xi,\eta=1}^{3} \Psi_{i,\xi\eta} \cdot s_\xi s_\eta + \cdots \tag{14}$$

where $\xi, \eta = 1, 2, 3$ and

$$b_0 = (1 - a_2/2 + \cdots), \quad b_1 = (a_1 + \cdots), \quad b_2 = (3a_2/2 + \cdots), \quad \cdots$$

$$\Psi_{i,0} = \sum_{j=1}^{L} D_{ji} W_j f_j(\hat{s}_i), \quad \Psi_{i,\xi} = \sum_{j=1}^{L} D_{ji} W_j f_j(\hat{s}_i) s_{\xi,j}' \tag{15}$$

$$\Psi_{i,\xi\mu} = \sum_{j=1}^{L} D_{ji} W_j f_j(\hat{s}_i) s_{\xi,j}' s_{\eta,j}', \quad \cdots$$

Equation (14) takes the form of 3-variable polynomials of $\hat{s}=(s_1,s_2,s_3)$ that have coefficients relying on the weighted-summations of the incident radiosities. Although the radiosities are scalars, the weights that are obtained by vectorlike summations taking account of the directional distribution of the incident radiosities in a physical sense. Likewise, the other phase functions can also be cast into the 3-variable polynomials in a similar fashion. By Eq. (14) it is convenient to sum up the incident radiosities in advance and then distribute the scattered energy in a whole manner later. This means that we have readily found a way to assess the scattering/reflecting term by $L$-order operations (Fig. 1(*b*)).

Substitution of Eq. (14) into Eq. (6) leads to

$$F_i W_i f(\hat{s}_j) = F_i(1 - \omega_i) E_{b,i} + \omega_i S_i(\hat{s}_j) \tag{16}$$

The radiosity $W_i$ is

$$W_i = (1 - \omega_i) E_{b,i} + \left( \omega_i \sum_{j=1}^{L} D_{ji} W_j f_j(\hat{s}_i) \right) \Big/ F_i \tag{17}$$

The correction $f_i(\hat{s}_j)$ becomes accordingly

$$f_i(\hat{s}_j) = W_{ij}/W_i = \lfloor (1 - \omega_i) E_{b,i} + \omega_i S_i(\hat{s}_j)/F_i \rfloor / W_i \tag{18}$$

The subscripts $i$ and $j$ stand that it is a function of the anisotropic radiosity $W_i$ and the scattering/reflecting direction $\hat{s}_j$ pointing to an element $j$.

In a similar way we are able to rewrite Eqs. (3)–(5) with respect to anisotropic media. Equation (3) is only concerned with energy exchange so that

$$F_i Q_i = F_i(1 - \omega_i) E_{b,i} - (1 - \omega_i) \sum_{j=1}^{L} D_{ji} W_j f_j(\hat{s}_i) \tag{19}$$

Substituting Eq. (19) into Eq. (16) for $E_{b,i}$ yields an equation that corresponds to Eq. (4), reading

$$F_i W_i f_{ij} = F_i Q_i + (1 - \omega_i) \sum_{j=1}^{L} D_{ji} W_j f_j(\hat{s}_i) + \omega_i S_i(\hat{s}_j) \tag{20}$$

where the radiosity $W_i$ is

$$W_i = Q_i + \left( \sum_{j=1}^{L} D_{ji} W_j f_j(\hat{s}_i) \right) \Big/ F_i \tag{21}$$

and the correction $f_i(\hat{s}_j)$ becomes

$$f_i(\hat{s}_j) = \left\{ Q_i + \left\lfloor (1 - \omega_i) \sum_{j=1}^{L} D_{ji} W_j f_j(\hat{s}_i) + \omega_i S_i(\hat{s}_j) \right\rfloor \Big/ F_i \right\} \Big/ W_i \tag{22}$$

Equation (5) is transformed into

$$C_{i,j} = (1 - \omega_j) \sum_{k=1}^{L} D_{kj} W_k f_k(\hat{s}_j) \tag{23}$$

In a previous study, Jiang [12] proposed a scheme regarding the anisotropic scattering by a simple vector summation, which can be considered as a linear part of Eq. (14) by truncating the higher-order terms and is hence conditionally tenable.

As for the wall reflection, the aforementioned formulations are still applicable once the phase function in Eq. (9) is replaced by a reflection phase.

**2.3 Equation Solving by Traditional Method.** Having computed for $D_{ij}$ and the constants $b_m$ in Eq. (15), one can solve this GEAM by an iterative algorithm (referred to as GEAM-IM hereafter), which includes in principle three steps: (1) solving for radiosities of the equation group composed by Eq. (17) or by Eqs. (17) and (21) (2) renewing the corrections $f_i(\hat{s})$ by Eq. (18) or Eq. (22) using the new radiositiesm, and (3) repeating the first two steps until $f_i(\hat{s})$ and $W_i$ converge at fixed values, so as to output the solutions for heat exchange and temperature. One suggestion is that the new values of $f_i(\hat{s})$ should be normalized with regard to energy conservation. In Eq. (18) $W_{ij}=W_i$ for $\hat{s}_j=0$, so that the coefficients of $f_i(\hat{s}_j)$ should be normalized to fit this condition.

**2.4 Equation Solving by a Two-Step Method.** The problem can also be solved by a two-step method (TSM) proposed in Ref. [12]. TSM is based on a concept that the coincident processes of absorption and scattering/reflection can be separated fictitiously.

All medium elements and wall surfaces are supposed to be pure-absorbing when receiving incident radiation. Afterwards they emit the scattered/reflected radiation. The absorption of both the initial and the secondary radiation can be assessed by DEA. Instead of equation solving, TSM works by following the absorption and scattering/reflection processes in a numerical way. The detailed formulations, as well as the validation, were given in Ref. [12] so that the implementation is briefly described here under the frame of GEAM. In the following section we present three nested versions of the model for heat exchange calculation, equilibrium temperature solving, and TEA derivation. They do not differ too much in computational implementations. We refer this method as GEAM-TSM hereafter.

*2.4.1 Heat Transfer Calculation*. In this situation the temperature $T_i$ is known. The initial emissive power of an element is $q_i^{(1)}=(1-\omega_i)E_{b,i}$, which is isotropic, making $f_i(\hat{s}_j)=1$. For convenience we define a summation of the initial emissions that $Q_\Sigma^{(1)}=\Sigma_{i=1}^{L}q_i^{(1)}F_i$. The computation procedure includes two steps. (1) At the first step, every element absorbs the incident radiation $q_j^{(1)}$ from the others, and the total absorption of the element $i$ is

$$Q_{a,i}^{(1)}=\sum_{j=1}^{L}D_{ji}q_j^{(1)}f_j(\hat{s}_i) \tag{24}$$

The scattered/reflected radiosity $S_i(\hat{s})$ is derived by substituting $q_j^{(1)}$ into Eq. (14) for $W_j$.

(2) At the second step, every element emits the scattered/reflected radiation, which is

$$q_i^{(2)}=\omega_i Q_{a,i}^{(1)}/F_i \tag{25}$$

The new correction to $q_i^{(2)}$ is found to be

$$f_i(\hat{s}_j)=S_i(\hat{s}_j)/Q_{a,i}^{(1)} \tag{26}$$

This secondary radiation is absorbed again according to Process (1). The above two processes are repeated until the remaining secondary radiation are insignificant, i.e., the iteration terminates at step $n$ if there is

$$Q_\Sigma^{(n)}/Q_\Sigma^{(1)}<\Delta \tag{27}$$

where $\Delta$ is a residual tolerance. Note that the purely absorbed energy by the element $i$ is $(1-\omega_i)Q_{a,i}^{(t)}/F_i$ at every step $t$ ($t=1,\ldots,n$), and the initial emissive power is $(1-\omega_i)E_{b,i}$, so that the net heat generation of the element yields

$$F_iQ_i=F_i(1-\omega_i)E_{b,i}-(1-\omega_i)\sum_{t=1}^{n}Q_{a,i}^{(t)},\quad i=1,2,\ldots,L \tag{28}$$

Equation (28) is essentially Eq. (19) with the exception of the expression of the second rhs term that stands for total absorption. In a traditional model the term is estimated by solving equations for gross radiosity $W_j$ but in TSM it becomes a summation of a time series of absorptions. The heat flux divergence is given by $q_i=F_iQ_i/V_i$ for a medium element and the heat flux is $q_i=F_iQ_i/A_i$ for a surface.

*2.4.2 Equilibrium Temperature Solving*. This version resembles the aforementioned one except that an equation group composed of Eqs. (17) and (21) is to be solved. For an element where the temperature is given (e.g., a boundary surface) the operations are the same as that in Sec. 2.4.1 For an element with an unknown temperature, which is under radiation equilibrium, Eq. (22) suggests that the initial emission is $q_i^{(1)}=Q_i$ with $f_i(\hat{s}_j)=1$. The total absorption is the same as Eq. (24), but Eq. (21) suggests that the secondary radiosity becomes

$$q_i^{(2)}=Q_{a,i}^{(1)}/F_i \tag{29}$$

The new corrections are obtained by substituting $q_j^{(1)}$ into Eq. (22) for $W_j$. As soon as the whole computation is finished, one can obtain the gross radiosity $W_i$, reading,

$$W_i=\left(Q_i+\sum_{t=1}^{n}Q_{a,i}^{(t)}\right)\Big/F_i \tag{30}$$

Equation (30) is essentially Eq. (21) apart from the second rhs term, which is replaced by a summation of a time series of the secondary absorptions. The blackbody emission, or say the unknown temperature, can be obtained from Eq. (28) that

$$F_i(1-\omega_i)E_{b,i}=F_iQ_i+(1-\omega_i)\sum_{t=1}^{n}Q_{a,i}^{(t)} \tag{31}$$

*2.4.3 TEA Derivation*. In the TEA calculation, we let the emissive power of a specified element $i_e$ be $q_{i_e}^{(1)}=(1-\omega_{i_e})$ and the others be $q_j^{(1)}=0$ ($j\neq i_e$). By performing the same procedure as that in Sec. 2.4.1, one can deduce the TEA between $i_e$ and the other elements, that

$$C_{i_ej}=(1-\omega_j)\sum_{t=1}^{n}Q_{a,j}^{(t)} \tag{32}$$

It is necessary to carry out the computation $L$ times for $i_e=1,2,\ldots,L$.

Although the two algorithms are mathematically equivalent, in the computation GEAM-IM needs an additional $L^2$-dimensional array to deposit the coefficient matrix in Eqs. (17) and (21). GEAM-TSM works by only DEA, which calls for the least memory. As will be shown in the applications, the computation performances of the two algorithms are determined by a real condition. The convergence speed of GEAM-TSM depends on the system's gross absorptivity, which is less efficient for highly scattering media.

In both algorithms, the calculation of the corrections $f_i(\hat{s}_j)$ does not give rise to heavy computations because it is not tedious to obtain the vector products if the coordinates of the elements are given. As for self-emitting-absorption ($i=j$) both the vectors are $\hat{s}=\hat{s}'=0$ and thus $f_i(0)\equiv 1$.

## 3 Applications

**3.1 Application to Three-Dimensional Inhomogeneous Gray Media Contained in a Cube.** The discussion is on a cubic geometry filled with participating media. The coordinates originate from the center and the computation domain is bounded in $-0.5\leqslant(x,y,z)\leqslant 0.5$. In Ref. [13] several benchmark problems were discussed, where the radiative transfer occurs between inhomogeneous gray media and black walls. The distribution of optical thickness $\tau$ (extinction coefficient times the side length) is given by

$$\tau(x,y,z)=a\left(1-\frac{|x|}{0.5}\right)\left(1-\frac{|y|}{0.5}\right)\left(1-\frac{|z|}{0.5}\right)+b \tag{33}$$

An anisotropic linear phase function is set to the medium, that

$$\Phi(\mu)=1+\beta\mu \tag{34}$$

where $\beta$ is a coefficient bounded in $(-1,1)$. Table 1 lists the parameters of the two cases being considered. The wall at $x=-0.5$ has a unit emissive power $\sigma T^4=1$ and the medium is in radiation equilibrium. In the present study, DEA was calculated by the Monte-Carlo method, where 1000 rays were traced for every element.

Here the constants in Eq. (15) is $b_0=1$ and $b_1=\beta$. The problems

**Table 1 Parameters of the benchmark computation cases**

| Case | Scattering albedo $\omega$ | $\beta$ in Eq. (32) | $a$, $b$ in Eq. (31) | Boundary conditions |
|---|---|---|---|---|
| A1 | 0.9 | −1 | $a$=0.9, $b$=0.1 | 1 hot /5 cold walls |
| A2 | 0.9 | 1 | $a$=5.0, $b$=5.0 | 1 hot /5 cold walls |

were solved by both the GEAM-IM and GEAM-TSM methods. By using the TSM scheme described in Sec. 2.4.2, the scattering term for a volume element at step $t$ becomes

$$S_i(\hat{s}) = \sum_{j=1}^{L} D_{ji} q_j^{(t)} f_j(\hat{s}_i) + \beta \sum_{\xi=1}^{3} \left( s_\xi \sum_{j=1}^{L} D_{ji} q_j^{(t)} f_j(\hat{s}_i) s'_{\xi,j} \right) \quad (35)$$

The next step radiosity is given by Eq. (27) with a correction reading

$$f_i(\hat{s}_j) = \left[ (1-\omega_i) \sum_{j=1}^{L} D_{ji} q_j^t f_j(\hat{s}_i) + \omega_i S_i(\hat{s}_j) \right] \Big/ Q_{a,i}^{(t)} \quad (36)$$

Tables 2 and 3 list the distributions of the equilibrium emissive power at $Y=Z=0$ and the surface heat flux at $X=-0.5$ and $Y=0$, respectively, in comparison with the Monte-Carlo results in Ref. [13]. Case A1 is an optical-thin medium. The domain was divided into $9^3$ volume elements. The results are in very close agreements with Ref. [13]. Case A2 is characterized by an optical-thick medium. The calculation was performed using a $27^3$ grid. It is also shown that the results agree with that in Ref. [13] very well. Nevertheless the differences of GEAM-IM is somewhat large than GEAM-TSM and the reference.

Compared are the computational time of variant GEAM schemes relative to that for solving an isotropic radiation problem (Fig. 2). The computations were conducted in an Altix-350 machine (4.2GFlops), where the residual tolerance was set to be $10^{-6}$. The linear equations were solved by an incomplete Choleski conjugated gradient (ICCG) method. By isotropic radiation problem, we mean that the time taken by solving the same problem with $\beta=0$ where the iteration for deriving $f(\hat{s})$ is unnecessary. It is noted that the computational time taken by both the GEAM-IM and GEAM-TSM for solving anisotropic radiation are only a few times longer than that for isotropic radiation, while the time for solving the GEAM model of Ref. [10] (i.e., Eqs. (6)–(8)) are several orders longer. In this sense we state that the present model is really a practicable GEAM scheme for application. Additionally in the GEAM model in Ref. [10] it is necessary to take additional time to calculate the scattering/reflection area.

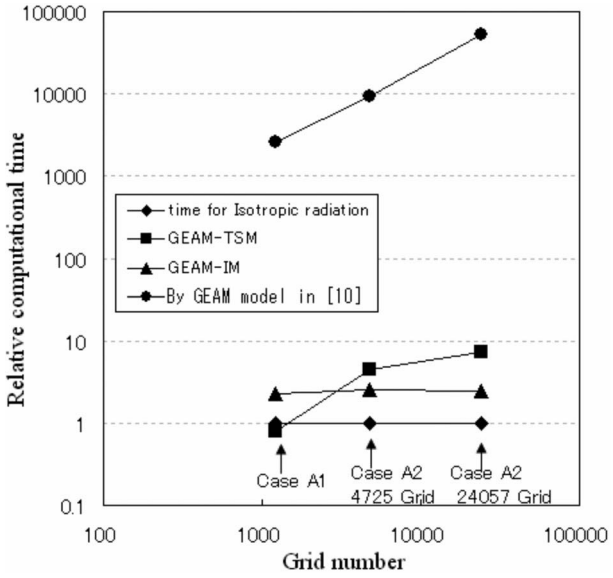


**Fig. 2 Comparisons of the computational time relative to EAM for isotropic media**

**3.2 Application to a One-Dimensional Purely Scattering Slab.** Considered is a purely anisotropic scattering layer ($\omega=1$) bounded by black walls (Fig. 3). The medium is composed of $N$ volume elements and $M=2$ surface elements $\Gamma_1$ and $\Gamma_{N+1}$, so that the number of elements is $L=N+2$. Layer thickness is a unit and the optical thickness is $\tau=\alpha\times 1$. Each volume element $g_i$ is confined by two virtual surfaces $\Gamma_i$ and $\Gamma_{i+1}$ located at $z_i$ and $z_{i+1}$. The

**Table 2 Comparisons of the emissive power at $y=z=0$ with the results in Ref. [13]**

| | A1 | | | A2 | | |
|---|---|---|---|---|---|---|
| $x$ | MCM [13] | GEAM-IM | GEAM-TSM | MCM [13] | GEAM-IM | GEAM-TSM |
| −4/9 | 0.47660 | 0.47892 | 0.47898 | 0.64420 | 0.65379 | 0.64946 |
| −3/9 | 0.37990 | 0.37958 | 0.37977 | 0.48220 | 0.48696 | 0.48261 |
| −2/9 | 0.29450 | 0.30146 | 0.30147 | 0.35100 | 0.35819 | 0.35509 |
| −1/9 | 0.22430 | 0.22041 | 0.22036 | 0.24700 | 0.24836 | 0.24648 |
| 0 | 0.16640 | 0.16274 | 0.16264 | 0.16640 | 0.16743 | 0.16659 |
| 1/9 | 0.12120 | 0.12037 | 0.12028 | 0.10760 | 0.10771 | 0.10755 |
| 2/9 | 0.08987 | 0.09067 | 0.09054 | 0.06878 | 0.06829 | 0.06848 |
| 3/9 | 0.06820 | 0.06819 | 0.06816 | 0.04310 | 0.04271 | 0.04306 |
| 4/9 | 0.05326 | 0.05371 | 0.05371 | 0.02484 | 0.02469 | 0.02507 |

**Table 3 Comparisons of the surface heat flux at $x=-0.5$, $y=0$ with the results in Ref. [13]**

| | A1 | | | A2 | | |
|---|---|---|---|---|---|---|
| $z$ | MCM [13] | GEAM-IM | GEAM-TSM | MCM [13] | GEAM-IM | GEAM-TSM |
| −4/9 | 0.9656 | 0.9668 | 0.9668 | 0.73260 | 0.72592 | 0.73325 |
| −3/9 | 0.9510 | 0.9514 | 0.9514 | 0.62550 | 0.62233 | 0.62542 |
| −2/9 | 0.9387 | 0.9403 | 0.9404 | 0.56670 | 0.56386 | 0.56946 |
| −1/9 | 0.9295 | 0.9287 | 0.9289 | 0.53450 | 0.53068 | 0.53626 |
| 0 | 0.9253 | 0.9262 | 0.9264 | 0.52340 | 0.51704 | 0.52412 |

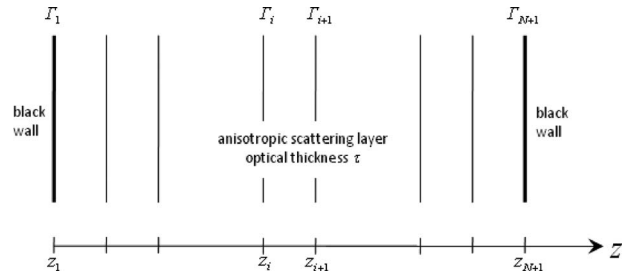


**Fig. 3 Purely anisotropic scattering layer bounded by black walls**

linear phase function in Eq. (34) is set to the medium. We let $\Gamma_1$ and $\Gamma_{N+1}$ be the first and the $L$ elements, and the volume elements be the 2 to $L-1$ elements. Many have computed the TEA $C_{11}$ by various methods [8,9,14–16], and this case is to demonstrate how the vector GEAM is applied. However, this special case gives rise to additional complex in the operation of scattering because here DEA is given in an integrated form so that it is essentially a quasi-two-dimensional problem.

The DEA between two surfaces $\Gamma_i$ and $\Gamma_j$ is given by [3],

$$(\Gamma_i\Gamma_j) = 2\int_0^1 \mu \exp(-\alpha\Delta z_{ij}/\mu)d\mu \tag{37}$$

where $\Delta z_{ij}=|z_i-z_j|$ and $\mu$ is the cosine relative to the $z$-direction. Upon computation Eq. (37) is thus rewritten as a quadrature

$$(\Gamma_i\Gamma_j) = 2\sum_{k=1}^{K} \mu_k \exp(-\alpha\Delta z_{ij}/\mu_k)\Delta\mu = 2\Delta\mu\sum_{k=1}^{K} \mu_k E_k(\Delta z_{ij}) \tag{38}$$

where $K$ is the partition number of $\mu$ in (0,1) and $E_k(\Delta z_{ij}) = \exp(-\alpha\Delta z_{ij}/\mu_k)$. The DEA for all elements are derived in a sequence, i.e.,

$$D_{ij} = \sum_{k=1}^{K} D_{ij}^k \tag{39}$$

where

$$\begin{aligned}
D_{1L}^k &= 2\mu_k E_k(\Delta z_{1L})\Delta\mu \\
D_{1j}^k &= 2\mu_k E_k(\Delta z_{1j})[1 - E_k(\Delta z_{jj+1})]\Delta\mu \\
D_{jL}^k &= 2\mu_k E_k(\Delta z_{j+1L})[1 - E_k(\Delta z_{jj+1})]\Delta\mu \\
D_{ij}^k &= 2\mu_k E_k(\Delta z_{i+1j})[1 - E_k(\Delta z_{jj+1})]\cdot[1 - E_k(\Delta z_{ii+1})]\Delta\mu \\
& \quad i,j = 2,3,\ldots,L-1
\end{aligned} \tag{40}$$

The self-DEA $D_{ii}$ are obtained by the energy conservation relation noting that $F_1=F_L=1$ and $F_i=4\alpha\Delta z_{ii+1}$ for volume elements.

The initial emissive power is taken as $q_1^{(1)}=(1-\omega_1)=1$ and $q_i^{(1)}=0$ $(i=2,3,\ldots,L)$ to compute $C_{11}$ by TSM. Given the initial values $f_i(\hat{s}_j)=1$, the iterative procedures of TSM are performed so as to give the time series of $Q_{a,i}^{(t)}$ $(t=1,\ldots,n)$ by Eq. (24). For gas elements $(i=2,3,\ldots,L-1)$ $b_0=1$ and $b_1=\beta$, $S_i(\hat{s})$ becomes

$$S_i(\mu_k) = \sum_{j=1}^{L} q_j^{(t)}\sum_{k=1}^{K} D_{ji}^k f_j(\hat{s}_k) + \beta\cdot\mu_k\sum_{j=1}^{L} q_j^{(t)}\sum_{k=1}^{K} \mu_k' D_{ji}^k f_j(\hat{s}_k) \tag{41}$$

$$f_i(\hat{s}_k) = S_i(\mu_k)/Q_{a,i}^{(t)} \tag{42}$$

In the current one-dimensional frame, the unit scattering vector $\hat{s}$ is cast into $\mu_k$, which is positive for an element $j$ located at the right side of $i$ $(j>i)$ and negative for an element at left side $(j<i)$. Likewise the incident unit vector $\hat{s}'$ is taken as $\mu_k'$, which is negative if an emitting element $j$ is located at the right side and vice versa. For the surfaces $\Gamma_1$ and $\Gamma_{N+1}$, we have $S_1(\hat{s})=S_L(\hat{s}) = \Sigma_{j=1}^{L} q_j^{(t)}\Sigma_{k=1}^{K} D_{ji}^k f_j(\hat{s}_k)$. Besides the light computational effort, an additional advantage of the current GEAM over those in Ref. [8,9] is that it is not needed to compute for the complex indirect-exchange-area or scattering-exchange-area.

We used $N=20$ volume elements and discretized $\mu$ for $K=100$ in the computation. The TEA $C_{11}$ is calculated by Eq. (32). Table 4 lists the values of $C_{11}$ for different optical thicknesses $\tau$ and coefficients $\beta$. The values are in excellent agreement with what were given by the other methods (summarized in Ref. [8]). For future possible validation Fig. 4 diagrams the distribution of the virtual total absorbed energy $\Sigma_{t=1}^{n} Q_{a,i}^{(t)}$, where the residual tolerance was taken as $10^{-8}$.

## 4 Conclusions and Remarks

In the current article a vector form GEAM is proposed for computing the anisotropic radiative transfer. It is based on the stepwise treatment of the Lengendre polynomials of scattering/reflecting phase function: first, by making vectorlike summations of incident radiation and second, by distributing the scattering/

**Table 4 Total-exchange-area $C_{11}$ in a purely anisotropic scattering slab, computed with $N=20$, $K=100$**

| | | $\beta$ | | | | | | |
|---|---|---|---|---|---|---|---|---|
| $\tau$ | | −1 | −0.7 | −0.5 | 0 | 0.5 | 0.7 | 1 |
| 0.1 | This work | 0.1048 | 0.0988 | 0.0947 | 0.0843 | 0.0737 | 0.0694 | 0.0629 |
| | [7] | | 0.0987 | | 0.0843 | | 0.0694 | 0.0631 |
| | [8] | 0.1050 | 0.0988 | | 0.0843 | | 0.0695 | 0.0628 |
| 1 | This work | 0.5143 | 0.4956 | 0.4824 | 0.4464 | 0.4055 | 0.3876 | 0.3588 |
| | [7] | | 0.497 | | 0.4465 | | 0.3872 | 0.3577 |
| | [8] | 0.5164 | 0.4967 | | 0.4465 | | 0.3891 | 0.3619 |
| 10 | This work | 0.9053 | 0.8979 | 0.8925 | 0.8772 | 0.8585 | 0.8499 | 0.8353 |
| | [7] | | 0.9026 | | 0.8828 | | 0.8529 | 0.8348 |
| | [8] | 0.9089 | 0.9014 | | 0.8804 | | 0.8531 | 0.8386 |

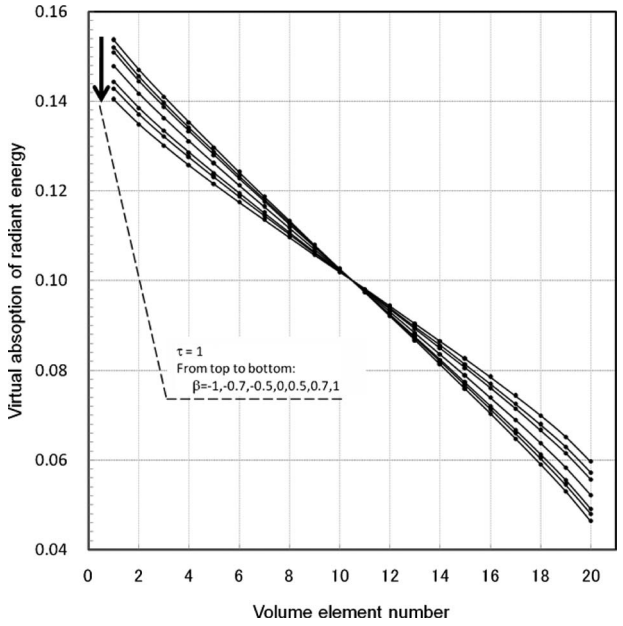


**Fig. 4 Distribution of the virtual absorption $\Sigma_{t=1}^{n} Q_{a,j}^{(t)}$ of radiant energy**

reflection in a gross mode. On the implementation of the model, the core issue is to derive the vectorlike weighted-summations of radiant energy. The operations rely on two radiation vectors. One is the incident radiation vector $\hat{s}'$, which is from an emitting element. This vector is involved in the expression for $S_i(\hat{s})$. The other one is the outgoing emitting vector $\hat{s}$, which points to an absorbing element and is included in the expression of the correction coefficient $f(\hat{s})$. In principle the scheme can be readily applied to any anisotropic phase function that can be formulated in terms of the cosine between incidence and scattering/reflection directions.

The model can be solved by both the traditional iterative algorithm and a two-step method. Applications to a one-dimensional and a three-dimensional benchmark problem have validated the model with showing its high performance in computation.

## Nomenclature

### Alphabet

$a$ = constant in Eq. (9)
$b$ = constant in Eq. (15)
$C_{ij}$ = total-exchange-area ($m^2$)
$D_{ij}$ = direct-exchange-area, ($m^2$)
$E_b$ = blackbody emissivity, $=\sigma T^4$ ($W/m^2$)
$f(\hat{s})$ = correction coefficient to radiosity in terms of the anisotropic distribution
$F$ = equivalent absorption area ($m^2$)
$K$ = partition number of $\mu$
$L,M,N$ = numbers of total, surface and medium elements
$q$ = surface heat flux ($W/m^2$)
$Q$ = heat flux divergence ($W/m^3$)
$\hat{s},\hat{s}'$ = scattering and incidence vectors
$S(\hat{s})$ = scattering term, see Eq. (14)
$T$ = temperature, (K)
$W$ = radiosity ($W/m^2$)

### Greek

$\alpha$ = medium extinction coefficient ($m^{-1}$)
$\beta$ = coefficient of linear phase function, see Eq. (34)
$\mu$ = cosine of two vectors $=\hat{s}\cdot\hat{s}'=\cos\theta$
$\theta$ = angle (deg)
$\sigma$ = Stefan–Boltzmann const $=5.67\times10^{-8}$ ($W/m^2\,K^4$)
$\omega$ = scattering/reflecting albedo
$\tau$ = optical thickness
$\Phi$ = phase function
$\Psi$ = weighted-summations of incident radiation, see Eq. (15) (W)

### Subscripts and Superscripts

$i,j,k$ = index of element number
$(m)$ = order of Legendre polynomials,
$(t)$ = index of iteration step
$\xi,\eta$ = index of the components of a three-dimensional vector

## References


[1] Carvalho, M. G., and Farias, T. L., 1998, "Modeling of Heat Transfer in Radiating and Combusting Systems," Trans. IChemE, Part C, **76**(A), pp. 175–184.
[2] Yuen, W. W., and Takana, E. E., 1997, "The Zonal Method, A. Practical Solution Method for Radiative Heat Transfer in Non-Heat Transfer Uniform, Non-Isothermal Absorbing, Emitting and Scattering Media," Annu. Rev. Heat Transfer, **8**, pp. 153–215.
[3] Hottel, H. C., and Sarafim, A. F., 1967, *Radiative Transfer*, McGraw-Hill, New York.
[4] Noble, J. J., 1975, "The Zone Method, Explicit Matrix Relations for Total Exchange Areas," Int. J. Heat Mass Transfer, **18**, pp. 261–269.
[5] Maruyama, S., and Aihara, T., 1997, "Radiation Heat Transfer of Arbitrary Three-Dimensional Absorbing, Emitting and Scattering Media and Specular and Diffuse Surfaces," ASME Trans. J. Heat Transfer, **119**(1), pp. 129–136.
[6] Howell, J. R., 1998, "The Monte Carlo Method in Radiative Heat Transfer," ASME J. Heat Transfer, **120**(3), pp. 547–560.
[7] Bynn, K. H., and Smith, T. F., 1988, "Development of the Zone Method for Linearly Anisotropic Scattering Media," J. Quant. Spectrosc. Radiat. Transf., **40**, pp. 591–604.
[8] Goyheneche, J. M., and Sacadura, J. F., 2002, "The Zone Method, a New Explicit Matrix Relation to Calculation the Total Exchange Areas in Anisotropically Scattering Medium Bounded by Anisotropically Reflecting Walls," ASME J. Heat Transfer, **124**(3), pp. 696–703.
[9] Ma, A. K., 1995, "Generalized Zoning Method in One-Dimensional Participating Media," ASME J. Heat Transfer, **117**(2), pp. 520–526.
[10] Yuen, W. W., and Takana, E. E., 1994, "Development of, a Generalized Zonal Method for Analysis of Radiative Transfer in Absorbing and Anisotropically Scattering Media," Numer. Heat Transfer, Part B, **25**, pp. 75–96.
[11] Siegel, R., and Howell, J. R., 2002, *Thermal Radiation Heat Transfer*, 4th ed., Taylor & Francis, New York.
[12] Jiang, Y. Y., 2008, "A Two-Step Strategy for Numerical Simulation of Radiative Transfer With Anisotropic Scattering and Reflection," J. Quant. Spectrosc. Radiat. Transf., **109**(4), pp. 636–649.
[13] Hsu, P. F., and Farmer, J. T., 1997, "Benchmark Solution of Radiative Heat Transfer Within Nonhomogeneous Participating Media Using the Monte Carlo and YIX Method," ASME J. Heat Transfer, **119**(1), pp. 185–188.
[14] Dayan, A., and Tien, C. L., 1975, "Heat Transfer in a Gray Planar Medium With Linear Anisotropic Scattering," ASME J. Heat Transfer, **97**, pp. 391–397.
[15] Sutton, W. H., and Ozisik, M. N., 1979, "An Iterative Solution for Anisotropic Radiative Transfer in a Slab," ASME J. Heat Transfer, **102**, pp. 695–698.
[16] Yuen, W. W., and Tien, C. L., 1980, "A Successive Approximation Approach to Problems in Radiative Transfer With Difference Formulation," ASME J. Heat Transfer, **102**, pp. 86–91.

**Coquard Rémi**
e-mail: remi.coquardl@insa-lyon.fr

**Baillis Dominique**

Centre Thermique de Lyon (CETHIL),
UMR CNRS 5008,
Domaine Scientifique de la Doua,
INSA de Lyon, Bâtiment Sadi Carnot,
9, rue de la physique,
69621 Villeurbanne CEDEX, France

**Quenard Daniel**
Centre Scientifique et Technique du Bâtiment (CSTB),
24, rue Joseph FOURIER,
38400 Saint Martin d'Hères, France
e-mail: quenard@cstb.fr

# Radiative Properties of Expanded Polystyrene Foams

*Expanded polystyrene foams are one of the most widely used materials for a building's thermal insulation. Owing to their very low density, a substantial proportion of the heat transfer is due to thermal radiation propagating through their porous structure. In order to envisage an optimization of their thermal performances, an accurate modeling of their radiative behavior is required. However, the previous studies on this subject used several drastic simplifications regarding their radiative behavior (optically thick material) or their porous morphology (homogeneous cellular material, dodecahedral cells). In this study, we propose a more accurate model based on a detailed representation of their complex morphology allowing us to predict their entire monochromatic radiative properties. We investigated the influence of the different structural parameters on these properties. We checked the validity of our model by comparing the spectral hemispherical reflectance and transmittance measured on slabs of foam samples with values predicted by our model. A good accordance was found globally.* [DOI: 10.1115/1.2994764]

*Keywords: thermal insulation, EPS foams, radiative heat transfer, extinction coefficient, scattering*

## 1 Introduction

Expanded polystyrene (EPS) foams are cellular plastics, which are mostly used for the thermal insulation of buildings. In addition to a complex structure exhibiting a double-scale porosity, they are characterized by a particularly low density (comprised between 10 $kg/m^3$ and 30 $kg/m^3$). Even at ambient temperature, the radiative transfer could contribute up to 40% of the total heat transferred. Thus, it is relatively important to model as accurately as possible this mode of heat transfer.

Classical methods of modeling of the radiative transfer in porous structures assimilate the porous material to an equivalent semitransparent medium whose radiative properties accurately match the radiative behavior of the material. An extensive review on this subject, summarizing the results published for numerous dispersed media, was recently conducted by Baillis and Sacadura [1]. Fibrous materials [2], glass foams [3], carbon foams [4], packed beds [5], cellular foams [6], or metallic foams [7] were the most widely studied. Paradoxically, only few studies have focused on EPS foams, certainly because of their complex porous morphology.

Actually, Glicksman et al. [6] were interested in the modeling of EPS foams but their work belongs to a more general study dealing with radiative and conductive transfer through classical cellular plastics so that they greatly simplified their complex porous structure. Indeed, EPS foams were assimilated to porous materials with homogeneous cellular structure composed of windows and cylindrical struts. Moreover, the densities considered were much greater than that of EPS foams.

Kuhn et al. [8] and Placido et al. [9] studied more precisely the heat transfer through EPS foams. However, like Glicksman et al. [6], they also considered that the cellular structure is homogeneous and composed of pentagonal windows and cylindrical struts. Thus, they neglected the influence of macroscopic porosities. Additionally, these studies were especially interested in EPS foams with relatively high densities.

All of these studies have always considered that the cellular material forming the foam is made of dodecahedral (DODE) cells. Moreover, they always used the Rosseland approximation to treat the radiative transfer, which is a strong simplification of the radiative phenomenon occurring in the material. Actually, the previous works were especially interested in EPS foams with relatively high densities for which the assumption of an optically thick material (Rosseland approximation) is valid. Then, the authors had recourse to only one parameter to take into account the radiative heat transfer: the weighted Rosseland extinction coefficient $\beta_\lambda^*$. That is the reason why their theoretical results did not show good agreements with experimental measurements for foams with relatively low densities, which could no more be considered as optically thick materials. Indeed, in this case, the complete radiative properties appearing in the radiative transfer equation and characterizing the interaction between the radiation and the porous structure are required. These properties are the spectral extinction coefficient $\beta_\lambda(m^{-1})$, the spectral scattering coefficient $\sigma_\lambda(m^{-1})$, the spectral absorption coefficient $\kappa_\lambda(m^{-1})$, and the scattering phase function $P_\lambda(\theta)$. In our previous study [10] on the modeling of the coupled one dimensional heat transfer in EPS foams, we have computed theoretically these entire radiative properties, taking into account the structural characteristics of EPS foams such as foam density or cell diameter. However, we were primarily interested in the evaluation of the global thermal performances and we did not highlight the variations of the radiative behavior of the foam. Moreover, we only considered dodecahedral cells.

In the present study, a more specific emphasis is put on radiative heat transfer. We use the model of prediction of the radiative behavior of low-density EPS foams presented in our previous paper [10] at which we have added two other possible cell shapes in addition to the dodecahedron: cube and tetrakaidecahedron. This allowed us to investigate the variations of the entire monochromatic radiative properties with the parameters characterizing the foam (density, cell diameter, bead diameter and macroscopic porosity) and with the cell shapes considered. Finally, we check the validity of these radiative properties by comparing theoretical and experimental spectrometric measurements made on several slices of EPS foams.

## 2 Structure of EPS Foams

The structure of EPS foams is more complex than a simple cellular matrix. They are characterized by a double-scale porosity directly due to their production process. As shown in the photo-

Contributed by the Heat Transfer Division of ASME for publication in the JOURNAL OF HEAT TRANSFER. Manuscript received December 14, 2007; final manuscript received April 8, 2008; published online October 22, 2008. Review conducted by Walter W. Yuen.

  

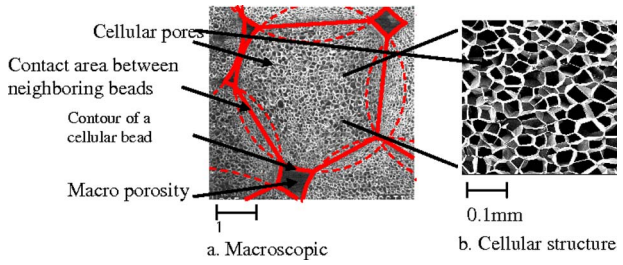


**Fig. 1 SEM photographs representing the porous morphology of EPS: (*a*) macroscopic structure and (*b*) cellular structure**

graph in Fig. 1, the porous structure is not homogeneous and is actually composed of two different types of pores: small cellular pores ($D_{cell} \approx 100-300\ \mu m$) with a regular shape contained in the polystyrene beads and large pores ($D \approx 1$ mm) with an irregular shape corresponding to the interparticle space. The porosity $\varepsilon_{cell}$ of the cellular material contained in the beads is very important ($\varepsilon_{cell} \approx 97-99\%$) whereas the macroporosity, noted $\varepsilon_{interbead}$, is relatively low ($\varepsilon_{interbead} \approx 4-10\%$). This macroscopic structure of the EPS foams could be accurately reproduced by an arrangement of overlapping spherical particles with diameter $D_{bead}$ representing the compressed beads (Fig. 1(*a*)).

With regard to the cellular medium contained in the compressed beads, it is composed of perfectly closed cells with homogeneous shape and size. Moreover, microscopic analysis show that most of the polymer is contained in the cellular windows and that the struts of matter generally observed at the junction of two cellular faces could be neglected in EPS foams. All the previous studies assumed that the cellular medium has a dodecahedral shape (pentagonal windows). However, microscopic photographs show windows of different shapes: square, pentagonal, or hexagonal. Then, the cells are not perfect dodecahedrons. That is the reason why, in order to investigate the influence of the shape of the cells, we model three different types of cells (Fig. 2): cubic (CUBE) (square faces), dodecahedron (pentagonal faces), and tetrakaidecahedral (TETRA) (square and hexagonal faces).

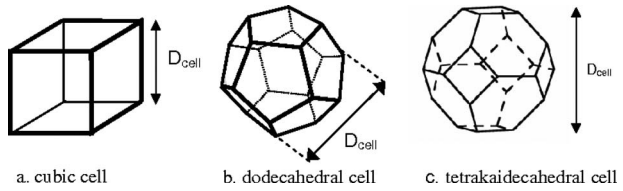


**Fig. 2 Illustration of the different shapes of cells: (*a*) cubic cell, (*b*) dodecahedral cell, and (*c*) tetrakaidecahedral cell**

To quantify the dimensions of the cells, we use the parameter $D_{cell}$ (Fig. 2). We will assume subsequently that the cellular medium is made of cells of constant shape and dimensions. The volume of the cell is related to this diameter according to the shape of the cell considered (Table 1).

Assuming that the entire polymer is contained in the cell windows of constant thickness $h$ and that $h$ is very small compared with $D_{cell}$, we can express $h$ from $D_{cell}$ and $\varepsilon_{cell}$. The expression relating the structural parameters are summarized in Table 1.

In conclusion, our representation of the porous structure of EPS foams is entirely described using five different structural characteristics:

- the bead diameter $D_{bead}$
- the macroporosity $\varepsilon_{interbead}$
- the cell diameter $D_{cell}$
- the porosity of the cellular medium $\varepsilon_{cell}$
- the shape of the cell: dodecahedron, cube, or tetrakaidecahedron

Generally, one prefers to use the density $\rho_{EPS}$ of the foam instead of $\varepsilon_{cell}$ given that it could be measured directly. Indeed, we have

$$\rho_{EPS} = (1-\varepsilon_{cell}) \times (1-\varepsilon_{interbeads}) \times \rho_{PS}$$

$$\Leftrightarrow \varepsilon_{cell} = 1 - \frac{\rho_{EPS}}{\rho_{PS}} \times (1-\varepsilon_{interbeads})^{-1} \quad (1)$$

## 3 Modeling of the Radiative Properties of EPS Foams

Radiative heat transfer in $\alpha$ low-density porous medium is a relatively complex problem given that it takes into account not only the emission and absorption but also the scattering of radiation by the porous material. This radiative behavior may also vary with the radiation wavelength $\lambda$. Thus, one has to recourse to three different spectral characteristics:

- the extinction coefficient $\beta_\lambda (m^{-1})$,
- the albedo $\omega_\lambda = \sigma_\lambda / \beta_\lambda$, and
- the scattering phase function $P_\lambda(\theta)$

These radiative properties are closely related to the porous microstructure. For EPS foams, it is necessary to take into account accurately the real morphology and, especially, the macroscopic pores, which could represent 10% of the total volume. We use an

**Table 1 Expression relating the structural parameters for the three cell shapes considered**

| | Dodecahedron | Cube | Tetrakaedecaehedron |
|---|---|---|---|
| Cell volume | $V_{dode} \approx 0.427 \times D_{cell}^3$ | $V_{cube} = D_{cell}^3$ | $V_{tetr} = 0.5 \times D_{cell}^3$ |
| Window area | $S_{win} \approx 0.251 \times D_{cell}^2$ | $S_{win} \approx D_{cell}^2$ | $S_{win,1} \approx 0.32476 D_{cell}^2$ (hexagon)<br>$S_{win,2} = 0.125 D_{cell}^2$ (square) |
| Cell total window area | $S_{dode} = 6 \times S_{win}$<br>$S_{dode} \approx 3.0122 \times D_{cell}^2$ | $S_{cube} = 6 \times S_{win}$<br>$S_{cube} = 6 \times D_{cell}^2$ | $S_{tetr} = 8 \times S_{win,1} + 6 \times S_{win,2}$<br>$S_{tetr} \approx 3.3480 \times D_{cell}^2$ |
| Particles per unit volume | $N = \frac{6}{V_{cell}} \approx \frac{14.006}{D_{cell}^3}$ | $N = \frac{3}{V_{cell}} = \frac{3}{D_{cell}^3}$ | $N_1 = \frac{4}{V_{cell}} = \frac{8}{D_{cell}^3}$ (hexagon)<br>$N_2 = \frac{3}{V_{cell}} = \frac{6}{D_{cell}^3}$ (square) |
| Relation $\varepsilon_{cell}/h$ | $h \approx 0.2836 \times (1-\varepsilon_{cell}) \times D_{cell}$ | $h = \frac{(1-\varepsilon_{cell}) \times D_{cell}}{3}$ | $h \approx 0.29898 \times (1-\varepsilon_{cell}) \times D_{cell}$ |

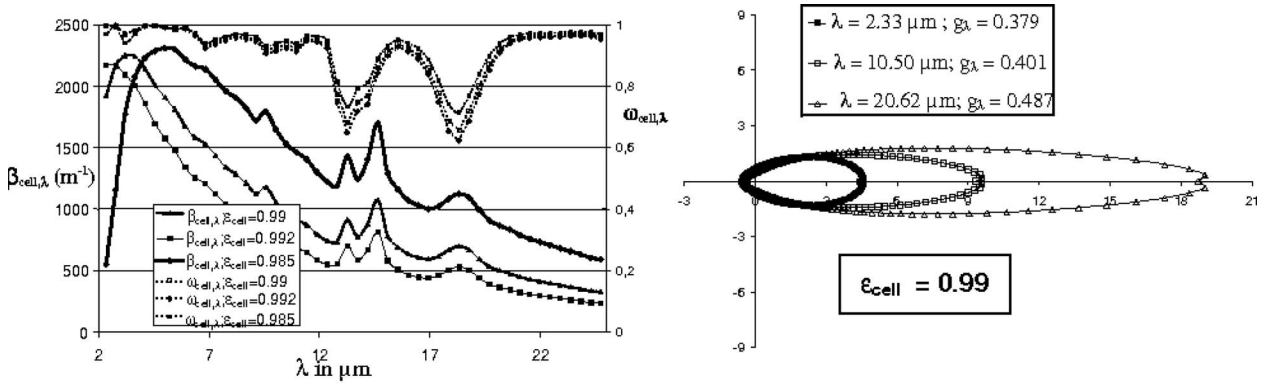


a. extinction coefficient and albedo

b. scattering phase function

**Fig. 3 Evolution of the extinction coefficient, scattering albedo (*a*) and scattering phase function (*b*) with the radiation wavelength for a dodecahedral cellular material with $D_{cell}$=200 $\mu$m and various densities**

innovative model to determine the extinction, absorption, and scattering coefficients and the phase functions. It is divided in to two stages.

- First, we focus on the equivalent radiative properties $\beta_{cell,\lambda}$, $\omega_{cell,\lambda}$, and $P_{cell,\lambda}(\mu' \rightarrow \mu)$, of the cellular material
- Then, the properties of the entire foam are calculated by assimilating the foam to an arrangement of overlapping spherical particles containing a homogeneous absorbing and scattering medium with known radiative properties

**3.1 Equivalent Radiative Properties of the Cellular Medium.** In order to compute for the equivalent radiative properties of porous media, we have assimilated the porous structure to a random arrangement of particles whose shape and size permit us to reproduce the internal structure. For the cellular medium, we assumed that it is made of a cloud of randomly oriented identical cell windows. Given the very high porosity, we have considered that the particles scatter radiation independently. Under these assumptions $\sigma_{cell,\lambda}$, $\kappa_{cell,\lambda}$, $\beta_{cell,\lambda}$, and $P_{cell,\lambda}(\mu' \rightarrow \mu)$ are calculated by adding the radiative characteristics of all the different particles present in an elementary volume ($N_i$). These characteristics are the absorption cross section $C_{a,\lambda}(m^2)$, the scattering cross section $C_{s,\lambda}(m^2)$, the extinction cross section $C_{e,\lambda}=C_{a,\lambda}+C_{s,\lambda}(m^2)$, and the scattering phase function $\Phi_\lambda(\theta)$. They are computed by analyzing the interaction of the particle with a plane incident wave. Moreover, the characteristics must be averaged over all the possible directions of the incident wave (sign $\langle\rangle$). We then have

$$\kappa_{cell,\lambda} = \sum_i N_i \cdot \langle C_{a,\lambda,i} \rangle, \quad \sigma_{cell,\lambda} = \sum_i N_i \cdot \langle C_{s,\lambda,i} \rangle$$

$$\beta_{cell,\lambda} = \sum_i N_i \cdot \langle C_{e,\lambda,i} \rangle, \quad P_{cell,\lambda}(\theta) = \frac{1}{\sigma_{cell,\lambda}} \sum_i C_{s,\lambda,i} \cdot \Phi_{\lambda,i}(\theta) \cdot N_i \tag{2}$$

We have applied the approach previously described to cellular materials with pentagonal, square, and hexagonal cell windows. In order to compute for the radiative characteristics of a particle, it is theoretically necessary to consider a plane monochromatic wave incident on this particle and apply Maxwell's equation. However, in the case of EPS foams, the particle size parameter $x = \pi \cdot D_{cell}/\lambda$ is very large (100 $\mu$m$<D_{cell}<$300 $\mu$m; $\lambda \approx 10$ $\mu$m) and the geometric optics approximation (GOA: Fresnel relations) alone could be used to treat the radiation/matter interaction.

We checked the validity of the previous assumption for pentagonal windows oriented normally to the plane wave by comparing the radiative characteristics stemming from the GOA with the results of a numerical method based on the discrete dipole approximation (DDA) developed by Draine and Flatau [11]. With regard to the cross sections, the comparisons show that the GOA leads to errors lower than 5% for windows with $t_{win}$ as small as 30 $\mu$m. The phase function given by the DDA for windows oriented normally to the plane wave also proves to be very close to that predicted by GOA. In the rest of the study we assumed that these conclusions are valid whatever the orientation of the windows.

According to the GOA, the absorption and scattering cross sections are computed by multiplying the cross section of the particle by its absorptivity and reflectivity calculated by the Fresnel relations. Given that the particles are supposed to be randomly oriented, one must integrate over all the possible incident angles $\theta_{inc}$

$$C_{e,\lambda} = \int_{\theta inc=0}^{\pi/2} (1 - \mathrm{Tr}_{win}(\theta_{inc})) \cdot S_{win} \cos\theta_{inc} \sin\theta_{inc} \cdot d\theta_{inc}$$

$$C_{s,\lambda} = \int_{\theta inc=0}^{\pi/2} R_{win}(\theta_{inc}) \cdot S_{win} \cos\theta_{inc} \sin\theta_{inc} \cdot d\theta_{inc}$$

$$C_{a,\lambda} = \int_{\theta inc=0}^{\pi/2} A_{win}(\theta_{inc}) \cdot S_{win} \cos\theta_{inc} \sin\theta_{inc} \cdot d\theta_{inc} \tag{3}$$

$$\Phi(\theta) = \frac{2 \cdot R_{win}(\theta_{inc})}{\int_{\theta=0}^{\pi} R_{win}(\theta_{inc}) \sin\theta \cdot d\theta} \quad \text{with } \theta_{inc} = \pi/2 - \theta/2$$

The thickness $h$ is comparable to the radiation wavelengths. Therefore, $A_{win}$, $R_{win}$, and $\mathrm{Tr}_{win}$, are computed from the thin film optic laws, which take into account the interference effects. These relations are well-described in [12].

The radiative properties could be determined from the average radiative characteristics of one particle (Eq. (2)). We conducted our computations for the three different types of cells. For each shape, the equation relating the morphological parameters to $\varepsilon_{cell}$ and $D_{cell}$ are summarized in Table 1.

We have determined the complex refractive index $\tilde{n}=n-ik$ of polystyrene for infrared wavelength using an identification method based on transmittance and reflectance measurements on thin and thick polystyrene films. The variations of this index with the wavelength can be found in our previous paper [10].

We have computed the variation of $\kappa_{cell,\lambda}$, $\sigma_{cell,\lambda}$, $\beta_{cell,\lambda}$, and $P_{cell,\lambda}(\theta)$ with the radiation wavelength for cellular materials with different morphologies using the identified refractive index. Some results are illustrated in Fig. 3 where the variations of the extinction coefficient $\beta_{cell,\lambda}$, scattering albedo $\omega_{cell,\lambda}=\sigma_{cell,\lambda}/\beta_{cell,\lambda}$, and

phase function are depicted for dodecahedral cellular media with $D_{cell}=200\ \mu m$. For the phase function, we also indicate some values of the asymmetry parameter $g_\lambda$, which illustrates the ability of the material to scatter predominantly in the forward ($>0$) or backward ($<0$) hemisphere. This parameter comprised between $-1$ and 1 is defined by $g_\lambda=0.5\int_0^\pi P_{cell,\lambda}(\theta)\cdot\sin\theta\cdot\cos\theta d\theta = 0.5\int_{-1}^{1} P_{cell,\lambda}(\mu)\cdot\mu\cdot d\mu$. This figure shows that the radiation/matter interaction strongly depends on the wavelength considered and is dominated by scattering ($\omega_{cell,\lambda}\approx 1$) except for some wavelengths belonging to a polystyrene absorption peak. Moreover, one can observe that the scattering phase function is oriented predominantly in the forward direction whatever the wavelength considered.

**3.2 Radiative Properties of the Entire Foam.** Once the radiative properties of the cellular medium have been determined, the foam is assimilated to a random arrangement of spherical overlapping particles containing a homogeneous absorbing and scattering medium whose equivalent radiative properties are those of the cellular material. This representation is very close to the real macroscopic structure of EPS foams (see Fig. 1). The porosity and the particle diameter of the arrangement must, respectively, be equal to the macroporosity $\varepsilon_{interbead}$ and the mean bead diameter $D_{bead}$ of the EPS foam. The generation of the arrangement of spheres and the computation of the properties of the entire foam are detailed in our previous paper on packed beds of semitransparent [13] spheres.

First, a ray-tracing procedure is applied in a spherical domain of the arrangement much larger than $D_{bead}$ and permit to compute three variables entirely describing the radiative behavior of the packed bed. The three variables correspond to the proportion of starting energy traveling through the spherical domain without being neither absorbed nor scattered, the proportion leaving after one or several scattering inside the particles and the angular repartition of this latter energy. The traveling of the rays through the absorbing and scattering medium representing the cellular material is dictated by the radiative properties $\kappa_{cell}$, $\sigma_{cell}$, $\beta_{cell}$, and $P_{cell}(\theta)$. Secondly, an identification procedure determines the equivalent radiative properties $\kappa_\lambda$, $\sigma_\lambda$, $\beta_\lambda$, and $P_\lambda(\theta)$ of the homogeneous semitransparent medium that best match the radiative behavior of the arrangement of spheres previously characterized. For more details about the method, one can consult the paper of reference [13].

## 4 Results

We have applied our model to several fictive foams by varying the density, cell diameter, bead diameter, and interbead porosity in the ranges of values commonly encountered. We conducted our computations for the three different cell shapes considered. This allows us to investigate the influence of the structural parameters on the monochromatic radiative behavior of the foam.

Moreover, in order to check the validity of our computed properties, we compared the spectral transmittances and reflectances measured on thin slices of different EPS foams of various morphological properties with the ones predicted.

**4.1 Evolution of the Radiative Properties With the Structural Characteristics.** The radiative properties of the foam vary strongly with the wavelength considered, as illustrated in Fig. 3. In order to lighten the theoretical analysis, we focused on the global radiative properties $\beta$, $\omega$, and $P(\theta)$, which corresponds to the spectral properties integrated over all the wavelengths. Their calculations are inspired from the expression of the Rosseland global extinction coefficient

$$\frac{1}{\beta}=\frac{\int_{2\ \mu m}^{25\ \mu m}(1/\beta_\lambda)\cdot I_\lambda^0(T)\cdot d\lambda}{\int_{2\ \mu m}^{25\ \mu m} I_\lambda^0(T)\cdot d\lambda},\quad \frac{1}{\sigma}=\frac{\int_{2\ \mu m}^{25\ \mu m}(1/\sigma_\lambda)\cdot I_\lambda^0(T)\cdot d\lambda}{\int_{2\ \mu m}^{25\ \mu m} I_\lambda^0(T)\cdot d\lambda}$$

$$\frac{1}{\sigma\cdot P(\theta)}=\frac{\int_{2\ \mu m}^{25\ \mu m}1/(\sigma_\lambda\cdot P_\lambda(\theta))\cdot I_\lambda^0(T)\cdot d\lambda}{\int_{2\ \mu m}^{25\ \mu m} I_\lambda^0(T)\cdot d\lambda}\quad \text{and } \omega=\frac{\sigma}{\beta} \tag{4}$$

Moreover, as the representation of the scattering phase function is weighty, we rather depict, in the next, the variations of its global asymmetric parameter $g$. Finally, in order to summarize the radiative behavior of the foam in a unique parameter, we also compute the weighted extinction coefficient $\beta^*$

$$\frac{1}{\beta^*}=\frac{\int_{2\ \mu m}^{25\ \mu m}(1/\beta_\lambda^*)\cdot I_\lambda^0(T)\cdot d\lambda}{\int_{2\ \mu m}^{25\ \mu m} I_\lambda^0(T)\cdot d\lambda}\quad \text{with}\begin{cases}\beta_\lambda^*=\kappa_\lambda+\sigma_\lambda^*\\ \sigma_\lambda^*=\sigma_\lambda\cdot(1-g_\lambda)\end{cases} \tag{5}$$

Note that this weighted extinction coefficient $\beta^*$ is useful in the Rosseland approximation.

*4.1.1 Influence of the Foam Density*. The results illustrated in this paragraph (Fig. 4) Nere computed for a variety of EPS foams with the following characteristics: $\varepsilon_{interbead}=6\%$, $D_{bead}=4$ mm, and $100\ \mu m<D_{cell}<300\ \mu m$. The density of the foam varies between 8.95 kg/m$^3$ ($\varepsilon_{cell}=0.992$) and 19.0 kg/m$^3$ ($\varepsilon_{cell}=0.983$). We simulated DODE, (CUBE), and TETRA cells. However, we only depict the results for all the three cell shapes (DODE, CUBE, TETRA) for $D_{cell}=200\ \mu m$.

The theoretical results show that the density has a strong influence on the global radiative properties and especially on the extinction coefficient of the foam. As expected, the extinction coefficient increases with an increase of the density. This can be explained by the fact that when the foam is denser, a more important quantity of matter interact with thermal radiation and prevent its propagation. This remark is valid whatever the diameter of the cells. However, the evolutions are somewhat different according to the size of the cells. For foams made of relatively small cells ($D_{cell}=100\ \mu m$), the increase is more pronounced than for relatively large cells.

With regard to the scattering albedo of the foam, one can remark that it is always close to 1 ($>0.85$), whatever the shape of cells considered. This means that, in EPS foams, the extinction phenomenon is dominated by scattering. Moreover, the variation of the albedo with the density is less significant than for the extinction coefficient. Actually, for a given cell size, one can observe a slight increase of $\omega$ with $\rho_{EPS}$. In addition, this increase is less important for relatively large cells. Then, for a cell diameter $D_{cell}=300\ \mu m$, it is practically imperceptible.

Finally, the evolution of the asymmetry parameter of the phase function with $\rho_{EPS}$ indicates that the complex porous structure scatters radiation predominantly in the forward direction ($g>0$), as it was observed for the cellular medium contained in the beads. Theoretical results also show that, when $\rho_{EPS}$ increases, the scattering in the forward direction is less predominant.

This later remark, as well as the previous observation, clearly indicates that an increase in the density noticeably reduces the thermal radiative heat transfer in EPS foams. This is confirmed qualitatively by the significant increase of $\beta^*$ with the density. This conclusion confirms the general observation concerning the

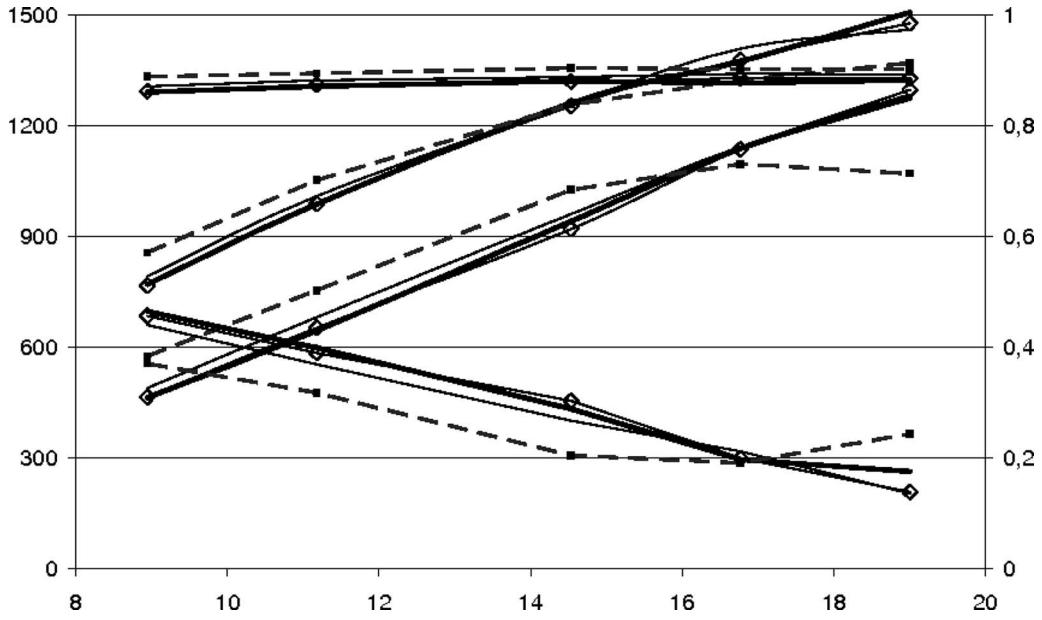


**Fig. 4 Variation of the global radiative properties with the density for an EPS foam with $\varepsilon_{interbead}$ =6% and $D_{bead}$=4 mm**

evolution of the insulating performances of EPS foams with $\rho_{EPS}$. Additionally, it seems that this decrease in the radiative heat transfer with the increasing density is less pronounced when the cells are large.

*4.1.2 Influence of the Cell Diameter*. The results presented in Fig. 5 were obtained for fictive EPS foams with $\varepsilon_{interbead}$=6%, $D_{bead}$=4 mm, and a density varying between 8.95 kg/m$^3$ and 19.0 kg/m$^3$. Like in the previous paragraph, we only depict the results for all the three cell shapes for $\rho$=8.95 kg/m$^3$.

The evolutions of the radiative properties with the cell diameter are more complex than with the foam density

- With regard to $\beta$, one can remark that it reaches a maximum value for a given cell diameter. This optimal cell diameter varies with the density and the shape of the cells. The denser the foam is, the lower the optimal diameter is. This optimal diameter is approximately identical for dodecahedral and tetrakaidecahedral cells and somewhat lower for cubic cells. Then, for $\rho<9$ kg/m$^3$, the optimal diameter is greater than 300 $\mu$m whatever the shape of the cells. On the other hand, for foams with densities of 14.5 kg/m$^3$ and 19 kg/m$^3$, the optimal diameter is approximately 250 $\mu$m and 200 $\mu$m for dodecahedral and tetrakaidecahedral cells and 200 $\mu$m and 150 $\mu$m for cubic cells, respectively.
- The scattering albedo varies much more slightly with $D_{cell}$. Actually, it is always comprised between 0.85 and 0.93. The albedo is inclined to increase when the cells get larger whatever the density of the foam. However, one can also notice

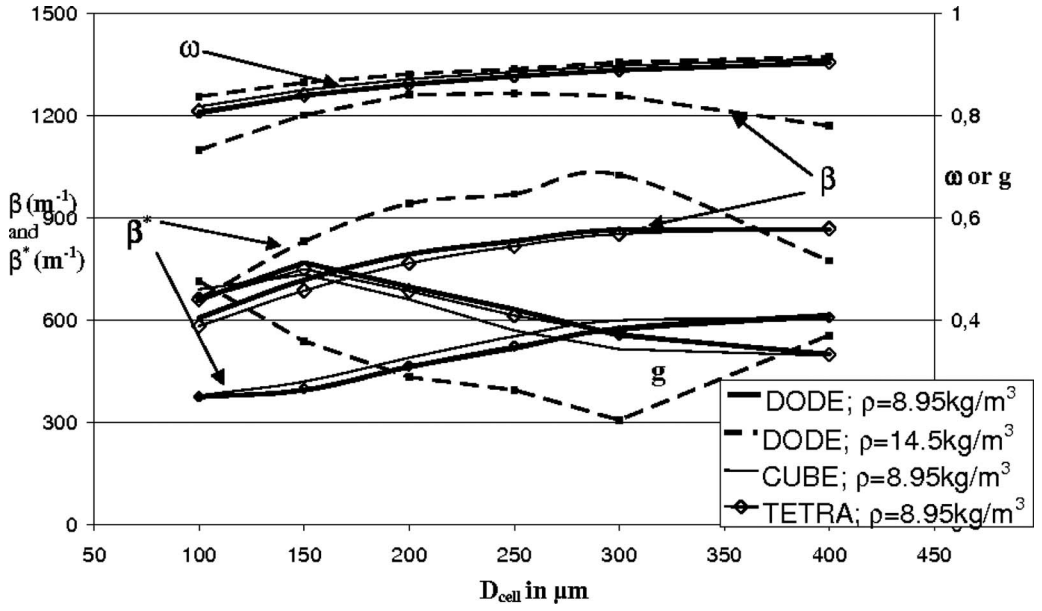


**Fig. 5 Variation of the global radiative properties with the cell diameter for EPS foams with $\varepsilon_{interbead}$=6%, $D_{bead}$=4 mm, and $\rho$=8.95 kg/m$^3$ or $\rho$=14.0 kg/m$^3$**

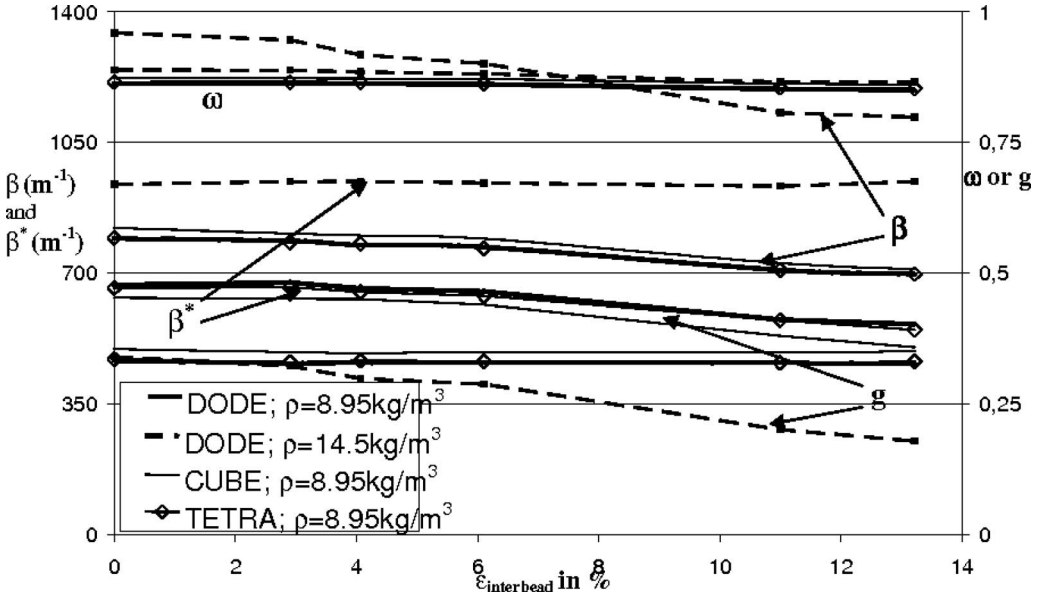


**Fig. 6 Variation of the global radiative properties with the interbead porosity for an EPS foam with $D_{bead}$=4 mm, $D_{cell}$=200 $\mu$m, and $\rho$=8.95 kg/m$^3$ or $\rho$=14.5 kg/m$^3$**

that this tendency is more pronounced for low-density foams.

- $D_{cell}$ has also a strong influence on the directional distribution of the energy scattered. Besides, the evolution of $g$ can be compared to that observed for $\beta$. Indeed, for foams with small densities, the presence of relatively small cells favors the forward scattering. The propagation of the radiation in the material is then easier for small cells than for large ones, which enhance the radiative transfer. However, for greater densities, the value of $g$ reaches a minimum value for a given cell diameter. The denser the foam is, the lower this diameter is. For this cell diameter, the radiative heat transfer is restrained. One can also notice that, whatever the density considered, the optimal diameter for $P(\theta)$ is approximately the same as the optimal diameter observed for $\beta$. All the previous observations are valid for the three cell shapes.

We can conclude that the comprised $D_{cell}$ is a parameter of great influence. It appears that there exists, for each density, an optimal diameter minimizing the penetration length of the IR radiation. This diameter is larger for light foams than for dense foams. For this diameter, the insulating performances are optimal. The conclusions are summarized qualitatively by the evolution of the weighted extinction coefficient $\beta^*$ with $D_{cell}$. It exhibits a maximal value for foams of 14.5 kg/m$^3$ and 19.0 kg/m$^3$ in density whereas it increases continuously for the lightest foam in the range of cell diameters considered.

*4.1.3 Influence of the Interbead Porosity*. The results presented in this section were calculated for the following characteristics: $D_{bead}$=4 mm, $D_{cell}$=200 $\mu$m, and $\rho$=8.95 kg/m$^3$ and 14.5 kg/m$^3$. Like in the previous paragraphs, we only depict the results for all the three cell for $\rho$=8.95 kg/m$^3$ (Fig. 6).

It is interesting to note that $\varepsilon_{interbead}$ affects the radiative properties in a very weak manner.

Its influence on $\beta$ is relatively limited when we consider foams with low densities for which the radiation-matter interaction is weak. However, we notice a regular decrease of $\beta$ when $\varepsilon_{interbead}$ increases. This decrease is more important for denser foams.

With regard to $\omega$, it very slightly decreases when $\varepsilon_{interbead}$ gets larger. This decrease is somewhat more pronounced for denser foams.

Finally for $P(\theta)$, when $\varepsilon_{interbead}$ increases, the asymmetry parameter varies in a manner that is obviously identical to the variation of $\beta$. Indeed, a high interbead porosity is less favorable to the forward scattering as $g$ decreases. This is a consequence of the "back-scattering effect" due to the spherical shape of the beads, which is underlined in our paper [13]. Actually, when $\varepsilon_{interbead}$ increases, the macroscopic morphology of the foam come close to an arrangement of touching spheres and thus, the shape of the particle has a significant influence. On the other hand, when $\varepsilon_{interbead} \to 0$, the macroscopic morphology of the foam comes close to a homogeneous material. The back-scattering effect tends to become negligible.

According to the previous observations, it is not possible to draw a general conclusion concerning the influence of $\varepsilon_{interbead}$ on the radiative heat transfer since $\beta$ and $P(\theta)$ are influenced in an antagonistic manner. However, the variations of the weighted extinction coefficient $\beta^*$, which are almost negligible, clearly indicate that radiative heat transfer is globally not influenced by $\varepsilon_{interbead}$.

*4.1.4 Influence of the Bead Diameter*. The results reported in Fig. 7 were obtained for EPS foams with $\varepsilon_{interbead}$=6%, $D_{cell}$=200 $\mu$m, and 8.95 kg/m$^3$ $< \rho_{EPS} <$ 19.0 kg/m$^3$. Like in the previous paragraphs, we only depict the results for all the three cell shapes for $\rho$=8.95 kg/m$^3$.

The analysis of the graphs shows that $D_{bead}$ has a non-negligible influence on the global radiative properties. Actually, as for the interbead porosity, we notice a regular decrease of $\beta$ when $D_{bead}$ increases. This remark is valid whatever the cell diameter and density of the foam. Consequently, for given $\rho_{EPS}$ and $D_{cell}$, the radiation-matter interaction is enhanced for small beads. This influence is more important for foams with relatively large densities.

The influence of $D_{bead}$ on $\omega$ is practically imperceptible. However, we can notice that it tends to decrease when the beads gets larger.

$g$ is influenced by $D_{bead}$ in a manner that is quite the same as $\beta$. Indeed, $g$ decreases regularly when the diameter increases and this evolution is more pronounced for relatively dense foams. Moreover, the value of g remains always positive, which indicates that the forward scattering is always predominant. This decreases of $g$

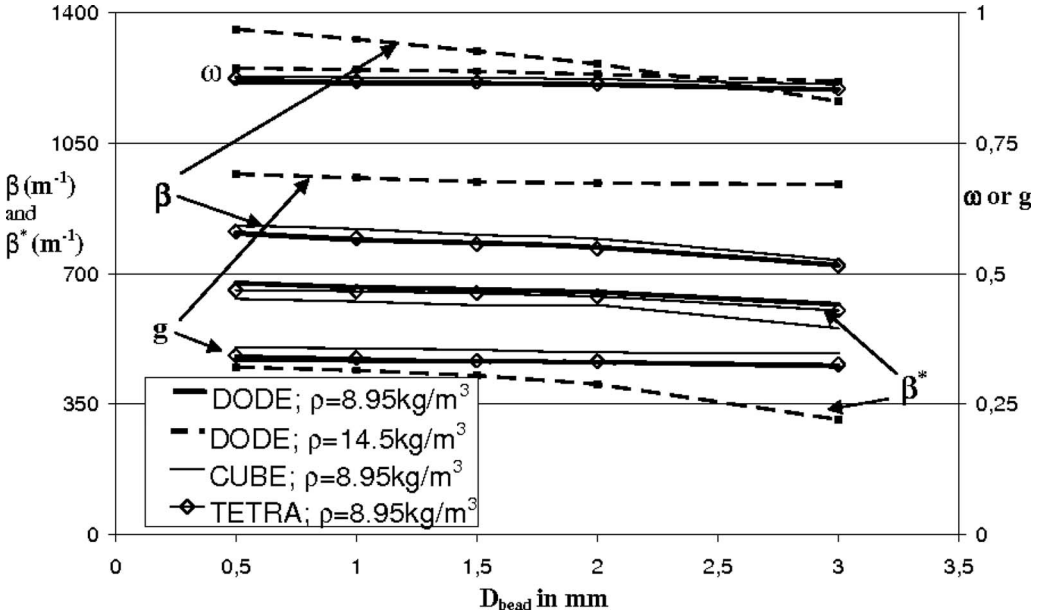


**Fig. 7 Variation of the global radiative properties with the bead diameter for an EPS foam with $\varepsilon_{interbead}$=6%, $D_{cell}$=200 $\mu$m, and $\rho$=8.95 kg/m$^3$ or $\rho$=14.5 kg/m$^3$**

with $D_{bead}$ is due to the back-scattering effect already evocated in the previous paragraph. Indeed, this effect caused by the spherical shape of the particle is more pronounced when the dimensionless number $\beta_{ins} \cdot R$ is large.

The previous remarks indicate that the global influence of $D_{bead}$ on the radiative properties is quite similar to that of $\varepsilon_{interbead}$. The variations of $\beta$ and $P(\theta)$ with $D_{bead}$ are antagonistic. Moreover, the variations of $\beta^*$ show, that radiative heat transfer is globally not influenced by $D_{bead}$.

*4.1.5 Influence of the Cells Shape*. We have seen that the shape of the cellular material is not well-defined and is rather a combination of cubic, dodecahedral, and tetrakaidecahedral cells. The radiative behavior is then intermediate between these three kinds of cells.

Now, from the theoretical results, it appears clearly that the global behaviors of these three different cellular morphologies follow a similar trend. Indeed, the variations of the three global radiative properties with the parameters characterizing the cellular structure are the same. However, some minor differences are found notably in the algebraic values of $\beta$, $\omega$, and $g$. Then, it seems that a cubical shape leads to a stronger radiation-matter interaction whereas the results obtained for dodecahedral or tetrakaidecahedral cells are practically identical. This can be explained by the fact that the morphological relations illustrated in Table 1 are very close to each other. Actually, the most noteworthy difference observed concerns the value of the optimal cellular diameter (Sec. 4.1.2), which is slightly lower for cubes.

*4.1.6 Conclusions*. The study on the variation of $\beta$, $\omega$, and $P(\theta)$ with the structural parameters has revealed that, whatever the structural characteristics (density, $D_{cell}$, cell shape, $\varepsilon_{interbead}$, and $D_{bead}$) the interaction of the porous structure of EPS foams with radiation is dominated by scattering and that the radiant energy is predominantly forward scattered. We also show that the most influent characteristics are $\rho_{EPS}$ and $D_{cell}$. As expected, a higher foam density enhances the radiation/matter interaction and leads to a substantial increase of $\beta$. On the other hand, the variations of $\beta$, $\omega$, and $P(\theta)$ with $D_{cell}$ is not so evident since there actually exists, for each foam density, an optimal cell diameter minimizing the propagation of radiation. For this diameter, $\beta$ reaches a maximum value and $g$ is minimal. This diameter increases with the foam density. With regard to the parameters related to the macroscopic structure, the theoretical investigations revealed that their influence on the propagation of the radiation is relatively limited although $\beta$ and $P(\theta)$ may be noticeably affected by a variation of $D_{bead}$ or $\varepsilon_{interbead}$. Indeed, the influence of $D_{bead}$ and $\varepsilon_{interbead}$ on $\beta$ and $P(\theta)$ are antagonistic. Thus, a detailed consideration of the macrostructure of EPS foams is not of primary importance. This conclusion permits us to validate the assumptions made by the previous authors [6,8,9], which neglected the macroporosity and assimilated EPS foams to macroscopically homogeneous materials. Finally, the theoretical results also reveal that the shape of the cells has a relatively weak influence as the three cell models considered demonstrated a similar behavior.

**4.2 Validation.** The model of computation of the radiative properties presented in the previous paragraph makes several assumptions concerning the radiation-matter interaction or the representation of the porous morphology. In order to check that the properties obtained accurately represent the radiative behavior of the foam, we developed a validation procedure based on spectroscopic measurements on thin slices of EPS foams.

We choose different EPS foam samples whose morphologic properties are measured (see Table 2). In each foam sample, we cut up thin slices of thicknesses Th. We measured the hemispherical transmittance $Tr_{h,\lambda}$ and reflectance $R_{h,\lambda}$ of these slices using a Fourier transform spectrometer fitted out with an integrating sphere. Measurements are made in the spectral range 2–25 $\mu$m. The slices obtained are relatively inhomogeneous as the proportion of the thickness occupied by the cellular medium varies with the zone considered. In order to reduce the influence of this inhomogeneity, numerous measurements are made by varying the position of the IR beam. The experimental values are then obtained

**Table 2 Characteristics of the EPS foam samples used for the validation**

| Sample No. | $\rho$ (kg/m$^3$) | $D_{cell}$ ($\mu$m) | $D_{bead}$ (mm) | $\varepsilon_{interbead}$ (%) | $\varepsilon_{cell}$ (%) |
|---|---|---|---|---|---|
| 1 | 8.7 | 200 | 5.6 | 6.1 | 99.1175 |
| 2 | 12.8 | 160 | 5.1 | 7.1 | 98.6846 |
| 3 | 17 | 80 | 3.2 | 8.1 | 98.2378 |

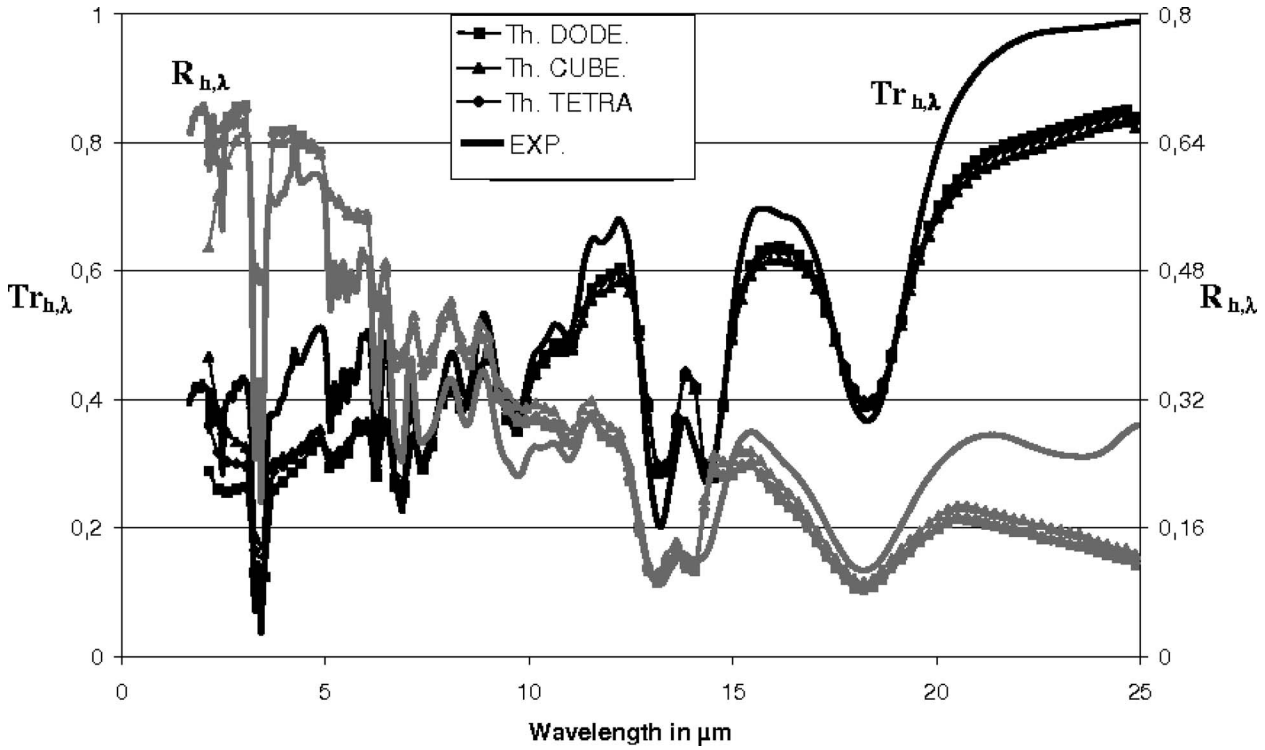


**Fig. 8 Comparison of the experimental and theoretical spectral transmittances and reflectances for sample No. 1 (slice thickness: 3 mm)**

by averaging over all the measurements.

Thereafter, the experimental transmittance (noted expt·$\mathrm{Tr}_{h,\lambda}$) and reflectance (noted expt·$R_{h,\lambda}$) are compared with the theoretical values stemming from the model previously presented. To do that, we first compute for the monochromatic radiative properties of the cellular medium from its measured porosity and $D_{\mathrm{cell}}$. Then, the theoretical hemispherical transmittance and reflectance are determined using a ray-tracing approach.

From the value of $\varepsilon_{\mathrm{interbead}}$ and $D_{\mathrm{bead}}$ measured, we generate a bed of compressed spheres simulating the macroscopic morphology of the foam. Rays are then generated from random points of the bed with random starting directions. The path of each ray is tracked until it leaves the fictitious slice perpendicular to the starting direction and whose enter face is located on the starting point. This fictitious slice represents the real foam slice. The rays can pass through the slice without being intercepted. They can also undergo one or several scattering or be absorbed into the cellular beads before leaving the slice by the forward or backward faces. The distance traveled by the rays inside the cellular medium before interception, the probability for an intercepted ray to be scattered, and the direction in which the ray is scattered are closely related to $\beta_{\mathrm{cell},\lambda}$, $\omega_{\mathrm{cell},\lambda}$, and $P_{\mathrm{cell},\lambda}(\theta)$, respectively. For each ray, these probabilities are randomly determined using random-generated numbers. For a great number of rays, we can determine the theoretical transmittance and reflectance by simply counting the proportion of rays leaving the slices by the forward or backward faces. The fact that the fictitious slices are randomly chosen permits to obtain average values for the transmittance and reflectance and to homogenize the influence of the macroporosities. Thus, they have the same significance as the averaged values $\mathrm{Tr}_{h,\lambda}$ and $R_{h,\lambda}$ obtained experimentally from numerous measurements at many locations on different slices. The comparisons of experimental (expt) and theoretical (th) results are illustrated in Figs. 8–10.

We can see that the monochromatic hemispherical transmittance and reflectance obtained theoretically accurately match the measurements made on the foam samples. The results also confirm that the radiative behavior calculated assuming that cubic, dodecahedral, or tetrakaidecahedral cellular media are very close to each other. However, one can notice that a dodecahedral or tetrakaidecahedral cellular structure favors the propagation of the radiation in comparison with a cubic structure. As a conclusion, we can affirm that the results of our model are in good agreement with the radiative behavior of the real foams.

## 5 Conclusion

Expanded polystyrene foams are widely used as thermal insulators for building. Owing to their low density, a significant part of the heat may be transferred by thermal radiation even at ambient temperature. An accurate modeling of the interaction of their porous structure with IR radiation is thus of primary importance. However, the previous works on the subject have usually used drastic simplifications for the modeling of the radiative contribution, notably concerning their morphology. Moreover, they generally had recourse to only one radiative parameter to describe the radiation-matter interaction.

In the present paper, we use a new model of prediction of the entire radiative properties of EPS foams. This model takes into account, as faithfully as possible, their real morphology and notably their macroscopic porosity. Thereby, we used a representation of the porous structure, which reproduces their double-scale porosity. Moreover, the cells forming the cellular materials could be tetrakaidecahedral, dodecahedral, or cubic, which allowed us to analyze the influence of the cell shapes on the radiative behavior. Thanks to this model, we managed to grasp the influence of the structural parameters on each radiative property. The foam density and the cell diameter were proved to be the most influent morphological characteristics. As expected, a higher density enhances the radiation-matter interaction, while there exists, for each density, an optimal cell diameter minimizing the propagation of radiation. It also appears that the macroscopic structure of the foam has a

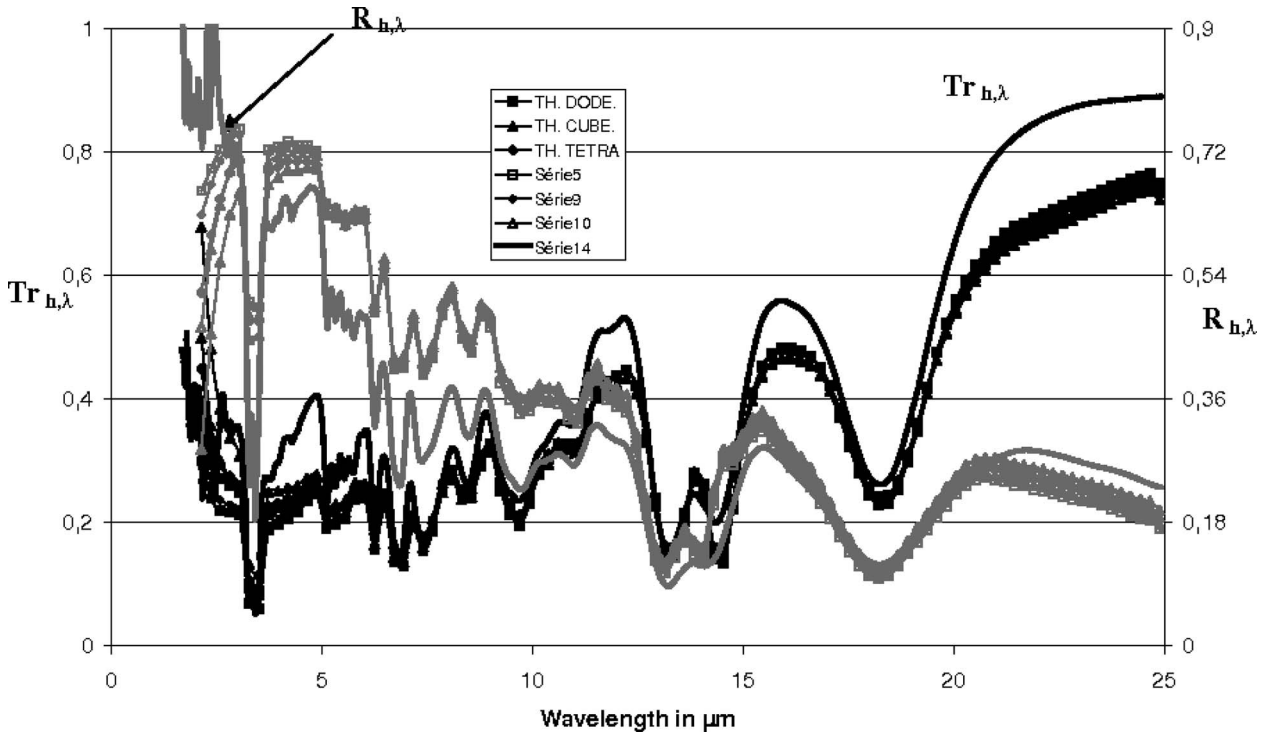


**Fig. 9 Comparison of the experimental and theoretical spectral transmittances and reflectances for sample No. 2 (slice thickness: 3 mm)**

very weak influence on the radiative behavior although the extinction coefficient and the phase function could vary with $D_{bead}$ and $\varepsilon_{interbead}$.

Thereafter, the theoretical monochromatic radiative properties obtained were validated by comparing measured transmittances and reflectances made on different EPS foam slices to predicted values. The agreement proved to be quite good. Additional computations of the reflectances and transmittances when the representation of the macroscopic structure is simplified allowed us to confirm the general trend concerning the negligible influence of the macroscopic parameters.

## Nomenclature

$A$ = absorptivity

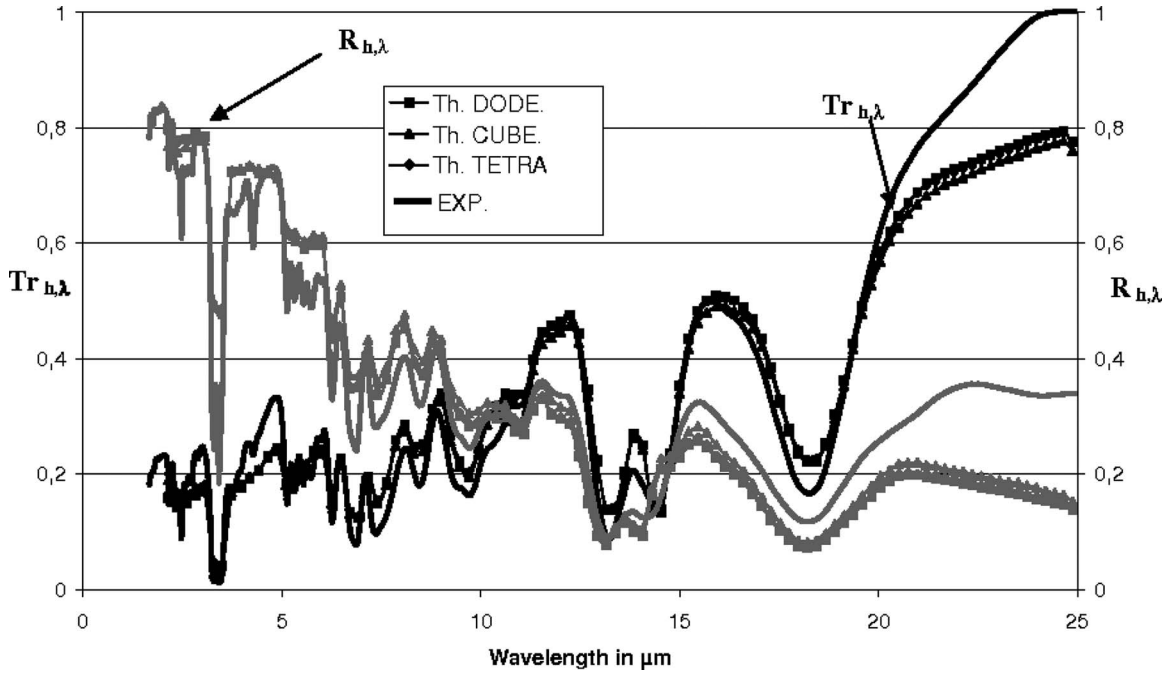


**Fig. 10 Comparison of the experimental and theoretical spectral transmittances and reflectances for sample No. 3 (slice thickness 2.5 mm)**

$C$ = cross section ($m^2$)
$D$ = mean diameter (m)
$d\Omega_{inc}$ = solid angle around incident direction (str)
$g$ = asymmetry parameter of the phase function
$h$ = thickness of the cell windows (m)
$I(T)$ = monochromatic radiation intensity of the blackbody at temperature $T$ ($W/m^2/Str/\mu m$)
$\tilde{n}=n-ik$ = complex refractive index of polystyrene
$N_i$ = number of particle of type $i$ per unit volume ($m^{-3}$)
$P(\mu' \rightarrow \mu)$
$=P(\theta)$ = scattering phase function of the equivalent semitransparent material
$R$ = reflectance
$S$ = surface area ($m^2$)
$t_{win}$ = height (m)
$T$ = temperature (K)
Th = thickness of the slice of foam sample (m)
Tr = transmittance
$V$ = volume ($m^3$)
$w$ = weighting factors of the discretized directions
$x$ = size parameter of the particle

**Greek Symbols**

$\beta$ = global extinction coefficient ($m^{-1}$)
$\beta^*$ = weighted Rosseland extinction coefficient ($m^{-1}$)
$\varepsilon$ = porosity
$\varepsilon_{interbead}$ = interbead porosity due to the macroscopic pores generated during the compression of beads
$\rho$ = density ($kg/m^3$)
$\sigma$ = scattering coefficient ($m^{-1}$)
$\kappa$ = absorption coefficient ($m^{-1}$)
$\Phi(\mu)=\Phi(\theta)$ = scattering phase function of a particle
$\mu$ = cos $\theta$
$\theta$ = angle between the incident and scattering directions (rad)
$\theta_{inc}$ = angle between the incident direction and the normal to the surface (rad)
$\theta_{ref}$ = refraction angle (rad)
$\omega$ = scattering albedo
$\lambda$ = radiation wavelength ($\mu m$)

**Subscripts**

$\parallel$ = parallel polarization
$\perp$ = normal polarization
12 = from Medium 1 to Medium 2
$a$ = absorption
bead = of the beads
cell = of the cellular material contained in the beads
cube, dode, tetra = of the cubic, dodecahedral, or tetrakaidecahedral cells
$e$ = extinction
EPS = of the EPS foam
h = hemispherical
part = of the particle
PS = of the polystyrene polymer
ref = reflected
s = scattered
win = of the cell windows
$\lambda$ = spectral value

## References


[1] Baillis, D., and Sacadura, J. F., 2000, "Thermal Radiation Properties of Dispersed Media: Theoretical Prediction and Experimental Characterization," J. Quant. Spectrosc. Radiat. Transf., **67**, pp. 327–363.
[2] Lee, S. C., 1989, "Effect of Fibre Orientation on Thermal Radiation in Fibrous Media," Int. J. Heat Mass Transfer, **32**(2), pp. 311–319.
[3] Fedorov, A. G., and Viskanta, R., 2000, "Radiation Characteristics of Glass Foams," J. Am. Ceram. Soc., **83**(11), pp. 2769–2776.
[4] Baillis, D., Raynaud, M., and Sacadura, J. F., 2000, "Determination of Spectral Radiative Properties of Open Cell Foam Model Validation," J. Thermophys. Heat Transfer, **14**(2), pp. 137–143.
[5] Kaviany, M., and Singh, B. P., 1992, "Modelling Radiative Transfer in Packed Beds," Int. J. Heat Mass Transfer, **35**(6), pp. 1397–1405.
[6] Glicksman, L., Schuetz, M., and Sinofsky, M., 1987, "Radiation Heat Transfer in Foam Insulation," ASME J. Heat Transfer, **109** pp. 809–812.
[7] Calmidi, V. V., and Mahajan, R. L., 1999, "The Effective Thermal Conductivity of High Porosity Fibrous Metal Foams," ASME J. Heat Transfer, **121**, pp. 466–471.
[8] Kuhn, J., Ebert, H. P., Arduini-Schuster, M. P., Buttner, D., and Fricke, J., 1992, "Thermal Transport in Polystyrene and Polyurethanes Foam Insulations," Int. J. Heat Mass Transfer, **35**(7), pp. 1795–1801.
[9] Placido, E., Arduini-Schuster, M. C., and Kuhn, J., 2005, "Thermal Properties Predictive Model for Insulating Foams," Infrared Phys. Technol., **46**, pp. 219–231.
[10] Coquard, R., and Baillis, D., 2006, "Modeling of Heat Transfer in Low-Density EPS Foams," ASME J. Heat Transfer, **128**(6), pp. 538–549.
[11] Draine, B. T., and Flatau, P. J., 1994, "Discrete Dipole Approximations for Scattering Calculations," J. Opt. Soc. Am. A, **11**, pp. 1491–1499.
[12] Siegel, R., and Howell, J. R., 1992, *Thermal Radiation Heat Transfer*, 3rd ed., Hemisphere, Washington DC.
[13] Coquard, R., and Baillis, D., 2004, "Radiative Characteristics of Beds of Spheres Containing an Absorbing and Scattering Medium," J. Thermophys. Heat Transfer, **18**(2), pp. 178–186.

# Developing Nonthermal-Equilibrium Convection in Porous Media With Negligible Fluid Conduction

**Nihad Dukhan**
Department of Mechanical Engineering,
University of Detroit Mercy,
4001 W. McNichols Road,
Detroit, MI 48221
e-mail: nihad.dukhan@udmercy.edu

*In certain contemporary technologies, porous media with high solid-phase conductivity are impregnated with low-conductivity fluids, e.g., metal and graphite foam cooled by air. For such cases, an approximate analytical model for the developing heat transfer inside a two-dimensional rectangular porous medium subjected to constant heat flux is presented. The model neglects conduction in the fluid and assumes plug flow. The resulting nonthermal-equilibrium equations are solved for the solid and fluid temperatures by separation of variables. The temperatures decay exponentially as the distance from the heated base increases. The effects of the Biot and Peclet numbers are presented. Fully developed heat-transfer conditions are achieved at an axial distance equal to five times the height of the porous medium, with a constant Nusselt number equal to 3.* [DOI: 10.1115/1.2993540]

*Keywords: convection, heat sink, metal foam, graphite foam*

## 1 Introduction

Metal and graphite foams are a relatively new class of porous media characterized by having relatively high solid-phase conductivities. This is especially true if the pores are occupied by a low-conductivity fluid such as air. Simple models for heat transfer in these foams are needed.

The complex internal structure of these foams leads to complex flow fields and heat transfer. Exact solutions of the complete transport equations inside the pores are virtually impossible [1,2]. Bhattacharya et al. [3] experimentally and numerically studied forced convection in high-porosity metal foam using air as the working fluid. In a similar study, Hwang et al. [4] showed that the local Nusselt number increased with increasing Reynolds number.

Kim and Kim [5] solved the governing equations of heat transfer and fluid flow in a microchannel heat sink by treating it as a fluid-saturated porous medium. Lee and Vafai [6] presented an analytical model for the solid and fluid temperatures for Darcian flow in porous media. The wall temperature was obtained as part of the solution. Many researchers invoked the local thermal equilibrium assumption in their studies [7–12]. Kim and Jang [13] investigated the local thermal equilibrium assumption. Kim and Kim [14] discussed the different types of thermal boundary conditions for porous media.

All of the above studies assumed fully developed conditions. The present work provides an approximate engineering model for developing heat transfer in porous media with high solid-phase conductivity cooled by a low-conductivity fluid. The model ignores conduction in the fluid. Such an engineering model may help the design and application communities by saving computational efforts.

Contributed by the Heat Transfer Division of ASME for publication in the JOURNAL OF HEAT TRANSFER. Manuscript received November 2, 2007; final manuscript received July 8, 2008; published online October 16, 2008. Review conducted by Jamal Seyed-Yagoobi.

## 2 Heat Transfer Model

Consider a two-dimensional rectangular block of open-cell porous medium having a constant cross-sectional area that is heated from above with a constant uniform heat flux $q''$. The block has a height $H$ and is bounded by solid surfaces at the top and bottom, as shown in Fig. 1. There is a confined one-dimensional fluid flow in the positive $x$-direction, with an average approach velocity $u_\infty$ and freestream temperature $T_\infty$, that enters the porous medium at $x=0$.

The assumptions are given as follows:

- Radiation is negligible
- Constant thermophysical properties of the solid and fluid
- Isotropic and homogeneous porous medium
- Laminar steady macroscopic plug flow
- Longitudinal conduction terms for solid and fluid are negligible (high Peclet number) [11]. For inclusion of these terms, see Ref. [12].

Applying conservation of energy to the solid and fluid within a control volume inside the porous medium, we obtain

$$k_s \frac{\partial^2 T_s}{\partial y^2} - h\sigma(T_s - T_f) = 0 \tag{1}$$

$$k_f \frac{\partial^2 T_f}{\partial y^2} + h\sigma(T_s - T_f) = \rho c u \frac{\partial T_f}{\partial x} \tag{2}$$

where $k_s$ and $k_f$ are the effective thermal conductivities, $T_s$ and $T_f$ are the volume-averaged temperatures of the solid and fluid, respectively, $h$ is the heat-transfer coefficient between the solid and fluid, $\sigma$ is the surface area per unit volume, $\rho$ is the density, $c$ is the heat capacity, and $u$ is the volume-averaged velocity of the cooling fluid. These equations have been used extensively [3,5,6,11,15–20]. Sometimes thermal dispersion is included in the fluid's energy equation [3,14,15,21]. However, due to the assumed dominance of solid conduction in the present model, dispersion is neglected [3].

For air cooling of metals and graphite foam, the transverse conduction term in the fluid is a few orders of magnitude smaller than the convection and bulk flow terms in Eq. (2). Eliminating fluid conduction, solving Eq. (2) for the solid temperature, substituting in Eq. (1), and casting the resulting equation in a nondimensional form, we obtain

$$\frac{\partial^2}{\partial Y^2}\left(a\frac{\partial \theta_f}{\partial X} + \theta_f\right) - \mathrm{Pe}\frac{\partial \theta_f}{\partial X} = 0 \tag{3}$$

$$\text{at} \quad Y = 0 \quad \frac{\partial \theta_f}{\partial Y} = 0 \tag{4}$$

$$\text{at} \quad Y = 1 \quad \frac{\partial \theta_f}{\partial Y} = 1 \tag{5}$$

$$\text{at} \quad X = 0 \quad \theta_f = 0 \tag{6}$$

where $X=x/H$, $Y=y/H$, $\theta_f=(T_f-T_\infty)/q''H/k_s$, $a=\rho c u_D/h\sigma H$, and $\mathrm{Pe}=\rho c u_D H/k_s$. To get an engineering first estimate, we used a plug-flow approximation [2,4], so the volume-averaged pore velocity $u$ is replaced by the Darcian velocity $u_D$, which is defined by $u_D=u_\infty/\varepsilon$, where $\varepsilon$ is the porosity. $a$ is a nondimensional number that represents the ratio of the rate of heat gained by the fluid to the heat transfer by convection per unit area per degree, while Pe is the Peclet number. The ratio $\mathrm{Pe}/a=h\sigma H^2/k_s \equiv \mathrm{Bi}$ represents the Biot number of the porous medium. Boundary condition (5) is the continuity of the heat flux at the interface. $\partial\theta_f/\partial X$ is not constant for developing heat transfer.

  

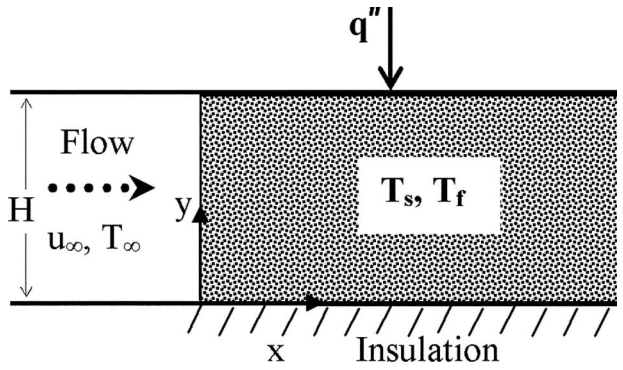


**Fig. 1 Schematic of the heat-transfer problem**

Using separation of variables (see, for example, Ref. [22]) and assuming a solution of the form $\theta_f(X,Y)=f(X)+g(y)+w(X,Y)$, one obtains

$$\theta_f(X,Y)=\frac{X}{\mathrm{Pe}}+\frac{Y^2}{2}-\frac{1}{6}-2\sum_{n=1}^{\infty}\frac{(-1)^n}{(n\pi)^2}\cos(n\pi Y)\exp\left(\frac{-(n\pi)^2}{\mathrm{Pe}\left(\frac{(n\pi)^2}{\mathrm{Bi}}+1\right)}X\right) \quad (7)$$

This series converges quickly as $1/n^2$, and we only need to consider the first five to ten terms. The nondimensional form of the solid temperature follows as

$$\theta_s(X,Y)=\frac{X}{\mathrm{Pe}}+\frac{Y^2}{2}+\frac{1}{\mathrm{Bi}}-\frac{1}{6}-2\sum_{n=1}^{\infty}\frac{(-1)^n}{(n\pi)^2\left(\frac{(n\pi)^2}{\mathrm{Bi}}+1\right)}\times\cos(n\pi Y)\exp\left(\frac{-(n\pi)^2}{\mathrm{Pe}\left(\frac{(n\pi)^2}{\mathrm{Bi}}+1\right)}X\right) \quad (8)$$

where $\theta_s=(T_s-T_\infty)/q''H/k_s$. The maximum fluid and solid temperatures are obtained by setting $Y=1$ in Eqs. (7) and (8), respectively, while the solid-fluid temperature difference is obtained by subtracting Eq. (7) from Eq. (8).

## 3 Results and Discussion

The fluid temperature inside the porous medium at different axial distances and two values of Bi is presented. Figure 2(*a*) is for Bi=0.1, which means that the conduction resistance is 0.1 of the convection resistance, i.e., very low convection. For this case, the fluid temperature reaches higher values. As the Bi increases, the fluid temperature decreases, as seen in Fig. 2(*b*). Similar trends were observed in Ref. [6].

The mean fluid temperature $\theta_{fm}$ can be obtained by integrating the fluid temperature over the cross section:

$$\theta_{fm}(X)=\int_0^1\theta_f(X,Y)dY=\frac{X}{\mathrm{Pe}} \quad (9)$$

The Nusselt number is

$$\mathrm{Nu}(X)=\frac{Hq''/k_s}{T_{fH}-T_{fm}}=\frac{1}{\theta_{fH}-\theta_{fm}}=\left[\frac{1}{3}-2\sum_{n=1}^{\infty}\frac{1}{(n\pi)^2}\exp\left(\frac{-(n\pi)^2}{\mathrm{Pe}\left(\frac{(n\pi)^2}{\mathrm{Bi}}+1\right)}X\right)\right]^{-1} \quad (10)$$

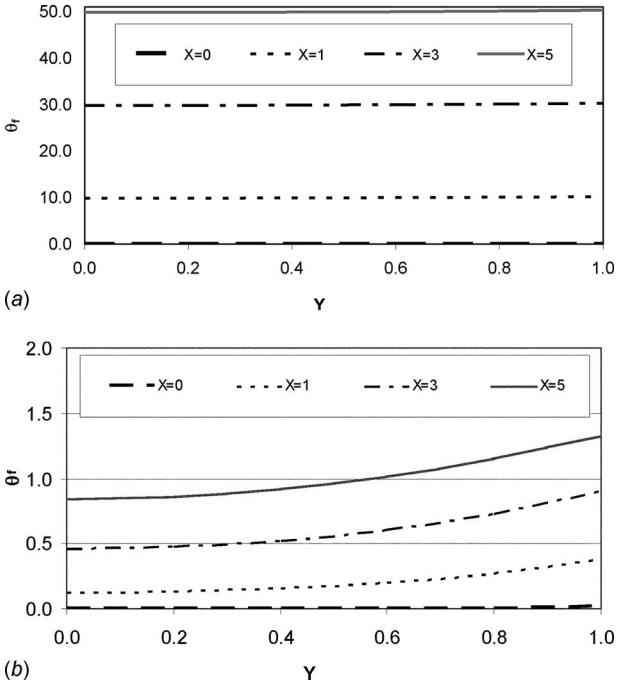


**Fig. 2 Fluid temperature: (*a*) Bi=0.1 and (*b*) Bi=5**

Figure 3 is a plot of Nu as a function of $X$ for Bi=15 and Pe=7.5. It is clear that Nu approaches an asymptotic value of 3 at $X=5$. This is the axial distance for which the heat transfer is considered fully developed. The general trend in Fig. 3 is in agreement with Refs. [12,17]. The fully developed value of Nu was 2.873 in Ref. [12]. The difference is due to the fact that Ref. [12] used the thermal-local-equilibrium assumption and included axial conduction in the governing equations. Figure 4 is a plot of the Nu as a function of Pe at a fixed location $X=1$ and for Bi=15. The Nusselt number is seen to increase with increasing Pe, which is expected, and is in agreement with the data reported in Refs. [4,6,7,13,17].

## 4 Conclusion

Nonthermal-equilibrium convection heat-transfer analysis in the developing region of a two-dimensional porous media channel having low effective fluid conductivity compared with effective solid conductivity was presented. The two-equation model was simplified by neglecting the fluid's longitudinal conduction, which overcame the coupling of the governing equations. Assuming plug flow and using separation of variables, the temperature profiles of

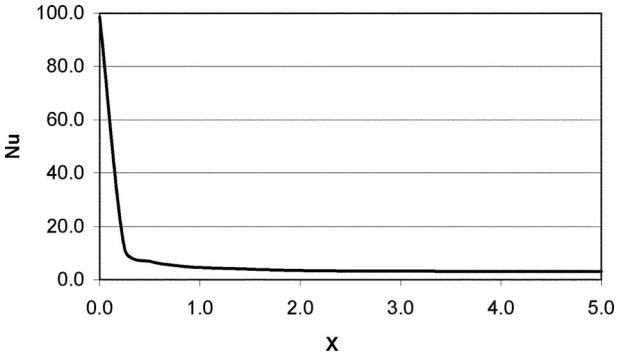


**Fig. 3 Local Nusselt number as a function of axial location for Bi=15 and Pe=7.5**

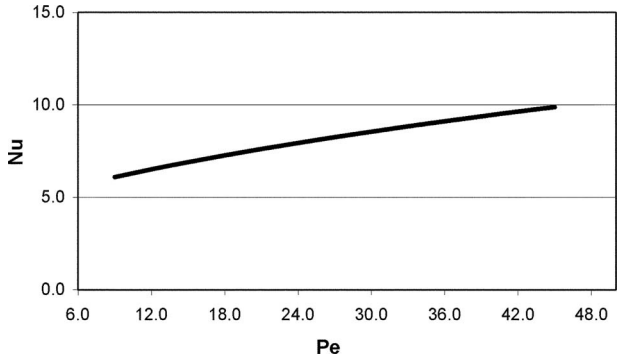


**Fig. 4 Local Nusselt number as a function of Peclet number for Bi=15 at $X=1$**

the fluid and solid as functions of axial and transverse distances were obtained. The behavior of the Nusselt number as a function of Bio and Peclet numbers was presented. The solution was in qualitative agreement with previous more complex analytical and numerical solutions.

## Nomenclature

$a$ = dimensionless parameter $=\rho c u_D / h\sigma H$
Bi = porous media Biot number $=h\sigma H^2/k_s$
$c$ = heat capacity of fluid
$h$ = heat-transfer coefficient
$H$ = height of porous medium
$k$ = effective thermal conductivity
Nu = local Nusselt number $=Hq''/k_s/T_{fH}-T_{fm}$
Pe = Peclet number $=\rho c u_D H/k_s$
$q''$ = heat flux
$T$ = temperature
$u$ = volume-averaged pore velocity
$u_D$ = Darcian velocity
$u_\infty$ = average flow velocity entering porous medium
$x$ = axial coordinate
$X$ = dimensionless axial coordinate
$y$ = transverse coordinate
$Y$ = dimensionless transverse coordinate

### Greek

$\varepsilon$ = porosity
$\theta$ = dimensionless temperature
$\rho$ = density of fluid
$\sigma$ = surface area per unit volume

### Subscripts

$f$ = fluid
$H$ = heated wall
$s$ = solid
$\infty$ = ambient

## References


[1] Vafai, K., and Tien, C. L., 1982, "Boundary and Inertia Effects on Convective Mass Transfer in Porous Media," Int. J. Heat Mass Transfer, **25**(8), pp. 1183–1190.
[2] Hunt, M. L., and Tien, C. L., 1988, "Effect of Thermal Dispersion on Forced Convection in Fibrous Media," Int. J. Heat Mass Transfer, **31**(2), pp. 301–309.
[3] Bhattacharya, A., Calmidi, V. V., and Mahajan, R. L., 2002, "Thermophysical Properties of High Porosity Metal Foams," Int. J. Heat Mass Transfer, **45**, pp. 1017–1031.
[4] Hwang, J. J., Hwang, G. J., Yeh, R. H., and Chao, C. H., 2002, "Measurement of the Interstitial Convection Heat Transfer and Frictional Drag for Flow Across Metal Foam," ASME J. Heat Transfer, **124**, pp. 120–129.
[5] Kim, S. J., and Kim, D., 1999, "Forced Convection in Microstructures for Electronic Equipment Cooling," ASME J. Heat Transfer, **121**, pp. 639–645.
[6] Lee, D. Y., and Vafai, K., 1999, "Analytical Characterization and Conceptual Assessment of Solid and Fluid Temperature Differentials in Porous Media," Int. J. Heat Mass Transfer, **42**, pp. 423–435.
[7] Angirasa, D., 2002, "Forced Convective Heat Transfer in Metallic Fibrous Materials," ASME J. Heat Transfer, **124**, pp. 739–745.
[8] Poulikakos, D., and Renken, K., 1987, "Forced Convection in a Channel Filled With Porous Medium, Including the Effect of Flow Inertia, Variable Porosity and Brinkman Friction," ASME J. Heat Transfer, **109**, pp. 880–888.
[9] Vafai, K., and Kim, S. J., 1989, "Forced Convection in a Channel Filled With a Porous Medium: An Exact Solution," ASME J. Heat Transfer, **111**, pp. 1103–1106.
[10] Haji-Sheikh, A., and Vafai, K., 2004, "Analysis of Flow and Heat Transfer in Porous Media Imbedded Inside Various-Shaped Ducts," Int. J. Heat Mass Transfer, **47**, pp. 1889–1905.
[11] Narasimhan, A., Lage, J., and Nield, D. A., 2001, "New Theory for Forced Convection Through Porous Media by Fluids With Temperature-Dependent Viscosity," ASME J. Heat Transfer, **123**, pp. 1045–1051.
[12] Minkowycz, W. J., and Haji-Sheikh, A., 2006, "Heat Transfer in Parallel Plates and Circular Porous Passages With Axial Conduction," Int. J. Heat Mass Transfer, **49**(13-14), pp. 2381–2390.
[13] Kim, S. J., and Jang, S. P., 2002, "Effects of the Darcy Number, the Prandtl Number and the Reynolds Number on the Local Thermal Non-Equilibrium," Int. J. Heat Mass Transfer, **45**, pp. 3885–3896.
[14] Kim, S. J., and Kim, D., 2001, "The Thermal Interaction at the Interface Between a Porous Medium and an Impermeable Wall," ASME J. Heat Transfer, **123**, pp. 527–533.
[15] Krishnan, S., Murthy, J. Y., and Garimella, S. V., 2004, "A Two-Temperature Model for the Analysis of Passive Thermal Control System," ASME J. Heat Transfer, **126**, pp. 628–637.
[16] Amiri, A., and Vafai, K., 1994, "Analysis of Dispersion Effects and Non-Thermal Equilibrium, Non-Darcian, Variable Porosity Incompressible Flow Through Porous Media," Int. J. Heat Mass Transfer, **37**(6), pp. 939–954.
[17] Hwang, G. J., and Chao, C. H., 1994, "Heat Transfer Measurement and Analysis for Sintered Porous Channels," ASME J. Heat Transfer, **116**, pp. 456–464.
[18] Amiri, A., Vafai, K., and Kuzay, T. M., 1995, "Effects of Boundary Conditions on Non-Darcian Heat Transfer Through Porous Media and Experimental Comparisons," Numer. Heat Transfer, Part A, **27**, pp. 651–664.
[19] Alazmi, B., and Vafai, K., 2002, "Constant Wall Heat Flux Boundary Conditions in Porous Media Under Local Thermal Non-Equilibrium Conditions," Int. J. Heat Mass Transfer, **45**, pp. 3071–3087.
[20] Quintard, M., Kaviany, M., and Whitaker, S., 1997, "Two-Medium Treatment of Heat Transfer in Porous Media: Numerical Results for Effectvive Properties," Adv. Water Resour., **20**(2-3), pp. 77–94.
[21] Deleglise, M., Simacek, P., Binetruy, C., and Advani, S., 2003, "Determination of the Thermal Dispersion Coefficient During Radial Filling of a Porous Medium," ASME J. Heat Transfer, **125**, pp. 875–880.
[22] Myers, G. E., 1998, *Analytical Methods in Conduction Heat Transfer*, 2nd ed., AMCHT, Madison, WI, Chap. 3.

# Mixed Convection in a Vertical Microannulus Between Two Concentric Microtubes

**Mete Avcı**

**Orhan Aydın**[1]
e-mail: oaydin@ktu.edu.tr

Department of Mechanical Engineering,
Karadeniz Technical University,
61080 Trabzon, Turkey

*In this study, fully developed mixed convective heat transfer of a Newtonian fluid in a vertical microannulus between two concentric microtubes is analytically investigated by taking the velocity slip and the temperature jump at the wall into account. The effects of the mixed convection parameter Gr/Re, the Knudsen number Kn, and the aspect ratio r* on the microchannel hydrodynamic and thermal behaviors are determined. Finally, a Nu $=f(Gr/Re, Kn, r^*)$ expression is developed. It is disclosed that increasing Gr/Re enhances heat transfer while rarefaction effects considered by the velocity slip and the temperature jump in the slip flow regime decreases it.* [DOI: 10.1115/1.2977552]

*Keywords: microfluidics, vertical microannulus, mixed convection, temperature jump, velocity slip*

## 1 Introduction

Understanding the microscale heat and fluid flow phenomena is very important for design and optimization of microdevices in microelectromechanical systems (MEMS) and biomedical applications such as drug delivery, DNA sequencing, and bio-MEMS.

When compared to an abundant volume of forced convection studies in microscale [1–5], studies on free or mixed convection are much less. In a recent study, Chen and Weng [6] analytically studied the fully developed natural convection in an open-ended vertical parallel plate microchannel with asymmetric wall temperatures. The effects of rarefaction and fluid-wall interaction were shown to increase the volume flow and to decrease the heat transfer rate. In a following article, Chen and Weng [7] numerically studied the creep effect on the flow and heat transfer characteristics for developing natural convective microflow in the same geometry. Khadrawi et al. [8,9] analytically investigated the transient hydrodynamics and thermal behaviors of fluid flow in an open-ended vertical parallel-plate microchannel under the effect of the hyperbolic and dual-phase-lag heat conduction model.

Haddad et al. [10] numerically investigated the developing hydrodynamical behaviors of free convection gas flow in a vertical open-ended parallel-plate microchannel filled with porous media. Recently, Aydin and Avci [11,12] analytically investigated mixed convection of rarefied gas in a vertical asymmetrically heated microchannel between two parallel plates for the isothermal [11] and isoflux [12] thermal conditions at walls.

The present study is aimed at theoretically investigating mixed convection flow of a rarefied gas in a vertical concentric annular microduct representing a microheat exchanger for the hydrodynamically and thermally fully developed case. The effects of the mixed convection parameter Gr/Re, the Knudsen number Kn, and the aspect ratio of the annular geometry on the temperature profile and subsequently on the Nusselt number are determined.

## 2 Analysis

Let's consider internal mixed convection in a vertical microannulus between two concentric isothermal microtubes shown in Fig. 1. The flow is assumed to be fully developed both hydrodynamically and thermally. Steady laminar flow having constant properties is considered. The axial heat conduction in the fluid and in the wall is assumed to be negligible. The viscous dissipation and compressibility effects in the fluid and radiation effects are neglected.

In the slip flow regime (Kn=0.001–0.1) of microscale flow, it is usual to couple the continuum approach with the two main characteristics of the microscale phenomena, the velocity slip, and the temperature jump because the gas no longer reaches the velocity or the temperature of the surface. Velocity slip is defined as [13]

$$u_s = -\frac{2-F_v}{F_v}\lambda \left.\frac{\partial u}{\partial r}\right|_{r=r_2} \tag{1}$$

where $u_s$ is the slip velocity, $\lambda(=\mathrm{Kn}D_h)$ is the molecular mean free path, and $F_v$ is the tangential momentum accommodation coefficient, and the temperature jump is defined as [13]

$$T_s - T_w = -\frac{2-F_t}{F_t}\frac{2\gamma}{\gamma+1}\frac{\lambda}{\mathrm{Pr}}\left.\frac{\partial T}{\partial r}\right|_{r=r_2} \tag{2}$$

where $T_s$ is the temperature of the gas at the wall, $T_w$ is the wall temperature, and $F_t$ is the thermal accommodation coefficient, which depends on the gas and surface materials. Particularly for air, it assumes typical values near unity [13]. For the rest of the analysis, $F_v$ and $F_t$ will be assumed to be 1.

In a sufficiently long channel, the velocity and the temperature profiles will cease to change with distance along the channel, i.e., a fully developed flow will exist [14].

The Boussinesq approximation, the equations governing the present flow can be written as follows:

$$0 = -\frac{dp}{dz} + \frac{\mu}{r}\frac{d}{dr}\left(r\frac{du}{dr}\right) + \beta g \rho_0 (T - T_0) \tag{3}$$

$$0 = \frac{d}{dr}\left(r\frac{dT}{dr}\right) \tag{4}$$

where $\beta$ is the thermal expansion coefficient, $\rho_0$ is the mass density at temperature $T_0$, and $T_0$ is the reference fluid temperature, which ensures a linear relation between the local mass density and the local temperature.

$$\rho = \rho_0[1 - \beta(T - T_0)]$$

As is suggested in Ref. [15], the reference temperature is chosen as the mean fluid temperature in any cross section of the duct, i.e.,

$$T_0 = \frac{2}{r_2^2 - r_1^2}\int_{r_1}^{r_2} Tr dr \tag{5}$$

The boundary conditions are as follows:

$$u = u_{s_1} \quad \text{at } r = r_1$$

$$u = u_{s_2} \quad \text{at } r = r_2$$

$$T = T_{s_1} \quad \text{at } r = r_1$$

$$T = T_{s_2} \quad \text{at } r = r_2 \tag{6}$$

By introducing the following nondimensional quantities

[1]Corresponding author.

Contributed by the Heat Transfer Division of ASME for publication in the JOURNAL OF HEAT TRANSFER. Manuscript received February 4, 2008; final manuscript received April 22, 2008; published online October 17, 2008. Review conducted by Sung Jin Kim.

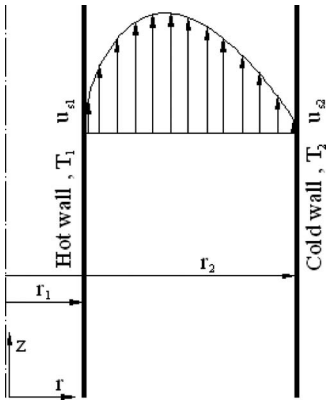


**Fig. 1 Schematic of the flow domain**

$$R = \frac{r}{r_2}, \quad r^* = \frac{r_1}{r_2}, \quad Z = \frac{z}{\mathrm{Re}\, D_h}, \quad \theta = \frac{T - T_0}{T_1 - T_2}$$

$$U = \frac{u}{u_m}, \quad \mathrm{Kn} = \frac{\lambda}{D_h}$$

$$\beta_v = \frac{2 - F_v}{F_v}, \quad \beta_t = \frac{2 - F_t}{F_t}\frac{2\gamma}{\gamma + 1}\frac{1}{\mathrm{Pr}}$$

$$P = \frac{p}{\rho_0 u_m^2}, \quad \mathrm{Gr} = \frac{g\beta\rho_0^2(T_1 - T_2)D_h^3}{\mu^2}$$

$$\mathrm{Re} = \frac{\rho_0 u_m D_h}{\mu}, \quad w = \frac{T_1 - T_0}{T_1 - T_2} \tag{7}$$

Eqs. (3) and (4) can be written as

$$0 = -\frac{dP}{dZ} + (2(1 - r^*))^2 \frac{1}{R}\frac{d}{dR}\left(R\frac{dU}{dR}\right) + \frac{\mathrm{Gr}}{\mathrm{Re}}\theta \tag{8}$$

$$0 = \frac{d}{dR}\left(R\frac{d\theta}{dR}\right) \tag{9}$$

In terms of the dimensionless variables introduced in Eq. (7), the boundary conditions given in Eq. (6) can be shown as

$$U = 2\beta_v \mathrm{Kn}(1 - r^*)\frac{dU}{dR} \quad \text{at } R = r^*$$

$$U = -2\beta_v \mathrm{Kn}(1 - r^*)\frac{dU}{dR} \quad \text{at } R = 1$$

$$\theta = \frac{T_{s1} - T_0}{T_1 - T_2} = w + 2\beta_T \mathrm{Kn}(1 - r^*)\frac{d\theta}{dR} \quad \text{at } R = r^*$$

$$\theta = \frac{T_{s2} - T_0}{T_2 - T_0} = w - 1 - 2\beta_T \mathrm{Kn}(1 - r^*)\frac{d\theta}{dR} \quad \text{at } R = 1 \tag{10}$$

From Eqs. (5) and (7), one can obtain the following constraint on $\theta$:

$$\int_{r^*}^{1} \theta R dR = 0 \tag{11}$$

Equation (9) indicates that the dimensionless temperature varies logarithmically across the duct. Integrating Eq. (9) and applying the boundary conditions given in Eq. (10) with Eq. (11) give

$$\theta = C_0 + C_1 \ln R \tag{12}$$

where $C_0$ and $C_1$ are

$$C_0 = C_1\left(\frac{1}{2} + \frac{r^{*2}\ln r^*}{1 - r^{*2}}\right), \quad C_1 = \frac{1}{\ln r^* - 2\beta_T \mathrm{Kn}(1 - r^*)(1 + 1/r^*)}$$

$$w = 1 + C_1\left(\frac{1}{2} + \frac{r^{*2}\ln r^*}{1 - r^{*2}} + 2\beta_T \mathrm{Kn}(1 - r^*)\right) \tag{13}$$

For the macroscale case (Kn=0), the dimensionless temperature distribution obtained above is the same as that given by Zanchini [16].

$$\theta = \frac{\ln R}{\ln r^*} + \frac{r^{*2}}{1 - r^{*2}} + \frac{1}{2\ln r^*} \tag{14}$$

Substituting Eq. (12) into the momentum equation, Eq. (8) gives

$$0 = -\frac{dP}{dZ} + (2(1 - r^*))^2 \frac{1}{R}\frac{d}{dR}\left(R\frac{dU}{dR}\right) + \frac{\mathrm{Gr}}{\mathrm{Re}}(C_0 + C_1 \ln R) \tag{15}$$

Rearranging the momentum equation then gives

$$\frac{1}{R}\frac{d}{dR}\left(R\frac{dU}{dR}\right) = C_2 - C_3(C_0 + C_1 \ln R) \tag{16}$$

where $C_2$ and $C_3$ are

$$C_2 = \frac{1}{(2(1 - r^*))^2}\frac{dP}{dZ}, \quad C_3 = \frac{1}{(2(1 - r^*))^2}\frac{\mathrm{Gr}}{\mathrm{Re}} \tag{17}$$

Integrating this equation twice then gives

$$U = \frac{C_2}{4}R^2 - \frac{C_3}{4}((C_0 - C_1)R^2 + C_1 R^2 \ln R) + C_4 \ln R + C_5 \tag{18}$$

At any cross section in the channel, the dimensionless mean velocity $U_m$ can be written as

$$U_m = \frac{\int_{r^*}^{1} URdR}{\int_{r^*}^{1} RdR} = 1 \tag{19}$$

By applying the boundary conditions given in Eq. (10) and using Eq. (19), the three unknown constants $C_2$, $C_4$, and $C_5$ can be obtained analytically. Because of their complex structures, the expressions of these constants are not given here.

The dimensionless bulk temperature can be defined as

$$\theta_b = \frac{T_b - T_0}{T_1 - T_2} = \frac{\int_{r^*}^{1} U\theta R dR}{\int_{r^*}^{1} UR dR} \tag{20}$$

Using Eq. (12), the convective heat transfer coefficient at the inner wall can be obtained as follows:

$$h = \frac{-k\left.\frac{dT}{dr}\right|_{r=r_1}}{T_1 - T_b} = \frac{kC_1}{r_1}\frac{1}{\theta_b - w} = \frac{kC_1}{r_2 r^*}\frac{1}{\theta_b - w} \tag{21}$$

Similarly, the Nusselt number at the inner wall can be written as

$$\mathrm{Nu} = \frac{2C_1(1/r^* - 1)}{\theta_b - w} \tag{22}$$

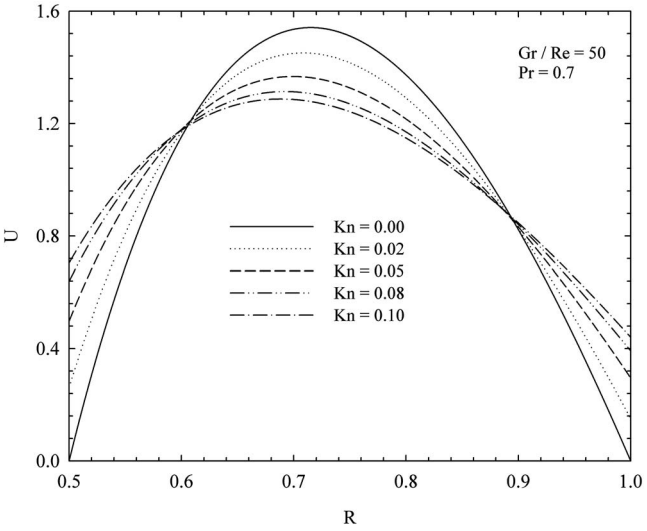


**Fig. 2 Dimensionless velocity distribution at different values of Kn for Gr/Re=50**

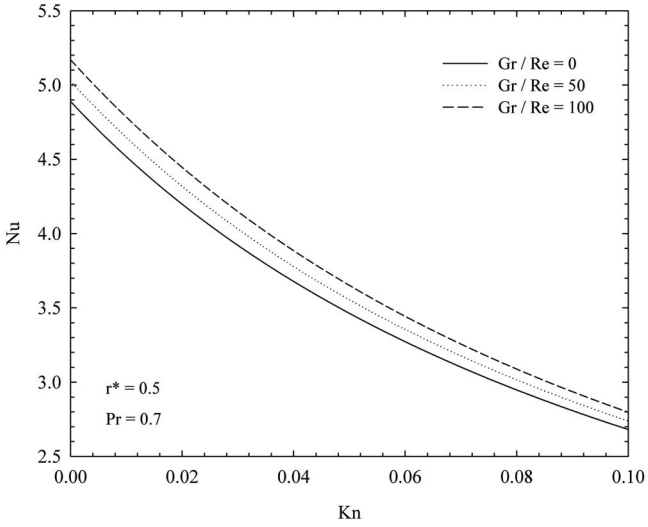


**Fig. 4 The variation of the Nu with Kn at different values of Gr/Re=50 for $r^*$=0.5**

## 3 Results and Discussion

In this study, the interactive effects of the mixed convection parameter Gr/Re the Knudsen number Kn, and the aspect ratio $r^*$ on heat and fluid flow in a microannulus between two vertical concentric microtubes are investigated for both hydrodynamically and thermally fully developed case. Kn values in the range of $0 \leqslant \mathrm{Kn} \leqslant 0.1$ were considered. The following values of the mixed convection parameter are covered: Gr/Re=0, 50, and 100.

For a constant value of Gr/Re(=50), the influence of the Knudsen number Kn on the velocity and temperature profiles are illustrated in Figs. 2 and 3, respectively. It can be seen that increasing Kn increases velocity slips at the walls. With an increase in Kn, the maximum velocity decreases and its position shifts towards the inner hot wall since the slip effect is higher at the hot inner wall than that at the cold outer wall. The influence of Kn is to decrease temperature gradients at the walls, as seen from Fig. 3.

Finally, the variation of Nu with Kn is plotted in Fig. 4. As seen, increasing Kn decreases Nu as a result of decreased temperature gradient at the hot inner wall due to the velocity slip and the temperature jump. Figure 5 gives Nu variation with $r^*$ for various values of Kn.

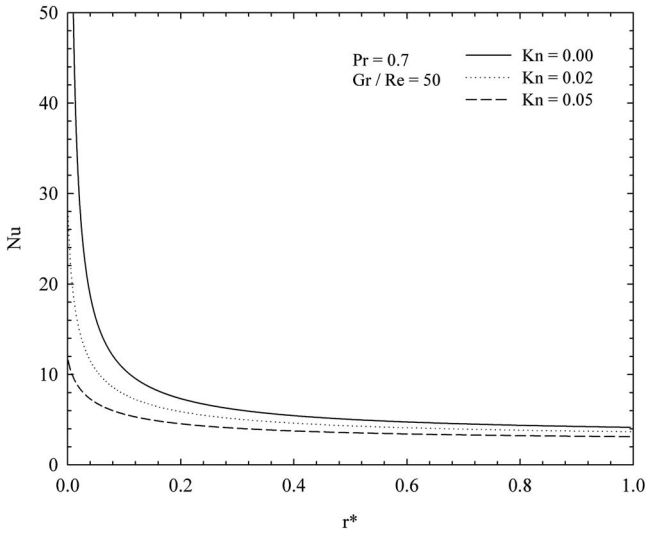


**Fig. 5 The variation of the Nu with $r^*$ at different values of Kn for Gr/Re=50**

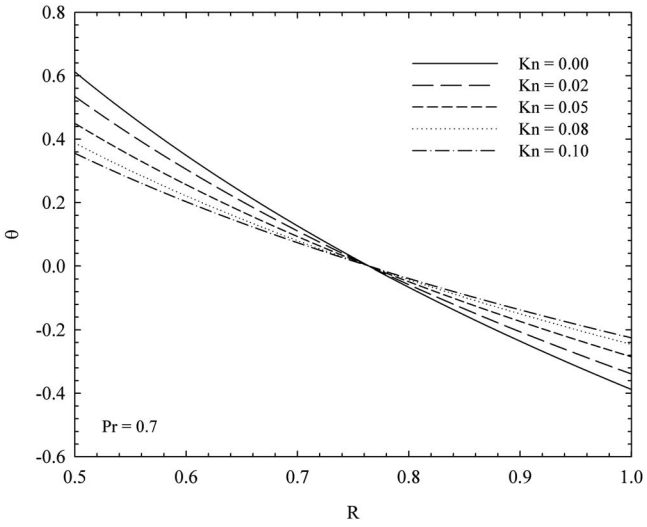


**Fig. 3 Dimensionless temperature distribution at different values of Kn**


## Acknowledgment

The authors greatly acknowledge the financial support of this work by the Scientific and Technological Research Council of Turkey (TUBITAK) under Grant No. 104M436.


## Nomenclature

$c_p$ = specific heat at constant pressure
$D_h$ = hydraulic diameter, $2(r_2-r_1)$
$F$ = tangential momentum accommodation coefficient
$F_t$ = thermal accommodation coefficient
$g$ = gravitational acceleration
Gr = Grashof number, $g\beta\rho_0^2(T_1-T_2)D_h^3/\mu^2$
$h$ = convective heat transfer coefficient
$k$ = thermal conductivity

Kn = Knudsen number, $\lambda/D_h$
Nu = Nusselt number
$p$ = pressure difference, $p'-p''$
$p'$ = static pressure
$p''$ = hydrostatic pressure
Pr = Prandtl number
Re = Reynolds number, $u_m D_h/\upsilon$
$r^*$ = ratio of radiuses$=r_1/r_2$
$r_1$ = inner radius
$r_2$ = outer radius
$w$ = ratio of wall temperature differences, Eq. (7)
$T$ = temperature
$u$ = axial velocity
$U$ = dimensionless axial velocity
$z,r$ = axial and radial coordinate
$Z,R$ = dimensionless axial and radial coordinate

**Greek Symbols**

$\alpha$ = thermal diffusivity
$\beta$ = thermal expansion coefficient
$\beta_\upsilon,\beta_t$ = dimensionless variables, Eq. (7)
$\gamma$ = specific heat ratio
$\lambda$ = molecular mean free path
$\mu$ = dynamic viscosity
$\rho$ = density
$\upsilon$ = kinematic viscosity
$\theta$ = dimensionless temperature, Eq. (7)

**Subscripts**

1 = value on inner wall (i.e., at $r=r_1$)
2 = value on outer wall (i.e., at $r=r_2$)
$b$ = bulk value
$m$ = mean value
$s$ = fluid properties on wall
$s_1$ = fluid properties on inner wall
$s_2$ = fluid properties on outer wall
$w$ = wall

## References


[1] Aydın, O., and Avcı, M., 2006, "Heat and Fluid Flow Characteristics of Gases in Micropipes," Int. J. Heat Mass Transfer, **49**, pp. 1723–1730.
[2] Aydın, O., and Avcı, M., 2006, "Analsysis of Micro-Graetz Problem in a Microtube," Nanoscale Microscale Thermophys. Eng., **10**(4), pp. 345–358.
[3] Aydın, O., and Avcı, M., 2006, "Thermally Developing Flow in Microchannels," J. Thermophys. Heat Transfer, **20**(3), pp. 628–631.
[4] Aydın, O., and Avcı, M., 2007, "Analysis of Laminar Heat Transfer in Micro-Poiseuille Flow," Int. J. Therm. Sci., **46**(1), pp. 30–37.
[5] Avcı, M., and Aydın, O., 2008, "Laminar Forced Convection Slip-Flow in a Micro-Annulus Between Two Concentric Cylinders," Int. J. Heat Mass Transfer, **51**(13-14), pp. 3460–3467.
[6] Chen, C. K., and Weng, H. C., 2005, "Natural Convection in a Vertical Microchannel," ASME J. Heat Transfer, **127**, pp. 1053–1056.
[7] Chen, C. K., and Weng, H. C., 2006, "Developing Natural Convection With Thermal Creep in a Vertical Microchannel," J. Phys. D: Appl. Phys., **39**, pp. 3107–3118.
[8] Khadrawi, A. F., Othman, A., and Al-Nimr, M. A., 2005, "Transient Free Convection Fluid Flow in a Vertical Microchannel as Described by the Hyperbolic Heat Conduction Model," Int. J. Thermophys., **26**(3), pp. 905–918.
[9] Khadrawi, A. F., and Al-Nimr, M. A., 2007, "Unsteady Natural Convection Fluid Flow I a Vertical Microchannel Under the Effect of the Dual-Phase-Lag Heat Conduction Model," Int. J. Thermophys., **28**(4), pp. 1387–1400.
[10] Haddad, O. M., Abuzaid, M. M., and Al-Nimr, M. A., 2005, "Developing Free-Convection Gas Flow in a Vertical Open-Ended Microchannel Filled With Porous Media," Numer. Heat Transfer, Part A, **48**, pp. 693–710.
[11] Avcı, M., and Aydın, O., 2007, "Mixed Convection in a Vertical Parallel Plate Microchannel," ASME J. Heat Transfer, **129**(2), pp. 162–166.
[12] Avcı, M., and Aydın, O., 2007, "Mixed Convection in a Vertical Parallel Plate Microchannel With Asymmetric Wall Heat Fluxes," ASME J. Heat Transfer, **129**(8), pp. 1091–1095.
[13] Ameel, T. A., Wang, X. M., Baron, R. F., and Warrington, R. O., 1997, "Laminar Forced Convection in a Circular Tube With Constant Heat Flux and Slip Flow," Microscale Thermophys. Eng., **1**(4), pp. 303–320.
[14] Aung, W., and Worku, G., 1986, "Theory of Fully Developed, Combined Convection Including Flow Reversal," ASME J. Heat Transfer, **108**, pp. 485–488.
[15] Barletta, A., and Zanchini, E., 1999, "On the Choice of the Reference Temperature for Fully Developed Mixed Convection in a Vertical Channel," Int. J. Heat Mass Transfer, **42**, pp. 3169–3181.
[16] Zanchini, E., 2008, "Mixed Convection With Variable Viscosity in a Vertical Annulus With Uniform Wall Temperatures," Int. J. Heat Mass Transfer, **51**(1–2), pp. 30–40.

# Analytical Solution of Nonequilibrium Heat Conduction in Porous Medium Incorporating a Variable Porosity Model With Heat Generation

**M. Nazari**
e-mail: mnazari@alum.sharif.edu

**F. Kowsary**
e-mail: fkowsari@ut.ac.ir

School of Mechanical Engineering,
Tehran University,
P.O. Box 14395-515,
Tehran, Iran

*This paper is concerned with the conduction heat transfer between two parallel plates filled with a porous medium with uniform heat generation under a nonequilibrium condition. Analytical solution is obtained for both fluid and solid temperature fields at constant porosity incorporating the effects of thermal conductivity ratio, porosity, and a nondimensional heat transfer coefficient at pore level. The two coupled energy equations for the case of variable porosity condition are transformed into a third order ordinary equation for each phase, which is solved numerically. This transformation is a valuable solution for heat conduction regime for any distribution of porosity in the channel. The effects of the variable porosity on temperature distribution are shown and compared with the constant porosity model. For the case of the exponential decaying porosity distribution, the numerical results lead to a correlation incorporating conductivity ratio and interstitial heat transfer coefficient.* [DOI: 10.1115/1.2977544]

*Keywords: analytical solution, porous media, nonthermal equilibrium, variable porosity*

## Introduction

Analysis of fluid flow and heat transfer in a porous medium has been a subject of continuous interest for the past decades because of the wide range of engineering applications such as heat exchangers, energy storage units, drying technology, and geothermal systems.

There is abundance of literature on heat transfer analysis in porous media under thermal equilibrium condition. Although the local thermal equilibrium assumption may be sufficiently accurate in many industrial applications, this assumption breaks down when a substantial temperature difference exists between the solid and the fluid phases.

The nonequilibrium two-energy equation model for conduction and convection is proposed by Nakayama et al. [1] in which the two-energy equations for the individual phases at constant porosity are combined together and solved analytically. Amiri and Vafai [2] employed a general fluid flow model and two-phase energy equations to investigate the forced convection heat transfer within a channel with constant wall temperature. Nield et al. [3] also treated the effect of local thermal nonequilibrium on thermally developing forced convection in a porous medium for various values of the fluid-solid conductivity ratio.

Marafie and Vafai [4] investigated forced convection in a porous medium using the Darcy–Forchheimer–Brinkman model under the nonthermal equilibrium assumption.

Various boundary conditions modeling of wall heat flux in the absence of local thermal equilibrium conditions was analyzed by Alazmi and Vafai [5]. Various effects such as variable porosity and solid-to-fluid conductivity ratio were investigated. Viscous dissipation effects of forced convection heat transfer in porous media using a thermal nonequilibrium model wave investigated by Jiang and Ren [6]. In that paper the boundary condition assumptions were analyzed using a numerical model. The results from Minkowycza et al. [7] confirm that local thermal equilibrium in a fluidized bed depends on the size of the layer, mean pore size, and interstitial heat transfer coefficient.

In the present paper an analytical solution is obtained for thermal nonequilibrium energy equations including the variable porosity model in the conduction heat transfer limit with internal heat generation. We concentrate on the case of a parallel plate channel with uniform temperature at the boundary walls. The two-energy equation model is also used to represent the effect of conductivity ratio and porosity distribution on the fluid and solid phases. By comparing the results for the constant and variable porosity model in the conduction regime, it is shown that the variable porosity model can greatly affect the temperature of each phase.

## Model Development

Consider a channel filled with porous medium and bounded by two parallel flat plates maintained at constant temperature $T_w$. The distance between two plates is assumed to be $2H$.

Using a steady-state and one dimensional heat conduction, the energy equations of the solid and fluid phases are, respectively, as follows [8].

$$K_f \nabla \cdot (\varepsilon \nabla T_f) + h(T_s - T_f) = 0 \tag{1}$$

$$K_s \nabla \cdot ((1-\varepsilon) \nabla T_s) - h(T_s - T_f) + (1-\varepsilon) q_s''' = 0 \tag{2}$$

where $q_s'''$ is the heat generation per unit solid volume, which takes place within the solid phase. The second terms in energy equations represent the coupled heat transfer between the two phases because of the existing temperature difference. Assuming a high thermal conductivity at the boundary, the temperature of the solid and fluid at the wall interface will be the same, and

$$T_s(x, y = H) = T_f(x, y = H) = T_w \tag{3}$$

The symmetry condition at the centerline will be

$$\frac{dT_f}{dy}(x, y = 0) = \frac{dT_s}{dy}(x, y = 0) = 0 \tag{4}$$

The governing equations (Eqs. (1) and (2)) can be nondimensionalized as

$$\frac{d}{dy^*}\left(\varepsilon \frac{\partial}{\partial y^*}\theta_f\right) + (A)(\theta_s - \theta_f) = 0 \tag{5}$$

$$\frac{d}{dy^*}\left((1-\varepsilon)\frac{d}{dy^*}\theta_s\right) - (A)(k)(\theta_s - \theta_f) + (1-\varepsilon)Ak = 0 \tag{6}$$

We introduce the following dimensionless parameters:

$$\theta = \frac{(T - T_w)}{\dfrac{q_s''}{h}}, \quad Y^* = \frac{y}{H}, \quad A = \frac{hH^2}{k_f}, \quad k = \frac{k_f}{k_s} \tag{7}$$

After some mathematical manipulations, the governing equations yield

Contributed by the Heat Transfer Division of ASME for publication in the JOURNAL OF HEAT TRANSFER. Manuscript received December 27, 2007; final manuscript received June 18, 2008; published online October 20, 2008. Review conducted by Jamal Seyed-Yagoobi.

$$\frac{d^3}{dy^{*3}}(\Gamma_f) - \frac{\frac{d}{dy^*}(\varepsilon)}{1-\varepsilon}\frac{d^2}{dy^{*2}}(\Gamma_f) - \frac{A}{\varepsilon}\left(1+\frac{\varepsilon}{1-\varepsilon}k\right)\frac{d}{dy^*}(\Gamma_f) + A\frac{d}{dy^*}(\varepsilon)\frac{1}{(1-\varepsilon)\varepsilon^2}\Gamma_f = A^2k \tag{8}$$

where $\Gamma_f = \varepsilon(d/dy^*)(\theta_f)$.

If we neglect the effects of porosity variation in the above equation, it will be simplified to Eq. (8) in Ref. [1], without considering the effects of tortuosity parameter.

Following a similar procedure for solid phase yields

$$\frac{d^3}{dy^{*3}}(\Gamma_s) + \frac{\frac{d}{dy^*}(\varepsilon)}{\varepsilon}\frac{d^2}{dy^{*2}}(\Gamma_s) - \frac{A}{\varepsilon}\left(1+\frac{\varepsilon}{1-\varepsilon}k\right)\frac{d}{dy^*}(\Gamma_s) - Ak\frac{d}{dy^*}(\varepsilon)\frac{1}{(1-\varepsilon)^2\varepsilon}\Gamma_s = A^2k\frac{1-\varepsilon}{\varepsilon} + Ak\left[\frac{1}{\varepsilon}\left(\frac{d}{dy^*}(\varepsilon)\right)^2 + \frac{d^2}{dy^{*2}}(\varepsilon)\right] \tag{9}$$

where $\Gamma_s = (1-\varepsilon)d/dy^*(\theta_s)$.

Transforming the mentioned boundary conditions, Eqs. (3) and (4), in terms of the previously defined parameter $\Gamma$ yields the following: at $y^*=1$,

$$\frac{d}{dy^*}\Gamma_f = 0, \quad \frac{d}{dy^*}\Gamma_s = -(1-\varepsilon)Ak \tag{10}$$

at $y^*=0$,

$$\frac{d^2}{dy^{*2}}(\Gamma_f) = 0, \quad \frac{d^2}{dy^{*2}}(\Gamma_s) = Ak\frac{d}{dy^*}(\varepsilon) \tag{11}$$

at $y^*=0$,

$$\Gamma_f = \Gamma_s = 0 \tag{12}$$

## Constant Porosity Solution

For constant porosity Eqs. (8) and (9) reduce to

$$\frac{d^4}{dy^{*4}}(\theta_f) - \frac{A}{\varepsilon}\left(1+\frac{\varepsilon}{1-\varepsilon}k\right)\frac{d^2}{dy^{*2}}(\theta_f) = A^2k/\varepsilon \tag{13}$$

and

$$\frac{d^4}{dy^{*4}}(\theta_s) - \frac{A}{\varepsilon}\left(1+\frac{\varepsilon}{1-\varepsilon}k\right)\frac{d^2}{dy^{*2}}(\theta_s) = A^2k/\varepsilon \tag{14}$$

The appropriate boundary conditions are

$$\frac{d\theta_f}{dY^*}(X^*,0) = 0, \quad \frac{d^3\theta_f}{dY^{*3}}(X^*,0) = 0$$
$$\theta_f(X^*,1) = 0, \quad \frac{d^2\theta_f}{dY^{*2}}(X^*,1) = 0 \tag{15}$$

$$\frac{d\theta_s}{dY^*}(X^*,0) = 0, \quad \frac{d^3\theta_s}{dY^{*3}}(X^*,0) = 0$$
$$\theta_s(X^*,1) = 0, \quad \frac{d^2\theta_s}{dY^{*2}}(X^*,1) = Ak \tag{16}$$

The above fourth order ordinary differential equation (ODE) has a closed-form analytical solution as

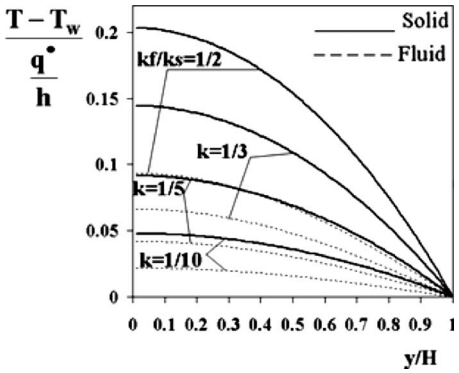


**Fig. 1 Nondimensional temperature distribution in a porous channel with constant porosity ($\varepsilon=0.5$) at different conductivity ratios between solid and fluid for $A=1$**

$$\theta_f = \frac{\varepsilon K_f}{\sigma^2 K_s}\left(\frac{\cosh(A'Y^*)}{\cosh(A')} - 1\right) + \frac{K_f}{2\sigma K_s}\left(\frac{H^2}{\frac{K_f}{h}}\right)(1-Y^{*2}) \tag{17}$$

Similarly the solution for the solid temperature would become

$$\theta_s = \frac{\varepsilon}{\sigma^2}(\sigma-1)\left(\frac{K_f}{K_s}\right)\left(1-\frac{\cosh(A'Y^*)}{\cosh(A')}\right) + \frac{K_f}{2\sigma K_s}\left(\frac{H^2}{\frac{K_f}{h}}\right)(1-Y^{*2}) \tag{18}$$

where

$$A' = H\sqrt{\frac{\sigma h}{\varepsilon K_f}}, \quad \sigma = \frac{(1-\varepsilon)K_s + \varepsilon K_f}{(1-\varepsilon)K_s} = 1 + \frac{\varepsilon}{1-\varepsilon}k \tag{19}$$

## Variable Porosity Solution

For the variable porosity channel, many authors [9–12] have suggested an exponential expression for porosity variation from the impermeable wall to the freestream as

$$\varepsilon = \varepsilon_\infty[1 + a\exp(-by^*H/d_P)] \tag{20}$$

where $a$ and $b$ are empirical constants, $d_p$ is the particle diameter, and $\varepsilon_\infty$ is the freestream porosity. In this paper the empirical coefficients are chosen: $a=1.7$ and $b=6$ [10]. The above mentioned porosity function is a suitable expression for the case of spherical beds [13,8].

Assuming such a porosity function, the governing ordinary differential equations for temperature fields must be solved numerically as closed-form solution does not exist to the best knowledge of the authors.

Equations (8) and (9) are the general ODE forms of the energy equation in the conduction regime in a porous channel.

## Results and Discussion

The effects of variation in the conductivity ratio ($k_f/k_s$) on the fluid and solid phases are shown in Fig. 1. Results presented in this figure refer to the analytical solution with constant porosity ($\varepsilon=0.5$ and $A=1$). By increasing the fluid to solid conductivity ratio, the temperature values for both solid and fluid phases increase substantially. Results show that the temperature differences between solid and fluid increase as the conductivity ratio increases. On the other hand, the assumption of local thermal equilibrium breaks down in the case of high conductivity ratio ($k_f/k_s$). For a given $A$, results show that increasing $k_f/k_s$ would cause a greater deviation from the thermal equilibrium. It is also important that the maximum temperature differences occur in the channel center. The temperature differences obtained from the constant

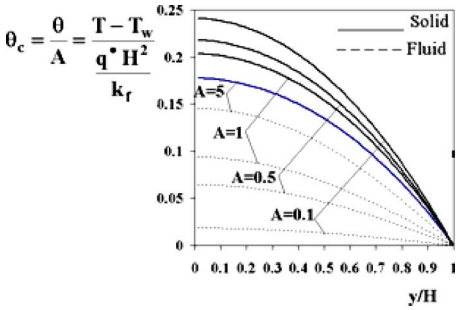


**Fig. 2 Nondimensional temperature distribution in a porous channel with constant porosity ($\varepsilon=0.5$) at different values of $A$ for $k=1/2$**

porosity are shown in Fig. 2 for both solid and fluid phases for the case of $k=1/2$ and $\varepsilon=0.5$ taking $A$ as the varying parameter. As expected, increasing the coefficient $A$ will result in a decrease in the temperature difference between solid and fluid. This increase may be due to a large interstitial heat transfer between solid and fluid phases. In the case of a very small value for coefficient $A$, the temperature differences can be calculated from

$$\left(\frac{\Delta\theta}{A}\right)_{A\to 0} = \frac{k}{2}(1 - y^{*2}) \tag{21}$$

which is identical in form to the one dimensional steady-state heat conduction solution in a heat generating slab. The maximum temperature differences between two phases and the limit curve for coefficient $A$ as it approaches zero are shown in Fig. 3. It is clear that the thermal nonequilibrium assumption is a suitable hypothesis when $A$ approaches zero.

The maximum temperature for each phase is shown in Fig. 4 with respect to the porosity. It is interesting to notice that as the porosity increases, the temperature difference between solid and fluid approaches a maximum value in a specific porosity value.

Temperature distributions in a porous channel with variable porosity at different values of $k_f/k_s$ are shown in Fig. 5 for the case of $A=1$ and $\varepsilon=0.37$. By raising the fluid to solid conductivity ratio, the temperature values for solid and fluid phases increase substantially. The figure clearly shows that heat generated in the solid phase is transferred to the fluid phase, and the local thermal equilibrium assumption may not be valid for the case of a large conductivity ratio $(k_f/k_s)$ especially near the wall.

For the variable porosity model, the maximum temperatures of each phase are plotted as a function of the inverse of the conductivity ratio for different values of $A$. As shown in Fig. 6, all these results can be correlated with the two functions below:

$$\theta_{S,\max} \times A^{-N} = 0.4656\left(\frac{k_s}{k_f}\right)^{-0.7472} \tag{22a}$$

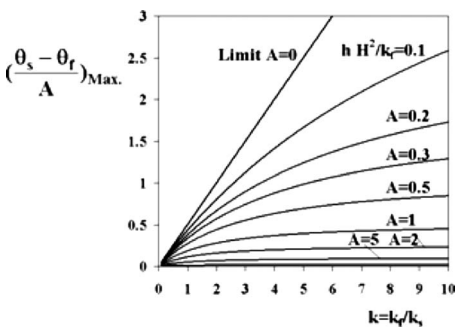


**Fig. 3 Maximum temperature difference in a porous channel incorporating the limit values ($\varepsilon=0.5$)**

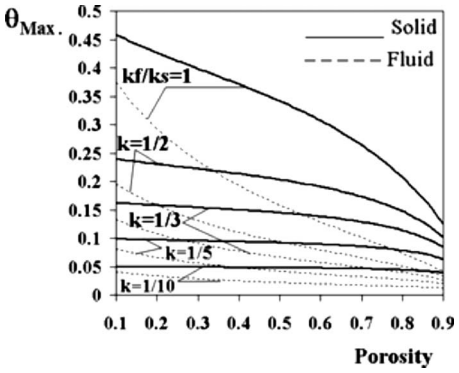


**Fig. 4 Maximum temperature in a porous channel at different porosity and conductivity values ($A=1$)**

$$\theta_{F,\max} \times A^{-N} = 0.3772\left(\frac{k_s}{k_f}\right)^{-0.7462} \tag{22b}$$

As indicated in the previous works in porous media, the conductivity ratio is one of the most important parameters in porous media modeling and has significant effects in temperature distribution and temperature difference between the two phases.

## Conclusion

In this work, conduction heat transfer in a channel filled with a heat generating porous medium was investigated analytically. An analytical representation of the temperature fields was obtained incorporating the effect of conductivity ratio and porosity variation. The temperature difference between fluid and solid phases was found to increase with an increase in conductivity ratio.

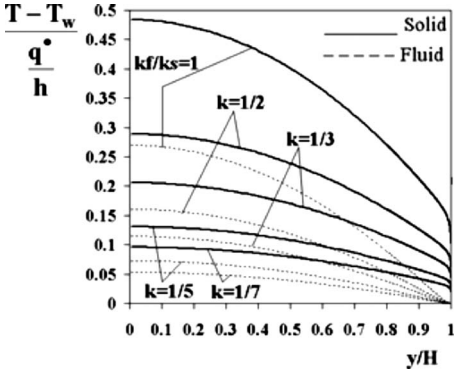


**Fig. 5 Temperature distribution in a porous channel with variable porosity at different values of $k$ for $A=1$**

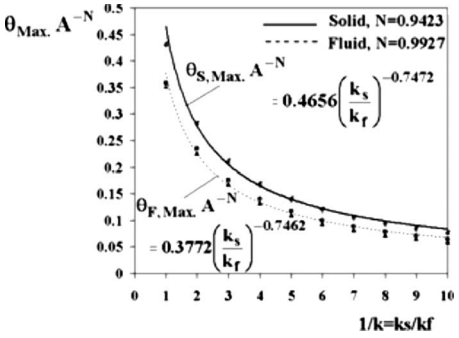


**Fig. 6 Maximum temperature of solid and fluid phases in a porous channel with variable porosity model**

Based on the obtained results one can infer the domain in which the local thermal equilibrium is not valid. Solving the ordinary differential equations for the case of exponential porosity function leads to a correlation for the maximum temperature in the heat generating porous slabs.

## Nomenclature

$C_p$ = specific heat of the fluid (J/kg K)
$h$ = convection heat transfer coefficient at the pore level
$H$ = semi height of the channel (m)
$k_s$ = solid conductivity (W/m K)
$k_f$ = fluid conductivity (W/m K)
$k$ = conductivity ratio
$q'''s$ = internal heat source ($W/m^2$)
$T$ = temperature (K)

### Greek

$\epsilon$ = porosity
$\theta$ = nondimensional temperature ($T-T_w/q'''/h$)

### Subscripts

$f$ = fluid
$s$ = solid
$w$ = impermeable wall

## References


[1] Nakayama, A., Kuwahara, F., Sugiyama, M., and Xu, G., 2001, "A Two-Energy Equation Model for Conduction and Convection in Porous Media," Int. J. Heat Mass Transfer, **44**, pp. 4375–4379.

[2] Amiri, A., and Vafai, K., 1994, "Analysis of Dispersion Effects and Non-Thermal Equilibrium, Non-Darcian, Variable Porosity Incompressible Flow Through Porous Media," Int. J. Heat Mass Transfer, **37**, pp. 939–954.

[3] Nield, D. A., Kuznetsov, A. V., and Xiong, M., 2002, "Effect of Local Thermal Non-Equilibrium on Thermally Developing Forced Convection in a Porous Medium," Int. J. Heat Mass Transfer, **45**, pp. 4949–4955.

[4] Marafie, A., and Vafai, K., 2001, "Analysis of Non-Darcian Effects on Temperature Difference in Porous Media," Int. J. Heat Mass Transfer, **44**, pp. 4401–4411.

[5] Alazmi, B., and Vafai, K., 2002, "Constant Wall Heat Flux Boundary Conditions in Porous Media Under Local Thermal Non-Equilibrium Conditions," Int. J. Heat Mass Transfer, **45**, pp. 3071–3087.

[6] Jiang, P.-X., and Ren, Z.-P., 2001, "Numerical Investigation of Forced Convection Heat Transfer in Porous Media Using a Thermal Non-Equilibrium Model," Int. J. Heat Fluid Flow, **22**, pp. 102–110.

[7] Minkowycza, W. J., Haji-Sheikh, A., and Vafai, K., 1999, "On Departure From Local Thermal Equilibrium in Porous Media Due to a Rapidly Changing Heat Source: The Sparrow Number," Int. J. Heat Mass Transfer, **42**, pp. 3373–3385.

[8] Nield, D. A., and Bejan, A., 1998, *Convection in Porous Media*, 2nd ed., Springer, Berlin.

[9] David, E., Lauriat, G., and Cheng, P., 1991, "A Numerical Solution of Variable Porosity Effects on Natural Convection in a Packed-Sphere Cavity," ASME J. Heat Transfer, **113**, pp. 391–399.

[10] Poulikakos, D., and Renken, K., 1987, "Forced Convection in a Channel Filled With Porous Medium Including the Effects of Flow Inertia, Variable Porosity and Brinkman Friction," ASME J. Heat Transfer, **109**, pp. 880–888.

[11] Renken, K. J., and Poulikakos, D., 1988, "Experiment and Analysis of Forced Convective Heat Transport in a Packed Bed of Spheres," Int. J. Heat Mass Transfer, **31**, pp. 1399–1408.

[12] Amiri, A., and Vafai, K., 1998, "Transient Analysis of Incompressible Flow Through a Packed Bed," Int. J. Heat Mass Transfer, **41**, pp. 4259–4279.

[13] Kaviany, M., 1995, *Principle of Heat Transfer in Porous Media*, 2nd ed., Springer, Berlin.

# The Efficient Iterative Solution of the $P_1$ Equation

**P. Hassanzadeh**

**G. D. Raithby**[1]
e-mail: graith@mecheng1.uwaterloo.ca

Department of Mechanical and Mechatronics Engineering,
University of Waterloo,
Waterloo, ON, N2L 3G1, Canada

*The $P_1$ model is often used to obtain approximate solutions of the radiative transfer equation for heat transfer in a participating medium. For large problems, the algebraic equations used to obtain the $P_1$ solution are solved by iteration, and the convergence rate can be very slow. This paper compares the performance of the corrective acceleration scheme of and Li and Modest (2002, "A Method to Accelerate Convergence and to Preserve Radiative Energy Balance in Solving the $P_1$ Equation by Iterative Methods," ASME J. Heat Transfer, **124**, pp. 580–582), and the additive correction multigrid method, to that of the Gauss–Seidel solver alone. Additive correction multigrid is found to outperform the other solvers. Hence, multigrid is a superior solver for the $P_1$ equation.*
[DOI: 10.1115/1.2993546]

*Keywords: $P_1$ model, efficient iterative solver, additive correction multigrid solver, acceleration*

## 1 Introduction

The $P_1$ model approximates the radiative transfer equation (RTE), an integrodifferential equation describing thermal radiation, by a simple differential equation. This model represents intensity by the leading term of a spherical harmonics expansion [1] but can be more easily derived directly from the RTE [2–4]. The $P_1$ model is widely used, for example, as an option in the FLUENT [5] and CFX [6] commercial codes, because radiation is computed from a single equation. This is simple to implement and allows radiation and thermal energy to be solved as a coupled set of equations. The disadvantages of the $P_1$ model are loss of accuracy when the radiation intensity is highly anisotropic and inability to impose nonlinear scattering phase functions.

The $P_1$ equation is elliptic with a boundary condition of the third kind. The solution is usually obtained by application of a discrete method (finite element or finite volume) that replaces the continuous equations by a set of $N$ algebraic equations. For large $N$, the solution of the equations is obtained by application of an iterative solver.

Li and Modest [7] pointed out that the iterative solution of the $P_1$ equations can be very costly, especially for weak medium participation or highly reflective boundaries. They then proposed a method that dramatically reduced the cost. This Technical Brief verifies the Li–Modest results for the two types of radiation problems and also examines the performance of the multigrid solver that is often used in computational fluid dynamics (CFD) codes for the solution of the continuity, momentum, thermal energy, and other equations.

[1]Corresponding author.

Contributed by the Heat Transfer Division of ASME for publication in the JOURNAL OF HEAT TRANSFER. Manuscript received December 3, 2007; final manuscript received July 11, 2008; published online October 22, 2008. Review conducted by Walter W. Yuen.

## 2 Background

**2.1 Conservation of Radiative Energy.** Consider an enclosure containing a gray medium at temperature $T$ with absorption coefficient $\kappa$ and scattering coefficient $\sigma_s$. Conservation of radiative energy requires [1]

$$\nabla \cdot \mathbf{q} = 4\pi\kappa(I_b - I_a) \tag{1}$$

where $\mathbf{q}$ is the radiation heat flux, $I_b = \sigma T^4/\pi$ is the blackbody intensity, and $I_a = \int_{4\pi} I d\omega/4\pi$ is the average intensity. If the walls of the enclosure are diffuse gray with temperature $T_w$ and emissivity $\varepsilon_w$, and if the outward unit normal (from the wall toward the medium) is $\mathbf{n}$, the boundary condition for Eq. (1) is [1]

$$\mathbf{q} \cdot \mathbf{n} = \frac{2\varepsilon_w}{(2-\varepsilon_w)}(\sigma T_w^4 - \pi I_a) \tag{2}$$

where $\sigma$ is the Stefan–Boltzmann constant.

**2.2 $P_1$ Model.** For isotropic scattering, the $P_1$ approximation of the heat flux is [1]

$$\mathbf{q} = -\frac{4\pi}{3\beta}\nabla I_a \tag{3}$$

where $\beta = \kappa + \sigma_s$ is the extinction coefficient. Substituting Eq. (3) into Eqs. (1) and (2) gives the $P_1$ model in which the dependent variable is $I_a$. If the extinction coefficient of the medium is uniform, the $P_1$ model is

$$\nabla^2 I_a = 3\beta\kappa(I_a - I_b) \tag{4}$$

with boundary condition

$$\nabla I_a \cdot \mathbf{n} = \frac{3\beta\varepsilon_w}{2\pi(2-\varepsilon_w)}(\pi I_a - \sigma T_w^4) \tag{5}$$

## 3 Numerical Solution

**3.1 Algebraic Equation.** In the present study, a square computational domain was first subdivided into Cartesian elements. A vertex-centered finite volume method was then applied, with bilinear shape functions within the element, to replace Eqs. (4) and (5) by a set of $N$ algebraic equations. The algebraic equation for $I_a$ at node $P$, with neighbor nodes $nb$, has the form

$$a_P I_{a,P} + \sum_{nb} a_{nb} I_{a,nb} = b_P \tag{6}$$

At an interior node $a_P = -\Sigma_{nb} a_{nb} + 3\beta\kappa V_P$ and $b_P = 3\beta\kappa V_P I_{b,P}$, where $V_P$ is the volume associated with node $P$. At the boundary nodes, $a_P = -\Sigma_{nb} a_{nb} + 3\beta\kappa V_P + 1.5\beta A_{B,P}\varepsilon_w/(2-\varepsilon_w)$ and $b_P = 3\beta\kappa V_P I_{b,P} + 1.5\beta(\sigma T_w^4/\pi) A_{B,P}\varepsilon_w/(2-\varepsilon_w)$, where $A_{B,P}$ is the area of that part of the control volume $P$, which lies on the boundary surface.

**3.2 Iterative Solution.** After iteration $m$ of Eq. (6), the computed intensities are denoted as $I_a^m$, and the residual $R^m$ is defined by

$$R^m = \max\left\{\frac{\left|a_P I_{a,P}^m + \sum_{nb} a_{nb} I_{a,nb}^m - b_P\right|}{a_P \times (\sigma T_h^4/\pi)}\right\}$$

where $T_h$ will be defined later. The initial intensities were taken as $I_a^o = 10^{-5}$ W/m$^2$ sr. The iterative solution was continued until $R^m/R^1 \le 10^{-5}$ was achieved.

**3.3 Convergence Rate.** For a given problem, the radiation heat transfer depends on the parameters that appear in Eqs. (4) and (5): $\beta$, $\kappa$, and $\varepsilon_w$. The dependence of the convergence rate of iterative solvers on these parameters can be anticipated by examining the coefficients in the algebraic equations. If the medium temperature is specified and nonzero, then $a_P > \Sigma_{nb}|a_{nb}|$ for all

  

**Table 1 Convergence and cost of the $P_1$ solution for an emitting-absorbing medium with specified temperature**

| | | GS | | GS-CAS | | ACM | |
|---|---|---|---|---|---|---|---|
| $\tau$ | $\varepsilon_w$ | it | WU | it | WU | it | WU |
| 0.01 | 1 | 127299 | 1264.2 | 518 | 5.3 | 90 | 0.7 |
| 0.1 | 1 | 12409 | 126.1 | 333 | 3.4 | 84 | 0.7 |
| | 0.1 | 2311 | 23.0 | 245 | 2.5 | 82 | 0.6 |
| 1 | 0.5 | 1568 | 15.6 | 215 | 2.2 | 68 | 0.5 |
| | 1 | 977 | 9.8 | 172 | 1.8 | 61 | 0.5 |
| 10 | 1 | 28 | 0.3 | 21 | 0.2 | 15 | 0.1 |

**Table 2 Convergence and cost of the $P_1$ solution for an emitting-absorbing medium in radiative equilibrium**

| | | GS | | GS-CAS | | ACM | |
|---|---|---|---|---|---|---|---|
| $\tau$ | $\varepsilon_w$ | it | WU | it | WU | it | **WU** |
| 0.01 | 1 | 110875 | 1098.8 | 1089 | 11.0 | 120 | 1.0 |
| 0.1 | 1 | 11266 | 112.2 | 864 | 8.7 | 111 | 0.9 |
| | 0.1 | 21227 | 211.2 | 943 | 9.5 | 115 | 1.0 |
| 1 | 0.5 | 3526 | 35.1 | 665 | 6.7 | 94 | 0.8 |
| | 1 | 1337 | 13.3 | 451 | 4.6 | 71 | 0.6 |
| 10 | 1 | 407 | 4.1 | 240 | 2.4 | 47 | 0.4 |

interior equations, and the strength of the inequality increases with $\beta\kappa$. The equation for $I_a$ at boundary nodes is also diagonally dominant for $\beta\varepsilon_w \neq 0$, with the strength increasing with $\beta\varepsilon_w$. Convergence is therefore guaranteed for a Gauss–Seidel (GS) or Jacobi solver, with the rate increasing with $\kappa$, $\beta$, and $\varepsilon_w$.

For radiative equilibrium $I_b = I_a$, the right side of Eq. (4) is zero; therefore, $a_P = \Sigma_{nb}|a_{nb}|$ at interior nodes and the equations are weakly diagonally dominant. As a result, convergence will be slower than for a specified temperature medium, for the same values of $\beta$ and $\varepsilon_w$.

In both cases, for $\beta \to 0$, Eqs. (4) and (5) are satisfied by any constant value of $I_a$, so the algebraic equation set becomes singular. In radiative equilibrium, this also occurs for any $\beta$ if $\varepsilon_w \to 0$.

It is therefore expected that the convergence rate of any iterative solver will diminish with decreasing $\beta$ and $\varepsilon_w$. The convergence rate for radiative equilibrium should also be slower than when the medium temperature is specified for given positive values of $\beta$, $\kappa$, and $\varepsilon_w$, especially if $\beta\kappa$ is large.

**3.4 Iterative Solvers Tested.** Equation (6) has been solved in this study using three iterative solvers: GS, GS with the corrective acceleration scheme (GS-CAS) of Li and Modest [7], and GS with the additive correction multigrid (ACM) method of Hutchinson and Raithby [8]. In the GS-CAS, $I_a$ at every node is corrected after each iteration by a factor $f$ that is calculated to restore the radiative energy balance over the entire domain. This procedure has been recently employed in parallelization of the $P_1$ model by Krishnamoorthy et al. [9]. In the ACM method, a V-cycle was used with one GS smoother for each restriction and prolongation, and with $2 \times 2$ agglomeration of control volumes until the coarsest grid had just one control volume. In the GS and GS-CAS solvers, for the 2D Cartesian grid, one GS iteration updates the solution of Eq. (6) by sweeping the grid in all eight distinct patterns. In the ACM solver, one GS iteration updates the solution of Eq. (6) by sweeping the grid in only one direction, from the bottom-left corner to the top-right one.

The computational time to satisfy the convergence criterion is reported in work unit (WU) in order to make the results less sensitive to computer speed and to the size of the computational grid. One WU is defined as the time to do 100 GS (with eight patterns) iterations for a given grid, $\beta$, $\kappa$, and $\varepsilon_w$.

## 4 Results

The results for two problems are reported. In both cases, the 2D computational domain has dimensions $L \times L$. A grid of $63 \times 63$ elements of equal size is used, giving a total of 4096 nodes. The results are reported for a range of $\tau = \kappa L$ and surface emissivity $\varepsilon_w$.

**4.1 Specified Temperature.** As a parallel to the problem solved by Li and Modest [7], the temperature of the medium is given as $T(x,y) = T_h \times (x/L)(1-x/L)(y/L)(1-y/L)$ where $T_h = 1000$ K. The number of iterations (it) and the number of WUs are presented in Table 1 for a wide range of conditions. These results confirm that the convergence rate of all solvers diminishes as $\tau$ and $\varepsilon_w$ are decreased. It also confirms that the GS-CAS method of Li and Modest [7] dramatically reduces the solution time compared with GS alone. The ACM has even better performance, reducing the solution time further by factors of between 2 and 7.

**4.2 Radiative Equilibrium.** For the same enclosure, the side and top walls are taken as cold $T_c = 0$ K, the bottom wall is heated to $T_h = 100$ K, and the medium temperature is established by radiative equilibrium. Table 2 summarizes the results for a range of

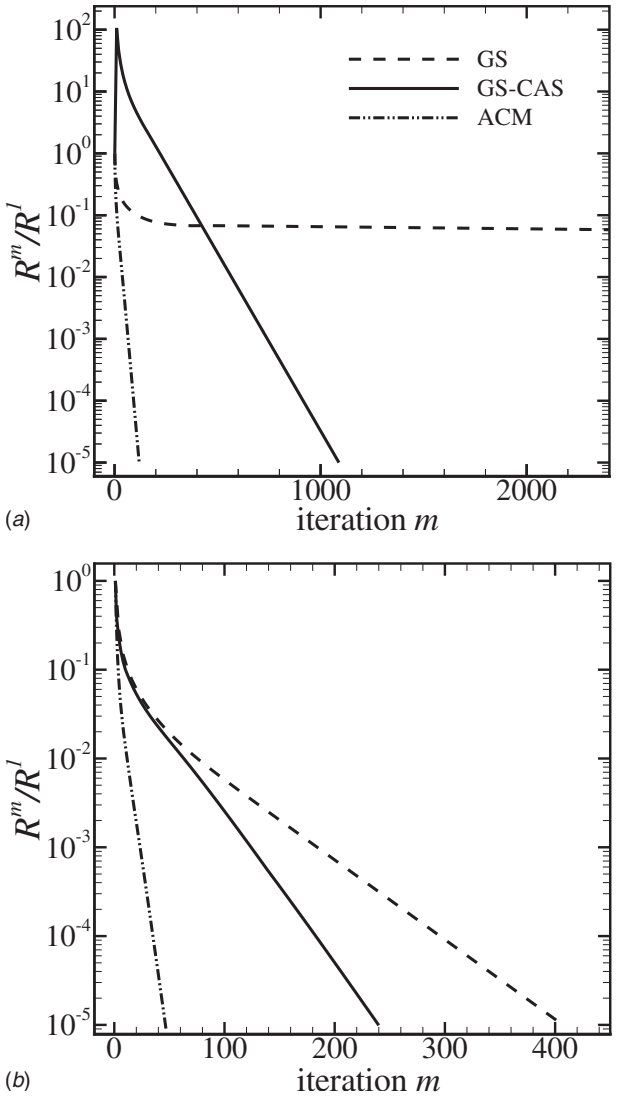


**Fig. 1 Maximum scaled residuals versus iterations for (*a*) $\tau = 0.01$ and (*b*) $\tau = 10$**

$\tau$ and $\varepsilon_w$. These results show the expected trends: solution times for the large $\tau$ values are much larger than when the medium temperature was specified and increase with a decrease of $\tau$ and $\varepsilon_w$. As before, the GS-CAS solver of Li and Modest [7] substantially decreases the time to achieve convergence compared with GS alone, and the ACM method again performs better than GS-CAS, reducing the solution time by about a further order of magnitude.

The rate of residual reduction with iterations for these three solvers is shown in Fig. 1 for black walls for $\tau=0.01$ (Fig. 1($a$)) and $\tau=10$ (Fig. 1($b$)). The rapid initial residual reduction with GS indicates that the high frequency components of the residual are quickly removed, but the solver stalls in the removal of the low frequency components [8]. As a result of this failure, GS needs more than $10^5$ iterations to converge for $\tau=0.01$, in which the equation set has a weak diagonal dominance. For $\tau=0.01$, the GS-CAS initially increases the residual but then decreases it fairly quickly. In all cases studied, the ACM method monotonically and rapidly reduces the residual. Monotonicity is important because a CFD code solving multiprocess problems reduces the residual of the linearized equations by only an order of magnitude or less before updating coefficients. To reduce the residuals by 1/10 in Fig. 1($a$) requires 2.2 WU for GS-CAS and 0.1 WU for ACM.

## 5 Conclusions

The $P_1$ equations for the prediction of radiation heat transfer in a participating medium can be difficult to solve by iteration. The conditions for slow convergence, expected from the coefficients of the algebraic equations, are confirmed in two problems. The corrective acceleration scheme of Li and Modest [7] applied with Gauss–Seidel performs much better than Gauss–Seidel alone. The additive correction multigrid solver is better still and has the added important property that the residuals are monotonically reduced. It is also convenient that the multigrid solver works well for the $P_1$ equation because it is usually available and used to solve the other governing equations in the CFD codes.

## Acknowledgment

This work was financially supported by the Climate Change Technology and Innovation Initiative (CCTII) through CANMET Energy Technology Centre, Natural Resources Canada, of the Canadian Federal Government, and through an Operating Grant to the second author from the Natural Sciences and Engineering Council of Canada. The authors also gratefully acknowledge the contributions of Dr. E. H. Chui and Professor G. D. Stubley.

## References

[1] Modest, M. F., 2003, *Radiative Heat Transfer*, Academic, New York.
[2] Hassanzadeh, P., Raithby, G. D., and Chui, E. H., 2008, "The Efficient Calculation of Radiation Heat Transfer in the Participating Media," J. Thermophys. Heat Transfer, **22**, pp. 129–139.
[3] Hassanzadeh, P., Raithby, G. D., and Chui, E. H., 2008, "The Efficient Computation of Radiation Heat Transfer in the Participating Media," presented at the 40th AIAA Thermophysics Conference, Seattle, WA, June 23–26, Paper No. 2008-4244.
[4] Hassanzadeh, P., 2007, "An Efficient Computational Method for Thermal Radiation in Participating Media," M.S. thesis, University of Waterloo, Waterloo, Ontario, Canada, Available from http://hdl.handle.net/10012/3135.
[5] FLUENT 5 User's Guide, 1998, Version 5.
[6] ANSYS-CFX Solver, Release 10: Theory.
[7] Li, G., and Modest, M. F., 2002, "A Method to Accelerate Convergence and to Preserve Radiative Energy Balance in Solving the $P_1$ Equation by Iterative Methods," ASME J. Heat Transfer, **124**, pp. 580–582.
[8] Hutchinson, B. R., and Raithby, G. D., 1986, "A Multigrid Method Based on the Additive Correction Strategy," Numer. Heat Transfer, **9**, pp. 511–537.
[9] Krishnamoorthy, G., Rawat, R., and Smith, P. J., 2006, "Parallelization of the $P_1$ Radiation Model," Numer. Heat Transfer, **49**, pp. 1–17.